Fabrication of Solid Dispersion Based Patches Using Hot Melt Injection Moulding and Fused Deposition Modelling 3D Printing

Muqdad Athab Muosa Alhijjaj

B.Sc. Pharmacy; M.Sc. Pharmaceutics

Thesis submitted to the School of Pharmacy, University of East Anglia in fulfilment of the requirement for the degree of Doctor of Philosophy

March 2017

© This copy of the thesis has been supplied on condition that anyone who consults it is understood to recognise that its copyright rests with the author and that use of any information derived there from must be in accordance with current UK copyright Law. In addition, any quotation or extract must include full attribution

Acknowledgments

My PhD study at the School of Pharmacy/University of East Anglia was a very special period of my life where experience and achievements are sometimes mixed with challenges and difficulties. Progressing at the different stages of this fruitful work was not reachable without the help and support of a number of people whom I would like to take the opportunity to express my deepest thanks.

I am eternally grateful to my supervisors Dr Sheng Qi and Professor Peter Belton for their guidance, vast knowledge, support and encouragement in all stages of my PhD. It is a real privilege and honour to study under their supervision. I am sincerely thankful to Professor Mike Reading (Cyversa, Norwich, UK) for offering the chance to work on TASC and for his scientific advice. Many thanks for Dr Nikolaus Wellner (Institute of Food Research (IFR), Norwich, UK) for providing the access to use the texture analyser and for helping with the IR imaging. I would like to extend my thanks to Dr Jacob Bouman (Wageningen University, The Netherlands), Dr Axel Zeitler and Dr Samy Yassin (University of Cambridge, UK), Dr Rudy Lapeer and Mr Zelimkhan Gerikhanov (University of East Anglia/School of Computing, Norwich, UK) and Mr Nick Corps from Bruker for their help with XμCT analysis.

I am sincerely thankful to the Higher Committee of Education Development (HCED) and University of Basrah in Iraq for their generous financial support. Many thanks for Linkam Scientific Instruments for providing the temperature controlled microscopy system used in this project and Mr Michael Morton for installing the TASC software.

Many thanks to the academic staff members of the Drug Delivery Department in the UEA School of Pharmacy for their continuous help and support. Special thanks to Dr Pratchaya Tipduangta, Dr Khaled Takieddin, Dr Esra'a Albarahmieh, Dr Doroty Codoni, Dr Claudia Pigliacelli, Dr Ziyi Yang and Miss Susana Campos E Menezes, Mr Bertrand Leze, Mr Peter Mayes and Mr Roy Carter for their help during my PhD study.

Deep thanks to Assistant Professor Ali Mohammed Hadi, Mr Aws Al-Saffar, Mr Sameer Talib, Assistant Professor Falah Hassan, Dr Mohammed Sattar Al-Hititawi, Professor Mohamad Alhajaj, Mrs Saham Al-Jawahiri, Professor Shaker Al-Jadaan, Assistant Professor Abdulelah Al-Mayah, Assistant Professor Ausama Yacob, Mr KaramAllah Shaker, Mr Muayyad Al-Shinnayin, and all other academic staff members of the College of Pharmacy/University of Basrah for their help and support during the early stages of my PhD.

I would like also to express my grateful thanks and love to my parents, brothers, sisters, lovely wife ‘Ibtisam’, daughters ‘Halah and Massara’ and son ‘Mohammed’ for their support and love.

Last but not least, I would like to extend my thanks to all other people in Iraq and the UK who helped me to make this work possible.

Muqdad Alhijjaj

Abstract

The poor aqueous solubility of many APIs, such as felodipine, are significant dissolution rate limiting factors that often lead to poor oral systemic bioavailability. Solid dispersions have been used as a formulation approach to improve drugs dissolution properties. Most of the reported solid dispersion formulations in the literature are binary mixtures with limited functionalities (with enhancing dissolution being the primary function). The aim of this study is to design, characterise and evaluate complex solid dispersions with intentionally designed microstructures (in the form of phase separations). The potential functionalities of these microstructures were explored by this project. In our view, the complex formulations are more representative of real pharmaceutical products in their final forms.

HME-IM is a single processing technique for fabricating formulations with high geometric precision in a rapid, efficient and environmentally friendly way. It was used as the main processing method to produce the solid dispersion based buccal patches in this project. The patches were thoroughly characterised using conventional techniques including DSC, MTDSC, TGA, DVS, ATR-FTIR, PXRD, SEM, EDS, IR imaging, mucoadhesion and *in vitro* dissolution testing. In order to address the spatial distribution of the phase separations, two non-conventional characterisation methods, thermal analysis by structural characterisation and X-ray micro-computed tomography, were introduced to provide novel insights into the heterogeneity and phase distribution of these formulations. The results revealed that HME-IM patches with 10% drug loading were unsaturated while those with 20-30% w/w drug concentration were saturated or even supersaturated. HME-IM patches containing TPGS were more solubilising to felodipine and more stable compared to Tween 80 containing systems. Thermal analysis by structural characterisation provided rapid detection of heterogeneity and the thermal dissolution of crystalline drug fraction while XμCT provided microscale spatial distribution of different phases. Having shown the advantages of using polymeric blends to formulate solid dispersions that were demonstrated by the felodipine buccal patches, we further explored the use of polymer blends for improving the FDM 3D printability of pharmaceutical solid dosage forms with the potential applications in personalised medicine.

This project demonstrated the potential and formulation principles of using HME-IM and FDM 3D printing as formulation methods for production of polymer blend based complex solid dispersions for the purposes of enhanced bioavailability of poorly soluble drugs and providing personalised medicines.

Table of Contents

Table of Contents v
List of Abbreviations xiii
List of Figures xvii
List of Tables xxx
1. Chapter 1. Introduction 1
1.1 The mystery of poor water solubility of active pharmaceuticals 2
1.2 Solid dispersions 4
1.2.1 Classification of solid dispersions according to the physical state of the drug and the carrier 6
1.2.1.1 Eutectic mixtures 7
1.2.1.2 Solid solutions 8
1.2.1.3 Glass solutions and suspensions 10
1.2.1.4 Amorphous precipitations in crystalline carrier 12
1.2.1.5 Compound or complex formation 12
1.2.1.6 Combination solid dispersions 13
1.3 Drug-polymer miscibility predictions for solid dispersion development 13
1.3.1 Solubility parameter approach 14
1.3.2 Melting point depression approach 16
1.4 Thermodynamics of solid dispersions 19
1.4.1 Physical stability of solid dispersions 19
1.4.1.1 Glass transition (T_g) 19
1.4.1.2 Molecular mobility 21
1.4.2 Factors affecting physical stability of solid dispersions 22
1.4.3 Phase separation 23
1.4.4 Approaches developed to improve physical stability of solid dispersions 24
1.4.5 Other drawbacks of solid dispersions 26
1.4.5.1 Impacts of thermal degradation 27
1.4.5.2 Impacts of residual solvents 27
1.4.5.3 Impact of downstream processing 28
1.5 Manufacturing of solid dispersions 29
1.5.1 Hot melt extrusion (HME) 30
1.5.1.1 Types of extruders 31
1.5.1.2 Requirements of successful processing 34
1.5.1.3 Suitable APIs candidates for HME 35
1.5.1.4 Functional excipients used in HME solid dispersions 35

Carriers 36
Release-modifying agents 37
Plasticisers 38
Antioxidants 38
1.5.2 Injection moulding (IM) 39
1.5.2.1 Injection moulding processing 40
1.5.2.2 Scale-up of solid dispersions to manufacturing level 42
1.5.3 Fused deposition modelling (FDM) 3D printing as a new method for fabricating solid dispersions 42
1.5.3.1 FDM 3D printing process 43
1.5.3.2 Pharmaceutical applications of FDM 3D printing technology 44
1.6 Drug delivery through peroral routes 46
1.6.1 Buccal drug delivery 46
1.6.1.1 Physiology of oral cavity 46
Mucus 48
Saliva 50
1.6.2 Drug absorption through buccal route 50
1.6.3 Buccal formulation design 51
1.6.3.1 Matrix tablets 53
1.6.3.2 Buccal patches 53
1.6.4 Mucoadhesive drug delivery systems 54
1.6.5 Mechanisms of mucoadhesion 55
Electronic (electrostatic) theory 56
Adsorption theory 56
Diffusion theory 56
Wetting theory 56
Fracture theory 57
1.7 Objectives of this project 57
2. Chapter 2. Materials and methods 59
2.1 Introduction 60
2.2 Materials 61
2.2.1 Model drug 61
2.2.1.1 Physicochemical and pharmacokinetic properties 61
2.2.2 Excipients 64
2.2.2.1 Polyethylene glycol (PEG) 4000 64
2.2.2.2 Polyethylene oxide (PEO) 68

2.2.2.3 Polysorbate (Tween®) 80 70
2.2.2.4 D-α-tocopheryl polyethylene glycol 1000 succinate (vitamin E TPGS, Kolliphor® TPGS) 71
2.2.2.5 Poly(butyl methacrylate-co-(2-dimethylaminoethyl)methacrylate-co-methyl methacrylate) (Eudragit® E PO) 72
2.2.2.6 Polyvinyl caprolactam-polyvinyl acetate-polyethylene glycol graft copolymer (Soluplus) 74
2.2.2.7 Polyvinyl alcohol (PVA) 75
2.3 Characterisation methods 77
2.3.1 Thermogravimetric analysis (TGA) 77
2.3.2 Differential scanning calorimetry (DSC) and modulated temperature differential scanning calorimetry (MTDSC) 78
2.3.3 Thermal analysis by structural characterisation (TASC) 80
2.3.4 Dynamic vapour sorption (DVS) 83
2.3.5 Polarised-light hot stage microscopy (HSM) 83
2.3.6 Scanning electron microscopy (SEM) 84
2.3.7 Energy dispersive spectroscopy (EDS) 84
2.3.8 Powder X-ray diffraction (PXRD) 85
2.3.9 X-ray micro computed tomography (XμCT) 85
2.3.10 Attenuated total reflectance-Fourier transform infrared (ATR-FTIR) spectroscopy 86
2.3.11 Fourier transform Infrared (FTIR) imaging 88
2.3.12 Laser diffraction (LD) particle size analysis 88
2.4 Evaluation methods 89
2.4.1 In vitro release profiles 89
2.4.2 Determination of drug loading efficiency 90
2.4.3 In vitro mucoadhesion study 90
3 Chapter 3. Characterisation of raw materials 92
3.1 Introduction 93
3.2 Materials and Methods 94
3.2.1 Materials 94
3.2.2 Methods 94
3.2.2.1 Preparation of amorphous felodipine 94
3.2.2.2 Preparation of binary and ternary excipients' extrudates 94
3.2.2.3 Physicochemical characterisation of raw materials 95
3.2.2.3.1 Thermogravimetric analysis (TGA) 95

3.2.2.3.2 Differential scanning calorimetry (DSC) and modulated temperature DSC (MTDSC).. 95
3.2.2.3.3 Dynamic vapour sorption (DVS) 95
3.2.2.3.4 Attenuated total reflectance-Fourier transform infrared spectroscopy (ATR-FTIR)…… 96
3.2.2.3.5 Scanning electron microscopy (SEM) 96
3.2.2.3.6 Powder X-ray diffraction (PXRD) 96
3.2.2.3.7 Solubility measurements 97
3.3 Results 97
3.3.1 Physicochemical characterisation of raw materials 97
3.3.1.1 Felodipine 97
3.3.1.2 PEG 4000 103
3.3.1.3 PEO WSR 1105 (PEO K900) 107
3.3.1.4 Tween 80 111
3.3.1.5 TPGS 114
3.3.1.6 PEO WSR N10 LEO (PEO K100) 118
3.3.1.7 Eudragit E PO 121
3.3.1.8 Soluplus 124
3.3.1.9 Polyvinyl alcohol (PVA) 127
3.3.2 Theoretical calculations of the solubility parameters of the ingredients 130
3.3.3 Experimental estimation of the miscibility of PEG 4000 and PEO K900 using DSC…… 131
3.3.4 Estimation of the miscibility of felodipine and excipients used in HME-IM formulations 136
3.4 Discussion 136
3.5 Conclusion 138
4. Chapter 4. Design, characterisation and evaluation of felodipine loaded HME-IM mucoadhesive buccal patches 139
4.1 Introduction 140
4.2 Materials and Methods 141
4.2.1 Materials 141
4.2.2 Felodipine loaded buccal patches prepared by HME-IM 141
4.2.3 Physicochemical characterisation and evaluation of CM1 and CM2 formulations… 144
4.2.3.1 Differential scanning calorimetry (DSC) and modulated temperature DSC (MTDSC) 144

4.2.3.2 Scanning electron microscopy (SEM) and energy dispersive spectroscopy (EDS)….. 144
4.2.3.3 Powder X-ray diffraction (PXRD) 144
4.2.3.4 Attenuated total reflectance-Fourier transform infrared spectroscopy (ATR-FTIR)……. 145
4.2.3.5 Fourier transform infrared microscopy imaging 145
4.2.3.6 In vitro mucoadhesion study 145
4.2.3.7 In vitro drug release studies 145
4.3 Results 146
4.3.1 Physicochemical characterisation of placebo and felodipine loaded HME-IM buccal patches 146
4.3.1.1 Thermal characterisation of CM1 and CM2 146
CM1 patches 147
CM2 patches 153
4.3.1.2 Comparisons of morphological properties of CM1 and CM2 patches 157
4.3.1.3 PXRD and IR characterisation of CM1 and CM2 patches 161
4.3.1.4 Investigation of heterogeneity HME-IM patches using IR imaging 165
4.3.2 Influence of drug loading and phase separation on mucoadhesion 169
4.3.3 Influence of drug loading and phase separation on the in vitro felodipine release profiles from the HME-IM patches 171
4.4 Discussion 174
4.5 Conclusion 176
5. Chapter 5. Characterisation of heterogeneity and spatial distribution of phases in felodipine HME-IM patches using thermal analysis by structural characterisation and X-ray micro computed tomography 177
5.1 Introduction 178
5.2 Materials and Methods 180
5.2.1 Materials 180
5.2.2 Methods 180
5.2.2.1 Thermal analysis by structural characterisation (TASC) 180
5.2.2.2 Differential scanning calorimetry (DSC) and modulated temperature DSC (MTDSC) 181
5.2.2.3 Variable temperature attenuated total reflectance Fourier transform infrared spectroscopy (VT-ATR-FTIR) 181
5.2.2.4 X-ray micro computed tomography (XμCT) 181
5.3 Results 182

5.3.1 TASC analysis of the phase separation of the HME-IM patches 182
5.3.1.1 Fast detection of heterogeneity in solid dosage forms 182
5.3.1.2 Detection of thermal dissolution of crystalline drug in excipients 192
5.3.1.3 Sensitivity to the presence of metastable form of PEG 194
5.3.1.4 Scanning rate effects on the detection sensitivity 199
5.3.2 XμCT analysis of phase separations in the HME-IM patches 200
5.3.2.1 XμCT analysis of internal microstructure and spatial distribution of phase separations 200
5.3.2.2 XμCT analysis as a potential semi-quantitative method to study crystalline drug content 205
5.3.3 Comparison of heterogeneity assessment by XμCT and TASC 208
5.4 Discussion 209
5.5 Conclusion 211
6. Chapter 6. Effect of surfactants on the physical stability of solid dispersions and felodipine crystallisation 212
6.1 Introduction 213
6.2 Materials and Methods 214
6.2.1 Materials 214
6.2.2 Methods 215
6.2.2.1 Storage conditions for HME-IM patches and amorphous felodipine 215
6.2.3 Characterisation of HME-IM aged solid dispersions 215
6.3 Results 216
6.3.1 Effect of surfactant on the stability of semi-crystalline carrier in placebo patches 216
6.3.2 Effect of drug loading on semi-crystalline carrier 223
6.3.3 Carrier stability of drug loaded patches aged under 0%RH 238
6.3.4 Carrier stability of drug loaded patches under 75%RH 241
6.3.5 Effect of surfactant on crystallisation tendency and crystal growth of felodipine on ageing 241
6.3.6 Characterisation of felodipine recrystallised from its glassy state under stressful conditions of temperature and humidity 253
6.4 Discussion 257
6.5 Conclusions 258
7. Chapter 7. Design, characterisation and evaluation of FDM 3D printed felodipine solid dispersions 259
7.1 Introduction 260

7.2 Materials and Methods 261
7.2.1 Materials 261
7.2.2 Preparation of placebo and felodipine loaded FDM filaments using HME 262
7.2.3 Using FDM 3D printing to fabricate solid dispersions 263
7.2.4 Characterisation and evaluation of FDM 3D printed solid dispersions 264
7.2.4.1 Thermal gravimetric analysis (TGA) 264
7.2.4.2 Differential scanning calorimetry (DSC) and temperature modulated DSC (MTDSC) 264
7.2.4.3 Attenuated total reflectance Fourier transform infrared spectroscopy (ATR-FTIR)…… 265
7.2.4.4 Scanning electron microscopy (SEM) 265
7.2.4.5 Powder X-ray diffraction (PXRD) 265
7.2.4.6 X-ray micro-computed tomography (XμCT) 265
7.2.4.7 Determination of drug loading efficiency 265
7.2.4.8 In vitro drug release studies 266
7.3 Results 266
7.3.1 FDM 3D printing processability of placebo and drug loaded solid dispersions…… 266
7.3.2 Loading efficiency of FDM 3D printed felodipine solid dispersions 269
7.3.3 Physical characterisation of the FDM 3D printed solid dispersions 272
7.3.4 In vitro disintegration and drug release study of FDM printed felodipine dispersions 278
7.4 Discussion 286
7.4.1 Linking phase behaviour with FDM printability of the dispersions 286
7.4.2 Linking phase behaviour with in vitro disintegration and dissolution performance.... 287
7.5 Conclusion 288
8. Chapter 8. Concluding remarks and future work 290
8.1 Conclusions 291
8.1.1 Preformulation studies 291
8.1.2 Formulation development strategies of felodipine HME-IM buccal patches ... 291
8.1.3 Characterisation challenges for investigating the microstructures of HME-IM patches…. 293
8.1.4 Evaluations of physical stabilities of the HME-IM patches and their implications in formulation optimisation 295

8.1.5 Using polymer blends as a strategy to improve FDM 3D printability of pharmaceutical solid dosage forms 297
8.2 Future outlook 298
References 300
Appendices 340
Appendix 1: Solubility parameter calculations using group contribution methods 341
Appendix 2: UV-Visible scans and standard calibration curves of felodipine in different dissolution media 353
Appendix 3: Characterisation of different batches of pure felodipine samples 355
Appendix 4: Calculation of T_g using Fox equation 359

List of Abbreviations

2D	Two dimensional
3D	Three dimensional
AFM	Atomic force microscopy
AM	Additive manufacturing
ANOVA	Analysis of variance
APIs	Active pharmaceutical ingredients
ATR-FTIR	Attenuated total reflectance Fourier transform infrared spectroscopy
BCS	Biopharmaceutics classification system
C_{max}	Maximum concentration
Cl	Clearance
CLIP	Continuous liquid interface production
CM	Carrier mixture
CMC	Critical micelle concentration
C_p	Heat capacity
DLP	Digital light projection
DSC	Differential scanning calorimetry
DVS	Dynamic vapour sorption
EC	Ethyl cellulose
EDS	Element dispersive spectroscopy
EDTA	Ethylene diamine tetra-acetic acid
FDA	Food and Drug Administration
FDM	Fused deposition modelling
EMA	European Medicines Agency
FFF	Fused filament fabrication
F-H	Flory-Huggins

FTIR	Fourier transform infrared spectroscopy
GI	Gastrointestinal
G-T	Gordon-Taylor
H_c	Heat of crystallisation
H_f	Heat of fusion
HLB	Hydrophilic-lipophilic balance
HME	Hot melt extrusion
HME-IM	Hot melt extrusion conjunction with injection moulding
HPC	Hydroxypropyl cellulose
HPMC	Hydroxypropyl methyl cellulose
HPMC-AS	Hydroxypropyl methyl cellulose acetyl succinate
IDR	Intrinsic dissolution rate
IM	Injection moulding
IR	Infrared
LD	Laser diffraction
Log P	Partition coefficient (logarithmic scale)
LOM	Laminated object manufacturing
MTDSC	Modulated temperature differential scanning calorimetry
NMR	Nuclear magnetic resonance
PBS	Phosphate buffer saline
PCA	Principal component analysis
PCL	Polycaprolactone
PEG	Polyethylene glycol
PEO	Polyethylene oxide
PKa	Acid dissociation constant (logarithmic scale)
PLA	Polylactic acid
PL-HSM	Polarised-light hot stage microscopy

PM	Physical mixture
PVA	Polyvinyl alcohol
PVAc	Polyvinyl acetate
PVP	Polyvinyl pyrrolidone
PVPVA	Polyvinyl pyrrolidone vinyl acetate
PXRD	Powder X-ray diffraction
RH	Relative humidity
ROI	Region of interest
SCF	Supercritical fluid
SD	Standard deviation
SEM	Scanning electron microscopy
SGF	Simulated gastric fluid
SHS	Selective heat sintering
SLA	Stereolithography apparatus
SLS	Selective laser sintering
STM	Scanning tunneling microscopy
$\mathbf{t_{1/2}}$	Half life
TA	Target area
TASC	Thermal analysis by structural characterisation
TEM	Transmission electron microscopy
$\mathbf{T_g}$	Glass transition
TGA	Thermogravimetric analysis
$\mathbf{T_m}$	Melting temperature
$\mathbf{t_{max}}$	Time to reach maximum concentration
TPGS	Tocopheryl polyethylene glycol succinate
TRH	Thyrotropin-releasing hormone
TTM	Transition temperature microscopy

USP	United States Pharmacopeia
UV-VIS	Ultraviolet-visible
VT-ATR-FTIR	Variable temperature attenuated total reflectance Fourier transform infrared spectroscopy
WHO	World Health Organisation
XμCT	X-ray micro computed tomography

List of Figures

Figure 1.1: Biopharmaceutics classification system (BCS) with examples; adapted from references (6-8) 2
Figure 1.2: An illustration of phase composition of different types of solid dispersions 5
Figure 1.3: Surface free energy of crystalline compared to amorphous and molecularly dispersed drugs in solid dispersions; adapted from reference (38). 6
Figure 1.4: Classification of solid dispersions based on the physical state and distribution of phases; adapted from reference (36) 7
Figure 1.5: Simple eutectic mixture phase diagram with negligible solid solubility 8
Figure 1.6: Continuous (A) and discontinuous (B) solid solution phase diagrams 9
Figure 1.7: Schematic representation of substitutional solid solution (left) and interstitial solid solution (right). Black hexagons represent drug molecules (guest) while the orange hexagons represent the carrier (host) molecules 10
Figure 1.8: Schematic representation of glass solutions and suspensions 11
Figure 1.9: Schematic representation of drug-PEG inclusion complexes; adapted from reference (54) 13
Figure 1.10: Typical phase diagram for binary drug-polymer blends as a function of temperature and composition; adapted from reference (90) 18
Figure 1.11: Schematic representation of glass transition (Tg) and comparison between the behaviours of crystalline and glass forming systems; adapted from reference (94) 20
Figure 1.12: Schematic representation of intentionally phase separated drug loaded polymeric blend; adapted from reference (73) 24
Figure 1.13: Types of hot melt extruders; A and B are single and twin screw extruders; C and D are the co-rotating and the counter rotating types; adapted from reference (30) 32
Figure 1.14: General design of extruder screw; adapted from reference (181) 33
Figure 1.15: Injection moulding (IM) machine, adapted from reference (208) 41
Figure 1.16: An illustration explains fused deposition modelling (FDM) 3D printing technology; adapted from reference (223) 44
Figure 1.17: Cross-section of the mucosa of the buccal cavity; adapted from reference (237) .. 47
Figure 2.1: Chemical structure of felodipine, adapted from reference (312) 62
Figure 2.2: Schematic representation of the crystalline-amorphous structures of PEG, adapted from reference (329) 64
Figure 2.3: a) Molecular model representing single-stranded helix of PEG consisting of seven monomer units with two turns per repeat unit and b) STM image of single- and double-stranded

helices of PEG; adapted from reference (331). Reproduced with permission from the publisher 65
Figure 2.4: a) Model illustrating single layer extended chain PEG crystal; adapted from reference (332) and b) polarised light hot stage microscope image of crystallised PEG 4000; adapted from reference (336) 66
Figure 2.5: Influence of PEO molecular weight on the release profile of theophylline from the hot melt extrudates in phosphate buffer pH 7.4; adapted from reference (357) 69
Figure 2.6: Chemical structure of Tween 80 (x + y + z = 20); adapted from reference (364).... 70
Figure 2.7: Chemical structure of vitamin E TPGS; adapted from reference (376) 71
Figure 2.8: Chemical structure of eudragit® E PO; adapted from reference (391) 73
Figure 2.9: Chemical structure of soluplus; adapted from reference (404) 75
Figure 2.10: Chemical structure of hydrolysed PVA; adapted from reference (412) 76
Figure 2.11: Thermal analysis by structural characterisation (TASC) of felodipine melting at 10 °C/ min; A) selection of ROI and TA for TASC analysis and B) TASC signal corresponding to felodipine melting 80
Figure 2.12: Working principle of TASC a) represents an image of 7×7 pixels that is the Target Area (TA). The Region of Interest (ROI) is designated by the dashed box and the black pixel represents the only structure in the ROI. b) is the extracted ROI which acts as a template that is raster scanned over the TA. Under b) the results of subtracting the different values for the pixels are given; in this simplified case subtracting the same values gives zero and subtracting different pixels gives 1. The raster scan starts in the top left corner as shown in c) with the dashed line, the sum of all differences in this case is 1 (only one pixel is different). When the ROI is moved one pixel to the right as shown in d) (the next step in the raster scan) the same value is obtained. If the black pixel moves as shown in e) the value at the start of the raster scan is zero 82
Figure 2.13: Schematic representation of the paddle over disc apparatus used for dissolution profile study; adapted from reference (441)..... 89
Figure 3.1: a) TGA analysis of felodipine using heating program of 10˚C / min from ambient to 300 °C (n=2); b) standard DSC thermogram of crystalline felodipine form I using 10˚C / min heating ramp (n=3); c) reverse signal of MTDSC thermogram showing amorphous felodipine glass transition (Tg) using 2˚C / min, 0.318 amplitude and 60 sec.s period (n=3) 98
Figure 3.2: Moisture uptake capacity of pure crystalline felodipine form I at 25℃ and 75% RH (n=3)..... 99
Figure 3.3: ATR-FTIR spectrum of a) pure crystalline felodipine form I and b) amorphous felodipine (n=3) 100
Figure 3.4: PXRD diffractograms of crystalline felodipine forms I-IV; adapted from reference (312)..... 102

Figure 3.5: PXRD pattern of pure crystalline felodipine form I used in this study 102
Figure 3.6: SEM image of pure crystalline felodipine form I particles 103
Figure 3.7: a) TGA analysis of PEG 4000 using heating program of 10℃ / min from ambient temperature to 450℃ (n=2) and b) the moisture uptake capacity of PEG 4000 at 25℃ and 75% RH (n=3) 104
Figure 3.8: Partial standard DSC thermograms showing semicrystalline PEG 4000 melting (a), crystallisation (b) and re-melting (c) transitions using 10˚C / min heating and cooling ramps (n=3) 105
Figure 3.9: a) ATR-FTIR spectrum (n=3) and b) PXRD PEG 4000 106
Figure 3.10: a) TGA analysis of PEO K900 using heating program of 10˚C / min from room temperature to 500˚C (n=2); b) MTDSC thermogram showing PEO K900 glass transition (T_g) using 2˚C / min, 0.318 amplitude and 60 sec.s period (n=3) and c) moisture uptake capacity of PEO K900 at 25℃ and 75% RH (n=3) 108
Figure 3.11: Partial standard DSC thermograms show semicrystalline PEO K900 melting (a), crystallisation (b) and re-melting (c) transitions using 10˚C / min heating and cooling ramps (n=3) 110
Figure 3.12: a) ATR-FTIR spectrum (n=3) and PXRD pattern of PEO K900 111
Figure 3.13: a) TGA analysis of Tween 80 using heating program of 10˚C / min from ambient to 500℃ (n=2); b) MTDSC thermogram showing the thermal events (glass transition T_g, crystallisation and melting) of Tween 80 using temperature program of 2˚C / min, 0.318 amplitude and 60 sec.s period (n=3) and c) moisture uptake capacity of Tween 80 at 25℃ and 75% RH (n=3) 113
Figure 3.14: ATR-FTIR spectrum of Tween 80 (n=3) 114
Figure 3.15: a) TGA analysis of TPGS using heating program of 10˚C / min from ambient to 500˚C (n=2) and b) moisture uptake capacity of TPGS at 25℃ and 75% RH (n=3) 115
Figure 3.16: Partial standard DSC thermograms showing semicrystalline TPGS melting (a), crystallisation (b) and glass transition (T_g) with re-melting (c) events using 10˚C / min heating and cooling ramps (n=3) 116
Figure 3.17: a) ATR-FTIR spectrum (n=3) and b) PXRD pattern of TPGS 117
Figure 3.18: TGA analysis of PEO K100 using heating program of 10˚C / min from room temperature to 475˚C (n=2) 118
Figure 3.19: Partial standard DSC thermograms show semicrystalline PEO K100 melting (a), crystallisation (b) and re-melting (c) events using 10˚C / min heating and cooling ramps (n=3) 120
Figure 3.20: a) ATR-FTIR spectrum (n=3) and b) PXRD pattern of PEO K100 121

Figure 3.21: a) TGA analysis of eudragit E PO using heating program of 10˚C / min from ambient temperature to 500˚C (n=2) and b) reverse signal of MTDSC thermogram showing eudragit E PO glass transition (T_g) using 2˚C / min, 0.318 amplitude and 60 sec.s period (n=3) 122
Figure 3.22: a) ATR-FTIR spectrum (n=3) and b) PXRD pattern of eudragit E PO..... 123
Figure 3.23: a) TGA analysis of soluplus using heating program of 10˚C / min from room temperature to 500˚C (n=3) and b) reverse signal of MTDSC thermogram showing soluplus glass transition (T_g) using 2˚C / min, 0.318 amplitude and 60 sec.s period (n=3) 125
Figure 3.24: a) ATR-FTIR spectrum (n=3) and b) PXRD pattern of soluplus 126
Figure 3.25: a) TGA analysis of PVA using heating program of 10˚C / min from room temperature to 500˚C (n=3) and b) reverse signal of MTDSC thermogram showing PVA glass transition (T_g) using 2˚C / min, 0.318 amplitude and 60 sec.s period (n=3)..... 128
Figure 3.26: a) ATR-FTIR spectrum (n=3) and PXRD pattern of PVA..... 129
Figure 3.27: Standard DSC thermogram showing the a) heating cycle melting peaks; b) cooling cycle crystallisation peaks and c) reheating cycle melting peaks of PEG 4000 and PEO K900 physical mixtures with different proportions using 10˚C / min heating and cooling ramps (n=3) 132
Figure 3.28: Standard DSC thermogram showing melting peaks of PEG 4000 and PEO WSR 1105 extrudates using 10˚C / min heating ramp (n=3)..... 133
Figure 3.29: MTDSC thermogram showing transitions of PEG 4000- PEO K900-Tween 80 (4:3:3) physical mixture (a) and extrudate (b) using 2˚C / min, 0.318 amplitude and 60 sec.s period (n=3) 134
Figure 3.30: MTDSC thermogram showing transitions of PEG 4000- PEO K900-TPGS (4:3:3) physical mixture (a) and extrudate (b) using 2˚C / min, 0.318 amplitude and 60 sec.s period (n=3) 135
Figure 3.31: Depression in the extrapolated onset of melting of felodipine in different excipients as a function of felodipine weight fraction (n=3) 136
Figure 4.1: Images of the felodipine loaded HME-IM extrudates and buccal patches: A and C are placebo CM1 and CM2 extrudates respectively, B and D are placebo CM1 and CM2 buccal patches respectively, E and G are 10% w/w felodipine CM1 and CM2 extrudates respectively, F and H are 10% felodipine CM1 and CM2 buccal patches respectively, I and K are 20% w/w felodipine CM1 and CM2 extrudates respectively, J and L are 20% felodipine CM1 and CM2 buccal patches respectively, M and O are 30% w/w felodipine CM1 and CM2 extrudates respectively and N and P are 30% felodipine CM1 and CM2 buccal patches respectively..... 143
Figure 4.2: Standard DSC (10ºC/min scanning rate) thermograms of CM1 physical mixtures and drug loaded patches with 10-30% loading (n=3) 148

Figure 4.3: Non-reversing heat flow signal of the MTDSC results of CM1 physical mixes and buccal patches of placebo and patches loaded with 10% - 30% w/w felodipine (n=3) 150
Figure 4.4: MTDSC Reversing heat flow signals of CM1 physical mixes and buccal patches of placebo and patches loaded with 10% - 30% w/w felodipine (n=3)..... 151
Figure 4.5: T_g and ΔC_p values of the CM1 samples plotted against felodipine loading percentage (10% - 30% w/w) using MTDSC (n=3; average ± SD) 153
Figure 4.6: Standard DSC (10ºC/min scanning rate) thermogram of CM2 physical mixtures and drug loaded patches with 10-30% loading (n=3)..... 154
Figure 4.7: Standard DSC results of CM2 physical mixes and buccal patches of placebo and patches loaded with 10% - 30% w/w felodipine (n=3)..... 156
Figure 4.8: SEM images surfaces (a, c, e, g) of CM1 placebo and patches with 10%, 20% and 30% felodipine loading and their corresponding cross-sections (b, d, f, h)..... 158
Figure 4.9: SEM images surfaces (a, c, e, g) of CM2 placebo and patches with 10%, 20% and 30% felodipine loading and their corresponding cross-sections (b, d, f, h)..... 159
Figure 4.10: Scanning electron microscopic (left) and elemental analysis images (right) of the surfaces of CM1 and CM2 patches with different drug loadings 160
Figure 4.11: PXRD patterns of A) raw materials, CM1 placebo and 10-30% (w/w) felodipine loaded felodipine patches and B) raw materials, CM2 placebo and 10-30% (w/w) felodipine loaded felodipine patches..... 161
Figure 4.12: Partial ATR-FTIR spectra of felodipine NH stretching region of CM1 (a) and CM2 (b) HME-IM patches with different drug loadings in comparison to crystalline and amorphous felodipine. The dotted lines highlight the signature crystallisation and amorphous felodipine peaks (n=3)..... 162
Figure 4.13: Partial ATR-FTIR spectra of felodipine C=O carbonyl region of CM1 (a) and CM2 (b) HME-IM patches with different drug loadings in comparison to crystalline and amorphous felodipine (n=3) 164
Figure 4.14: Partial ATR-FTIR spectra of felodipine CN stretching region of CM1 and CM2 HME-IM patches with different drug loadings in comparison to crystalline and amorphous felodipine (n=3) 165
Figure 4.15: (a) IR reflectance spectra are coding for the composition of different colours in the IR images. Red spectrum indicates areas containing drug as molecularly dispersed or amorphous form; green spectrum indicating areas indicating areas rich with the drug (supersaturated matrix which may contain very tiny crystals); purple spectrum indicating areas with crystalline drug); correlation IR map (left), optical image (right) and the IR spectrum of the point of interest (bottom) of the surfaces of CM1 HME-IM patches with (b) placebo, (c) 10%, (d) 20% and (e) 30% felodipine loading 167

Figure 4.16: Correlation IR maps for placebo (a), 10% (b), 20% (c) and 30% (d) CM2 HME-IM patches; (e) is the IR reflectance spectra for the different areas of the maps..... 168
Figure 4.17: Mucoadhesion analysis for placebo CM1 sample using TA-XT2 Texture Analyser 170
Figure 4.18: In vitro release profiles of felodipine from HME-IM buccal mucoadhesive patches; a) CM1 patches under sink conditions, a) CM1 patches under non-sink conditions and c) CM2 patches under non-sink conditions (n=3; average ± SD) 173
Figure 5.1: Light microscopic image of an example slice of 10% w/w CM1 felodipine mucoadhesive buccal patch analysed by TASC software..... 183
Figure 5.2: Thermal events of placebo CM2 sample detected by TASC at different points (-10°C, 40°C, and 80°C) during the heating ramp at 10 °C/ min 183
Figure 5.3: TASC compared to standard DSC averaged thermograms of placebo CM1 during the heating (A and B), cooling (C and D) and reheating (E and F) cycles and placebo CM2 during the heating (G and H), cooling (I and J) and reheating (K and L) cycles at 10 °C/ min for all cycles (n=3; average ± SD)..... 185
Figure 5.4: TASC thermograms of 10% felodipine in CM1 during the heating (A), cooling (C) and reheating (E) cycles; and 10% felodipine in CM2 during the heating (B), cooling (D) and reheating (F) cycles using 10 °C/ min for all cycles (n=3; average ± SD)..... 186
Figure 5.5: TASC thermograms of 20% felodipine in CM1 during the heating (A), cooling (C) and reheating (E) cycles; and 20% felodipine in CM2 during the heating (B), cooling (D) and reheating (F) cycles using 10 °C/ min for all cycles (n=3; average ± SD)..... 187
Figure 5.6: TASC thermograms of 30% felodipine in CM1 during the heating (A), cooling (C) and reheating (E) cycles; and 30% felodipine in CM2 during the heating (B), cooling (D) and reheating (F) cycles using 10 °C/ min for all cycles (n=3; average ± SD)..... 188
Figure 5.7: TASC and DSC results of the heating cycle of CM1 (A and B) and CM2 (C and D) placebo and felodipine loaded mucoadhesive buccal patches with 10, 20 and 30% w/w loading (n=3; average ± SD)..... 189
Figure 5.8: Comparison of the TASC results of the heating cycle of CM1 (left) and CM2 (right) 30% w/w felodipine patches using (A, B) small sampling spots (to provide localise thermal analysis), (C and D) larger sampling spots; (E and F) extended heating to 150ºC to demonstrate that the drug dissolution/melting occurred in the 30% drug loaded samples as the TASC signal reaches the plateau at higher temperature above 100 °C (n=3; average ± SD)..... 190
Figure 5.9: The TASC results of the heating cycle of 10% (A and B) and 30% (C and D) CM2 felodipine loaded patches using a small sampling area (A and C) and a larger sampling area (B and D). It can be seen that there is no obvious difference in the error bars of the data collected

from the two areas with different sizes for 10% indicating the high homogeneity of the samples with low drug loading compared to 30% loading (n=3; average ± SD)..... 191
Figure 5.10: TASC and DSC results of the cooling cycle of CM1 (A and B) and CM2 (C and D) placebo and felodipine loaded mucoadhesive buccal patches with 10, 20 and 30% w/w loading (n=3; average ± SD) 192
Figure 5.11: VT- ATR-FTIR (a) 2D and (b) 3D spectra of demonstrating the dissolution of the crystalline drug in CM1 matrix in the patches with 30% drug loading during heating 193
Figure 5.12: TASC and DSC results of the reheating cycle of CM1 (A and B) and CM2 (C and D) placebo and felodipine loaded mucoadhesive buccal patches with 10, 20 and 30% w/w loading showing the detection of metastable folded form of PEG by TASC (n=3; average ± SD)..... 195
Figure 5.13: Enhanced sensitivity for the detection of hidden thermal transitions. Optical images at different temperatures of the TASC measurement during heating of the PEG/PEO K900 based CM1 patch with 10% drug loading. The areas with no specular effect were chosen for the measurements..... 196
Figure 5.14: MTDSC results of the melting region of CM1 patches with 10% drug loading indicating the present of solid form transformation of PEG at the transition temperature identified by TASC during the reheating cycle (n=3; average ± SD) 197
Figure 5.15: VT- ATR-FTIR spectra of the heating a and c reheating cycle of the CM1 10% loaded patches indicating the crystallisation and melting of the metastable form of PEG; and (d) the ATR-FTIR spectra intensity changes of the additional peak at 1106 cm^{-1} with temperature indicating the presence of metastable form PEG 198
Figure 5.16: Influence of heating rate on TASC response in comparison to conventional DSC. CM1 patches loaded with 10% felodipine were tested using TASC and DSC at 10, 20 and 40ºC/min. First heating and reheating cycle were recorded and compared (n=3; average ± SD) 199
Figure 5.17: XμCT images of CM1 placebo surface and cross-section images (a, b) and CM1 10% surface and cross-section images (c, d)..... 200
Figure 5.18: XμCT images of CM1 HME-IM patches containing 20% (w/w) felodipine 201
Figure 5.19: XμCT images HME-IM CM1 patches containing 30% (w/w) felodipine..... 202
Figure 5.20: XμCT analysis of CM2 placebo sample; A) an example of a reconstructed binary image; B) selected Region of Interest (ROI) for analysis C) 3D object representing the different components according to their densities present in the selected ROI..... 203
Figure 5.21: (a) XμCT reconstruction of binary image of 10% CM2 loaded sample with selected Region of Interest (ROI) for analysis; b) 3D object representing the different components according to their densities present in the selected ROI; (c) XμCT reconstruction of binary image of 20% CM2 loaded patches with selected Region of Interest (ROI) for analysis; d) 3D object

representing the different components according to their densities present in the selected ROI 204
Figure 5.22: XμCT analysis of CM2 30% loaded sample; a) an example of reconstructed binary image with selected Region of Interest (ROI) for analysis b) 3D object representing the air pockets entrapped in the sample; c) 3D object representing the phase separated crystalline felodipine particles; d) 3D object representing the matrix 205
Figure 5.23: Representative 3D XμCT images of the distribution of crystalline felodipine in the compacts made of the physical mixes of crystalline felodipine-TPGS-PEG-PEO K900 with (a) 10%; (b) 30%; and (c) 60% crystalline felodipine loadings. (d) the correlation between crystalline drug content in these compacts and measured volume fraction of felodipine in their 3D XμCT images, which was used as a calibration curve for the quantitative estimation of crystalline felodipine in HME-IM patches with 30% drug loading..... 207
Figure 5.24: Estimation of heterogeneity by XμCT: (a) Illustration of the selection of a range of ROIs with different sizes on a representative 2D XμCT image of CM2 patches with 30% drug loading; (b) the comparison of the calculated volume fraction of crystalline felodipine in the ROIs with large (300×300 μm) and small (100×100 μm) areas 208
Figure 6.1: DSC thermograms of placebo CM1 fresh and aged samples using 10℃/ min (n=3) 217
Figure 6.2: DSC thermograms of placebo CM2 fresh and aged samples using 10℃/ min (n=3) 218
Figure 6.3: SEM images for CM1 placebo fresh and 3 months aged samples; (a and b) are surface and cross-section of fresh sample, (c and d) are surface and cross-section of sample stored at condition A, (e and f) are surface and cross-section of sample stored at condition B and (g and h) are surface and cross-section of sample stored at condition C..... 219
Figure 6.4: SEM images for CM2 placebo fresh and 3 months aged samples; (a and b) are surface and cross-section of fresh sample, (c and d) are surface and cross-section of sample stored at condition A, (e and f) are surface and cross-section of sample stored at condition B, (g and h) are surface and cross-section of sample stored at condition C, and (i and j) are surface and cross-section of sample stored at condition D 220
Figure 6.5: TGA results of 3-month aged CM1 placebo patches (n=3)..... 221
Figure 6.6: A) The high wavenumber and B) is the low wavenumber ATR-FTIR spectra of placebo CM1 fresh and aged samples (n=3) 223
Figure 6.7: SEM images for 10% CM1 fresh and 3 months aged samples; (a and b) are surface and cross-section of fresh sample, (c and d) are surface and cross-section of sample stored at condition A, (e and f) are surface and cross-section of sample stored at condition B, (g and h) are

surface and cross-section of sample stored at condition C, and (i and j) are surface and cross-section of sample stored at condition D 224
Figure 6.8: SEM images for 10% CM2 fresh and 3 months aged samples; (a and b) are surface and cross-section of fresh sample, (c and d) are surface and cross-section of sample stored at condition A, (e and f) are surface and cross-section of sample stored at condition B, (g and h) are surface and cross-section of sample stored at condition C, and (i and j) are surface and cross-section of sample stored at condition D 225
Figure 6.9: SEM images for 20% CM1 fresh and 3 months aged samples; (a and b) are surface and cross-section of fresh sample, (c and d) are surface and cross-section of sample stored at condition A, (e and f) are surface and cross-section of sample stored at condition B, (g and h) are surface and cross-section of sample stored at condition C, and (i and j) are surface and cross-section of sample stored at condition D 226
Figure 6.10: SEM images for 20% CM2 fresh and 3 months aged samples; (a and b) are surface and cross-section of fresh sample, (c and d) are surface and cross-section of sample stored at condition A, (e and f) are surface and cross-section of sample stored at condition B, (g and h) are surface and cross-section of sample stored at condition C, and (i and j) are surface and cross-section of sample stored at condition D 227
Figure 6.11: SEM images for 30% CM1 fresh and 3 months aged samples; (a and b) are surface and cross-section of fresh sample, (c and d) are surface and cross-section of sample stored at condition A, (e and f) are surface and cross-section of sample stored at condition B, (g and h) are surface and cross-section of sample stored at condition C, and (i and j) are surface and cross-section of sample stored at condition D 228
Figure 6.12: SEM images for 30% CM2 fresh and 3 months aged samples; (a and b) are surface and cross-section of fresh sample, (c and d) are surface and cross-section of sample stored at condition A, (e and f) are surface and cross-section of sample stored at condition B, (g and h) are surface and cross-section of sample stored at condition C, and (i and j) are surface and cross-section of sample stored at condition D 229
Figure 6.13: DSC thermograms of 10% CM1 fresh and three months aged samples using 10℃/ min heating ramp (n=3) 230
Figure 6.14: DSC thermograms of 20% CM1 fresh and three months aged samples using 10℃/ min heating ramp (n=3) 231
Figure 6.15: DSC thermograms of 30% CM1 fresh and three months aged samples using 10℃/ min heating ramp (n=3) 231
Figure 6.16: Part of DSC thermograms samples showing the T_g regions of 10% CM1 fresh and three months aged samples using 10℃/ min heating rate (n=3) 232

Figure 6.17: Part of DSC thermograms samples showing the T_g regions of 20% CM1 fresh and three months aged samples using 10℃/ min heating rate (n=3) 233
Figure 6.18: Part of DSC thermograms samples showing the T_g regions of 30% CM1 fresh and three months aged samples using 10℃/ min heating rate (n=3) 234
Figure 6.19: DSC thermograms of 10% CM2 fresh and three months aged samples using 10℃/ min heating ramp (n=3) 235
Figure 6.20: DSC thermograms of 20% CM2 fresh and three months aged samples using 10℃/ min heating ramp (n=3) 235
Figure 6.21: DSC thermograms of 30% CM2 fresh and three months aged samples using 10℃/ min heating ramp (n=3) 236
Figure 6.22: Part of DSC thermograms samples showing the T_g regions of 10% CM2 fresh and three months aged samples using 10℃/ min heating rate (n=3) 237
Figure 6.23: Part of DSC thermograms samples showing the T_g regions of 20% CM2 fresh and three months aged samples using 10℃/ min heating rate (n=3) 237
Figure 6.24: Part of DSC thermograms samples showing the T_g regions of 30% CM2 fresh and three months aged samples using 10℃/ min heating rate (n=3) 238
Figure 6.25: PXRD patterns of 10% w/w fresh and three months aged CM1 drug loaded patches 243
Figure 6.26: PXRD patterns of 10% w/w fresh and three months aged CM2 drug loaded patches 243
Figure 6.27: PXRD patterns of 20% w/w fresh and three months aged CM1 drug loaded patches 244
Figure 6.28: PXRD patterns of 20% w/w fresh and three months aged CM2 drug loaded patches 245
Figure 6.29: PXRD patterns of 30% w/w fresh and three months aged CM1 drug loaded patches 246
Figure 6.30: PXRD patterns of 30% w/w fresh and three months aged CM2 drug loaded patches 246
Figure 6.31: The NH stretching region of the ATR-FTIR spectra of CM1 10% fresh and aged samples (n=3)..... 247
Figure 6.32: Partial ATR-FTIR spectra of CM1 10% fresh and aged samples for the low wavenumber range (n=3) 247
Figure 6.33: The NH stretching region of the ATR-FTIR spectra of CM2 10% fresh and aged samples (n=3)..... 248
Figure 6.34: Partial ATR-FTIR spectra of CM2 10% fresh and aged samples for the low wavenumber range (n=3) 248

Figure 6.35: The NH stretching region of the ATR-FTIR spectra of CM1 20% fresh and aged samples (n=3) 249
Figure 6.36: Partial ATR-FTIR spectra of CM1 20% fresh and aged samples for the low wavenumber range (n=3) 249
Figure 6.37: The NH stretching region of the ATR-FTIR spectra of CM2 20% fresh and aged samples (n=3) 250
Figure 6.38: Partial ATR-FTIR spectra of CM2 20% fresh and aged samples for the low wavenumber range (n=3) 250
Figure 6.39: The NH stretching region of the ATR-FTIR spectra of CM1 30% fresh and aged samples (n=3) 251
Figure 6.40: Partial ATR-FTIR spectra of CM1 30% fresh and aged samples for the low wavenumber range (n=3) 251
Figure 6.41: The NH stretching region of the ATR-FTIR spectra of CM2 30% fresh and aged samples (n=3) 252
Figure 6.42: Partial ATR-FTIR spectra of CM2 30% fresh and aged samples for the low wavenumber range (n=3) 252
Figure 6.43: Images of felodipine in its glassy state (A) and after recrystallisation at 40℃ and 75% RH (B) 253
Figure 6.44: SEM images of felodipine after recrystallisation at 40℃ and 75% RH; A is the upper surface and (B) is the lower surface of the sample 254
Figure 6.45: DSC thermograms illustrating melting transition of pure felodipine form I and recrystallised felodipine at 40℃ and 75% RH before and after milling (n=3) 255
Figure 6.46: PXRD patterns of pure felodipine form I and recrystallised felodipine at 40℃ and 75% RH before and after milling 255
Figure 6.47: Partial ATR-FTIR spectra of pure felodipine form I and recrystallised felodipine at 40℃ and 75% RH before and after powdering; A and B are high and low wavenumber ranges respectively (n=3) 256
Figure 7.1: Images of the prepared HME filaments and FDM 3D printed discs 264
Figure 7.2: SEM images for 10% w/w felodipine loaded FDM 3D printed discs. CME (a) surface and (b) cross-section; CMS (c) surface and (d) cross-section; CMV (e) surface and (f) cross-section. The dotted lines indicate the widths of filaments strips after FDM printing 268
Figure 7.3: Representative XμCT reconstructed 3D images of CME placebo and 10% w/w felodipine loaded CME discs. HME filaments (left) and FDM 3D printed discs (right). The phase separate particles are likely to be metal contaminations introduced during HME and FDM printing and/or some inorganic additives included in the raw polymers (499) 269

Figure 7.4: Thermal degradation of placebo and 10% w/w felodipine loaded physical mixture, filament and 3D printed discs. A) CME, B) CMS and C) CMV mixtures (n=3) 271
Figure 7.5: DSC thermograms illustrating different thermal events for physical mixtures and FDM 3D printed discs of placebo and 10% w/w felodipine loaded CME, CMS and CMV (n=3) 272
Figure 7.6: MTDSC thermograms showing the T_g events of (a) CME formulations using temperature program of 1.0 ˚C amplitude, 60 sec period and 2 ˚C/ min heating rate and (b) CMS mixtures using a heat only temperature program of 0.318 ˚C amplitude, 60 sec period and 2 ˚C/ min heating rate (n=3)..... 273
Figure 7.7: MTDSC thermograms showing the T_g events of CMV mixtures using a heat only temperature program of 0.318 ˚C amplitude, 60 sec period and 2 ˚C/ min heating rate (n=3). 274
Figure 7.8: Partial ATR-FTIR spectra of the physical mixtures (PM) and felodipine loaded FDM printed discs. The NH stretching peak of crystalline felodipine is highlighted with the dashed line (n=3)..... 277
Figure 7.9: Moisture content of different FDM 3D printed discs using TGA at 10 ºC/min (n=3) 277
Figure 7.10: PXRD Diffraction patterns of physical mixtures and 10% w/w felodipine loaded FDM printed CME, CMS and CMV discs..... 278
Figure 7.11: Felodipine release profile of FDM 3D printed discs using a) pH 1.2 HCl (simulated gastric fluid without enzyme) and b) pH 6.8 phosphate buffer saline (PBS) (n=3; average ± SD) 279
Figure 7.12: Visual appearances of felodipine loaded FDM printed CME discs during dissolution in pH 1.2 HCl and pH 6.8 PBS. The dash circles represent the diameters of freshly prepared dry CME discs..... 280
Figure 7.13: Visual appearances of the felodipine loaded FDM printed CMS discs during the dissolution tests in (a) pH 1.2 HCl and (b) pH 6.8 PBS. The dash circles in (a) and (b) represent the diameters of the dry and freshly prepared CMS discs 281
Figure 7.14: Partial ATR-FTIR spectra of CMS discs taken out of the media and dried after 6 hours dissolution. The dash lines in (c) highlight the felodipine related IR peaks and arrows highlight the changes of PEG/PEO K100 related peaks labelled with * before dissolution (n=3) 282
Figure 7.15: Images (A and C) and SEM images (B and D) of 10% CMS samples after dissolution for 6 hours and drying. A and B in SGF pH 1.2, while C and D in PBS pH 6.8 283
Figure 7.16: DSC thermographs of CMS discs taken out of the media and dried after 6 hours dissolution (n=3) 283
Figure 7.17: Visual appearances of the felodipine loaded FDM printed CMV discs during the dissolution tests in (a) pH 1.2 HCl and (b) pH 6.8 PBS..... 284

Figure 7.18: Partial ATR-FTIR spectra of CMV discs taken out of the media and dried after 6 hours dissolution. The arrows highlight felodipine related IR peaks (n=3)..... 285
Figure 7.19: DSC thermographs of CMV discs taken out of the media and dried after 6 hours dissolution (n=3)..... 285
Figure 8.1: Proposed schematic illustration of felodipine loaded phase separated solubilisation compartments created by HME-IM 292
Figure 8.2: An illustration showing the impacts of storing temperature and relative humidity on the stability of felodipine loaded HME-IM patches..... 296

List of Tables

Table 1.1: Chemical classes of carriers with examples used as vehicles for solid dispersions preparation by HME; adapted from reference (165) 36
Table 1.2: Summary of 3D printing techniques, their operation principles and materials used in the fabrication of objects, adapted from reference (223) 43
Table 2.1: Physicochemical and pharmacokinetic properties of felodipine 63
Table 3.1: Characteristic ATR-FTIR absorption peaks of felodipine and other excipients used in this study 101
Table 3.2: Summary of solubility parameter predictions calculated using group contribution methods 130
Table 4.1: Composition of felodipine loaded CM1 and CM2 buccal patches produced by HME-IM technique 142
Table 4.2: Melting Temperature (T_m) depression of PEG-PEO K900 and surfactant phases caused by drug loading in different CM1 HME-IM patches (3 replicates for each sample) using DSC at 10°C/ min 149
Table 4.3: T_g and ΔC_p values of placebo and felodipine loaded CM1 physical mixtures and HME-IM patches (10% - 30% w/w) measured using MTDSC 152
Table 4.4: Melting temperature (T_m) depression of PEG-PEO K900 and surfactant phases caused by drug loading in different CM2 HME-IM patches (3 replicates for each sample) DSC 10°C/ min 155
Table 4.5: In vitro mucoadhesion measurements of CM1 and CM2 placebo and felodipine loaded HME-IM buccal patches (n = 5, mean ± SD) 170
Table 6.1: Percentage of weight loss of the formulations measured by TGA after three months ageing 222
Table 6.2: Summary of the changes of thermal properties of the aged patches in comparison to the properties of the fresh patches 239
Table 6.3: Summary of surface morphology and crystal growth of the 3-month aged HME-IM patches 242
Table 7.1: Composition of placebo and 10% w/w felodipine loaded FDM dispersions. Proportions are expressed as % w/w 262
Table 7.2: HME-3D printing processing parameters of placebo and 10% w/w loaded felodipine filaments and 3D printed discs 263
Table 7.3: Weights of placebo and 10% w/w felodipine loaded FDM printed discs 270

Table 7.4: Experimental % crystallinity of PEG-PEO polymers in CME and CMS blends compared to the 100% theoretical values 275
Table 7.5: Fox equation predicted T_g temperatures for different formulations..... 276

Chapter 1. Introduction

1.1 The mystery of poor water solubility of active pharmaceuticals

Poor water solubility due to the hydrophobic nature of ~ 40% of the newly discovered pharmaceutically active chemical entities (due to the chemistry of their active forms) comprises a challenging problem that affects their dissolution from the final products (1, 2). The equilibrium solubility of any chemical compound is an essential feature that can be changed only by chemical structure modification while the dissolution rate is an extrinsic property that can be modified by chemical, physical, and crystallographic changes like complexation, surface properties, particle size, solid state modification and formulation based solubilisation (3). According to U.S Food and Drug Administration (FDA), World Health Organisation (WHO) and European Medicines Agency (EMA), drugs are generally classified into four classes according to biopharmaceutics classification system (BCS). The classification is based on their aqueous solubility and permeability through the intestinal barriers at the site of absorption as a tool to predict their pharmacokinetic performances (4). Drugs are termed highly soluble when their highest strength is soluble in 250 mL or less aqueous solution within the pH range of 1- 6.8 at 37 ± 1 ℃. In addition, the expression 'high permeable' indicates not less than 85% of the administered dose (based on mass balance or in comparison to an intravenous reference dose) is absorbed through the intestinal site of absorption (5). The different classes with examples of various drugs are presented in **Figure 1.1**.

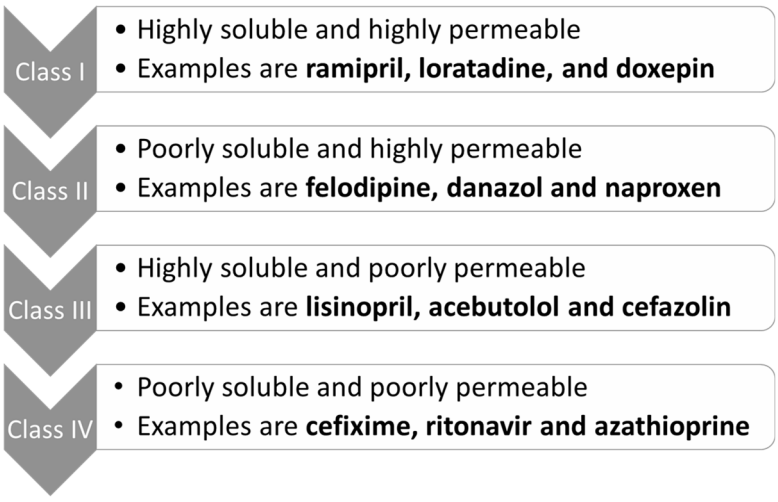

Figure 1.1: Biopharmaceutics classification system (BCS) with examples; adapted from references (6-8)

Solubility and/or dissolution rate are considered as critical parameters that control the development of any pharmaceutical product starting from the formulation process and ending by the different drug disposition stages inside the human body. Also, their impacts extend to later stages after the intake of medication to include the release profile, absorption, bioavailability, distribution, metabolism and excretion (3, 9, 10).

Over the last decades, researchers have developed a variety of strategies to overcome this problem like salt formation, complexation, co-crystals, nanocrystals, prodrug formation, lipid-based drug delivery systems and solid dispersions. Each one of these approaches has its advantages and limitations. Salt formation significantly increases the solubility, however, it is only applicable to acidic and basic drugs (11). Complexation using inclusion excipients like cyclodextrins enhance the solubility of hydrophobic drugs by trapping them in their central cavity. The formation of these solubilisation complexes is controlled by the size of the cyclodextrin ring and the guest molecule and the presence of interaction between them (12). Co-crystals can increase the solubility of this category of drugs by lowering the lattice energy and increasing the solvent affinity. However, the flexibility to formulate those drugs as co-crystals is limited by safety restrictions on the concentrations of coformers such as malic acids which forms co-crystals with itraconazole in a maximum allowable combination of less than 7% (13). Also, reducing the particle size by using nanocrystals approach led to the development of marketed products such as nabilone (Cesamet®/Lilly) and fenofibrate (Tricor®/Abbott) oral nanocrystal formulations through enhancing the dissolution rate by the enormous increase in the surface area exposed to solvent action (14). However, it was reported that physiological factors like pH variations, the composition of the gastric juices and GI peristalsis could affect the redispersion of nanocrystals resulting in a failure to achieve good *in vivo* performance (15). Reducing particle size may also be compromised by the extensive precipitation and the high recrystallisation tendency of the drug. It should be mentioned that very fine particles may express poor wetting properties, aggregation and agglomeration and difficulty in handling such particles during formulation and manufacturing processes (16-18). Furthermore, prodrug approach was shown to improve the solubility of poorly water soluble drugs, but this involves modification of drug's chemical structure which is generally not favourable to overcome solubility limitations (19). Lipid-based drug delivery systems offer the advantage of dissolving lipophilic drugs. A variety of lipids, surfactants or mixtures of lipids and surfactants were used to omit the dissolution step which acts as the limiting parameter for the absorption of poorly water soluble drugs (20-22). However, this formulation strategy may be affected by some challenges like physical changes and oxidative degradation over time which might have a potential impact on drug stability and formulation performance (23). Another

approach to improve the solubility and dissolution rate of poorly water soluble drugs is through the use of solid dispersions. The solubility and/or dissolution enhancement by this method is achieved majorly by converting the drug from its crystalline state to typically molecularly level solid dispersion. The major drawback of this formulation based technology is the physical stability of the dispersed drug in the formulation (24, 25). It should be mentioned that lipid-based formulations can be processed as solid dispersions to prepare drug delivery systems for improved dissolution properties of poorly water soluble drugs (21, 26).

1.2 Solid dispersions

Pharmaceutical solid dispersions are systems in which the APIs are distributed in a carrier composed of one or more pharmaceutical excipients (27, 28). The interest in solid dispersions is growing rapidly in the last five decades owing to the advantages offered by this type of preparations like the improvement in the bioavailability of poorly water-soluble drugs (BCS class II) through increasing their solubility and/or dissolution rates (18). The importance of this approach compared to other methods used for achieving this purpose is attributed to the flexibility in combining the drugs with a very wide range of pharmaceutically approved excipients having different functionalities to achieve the desired objectives of formulation. Excipients with wide variety of physicochemical properties like different chemical structures, molecular weights, crystalline, amorphous, lipidic, hydrophilic, amphiphilic, viscous, liquids, semisolids, solids can be used in fabricating solid dispersions. In addition, solid dispersions as blends are not restricted with certain stoichiometric mixing ratios which enable researchers to use a wide range of concentrations depending on the miscibility between the different components. Furthermore, there are several methods can be utilised for the fabrication of these formulations with different formulation strategies and applications that may be used to overcome preparation challenges (29-32). However, there are only a few products marketed as therapeutically effective and stable formulations to be used by the patients to cure diseases mainly due to physical stability issues (18). An illustration of the structure of different solid dispersions is shown in **Figure 1.2**. Depending on the physical states of the drug and the carrier, several types of solid dispersions with single or multiple phases can be formed.

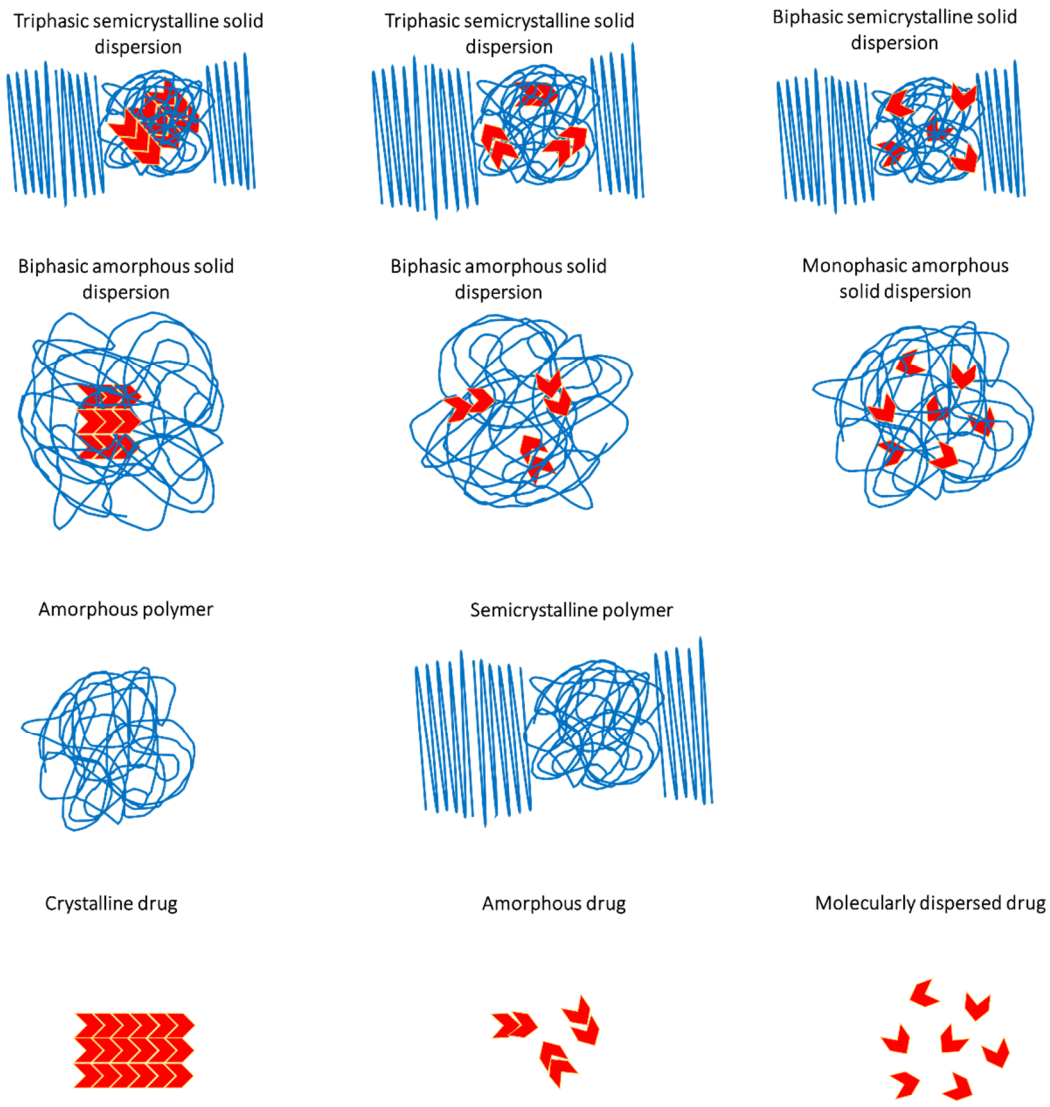

Figure 1.2: An illustration of phase composition of different types of solid dispersions

Poorly water soluble drugs are mostly crystalline compounds characterised by long-range three-dimensional order of arrangement of molecules (**Figure 1.2**). On the other hand, amorphous forms are disordered compounds lacking this property and have only short range of order (33). Also, polymorphic forms are crystalline forms belong to the same drug with different crystalline structures having various molecular arrangements caused by differences in packing and/or molecular conformations (34). Polymorphic forms are different in their thermodynamic (like melting temperature), kinetic (such as dissolution rate), packing (like density), surface (such as surface free energy) and mechanical properties (like hardness) (35).

Solid dispersions enhance the solubility and/or dissolution of poorly water-soluble drugs by different mechanisms. These mechanisms include converting the drug into molecular level,

amorphous or other polymorphic forms having higher solubility and/or dissolution properties (27, 36). The higher surface free energy of the molecularly dispersed and amorphous forms compared to crystalline form is the driving force responsible for the improvement in solubility and/or dissolution characteristics as shown in **Figure 1.3**. In addition, other factors like the decrease in particle size, reduction in agglomeration and aggregation, interaction with other excipients to form complexes and enhanced wettability are also contributing to such improvement in drug solubility and/or dissolution properties (27, 36). Increasing the dissolution properties by solid dispersions through particle size reduction is based on the assumption that the components of these dispersions crystallise as very small particles. Consequently, when these particles come into contact with the dissolution media, the larger surface area exposed to the solvent action of these small particles enhance the dissolution rate (37).

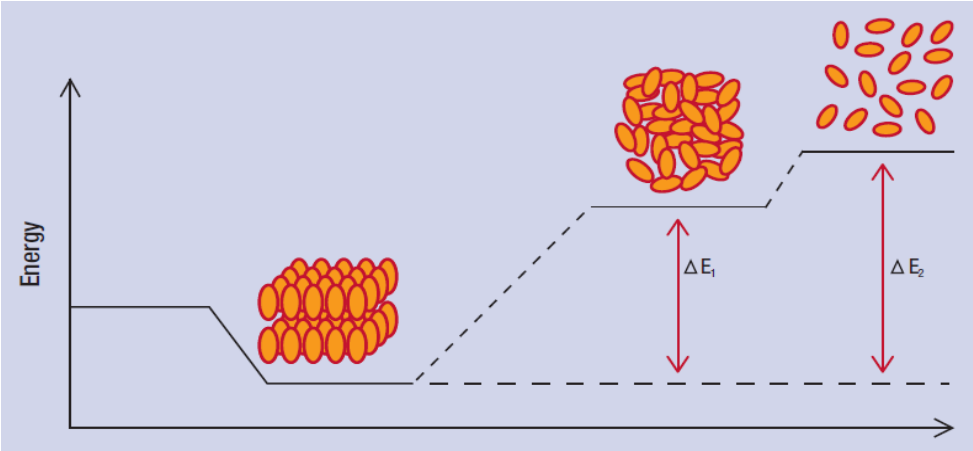

Figure 1.3: Surface free energy of crystalline compared to amorphous and molecularly dispersed drugs in solid dispersions; adapted from reference (38).

1.2.1 Classification of solid dispersions according to the physical state of the drug and the carrier

Based on the physical state of the drug and the carrier excipient(s), solid dispersions can be classified into many classes as illustrated in **Figure 1.4**

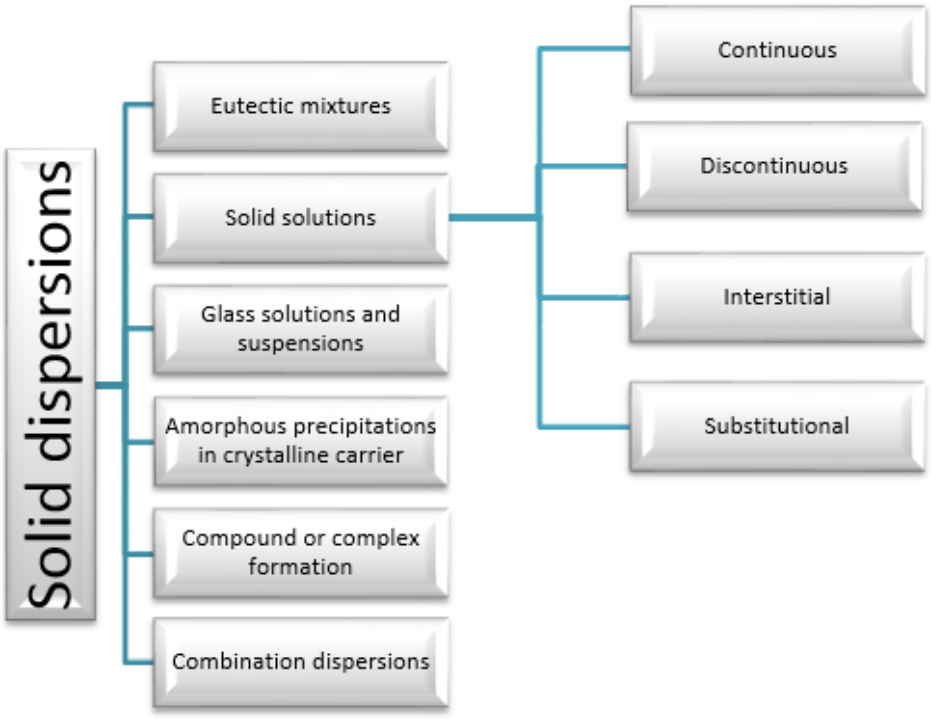

Figure 1.4: Classification of solid dispersions based on the physical state and distribution of phases; adapted from reference (36)

1.2.1.1 Eutectic mixtures

Eutectic mixtures are solid dispersions having a melting point (eutectic temperature) lower than that of its original components. The mixture is single phase in the liquid state and phase separated crystalline mixture in the solid state (36, 38, 39). An intimate physical interaction such as hydrogen bonding is a critical factor in causing the melting point depression of the system in the solid state. This kind of solid dispersions can be formed between drugs, excipients and their mixtures (40). Eutectic mixtures are further classified into monotectic and typical eutectic solid dispersion depending on how close the eutectic temperature to the melting point of individual constituents. Monotectic solid dispersions have eutectic point close to one of the mixture ingredients while in the case of typical eutectic systems the eutectic temperature lies in the middle area away from individual constituents (38, 39).

Several poorly water soluble drugs showed to form eutectic mixtures resulting in an enhancement in their dissolution properties. It was reported that ibuprofen solubility is improved by eutectic

mixture formation with menthol resulting in a significant improvement in the initial plasma concentration of the drug (41). Also, the dissolution rates of acetylsalicylic acid, benzoic acid and phenylacetic acid were found to be higher by the formation of eutectic mixtures with choline chloride and menthol at specific mixing proportions (42).

Furthermore, eutectic mixture of urea and efonidipine hydrochloride ethanolate was reported to be formed by microwave radiation treatment in which the eutectic point was depressed 70℃ and 40℃ with respect to the melting temperature of the drug and urea respectively (43). The phase diagram of this class of solid dispersions is illustrated in **Figure 1.5**.

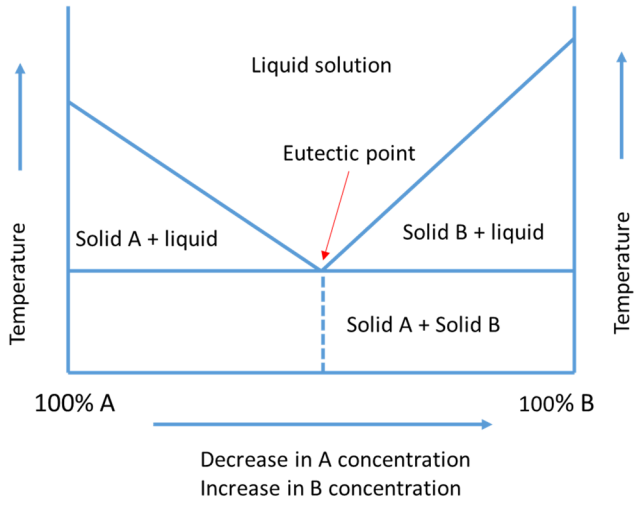

Figure 1.5: Simple eutectic mixture phase diagram with negligible solid solubility

1.2.1.2 Solid solutions

Solid solutions or often called mixed crystals are solid dispersions in which the components of the mixture in the solid state are crystallised together as a single phase homogeneous system. The dissolution properties of poorly water soluble drugs using this system are higher compared to the aforementioned eutectic mixture. The improved dissolution is attributed to particle size reduction to the maximum degree in which the drug is existing at the molecular level (36). Solid solutions are classified according to the extent of miscibility between the components of the system into continuous and discontinuous solid solutions. In the former, the constituents of the blends are miscible in all proportions while in the later there is incomplete miscibility between the individual ingredients. They also are subdivided into interstitial and substitutional solid dispersions.

Interstitial solid solutions, the solid solute molecules fill the interstitial spaces between the solid solvent molecules while in the case of substitutional type, the guest solute molecules substitute the solvent ones (27, 36, 44, 45). According to the similarities in their structure and/or the open spaces in the crystal of the solvent (host crystal), the solute (guest) can orient itself in a specific manner giving the dispersion its final characteristics.

The phase diagrams of the continuous and the discontinuous solid solutions are illustrated in **Figures 1.6 A and B**, respectively. Also, an illustration of the substitutional and the interstitial types of solid solutions is shown in **Figure 1.7**.

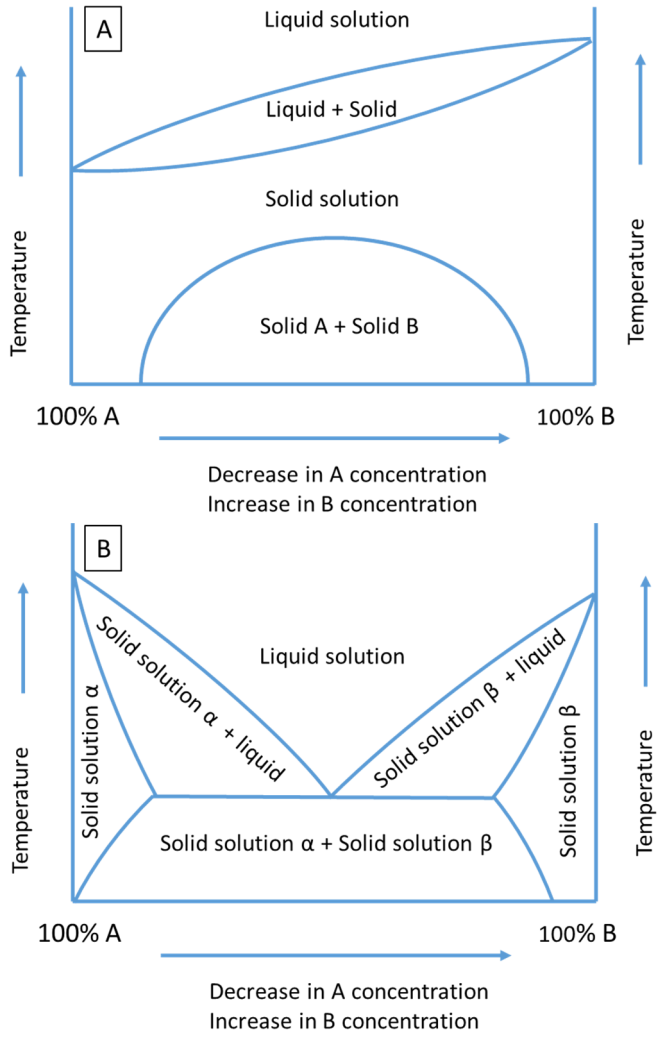

Figure 1.6: Continuous (A) and discontinuous (B) solid solution phase diagrams

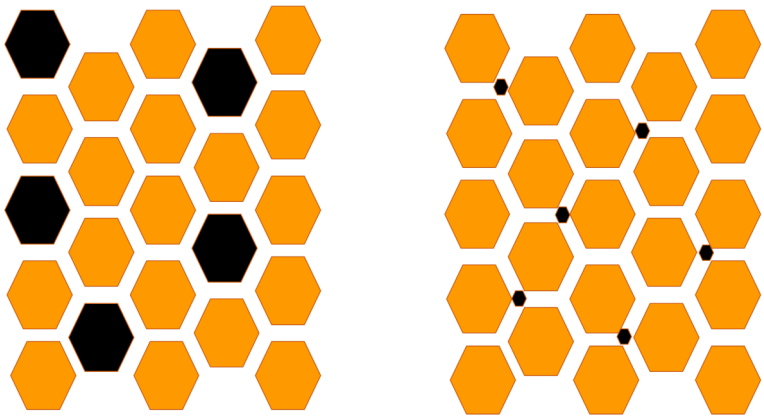

Figure 1.7: Schematic representation of substitutional solid solution (left) and interstitial solid solution (right). Black hexagons represent drug molecules (guest) while the orange hexagons represent the carrier (host) molecules

In the literature, it has been reported that several hydrophobic drugs form crystalline solid solutions with some excipients. The possible formation of interstitial solid solution between clofibrate and various molecular weight grades of PEG was considered as the contributing factor for enhancing the dissolution properties of the drug (46). Similar findings were concluded in the case of the oxazepam where its dissolution profiles are significantly enhanced by solid solution formation with PEG (47). However, other more recent studies showed that drugs dispersed in PEG are more likely distributed as molecularly dispersed in the amorphous fraction of these polymers or as nanocrystals that reported to be distributed into the interfibrillar, interlamellar or interspherulitic spaces of the PEG/PEO polymer carriers (48-51). Nevertheless, members of PEG polymers and other polymers are also reported to form cocrystals or mixed crystals with several drugs such as griseofulvin (52-55).

1.2.1.3 Glass solutions and suspensions

The third category of solid dispersions is glass dispersions in which the drug is either molecularly dispersed as single phase (glass solution) or phase separated mixtures in which the drug present as amorphous domains and/or crystalline fraction distributed in an amorphous polymer or polymeric blend (glass suspension) as illustrated in **Figure 1.8** (56, 57).

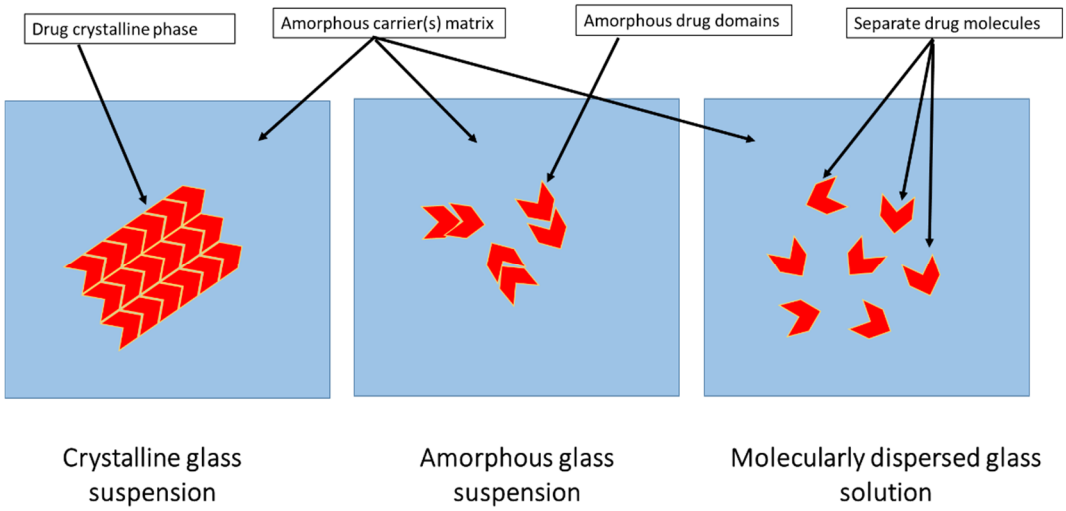

Figure 1.8: Schematic representation of glass solutions and suspensions

This class has attracted the attention of researchers to formulate amorphous solid solutions for poorly water soluble drugs like BCS class II because these mixtures have the maximum ability to improve the dissolution rate and the solubility of these drugs. Unlike crystalline or semi-crystalline systems, the individual molecules of amorphous systems lack the repetitious order and distributed randomly which makes the incorporation of the drug in the interstitial spaces between the polymer chains easier compared to crystalline polymers. Due to the lack of crystallinity, amorphous systems exhibit a characteristic behaviour of existing in the solid-like (glass) and liquid-like (supercooled liquid or rubbery) states depending on their temperature. The range of temperatures in which the system transforms from its glass to supercooled liquid states is termed the glass transition (T_g). Several theories explained the physics behind this thermal event like the free volume, configurational entropy, potential energy landscape and mode coupling theories. The T_g is mostly considered as an important parameter to estimate the stability and miscibility of amorphous solid dispersions due to the significant variation in the properties of the system above and below this thermal event. The solubility/dissolution properties of many poorly water soluble drugs have been reported to be significantly enhanced by the formation of molecular level amorphous solid dispersions (24, 25, 29, 44).

Amorphous polymers like PVP, HPMC and HPMC-AS are found to stabilise molecularly dispersed celecoxib resulting in an improvement in its release profile (58). The same polymers have found to improve the dissolution and maintain supersaturation in solution state for variable periods depending on the type of polymer and the loading percentage of the model drug danazol (59). Furthermore, an amorphous polymeric blend of PVP K90 and Eudragit E100 showed

significant enhancement in the dissolution profile and stability of molecularly dispersed poorly water soluble drug indomethacin (60).

1.2.1.4 Amorphous precipitations in crystalline carrier

In this type of solid dispersions, the solute (drug) phase is separated as amorphous domains in the crystalline carrier. Since the amorphous form is expected to have higher solubility compare to crystalline form, this category of solid dispersions can be considered as a mean to improve the dissolution properties of poorly water soluble drugs (44). The presence of phase separated fraction of amorphous indomethacin in the semicrystalline polymer PEG 6000 is an indication of the presence of this kind of solid dispersion (48). Similar findings have also confirmed the precipitation of amorphous bifonazole and acetaminophen in semicrystalline PEO−PPO−PEO triblock copolymers (Poloxamers® 188 and 407) solid dispersions (61). It was reported that amorphous glibenclamide precipitated in the semi-crystalline PEG 4000 is a possible explanation for the improvement in the dissolution properties of the drug (62).

1.2.1.5 Compound or complex formation

Complex formation between poorly water soluble drugs and hydrophilic carriers can also be considered as mean to improve their dissolution profiles and consequently enhance their bioavailability. Several examples of hydrophilic carriers have demonstrated their ability to form complexes with drugs such as cyclodextrins, PVP, PEG and PEO. Cyclodextrins are cyclic compounds characterised by hydrophobic interior cavities and the ability to form noncovalent inclusion complexes with a variety of drugs (27, 63-66). PVP as a hydrophilic amorphous polymer used widely for preparing solid dispersions has also reported to form complexes with BCS class II drugs resulting in an increase in their aqueous dissolution properties (67-69). In addition, hydrophilic solid dispersions of PEG and PEO have been shown to form soluble complexes with hydrophobic drug molecules such as griseofulvin, diflunisal and carbamazepine (54, 70, 71). The schematic representation of these complexes is illustrated in **Figure 1.9**.

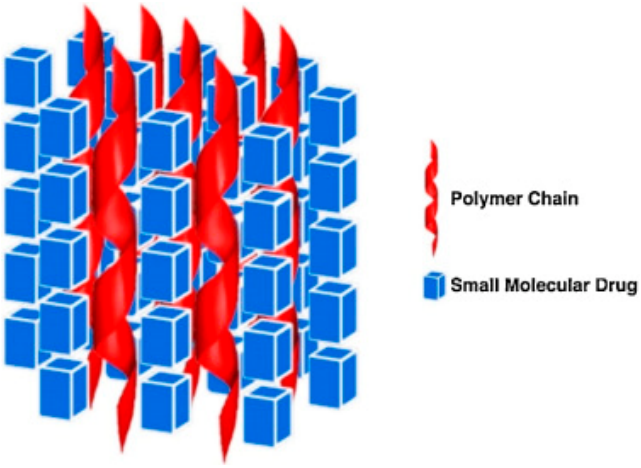

Figure 1.9: Schematic representation of drug-PEG inclusion complexes; adapted from reference (54)

1.2.1.6 Combination solid dispersions

Solid dispersions can exist as a mixture of two or more of the previously mentioned classes in single system depending on the number, characteristics and the degree of interaction between their constituents. Consequently, the global improvement in the dissolution profile of poorly water soluble drugs can be explained based on the individual class of solid dispersions. It was reported that PEO based mucoadhesive buccal patches of the antifungal drug ciclopirox olamine were heterogeneous solid dispersions composed of multiple phases of molecularly dispersed, amorphous, crystalline fractions resulting in an overall improvement of the poorly water soluble drug from its final formulation (50). Also, the structural diversity of the polymeric carriers was found to control the formation of multiphasic solid dispersions of acetylsalicylic acid prepared by freeze drying as seen using solid state NMR (72). Furthermore, the immiscibility between different polymers in polymeric blend solid dispersions found to form multiphasic solid dispersions of different characteristics (73).

1.3 Drug-polymer miscibility predictions for solid dispersion development

Theoretical prediction methods are considered as important approaches during the development of pharmaceutical products for selecting the most suitable excipients candidates for active pharmaceuticals. These approaches have been widely used for predicting quantitative structure-property relationships like solubility, permeability and biopharmaceutical profiles using a variety of methods (74-76). Concerning solid dispersions, these methods are also adapted to predict the

miscibility and stability of drugs in the different carriers as a preformulation strategy to select the best excipient candidates that show the highest solubilisation and stabilisation properties (77-80). Maintaining the stability of molecular level solid dispersions is a key parameter to ensure the enhancement in the solubility/dissolution properties of poorly water soluble drugs. Failure to achieve this requirement is expected to partially or completely abolish the formulation objectives behind solid dispersions. Using these predictions, it would be possible to select with higher certainty and more time and cost effective way the suitable carrier excipients that are more likely producing successful formulations.

Solubility and miscibility are critical physical parameters in the formulation of solid dispersions (3). Quantitatively, solubility is the concentration of solute in a saturated solution at a certain temperature while qualitatively it can be defined as the spontaneous interaction of two or more compounds to form a homogenous molecular dispersion (3). On the other hand, miscibility is used as a term describing the mutual solubilities of the components of the solution in liquid-liquid systems (3). Based on this, solutions are classified as subsaturated, saturated and supersaturated depending on the concentration of the solute in the solution below, at or above the saturation limit at specified temperature respectively (81). The degree of saturation of the system is critically affecting the physical state of the drug in the solid dispersion. Systems with drug concentrations at or above the saturation limits are more likely subjected to physical stability problems like phase separation affecting the quality of the product (82). Thus, predicting the solubility of the drug in the polymeric carrier system is crucial as it gives an indication of the solubilisation limits of the carrier which in turn may affect the stability of the final formulation.

1.3.1 Solubility parameter approach

The solubility parameter (δ) approach is one of the widely used prediction methods for the estimation of the solubility between the components of mixtures including polymer-drug blends (83, 84). This approach is based on the observation that the solubility of a polymer in organic solvents can be expressed directly by its cohesive properties which can be quantitatively expressed as the cohesive energy. The cohesive energy per unit volume is termed as the cohesive energy density. Hildebrand in 1936 proposed the square root of the cohesive energy density as a parameter to describe the behaviour of certain solvents. In 1949, this parameter was named as solubility parameter and given its known symbol (δ). Because the chemical structure of the polymer is largely the determinant of its solubility in different organic solvents, the similarity in the chemical structure of both compounds is in favour of solubility 'like dissolves like' (3). This

means that the solubility of the two components is in favour if their solubility parameters are similar. It should be mentioned that the solubility parameter of the polymer is defined as the square root of the cohesive energy density at room temperature in its amorphous state as shown in **Equation 1.1**.

$$\delta = \sqrt{\frac{Ecoh}{V}} \text{ ..... } \textbf{Equation 1.1}$$

where δ is the solubility parameter at 298 K in $(J/cm^3)^{1/2}$ or $(MJ/m^3)^{1/2}$ or $MPa^{1/2}$, E_{coh} is the cohesive energy (J/mol) and V is the molar volume (cm^3. mol^{-1}). It should be mentioned that the E_{coh} is determined for low molecular weight liquids by calculating the closely related molar heat of evaporation (ΔH_{vap}) at constant temperature as seen in **Equation 1.2**.

$$Ecoh \approx \Delta Hvap - RT \text{ ..... } \textbf{Equation 1.2}$$

where R is representing gas constant and T is the absolute temperature.

The group contribution method was derived by Dunkel (1928) who considered the E_{coh} of low molecular weight compounds as additive property. The same approach was applied to the polymers by other researchers like Hayes (1961), Di Benedetto (1963), Hoftyzer and Van Krevelen (1970) and Fedors (1974). Depending on the method used for estimating the cohesive energy, the values obtained are different between authors. It was found that the solubility of many amorphous polymers and other liquids are not only dependent on the dispersion forces between structural units as stated by Hildebrand, but also dependent on polar interactions and hydrogen bonding of interacting groups. Thus, the refined cohesive energy can be formally expressed as:

$$E_{coh} = E_d + E_P + E_h \text{ ..... } \textbf{Equation 1.3}$$

where E_d is dispersive forces contribution, E_P is polar forces contribution and E_h is hydrogen bonding forces contribution. **Equation 1.3** can be expressed in terms of the solubility parameter based on the three contributing components as follow:

$$\delta^2 = \delta_d^2 + \delta_p^2 + \delta_h^2 \text{ ..... } \textbf{Equation 1.4}$$

Hoftyzer and Van Krevelen method was widely used to calculate the solubility parameters of the drug and polymer blends using **Equations 1.5-1.8**.

$$\delta = \sqrt{\delta_d^2 + \delta_p^2 + \delta_h^2} \text{ ..... } \textbf{Equation 1.5}$$

$$\delta_d = \frac{\Sigma\, Fdi}{V} \quad \text{..... Equation 1.6}$$

$$\delta_p = \frac{\sqrt{\Sigma\, F^2 pi}}{V} \quad \text{..... Equation 1.7}$$

$$\delta_h = \sqrt{\frac{\Sigma\, Ehi}{V}} \quad \text{..... Equation 1.8}$$

where δ is solubility parameter $(MJ/m^3)^{½}$, F_{di} is the dispersion component of the molar attraction constant $(MJ/m^3)^{½}$. mol^{-1}, F_{pi} is the polar component of the molar attraction constant (MJ/m^3). mol^{-1}, E_{hi} is hydrogen bonding energy component $J.mol^{-1}$ and V is molar volume cm^3. mol^{-1}. The solubility parameters of the drug and other excipients are also calculated by Hoy group contribution method using **Equations 1.9-1.11**.

$$\delta = \frac{(F_i + B)}{V} \quad \text{..... Equation 1.9}$$

$$\delta = \frac{(F_i + B/\mathbf{n})}{V} \quad \text{..... Equation 1.10}$$

$$n = 0.5/\Delta T \quad \text{.....Equation 1.11}$$

where δ is total Solubility parameter $(MJ/m^3)^{½}$, F_i is molar attraction function $(MJ/m^3)^{½}$. mol^{-1}, B is the base value (which is 277 in this case), n is the number of monomers per effective chain segment of the polymer, ΔT is Hoy correction for non-ideality for polymers and V is the molar volume $cm^3.mol^{-1}$.

1.3.2 Melting point depression approach

Melting point depression can also be used as an approach to investigate drug-polymer and polymer-polymer miscibilities as a preliminary step before solid dispersion preparation (85-87). This method is based on the fact that melting of compounds occurs at temperatures at which the chemical potential of the crystalline solid is equal to that of the molten state. If the drug and the polymer are miscible, the chemical potential of the mixture is expected to be less than that of pure amorphous form of the drug. In this case, the depression in melting temperatures of different drugs in the same polymer gives an indication of the miscibility of these drugs in that polymer (79, 85, 88). Thermodynamically, solubility can be an endothermic, athermic or exothermic event. Weak exothermic, athermic and endothermic mixing usually accompanied by small or no melting

point depressions. However, strong depressions are usually occurring with strong exothermic mixing. For immiscible drug-carrier blends, no depression in the onset of melting for the drug is expected to be observed as the melting of the drug is not affected by the presence or the absence of the carrier (79). Depression of melting can be used to construct plots of Gibbs of free energy of mixing and phase diagrams for drug-polymer mixtures using the experimental data from DSC and some theoretical equations derived from Flory-Huggins (F-H) interaction theory (77, 78, 89). F-H theory is widely used to investigate polymer-polymer miscibility and polymer-solvent miscibility as a modification of the original solution theory. By considering the amorphous form of drugs as a solvent, F-H lattice theory provides a rational explanation for the thermodynamics of drug-polymer solubility (85). Based on this theory, the ΔG_{mix} can be expressed in **Equations 1.12-1.13** (77, 85, 87):

$$\Delta G_{mix} = \Delta H_{mix} + T\Delta S_{mix} \quad \textbf{Equation 1.12}$$

$$\Delta G_{mix} = RT\,(\phi_{drug} \ln \phi_{drug} + (\phi_{polymer}/m) \ln\phi_{polymer} + \chi_{drug\text{-}polymer}\, \phi_{drug}\, \phi_{polymer} \quad \textbf{Equation 1.13}$$

where ΔG_{mix} is the Gibbs free energy of mixing, ΔH_{mix} is the enthalpy of mixing, T is the absolute temperature, ΔS_{mix} is the entropy of mixing, R is the gas constant, ϕ_{drug} is the drug volume fraction, $\phi_{polymer}$ is the polymer volume fraction, m is the ratio of the volume of polymer chain to the volume of the drug molecule and $\chi_{drug\text{-}polymer}$ is F-H drug-polymer interaction parameter.

Depression of melting due to the presence of the polymer can be correlated to interaction parameter (χ) at specified temperature using the DSC data and **Equation 1.14** (77-79, 85, 87, 88):

$$(1/T_{m\ depressed}) - (1/T_{m\ pure}) = R/\Delta H_f\, [\ln\phi_{drug} + (\phi_{polymer}/m) \ln\phi_{polymer} + \chi_{drug\text{-}polymer}\, \phi^2_{polymer}] \quad \textbf{Equation 1.14}$$

where $T_{m\ depressed}$ is the depressed melting temperature of the drug due to the presence of the polymer (sometimes expressed as the onset or offset of the melting peak), $T_{m\ pure}$ is the melting temperature of pure drug and ΔH_f is the melting enthalpy of pure drug. The interaction parameter ($\chi_{drug\text{-}polymer}$) can be obtained by plotting $(1/T_{m\ depressed}) - (1/T_{m\ pure}) * (\Delta H_f/-R) - \ln \phi_{drug} - (1- 1/m)\, \phi_{polymer}$ versus $\phi^2_{polymer}$ using the DSC results of the drug-polymer binary physical mixtures with high drug loadings (more than 70% w/w drug loading) and slow heating rates (0.5-1 ℃/min). The slope of the line is the interaction parameter at that temperature. The drug-polymer interaction parameter (χ) at room temperature can also be calculated from the solubility parameter using **Equation 1.15** (77, 78, 85, 88):

$$\chi_{drug\text{-}polymer} = (V_0/RT)\ (\delta_{drug} - \delta_{polymer})^2 \text{.....} \textbf{Equation 1.15}$$

where V_0 is representing the volume of the lattice site, δ_{drug} and $\delta_{polymer}$ are the solubility parameters of the API and the polymer respectively. In order to calculate the drug-polymer interaction parameter (χ) at any temperature, the interaction parameters determined from the previous two approaches (solubility parameter using **Equation 1.15** and melting point depression using **Equation 1.14**) can be substituted in the simplified **Equation 1.16** to generate a series of interaction parameters at different temperatures (77, 85).

$$\chi_{drug\text{-}polymer} = A + (B/T) \text{.....} \textbf{Equation 1.16}$$

where A and B are values of the temperature-independent term (entropic contribution) and the value of the temperature dependent term (enthalpic contribution), respectively. Plots $\Delta G_{mix}/RT$ versus volume fraction of the drug (ϕ_{drug}) using the calculated interaction parameters at different temperatures can be used as an indication about drug-polymer miscibility as a function of drug volume fraction. Negative values of $\Delta G_{mix}/RT$ give an indication about drug-polymer miscibility while positive values indicate immiscibility of the binary system. This can be further extended to constructing drug-polymer phase diagram using the calculated interaction parameters at different temperatures and drug concentrations as illustrated in **Figure 1.10**.

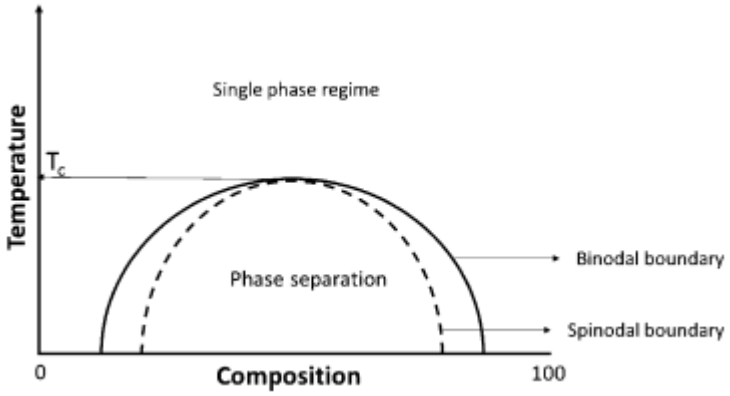

Figure 1.10: Typical phase diagram for binary drug-polymer blends as a function of temperature and composition; adapted from reference (90)

The phase diagram can provide predictions about the stability of drug-polymer mixtures with changes in temperature and composition during processing and storage. The binodal curve represents the phase boundary. Outside it, the system exists as a single phase molecularly miscible system in all compositions. This boundary can be determined using **Equations 1.13 and 1.16** and depends on the favourable mixing based on ΔG_{mix} (negative value). In this case, even if the mixing

is not achieved at ambient temperature, the system can be molecularly dispersed at elevated temperature and/or at lower drug loading due to the changes in the thermodynamics of the system (77, 78, 85, 90). On the other hand, the spinodal boundary is determined by setting the second derivative of ΔG_{mix} equal to zero as shown in **Equation 1.17** (77, 78, 85, 90).

$$(1/\phi_{drug}) + (1/\phi_{polymer}) + 2\chi_{drug\text{-}polymer} = 0 \quad \text{.....Equation 1.17}$$

The system below the spinodal boundary is unstable leading to phase separation without any significant energy barriers. Despite the thermodynamically unfavourable mixing below the spinodal curve, the system may be still kinetically stabilised 'trapped' by the reduced molecular mobility caused by the glassy nature of the polymer (77, 78, 85). The zone between the spinodal and binodal curves representing the metastability zone. In the metastable region, the system is predicted to form drug-rich and polymer-rich domains without drug recrystallisation (77, 78, 85).

1.4 Thermodynamics of solid dispersions

1.4.1 Physical stability of solid dispersions

Despite the valuable advantages of solid dispersions for improving the solubility and/or dissolution properties of poorly soluble drugs over the last 40 years, only a few number of these preparations have been translated into marketed products (27, 91-93). The most important reason behind this is their physical instability which may lead to drug recrystallisation resulting in a reduction in the dissolution profiles and bioavailability (27, 91-93). In order to fully understand the physical stability of solid dispersions, it is important to explain the key factors that affect physical behaviour of these preparations including glass transition temperature, molecular mobility, phase separation of the dispersed drug and/or the components of the carrier.

1.4.1.1 Glass transition (T_g)

Glass transition (T_g) is a physical property characteristic of amorphous materials which can be defined as a range of temperature degrees over which the material converts from its solid 'glassy' state to its liquid 'rubbery' state and vice versa. Typically, single phase amorphous system has single glass transition temperature (24). Unlike melting which is first order phase transition (the derivative of change in the free energy ΔG with respect to temperature is not equal to zero), the

T_g is a second order phase transition in which the second derivative of change in the free energy ΔG with respect to temperature is not equal to zero while the first derivative is equal to zero. Using DSC, the T_g is seen as a step reflecting a transition in the heat capacity (ΔC_p) during the heating or cooling cycles. **Figure 1.11** explains the possible pathways through which a crystalline material exists in a liquid state above melting converts into a solid state with crystalline or glassy properties passing through crystallisation or glass transition events respectively. When the cooling rate is slow enough, crystallisation process occurs at a temperature corresponding to melting point (assuming no supercooling happens). The formation of crystallised material (bottom line of **Figure 1.11**) shows a dramatic reduction in the thermodynamic parameters of the system (free volume 'the difference between the total volume and the volume occupied by the individual molecules of the system', enthalpy and entropy). The reduction in the free volume is attributed to the high order of arrangement of the molecules in the crystal lattice. However, when the cooling rate is too rapid for the crystallisation to occur, the liquid enters the super-cooled liquid 'rubbery' state without any discontinuity in the aforementioned thermodynamic parameters. Further cooling the rubbery state will lead to the glass transition step in which there is a loss of the kinetic equilibrium and the material becomes immobile as it acquires the characteristics of glass solid with a decrease the molecular mobility in a discontinuous manner. The T_g is a kinetic process affected by the cooling rate and therefore lower T_g values are expected for slow cooling rates as illustrated in **Figure 1.11** (94, 95). It should be mentioned that the average time scale of molecular motion of < 100 s and viscosity between 10^{-3} and 10^{12} Pa.s for the rubbery state while for the glassy state, the mobility is hugely reduced with an increase in the viscosity > 10^{12} Pa.s (95-97).

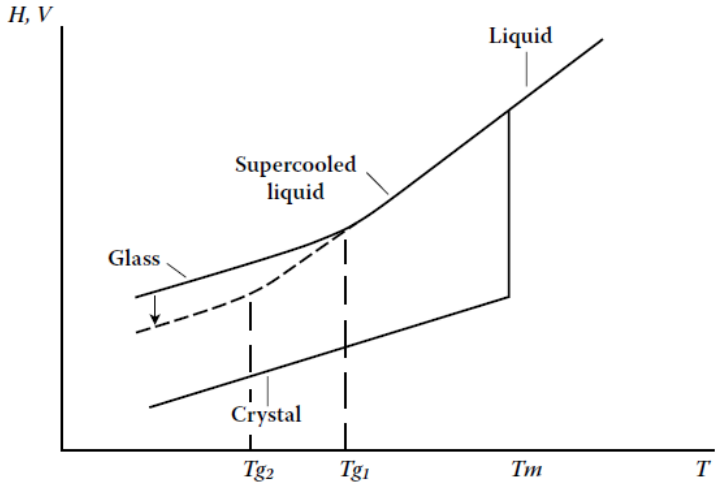

Figure 1.11: Schematic representation of glass transition (Tg) and comparison between the behaviours of crystalline and glass forming systems; adapted from reference (94)

The T_g of amorphous solid dispersion mixtures can be estimated using different theoretical and empirical equations like Fox and Gordon-Taylor (G-T) equations as a function of mixture composition. Compared to G-T equation, Fox equation assumes that the components of the amorphous blend have the same density and does not include the changes in thermal expansivity of the T_g in its expression. The two equations for binary drug-polymer mixture can be described in **Equations 1.18-1.20** (24, 98):

Fox equation:

$$1/T_{g\,mix} = (w_{drug}/T_{g\,drug}) + (w_{polymer}/T_{g\,polymer}) \quad \textbf{.....Equation 1.18}$$

G-T equation:

$$T_{g\,mix} = (w_{drug} \times T_{g\,drug}) + (Kw_{polymer} \times T_{g\,polymer})/(w_{drug} + Kw_{polymer}) \quad \textbf{.....Equation 1.19}$$

where $T_{g\,mix}$ is the predicted T_g of drug-polymer blend, w_{drug} is the weight fraction of the drug, $T_{g\,drug}$ is the T_g of the drug, $w_{polymer}$ is the weight fraction of the polymer, $T_{g\,polymer}$ is the T_g of the polymer, and K is a constant derived from the true densities (ρ_{drug} and $\rho_{polymer}$) and the change in thermal expansivity of T_g ($\Delta\alpha_{drug}$ and $\Delta\alpha_{polymer}$) of the two components of the mixture (24, 98).

$$K = (\rho_{drug} \times \Delta\alpha_{polymer})/(\rho_{polymer} \times \Delta\alpha_{drug}) \quad \textbf{.....Equation 1.20}$$

It should be mentioned that G-T equation assumes ideal volume additivity of both constituents and no specific interaction between them 'ideal mixing behaviour'(24). Experimentally, ideal mixing between the different components of solid dispersions is expected to give comparable results to the predicted results estimated using G-T equation. However, positive or negative deviations from the predicted T_g values reflects non-ideality of mixing. Positive deviation results from the interaction between the components of the mixture. On the other hand, the diffusion of the small molecular weight drug inside the polymer leading to a higher free volume than the anticipated one in G-T equation and/or the weaker drug-polymer interactions compared to the original drug-drug interactions causes the negative deviation (24, 99).

1.4.1.2 Molecular mobility

An essential parameter that governs the physical stability of any molecular level solid dispersion is the molecular mobility of the drug in the dispersion (97, 100). It was reported that the overall molecular mobility of molecularly dispersed drug is the result of different kinds of molecular

rearrangements including global mobility (α-relaxation), local mobility (β-relaxation) and secondary relaxations due to self-association through hydrogen bonding depending on the storage temperature and the T_g temperature of the system. α-relaxation has been thought as an important factor that determines the physical stability of molecularly dispersed drugs in solid dispersions (96).

Molecular mobility for amorphous systems is usually expressed in terms of the relaxation time (τ) and it may be caused by several processes including enthalpic relaxation, volume relaxation, dielectric relaxation and or spin-lattice relaxation (100-102). Molecular mobility as the reciprocal of relaxation time can be determined using a variety of methods like MTDSC, dielectric relaxation spectroscopy, and solid-state NMR spectroscopy. Using MTDSC, the relaxation time can be estimated using some empirical equations like the empirical Kohlrausch-William-Watts, Adam-Gibbs and Vogel-Tammann-Fulcher equations (103, 104).

1.4.2 Factors affecting physical stability of solid dispersions

Physical instability of molecular level amorphous solid dispersions is most commonly happened above rather than below the T_g. This second order phase transition is usually considered as a benchmark for monitoring the stability of these systems. As a general rule, amorphous dispersions stored at temperatures 50℃ below their T_g are mostly considered as physically stable with negligible crystallisation tendency (24). Accordingly, the effect of storage temperature relative to T_g is recognised as important parameter and its impacts are complex because it can control the physical stability in different pathways with variable outcomes. As an example, storing amorphous solid dispersions at low temperature can decrease the recrystallisation rate of molecularly dispersed drug due to the increased viscosity of the dispersing phase leading to reduction in the mobility. At the same time, this may support the formation of new nucleation sites leading to more crystal growth (105). Taking into consideration that storing the samples at lower temperatures reduces the thermodynamic solubility of the dispersed drug in the carrier (24). Thus, and depending on the observed growth, it can be concluded which pathway is the dominant; the diffusion or the thermodynamic and based on that the storing temperature may have a positive or negative impacts on the physical stability of the system under investigation (105).

It was observed that the presence of other excipients can affect the magnitude of α-relaxation process significantly. Global mobility was found to be directly proportional to the extent of the plasticising activity of the inactive components of the formulation. Water is one of the frequently

included excipients in the formulation either intentionally as a component of the preparation or accidently due to the entrapped moisture during processing and/or storage. In addition, it has low T_g and strong plasticising activity, therefore, it is shown to play a critical role in increasing the global mobility of the system and enhancing drug crystallisation from its dispersion (106, 107). In other words, the increased hygroscopicity of the formulation due to moisture uptake leads to increase the chemical potential of the dispersed drug and increase the degree of supersaturation and the thermodynamic driving force of crystallisation (108-110). On the other hand, some polymers with antiplasticising activity and/or hydrogen bonding ability help to maintain the physical stability of the dispersion and inhibit the recrystallisation process (111, 112).

For solid dispersions containing semicrystalline excipients, physical stability studies followed different approach compared to molecular level amorphous solid dispersions. For these heterogeneous systems, monitoring physical stability usually conducted by investigating parameters like the stability of crystalline relative to amorphous domains and the possibility of crystal thickening. In addition, the tendency of these complex mixtures to undergo phase separation of the molecularly dispersed drug in the amorphous fraction and its relationship with the percentage of drug loading and the effect of external factors like storage temperature and relative humidity on the whole system. These studies also provide information about the physical stability changes in the carrier like the increase in the crystalline fraction of the semicrystalline carrier at the expense of the amorphous domain which is responsible about the solubilisation of poorly water-soluble drugs on the molecular level (48, 113-117).

1.4.3 Phase separation

Physical instability of solid dispersions generally leads to phase separation of their individual components resulting in a partial or complete lack of the dissolution enhancement (3, 24). The concept of phase separation has been used to describe different cases related to solid dispersions. It has been used to indicate the conversion of the active pharmaceuticals from molecularly dispersed status to separated amorphous domains or crystalline fractions (3, 24). In this case, the phase separation is dependent on the inherent recrystallisation tendency of the drug, T_g of the system relative to storage temperature, viscosity of the dispersing phase, the presence or absence of interaction between the dissolved drug and the carrier, storage temperature and relative humidity (3, 24). In addition, phase separation sometimes used to describe the miscibility between immiscible/partially miscible polymeric blend as illustrated in **Figure 1.12**. These multiphasic matrices were recently demonstrated their superiority to solubilise, stabilise the drug as a

molecularly dispersed multicompartmental system with more resistance to mechanical stress caused by further formulation processing (73). Phase separation in both meanings is discussed in details in Chapter 4 as a formulation strategy for improving the solubility of poorly water soluble drugs.

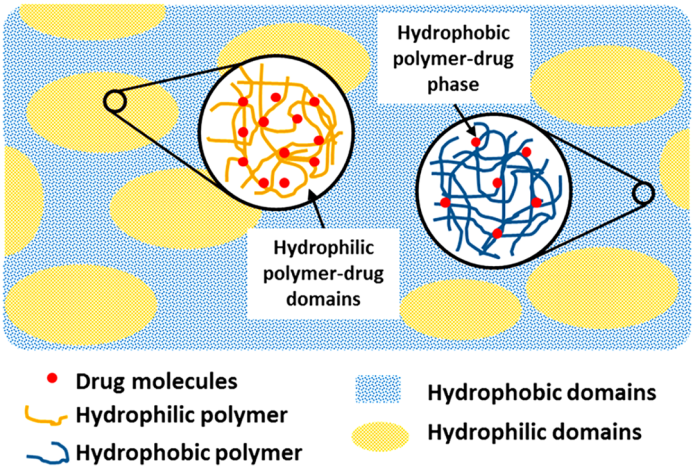

Figure 1.12: Schematic representation of intentionally phase separated drug loaded polymeric blend; adapted from reference (73)

1.4.4 Approaches developed to improve physical stability of solid dispersions

Several strategies have been adapted to reduce the molecular mobility of dispersed drugs to improve their physical stability in their dispersion. The use of polymeric carriers with higher T_g relative to storage temperature can help to restrict the mobility of molecularly solubilised drugs by antiplasticising effect. This can lead to an increase in the viscosity of the matrix and reduction in the diffusion of the drug to form aggregates as a preliminary step that leads to the formation of drug crystal lattice (118-120). This approach has been found to be unreliable as the inherent recrystallisation tendency of the drug plays a critical role in the devitrification process in addition to the difference between the T_g of the system and the temperature of storage (24, 121, 122). Thus, another mechanism that can be used to stabilise the solubilised drug by effective interaction with the carrier component(s) through ionic, hydrogen, dipole-dipole and ion-dipole interaction have been proven as a successful approach to improve the miscibility and stability of solid dispersions (111, 123, 124). It should be mentioned that the majority of polymers used in the fabrication of solid dispersions have structural sites to interact with drugs' molecules in the dispersions.

However, there are some examples of stable solid dispersions in which there is no specific interactions were detected between the dispersed drug and the carrier (120, 125).

Physical stability of the molecularly dispersed drug is a critical factor not only in the solid state during the storage period of the shelf life of the product which may be affected by factors like relative humidity and temperature, but also after dissolution in the aqueous dissolution medium at the site of dissolution and absorption. The enhanced apparent solubility and dissolution rates by solid dispersions generate thermodynamically metastable supersaturated solutions which may cause the precipitation of the drug in the more stable crystalline form. Recrystallisation of the drug at the site of absorption is most likely will reduce the concentration of the drug available for absorption abolishing the gained advantage of dissolution enhancement via the solid dispersion approach. Drug recrystallisation can happen either before the liberation of the drug from the matrix after contact with the dissolution medium or after achieving supersaturated concentrations under non-sink conditions (126-128). It should be mentioned that the recrystallisation of poorly water soluble drugs from their supersaturated solutions is dependent on the drug loading percentage and the type of the polymer included in the formulation (129).

In order to physically stabilise the drug in its supersaturated solution, several approaches have been used to inhibit drug recrystallisation through the use of different excipients like polymers, surfactants and cyclodextrins. Drugs recrystallisation involves several stages: formation of supersaturation, nucleation (formation of stable nuclei) and crystal growth. The formation of stable nuclei is the result of diffusion of drug molecules in the supersaturated state and collide to each other to form stable and effective nucleating cluster to start the growth process. The diffusion rate is an important parameter that controls the nucleation process (130, 131). Materials used to maintain supersaturation concentrations functions by different mechanisms that can inhibit the nucleation and/or crystal growth including (130, 131):

1. Changing the properties of the dissolution medium like saturated solubility and surface tension.
2. Altering crystal-medium adsorption layer interface.
3. Blocking crystal growth by selective adsorption to the interface of the crystal.
4. Disrupting surface growth layers by adsorption between these layers.
5. Adsorption into rough growth surfaces making them smooth and flat.
6. Changing crystal face surface energy which may alter the level of solvation.

It was found that polymers like PVP, PEG 400 and HPMC act as growth inhibitors by different mechanisms like hydrogen bonding, adsorption to the crystal and accumulating at the bulk crystal interface thus providing resistance to the diffusion of the molecules. Also, HPMC was found to act as crystal habit modifier by having different crystal faces adsorption capacities. The extent of adsorption is affected by the hydrogen bonding functional groups exposed at each face of the growing crystal (130-132). Furthermore, some polymers can prevent recrystallisation of certain drugs by increasing their saturated solubility and reduction in the level of supersaturation (133). Surfactants also have been shown to decrease the tendency to recrystallisation by micelles solubilisation and alteration the surface tension at the bulk crystal interface. They can also modify the habit and the size distribution of recrystallised materials (133-135). Additionally, the presence of surfactants during the recrystallisation of drugs from supersaturated solutions was shown to be the preferentially target the process into certain polymorphic forms by inhibiting the polymorphic transformation from metastable to stable polymorphic forms of drugs (136). It was reported that polymorph IV of celecoxib was generated from precipitated drug suspension in the presence of HPMC and Polysorbate 80. The formation of this polymorphic form was explained by changing in bulk diffusivity of drug molecules (bulk viscosity), surface tension and supersaturation induced by the presence of the two excipients. This leads to formulation controlled crystallisation (concentration and ratio dependent) which is thought as very important subject in pharmaceutical industry research investigations (137). Cyclodextrins also shown to play a role in inhibiting nucleation by the formation of inclusion complexes resulting in an enhancement in their solubility. These group of inclusion compounds were also reported to retard nucleation by non-complexation mechanisms similar to that of the aforementioned for polymers (131). It should be mentioned that the existence of cyclodextrins in drugs' supersaturated solutions can play a significant role in polymorphic transformation and crystal habit modifications (138, 139).

1.4.5 Other drawbacks of solid dispersions

Solid dispersions with their valuable advantages of improving the apparent solubility and dissolution rate of poorly water soluble drugs have some drawbacks reflected directly on the limited number of marketed products (27, 91-93). These problems are most importantly related to the physical stability of the dispersed drug in the carrier matrix during processing, storage and dissolution at the site of absorption (discussed in the previous section). Besides, impacts of thermal degradation, residual of solvents, downstream processing during and after solid dispersions formulation into their final dosage forms and ability to scale up to manufacturing

levels are also critical factors in the development of these preparations into marketed medicines (18, 24, 32).

1.4.5.1 Impacts of thermal degradation

Solid dispersions can be prepared by different methods including melting, solvent or melting-solvent methods. Depending on the method of preparation, there are some problems related to processing that hinder these preparations from reaching the marketing stage as safe, effective and convenient products. Preparation by melting methods sometimes involves the use of high temperatures to thermally incorporate the drug in the carrier(s) which may cause the thermal degradation of one or all the constituents of the mixture resulting from high shear forces and high processing temperatures (139). It was found that partially hydrolysed PVA polymers are more susceptible to thermo-mechanical degradation compared to fully hydrolysed PVA grades when exposed to multiple extrusions at an elevated temperature above 200℃. The degradation was attributed to the presence of the vinyl acetate group in their structures (140). In addition, it was reported that spray drying can cause the degradation of drugs during the rapid drying from their slurries affecting the quality of the final product (141). Furthermore, some excipients like PEG and Tween 80 were reported to be liable to random chain scission resulting in a reduction in the chain length (molecular weight) due to thermal oxidative degradation (142-145). For PEG polymers, members of low molecular weights are more susceptible to degradation compared to higher molecular grades (144). The chemical stability of the excipients during processing and storage is an important parameter to be investigated as it may affect the quality and safety of the product and determine the suitable processing and storing conditions required to keep the formulation within the design requirements. The details of PEG and Tween 80 degradation is studied in details in Chapter 6.

1.4.5.2 Impacts of residual solvents

Preparation of solid dispersion by solvent evaporation methods involves solubilisation of the components in an organic solvent followed by evaporation of the solvent using a variety of techniques. The problems facing this approach are related to the entrapment of certain quantity of the organic solvents in the dispersions which might affect their suitability for therapeutic applications. Also, since organic solvents have reduced T_g temperatures, their entrapment in solid dispersions may have a plasticising effect which may criticise the physical stability of molecularly

dispersed drugs in the final products during storage. Thus, efficient solvent removal is one of the essential requirements for designing high-quality products based on solid dispersion approach (32, 146, 147).

1.4.5.3 Impact of downstream processing

Solid dispersions prepared via different processing methods are mostly intermediate products that need further processing to reach the final product stage (148-150). According to pharmacopoeias, each dosage form should meet certain quality control and compendial requirements to be approved for marketing as a commercial medicine. As an example, tablets should have certain physical specifications including weight, weight variation, drug content uniformity, thickness, hardness, disintegration time and dissolution profile in addition to the general features like diameter, size, shape and colour (151). Adding to that the difficulty to give the dosage form its desired functionality like orally disintegrating and floating dosage forms using conventional fabrication methods of solid dispersions (148, 149, 151, 152). This makes the production of solid dispersions as final dosage forms in a single processing technique is challenging process and not easy to be achieved for the vast majority of formulations reported in the literature. The problems encountered during the attempts to produce commercially successful dosage forms like tablets and capsules for clinical applications based on solid dispersions involve many difficulties like milling, sifting, poor flow and mixing properties, poor compressibility characteristics, and stability problems (18). It was reported that milling can destabilise supersaturated amorphous solid dispersion produced by hot melt extrusion by increasing the molecular mobility leading to phase separation (153). Also, it was found that compression can increase the extent of crystallisation of amorphous indomethacin due to increase in the molecular mobility caused by mechanical deformation. The increased tendency of crystallisation was caused by the significant elevation of the heat of crystallisation (ΔHc) and the reduced onset of crystallisation (154). It was also reported that the force of compression induced the phase separation of naproxen-PVP K25 and itraconazole-soluplus amorphous solid dispersions by plastic deformation that causes weakening and/or disruption of intermolecular hydrogen bonding between drug and polymer (155, 156). However, other study showed that compression force at and above a critical value (250 MPa) significantly affects the intrinsic dissolution rate (IDR) (defined as drug release per accessible area mg/cm^2) of amorphous indomethacin compacts leading to significant change in the corresponding IDR of the drug containing solid dispersion. The reduction in the IDR was attributed to the change in the surface available for dissolution (157). Interestingly, compression force and dwell time of compression were found to improve the miscibility of supersaturated

phase separated amorphous solid dispersions prepared by spray drying. The improved miscibility of the double T_g phase system by the application of pressure is explained by the reduction in the drug-rich domain size of about 30 nm to lower size caused by stressful deformation of glassy polymer and glassy solid dispersion causing remixing of the phases and the formation of the more homogenous system (158).

1.5 Manufacturing of solid dispersions

Solid dispersions are prepared by three major methods namely melting (fusion), solvent evaporation and melting solvent methods. The first two methods are the most commonly used techniques for the preparation of solid dispersions (32). In thermal processing techniques like hot melt extrusion and injection moulding, the active pharmaceuticals and other formulation excipients are melted/softened and mixed at a temperature above the lowest melting/T_g of all or some ingredients of the mixture. After melting/softening and blending at elevated temperature, the melt is then cooled to the solid state using a variety of cooling techniques (32). Solvent evaporation can be achieved by using different methods like freeze drying (159), rotary evaporation (160), spray drying (161), electrospinning (162), electrospraying (163) and supercritical fluid (SCF) process (164). Solid dispersions prepared using solvent evaporation methods by dissolving the drug and the carrier in an organic solvent (or a mixture of solvents) followed by the evaporation of the solvent (32). The quality of the solid dispersion prepared by this method is highly affected by the solvent system used and its removal rate (165). Different organic solvents were used in this approach such as ethanol (166-168), chloroform (169), methanol/chloroform mixture (126) or ethanol/dichloromethane mixture (170). The major advantage of this method over thermal processing techniques is the avoidance of subjecting the drug to thermal degradation especially for drugs that are sensitive to heat (171). However, complete solvent removal from the final products and the environmental issues caused by the use of large quantities of organic solvents is often problematic (165). This study focused on the use of thermal based hot melt extrusion in conjunction of injection moulding (HME-IM) and fused deposition modelling (FDM) 3D printing methods for preparing solid dispersions of poorly water soluble drugs.

1.5.1 Hot melt extrusion (HME)

HME is a highly recognised technique in the fabrication of solid dispersions based formulations with high scalability and diversity of pharmaceutical applications. This method which is primarily used in plastic, rubber and food industries was first introduced in the early 1930s and then applied in the pharmaceutical field at the beginning of 1970s (30, 32, 172). HME has many advantages compared to other solid dispersions processing methods. In addition to improving the bioavailability of poorly water-soluble drugs via molecularly dispersing poorly soluble drugs in hydrophilic carriers, HME functions as a safe and environmentally friendly process that can exclude any organic solvents during preparation (30). Also, HME is anhydrous method thus aqueous hydrolytic pathway can be eliminated which may affect the integrity of the active ingredients (173). Furthermore, using HME, it can be possible to overcome the compressibility problems of poorly compactable drugs because dosage forms of these drugs can be made in different shapes and sizes using additional geometry designing techniques (173, 174). It should be mentioned that dosage forms produced by this method show a higher degree of content uniformity for low dose drugs compared to other methods of pharmaceutical products formulation (175). Depending on the processing temperature and residence time, it can be possible to load higher percentages of drug contents in solid dispersions compared to other methods (173). HME combined with injection moulding acts as a continuous process with minimum processing steps and high efficiency which means that it is time-consuming because it excludes the required time for drying when solvents are involved during the formulation (176). Due to the flexibility of using a variety of excipients and mixing proportions, this technique can be used to produce dosage forms with controlled or immediate release, floating, fast dissolving formulations (tablets, capsules, films, pellets and implants). These formulations can be utilised to deliver a variety of drugs through different sites like oral, transmucosal, transdermal and implantation routes of administration (32, 173, 177).

There are two types of HME processes based on the addition of solvents to the mixture before the extrusion process: wet and dry HME processes. Wet HME involves the addition of certain solvent before processing to improve the quality of the product due to the softening and plasticising advantages of the added solvent (178). This process is also used to minimise the heat employed during extrusion to avoid the degradation of the components of the formulation. The dry HME process is the most commonly used method without the incorporation of any solvent (green process) and the extrusion process is entirely achieved by the use of heat (179).

1.5.1.1 Types of extruders

Hot-melt extrudates are generally produced by two types of machines namely screw extruders and ram extruders. The difference between these two kinds of equipment is that the former contains a screw rotating in a heated barrel while the latter has a ram or piston capable of generating high pressure to pump the extrudate into the die (179). The main disadvantage of ram extrusion is the limited melting capacity which results in a poor thermal uniformity in all portions of the extrudate. On the other hand, high shearing stress and uniform mixing can be achieved by using screw extruder. Screw extruders are composed of three portions including a part for transport and mixing of the fed materials, a mould for forming, and downstream auxiliary equipment for solidification, milling and collection of the finished products. These types of extruders have a feeding hopper, heating barrel with controlled temperature, rotating screw, die, and heating and cooling systems. Also, the equipment may be provided with other parts like mass flow feeder to control the feeding rate, analytical devices to investigate the properties of the extrudates, liquid and solid side stuffers, vacuum pumps, pelletizers, and others (179).

There are two types of screw extruders: single and twin screw extruders depending on the number of screws contained within the barrel (**Figure 1.13 A and B**). The most commonly used is the single screw extruder in which single screw 'with various dimensions depending on the extruder' rotating within the barrel for the feeding, mixing, melting and pumping of the extrudates. Single screw extruders are either flood fed or starve fed and most commonly they are of the flood feed type in which the rate of output can be controlled by the hopper over the feed throat and the speed of screw rotation. Melting of the fed materials can be brought about by the energy of the heaters and the shear caused by the screw. At the end of the process, the extrudates are produced by pumping the melted mixture into the die (178).

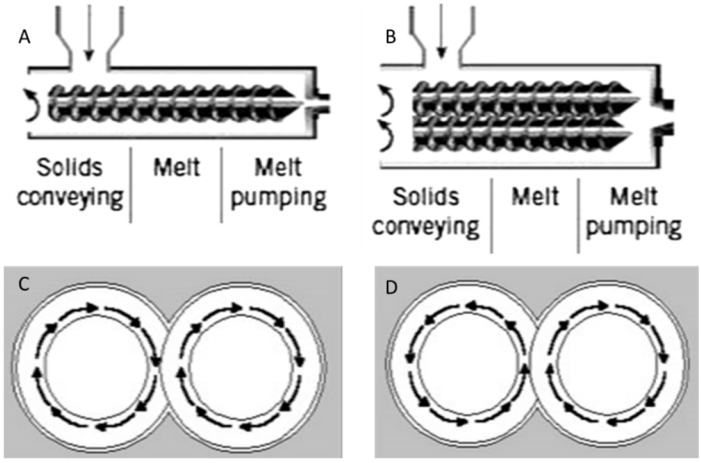

Figure 1.13: Types of hot melt extruders; A and B are single and twin screw extruders; C and D are the co-rotating and the counter rotating types; adapted from reference (30)

There are two types of twin extruders depending on the design of the screws contained within the extruder: co-rotating and counter-rotating twin extruders (**Figure 1.13 C and D**). The second one is used when very high stress is needed, but they have several drawbacks like the potential entrapment of air, excessive pressure generation and low maximum screw speed and output. On the contrast, the co-rotating twin extruders can produce higher output rates because the rotation of the screws is higher than that of the counter-rotating type. In addition, they exhibit good mixing and mass transport characteristics. Furthermore, the wearing of the barrel and the screws is found to be lower than that of the other type. Twin screw extruders are further classified into non-intermeshing and fully intermeshing where the latter is the most commonly used type because it provides self-wiping function thus preventing stasis of the soft mass which may lead to degradation (179). Twin-screw extruders may offer some advantages over the single-screw type involving including easier materials feeding, better dispersing abilities, substances processed are less subjected to overheating and shorter processing time. However, this type may be considered as more complicated compared to single screw extruders and more expensive (180).

The geometry of the screws is variable and dependent on the individual equipment as seen in **Figure 1.14**.

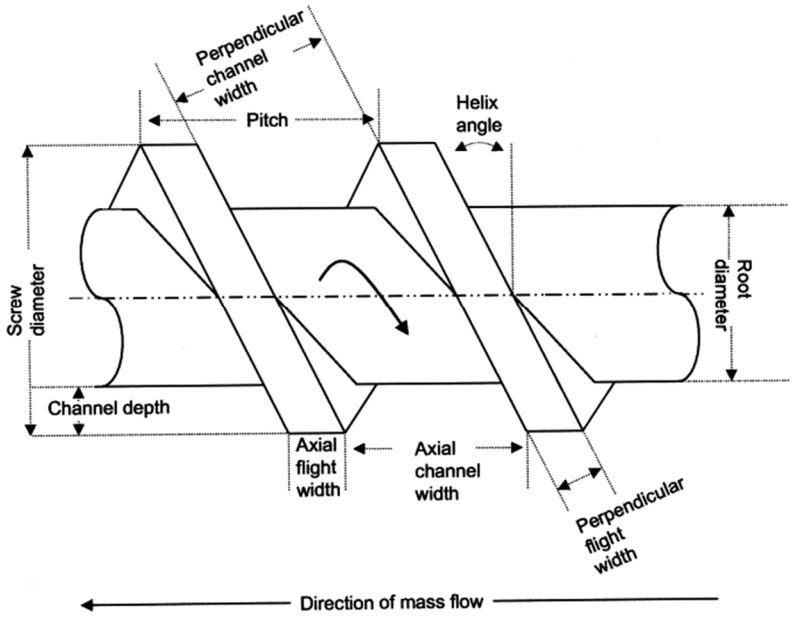

Figure 1.14: General design of extruder screw; adapted from reference (181)

The length and diameter are usually correlated and expressed as L/D ratio. It is important to note that the residence time within the extruder is also different and depends on many parameters such as the L/D ratio, the type of the device, the design of the screw(s) and the method of operation (179). Screws are designed to contain three distinct sections to perform the functions inside the barrel. The first region is responsible for the bulk transfer of the materials from the hopper to the barrel, while the next section is concerned to compression, softening and melting of the mixture. The melting of the feedstock is resulted by the energy generated from the shearing of the rotating screw (mechanical shearing stress) and the heating systems in the equipment by conduction (thermal stress). The diameter of the barrel cavity in the compression region is smaller than that of the conveying section to increase the pressure and remove any entrapped air bubbles within the melt. Finally, the metering section is responsible about the uniform pumping of the extrudate into the die which is attached to the end of the equipment. The final shape of the extrudates is determined by the shape and design of the dies. It should be mentioned that the size of the extrudate is not remained constant after cooling. This is attributed to the swelling in the cross-section of the product resulting from the recovery or relaxation of the individual polymer chains after the deformation caused by screw rotation. This phenomenon is called *die swell,* and it depends on the polymer viscoelastic features. The extrudates are then solidified by different methods like using air, N_2, stainless steel rolls or conveyors, or water (179).

The main controlling parameters that can affect the extrusion process are the barrel temperature, feeding rate, screw rotation speed and motor load and the generated pressure of the molten mass.

Barrel temperature is usually set based on the melting or glass transition of the material(s) to be extruded. Increasing the feeding rate and screw speed affect the load applied to the motor and the pressure generated inside the barrel (182). It was reported that the design of extruder screws might significantly influence the efficiency of the extrusion process and the properties of the processed materials like crystallinity and dissolution properties (180, 183, 184). The residence time inside the extruder is also an important factor that affects the extrusion process (5 seconds to 10 minutes), and it depends on the L/D ratio, type of the extruder, screw design and how is it operating (179).

1.5.1.2 Requirements of successful processing

In order to produce successful extrudates, the following requirements should be considered (179, 183, 185):

1. Substances to be extruded should possess high levels of purity and safety and have the ability to melt/soften easily and solidify rapidly after the completion of the process.
2. The mixture to be extruded should have good flowing characteristics, and this can be achieved by ensuring that the angle of the hopper is greater than the angle of repose of the mixture. This should be achieved to prevent the erratic flow of the feedstock in the extruder and the use of the force-feeding device can be used to fulfil this purpose.
3. Efficient feedstock transfer is an important factor to maintain the pressure at the compression and metering zones. Failure to achieve uniform feeding may cause the surge phenomenon in which cyclical changes in the output rate, head pressure, and the quality of the product.
4. The melting region should be within the temperature range 15-60 ˚C above the melting temperature of the semicrystalline polymer or the glass transition temperature (T_g) of the amorphous polymer.
5. In order to obtain an efficient fusion processing, polymers having low melt viscosities and high thermal conductivities should be employed.
6. Using screws with different designs may improve the melting process and also help to facilitate the transfer of feedstock through the extruder.
7. Care should be taken to ensure the melting of all the solid matter to avoid the blockage of the extruder cavity and the formation of surge phenomenon.
8. Excessive processing conditions can result in chain scission, depolymerisation or thermal degradation of the polymer.

HME as a process should be carried out under certain conditions, and the selection of the proper conditions is dependent on many parameters including (179, 186):

1. The chemical stability and physical properties of the drug and the carrier.
2. The viscosity of the melt.
3. The molecular weight of the polymer.
4. The T_g temperature of the amorphous polymers or the melting temperature (Tm) if it is semicrystalline.

1.5.1.3 Suitable APIs candidates for HME

Drugs liable to be processed by HME method should possess thermal, chemical and physical stability during and after the extrusion process (179). HME is widely used as thermal processing method to produce solid dispersions for water poorly soluble BCS class II drugs for the purpose of improving their bioavailability through dissolution enhancement (187). In addition, improving the dissolution BCS class IV drugs through fabrication as solid dispersions with hydrophilic excipients can be considered as an approach that may help to enhance their bioavailability (188-190). Because HME is solvent-free processing technique, it is considered as a very attractive approach for drugs exhibiting hydrolysis pathways during processing using solvent systems like water or hydroalcoholic mixtures. It should be mentioned that some extruder systems can be operated in an oxygen-free processing environment making the technology suitable for drug candidates exhibiting oxidation during preparation (179). Furthermore, HME may offer an advantage of overcoming the poor compressibility problem of some drugs by extruding formulation mixtures followed by improving the compressibility through solid dispersions or directly moulding them into their final dosage form geometry (191, 192).

1.5.1.4 Functional excipients used in HME solid dispersions

In addition to the active ingredients, the following components may be used in the formulation of solid dispersions using HME (83, 179):

1. Carriers
2. Release-modifying agents
3. Plasticisers
4. Antioxidants
5. Miscellaneous excipients like surfactants and bulking agents,

Carriers

In order to disperse drugs as molecular level solid dispersions using HME, a wide range of carriers having different physicochemical properties have been used as single or blend of two or more carrier components. The main classes of excipients used as carriers used in solid dispersion approach with examples are illustrated in **Table 1.1** (165).

Table 1.1: Chemical classes of carriers with examples used as vehicles for solid dispersions preparation by HME; adapted from reference (165)

Carrier type	Examples
Polymers	PVP, Eudragit, PVA, PEG, Zein
Sugars	Sucrose, dextrose, mannitol
Acids	Citric, succinic
Miscellaneous	Pentaerythritol, urea, urethane, hydroxyalkyl xanthins, cyclodextrins

These carriers are different in their melting and/or glass transition temperatures (T_g), crystallinity or amorphousness, water solubility, molecular weight, melt viscosity, thermoplasticity, and stability during and after processing. The following general characteristics were suggested as the general properties the carrier should possess (24, 29, 193):

1. Suitable aqueous solubility and rapid intrinsic dissolution properties if the immediate release is required.
2. Compatible and significantly interacting with the drug with complete miscibility to form single phase solid dispersion system.
3. Can increase the water solubility/ dissolution rate of the dispersed drug.
4. Ability to solubilise and stabilise the drug both in the solid and liquid states.
5. Chemically, physically and thermally stable.
6. Unable to form stable complexes that can retard the dissolution of the drug when fast dissolution is required.
7. The carrier should melt/soften at low temperature and solidify very quickly to maintain the drug dispersed as molecular dispersion.
8. Non-toxic within the pharmaceutical use limits.

9. It does not have any pharmacological activity.

Release-modifying agents

The release mechanism of drugs from solid dispersions designed for immediate release (to achieve maximum absorption) could be either drug or carrier dominant process. When the dispersions come into contact with aqueous medium, the carrier is either dissolves or swells to form a gel layer. In this case, the fraction of the drug in the solid dispersion relative to the carrier, ability of the drug to diffuse through the carrier layer and the layer viscosity are important factors that determine the carrier release controlling ability. However, if the drug is insoluble or sparingly soluble in the carrier's gel layer, it can be released directly into the dissolution medium, and its release is dependent on the properties of the drug itself like polymorphic form, particle size and inherent solubility. These two scenarios are often happening simultaneously in which the release is partly drug controlled and the other part is carrier dominant through the formed gel layer (27, 32). It was reported that the mechanism of release of felodipine from hydrophilic polymers like PEG and PVP is affected by many factors like the particle size of the drug, proportion of the drug, and the properties of the polymer in the dispersion. Concerning drug loading, carrier controlled release mechanism by diffusion through the polymer layer at low drug loadings and drug controlled release mechanism at high drug contents are the expected mechanisms of drug release from the different formulations (68).

Due to the advances in this technology and its flexibility to process a wide range of excipients with different formulation functionalities, a recent trend of using this approach for controlling the release of drugs in addition to enhancing their solubility/dissolution characteristics (27). Controlling the release of APIs dispersed in solid dispersions offers a number of potential advantages over traditional formulations like achieving uniform and extended therapeutic effect, reducing dosing frequency, improving the bioavailability, reducing dose strength, reducing adverse effects and improve patients' adherence to medications (66). Most commonly this formulation strategy can be achieved by a using a carrier with water insoluble or slowly dissolving properties instead of hydrophilic fast-dissolving ones. Depending on the characteristics of the prepared controlled release solid dispersions, the release mechanisms could be either diffusion, erosion or swelling followed by diffusion (32, 66). Examples of these release controlling agents are EC, HPMC, HPMC-AS, PVAc, chitosan, methacrylic acid copolymers and PEO which are widely used polymers to control the release of drugs (3, 194, 195). It was reported that domperidone buccal films prepared by hot melt extrusion using PEO N750 and HPMC E5 LV

were successfully sustaining the release of the drug resulting in a 93.62 ± 2.84% drug release and 63.36 ± 2.12% of drug permeation after 6 hours (196).

Plasticisers

Plasticisers are low molecular weight substances that have the ability to increase the free volume between the polymeric chains resulting in an increase in the entropy and mobility of the polymer chains and hence lowering the glass transition temperature (T_g) of plasticised polymers compared to non-plasticised ones. The increase in the mobility and entropy makes the polymer chains more flexible and the dispersion more diffusible which enables the dispersed drug to diffuse in higher rates depending on the concentration of the plasticiser (3, 187). The intermolecular forces of the secondary valence between the plasticiser and the polymer are responsible for this change in the characteristics of plasticised polymer (197). Examples of plasticising agents used in the process include triacetin, triethyl citrate, glycerol monostearate, diethyl phthalate, low molecular weight PEG, and surfactants (such as Tween 80, vitamin E TPGS and sodium docusate) (184, 198-201).

HME as a thermal processing technique is characterised by high shearing stress and therefore the presence of plasticiser in the formulation is reported to make the extrusion process more efficient and at relatively lower processing temperature (202). This potential advantage has an impact on reducing the thermal degradation of drugs and other formulation ingredients when processed at high temperatures (180). It was reported that plasticisers are effective in reducing the melt viscosity of viscous polymers resulting in extrudable mixtures at suitable processing temperatures. (203). They are also efficient in reducing the tensile strength of formulations prepared by hot melt extrusion compared to non-plasticised mixtures (203-205).

Antioxidants

Antioxidants are agents that protect the dispersed drug and any other formulation ingredient(s) from the oxidative degradation pathways (144). These agents are classified as preventive and chain-breaking antioxidants. The preventive antioxidants or oxygen scavengers act by preventing the initiation of a free radical chain reaction. Examples of such type are citric acid, ascorbic acid and EDTA. On the other hand, chain-breaking antioxidants act by blocking the oxidation reaction

and preventing their propagation. There are many examples of these agents like butylated hydroxyanisole, butylated hydroxytoluene, and vitamin E TPGS (179).

It was reported that polymers like PEG and PEO undergo thermal oxidative degradation when exposed to processing at elevated temperatures in the presence of oxygen (145). The degradation was attributed to random chain scission resulting from the free radical attack which leads to the formation of different degradation products with low molecular weights and melting points. These polymers are susceptible to thermal degradation due to a reduction in the activation energy required for hydrogen abstraction caused by the high strains exists at the chain folds of their lamellar structure (145). Because these polymers are semicrystalline, the degradation is shown to occur in the amorphous domains rather than the crystalline fractions which indicates that highly crystalline fractions are less susceptible to this chemical instability problem. This is attributed to the oxygen diffusion to the amorphous fraction is significantly higher compared to the highly ordered crystalline domains (144). Also, Tween 80 was reported to be degraded by autoxidation and hydrolysis mechanisms. Thermally activated autoxidation leads to the formation of free radicals that cause the degradation (142, 143, 206).

Vitamin E and its derivatives were found to possess antioxidant activity that can help to prevent the oxidation of drugs in their formulation. Vitamin E TPGS antioxidant micelles were found to solubilise and stabilise the new cytotoxic quinolinone derivatives against oxidation compared to cyclodextrins and other excipients contained in the formulations (207). It was also reported that vitamin E succinate and vitamin E TPGS are acting as stabilisers for PEO dispersions prepared by HME and their antioxidant activity is dependent on their hydrophilic character (144).

1.5.2 Injection moulding (IM)

Injection moulding (IM) is a rapid and versatile technique that introduced firstly in plastic manufacturing to produce objects with different geometries. This process entails the injection of the molten mass under specified conditions of temperature and pressure into a die with specific dimensions followed by cooling to achieve solidification then the final product is released from the mould (208). This technology was firstly patented to be used for the fabrication of medicines for oral administration by embedding drug(s) in a thermoplastic resinous material(s) suitable for injection moulding by Ciba-Geigy Corporation in 1969 (209). IM is also employed in the pharmaceutical field for the manufacturing of cosmetics, dosage form packaging and other advanced biomedical devices like scaffolds and microneedles (210, 211).

The advantages of using IM technology in the manufacturing of pharmaceutical products include:

1. It is entirely automated and continuous process that can be scaled up easily (208).
2. Dosage forms and other pharmaceutical devices can be produced in very defined shapes and geometries depending on the dimensions of the die used with higher composition uniformity (208).
3. It is highly efficient and time-saving technology because it needs only short time to produce the dosages in their final forms (208).
4. It excludes the use of solvents during processing which in turn lowers the cost of production and preserve the stability of drugs susceptible to degradation when manufactured in the presence of solvents (208).
5. Processing conditions like the heat and pressure provide the opportunity to kill the microbes and help in making the dosage form auto-sterilised by IM compared to the other preparation techniques (212).
6. IM produces solid dispersions with improved dissolution rates of poorly soluble drugs which may lead to enhancement in the bioavailability. It should be mentioned that improving drugs' bioavailability may have a great impact on reducing drugs' side effects by reducing the dose strength required to achieve the therapeutic effect (179, 213).
7. Using IM, the closure characteristics of capsules cap and body design can be modified to overcome problems associated with capsule manufacturing. Furthermore, IM can be used when dipping moulding is not suitable such as the case of manufacturing of capsules shells from non-gelatinous based sources (208). As it is known that some patients have certain restrictions regarding the use of gelatin shells due to dietary or religious reasons. The replacement of gelatin by other substances may exclude their manufacturing by dipping method, and IM can be an alternative method to produce gelatin free capsule shells (214, 215).
8. IM was used as a potential approach for the production of a variety of pharmaceutical products like matrix tablets (216-219), implants (220, 221) and intravaginal inserts (222).

1.5.2.1 Injection moulding processing

IM machines used for plastic and pharmaceutical application are consisting of two parts: plasticating/injecting unit and clamping unit with different configurations like horizontal or vertical (**Figure 1.15**). The plasticating/injecting unit has a design similar to that of the extruder where mixtures can be fed, mixed and melted by the actions of the rotating screw(s) and the heating systems present in the barrel of the system. The terminal portion of the IM machine is the

die which is generally composed of two halves that joined to form a 3D space that represents the final shape and size of the product. Moulds with many cavities can also be used to produce more than one unit in the same cycle. One of the two pieces of the mould is stationary, and the other is mobile to be easily coupled to form the closed die or separate to form the opened mould. The function of the clamping unit is to maintain the mould closed during the injection process. To achieve this purpose, the clamping force should be more than the injection force to prevent the opening of the mould during the injection process. After injection of the molten mixture, the mould is allowed to cool by the cooling system equipped with the device until the complete solidification of the matrix. The solidified product is then released by opening the die and ejected by pins present in the mobile half of the mould. Usually, IM process is a continuous process in which melting, injection, moulding, cooling and ejection of the final product are done in the same equipment. However, sometimes separated equipment can be used to achieve this purpose like the use of the extruder as the plasticating unit and then the matrix should be maintained at suitable conditions of temperature and transferred to another device where the injection process is to be completed (208).

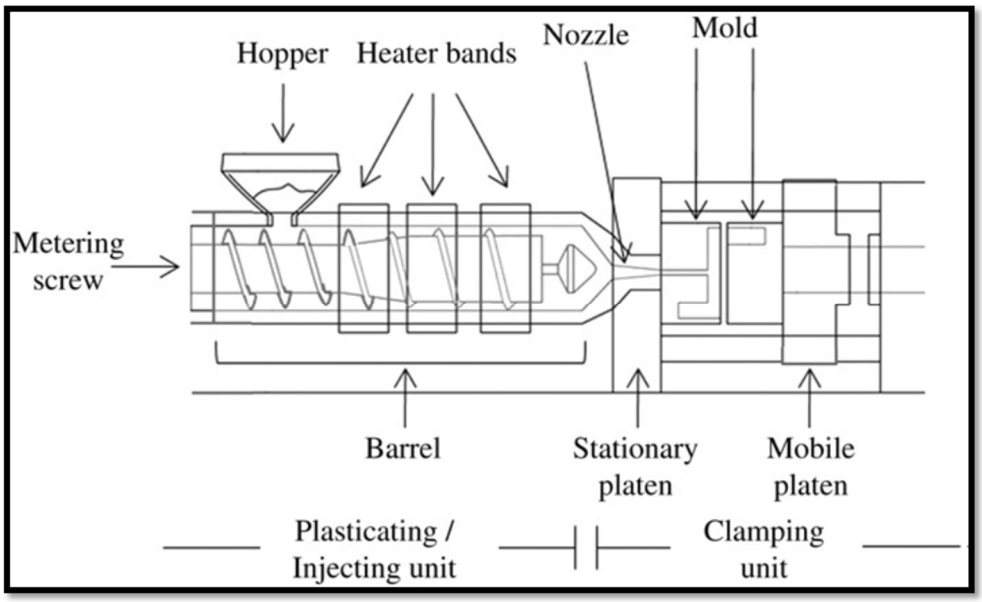

Figure 1.15: Injection moulding (IM) machine, adapted from reference (208)

1.5.2.2 Scale-up of solid dispersions to manufacturing level

Despite the enormous number of research conducted in the field of solid dispersions for improving the dissolution properties of poorly water soluble drugs especially BCS class II drugs, only very little number of pharmaceutical products were commercialised as approved medicines (32, 177). The limited commercialisation of these preparations is partly attributed to problems in scaling up into marketed products. These problems may be related to the physical instability of the molecularly dispersed drug in the system, thermal degradation, solvent residuals and changes during downstream processing. Also, the fabrication technologies may also play a major role in the commercialisation process. Examples of products that have been commercialised using hot melt extrusion and its advanced version Meltrex™ include Cesamet® (nabilone -PVP), Rezulin® (troglitazone-HPMC), Kaletra® (Meltrex™) (lopinavir - ritonavir- PVPVA) tablets. This is an indication of scalability of this processing technique compared to other solvent evaporation methods such as electrospinning (32).

1.5.3 Fused deposition modelling (FDM) 3D printing as a new method for fabricating solid dispersions

The process of forming objects in 3D generally falls into one of three major categories; forming, subtractive and additive manufacturing. The first class involves reshaping the object into different geometry without subtraction or addition like vacuum moulding. Subtractive manufacturing is another class in which the unwanted parts of the objects can be removed using certain cutting tool which is one of the techniques used in 3D object production. 3D printing is an example of the additive manufacturing process in which rapid synthesis of precisely modelled objects can be achieved with the assistance of computer-based designs. 3D printing as advanced and rapidly growing technology can be performed using a variety of technologies, operation principles and materials as illustrated in **Table 1.2** (223).

Table 1.2: Summary of 3D printing techniques, their operation principles and materials used in the fabrication of objects, adapted from reference (223)

3D printing technology	Principle of printing	materials used
Stereolithography apparatus (SLA)	Optical	polymer resin
Digital light projection (DLP)	Optical	polymer resin
Multijet /poly jet	Optical	polymer resin
Continuous liquid interface production (CLIP)	Optical	polymer resin
Selective laser sintering (SLS)	Optical	polymer powder
Selective heat sintering (SHS)	chemical/ mechanical	polymer powder
Binder jetting	chemical/ mechanical	polymer powder
Fused deposition modelling (FDM)	Thermal	polymer filament
Laminated object manufacturing (LOM)	Thermal	polymer films

Fused deposition modelling (FDM) or sometimes called fused filament fabrication (FFF) 3D printing was originally introduced during the 1980s as a branch of the additive manufacturing (AM) technology. FDM 3D printing is a thermal based 3D printing technique and has recently attracted the interest of researchers in many fields including pharmaceutical formulations design (224-226), food technology (227), and tissue engineering (228).

1.5.3.1 FDM 3D printing process

FDM 3D printing technology is an extension to the well-known hot melt extrusion (HME) or injection moulding (IM) techniques with the exception that the mould is not needed to get objects with specific and precise geometry (223, 229). The key element of FDM 3D printing is the extrusion process, which allows the thermally softened material strips to be deposited in a 'writing' mode. It principally works by converting a pre-designed software digital file coding the 3D object into a real object by adding a consecutive series of layers of molten or semi-liquid modelling material. Pre-made filaments with a specific diameter are needed for feeding into the printer. The modelling material in the printing state is pushed through a temperature-controlled 3D printing nozzle having a certain diameter at a pre-adjusted speed into a temperature controlled building

platform (**Figure 1.16**). Depending on the dimensions of the object, the printer nozzle moves in the X-Y plane in a particular pattern (determined by the shape of the object) creating the first layer. Successive layers are printed by moving either the nozzle or the platform through the Z plane with a distance equivalent to the layer thickness. The temperature of the platform is usually less than that of the extrusion head allowing the printed material to solidify between each layer. It should be mentioned that FDM printing can be performed using one or more printing heads depending on the design of the printer (223, 229).

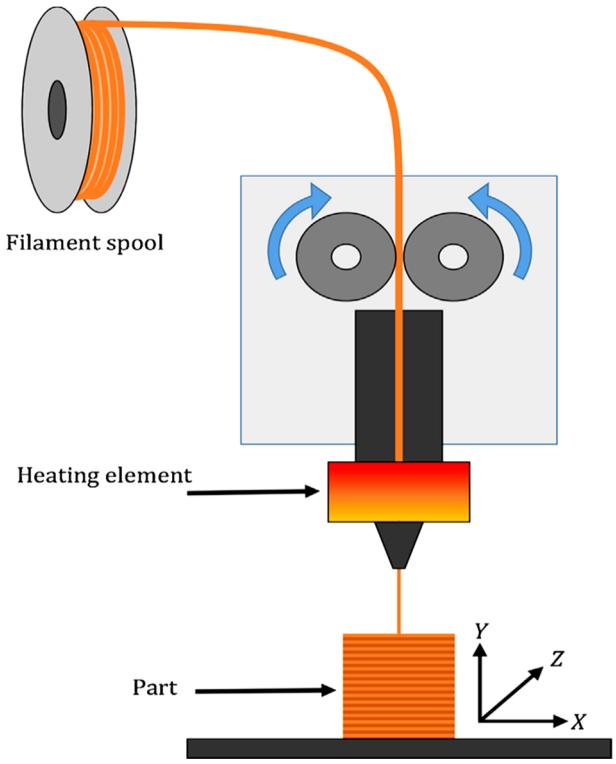

Figure 1.16: An illustration explains fused deposition modelling (FDM) 3D printing technology; adapted from reference (223)

1.5.3.2 Pharmaceutical applications of FDM 3D printing technology

An encouraging trend of using 3D printing in pharmaceutical manufacturing has been established by the approval of Spritam®, which is the first FDA-approved 3D printed oral dosage form. This first 3D printed commercial drug product used ZipDose® technology, which is a wet power deposition 3D printing method. There is a broad range of 3D printing technologies that operate via thermal or solvent evaporation mechanisms. Also, because FDM 3D printing is an advanced modification of HME and IM, it can be expected that the advantages mentioned for these two

techniques may apply to FDM 3D printing. The following advantages or applications can be achieved through the use of FDM 3D printing:

1. Fabricating medicines as combination drug therapies for treating patients with diseases require multiple actives such as complex cardiovascular treatment regimens or for patients suffering from multiple diseases at the same time (230).
2. Producing patients' personalised medicines according to patients' needs to improve the quality of treatment and consequently lead to higher percentages of patients' adherence to medications (230).
3. Using this technology with the advantages of flexibility in computer-aided design and the invention of multiple head 3D printers, it is possible to design products with different geometries and configurations. These products can be used to control the dissolution profiles of the incorporated drug(s) according to the desired effect (224).
4. Reducing the cost of production by eliminating the unnecessary resources. This can be achieved by saving the cost of the quantities of the actives and the excipients over the need of the patients (231).
5. This technology is fast for producing items such as prosthetics and implants compared to conventional methods which require milling, forging and long delivery time (232).
6. It is very flexible in producing dosage forms and drug delivery systems with a wide variety of applications and administration sites like oral fast disintegrating, floating, colon-targeted, multiple phasic and implantable systems (233).
7. Improving the solubility/dissolution of poorly water soluble drugs (especially BCS class II) via solid dispersion approach which leads to improved bioavailability of these drugs (233).

Currently, FDM 3D printing is facing some limitations in the pharmaceutical field to develop more personalised medications. The suitability of pharmaceutically approved excipients for FDM 3D printing purposes is one of the most important challenges. This is because nowadays commercially available filaments such as ABS, PVA, PLA and PCL filaments are either not suitable for pharmaceutical use or not flexible to fit with the broad field of FDM 3D printing application (233). In addition, thermal degradation may happen due to the use of high processing temperature required for FDM 3D printing which might cause the loss of the therapeutic activity of the APIs and the generation of the degradation products with the possibility of their harmful effects (230). Furthermore, the low and incomplete drug loading efficiency when drug loading performed by soaking of commercially available filaments (PVA) in saturated organic solutions of drugs (226).

1.6 Drug delivery through peroral routes

There are many different routes for drug administration to achieve the intended pharmacological activity. The most commonly used is the peroral route where the dosage form is administered through the oral cavity, and the drug is absorbed through the GI tract including the mouth cavity (234). This route offers a number of advantages compared to the other routes including its suitability for self-administration of drugs. Also, oral dosage forms do not need to be sterilised, and relatively larger amounts of drugs can be administered through the GI tract (9).

The factors that affect drug absorption through the GI tract are varied according to the different regions of this system. For example, drugs absorbed from the intestine may be affected by the gastric emptying time, presence of food and the influence of gastric secretions. However, some parts of the GI tract like the mouth cavity may offer interesting opportunities to overcome certain obstacles encountered when drugs are passing through the other parts of GI tract like the stomach and small intestine. These drawbacks may be related to the failure to achieve the effective plasma concentration of medication, drug destruction by the enzymatic attack and extensive first-pass metabolism in the liver after absorption. These reasons motivate researchers to investigate the possibility of delivering drugs via the mouth cavity. The delivery of APIs through the mouth cavity can be divided into three types including sublingual, buccal and local (235). Sublingual drug delivery in which drugs are delivered to the systemic circulation through the mucosal membranes lining of the ventral surface of the tongue and the floor of the mouth. On the other hand, drugs can also be delivered systemically through the buccal mucosa lining the cheeks and the area between the gums and upper and lower lips. Periodontal, gingival and odontal drug delivery systems are used for local treatment of diseases of the oral cavity, main aphthous ulcers, bacterial and fungal infections and periodontal conditions (220).

1.6.1 Buccal drug delivery

1.6.1.1 Physiology of oral cavity

The oral cavity is completely covered by membranes composed of relatively smooth mucus containing large number of small glands. It consists of the epithelium, basal lamina (links the epithelium to connective tissue), lamina propria (connective tissue) and submucosa (which

contains loose glandular or fatty connective tissue and main nerves and blood vessels) as illustrated in **Figure 1.17** (236, 237):

The epithelium is multilayered lining with various degrees of differentiation, and thus it differs from that of the GI which is simple and composed of a single layer of cells, (238). The outermost layer of the oral mucosa is composed of stratified squamous epithelium which has a mitotically active basal cell layer similar the stratified squamous epithelia present in the rest of the body. The differentiation is advancing as the layers become closer to the surface where cells are shed from the epithelium surface (239). It should be mentioned that most rodent models have keratinised outer layer while in humans, a non-keratinised buccal epithelium, much like other larger mammals including dog, pig and monkey (237).

The thickness of the epithelium of the buccal mucosa is about 40-50 cell layer thick (500-800 µm) while that of the sublingual region is somewhat thinner. The size of the epithelial cells is increased and the cells become flattened as they transfer from the basal layers to the surface of the epithelium. Also, the buccal epithelium has a turnover time estimated about 5-6 days. The composition of oral epithelium is different according to the various sites in the oral cavity. The epithelium of the gingiva and hard palate are keratinised and they are similar to that of the epidermis because these regions are more likely subjected to mechanical stress. However, a non-keratinised epithelium is found in the soft palate, sublingual and buccal regions (240).

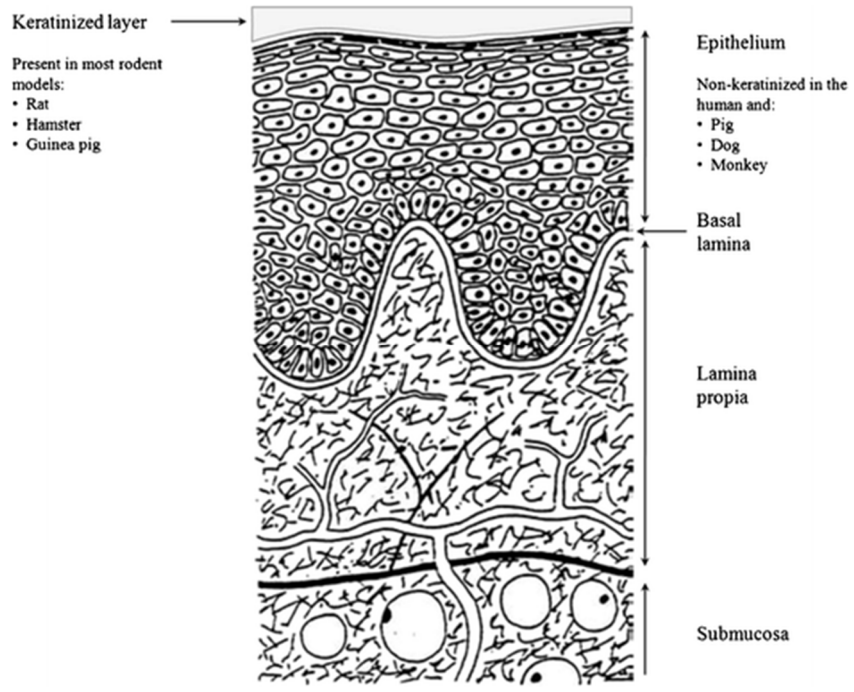

Figure 1.17: Cross-section of the mucosa of the buccal cavity; adapted from reference (237)

Keratinised tissue is characterised by being robust, dehydrated and capable of resisting chemical damage and it covers a surface area of about 50% of the oral cavity. On the other hand, non-keratinised tissue has higher flexibility, and it occupies approximately 30% of the total surface area. It should be mentioned that 60 to 75% of adults have sebaceous glands in their oral mucosa of the buccal mucosa and upper lip and they appear as pale yellow spots. In addition, small salivary glands openings can be seen in many areas. Concerning blood circulation, the oral mucosa has more blood vessels compared to the skin. The majority of the venous blood of the oral mucosa return circulates to the internal jugular vein. The lamina propria also contains lymphatic capillaries appear as blind cavities in the papillae (236).

Concerning the biochemical composition, the oral mucosa is characterised by the presence of large quantities of a protein in the cells of all layers in both keratinised and non-keratinised types of epithelia. This protein is termed keratin, and it has a relative molecular mass ranging from 40,000 to 70,000 g/mole. The lower molecular weight keratin is present in the non-keratinised cells mucosa. However, the higher keratins are predominantly present in the mucosa of the keratinised cells. It should be mentioned that keratinisation is a relative process, and the description noted above represents the extremes cases of keratinisation. It has been suggested that the water permeability of oral epithelium is related to its lipid content (241). The buccal mucosa is more permeable compared to other parts of oral cavity such as the gingiva and palate because it contains fewer quantities of acyl ceramides and ceramides. Epithelial cells are surrounded by material composed of carbohydrate-protein complexes. This intercellular ground substance is thought to be responsible for cells adhesion and serving as a lubricant to facilitate the movement of the cells relative to each other (241). The oral epithelium also contains some intercellular junctions such as gap junctions, tight junctions, and desmosomes and/or hemidesmosomes. The membranes of adjacent epithelial cell are separated by gap junctions of approximately 2-5 nm. These gaps are thought to be continuous which allow the passage of compounds having a molecular mass of several thousand daltons (240).

Mucus

Mucus is a gel-like complex aqueous mixture that covers the entire surface of the oral cavity. The function of this layer is providing protection to the underlying epithelial cells from the various environmental conditions and the effect of enzymes and other chemical substances. It is a viscous and elastic hydrogel composed mainly of water ~ 95%, 0.5-5% water-insoluble glycoproteins, together with small quantities of other substances like proteins, lipids, enzymes, electrolytes,

nucleic acid, sloughed epithelial cells and bacteria (242, 243). The constituents of mucus may differ depending on the site of secretion, the intended protective and mechanical function and the presence of illnesses (244).

The major component of mucus is mucin which has two forms: soluble secretory mucin and membrane-bound mucin (245). The former is responsible for the formation of the gel-like structure of the mucus due to its higher molecular weight and its ability to form intermolecular linkages through the disulfide bridges. The membrane-bound mucin does not have the ability to form the intermolecular disulfide linkages, but it has a hydrophobic portion that binds the molecule to the plasma membrane of the epithelial cells (246-248). Mucin is composed of oligosaccharides (70-80% of their total weight) which are linked via *O*-glycosidic linkages to a peptide core which constitutes 10-30% of the total weight of the mucin (242). The oligosaccharides are varying in their length (2-15 sugar units) and they have a branched structure (249). In general, mucins differ according to their molecular size, the composition of their sugar moiety, sequence and the length of their chains (250, 251). Mucins isolated from the same glands are not identical, and they do not have the same molecular size (252). The protein core of mucins composed of high quantities amino acids such as serine, threonine, alanine, glycine, proline and low levels of aromatic amino acids (253). The most common monosaccharides attached to the protein core are *N*-acetylgalactosamine, *N*-acetylglucosamine, galactose, fucose and sialic acid (250). The net negative charge of the oligosaccharides and the entire mucins are due to the presence of sialic acid and other sulphate residues (242).

Several studies demonstrated that mucous layer might act as a membrane that limits the absorption of drugs through the mucosa. On the contrary, this layer may provide an excellent mean for sustained or prolonged drug delivery by designing mucoadhesive drug delivery systems (243). The factors that affect the diffusion coefficient of the molecules through the mucous layer include the relative size of the drug molecule, the effective pore size of the of the mucus gel formed by the association of mucin macromolecules and any interaction between the drug and the components of the mucous membrane. As the molecule size of the drug increased the diffusion coefficient is decreased i.e. there is an inverse proportion between the molecular weight of the drug and the diffusion through the mucous membrane. The diffusion of small and uncharged molecules through the mucous layer seems not to be considerably affected by the mucous membrane compared to larger or charged (cationic) molecules. On the other hand, as the mesh size of the mucous network increase, the diffusivity of the drug is also increased (254). Furthermore, any interaction between the drug and the components of the mucous layer can reduce or prohibit the penetration of the drug through the mucous membrane (255-257).

Saliva

Salivary fluid is excreted into the human mouth cavity (1-2 litres/ day) as a continuous and low basal secretion rate of 0.5 mL/min. Higher rates of secretions of more than 7 mL/min increased rapidly by the thought, smell and/or taste of food. The parasympathetic system is responsible for the control of salivary secretion. Saliva is characterised by being viscous, opalescent, colourless and hypotonic compared to plasma. The specific gravity of the salivary fluid is about 1.003, and its pH varies between 7.4 - 6.2 with lower pH at higher secretion rates. The salivary fluid is a mixture of water, proteins, mucus, mineral salts and amylase (236). Saliva also contains ions such as Na^+, K^+, Cl^- and $HCO3^-$. Na^+ and Cl^- are reabsorbed in the ducts of the salivary glands while K^+ and $HCO3^-$ are secreted to control the electrolyte balance depending upon the rate of saliva secretion (236). Salivary fluid also contains enzymes such as α-amylase and ptyalin which can hydrolyze polysaccharides such as glycogen and starch to small molecules. Also, different esterases, mainly carboxylesterases also exist in the salivary fluid, and these may hydrolyse ester prodrugs or APIs containing susceptible ester groups (236, 258).

1.6.2 Drug absorption through buccal route

The absorption of APIs across the buccal mucosa involved two pathways: 1) intracellular (through the cells) and 2) intercellular or paracellular (between the cells). Both hydrophilic and lipophilic drug molecules can penetrate the buccal mucosa through these paths. The intracellular pathway offers a greater surface area for diffusion, but drugs passing by this mechanism may suffer from a significant diffusional resistance when they cross the aqueous and lipid compartments of the buccal epithelial cells. The mechanism by which water soluble compounds diffuse transcellularly involves the penetration of these molecules through the aqueous pores of the cell membrane. This is followed by the diffusion via the cytoplasm, and the process continued from cell to another across the epithelium (259). In addition, specialised transport mechanisms also participate in the absorption of drugs through the intracellular pathway (260-262). Lipophilic drugs can traverse by this pathway by partitioning through the lipid bi-layer of the cell envelope of the epithelial cells (259). On the other hand, drugs can also penetrate the buccal mucosa through the longer and tortuous pathway between the cells (intercellularly). In order to pass by this mechanism, the drug should have a certain affinity for and diffusivity in the intercellular fluid (240). Despite that this route offers a smaller surface area of diffusion compared to the intracellular one, this pathway appears as the most common route of penetration for most pharmacologically active compounds

(263). Several studies showed the uppermost 25-30% layer of the buccal epithelium is the limiting membrane for the absorption of many compounds like horseradish peroxidase (264), lanthanum (265), thyrotropin-releasing hormone (TRH) (266) and salicylic acid (267).

1.6.3 Buccal formulation design

Buccal drug delivery offers a number of valuable features such as the large surface area available for drug absorption (approximately 100 cm^2) and providing a useful alternative to the intestinal route for drug absorption in situations where the GI route is unfeasible. In addition, delivering drugs to the systemic circulation is expected to bypass the hepatic metabolism that affects the plasma concentration of drugs susceptible to liver metabolism. Due to the relative permeability and rich in blood supply of the buccal mucosa, it serves as an absorption site that can promote rapid and efficient delivery of drugs to the systemic circulation. Also, drugs administered through the buccal mucosa are usually avoid the enzymatic degradation that they might subject to during their passage through the rest of the GI tract. This is an important issue for the delivery of proteins and peptides to the systemic circulation. It should be mentioned that the potential of irritation and irreversible damage to the mucosal lining and the buccal mucosa is not a problem because of the rapid recovery of the buccal mucosa after stress or damage. It was also reported that buccal route of adminstration is more acceptable to patients compared to other non-oral routes of administration such as intravenous and intramuscular injections because buccal formulations are non-invasive and cost effective. It should be noted that this route offers easy withdrawal or termination of medication by the patient which is an important issue in the case of emergencies like hypersensitivity to the drug or excipients contained within the formulation (235, 243, 259). Due to their smaller size and reduced thickness, buccal films are reported to have an improved patients' compliance compared to tablets (268), and lozenges (269)

On the other hand, only potent drugs with poor absorption characteristics are suitable candidates for this route of drug delivery due to the limitations of dosage form size, residence time and the permeation through the buccal mucosa. Drugs with an effective plasma concentration within or less than ng/mL are considered as ideal candidates for buccal drug delivery. In addition, peptides and proteins may be subjected to the metabolic activity of the enzymes present in the oral cavity. This factor affecting these types of drugs to a lesser extent compared to the metabolic enzymatic activity in the GI tract. The mucus and salivary clearance can also decrease the retention time of drugs, and this may affect their absorption through the buccal mucosa. It should be mentioned that the mucus layer may act as a physical limiting membrane for the diffusion of APIs via the

buccal mucosa. Also, mucus may inhibit the penetration of drugs through the mucosa by binding with the drug (270).

Buccal dosage forms should possess certain general requirements to be suitable for the delivery of drugs through the buccal mucosa. These formulations should have specific adhesive characteristics to maintain the system in contact with the buccal mucosa but not so adhesive as it may cause damage to the underlying tissue upon the removal of the system. Also, the components of these products should be biocompatible, non-toxic, non-irritating to the buccal mucosa, not cause excessive salivary secretion, palatable and not bitter tasting. In addition, they should be convenient when applied and inconspicuous after application on the buccal mucosa. Furthermore, their surface should be smooth and not rough. It should be mentioned that unidirectional release buccal systems are more preferable to achieve buccal absorption and prevent swallowing of the drug to the GI tract (234, 271). These dosage forms are either used for treating local conditions within the buccal cavity or to deliver the pharmacologically active ingredients to the systemic circulation. Recently, many researchers have designed dosage forms that can deliver drugs through the buccal mucosa to overcome some problems related to their delivery by other routes or to get benefits from the advantages of this site. The most common dosage forms include matrix tablets, patches, lipophilic gels, and transfersomes (272).

The size and the shape of the buccal drug delivery systems are different according to the type of the dosage form. The buccal tablet may have a size range 5-8 mm in diameter, whereas buccal patches with flexible characteristics may have a surface area in the range 10-15 cm^2. It was reported that patients are more accepting buccal patches with an average size 1-3 cm^2 compared to buccal tablets. Buccal drug delivery systems are also variable with respect to their shapes, and the ellipsoid shaped systems seem to be more preferable (243). Because of the size limitations of buccal patches, only drugs with daily dosage 25 mg or less are suitable candidates for this route of administration (239). Buccal dosage forms should have a thickness not exceeds few millimetres and the maximum application time is expected to be within the time limit of 4-6 hours because food and/or liquid intake may restrict their application for longer periods (243, 273).

Buccal dosage forms can be classified according to their design into (274):

1) Reservoir systems: In which the drug is enveloped by a polymeric membrane that controls the rate of release. When the polymeric membrane is the rate limiting membrane, and there is an access of the drug, this system provides a constant release profile.

2) Matrix systems: In this system, there is a uniform distribution of the drug within the polymer. The release rate and profile are controlled by many factors including solubility of the polymer, polymer diffusivity, the thickness of the polymer diffusional path. In addition, the drug's aqueous solubility, partition coefficient and aqueous diffusivity are also important factors in controlling the release profiles. Furthermore, the thickness of the hydrodynamic diffusion layer, the amount of the drug loaded in the system and the surface area of the dosage form play a major role in the release pattern and rate of the incorporated drug.

1.6.3.1 Matrix tablets

The matrix tablets have a monolithic and a two-layered matrix structure that can be used for local or systemic purposes. The design of the simplest model of these tablets is a mixture of the active drug and a swelling polymer with sustained release and mucoadhesive features to liberate the drug in a bidirectional mechanism. This system can be modified by certain methods to obtain the desired release characteristics like for example the outer or all sides may be coated with water impermeable material to get a unidirectional release. Furthermore, the drug may be loaded in a release rate controlling layer that controls the drug release towards the buccal mucosa while the water impermeable layer ensures that the release is preceding to the direction of mucosa only. Matrix tablets are used for the delivery of different drugs such as naloxone HCl, propranolol, timolol, metronidazole, metoclopramide, morphine sulphate, nitroglycerin and codeine. This type of dosage forms is also used for the delivery of peptides, such as insulin, calcitonin and glucagon-like peptide (272, 275-277).

1.6.3.2 Buccal patches

Recently, several research approaches are focused on the formulation of buccal patches due to their patients' higher acceptability and compliance compared to buccal tablets due to their higher flexibility and the reduced thickness which make them more comfortable compared to buccal adhesive tablets. Buccal patches can be designed as multi-layered systems that composed of an outer impermeable layer and an underlying layer containing the drug substance in addition to other excipients. The drug containing layer has adhesive properties, and through this layer, the release of the drug to the mucosa in a unidirectional way is happened (272). This type of dosage

forms used for the delivery of many drugs such as diclofenac, thyrotropin-releasing hormone, octreotide, oxytocin, buserelin, calcitonin and leuenkephalin (278, 279).

1.6.4 Mucoadhesive drug delivery systems

The term 'bioadhesion' refers to the adherence of synthetic or natural macromolecules to biological tissues. Mucoadhesion represents the attachment of various polymeric macromolecules to the mucous membrane lining the mucosal epithelium (280). It was noticed that the attachment of the gut bacteria to the GI mucosa represents a natural example of mucoadhesion through the linkage between the proteins on the surface of the bacterial cells and the mucus membrane lining the GI mucosa (280, 281). The earlier attempts to use the bioadhesive drug delivery systems dated back to 1947 when researchers tried to deliver penicillin through the oral mucosa using tragacanth gum and dental adhesive powders (282). This approach became more interesting for researchers in the field of controlled-release drug delivery in the early 1980s (283). After that, many researchers are focused on the investigation of various biopolymers with bioadhesive characteristics for the development of many products for different therapeutic purposes. Bioadhesive polymers can generally be classified into two types: specific (like fimbrin and lectins) and non-specific (such as polyacrylic acid and cyanoacrylates) bioadhesive polymers. The difference between these two groups is related to their ability to bind to the biological membranes where the former have the potential to form a sort of attachment to specific chemical structure while the latter have the ability to adhere to both the surface membrane and the mucus layer (284).

Mucoadhesive systems are dosage forms that contain one or more mucoadhesive polymers that act as an essential part of their composition. They have the ability to adhere to the mucus layer by means of mucoadhesion, and they are useful for the targeted delivery of drugs where the drug retained at the site of absorption for extended periods (285). These systems were used to achieve sustained release purposes of medicines brought by the prolonged residence time on the ocular (286), nasal (287), vaginal (288) and buccal (289) mucosal membranes. More recently, bioadhesive drug delivery systems have gained a great interest for the delivery of peptides and proteins because the adhesive properties resulted from the use of bioadhesive polymers can provide an additional protection mechanism to the therapeutic drugs against enzymatic attack that may occur between the dosage form and mucosa (290, 291). Different kinds of forces are involved in binding the polymer with the biological tissue to promote bioadhesion which may include covalent (cyanoacrylate), hydrogen (carbopol, polycarbophil and acrylates) and weak electrostatic bonding (chitosan). Bioadhesion involves covalent bonding seems to be suitable if

the polymeric material is non-toxic. Several studies showed that most bioadhesive polymers are capable of forming weak polar or electrostatic interactions. To maintain the drug in contact with the biological tissue for the predetermined time period, there must be a relatively strong bonding between the polymer chemical group and the biological surface (292). Ideally, mucoadhesive polymers should promote mucoadhesion in different biological environments with different water contents. In addition, water and oil soluble drugs can be easily accommodated by the polymer for the controlled release purposes. Mucoadhesive polymers are also preferable if they possess additional properties such as the ability to inhibit local enzymes, help in enhancing the absorption of drugs, being safe, inert, biocompatible, provide excellent mechanical properties and being easily handled during the formulation and manufacturing processes (292, 293).

Polymers with mucoadhesive features are either of natural or synthetic sources. Examples of the synthetic type including polyacrylic acid derivatives (such as polyacrylic acid) and cellulose derivatives (such as carboxymethyl cellulose). On the other hand, natural materials can also be used as bioadhesive excipients such as chitosan and various gums such as xanthan, pectin and alginates (294).

1.6.5 Mechanisms of mucoadhesion

Mucoadhesion as a process involves three steps, in the first step there is an intimate contact between the mucoadhesive polymer and the biological tissue followed by the interpenetration between the macromolecules then the formation of interfacial bonds (295). These bonds are relatively weak bonds of the secondary type like hydrogen bonds, van der Waals forces, electrostatic forces and hydrophobic interactions (296). Due to the large number of charged groups such as hydroxyl (-OH), carboxyl (-COOH), sulfuric acid ($-SO_3H$), and amino ($-NH_2$), electrostatic interactions and hydrogen bonds seem to play an important role in the process of mucoadhesion. On the other hand, hydrophobic interactions result from the association of non-polar groups also participates in this process. The van der Waals binding energies between hydrophobic groups were estimated within the range 1-10 Kcal/mol, while the binding energy of hydrogen bonds between polar groups is about 6 Kcal/mol (297).

The process of mucoadhesion can be explained by several theories including electronic, adsorption, diffusion, wetting and fracture theories. In a particular situation, the formation of bioadhesive bonds can be explained by one or more of these theories (239).

Electronic (electrostatic) theory

This theory assumes the formation of an electrical double layer between the mucoadhesive material and the biological tissue. This electrical double layer is resulting from the electronic transfer between the two sides when they come in contact of each other as a result of their different electronic structures. The attractive forces across this electrical double layer are believed to be responsible about the mucoadhesion (298).

Adsorption theory

The adsorption theory states that the molecules of the biological tissue adsorbed at the surface of the mucoadhesive substrate resulting in a kind of interaction between these two systems (299, 300).

Diffusion theory

The diffusion theory suggested that the interpenetration and entanglement of the mucoadhesive polymer are responsible about mucoadhesion. The concentration gradient across the interface between the two substrates is the driving force for the interpenetration of the polymer chains into the biological side and vice versa. It is believed that interpenetration between the two substrates of about 0.2-0.5 μm is essential to produce an effective adhesion (301).

Wetting theory

The wetting theory suggests that for mucoadhesion to take place, there must be a certain degree of spreadability or wettability between the mucoadhesive material and the biological substrate. According to this theory, the angle of contact Θ is the reflection of the wetting power of liquid on solid and mucoadhesion is predicted as a function of wettability between the two substrates (280, 302, 303).

Fracture theory

This theory describes the force needed for the separation of two surfaces after mucoadhesion. The fracture strength is equal to mucoadhesive strength as explained in **Equation 1.21**. This theory is useful for the study of mucoadhesion by tensile apparatus.

$$\sigma = (E \times \varepsilon/L)^{1/2} \quad \text{.....Equation 1.21}$$

where σ is the fracture strength, *E* fracture energy, ε young modulus of elasticity, and L is the critical crack length (296).

1.7 Objectives of this project

Solid dispersions are most commonly prepared as binary drug-polymer models which are not necessarily reflecting the situation in real life complex pharmaceutical preparations. There is a lack of knowledge about the behaviour of complex solid dispersions with respect to the solubilisation of the drug, processing parameters, physical and chemical stability during and after preparation and the pharmaceutical properties of the fabricated products. This study aimed to prepare complex solid dispersions systems using a variety of blends of felodipine with different pharmaceutical excipients having various applications to produce final form products. These solid dispersions were designed using two different approaches with diversity in formulation objectives. The first approach was through the use of hot melt extrusion in conjunction with injection moulding (HME-IM) as a single step processing, environmentally friendly and efficient method to prepare felodipine buccal patches for enhancing the systemic bioavailability of felodipine via solubility/dissolution enhancement and avoidance of the extensive first pass effect of the drug. The second approach was the use of fused deposition modelling (FDM) 3D printing utilising various combinations of pharmaceutically approved excipients as a novel method of enhancing their printability. Successful preparation of dosage forms using FDM 3D printing is expected to play a major role towards more patient personalised medicines which in turn can improve patients' adherence to medications and treatment efficiency. Also, this study used two novel characterisation techniques: thermal analysis by structural characterisation (TASC) and X-ray micro computed tomography (XμCT) as a tool for investigating the heterogeneity and the spatial distribution of phases of the complex formulations prepared in this study.

The specific aims of the study include:

1. Investigating the physicochemical properties of the raw materials and their compatibility with the model drug that are used throughout this study.
2. Design, characterisation and evaluation of felodipine mucoadhesive buccal patches using HME-IM processing containing either Tween 80 or TPGS as surfactant-rich drug solubilisation and stabilisation phases.
3. Using TASC and XμCT as novel techniques for the assessment of heterogeneity and the phase distribution of the complex solid dispersions prepared by HME-IM.
4. Investigating the stability of the prepared HME-IM patches after storage at four different conditions of temperature and relative humidity and the impact of the role of surfactant type on the stability of the system and the recrystallisation of the incorporated drug.
5. Exploring the approach of using polymeric mixtures to improve the FDM 3D printability of pharmaceutical solid dispersions. This also involves the development of oral felodipine solid dispersions discs using FDM 3D printing and investigating their microstructure, loading efficiency and their release characteristics as a personalised oral dosage form for felodipine.

Chapter 2. Materials and methods

2.1 Introduction

In this study, the model drug selected was felodipine which was mixed with blends of a variety of pharmaceutical excipients including polyethylene glycol (PEG) 4000, polyethylene oxide (PEO), polyoxyethylene sorbitan monooleate (Tween) 80, d-α-tocopheryl polyethylene glycol 1000 succinate (vitamin E TPGS), polyvinyl caprolactam-polyvinyl acetate-polyethylene glycol graft copolymer (Soluplus), dimethylaminoethyl methacrylate-butyl methacrylate- methyl methacrylate copolymer (Eudragit E PO) and polyvinyl alcohol (PVA) in different combinations and loading percentages as solid dispersion based formulations. This chapter introduced the chemical and physical properties of these compounds and reviewed the current applications of these materials.

Solid dispersions were prepared using either hot melt extrusion in conjunction with injection moulding (HME-IM) or fused deposition modelling (FDM) 3D printing. HME-IM was used to prepare buccal patches containing felodipine which would bypass its extensive hepatic metabolism when taken orally, improving its systemic bioavailability and allowing a minimum dose to be given through the buccal route. FDM 3D printing was used the potential of providing patients personalised formulations based on pharmaceutically approved excipients with improved dissolution profiles via a solid dispersions approach.

In order to fully understand the characteristics of the HME-IM and FDM 3D printed products, it is essential to investigate the physicochemical properties of their individual components, intermediate blends, and finished products using a wide range of techniques. In this chapter, the characterisation tools used for the analytical purposes are introduced and discussed in details. These techniques include differential scanning calorimetry in standard (DSC) and modulated (MTDSC) modes, attenuated total reflectance Fourier transform infrared spectroscopy (ATR-FTIR), powder X-ray diffraction (PXRD), scanning electron microscopy (SEM), element dispersive spectroscopy (EDS), X-ray micro computed tomography (XμCT), thermal analysis by structural characterisation (TASC), thermogravimetric analysis (TGA), dynamic vapour sorption (DVS), polarised-light hot stage microscopy (PL-HSM) and Fourier transform infrared (FTIR) imaging. Furthermore, the techniques used to assess the *in vitro* performance of the formulations including stability testing, mucoadhesive study using texture analyser, and *in vitro* dissolution studies were also described in this chapter.

2.2 Materials

2.2.1 Model drug

In this study, felodipine as one of the potent calcium channel antagonists normally used to treat patients suffering from hypertension and for prevention of angina pectoris was used as the model drug. As a member of the dihydropyridine family, felodipine exerts its effect by selective relaxation of the vascular smooth muscles through inhibition of calcium influx via the slow channels (304, 305). Felodipine was used as the model drug to be formulated as buccal patches using HME-IM and personalised medicine prepared by FDM 3D printing. Felodipine was selected because:

1. It is poorly water soluble drug (practically insoluble in water) and has high permeability through body membranes. It is classified as class II according to Biopharmaceutical Classification System (BCS) and therefore using solid dispersion technology is expected to improve its dissolution and bioavailability which potentially improve the therapeutic outcomes of the drug (306, 307).
2. The drug is marketed as oral modified release tablets containing 2.5, 5, and 10 mg per tablet as single drug tablets and as combination film coated tablets with ramipril containing 2.5 and 5 mg felodipine (308). The daily dose of felodipine is 5-10 mg (307) and its small molecular weight make this model drug as a typical candidate to be delivered through buccal mucosa where minimum drug absorption is expected to reach its therapeutic window (239, 309). In addition, the single daily dosing of the drug suits well with the frequency of dosing using buccal drug delivery.
3. Felodipine shows an extensive first pass metabolism when absorbed through the gastrointestinal (GI) tract and approximately 84% of the administered dose deactivated through the liver (310). Therefore, buccal drug delivery is better alternative route of felodipine administration.

2.2.1.1 Physicochemical and pharmacokinetic properties

The chemical structure, physicochemical and pharmacokinetic properties of felodipine (ethyl methyl (4RS)-4-(2,3-dichlorophenyl)-2,6-dimethyl-1,4-dihydropyridine-3,5-dicarboxylate) are shown in **Figure 2.1** and **Table 2.1** (311).

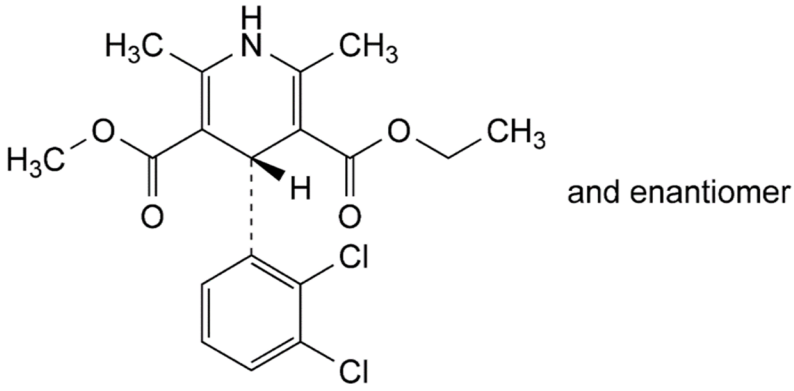

Figure 2.1: Chemical structure of felodipine, adapted from reference (312)

The complete single crystal structure details of four polymorphic forms of felodipine reported in literature. Their melting peak onsets are 143.8 ± 0.2, 134.8 ± 0.2, 143.7 ± 0.2 and 145.7 ± 0.2℃ for forms I-IV, respectively (312-314). In addition, the FTIR data indicated that these polymorphic forms showed different strengths of intermolecular hydrogen bonds between the NH group and the C=O groups. The NH stretching in their IR spectra have been reported at 3372, 3334, 3370, 3329 cm^{-1} for the four crystalline polymorphic forms I-IV, respectively (313-315). Furthermore, the amorphous form showed NH stretching peak at ~ 3339 cm^{-1}. The non-hydrogen bonded C=O group and the hydrogen-bonded C=O stretching peaks were detected at (1699 and 1690 cm^{-1}) for form I, (1698 and 1683 cm^{-1}) and form II, (1703 and 1654 cm^{-1}) for form IV and (1701 and 1682 cm^{-1}) for the amorphous form (313, 314, 316-318). No data is found for the C=O stretching of form III in literature. It should be mentioned that the crystal habits of the different forms were found to be blocky shaped for polymorphs I and II and platy like crystals for form III (319). No available information about the crystal habit of polymorph IV of felodipine has been reported (319).

Table 2.1: Physicochemical and pharmacokinetic properties of felodipine

Property	Details	References
CAS	72509-76-3	(311)
Chemical formula	$C_{18}H_{19}Cl_2NO_4$	(311)
Molecular weight	384.254 g/mole	
Polymorphic forms	4	
Melting temperature onsets (Tm)	Form I = 143.8 ± 0.2 ºC Form II = 134.8 ± 0.2 ºC Form III = 143.7 ± 0.2 ºC Form IV = 145.7 ± 0.2 ºC	(312, 314)
Glass transition temperature (T_g)	43.5 ºC	(320)
Solubility in water	Less than 0.5 mg/L	(321, 322)
PKa	5.71	(323)
Log P	4	(307)
Oral dose	5-10 mg/day	
C_{max}	12 ± 4 (nmol/L)	(324)
t_{max}	2.2 ± 1 (hrs)	
V_{ss}	10.3 ± 3 (L)	
Cl	934 ± 210 (mL/min)	
Cl_{oral}	10.3 ± 3 (L/min)	
$t_{1/2}$	13.6 ± 4 (hrs)	

2.2.2 Excipients

2.2.2.1 Polyethylene glycol (PEG) 4000

Polyethylene glycols (PEG) are widely utilised as pharmaceutical excipients in the formulation of different dosage forms including parenteral, topical, ophthalmic, oral, and rectal products (325). They are used as vehicles in the preparation of solid dispersions because they have good solubilising properties, low melting temperatures, high solidification rates, economic cost, and low toxicity (62, 326, 327). As shown in **Figure 2.2**, PEG is a group of hydrophilic semicrystalline polymers that show both amorphous and crystalline regions at different proportions depending on their method of manufacturing and thermal history involved during preparation (328, 329).

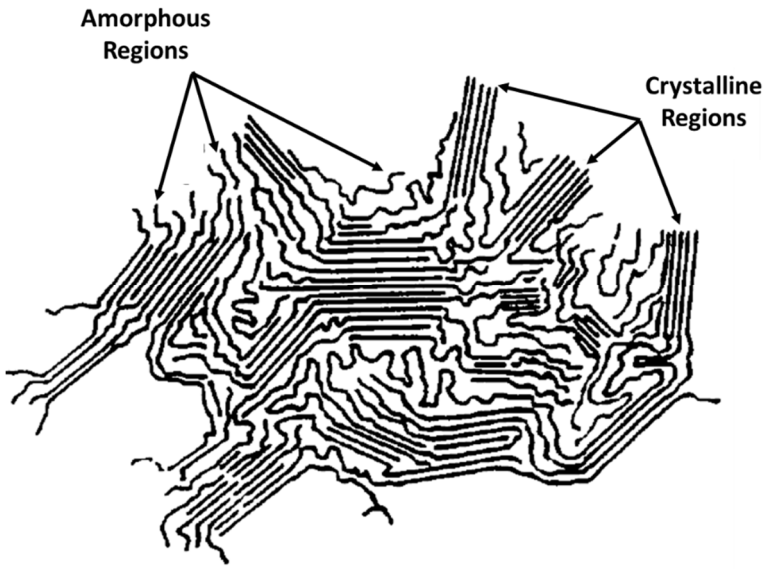

Figure 2.2: Schematic representation of the crystalline-amorphous structures of PEG, adapted from reference (329)

The molecular formula of PEG is $[H(-OCH_2CH_{2-})_nOH]$ where n represents the number of ethylene oxide $(-OCH_2CH_{2-})$ monomers within the polymer chain depending on its molecular weight (330). The chains of crystalline domains of PEG are composing of seven monomer units with two turns per fibre identity period (chain repetition distance) of 19.3 ˚A as illustrated in **Figure 2.3a**. It should be mentioned that the helical structures of PEG chain in their crystals was confirmed by using scanning tunneling microscopic (STM) imaging as shown in **Figure 2.3b** (331).

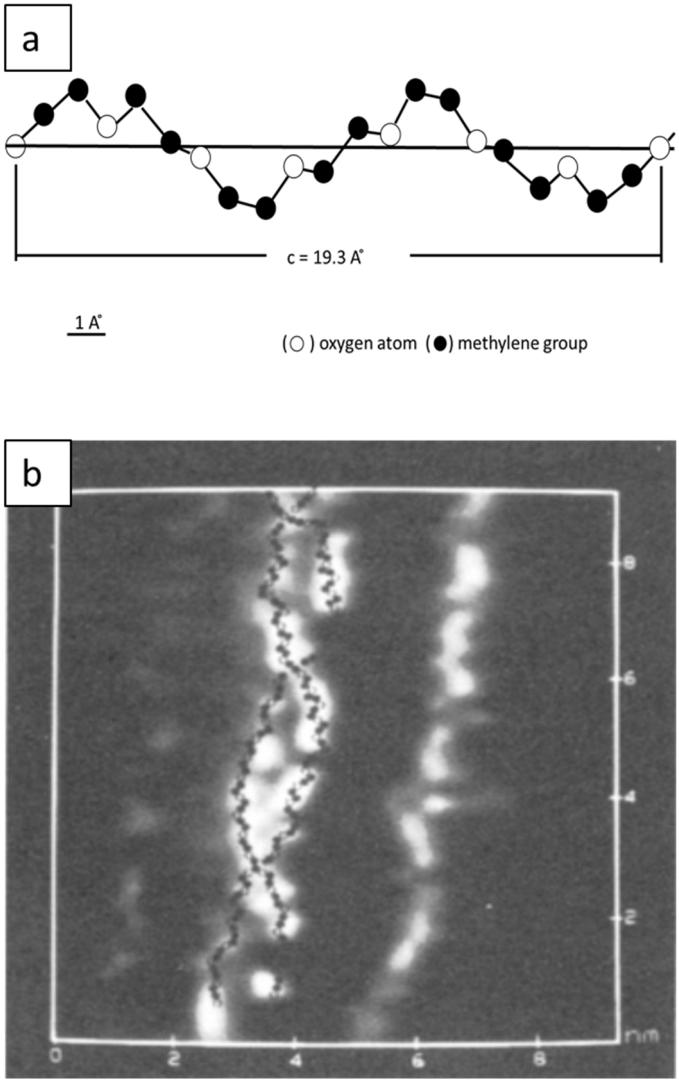

Figure 2.3: a) Molecular model representing single-stranded helix of PEG consisting of seven monomer units with two turns per repeat unit and b) STM image of single- and double-stranded helices of PEG; adapted from reference (331). Reproduced with permission from the publisher

The crystallographic unit cell of the PEG composes of four molecular chains with a monoclinic crystal system in which a = 7.96˚A, b = 13.11˚A, c = 19.39˚A and β = 124.48˚(332). The PEG single crystal has a flat or plate like structures named *lamellae* in which the helical chains extend perpendicular to the larger sides of the lamellae and the ends rejected to the surface of the crystal as illustrated in **Figure 2.4a** (332-334). The lamellae are organised in the spherulites in a way that the chains are oriented parallel to the tangential plane of the spherulite boundary which is responsible about the overall spherulitic morphology. The spherulites may be as big as 1 cm in diameter due to the slow nucleation rate of melt crystallisation (**Figure 2.4b**) (335).

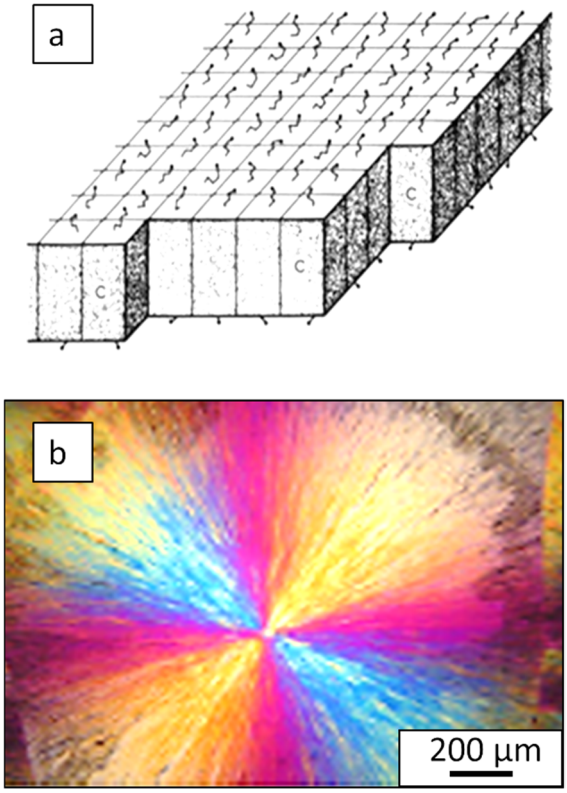

Figure 2.4: a) Model illustrating single layer extended chain PEG crystal; adapted from reference (332) and b) polarised light hot stage microscope image of crystallised PEG 4000; adapted from reference (336)

Inside each of the lamellae, the polymer chains are present in both the extended (stable) and the folded (metastable) forms in addition to the amorphous random coil fraction. The folded chains have lower melting points compared to the extended ones and are considered as the metastable form of the polymer. The melting point of the polymer is found to decrease as the number of folds in the chains increases. In addition, the kinetic stability of the metastable form increases as the molecular weight of the PEG increases (328, 330). The folded form may transform to the more stable extended form. The ordered helical structure of the polymer is converted completely into random coils on melting when the polymer melts (337).

PEG 4000 used in this study with an average molecular weight (4060 g/mole) is solid at room temperature and has a melting point of (58.9) °C measured by DSC using a heating rate of 4 °C /min (335). It is well known that PEG 4000 crystalline forms were detected in its lamellae as a mixture of single folded form with the more stable extended form (328, 330). The thickness of the crystal is found to decrease as the number of folds increased and thus the volume to surface

ratio being the lowest for the single folded form making it the less stable form of the polymer (328, 330). The fraction of the unstable folded form of this polymer is greatly affected by the cooling rate of the polymer when cooled from its molten state. It was reported that as the rate of cooling of this polymer from its molten state increased, the fraction of the folded form generated increased too (338).

PEG 4000 has been used widely as a carrier in the preparation of solid dispersions for enhancing the aqueous solubility and improving the bioavailability of many drugs (198, 339-342). It was found that the *in vitro* release profile of lonidamine was improved by formulating the drug with PEG 4000 and the extent of enhancement is dependent on the polymer content in the dispersion (340). In addition, the same polymer was reported to form solid dispersions with piroxicam with faster dissolution rate compared to simple physical mixtures resulting in a significant increase in the bioavailability of the drug in rabbits (341). Similarly, faster dissolution rate of extruded carbamazepine-PEG 4000 solid dispersions was achieved compared to simple physical mixtures with equivalent compositions (342). This polymer forms various kinds of solid dispersions in which the drugs might be either present as a molecular dispersion or as a nano amorphous aggregates dispersed in the amorphous phase of the polymer (343-345). In addition, monotectic solid dispersions of drugs with poor water solubility can also be produced using this polymer in which the eutectic temperature of the mixture is very close to one of the formulation components (PEG 4000) (38, 346). The stability of solid dispersions is dependent on many factors including the experimental conditions (temperature, humidity, duration of storage), nature of the dispersion components (drug and the carrier) and the physical characteristics of the dispersion formed. For example, it was found that PEG 4000 forms solid dispersion with oxazepam in which the dissolution behaviour was unchanged during the storage at room temperature for 6 months (47). On the other hand, the dissolution profile of the aged PEG 4000 dispersions of glyburide was found to be lower than that of the fresh samples due to the possible phase separation of the drug when aged at room temperature (339). The mechanism of dissolution/solubility enhancement of water poorly soluble drugs from solid dispersions using PEG 4000 was shown to be due to the increase in surface area of the molecularly dispersed drug from solid solutions (126), formation of the metastable highly soluble amorphous form of the drugs (339), increased solubility of drugs in the fluids of the diffusion layer (44) and/or improvement the wettability of the drug by the carrier used (126).

2.2.2.2 Polyethylene oxide (PEO)

Polyethylene oxide (PEO) is semi-crystalline, thermoplastic hydrophilic polymer has the same molecular formula as that of PEG [$H(-OCH_2CH_{2-})_nOH$]. The nomenclature of the two groups of polymers refers to the number of ethylene oxide monomers forming its chain. PEO polymer grades have a molecular weight range between 10^5 to 7×10^6 g/mole depending on the number of monomeric units included in its chain. These polymers are white to off-white, free-flowing powders with slight ammoniacal odour. They have a melting range of about 65–70 °C, true density 1.3 g/cm^3 and moisture content less than 1% w/w (347, 348). In contrast to PEG which is existing as relatively viscous fluid to waxy like solids, PEO is a real thermoplastic polymer having the ability to form tough and moulded shapes. This difference in physical properties is related principally to the molecular mass between the two groups of polymers and most importantly the higher fraction of hydroxyl terminal group in PEG compared to PEO (349). PEO has many applications in the formulation of various pharmaceutical products like sustained release tablets (350) matrix tablets (351), beads (352) and film dressing for wound healing (353). This polymer has many characteristic features including its excellent mucoadhesivness, good water solubility, high viscosity, good swelling capacity (higher molecular weight PEO), poorly absorbed by the GI tract, and low level of toxicity regardless the route of administration. This polymer is incompatible with strong oxidising agents (348).

The molecular weights for PEO used in this study are 900,000 g/mole (PEO K900) for HME-IM and 100,000 g/mole (PEO K100) for FDM 3D printing. The number of polyethylene oxide units in the polymeric chains for both grades are approximately 20,000 and 2,275 monomers respectively (348). This class of polymers are used to control the release of drugs by forming a strong swellable matrix upon hydration that is less liable to erosion compared to the lower molecular weight PEO grades (354, 355). PEO polymers have been recognised as a successful carrier for the preparation of solid dispersions by HME method due to their thermoplastic nature (144, 356). When used to control the release of drugs using HME, this polymer offers a number of advantages including the possibility of incorporating drugs with liable to degradation when processed at high temperatures, zero-order release kinetics, and easy preparation. It was reported that this polymer offers great flexibility in adjusting the release profiles by altering various formulation and processing parameters like the molecular weight of the polymer used in the formulation as shown in **Figure 2.5** (357).

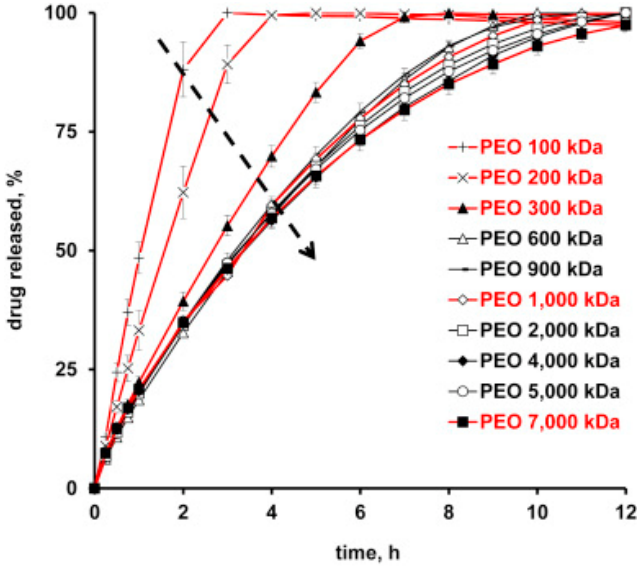

Figure 2.5: Influence of PEO molecular weight on the release profile of theophylline from the hot melt extrudates in phosphate buffer pH 7.4; adapted from reference (357)

As an example, this polymer was found to form a stable solid solution of chlorpheniramine maleate in which the drug is molecularly dispersed in the carrier polymer using low loading percentages. The release profile of the drug from the solid dispersion was sustained by polymeric erosion and the diffusion of the drug through the swollen layer formed at the surface of the tablet (356).

The thermal stability of pure PEO was found to be dependent on the storage temperature and the molecular weight of the polymer. It was shown that as the molecular weight of the polymer increased, the thermal stability resulting from resistance to thermal oxidative degradation was increased (144). This has been explained this in terms of the thickness of polymer crystals rather than the degree of crystallinity of the polymers. It was argued that the higher molecular weight polymers crystallise in thicker crystals which are less susceptible thermal oxidation compared to the thinner crystals formed by the polymer members of lower molecular weights (144). The stability of the practically insoluble drug clotrimazole in PEO N80 and PEO N750 (molecular weight 200,000 and 300,000 g/mole respectively) solid dispersions using HME method was investigated by Prodduturi and co-workers (358). It was found that the drug was more chemically stable in PEO N750 than in PEO N80 due to the lower water sorption capacity of the PEO N750 polymer grade. Also, it was noticed that the physical stability of the extruded films was good as solid dispersions for 1 month at 25 ˚C and 65% RH. However, the appearance of the characteristic PXRD peaks after 3 and 6 months indicated recrystallisation of the solubilised drug in the carrier polymer (358).

The bio/mucoadhesive properties of PEO polymers are very attractive for many researchers aiming to develop bioadhesive dosage forms with zero order release kinetics (358, 359). These polymers showed direct proportion between the molecular weight of the polymer and the adhesiveness and the work of adhesion of the prepared dosage forms. In this case, the mucoadhesion mechanism is explained according to the diffusion theory in which the magnitude of stickiness depends on the degree of penetration of the polymeric chains into the mucus glycoprotein chains (359).

2.2.2.3 Polysorbate (Tween®) 80

Polysorbate 80 (polyoxyethylene 20 sorbitan monooleate, molecular weight = 1310 g/mole) is a non-ionic surfactant commonly used in the production of cosmetics, food and pharmaceutical products. This surface active agent has an HLB value of 15 and used for its dispersing, emulsifying, solubilising, suspending, plasticising, penetration enhancing and wetting activities (360, 361). At 25 ˚C, it presents as yellow oily liquid miscible with water and ethanol and immiscible with vegetable and mineral oils. Tween 80 is regarded as hygroscopic material and should be stored in well-closed containers protected from light in a cool and dry place (360). In general, Tweens are stable compounds when mixed with electrolytes, weak acids and bases, however, they show gradual saponification with strong acids and bases and the oleic acid derivatives like Tween 80 were found to be sensitive to thermal autoxidation and hydrolysis. Tween 80 is moderately toxic when administered by intravenous (IV) route (LD_{50} = 4.5 g/kg) and mildly toxic after ingestion (LD_{50} = 25g/kg) in mouse (143, 360-362). Tween 80 has a CMC of 0.012 mM in water at 25 ˚C (363). The chemical structure of Tween 80 is shown in **Figure 2.6**.

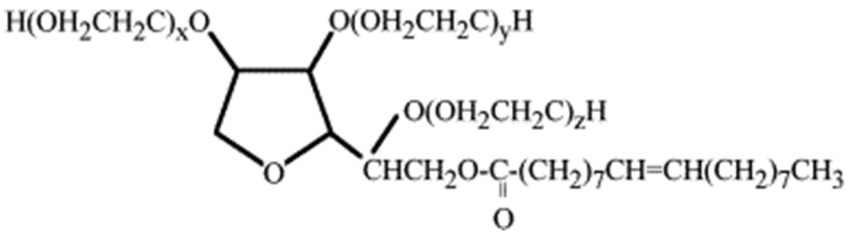

Figure 2.6: Chemical structure of Tween 80 (x + y + z = 20); adapted from reference (364)

Various surfactants were used in the preparation of solid dispersions for their plasticisation effect and their ability to improve the solubility of poorly soluble drugs in the carrier polymers. Many researchers demonstrated that these agents have the ability to enhance the solubility of drugs in their formulations by improving their wettability and the solubility. The capability of surfactants

to achieve this target is dependent on their HLB value, solubilisation power, and the possible interactions with both the drug and the carrier polymer (361, 365-368). Tween 80 has also been reported to act as a permeation enhancer to facilitate the penetration of various drugs into the systemic circulation across different biological membranes like the intestine (369), skin (370, 371) and buccal mucosa (372). Compared to anionic and cationic surfactants like sodium lauryl sulphate and cetyl trimethyl ammonium bromide, non-ionic surfactants were reported to be less damaging to the skin as permeation enhancers (373). It should be mentioned that the enhancement of drug penetration by using surfactants as chemical enhancers is variable because of its dependence on the type of the targeted membrane utilised in the experiment (373). Tween 80 is considered as an effective surfactant for stabilising and preventing the crystallisation of drugs from their supersaturated solid dispersions (374).

2.2.2.4 D-α-tocopheryl polyethylene glycol 1000 succinate (vitamin E TPGS, Kolliphor® TPGS)

Vitamin E TPGS is a water soluble non-ionic surfactant obtained by esterification of vitamin E with polyethylene glycol (PEG) 1000. Due to its hydrophilic-lipophilic moieties represented by the fat soluble vitamin and the water soluble PEG, this surface active agent shows an amphiphilic character with an HLB value of 13.2 and critical micelle concentration of 0.02% w/w in water (375). This compound is waxy solid at room temperature and has a melting point peak approximately at 37-41℃. The molecular weight of TPGS is 1513 g/mole (375). The chemical structure of vitamin E TPGS is illustrated in **Figure 2.7**.

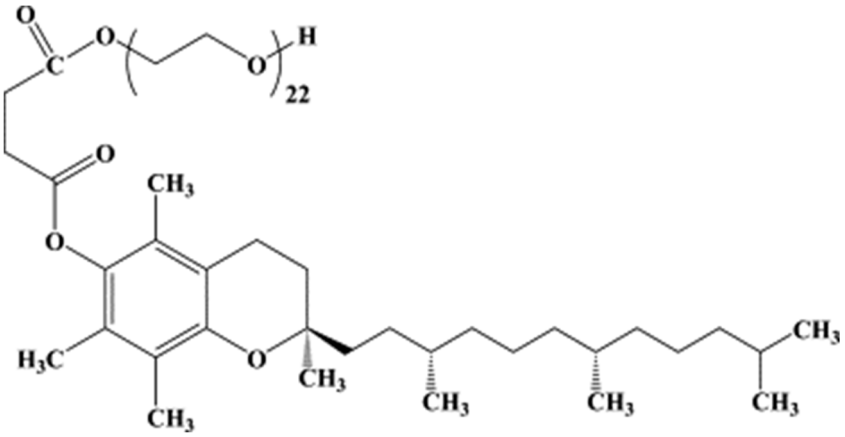

Figure 2.7: Chemical structure of vitamin E TPGS; adapted from reference (376)

TPGS has been widely used in pharmaceutical formulations for its valuable properties as solubilising (377, 378), plasticising (200), stabilising (379), antioxidant (144, 380), absorption enhancing (381), emulsifying agent (382), and as a nutritional supplement of vitamin E (383). For example, TPGS based formulations showed to significantly improve the solubility of poorly water soluble drug indomethacin over a wide range of pH values (377). Another case, the aqueous solubility of paclitaxel was found to be increased linearly as the concentration of TPGS increased (378). It was also reported that mixing this compound with blends of polymers containing hydroxypropyl cellulose (HPC) and polyethylene oxide (PEO) revealed a decrease of more than 11℃ in the T_g of the mixture indicating the plasticising action of TPGS (200). TPGS also showed to be able to solubilise and stabilise the amorphous form of itraconozole in solid dispersions prepared by microwave with the result of improving the dissolution properties of this poorly water soluble drug (384). The surfactant in a concentration of 1-2% solution was also reported to stabilise itraconozole in its supersaturated solutions compared to the drug alone (385). The TPGS needs to be hydrolysed to release the α-tocopherol succinate unit (vitamin E) which is well known to have free radical scavenger activity (386). Crowley and his co-workers showed that incorporating this surfactant successfully retarded the thermal oxidative degradation of PEO contained in chlorpheniramine maleate extrudates prepared by hot melt extrusion (144). In addition, this amphiphilic compound is shown to have a permeability enhancing effect by increasing the intraluminal amprenavir concentration in a concentration-dependent manner (387).

2.2.2.5 Poly(butyl methacrylate-co-(2-dimethylaminoethyl)methacrylate-co-methyl methacrylate) (Eudragit® E PO)

Eudragit E PO is a cationic polymethacrylate copolymer used to provide gastric targeted release profiles due to its pH dependent solubility in acidic media (pH < 5). The E PO grade of this polymer is a white powder with a characteristic amine-like odour (388). The average molecular weight of this amorphous polymer is about 74,000 g/mole, and its T_g is 48.6℃ (389, 390). The chemical structure of Eudragit® E PO is illustrated in **Figure 2.8**.

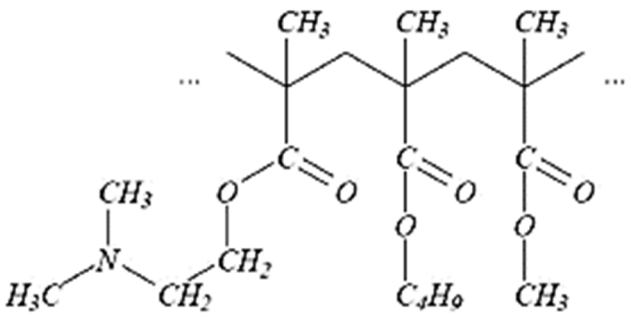

Figure 2.8: Chemical structure of eudragit® E PO; adapted from reference (391)

Eudragit® E PO has many applications in the pharmaceutical field including film coating (388), solid solution carrier to improve the dissolution properties of poorly water soluble drugs (392) and to mask the taste of bitter drugs (393). This copolymer has been used as a principle component of many formulations like solid dispersions (392), nanoparticles (394) and rapid disintegrating tablets (393). It has been used as a carrier in the preparation of solid dispersions using HME as a single polymer or as a polymeric blend to improve the dissolution properties of poorly water soluble drugs like felodipine and indomethacin (73, 389). This polymer has relatively low glass transition temperature which makes it as a good polymeric candidate for preparing solid dispersions for poorly water soluble drugs at an acceptable temperature. Eudragit E PO was found to significantly improve the dissolution properties of felodipine using 10% drug loadings as a binary and ternary mixture using PVPVA. Also, the concentration of Eudragit E PO in the dissolution medium of pH = 1.2 at 25℃ was found to solubilise felodipine in the aqueous solution to higher extent compared to corresponding concentrations of PVPVA and their polymeric blend (73). The thermal dissolution of indomethacin in Eudragit E PO melt was reported to be convective and can be enhanced by increasing processing temperature and extruder screw speed (389). In addition, it was found that a stable supersaturated concentration of indomethacin over 100 minutes of dissolution at pH 1.2 was achieved using a higher processing temperature indicating the formation of molecularly dispersed drug in the polymer matrix (389). It should be mentioned that due to the cationic character of this polymer, it can form strong interactions with anionic drugs resulting in stabilisation of their molecular level amorphous solid dispersions (395).

In this study, Eudragit E PO was used as a principle polymer in the fabrication of felodipine solid dispersions using FDM 3D printing technology due to its reported use as a carrier for drug loaded solid dispersions processed using HME indicating its good thermoplastic, solubilising and stabilising properties. In addition, the pH dependent solubility of this polymer makes it as a

suitable pharmaceutically approved carrier for immediate release of felodipine from the designed formulations.

2.2.2.6 Polyvinyl caprolactam-polyvinyl acetate-polyethylene glycol graft copolymer (Soluplus)

Soluplus is a novel amphiphilic graft copolymer designed specifically for improving the dissolution properties of poorly water soluble drugs (BCS class II) using HME. The copolymer performs this role by its interesting dual functionality of dispersing the drugs as molecularly dispersed in the polymeric matrix and its ability to form micelles in aqueous media (396). This recently developed polymer has a white to slightly yellowish freely flowing granules with a molecular weight within the range of 90,000-140,000 g/mole. The copolymer is soluble in water, acetone (up to 50%), methanol (up to 45%), ethanol (up to 25%) and dimethylformamide (DMF) (up to 50%) at room temperature. The chemical structure of soluplus is illustrated in **Figure 2.9** (56). The measured critical micelle concentration (CMC) for soluplus and its extrudates were found to be 1.93 µg/mL and 4.24 µg/mL at 37 °C, respectively. The determination of two critical micelles values for soluplus was attributed to the partial splitting of chains of the polymer (397).

It was reported that the presence of dissolved ions in the solution of hydrophilic polymers like soluplus which exhibit sol-gel behaviour can affect the solubility of the polymer (398, 399). Dissolved ions in the media have the ability to dehydrate this polymer by competing with it on the water of hydration resulting in precipitation of the polymer in a phenomenon called salting out (400). For these polymers, as the temperature increases, they start to precipitate and form a gel at the gelation temperature and thus the transmission of light will decrease due to precipitation. The temperature at which 50% of the transmission light is reduced is termed the cloud point (401). The presence of the dissolved ions was reported to reduce the cloud point and this phenomenon was also previously reported to happen in solutions of hydrophilic polymers like hypromellose (402), poloxamer (403) and soluplus (149).

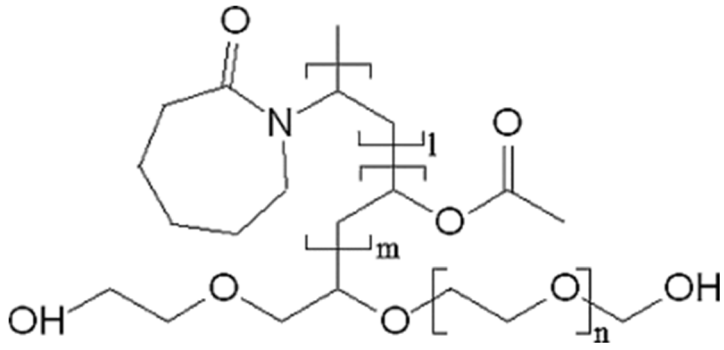

Figure 2.9: Chemical structure of soluplus; adapted from reference (404)

Soluplus is an amorphous polymer with a T_g of approximately 70℃ with excellent thermoplastic properties making it a suitable for HME as processing technique at relatively safe temperatures. This polymer was used principally as a solubiliser for BCS class II drugs for the production of amorphous solid dispersions using different fabrication techniques including HME, electrospining, spray drying and freeze drying, etc. (87, 396, 404). In addition, this amphiphilic copolymer showed an interesting absorption enhancing activity which can be used as additional functionality to improve the bioavailability of drugs through the biological membranes (405). This polymer was used effectively to improve the dissolution properties of drug like atorvastatin calcium (406), efavirenz (407) ezetimibe and lovastatin (408). It should be mentioned that this polymer was used as a single carrier or as a component of polymeric blend for the production of molecular level amorphous solid dispersions (118, 407). In this study, soluplus was used as the main polymer in a blend of excipient used for fabricating felodipine solid dispersions by FDM 3D printing.

2.2.2.7 Polyvinyl alcohol (PVA)

PVA is one of the widely used synthetic pharmaceutical polymers because it is water soluble, thermally stable, it has low gas permeability, good adhesiveness, biocompatibility and biodegradability (409). It functions as a coating, lubricant, stabilising and viscosity increasing agent in different pharmaceutical dosage forms and drug delivery systems. This partially crystalline polymer occurs as an odourless white to creamy granular powder with variable degrees of hydrolysis and molecular weights. This polymer exists as wholly or partly hydrolysed with different degrees of hydrolysis. The partially hydrolysed form is a copolymer of vinyl alcohol and vinyl acetate units originally synthesised by polymerisation of polyvinyl acetate followed by alkaline aqueous hydrolysis (in the presence of sodium hydroxide) to substitute the acetate by a

hydroxyl group. The extent of hydrolysis ranging from 30-99% and the hydrolysis is dependent on the concentration of the catalyst, reaction temperature and time and the molecular weight of the polymer (410). The degree PVA hydrolysis affects the aqueous solubility of the polymer which increases with the increase in the degree of hydrolysis. Also, the crystallinity is reported to increase with increasing the extent of hydrolysis (410). The reported melting points for the fully and partially hydrolysed grades are 228℃ and 180-190℃ respectively. The water solubility is reported to be higher for highly hydrolysed grades compared to the grades with the lower percentage of hydrolysis (185, 411). The molecular structure of this polymer is shown in **Figure 2.10**.

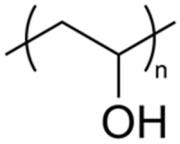

Figure 2.10: Chemical structure of hydrolysed PVA; adapted from reference (412)

PVA is considered as a component for the formulation of variety of pharmaceutical preparations such as hydrogels (413), solid dispersions (414) and nanoparticles (415).

PVA was used as a thermoplastic hydrophilic polymer for solubilising and stabilising drugs in solid dispersions prepared by HME. Indomethacin was found to be partially miscible in the amorphous domains of the semicrystalline structure of PVA as revealed by the consistent results of thermal analysis using hot stage microscopy and DSC. The same study indicated immiscibility between PVA and lacidipine as indicated by the detection of two glass transition temperature belonging to the amorphous drug and the amorphous fraction of the semicrystalline PVA (416).

Recently, it was reported that partially hydrolysed PVA grades with a degree of hydrolysis higher than 70% were able to solubilise celecoxib and hydrochlorothiazide with improved release profiles. The release profiles of the two drugs from the grades of the lower degree of hydrolysis were found to be influenced by the ionic strength of the dissolution medium. To overcome the degradation problems that may affect the stability of thermosensitive drugs due to the high processing temperature of the binary systems (180℃), sorbitol was used as a plasticiser to reduce the extrusion temperature of PVA. The plasticised extrudate was cryomilled, mixed with celecoxib and re-extruded at relatively acceptable processing temperature (140℃) with reduced mechanical shearing stress (screw speed reduced from 100 to 60 rpm). The dissolution profile of the ternary system for celecoxib was found to be superior in maintaining the supersaturation in

0.1 N HCl compared to the marketed product (Celebrex®) with highly comparable pharmacokinetic data (410).

PVA is one of most commonly used polymers in the recently introduced FDM 3D printing to the pharmaceutical research field to produce formulations loaded with a variety of APIs as a promising approach in the direction of personalised medicine. The standard PVA filaments produced for general printing purposes were used in the literature to print tablets loaded with drugs like 5- aminosalicylic acid (5-ASA, mesalazine), 4-aminosalicylic acid (4-ASA) and prednisolone using FDM 3D printing at processing temperature higher than 200℃ (226, 417). In order to load the prednisolone in PVA filaments, the filaments were incubated in a prednisolone saturated methanolic solution at 30℃ for 24 hours followed by drying at 40℃ and weighing the loaded filaments every hour until stable weight was achieved indicating evaporation of the organic solvent. It was found that PVA filaments loaded with prednisolone were able to be printed into regular ellipse-shaped tablets using this technology. The fabricated tablets with 1.9% w/w loading were able to extend the release of prednisolone to 24 hours (226). PVA was used as the benchmark polymer in this study because of its excellent thermoplasticity and good FDM 3D printability.

2.3 Characterisation methods

2.3.1 Thermogravimetric analysis (TGA)

In principle, this technique uses the mass change of the sample under investigation (as a function of temperature or time) to identify and quantify chemical or, to a lesser extent, physical events (like sublimation) caused by the application of certain temperature program under defined atmosphere. The temperature range of the commercially available TGA equipments are from ambient to more than 1000˚C enabling this technique to perform many flexible analytical tasks. The gaseous environment employed varies depending upon the experimental requirements and it could be an inert (like nitrogen, helium, and argon), oxidising (such as air or oxygen) or reducing (8-10% hydrogen in nitrogen) gases. The most important part of any TGA is the thermobalance which is responsible about the measurement of the mass change as a function of temperature or time (94).

In pharmaceutical practice, TGA has many applications like estimation the thermal degradability and desolvation studies of different pharmaceutical materials (94). In this project, TGA was used to evaluate the thermal stability of the raw materials involved in the preparation of felodipine formulations to prove their ability to withstand the temperature used during the HME-IM and FDM 3D printing techniques. In addition, the moisture content of these materials was also investigated as this considered as an important factor that affects the physical stability of the drug in the final solid dispersed patches.

In this study, TGA Q5000 (TA Instruments, Newcastle, USA) was used to evaluate the thermal stability of raw materials, physical mixtures and processed samples. In addition, TGA was used to assess the percentage of moisture entrapped within the samples under investigation.

2.3.2 Differential scanning calorimetry (DSC) and modulated temperature differential scanning calorimetry (MTDSC)

Differential scanning calorimetry (DSC) is an essential tool for the thermal analysis of materials in many fields including pharmaceutical product development. The principal of this analytical technique involves the detection heat changes accompanied thermal events like melting, crystallisation, glass transitions, and decomposition reactions induced by applying controlled temperature program (heating, cooling or isothermal) to the sample under a defined atmosphere (94). There are two kinds of DSC machines, these are heat flux and power compensation. Heat flux DSC uses two pans (crucibles) for the sample and the reference in a single furnace. Both crucibles are heated under the same temperature program and the difference in temperature between the pans is detected and converted into energy. On the other hand, power compensation DSC uses two furnaces for both of the sample and the reference and both of them are heated and maintained at the same temperature. The difference in energy supply to maintain the sample and the reference temperatures identical during the DSC experiment is then measured as sample thermal event (94). In this study, heat flux type of DSC was used.

Heat flow from the furnace to each crucible can be explained in **Equation 2.1**:

$$dQ/dt = \Delta T / R \quad \text{.....Equation 2.1}$$

where dQ/dt represents heat flow, ΔT is the temperature difference between the furnace and the pan and R is the thermal resistance in the heat flow between the furnace and the crucible (94).

The other fundamental parameter involved in DSC analysis is the heat capacity of the sample (C_p) which is defined as the energy supplied to increase the temperature of the certain material by one degree Kelvin (1 K). This parameter generally gives an estimation of the sample capability to hold energy at specified conditions. In DSC practice, this function can be expressed by the **Equation 2.2**:

$$dQ/dt = Cp \,.\, dT/dt \quad \text{.....Equation 2.2}$$

where dT/dt is the heating rate of the program (94).

Modulated temperature differential scanning calorimetry (MTDSC) is an extension of standard DSC in which the addition of sine waves to the temperature programme and a mathematical procedure are introduced for the purpose of separation (deconvolution) of various events that the sample might exhibit during the course of experiment. The deconvolution of these behaviours can be explained in **Equation 2.3**:

$$dQ/dt = Cp \,.\, dT/dt + f(t,T) \quad \text{.....Equation 2.3}$$

where f(t,T) is the time and temperature function that represents a response accompanying physical or chemical transitions. This equation separates between the reversible processes (processes in which the heat flows are correlated with the heat capacities of the samples) and irreversible processes (processes involve the contribution of the enthalpies of reactions) which cannot be separated using standard DSC. The temperature programme for MTDSC can be explained by **Equation 2.4**:

$$T = T_0 + bt + B \,.\, \sin(\omega t) \quad \text{.....Equation 2.4}$$

where T represents the temperature at time t, T_0 is the temperature at time zero, b is the heating rate, t is the time, B is the amplitude of oscillation, ω is the frequency of oscillation. Accordingly, the heat flow **Equation 2.3** can be rewritten in the following expression:

$$dQ/dt = Cp\,(b + B\omega \,.\, \cos(\omega t)) + f(t,T) + C\sin(\omega t) \quad \text{.....Equation 2.5}$$

where Bω . cos (ωt) represents the modulated heating rate, f(t,T) is the kinetic effect excluding the effect of modulation, and C is the amplitude of the kinetic response. The heating and cooling rates in MTDSC should be programmed in very slow rates for pharmaceuticals (1-3 ˚C/min) to prevent the appearance of artifacts into the reversing and non-reversing signals generated from the deconvolution of modulated heat flow signal (94).

In this study, thermal analysis of raw materials, their physical mixes, and processed formulations was conducted using the Q-2000 MTDSC (TA Instruments, Newcastle, USA) attached to RC90 cooling unit. Full calibration was performed before samples measurements. DSC in both standard and temperature modulated modes was used to investigate the thermal properties of raw materials, physical mixtures and fabricated formulations.

2.3.3 Thermal analysis by structural characterisation (TASC)

TASC is a recently developed technique by Reading et al as an optical analogue of micro/nano thermal analysis. This new microscopic tool has many applications like thermal dissolution analysis, glass transition kinetics, analysis of melting behaviour, analysis of heterogeneity as T-map mode and thermomechanical analysis (418, 419). This technique has the advantage of running the analysis in fast, easy and cheap cost in addition to its multiple applications. **Figure 2.11** represents the shape of the TASC signal corresponding to thermal events such as the melting of felodipine.

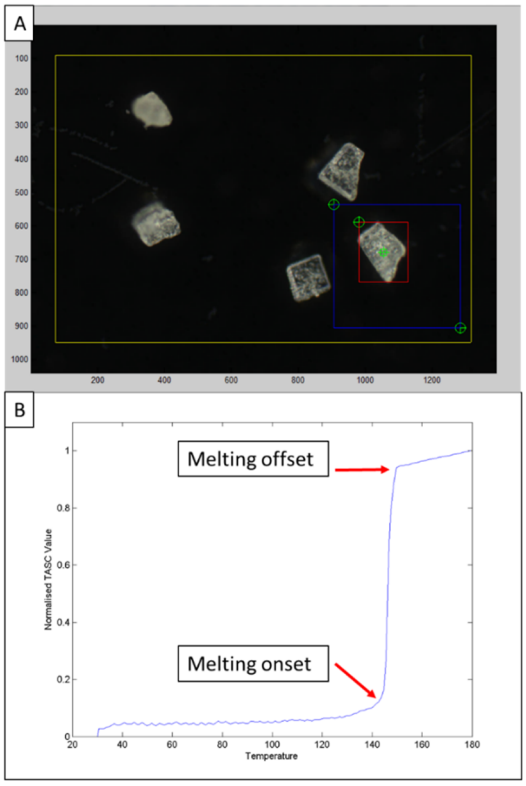

Figure 2.11: Thermal analysis by structural characterisation (TASC) of felodipine melting at 10 °C/ min; A) selection of ROI and TA for TASC analysis and B) TASC signal corresponding to felodipine melting

During the TASC experiment, heating, cooling and/or isothermal temperature programs with different ranges and rates can be applied to the sample under investigation. The method of analysis by TASC consists of quantifying changes in successive micrographs while at the same time allowing for any movement by the sample during the ramps. As illustrated in **Figure 2.12a**, a region of the sample is selected that is designated the region of interest or ROI (within which lies the structure of interest). Also, a larger area (the target area or TA) over which the ROI is scanned is selected (in this case, the TA is the entire 7 × 7 pixels). **Figure 2.12b** shows the extracted ROI that is the template that is raster scanned over the TA. At each point, in the scan, the corresponding pixels are subtracted and the sum of the modulus of all differences is calculated. In this simplified representation, subtracting the same pixel values gives zero and subtracting different pixels gives 1. After the scan is completed, it is the minimum value for the sum of all differences obtained during the course of the scan that is returned by the TASC algorithm. **Figure 2.12c** shows the start of the raster scan in the top left-hand corner. Because no structure is present in this part of the TA, when the ROI template is subtracted, the total sum of all subtractions is 1 (there is only one pixel where the ROI template is different from the selected region of the TA). The next step in the raster scan is to move the ROI template one pixel to the right as shown in **Figure 2.12d**; the value obtained is again 1. The ROI template is moved another pixel to the right, and the process continues until the entire TA has been scanned. The value zero is only obtained when the ROI template is in the centre of the TA as indicated in **Figure 2.12a**. This zero value is the minimum obtained during the course of the scan; thus, zero is returned by the TASC algorithm indicating no change. If the black pixel that represents the structure of interest moves as shown in **Figure 2.12e**, the value at the first point of the raster scan (such as the step illustrated in **Figure 2.12c**) is now zero. At all other positions, the value is greater than zero. It follows that the minimum value returned by the TASC algorithm at the end of the scan is still zero indicating no change even though the structure has moved. When the black pixel disappears, i.e., the structure has changed, the value returned at all points during the raster scan is 1 and TASC returns the value 1. Under this working principle, when the structure moves but does not change, the TASC value does not change, but when the structure changes, the TASC value increases. However, it is worth mentioning that for this to work the TA must be big enough so that the structure of interest does not travel outside of its limits. This is not difficult to achieve in practice simply by inspecting the first and last images.

For real-life samples of the type studied here, as the sample is heated, it often softens and all apparent structures vanish giving rise to a featureless image. In a typical experiment of this kind, there is no further change beyond this point; i.e., the intensity difference values are unchanging.

Thus, the TASC value reaches a plateau (of course decomposition will occur if the temperature is taken very high but this was always avoided in this study). All the values calculated relative to this plateau are then normalised because the absolute TASC values change with the size of the ROI and lighting conditions. Variations due to slight differences in lighting conditions are best removed by normalizing. Similarly, comparisons between different sized ROIs are best achieved by comparing normalised values.

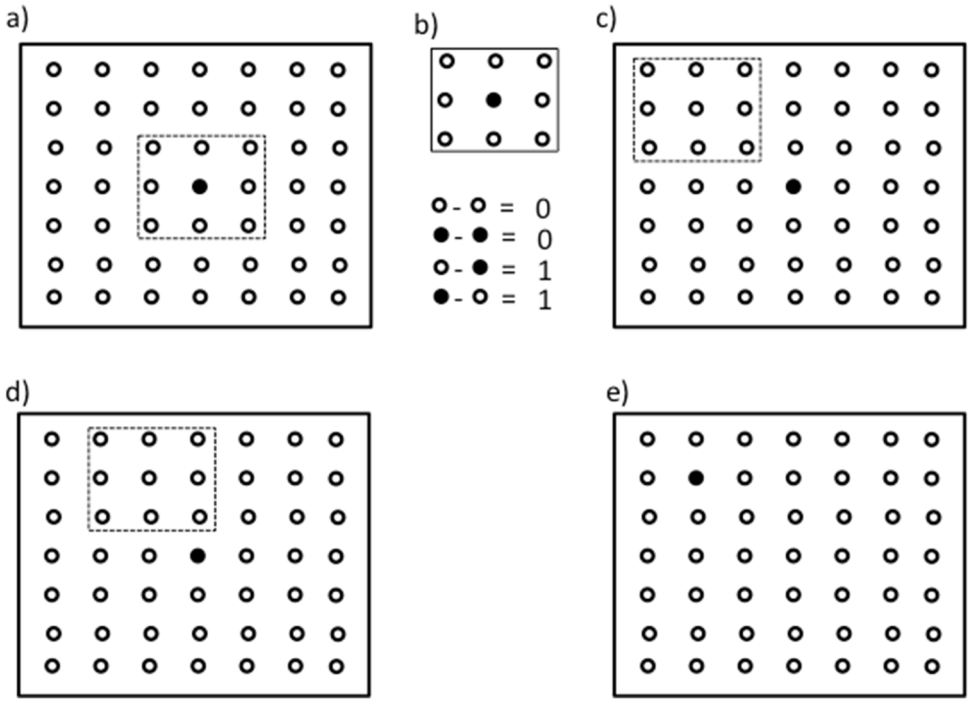

Figure 2.12: Working principle of TASC a) represents an image of 7×7 pixels that is the Target Area (TA). The Region of Interest (ROI) is designated by the dashed box and the black pixel represents the only structure in the ROI. b) is the extracted ROI which acts as a template that is raster scanned over the TA. Under b) the results of subtracting the different values for the pixels are given; in this simplified case subtracting the same values gives zero and subtracting different pixels gives 1. The raster scan starts in the top left corner as shown in c) with the dashed line, the sum of all differences in this case is 1 (only one pixel is different). When the ROI is moved one pixel to the right as shown in d) (the next step in the raster scan) the same value is obtained. If the black pixel moves as shown in e) the value at the start of the raster scan is zero

In this study, TASC was used as a novel thermal characterisation technique to investigate the heterogeneity of complex pharmaceutical solid dispersions prepared by HME-IM technology. The TASC system is composed of a Linkam MDSG600 automated temperature controlling (heating-cooling) stage (Linkam Scientific Instruments Ltd, Surry, UK), which is fixed to a

Linkam imaging station (Linkam Scientific Instruments Ltd, Surry, UK), and an imaging capture and analysis interface powered by TASC software provided by Cyversa (Cyversa, Norwich, UK). The microscope used in this study has a reflective LED light source and a lens with X10 magnification.

2.3.4 Dynamic vapour sorption (DVS)

Dynamic vapour sorption is a gravimetric method that measures the rate and the extent of solvent (like water) absorption and desorption by the sample under specified conditions of temperature and relative humidity as a function of time. This technique is widely utilised in the development of pharmaceutical products using a variety of modes in which the relative humidity inside the chamber is either stepped (sorption isotherm), ramped (adsorption-desorption isotherm) or maintained constant at constant temperature (isohume experiments) (420). DVS is normally used for many applications including modelling the process of moisture uptake, characterisation of recrystallisation, stability and structural changes of pharmaceuticals (420-423).

In this project, TGA Q5000 (TA Instruments, New Castel, USA) was used to measure the extent of moisture uptake by the raw materials and the impacts of processing techniques and the loading percentage of felodipine in the matrices. Isohume mode was used at constant relative humidity (RH) 75% and temperature 25 ˚C.

2.3.5 Polarised-light hot stage microscopy (HSM)

It is one of the thermoptometric methods in which the sample under investigation is analysed for its optical properties as a function of time or temperature using specific atmosphere. The recent advances in the design and applications of this analytical technique make it a very useful tool to understand the thermal behaviour of different compounds and mixtures (424). In this study, the system used consists of an AV camera attached to a microscope equipped with polarised light facility and the hot stage containing the sample on glass slide is placed on the stage of the microscope for visual observation. The main purpose of using this apparatus is to visualise thermal transitions like melting, thermal dissolution and crystallisation for raw materials and different forms of formulations as a complimentary analytical technique to support the results obtained by DSC. HSM experiments were conducted using a Mettler Toledo FP90 Central

Processor and an FP82HT Hot Stage, a Leica DM LS2 Microscope and a JVC digital colour video camera connected to a PC.

2.3.6 Scanning electron microscopy (SEM)

Scanning Electron Microscopy (SEM) is one of the most widely used technique for the analysis of microstructural properties of solid systems. The basic components of this versatile microscopic instrument are the lens system, electron gun, electron collector, cathode ray tubes for visual a photo recording and other related electronics. The electrons are generated and accelerated by the electron gun (tungsten hairpin) into small beam having an energy range (0.1-40 keV) which is then demagnetised and focused into the sample under investigation. SEM has many applications, but the most important use is to capture topographic images within the magnification range 10-1000,000X (425).

SEM used in this study was JSM 5900LV Field Emission Scanning Electron Microscope (Jeol Ltd, Japan) equipped with a tungsten hairpin electron gun. The purpose of the analysis was to scan the surfaces and cross-sections of the formulations to provide an understanding of the microstructure of the formulations as fresh and aged samples.

2.3.7 Energy dispersive spectroscopy (EDS)

EDS is one of the frequently used chemical characterisation techniques as an attachment to SEM or TEM. This tool offers a number of valuable advantages including rapid analysis, easy interpretation of results and good spatial resolution (426). The principle of this technique is the stimulation of the sample to emit characteristic X-rays by focusing high energy beam of photons, electrons or X-rays. The charged particles like the electrons cause the excitation of electron in an inner energy level and eject it creating an electron hole. This cause an electron from higher energy level to fill the hole and the energy difference between the outer and the inner energy levels may be released in the form of X-rays that can be detected and measured by the energy dispersive spectrophotometer. Because the difference in the energy levels is characteristic for the atomic structure of each emitting element, EDS can provide information (qualitative and quantitative) about the atomic composition of the sample spot under analysis (425). In order to confirm the identity of the detected crystal growth and taking advantage of the presence of the two chlorine

atoms in the structure of felodipine which serve as a chemical marker for the identification, EDS (INCA Energy manufactured by Oxford Instruments) combined with SEM was used in this study.

2.3.8 Powder X-ray diffraction (PXRD)

X-rays are high energetic electromagnetic radiations having an energy ranging from 200 eV to 1 MeV which specifies their location in the spectrum between γ-rays and ultraviolet (UV) radiations (427). The principle of X-ray diffraction is explained by Bragg who noticed that atoms or molecules of crystals are arranged in a regular way in space and this arrangement can be described as parallel plates separated by certain distance d. When X-rays applied on crystals, the scattering centres in the plane act as a mirror for the incident beam of X-rays. A constructive interference results from the reflection of X-rays by two planes separated by certain distance. This phenomenon is explained by Bragg's law (**Equation 2.6**):

$$2d \sin \Theta = n\lambda \quad \text{.....Equation 2.6}$$

where d is the interplanar spacing of the diffracting planes, Θ is the incidence angle of X-rays, n is an integral number of wavelengths, and λ is the wavelength of the X-ray beam.

Generally, X-ray diffraction is composed of three basic components including X-ray source, sample under investigation and the X-ray detector. These parts lie in the circumference of single circle known as the focusing circle and the angle between the X-ray source and the plane of the specimen is Θ while the angle between the X-ray projection and the detector is 2Θ. PXRD is considered as one of the fundamental methods for the analysis of crystalline structures in the pharmaceutical field. Because the majority of drugs are crystalline solids, this analytical technique has been used mainly for the determination of structural fingerprints of solid matter qualitatively and quantitatively (427, 428). The purpose of using PXRD (Thermo ARL Xtra X-ray diffractometer; Thermo Scientific, Switzerland) in this project is to investigate the presence or absence of crystalline felodipine and detecting the possible polymorphic transformation in different formulations.

2.3.9 X-ray micro computed tomography (XμCT)

XμCT is a 3D X-ray imaging technique that has been widely used in a diverse range of applications to study the microstructure of objects without causing damage to the original sample.

In contrast to X-ray diffraction methods, where X-rays are not absorbed but are reflected by an ordered array of matter, with a XμCT experiment it is the absorption of X-rays that results in the image, in a manner analogous to transmission microscopy. The differentiation of different phases by XμCT relies on the electron density differences that are characteristic of different elements. In the pharmaceutical industry, XμCT is used routinely to identify physical imperfections in solid dosage forms showing a high density contrast such as voids and cracks in tablets and coatings (429, 430). Therefore, the ability of the technique to distinguish materials with similar attenuation coefficients such as amorphous and crystalline forms of the same drug can be extremely limited (431) unless synchrotron radiation is used to improve the phase contrast (432, 433). However, for the conventional XμCT used in this study, in theory, if sufficient electron density differences are present between different phases contained within a sample, XμCT should be effective for resolving the distribution of these phases in 3D. The distribution of solid excipients in compressed tablets has been studied using XμCT based on this principle (434). However, it has not been widely used to investigate phase separation in solid dispersions. In this study, XμCT instruments have been used to investigate the heterogeneity and spatial distribution of different phases in felodipine solid dispersions with various drug loading percentages (0–30% w/w). Two types of XμCT equipment were used to achieve this objective; Phoenix v[tome]x m system (General Electric, Wunstorf, Germany) and SkyScan1172 high-resolution X-ray micro computed tomography (XμCT) scanner (Bruker-microCT, Kontich, Antwerp, Belgium).

2.3.10 Attenuated total reflectance-Fourier transform infrared (ATR-FTIR) spectroscopy

ATR-FTIR is considered as one of very common vibrational spectroscopic characterisation technique that has many applications in the pharmaceutical field basically for elucidating the chemical structure of different materials. Normally, this spectrophotometric tool uses the mid-infrared electromagnetic radiation within the wavenumber range of (4000-400 cm^{-1}) to stretch or bend the chemical bonds within the molecules absorbing these radiations resulting in a complex and unique fingerprint specific for the sample under investigation (435).

The sampling in ATR-FTIR is based on contact mode in which a crystal of high reflective index and excellent IR transmittance features such as diamond is used. This method offers a number of advantages compared to the other methods because this technique is quick and there is no need for further processing (such as milling and mixing with other materials) which is required during

sample preparation prior to scanning using other methods. This has great impact on removal of the destructive effect of preparation which might change the characteristics of the sample.

The basic principle of ATR accessory is depending on measuring the changes that occur in totally internally reflected infrared radiation when they come into contact with a sample. In order for the internal reflectance to occur, the angle of incidence of IR beam should be greater than a critical angle Θ_c (a function of the refractive indices between the sample and ATR crystal) as expressed in **Equation 2.7**.

$$\Theta_c = \sin^{-1}(n_2/n_1) \quad \text{.....Equation 2.7}$$

where n_2 is the refractive index of the sample and n_1 is the refractive index of the crystal. Moderate angles of incidence are obtained by using crystals like Ge, ZnSe, or diamond which have a much higher refractive index compared to that of organic compounds. As a result of the internal reflectance of the IR beam, the generation of an evanescent wave which extends behind the surface of the sample into the sample held into contact with the crystal. The effective penetration depth (dp) defined as the distance from the ATR crystal-sample interface to the depth at which the decay in the intensity of the evanescent wave reaches 37% of its original intensity and can be expressed by **Equation 2.8**:

$$dp = \lambda / 2\pi n_p (\sin^2\Theta - n_{sp}^2)^{1/2} \text{ .....Equation 2.8}$$

where λ is wave length of IR beam, n_p is the refractive index of the ATR crystal, Θ is the angle of incidence of IR radiation, and $n_{sp}= n_2/n_1$ is the ratio of the refractive indices between the sample and the internal reflective element (crystal) (436).

In this study ATR-FTIR was used to characterise felodipine solid dispersions prepared by HME-IM and FDM 3D printing. The attention was focused on understanding the fingerprints of the raw materials, physical mixes and processed samples and investigating the possibility of polymorphic transformation of the model drug and its ability to interact with the components of the carrier mixtures. IFS 66/S FTIR spectrometer (Bruker Optics Ltd, Coventry, UK) fitted with a Golden Gate® ATR accessory with temperature controllable top plate (Specac, Orpington, UK) and diamond internal reflection element was used in this study.

2.3.11 Fourier transform Infrared (FTIR) imaging

FT-IR imaging is a powerful characterisation techniques well suitable for investigating the distribution and the dynamics of different components in heterogeneous multicomponent formulations. In this method, the spatial resolution of individual components is achieved according to the spectral response of each detection element. The collected spectra are used to build up a chemical map of the sample under investigation (437, 438). This technique is operating in different methods including absorption, transmission or reflection modes (the last two modes through the use of ATR as complimentary accessary). ATR-FTIR imaging has many advantages over the original FTIR imaging including the minimal sample preparative procedures which may be useful to maintain the integrity of the sample and suitability for samples having high spectral absorption properties like water containing systems. Generally, ATR- FTIR imaging has many pharmaceutical applications including studying dynamic systems (tablets dissolution, water sorption, crystallisation and polymer dissolution in organic solvents) and the chemical distribution of heterogeneous samples (439). In this study, the heterogeneity of the surface composition was assayed with a Nicolet iN10MX infrared microscope operating in reflection mode.

2.3.12 Laser diffraction (LD) particle size analysis

Particle size is a critical formulation parameter that affects many physicochemical and biopharmaceutical properties of drugs in their final dosage forms like release profile, absorption rate, flow properties, mixing and segregation of powders and irritability of ophthalmic preparations. There are different methods used for the analysis of particle size including: microscopy and image analysis, laser diffraction, dynamic light scattering, coulter counter, etc. with different principles of operation and applications. Among these techniques, laser diffraction is widely used in pharmaceutical industry due to its fast analysis, robustness, reproducibility and precision of results and suitability for broad spectrum of products like liquid, solid, and gaseous dispersions. The principle of operation for laser diffraction is based on the relationship between the particle size and the angle and the intensity of the diffracted laser light. The detected information about the intensity and the angle of diffracted light is then processed using an algorithm based on Mie scattering theory that transform these data into particle size results (440). In this study, laser diffraction (Helos/Rodos 1636, Sympatec GmbH, Germany) was used to measure the particle size of felodipine form different batches as received from the supplier to investigate the impact batch to batch particle size variability on the formulation process.

Felodipine particles were dispersed in a filtered saturated aqueous solution of felodipine under sonication and stirring inside 50 mL quartz cuvette. Five replicates for each sample were analysed.

2.4 Evaluation methods

2.4.1 *In vitro* release profiles

In vitro drug release is a critical evaluation test to provide quantitative and kinetic information about the ability of the dosage form to liberate the drug and make it available at the site of absorption. For HME-IM patches designed for buccal administration, unidirectional dissolution studies to simulate the release profile for systemic buccal administration were conducted using the paddle over disc method (similar to USP apparatus 5) as illustrated in **Figure 2.13** using a dissolution apparatus (Caleva 8ST, Germany).

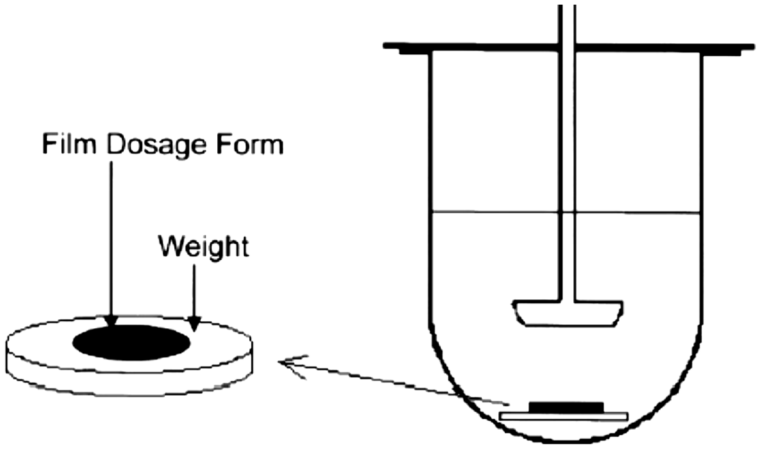

Figure 2.13: Schematic representation of the paddle over disc apparatus used for dissolution profile study; adapted from reference (441)

Under sink and non sink conditions, patch samples having the equivalent of the maximum daily dose of felodipine (10 mg) attached to a glass disc using double adhesive tape were immersed in 900 mL of phosphate buffer saline pH 6.8 (simulated salivary fluid) at 37 ± 0.5°C and 100 rpm paddle rotation. At different pre-determined time intervals, 5 mL samples were withdrawn and filtered using a 0.45 um filter unit (Minisart NML single use syringe, Sartorius, UK). The filtered samples were then diluted with an equal volume of absolute ethanol and the samples were analysed using a UV-VIS spectrophotometer (Perkin Elmer lambda 35, USA) at 363 nm. Samples

withdrawn were substituted with dissolution media at the same temperature after each sample was taken. All drug release studies were conducted in triplicate.

The *in vitro* drug release profiles for felodipine FDM 3D printed discs were measured in dissolution testing apparatus (Caleva 8ST, Germany) using the paddle method (USP apparatus 1). A paddle rotation speed of 100 rpm and 900 mL of pH 1.2 HCl or phosphate buffer pH 6.8 at 37 ± 0.5℃ were used for all experiments. The pure crystalline drug (approximately 5 mg in powder form) and disc shaped dispersions containing the equivalent of the daily dose (5 mg) of the drug were used in this study. Under non-sink conditions, 5 mL dissolution samples were withdrawn at pre-determined time intervals. The samples were directly filtered through a membrane filter with 0.45 μm pore size (Minisart NML single use syringe, Sartorius, UK). The filtered sample solutions were diluted with equal volume of ethanol. 5 mL of fresh pre-warmed (37 ± 5℃) dissolution media was added to the dissolution vessel after each sampling. The samples were analysed using a UV–VIS spectrophotometer (Perkin Elmer lambda 35, USA) at 363 nm. All dissolution tests were performed under non-sink conditions with no addition of surfactants in the media in order to minimise the effect of polymer-surfactant interactions on the drug release behaviour from the formulations. All drug release studies were conducted in triplicate.

2.4.2 Determination of drug loading efficiency

Accurately weighed drug loaded FDM 3D printed discs of different formulations were dissolved in a beaker containing 200 mL of 50:50 simulated gastric fluid pH 1.2 and absolute ethanol. The beaker was covered with a parafilm tape to minimise solvent evaporation during dissolution. The medium was stirred using magnetic stirrer at room temperature. After complete dissolution, 5 mL samples were withdrawn and filtered using 0.45 μm pore size (Minisart NML single use syringe, Sartorius, UK). The filtered samples then scanned for their content of felodipine using a UV–VIS spectrophotometer (Perkin Elmer lambda 35, USA) at 363 nm. The loading efficiency measurements for the loaded discs were carried out in triplicate.

2.4.3 *In vitro* mucoadhesion study

Mucoadhesion is considered as a critical parameter for the successful delivery of drugs from buccal patches to the systemic circulation. The description of mucoadhesion is generally related to the degree of interaction between the polymers with adhesive properties with the epithelium of

the site of application. Mucoadhesivness of buccal patches can be estimated by measuring the force required to detach the patch from substrate and work of adhesion or which give insights for the retention pattern of these patches at the application surface (441). There are many approaches for quantitative determination of mucoadhesion force based on measuring the shear strength to evaluate the force mucoadhesion (442-444). Measuring the tensile strength is the most widely and accurate method to assess the mucoadhesivness of buccal films especially after the development of benchtop texture analyser (441).

In this study, the mucoadhesive measurements were carried out on felodipine buccal patches prepared by HME-IM technique using a TA-XT2 Texture Analyser (Stable Micro Systems, Surrey, U.K.) fitted with a 5 kg load cell in tension mode. Felodipine loaded buccal patches (n = 5) having an area of 1.56 cm^2 were attached to the cylindrical perspex probe (1.2 cm diameter and 4.5 cm length) using double-sided adhesive tapes. Aqueous gelatin solution in a concentration of 6.67% w/v was allowed to set as solid gel in a Petri dish (diameter 88 mm), which was used to simulate the adhesion of buccal mucosa. Prior to each measurement, the gelatinous substrates were equilibrated with 1 mL of 2% w/v porcine mucin solution (pH of 6.8) and fixed on the platform of the texture analyser. For all tests, the probe moved at a pretest speed of 0.5 mm/s, a test speed of 0.5 mm/s, and a post-test speed of 1 mm/s, with an applied force of 0.5 kg, a return distance of 10 mm, and a contact time of 60 s. During the post-test period, the probe was lifted automatically with 0.05 kg force.

Chapter 3. Characterisation of raw materials

3.1 Introduction

The production of solid dispersions by thermal processing such as HME and FDM 3D printing is considered as an efficient approach to improve the dissolution properties of poorly water-soluble drugs (8, 445-447). Preformulation studies are essential part for the development of any pharmaceutical product as they provide the scientific basis needed during the formulation and evaluation processes. These studies involve physical and chemical characterisation of the drug(s) under investigation together with the pharmaceutical excipients needed for the fabrication of the intended product. These investigations use a wide variety of physicochemical characterisation techniques, prediction methods and evaluation studies to be used as a framework during the next stages of drug development process (151). In this chapter, the physicochemical properties of felodipine and the other excipients presented in Chapter 2 were characterised using different thermal and spectroscopic characterisation techniques including ATR-FTIR, DSC, MTDSC, PXRD, DVS and SEM. These tools were used to provide information about the thermal properties of the drug and the excipients including melting, glass transition (T_g), recrystallisation, thermal history, crystallinity, thermal stability and moisture uptake of the formulation components. In addition, spectroscopic methods were used to provide details about crystalline and amorphous transformations, detecting functional groups that may be involved in intermolecular interactions and morphological properties. Furthermore, DSC was used to investigate the suitable blends of the excipients to be used for the development of the loaded formulations. Estimating drug-excipient(s) miscibility using solubility parameter based on group contribution (Hoftyzer and Van Krevelen and Hoy) and melting point depression methods were used to predict the miscibility of the components as explained in Chapter 1 (83, 84).

Research Objectives:

1. To investigate the physicochemical properties of the raw and physical mixtures of drug-excipients materials used in the formulation of solid dispersions.
2. To study the thermal properties of PEG/PEO blends and how the addition of surfactants could affect their behaviour.
3. To estimate the solubility parameters of felodipine and other formulation components in order to predict their miscibilities.

3.2 Materials and Methods

3.2.1 Materials

Felodipine (MWT =384.25 g/mole) (batch no. FP140602) was purchased from Afine Chemicals Ltd (Hangzhou, China). Polyethylene glycol (PEG) 4000 (average MWT = 4060 g/mole) and polysorbate (Tween®) 80 (MWT = 1310 g/mole) were purchased from Sigma-Aldrich (Dorset, UK). Vitamin E TPGS (MWT = 1513 g/mole) and two grades of polyethylene oxide (PEO K900) WSR 1105 (MWT= 900,000 g/mole) and (PEO K100) WSR N10 LEO (MWT= 100,000 g/mole) were kindly donated by BASF (Ludwigshafen, Germany) and Colorcon Ltd (Dartford, UK) respectively. Soluplus (average MWT 116000 g/mole), eudragit® E PO (average MWT 116000 g/mole) and 33-38% partially hydrolysed polyvinyl alcohol (PVA LM 25) (MWT = 18,000-25,000) were kindly donated by BASF (Ludwigshafen, Germany), Evonik Industries (Darmstadt, Germany) and Kuraray Co., Ltd. (Tokyo, Japan), respectively.

3.2.2 Methods

3.2.2.1 Preparation of amorphous felodipine

Amorphous felodipine was prepared by melting the drug in an aluminium weighing dish using a preheated hot plate at 160℃ using melt-cool method.

3.2.2.2 Preparation of binary and ternary excipients' extrudates

PEG 4000/PEO K900 extrudates with or without surfactants (Tween 80 or TPGS) were prepared using co-rotating twin screw mini-extruder (HAAKE™ MiniLab II Micro Compounder, Thermo Electron, Karlsruhe, Germany). The physical mixtures of different binary and ternary combinations were mixed using mortar and pestle for at 2 minutes before feeding into the extruder. The extrusion process was performed at 65 ℃, 100 rpm for 5 minutes. After the specified residence time, excipients extrudates were flushed and collected for characterisation.

3.2.2.3 Physicochemical characterisation of raw materials

3.2.2.3.1 Thermogravimetric analysis (TGA)

In order to investigate the thermal stability of felodipine and other excipients and estimate the suitability of these materials to processing conditions, TGA analyses were conducted. A Q5000 (TA Instruments, Newcastle, USA) TGA equipment was used to analyse the samples (5-10 mg) by applying a temperature program of 10 ºC/min over the temperature range 25-500 ºC. 2-3 replicates for each sample were tested and Universal Analysis software was used to analyse the obtained results.

3.2.2.3.2 Differential scanning calorimetry (DSC) and modulated temperature DSC (MTDSC)

In this study, Q-2000 MTDSC equipped with an RC90 cooling unit (TA Instruments, Newcastle, USA) was used to detect the thermal transitions of raw and processed samples. Before analysis, baseline temperature and heat capacity calibrations were performed. The samples were prepared using standard aluminium pans and lids (TA Instruments, Newcastle, USA). Dry nitrogen gas was used as the purge gas with a flow rate of 50 mL/min. For standard DSC mode, temperature programs at a heating rate of 10 ˚C/min in a range of temperatures between -80 to 180 ˚C (depending on the individual experimental settings) were used to scan the samples for heating, cooling and/or reheating cycles. For MTDSC experiments, a temperature program with an amplitude of ± 0.318˚C, a period of 60 second and a scanning rate of 2 ˚C/min from -80 ˚C to 180 ˚C was used. Three replicates of each sample were measured. Universal Analysis software was utilised for the analysis of the collected thermograms.

3.2.2.3.3 Dynamic vapour sorption (DVS)

DVS was used to measure the extent of moisture uptake by the raw materials used in the fabrication of felodipine solid dispersions using HME-IM. Isohume mode was used at constant relative humidity (RH) 75% and temperature 25 ˚C. Raw materials and freshly prepared samples were loaded in a previously tared pan of the DVS (TGA Q5000) (TA Instruments, Newcastle, USA). For each experiment, a drying step is initially conducted to remove the already existing

water in the samples by holding the sample at 0% relative humidity (RH) at 25 ˚C for 2880 minutes or when the percentage of weight loss is ≤ 0.01% for 30 minutes indicating reaching equilibrium with complete removal of moisture. After that, an isohumic step is initiated at 75% relative humidity (RH) and 25 ˚C for 2880 minutes or when the percentage of weight gain is ≤ 0.01% for 30 minutes indicating reaching a plateau with the maximum percentage of moisture absorption by the sample. The analysis was conducted for each sample as triplicate, and the collected data were analysed using the Universal Analysis software.

3.2.2.3.4 Attenuated total reflectance-Fourier transform infrared spectroscopy (ATR-FTIR)

Raw and processed samples were scanned using an IFS 66/S FTIR spectrometer (Bruker Optics Ltd, Coventry, UK) fitted with a Golden Gate® ATR accessory (Specac, Orpington, UK) equipped with diamond internal reflection element. All ATR-FTIR spectra were obtained using a scanning resolution of 2 cm^{-1} with 32 repeated scans in absorbance mode in the range of wavenumbers of 4000-550 cm^{-1}. Opus software was used for analysing the collected results. All measurements were performed in triplicates.

3.2.2.3.5 Scanning electron microscopy (SEM)

The SEM images for felodipine particles was conducted using JSM 5900LV Field Emission Scanning Electron Microscope (Jeol Ltd, Japan) equipped with a tungsten hairpin electron gun. Felodipine particles were spread over the double adhesive of the SEM stubs using double adhesive tape and then coated with gold using a Polaron SC7640 sputter gold coater (Quorum Technologies, Laughton, UK) before imaging.

3.2.2.3.6 Powder X-ray diffraction (PXRD)

The diffraction patterns of felodipine and all other excipients were collected using Thermo ARL Xtra X-ray diffractometer (Thermo Scientific, Switzerland) equipped with a copper X-ray Tube (λ =1.540562 Å). All samples were measured using an X-ray beam with a voltage of 45 kV and a current of 40 mA. The measurements were performed using an angular scan range (5 ˚ < 2Θ < 60 ˚), step scan mode with a step width of 0.01˚ and scan speed of 1 sec/step.

3.2.2.3.7 Solubility measurements

The saturated solubility of felodipine in Tween 80 was measured by adding an excess amount of felodipine to 40 mL of Tween 80. The mixture was incubated at room temperature for 72 hours with continuous shaking at 200 rpm using a shaking incubator (MaxQ 4000, Thermo Scientific, USA) to facilitate the dissolution of the crystalline drug in Tween 80. After 72 hours, the supernatant was filtered using a 0.45 μm Millipore filter pore size membrane filters (Minisart NML single use syringe, Sartorius, U.K.) and 0.5 mL of the filtered solution was diluted to 100 mL with phosphate buffer saline PBS pH 6.8. Due to the high concentration of felodipine which gives higher absorbance values, the solution was further diluted to 2000 mL using PBS pH 6.8 containing 0.5% v/v Tween 80. The saturated solubility of felodipine in Tween 80 was determined by UV-VIS spectrophotometer (Perkin-Elmer Lambda 35, USA) at λmax 363 using the same standard curve constructed for measuring the solubility of felodipine in phosphate buffer saline (PBS) pH 6.8 containing 0.5% v/v Tween 80 (Appendix 2). All measurements were repeated three times.

3.3 Results

3.3.1 Physicochemical characterisation of raw materials

3.3.1.1 Felodipine

Figure 3.1a illustrates the percentage and derivative of weight loss signals of felodipine heated at 10˚C / min using TGA. The thermal degradation of felodipine occurred as a single step process with an onset at approximately 166˚C and complete decomposition at 280˚C. Standard DSC results show that felodipine form I has a melting peak at 144.6 ± 0.1℃ and ΔH_f about 81.66 ± 1.64 J/g using 10˚C / min (**Figure 3.1b**). Amorphous felodipine T_g and ΔC_p measured using MTDSC were 46.5 ± 0.2℃ and 0.34 ± 0.07 J/g.℃ respectively at a heating rate of 2˚C / min, 0.318 amplitude and 60 sec period as shown in **Figure 3.1c**. Due to the hydrophobic nature of felodipine, this drug has low tendency (0.21 ± 0.02% w/w) for moisture uptake as shown in **Figure 3.2**.

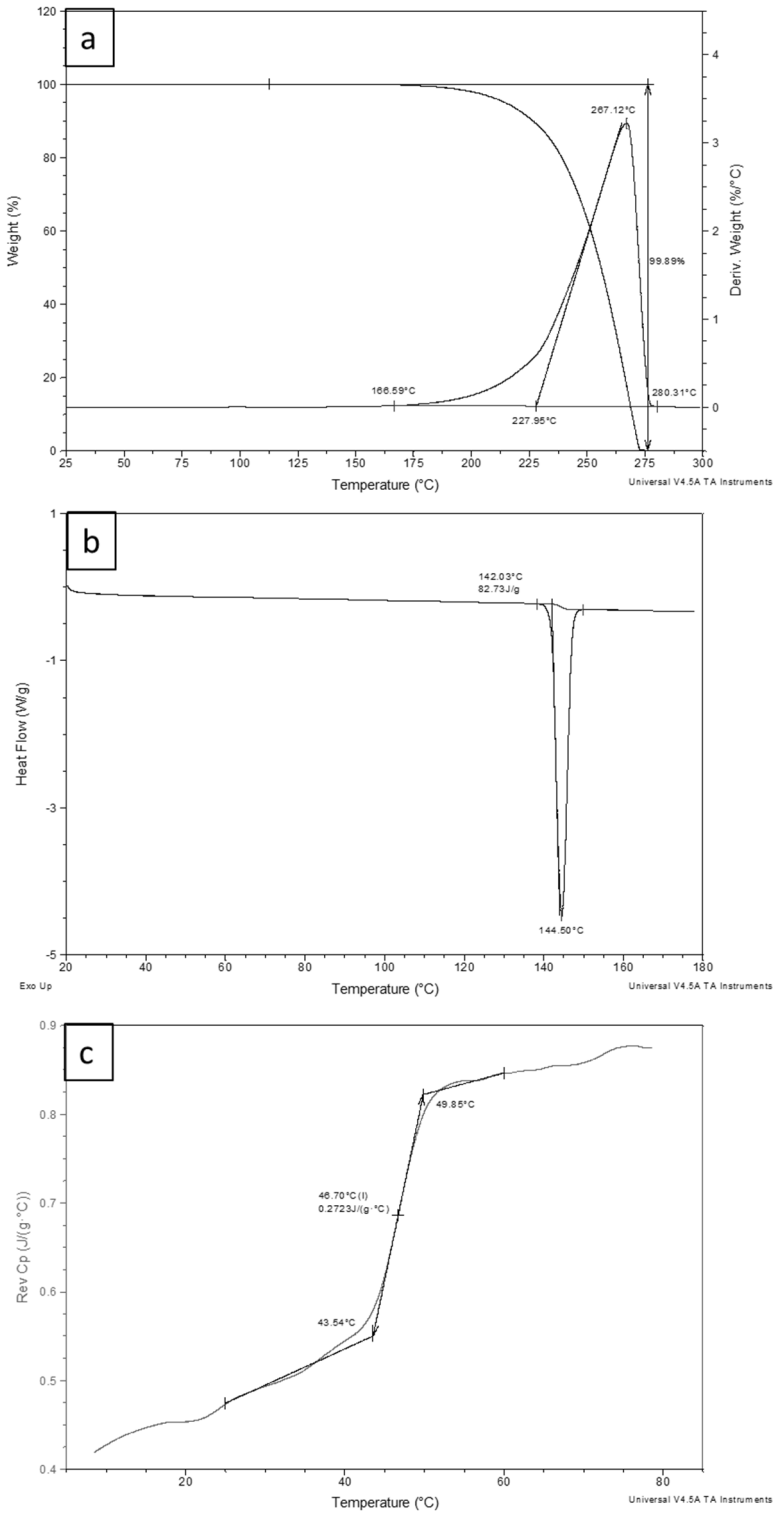

Figure 3.1: a) TGA analysis of felodipine using heating program of 10˚C / min from ambient to 300 ˚C (n=2); b) standard DSC thermogram of crystalline felodipine form I using 10˚C / min heating ramp (n=3); c) reverse signal of MTDSC thermogram showing amorphous felodipine glass transition (Tg) using 2˚C / min, 0.318 amplitude and 60 sec.s period (n=3)

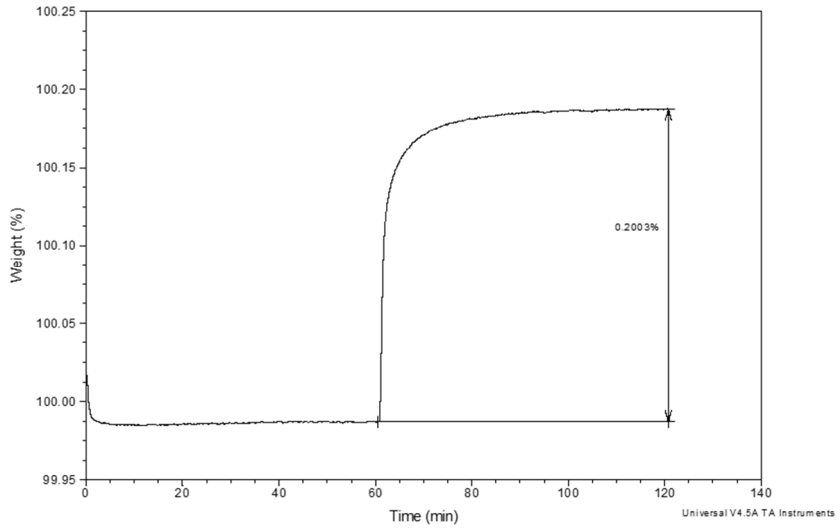

Figure 3.2: Moisture uptake capacity of pure crystalline felodipine form I at 25℃ and 75% RH (n=3)

The NH stretching vibrations in the IR spectra has been reported at 3372, 3334, 3370, 3329 cm^{-1} for the four crystalline polymorphic forms I-IV of felodipine, respectively (313-315, 318). Furthermore, the amorphous form shows an NH stretching peak at ~ 3339 cm^{-1} and peaks at 1701 and 1682 cm^{-1} corresponding to the non-hydrogen bonded C=O group and the hydrogen-bonded C=O group respectively. The ATR-FTIR spectra for crystalline felodipine form I used in this study and amorphous form prepared from it by rapid cooling of the melt are shown in **Figures 3.3a and b** respectively which are consistent with data reported in the literature (315, 317). The most important difference between the spectra of form I and the amorphous form of felodipine are the peaks associated with the NH stretching, C=O stretching and CN stretching which reflects different strengths of intermolecular hydrogen bonding (448). **Table 3.1** shows the characteristic absorption peaks of crystalline felodipine form I, amorphous felodipine and all other excipients used in this study.

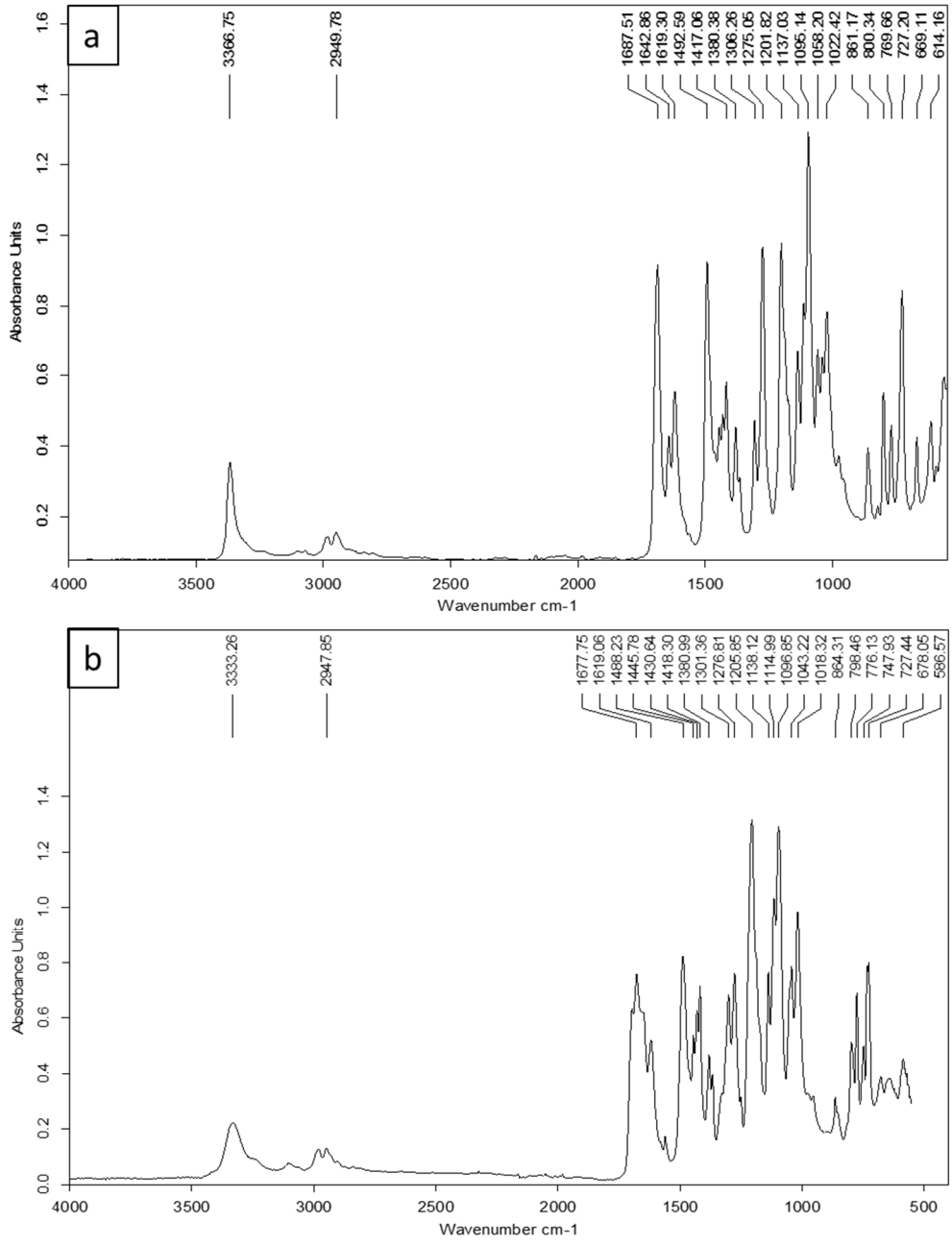

Figure 3.3: ATR-FTIR spectrum of a) pure crystalline felodipine form I and b) amorphous felodipine (n=3)

Table 3.1: Characteristic ATR-FTIR absorption peaks of crystalline and amorphous felodipine

Compound	Chemical group	Peak wavenumber (cm^{-1})
Crystalline felodipine form I	NH Stretching	3367
	aromatic CH stretching	3071
	CH stretching	2949
	C=O stretching	1688
	NH Bending	1643
	C = C ring stretching	1619, 1492 and 1445
	CN stretching	1202
	C-O-C stretching	1095
	Substituted benzene ring	725 and 800
	Cl stretching	561
Amorphous felodipine	NH stretching	3333
	aromatic CH stretching	3105
	CH stretching for CH_3	2979
	CH stretching for CH_2	2948
	C=O stretching	1697
	CN stretching	1206

Since the determination of felodipine form I crystal structure in 1986, several studies have been published reporting new polymorphic forms (II-IV) obtained from various solvents (312-315, 318, 319). The PXRD patterns of these forms are shown in **Figure 3.4**.

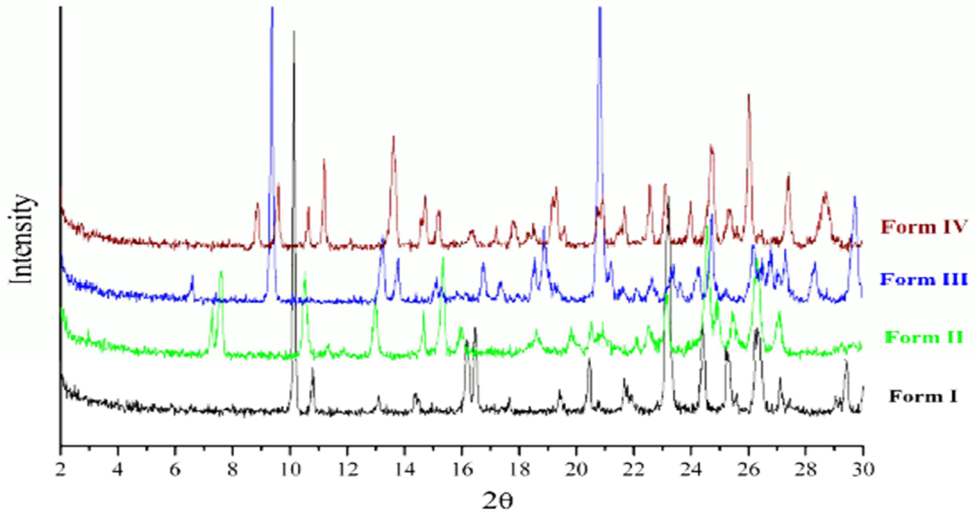

Figure 3.4: PXRD diffractograms of crystalline felodipine forms I-IV; adapted from reference (312)

In this study, crystalline felodipine with the characteristics PXRD patterns of form I was used in the preparation of felodipine solid dispersions using HME-IM and FDM 3D printing as illustrated in **Figure 3.5**.

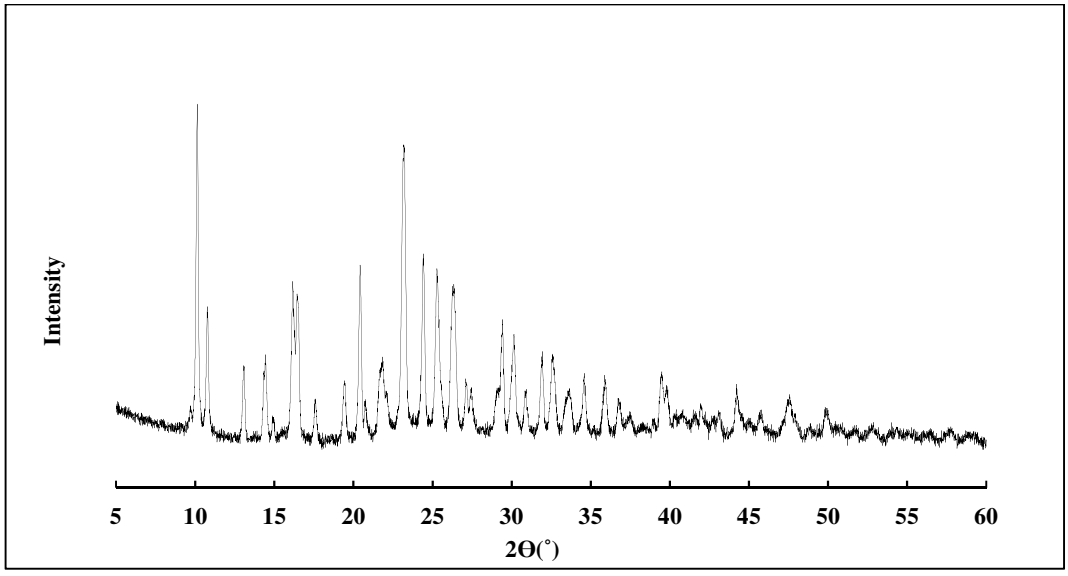

Figure 3.5: PXRD pattern of pure crystalline felodipine form I used in this study

It should be mentioned that the crystal habits of the polymorphs were reported to be block-shaped for polymorphs I (recrystallised from grown from methanol, ethanol or acetonitrile) and II (recrystallised in the presence of succinic acid, malonic acid or isonicotinamide in methanol). For form III (recrystallised in the presence of maleic acid or 4-hydroxybenzoic acid in acetonitrile),

plate-like crystals were reported (312, 319). However, there is no available information about the crystal habit of polymorph IV (recrystallised by slowly evaporation of methanol and NaOH mixture pH =10.0) of felodipine (319) is available. SEM image of felodipine particles is shown in **Figure 3.6**.

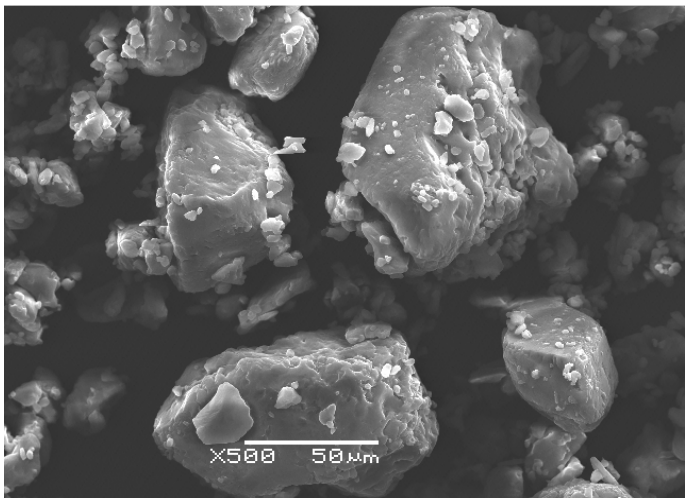

Figure 3.6: SEM image of pure crystalline felodipine form I particles

3.3.1.2 PEG 4000

In this study, PEG 4000 was used as the main polymer for preparing the solid dispersions of felodipine using HME-IM. It was also used as one of the polymeric blend mixtures for preparing felodipine matrices using FDM 3D printing technique. In order to understand the basic physicochemical properties of PEG 4000, characterisation using TGA, DSC, ATR-FTIR and PXRD techniques was performed. The TGA analysis of PEG 4000 is shown in **Figure 3.7a**. A single-step degradation process was observed with extrapolated degradation onset of 376.3 ± 5.0℃. The moisture uptake capacity of this hydrophilic partially crystalline polymer was shown in **Figure 3.7b**. The results revealed that the equilibrium water absorption capacity is 1.18 ± 0.02 using 25℃ and 75% RH. This low percentage of moisture uptake may be due to the small amorphous fraction of this polymer available for occupying moisture in addition to its high crystalline properties.

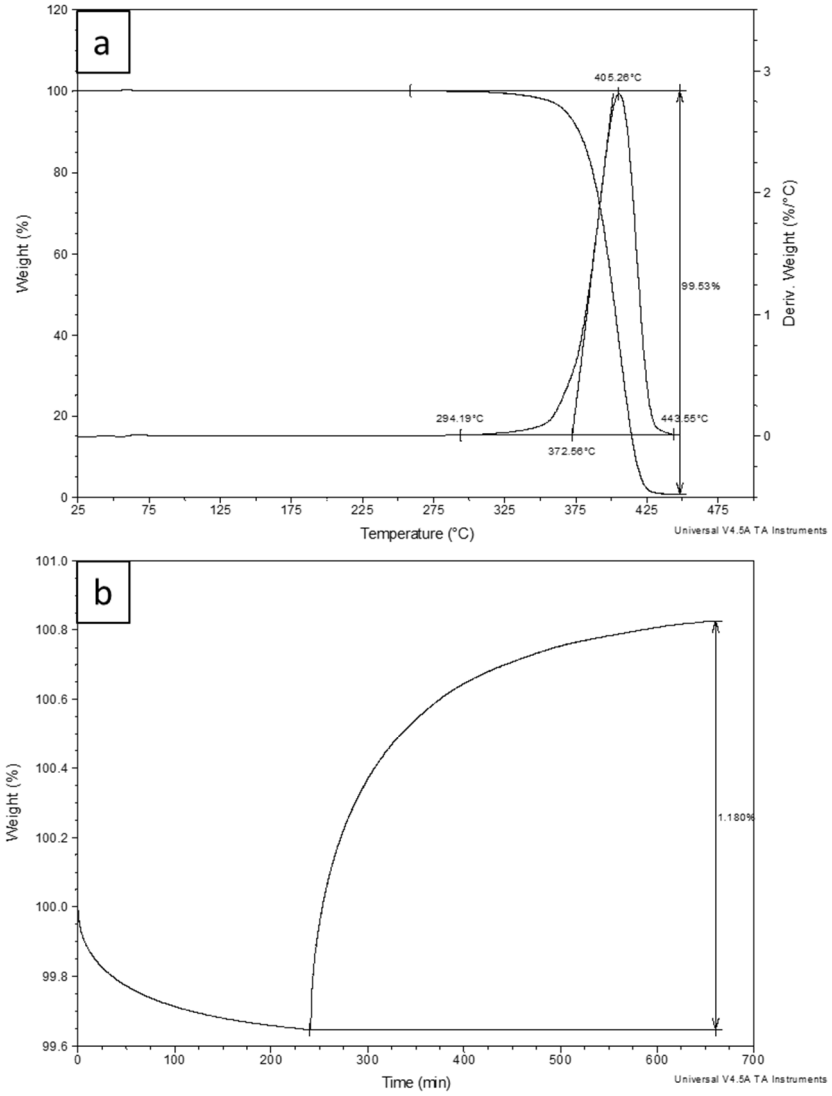

Figure 3.7: a) TGA analysis of PEG 4000 using heating program of 10℃ / min from ambient temperature to 450℃ (n=2) and b) the moisture uptake capacity of PEG 4000 at 25℃ and 75% RH (n=3)

DSC analysis of PEG 4000 using standard mode is shown in **Figures 3.8a-c**. This polymer has a melting onset and peak at 55.4 ± 0.2 and 59.0 ± 0.2℃ respectively using heating rate of 10℃/min as seen in **Figure 3.8a**. This makes this polymer as a good candidate for preparing solid dispersions of poorly water soluble drugs at relatively low processing temperature (38, 341, 343). The % crystallinity was calculated based on the results obtained from the DSC experiments (ΔH_f =187.9 ± 4.9) and the ΔH_f of the 100% crystalline form of PEG 4000 reported in literature (449) which is 214.6 J/g. Using **Equation 3.1**, the % crystallinity of the raw material can be calculated as 87.6%.

% Crystallinity = (ΔH_f raw / ΔH_f 100% crystalline) × 100% ……**Equation 3.1**

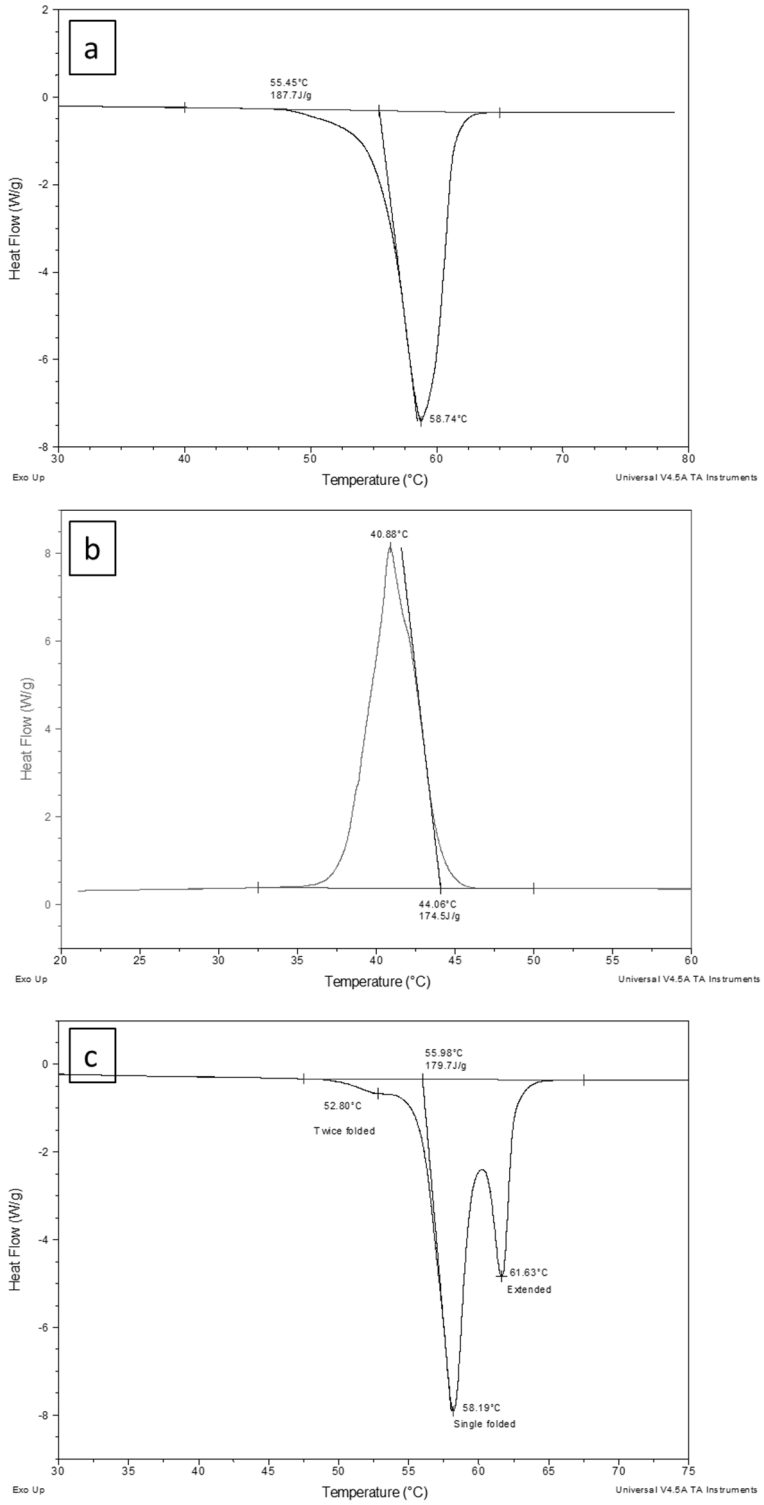

Figure 3.8: Partial standard DSC thermograms showing semicrystalline PEG 4000 melting (a), crystallisation (b) and re-melting (c) transitions using 10 °C / min heating and cooling ramps (n=3)

In addition, PEG 4000 also shows a recrystallisation peak at 40.9 ± 0.7℃ and ΔH_c =173.1 ± 1.2 J/g on cooling at a rate of 10℃ / min from 80℃ as shown in **Figure 3.8b**. The immediate reheating cycle (**Figure 3.8c)** of the recrystallised PEG after cooling revealed the presence of two partially separate peaks representing the single folded and the extended crystalline forms of PEG in addition to a shoulder indicating twice folded form (38, 328, 450-452). The metastable single folded and the stable extended forms show melting peaks at 58.2 ± 0.1 and 61.7 ± 0.1℃, respectively. It should be mentioned that the reported T_g for PEG 4000 is -61℃ (449, 453).

The ATR-FTIR spectrum of PEG 4000 is shown in **Figure 3.9a** and characteristic peaks summarised in **Table 3.2** which are consistent to the reported assigned peaks (454). For PXRD, due to the highly semicrystalline nature of PEG 4000, it shows a characteristic diffraction patterns associated with the crystal lattice arrangements as seen in **Figure 3.9b**.

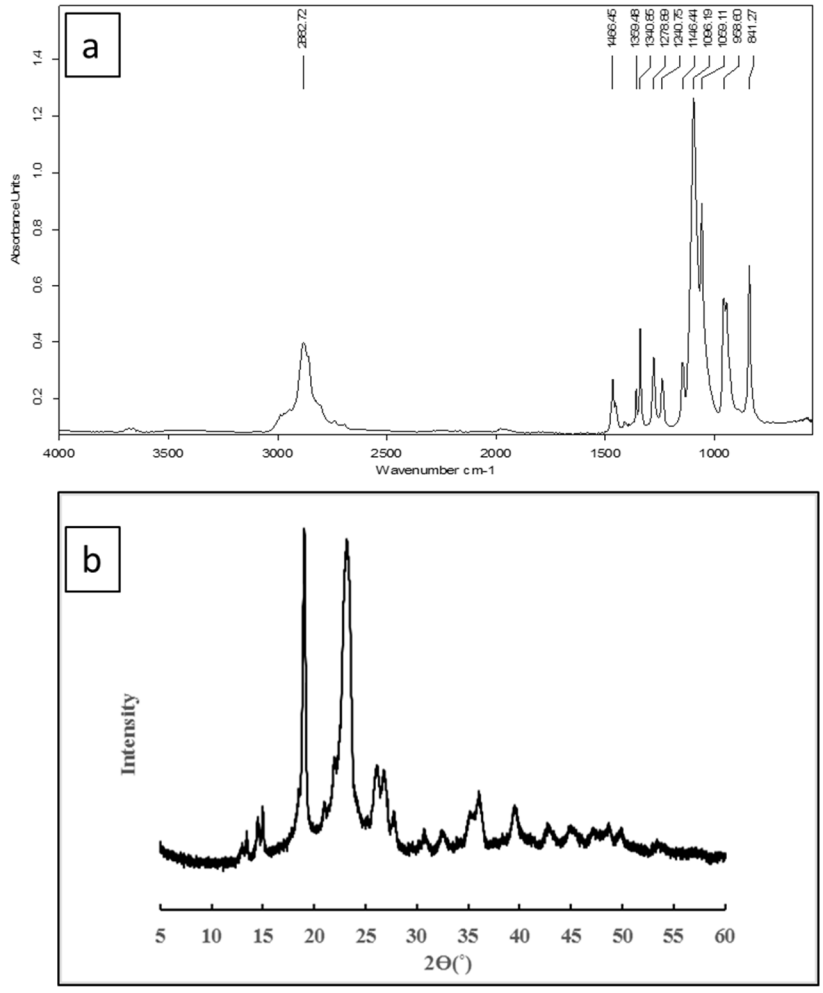

Figure 3.9: a) ATR-FTIR spectrum (n=3) and b) PXRD PEG 4000

Table 3.2: Characteristic ATR-FTIR absorption peaks of PEG 4000, PEO K900 and PEO K100

Compound	Chemical group	Peak wavenumber (cm^{-1})
PEG 4000, PEO K900 and PEO K100	OH stretching	3413
	CH stretching	2883
	C–O–C stretching	1145, 1096 and 1059
	crystal peak of PEO moiety	959
	C–C–O	841

3.3.1.3 PEO WSR 1105 (PEO K900)

PEO K900 was used in the fabrication of felodipine solid dispersions using HME-IM method. As mentioned in Chapter 2, this polymer has high molecular weight (900,000 g/mole) and good thermoplastic, drug release controlling and mucoadhesive properties (356-359). TGA, DSC, MTDSC, ATR-FTIR and PXRD techniques were used to investigate the basic physicochemical properties of this polymer. **Figure 3.10a** illustrates the thermal stability profile of PEO using 10℃ / min ramp from ambient temperature to 500℃. The degradation of PEO occurred as a single step process with an extrapolated degradation onset at 356.3 ± 0.3℃. The T_g of PEO K900 was found to be -53.9 ± 1.9℃ with ΔC_p of 0.01 ± 0.00 J/g.℃ measured using MTDSC using heating rate of 2˚C / min, 0.318 amplitude and 60 sec. period as shown in **Figure 3.10b**. The capacity of moisture uptake of PEO K900 was measured using DVS and found to be 1.80 ± 0.03% w/w after incubation at 25˚C and 75% RH as shown in **Figure 3.10c**.

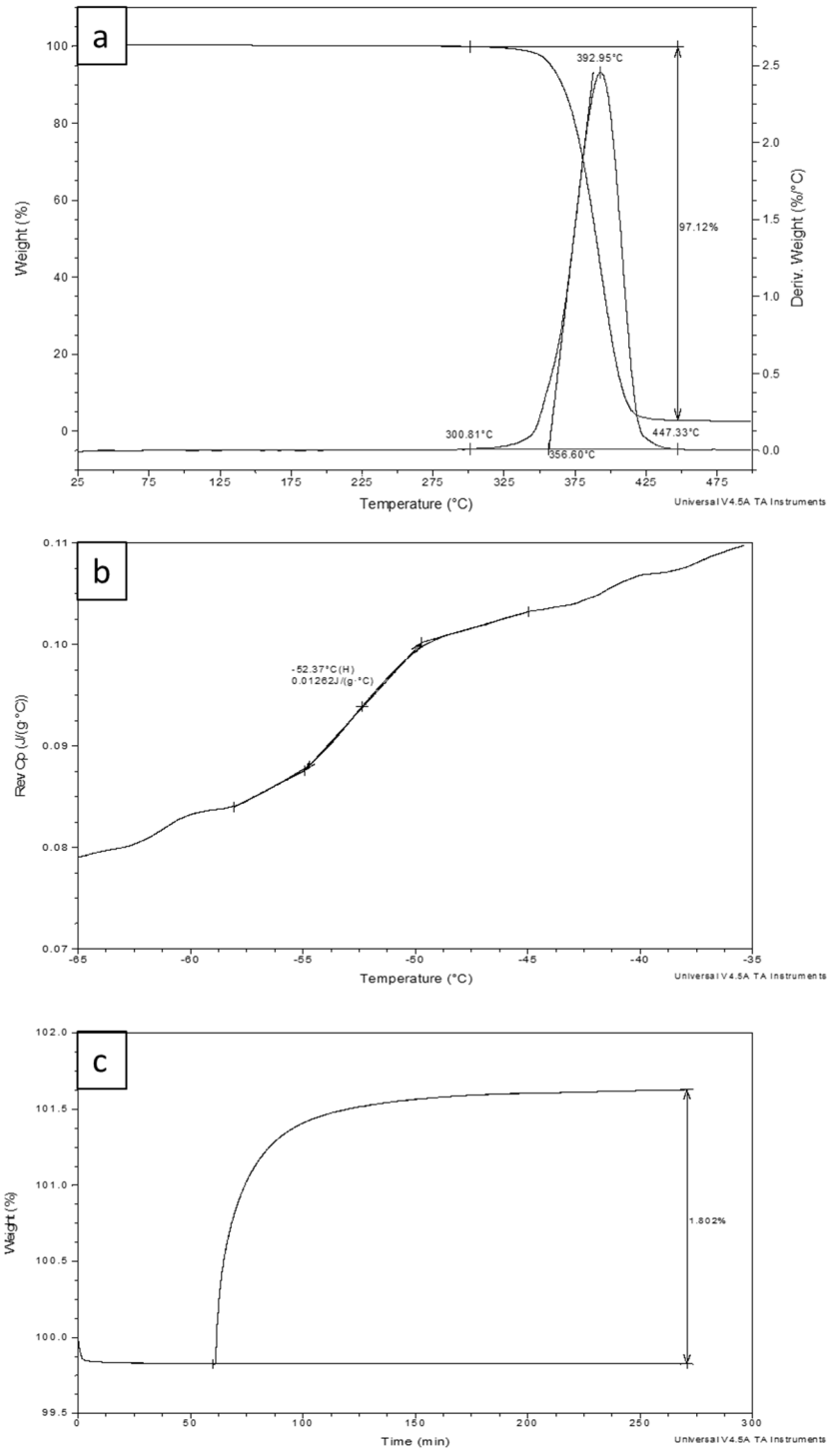

Figure 3.10: a) TGA analysis of PEO K900 using heating program of 10˚C / min from room temperature to 500˚C (n=2); b) MTDSC thermogram showing PEO K900 glass transition (T_g) using 2˚C / min, 0.318 amplitude and 60 sec.s period (n=3) and c) moisture uptake capacity of PEO K900 at 25℃ and 75% RH (n=3)

Due to the difference in their molecular weights, PEG/PEO polymers exist in different physical states with different physical properties. Members with molecular weights 300-600 g/mole are liquids, 1500 g/mole is semisolid, 3000-20000 are semicrystalline solids and polymers with molecular weight higher than 100000 have resinous nature. The difference in their molecular weight is also reflected on their melting, crystallisation, crystallinity and their existence in single or multiple crystal forms. It was reported that the melting temperatures of PEG.s increase with increasing the molecular weight up to 6000 g/mole above which the melting point remains practically constant as the melting is dependent on the thickness of the lamellae rather than the molecular weight of the polymer (452). The melting, crystallisation and re-melting of PEO K900 are shown in **Figure 3.11a-c**. PEO K900 showed a folded form melting peak at 70.2 ± 0.3 ℃ with a ΔH_f of 172.4 ± 3.9 J/g using a heating rate of 10 ℃/min (**Figure 3.11a**). This indicates that the % crystallinity of the raw polymer is 84.1% using 205 J/g as melting enthalpy for the 100% crystalline form reported in literature (455, 456). The polymer shows a crystallisation temperature at 50.3 ± 0.1 ℃ with a ΔH_c of 97.4 ± 3.0 J/g using 10 ℃/min cooling ramp as shown in **Figure 3.11b**. Furthermore, the immediately reheating cycle (**Figure 3.11c**) indicated lower melting temperature (66.0 ± 0.1 ℃) and heat of fusion (ΔH_f = 117.6 ± 2.3 J/g) compared to the first heating cycle using the same heating rate. This indicates that the recrystallised polymer in the reheating cycle is more folded (thinner lamellae) and metastable relative to the first cycle (452).

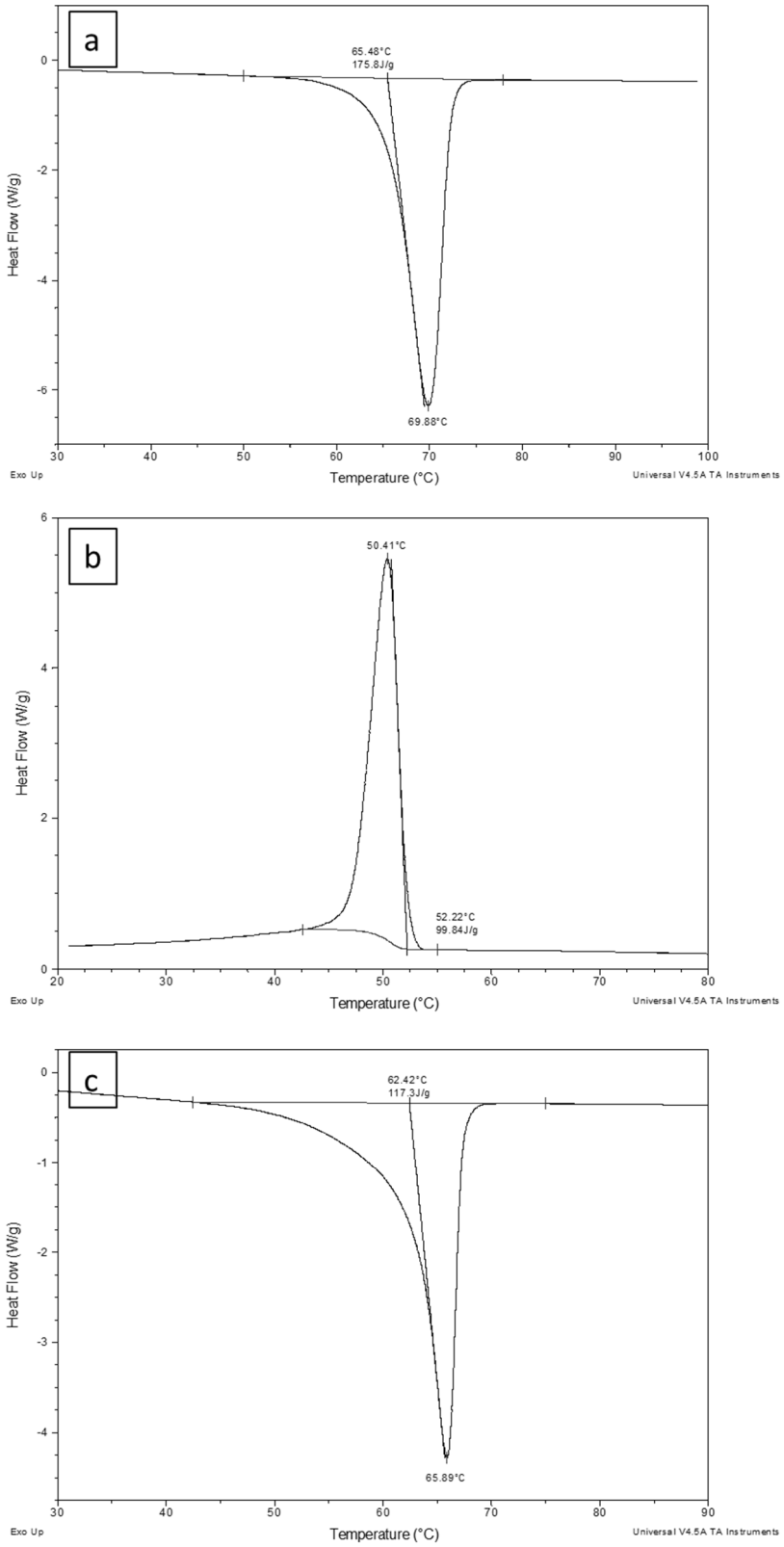

Figure 3.11: Partial standard DSC thermograms show semicrystalline PEO K900 melting (a), crystallisation (b) and re-melting (c) transitions using 10˚C / min heating and cooling ramps (n=3)

The ATR-FTIR spectrum of PEO K900 (**Figure 3.12a**) shows the same characteristic IR peaks like those of PEG 4000 (**Table 3.2**) because both polymers are composed of the same monomeric ethylene oxide units as mentioned in Chapter 2. In addition, **Figure 3.12b** shows the PXRD diffraction patterns of PEO K900 polymer with its characteristics peaks indicating its semicrystalline structure.

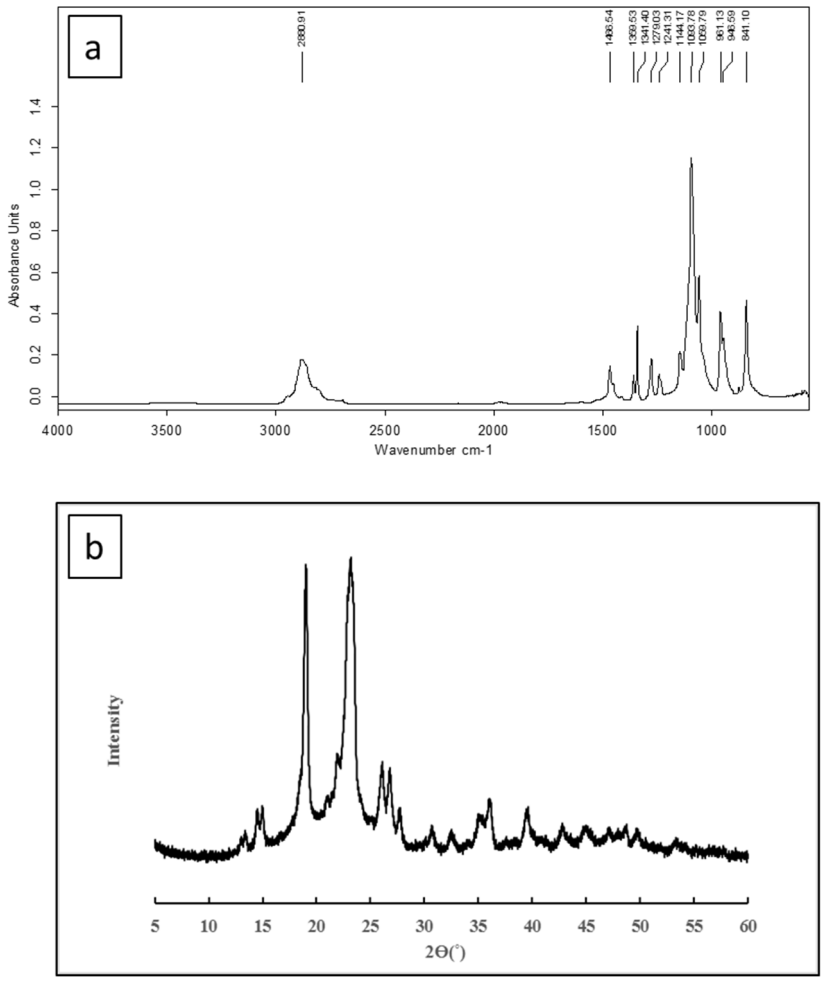

Figure 3.12: a) ATR-FTIR spectrum (n=3) and PXRD pattern of PEO K900

3.3.1.4 Tween 80

Tween 80 was used as solubilisation non-ionic surfactant for preparing felodipine solid dispersions using HME-IM and 3D FDM printing. This compound was selected for its solubilisation, plasticisation and absorption enhancing effects as mentioned in Chapter 2. The physicochemical properties of this surfactant were investigated using TGA, MTDSC, DVS and ATR-FTIR. The TGA profile for Tween 80 (**Figure 3.13a**) illustrated that Tween 80 has an

extrapolated degradation temperature onset of 372.4 ± 0.8℃ as a single step degradation process. Using MTDSC, the melting, crystallisation and glass transition (T_g) of Tween 80 were found to be -10.2 ± 2.3, -44.6 ± 1.2 and -64.2 ± 0.6℃, respectively (**Figure 3.13b**). In addition, this hydrophilic liquid surfactant has high tendency for moisture uptake estimated as 14.44 ± 0.89% w/w using DVS as shown in **Figure 3.13c**. This is an important parameter that may play a significant role in the physical stability of formulated solid dispersions exposed to high relative humidity environment.

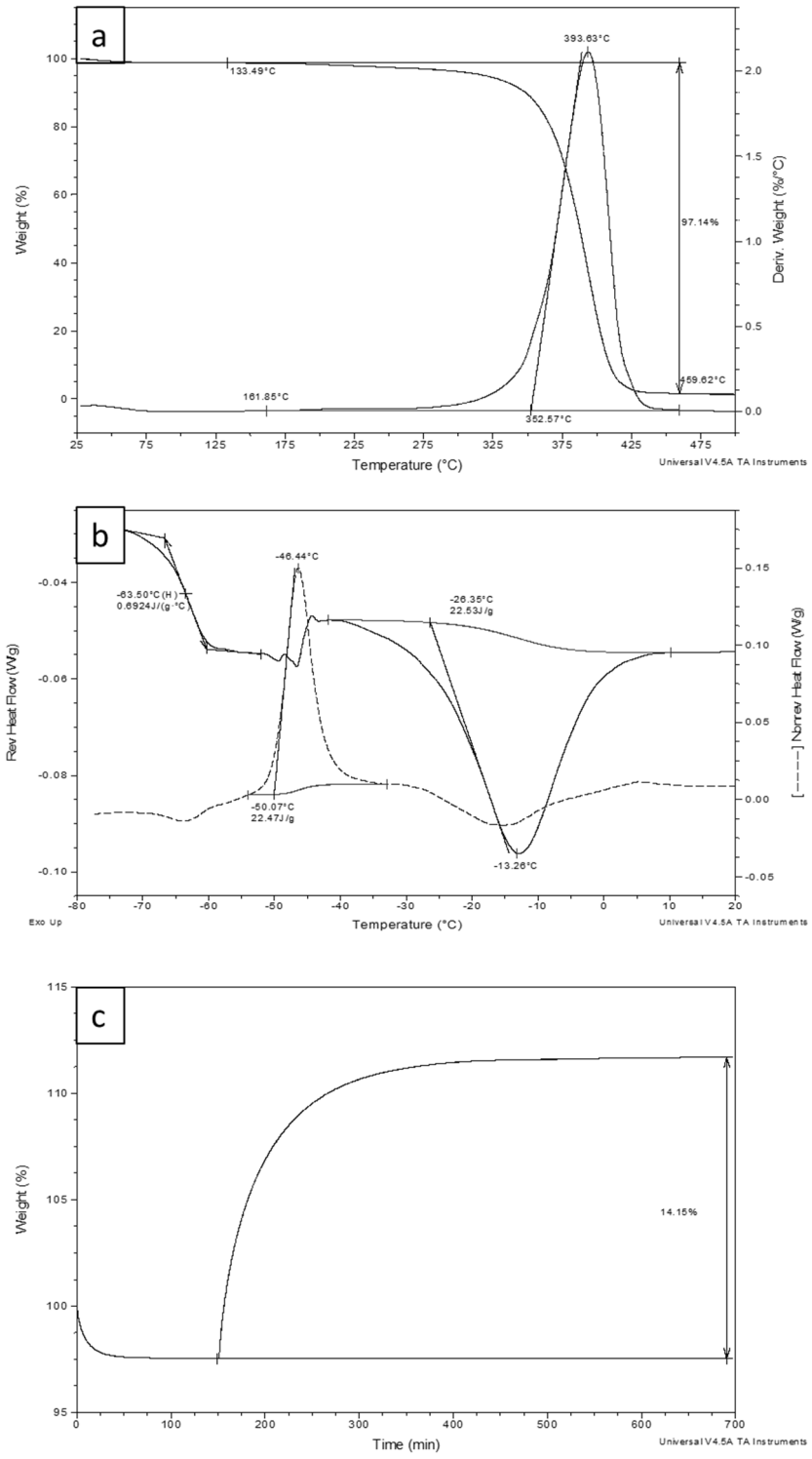

Figure 3.13: a) TGA analysis of Tween 80 using heating program of 10° C / min from ambient to 500℃ (n=2); b) MTDSC thermogram showing the thermal events (glass transition T_g, crystallisation and melting) of Tween 80 using temperature program of 2° C / min, 0.318 amplitude and 60 sec.s period (n=3) and c) moisture uptake capacity of Tween 80 at 25℃ and 75% RH (n=3)

The ATR-FTIR spectrum (**Figure 3.14**) shows the characteristic FTIR bands of Tween 80 which are listed in **Table 3.3**.

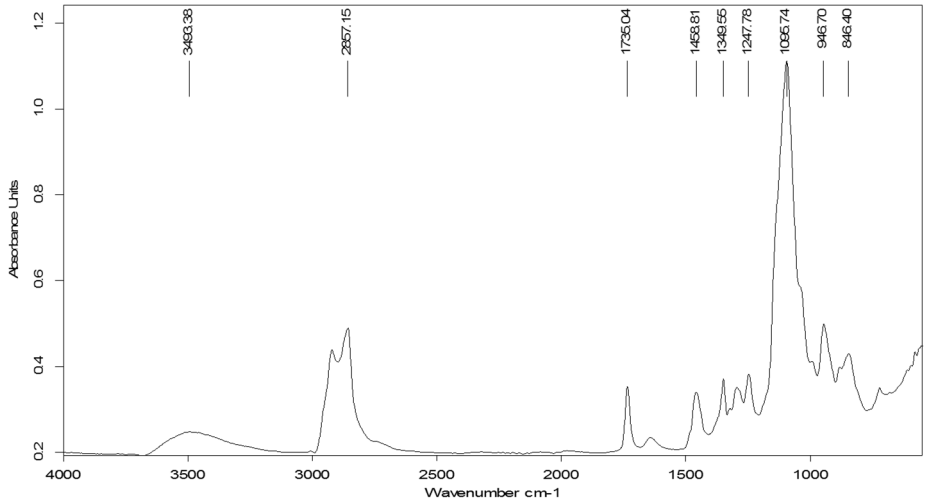

Figure 3.14: ATR-FTIR spectrum of Tween 80 (n=3)

Table 3.3: Characteristic ATR-FTIR absorption peaks of Tween 80

Compound	Chemical group	Peak wavenumber (cm^{-1})
Tween 80	OH stretching	3493
	CH stretching for CH_3	2922
	CH stretching for CH_2	2857
	C=O stretching	1735
	C–O–C stretching	1096

3.3.1.5 TPGS

Vitamin E TPGS was used in this study as a semisolid surfactant to illustrate the impacts of surfactant physical state on the solubility and stability of felodipine solid dispersions. TPGS showed an extrapolated degradation onset at 353.4 ± 1.1 ℃ (**Figure 3.15a**). TPGS has high ability to uptake moisture despite its semicrystalline structure and semisolid state. The equilibrium

moisture absorption capacity of this hydrophilic surfactant is 12.80 ± 0.72 % w/w measured using DVS which is only slightly less but much slower compared to Tween 80 (**Figure 3.15b**).

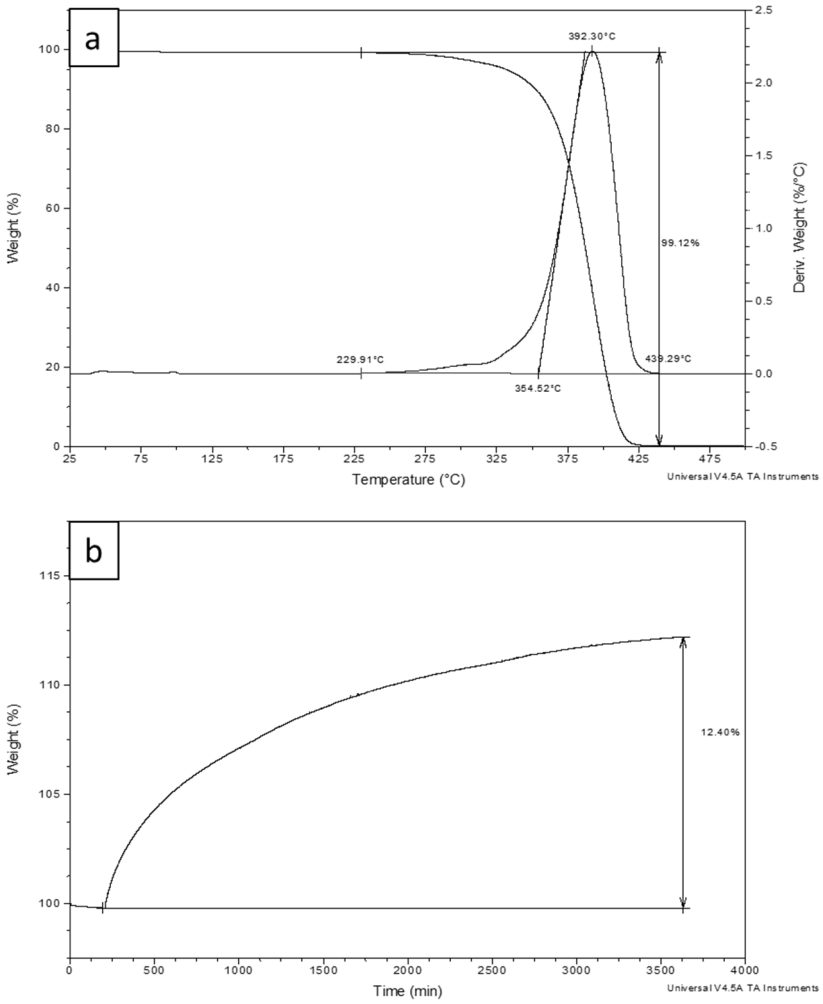

Figure 3.15: a) TGA analysis of TPGS using heating program of 10˚C / min from ambient to 500˚C (n=2) and b) moisture uptake capacity of TPGS at 25℃ and 75% RH (n=3)

TPGS is a semicrystalline non-ionic surfactant that has an asymmetric melting peak at 37.2 ± 0.2℃ and ΔH_f of 100.01 ± 1.09 J/g using 10℃/min temperature program as shown in **Figure 3.16a**. The surfactant recrystallised in two peaks at 0.3 ± 1.2 and -15.9 ± 0.2℃ as shown in **Figure 3.16b**. The asymmetric melting and the two distinct recrystallisation peaks suggest the presence of small fractions of the di-ester form of vitamin E TPGS in addition to the main mono-esterified form with free residuals of PEG 1000 (56, 457, 458). The reheating cycle indicates that the surfactant re-melted at 38.3 ± 0.4℃ and ΔH_f of 104.00 ± 1.3 J/g. The T_g of TPGS was measured

using the immediate reheating cycle at 10℃ after cooling at the same rate of standard DSC and found to be -20.0 ± 0.9℃ with ΔC_p of 0.32 ± 0.06 J/g.℃ as shown in **Figure 3.16c**.

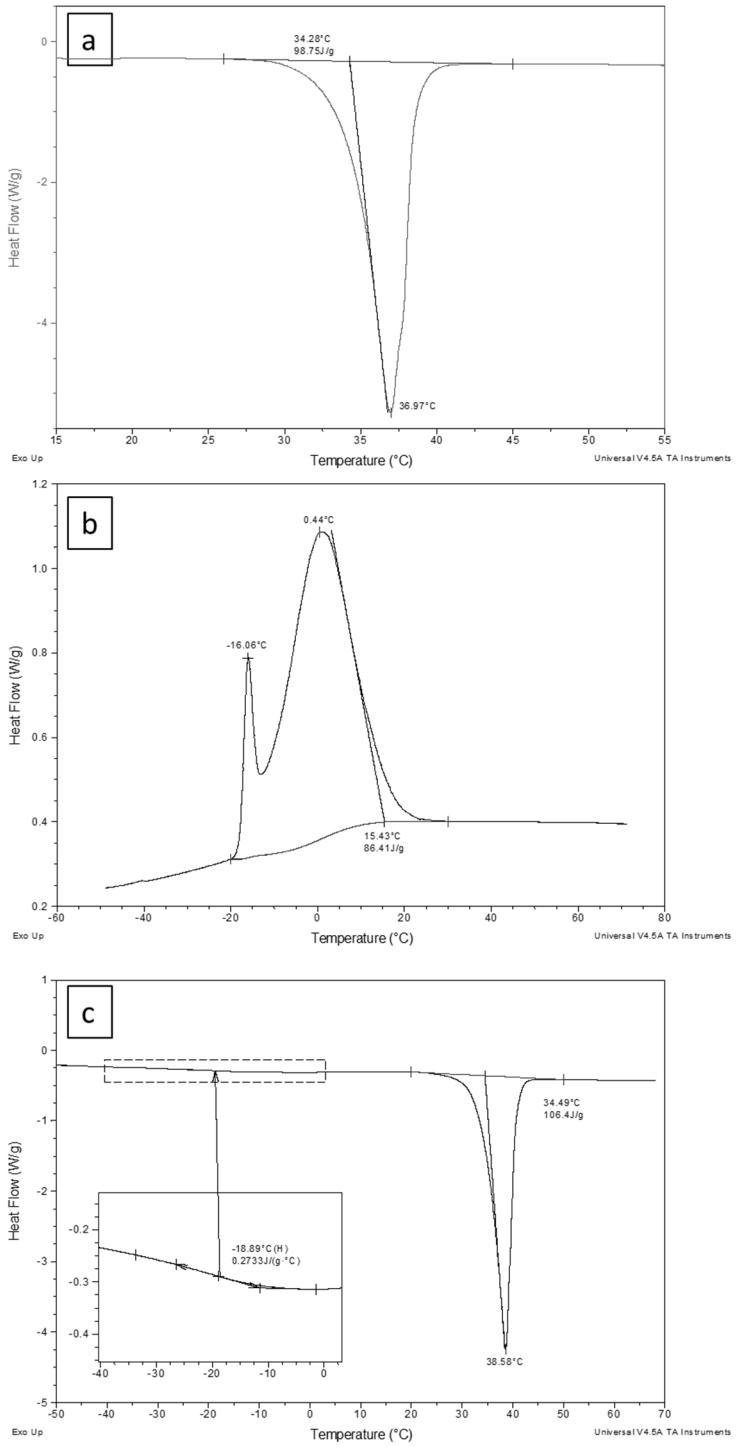

Figure 3.16: Partial standard DSC thermograms showing semicrystalline TPGS melting (a), crystallisation (b) and glass transition (T_g) with re-melting (c) events using 10˚C / min heating and cooling ramps (n=3)

The ATR-FTIR spectrum of TPGS indicated the presence of bands characteristics of polyethylene oxide (PEO) and vitamin E moieties in addition to the C=O band at 1735 cm^{-1} of the succinate group as shown in **Figure 3.17a and Table 3.4**. The PXRD pattern of TPGS (**Figure 3.17b**) revealed the presence of the diffraction peaks of the crystalline polyethylene oxide moiety especially those at 19.4° and 23.5° 2Θ indicating the semicrystalline nature of this surfactant (385).

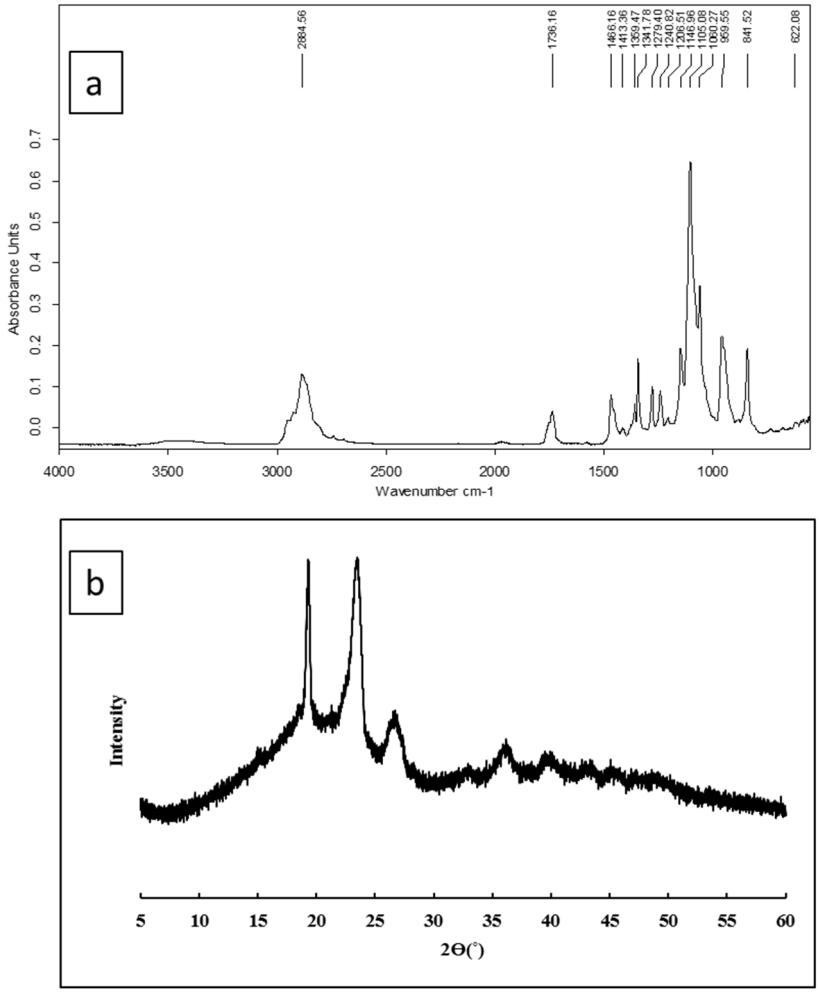

Figure 3.17: a) ATR-FTIR spectrum (n=3) and b) PXRD pattern of TPGS

Table 3.4: Characteristic ATR-FTIR absorption peaks of TPGS

Compound	Chemical group	Peak wavenumber (cm^{-1})
TPGS	OH stretching	3428
	CH stretching for CH_3	2885
	C=O	1735
	C–O–C stretching	1147, 1105 and 1060
	crystal peak of PEO moiety	969

3.3.1.6 PEO WSR N10 LEO (PEO K100)

PEO K100 was used as a constituent of the polymeric blend utilised in the fabrication of felodipine solid dispersions by FDM 3D printing. PEO K100 shows a single step degradation with extrapolated onset of 369.3 ± 0.3℃ as illustrated in **Figure 3.18**.

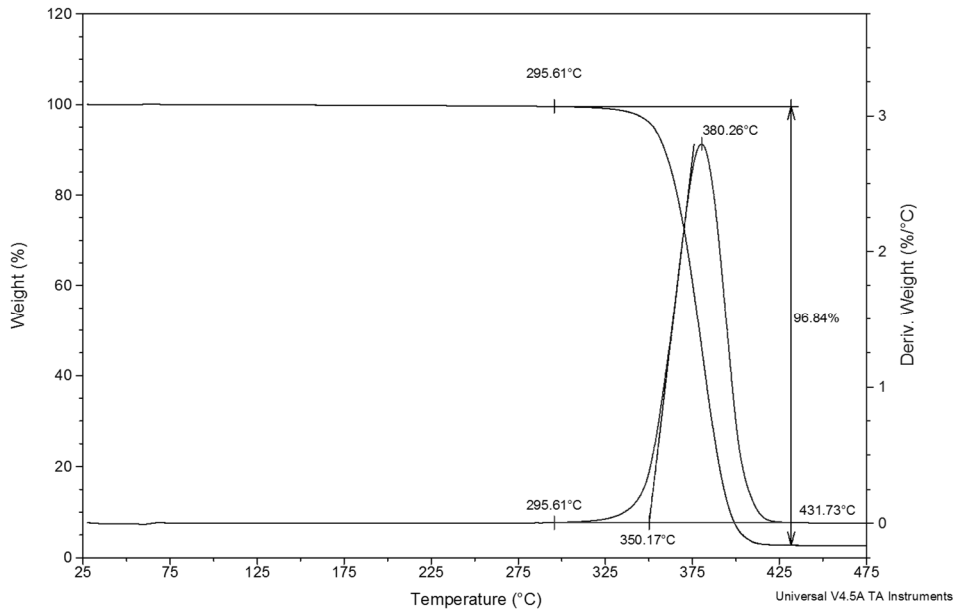

Figure 3.18: TGA analysis of PEO K100 using heating program of 10˚C / min from room temperature to 475˚C (n=2)

Thermal analysis using standard DSC revealed an intermediate melting peak between those of PEG 4000 and PEO K900 at 65.6 ± 0.1 ℃ with ΔH_f of 180.3 ± 4.4 J/g using 10 ℃/min temperature program as shown in **Figure 3.19a**. This grade of PEO shows a recrystallisation peak at 41.9 ± 0.4 ℃ with ΔH_c of 133.6 ± 10.2 J/g using 10 ℃/min cooling rate as shown in **Figure 3.19b**. In addition, using the same heating rate, the immediate reheating cycle showed an asymmetric melting peak of the polymer having peak at 62.4 ± 0.1 ℃ with ΔH_f of 143.0 ± 8.6 J/g revealing more folding and thinner crystals as shown in **Figure 3.19c** (328).

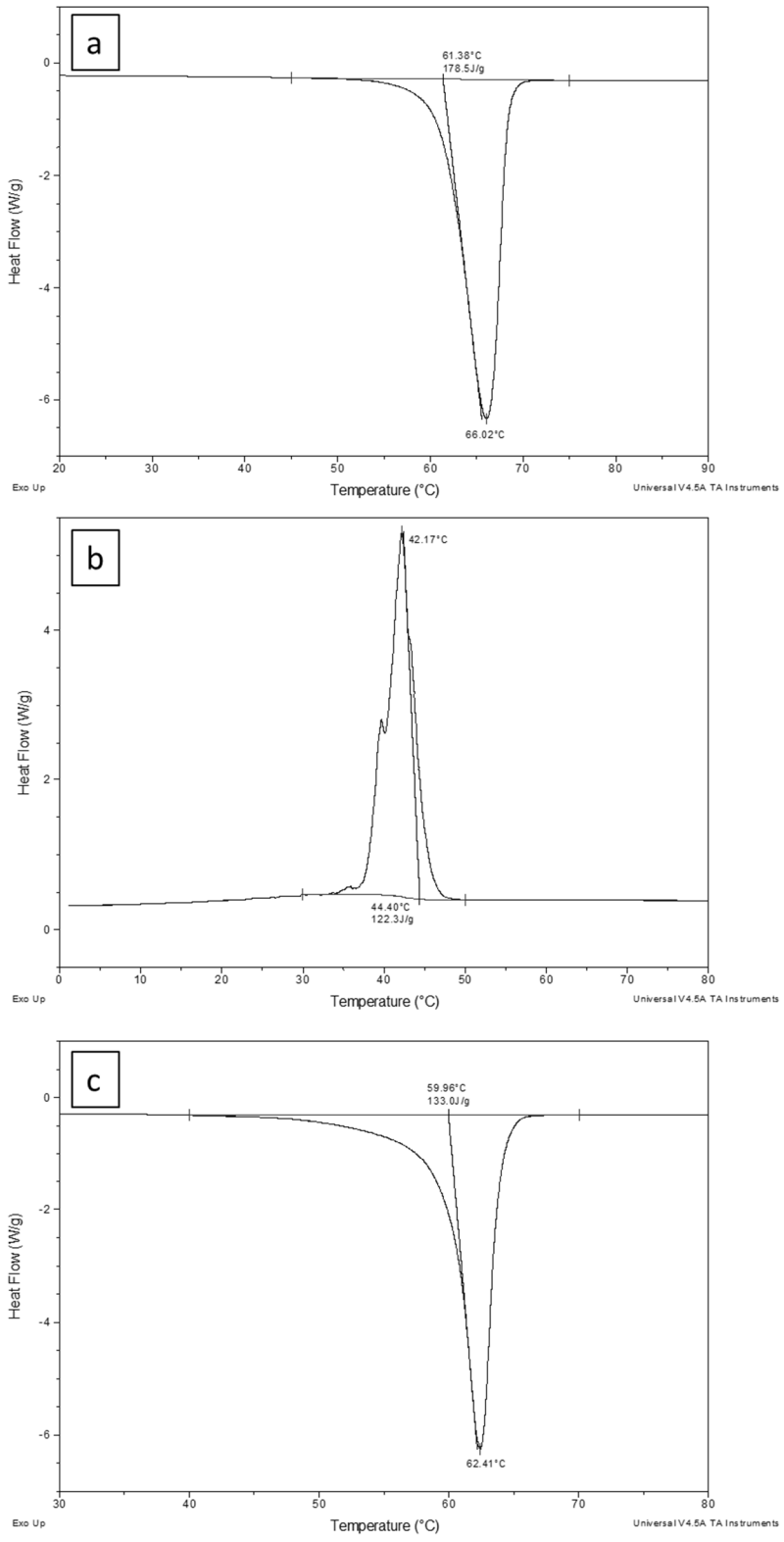

Figure 3.19: Partial standard DSC thermograms show semicrystalline PEO K100 melting (a), crystallisation (b) and re-melting (c) events using 10˚C / min heating and cooling ramps (n=3)

The ATR-FTIR spectrum and PXRD pattern for PEO K100 are shown in **Figures 3.20a and 3.20b** respectively. Due to the similarity in the monomeric unit of this polymer and PEG 4000 and PEO K900, this polymer showed similar IR absorption bands and diffraction peaks as summarised in **Table 3.2**.

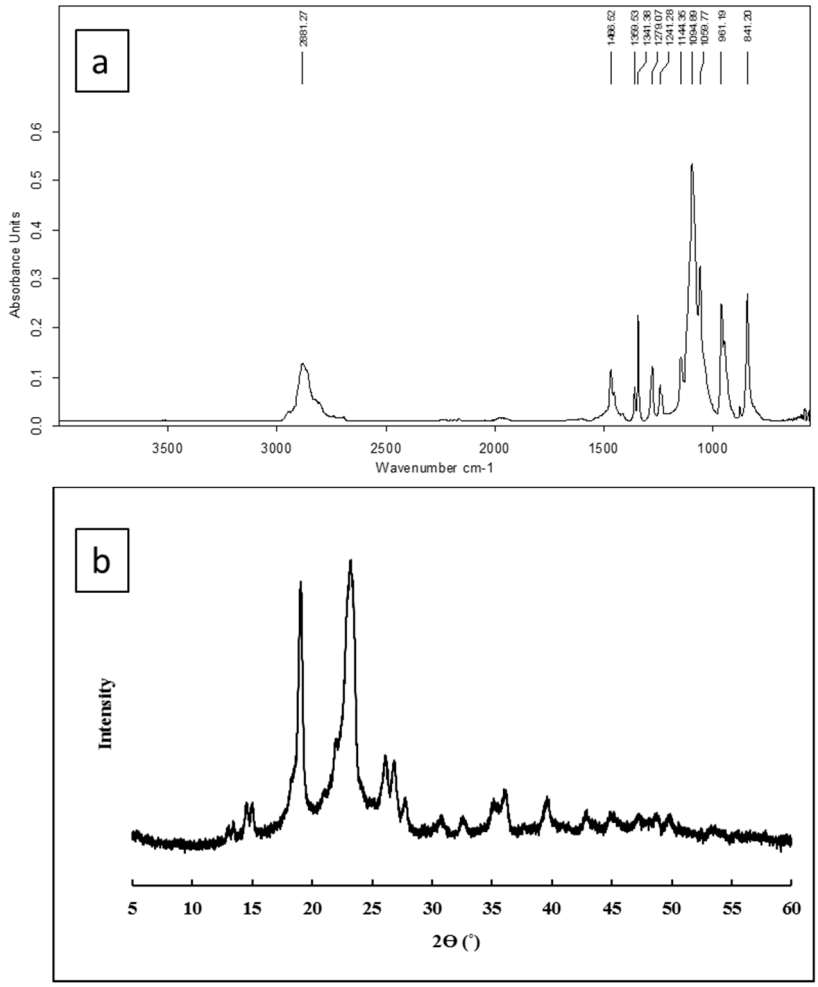

Figure 3.20: a) ATR-FTIR spectrum (n=3) and b) PXRD pattern of PEO K100

3.3.1.7 Eudragit E PO

Eudragit E PO is a copolymer used as a main constituent of felodipine solid dispersions prepared by FDM 3D printing. This polymer is degraded in a two steps process at 253.0 ± 2.8 and 362.4 ± 4.9℃ as shown in **Figure 3.21a**. Eudragit E PO is an amorphous polymer has a T_g at 46.7 ± 1.0℃ and ΔC_p of 0.40 ± 0.02 J/g.℃ as shown in **Figure 3.21b** using 2˚C / min, 0.318 amplitude and 60 sec.s period MTDSC program.

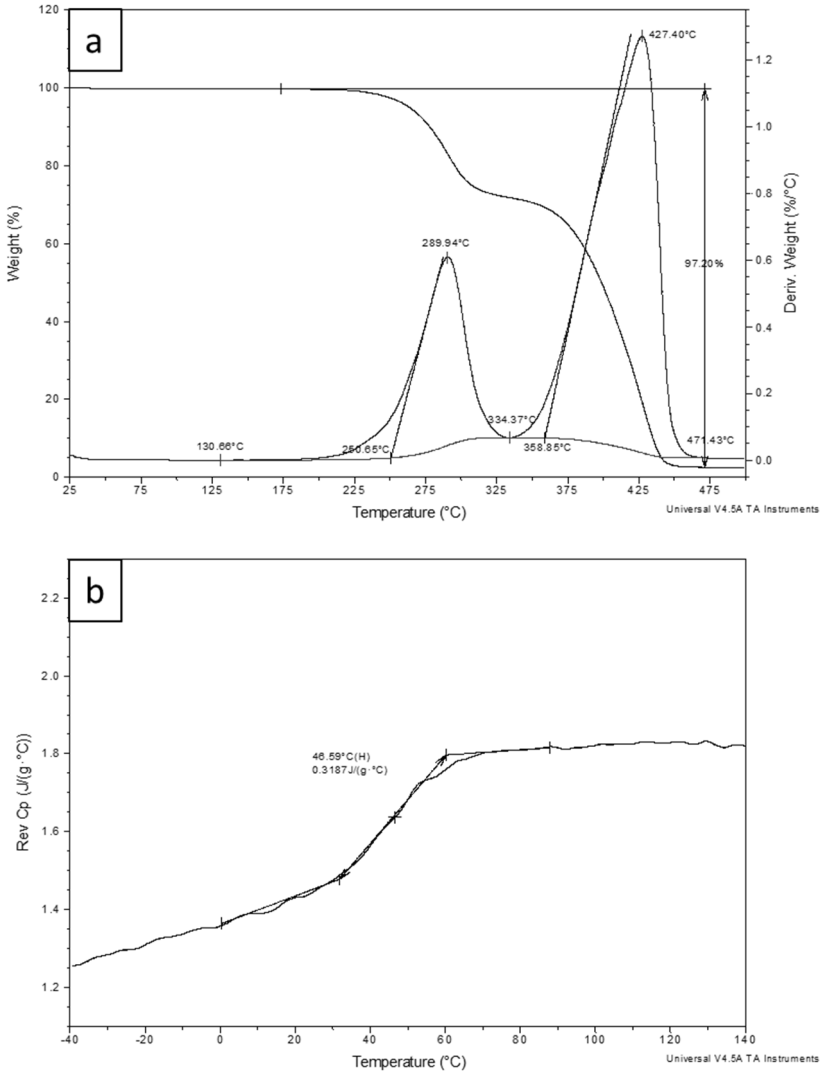

Figure 3.21: a) TGA analysis of eudragit E PO using heating program of 10˚C / min from ambient temperature to 500˚C (n=2) and b) reverse signal of MTDSC thermogram showing eudragit E PO glass transition (T_g) using 2˚C / min, 0.318 amplitude and 60 sec.s period (n=3)

The ATR-FTIR spectrum of Eudragit E PO is shown in **Figure 3.22a** reveals the characteristic IR peaks which are listed in **Table 3.5**. The PXRD pattern of eudragit E PO indicates the amorphous nature of this copolymer as illustrated in **Figure 3.22b**.

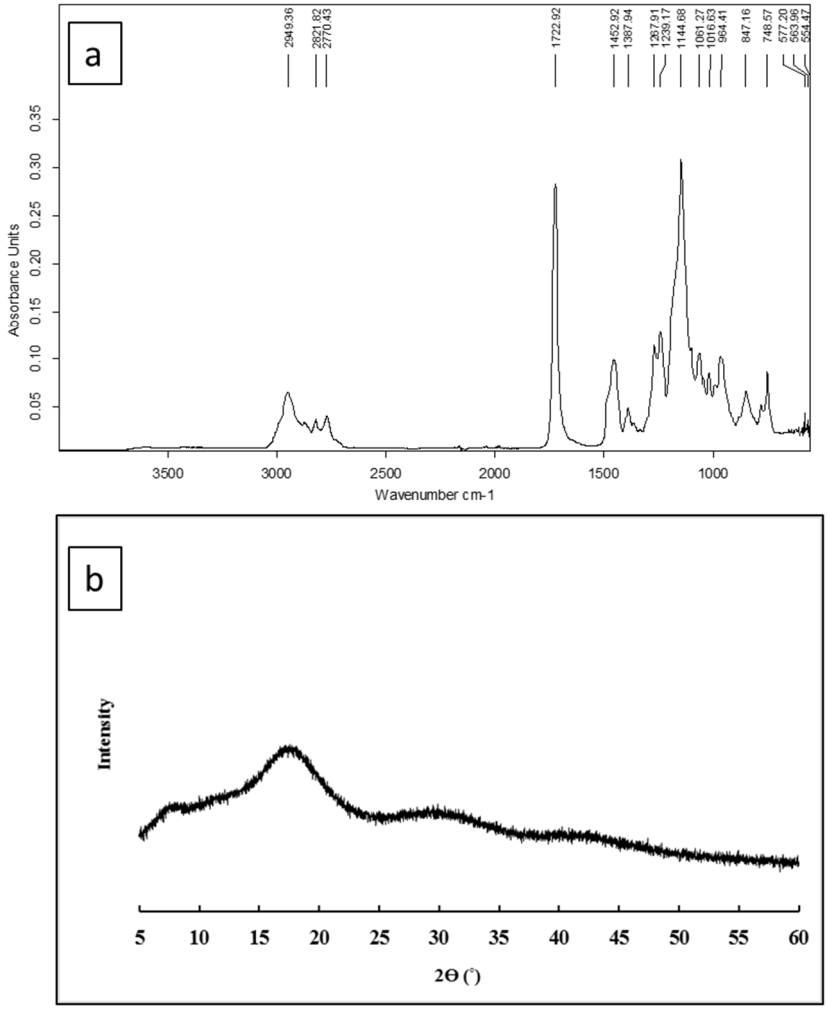

Figure 3.22: a) ATR-FTIR spectrum (n=3) and b) PXRD pattern of eudragit E PO

Table 3.5: Characteristic ATR-FTIR absorption peaks of eudragit E PO

Compound	Chemical group	Peak wavenumber (cm^{-1})
Eudragit E PO	CH stretching for CH_3	2949
	CH stretching for CH_2	2821
	CH stretching for CH	2770
	C=O stretching	1723
	CH bending	1453
	C-O stretching	1388
	C-O-C stretching	1268 and 1239
	C-C stretching	1144

3.3.1.8 Soluplus

Soluplus is also a copolymer used in this study as the main polymer for preparing felodipine solid dispersions using FDM 3D printing. The TGA of soluplus indicated the degradation in two step processes with extrapolated onsets at 282.7 ± 0.3 and 370.4 ± 1.1 ℃ as shown in **Figure 3.23a**. MTDSC thermogram using 2 ˚ C / min, 0.318 amplitude and 60 sec.s period indicated the amorphous character of soluplus with a T_g of 74.1 ± 0.3 ℃ and ΔC_p of 0.42 ± 0.04 J/g ℃ as shown in **Figure 3.23b**.

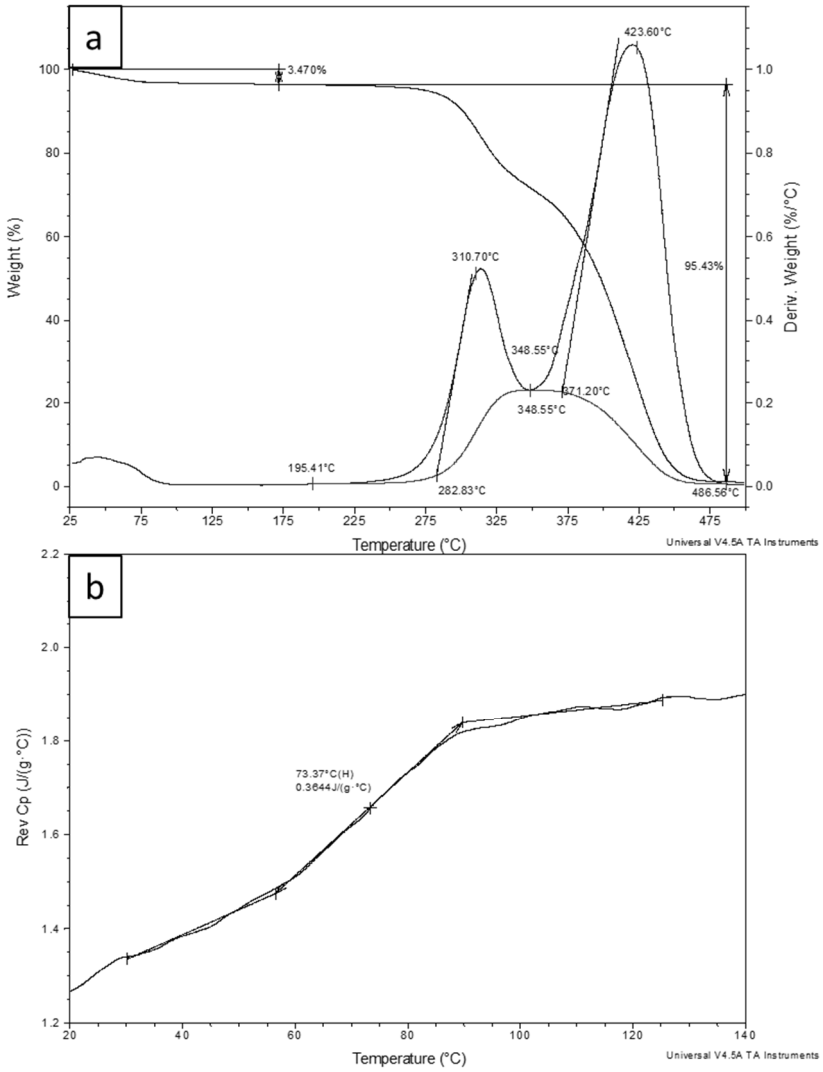

Figure 3.23: a) TGA analysis of soluplus using heating program of 10˚C / min from room temperature to 500˚C (n=3) and b) reverse signal of MTDSC thermogram showing soluplus glass transition (T_g) using 2˚C / min, 0.318 amplitude and 60 sec.s period (n=3)

The ATR-FTIR spectrum of soluplus is shown in **Figure 3.24a** revealing its absorbance peaks listed in **Table 3.6**. The PXRD pattern of this copolymer **Figure 3.24b** indicates its amorphous character due to the absence of any diffraction peaks.

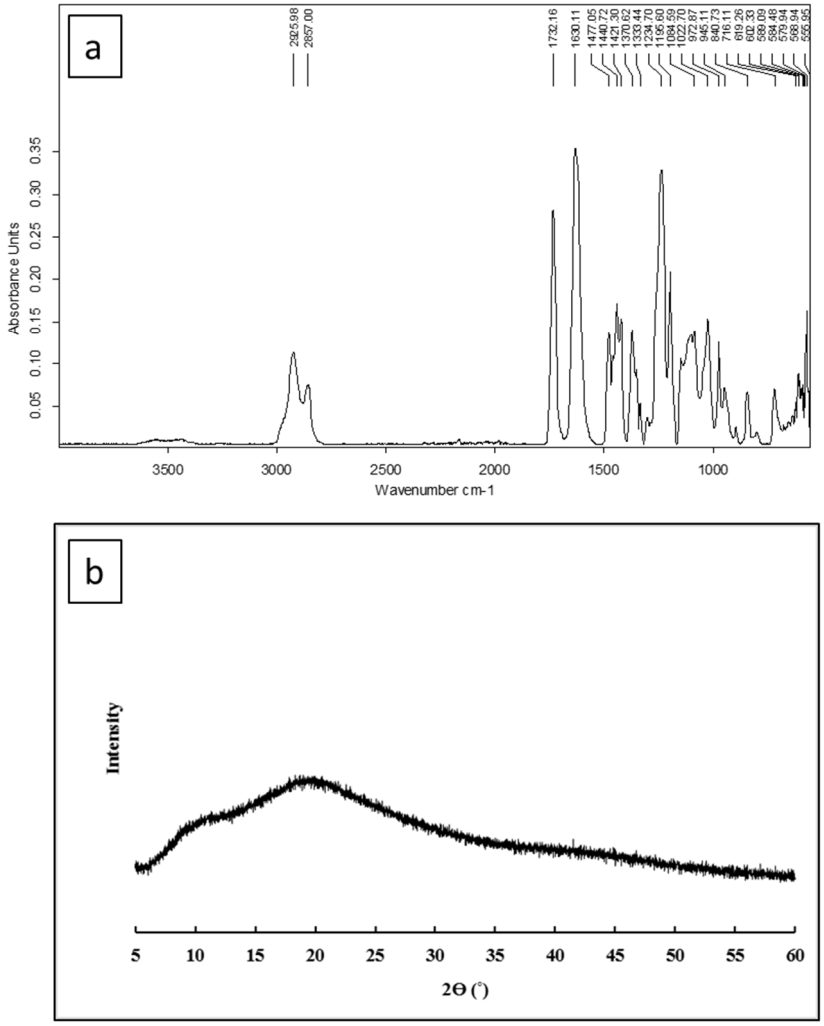

Figure 3.24: a) ATR-FTIR spectrum (n=3) and b) PXRD pattern of soluplus

Table 3.6: Characteristic ATR-FTIR absorption peaks of soluplus

Compound	Chemical group	Peak wavenumber (cm^{-1})
Soluplus	OH stretching	3447
	CH stretching for CH_3	2926
	CH stretching for CH_2	2857
	C=O stretching	1732
	O-C-N stretching	1630
	CH bending	1477
	C-O stretching	1370
	C-O-C stretching	1234
	C-C stretching	1195

3.3.1.9 Polyvinyl alcohol (PVA)

PVA was used as a benchmark FDM 3D printing polymer for fabricating felodipine solid dispersions due to the reported good printability properties. In order to understand the properties of this polymer, TGA, MTDSC, ATR-FTIR and PXRD techniques were used to investigate its physicochemical properties. The TGA of PVA is shown in **Figure 3.25a** revealing degradation in two-step degradation process due to the partial hydrolysis state of this polymer. Also, this grade of PVA is completely amorphous due to the absence of any melting peak and the presence of single T_g at 46.1 ± 0.2 ℃ with ΔC_p of 0.60 ± 0.02 J/g ℃ as shown in **Figure 3.25b**.

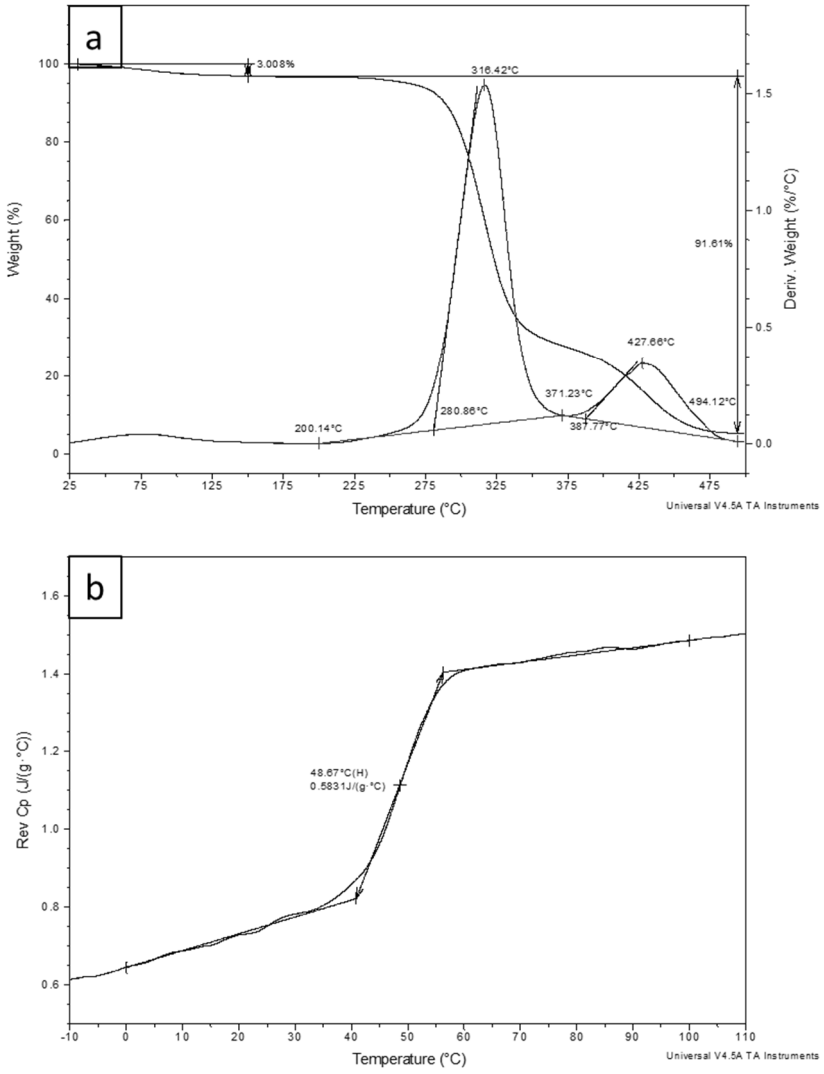

Figure 3.25: a) TGA analysis of PVA using heating program of 10˚C / min from room temperature to 500˚C (n=3) and b) reverse signal of MTDSC thermogram showing PVA glass transition (T_g) using 2˚C / min, 0.318 amplitude and 60 sec.s period (n=3)

The ATR-FTIR spectrum of PVA is shown **in Figure 3.26a** revealing the characteristic IR peaks listed in **Table 3.7**. The PXRD pattern of PVA (**Figure 3.26b**) indicates the absence of any crystalline diffraction peaks revealing the amorphous nature of this grade of PVA.

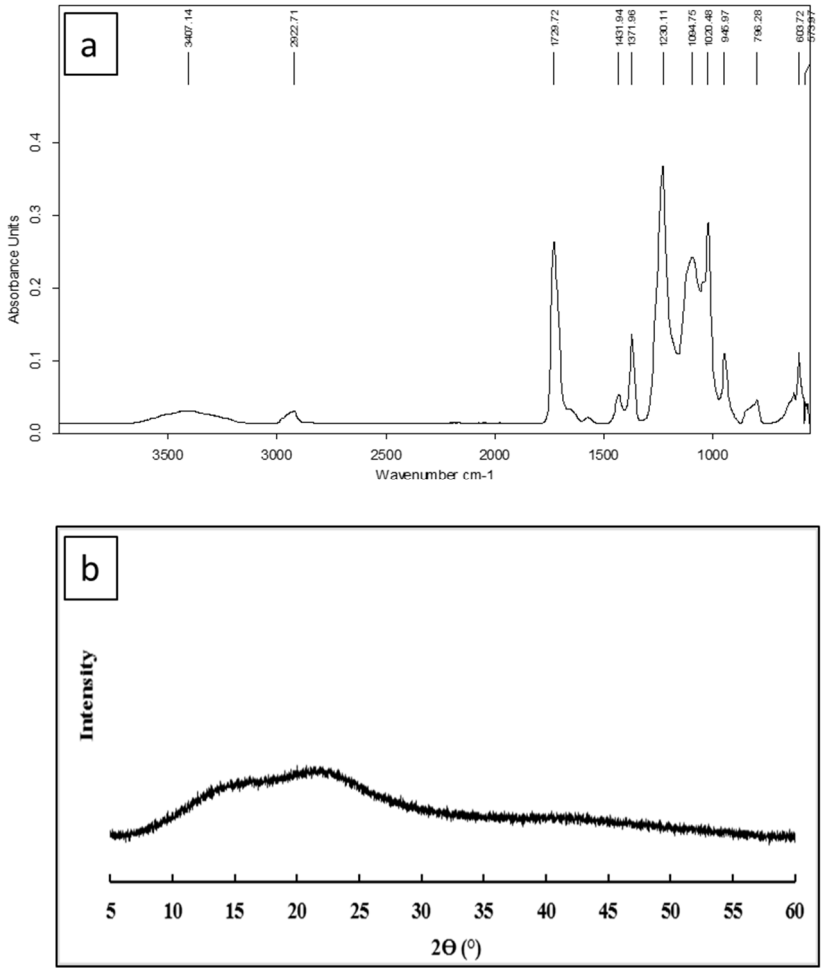

Figure 3.26: a) ATR-FTIR spectrum (n=3) and PXRD pattern of PVA

Table 3.7: Characteristic ATR-FTIR absorption peaks of PVA

Compound	Chemical group	Peak wavenumber (cm^{-1})
PVA	OH stretching	3424
	CH stretching for CH_2	2823
	C=O stretching	1730
	CH bending	1432
	C-O stretching	1372
	C-O-C stretching	1230
	C-C stretching	1095

3.3.2 Theoretical calculations of the solubility parameters of the ingredients

The calculations of solubility parameters of felodipine and other excipients (chemical structure are shown in Chapter 2) using Hoftyzer and Van Krevelen and Hoy methods can be found in Appendix 1. **Table 3.2** summarises the results of the calculations by averaging of the solubility parameters determined by the two approaches as recommended in literature to ensure the accuracy of prediction (459).

Table 3.8: Summary of solubility parameter predictions calculated using group contribution methods

Compound	δ Van Krevelen	δ Hoy	δ average	δ difference*
Felodipine	20.60	21.08	20.84	-
PEG 4000 PEO K900 PEO K100	22.00	21.44	21.72	0.88
Tween 80	20.90	22.71	21.81	0.97
TPGS	20.38	21.18	20.78	0.06
Eudragit E PO	18.80	18.55	18.68	2.17
Soluplus	18.94	24.34	21.64	0.80
PVA	30.53	28.79	29.66	8.82

*** (difference between the solubility parameters of the drug and each one of the excipients)**

Based on the results obtained from these prediction methods, the miscibility of felodipine in the individual excipients at room temperature can be ranked in the following order: TPGS > soluplus > (PEG 4000, PEO K900, PEO K100) > Tween 80 > eudragit E PO > PVA. The rule of thumb for estimating miscibility reported in literature is a difference in solubility parameter (Δδ) of less than 7 $(MJ/m^3)^{½}$ indicates that the substances are miscible; a Δδ value more than 10 $(MJ/m^3)^{½}$ predicts unfavourable interaction and immiscibility between the components of the blend leading to phase separation. A Δδ value of 7-10 $(MJ/m^3)^{½}$ indicates partial miscibility of the ingredients (60, 361). Based on this, all excipients used in this study are expected to possess good miscibility at room

temperature with felodipine except PVA which is predicated to form a partially miscible binary mixture with the model drug.

3.3.3 Experimental estimation of the miscibility of PEG 4000 and PEO K900 using DSC

PEG 4000 and PEO K900 are the main constituents used for preparing felodipine mucoadhesive buccal patches using HME-IM because they provide solubilisation, mucoadhesion, low temperature processing properties and most importantly their easy removal after moulding making them suitable candidate excipients for IM processing (151). Due to the difference in the molecular weights of these two grades and the inability of the theoretical methods to predict their miscibility due to the similarity in their monomeric units and molecular configurations, it is important to investigate their behaviour in order to select the most suitable combination blend. Thermal properties of the two polymers at different proportions using 10% w/w increments of PEG 4000 relative to PEO K900 were analysed using DSC. The results of the first heating cycle of the physical mixtures show both melting peaks and the magnitude of each peak is corresponding to the proportions of their mixing ratios as seen in **Figure 3.27a**. This indicates their immiscibility within the timescale and conditions of the DSC run. On cooling, the molten mixtures with the higher ratios of PEO K900 (PEG:PEO 1:9, PEG:PEO 2:8, and PEG:PEO 3:7) show two partially resolved crystallisation peaks corresponding to the crystallisation of the two polymers (**Figure 3.27b**). On the other hand, as the percentage of PEG 4000 increased the mixture started to form single crystallisation peak shifted to lower temperature as the amount of PEG 4000 increased in the mixture. However, the reheating cycles indicate the presence of two partial overlapped melting peaks shifted to lower temperatures compared to the first heating cycle as shown in **Figure 3.27c**. The appearance of two peaks during the heating, cooling and reheating cycles of the DSC runs with more peak separation for the mixtures containing high proportions of PEO K900 either indicates partial miscibility of the two polymers and/or the high viscosity of PEO K900 prevents the complete mixing between the two polymers inside the sealed DSC pans.

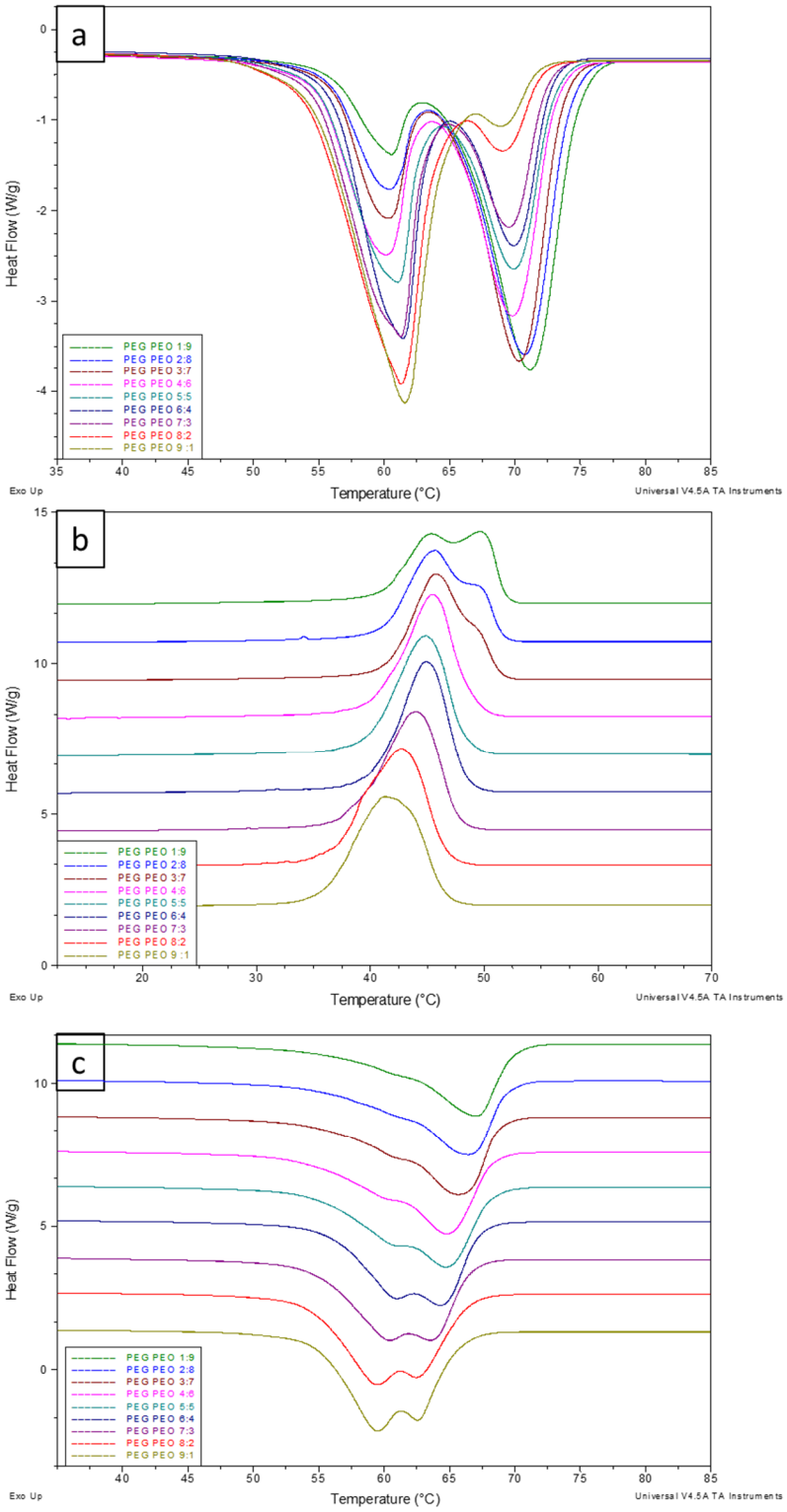

Figure 3.27: Standard DSC thermogram showing the a) heating cycle melting peaks; b) cooling cycle crystallisation peaks and c) reheating cycle melting peaks of PEG 4000 and PEO K900 physical mixtures with different proportions using 10˚C / min heating and cooling ramps (n=3)

In order to further understand the effect of preparing processes on the miscibility and crystallinity of PEG 4000 /PEO K900, extruded blends of mixtures with different mixing proportions (3:7, 4:3 and 7:3) were investigated using DSC after HME processing at 65 °C. The results revealed single asymmetric melting peaks for 7:3 and 4:3 and partially separated two melting peaks for 3:7 PEG/PEO extruded blends as shown in **Figure 3.28**. Compared to physical mixtures with same mixing proportions, HME processing significantly enhances the miscibility of the two polymers especially for mixtures contain higher percentage of PEG 4000. The observation of two melting peaks for the 3:7 PEG 4000 /PEO K900 mixture indicates their partial miscibility after processing using HME experimental conditions. No significant difference in the melting temperatures of the blends showing single melting peaks was observed. The resultant single melting peaks' temperatures are lower than that of PEO K900 and higher than that of PEG 4000. This may indicate that mixing different grades with different melting temperatures of this polymer can produce a miscible semicrystalline mixture with intermediate melting points depending on the proportion of mixing.

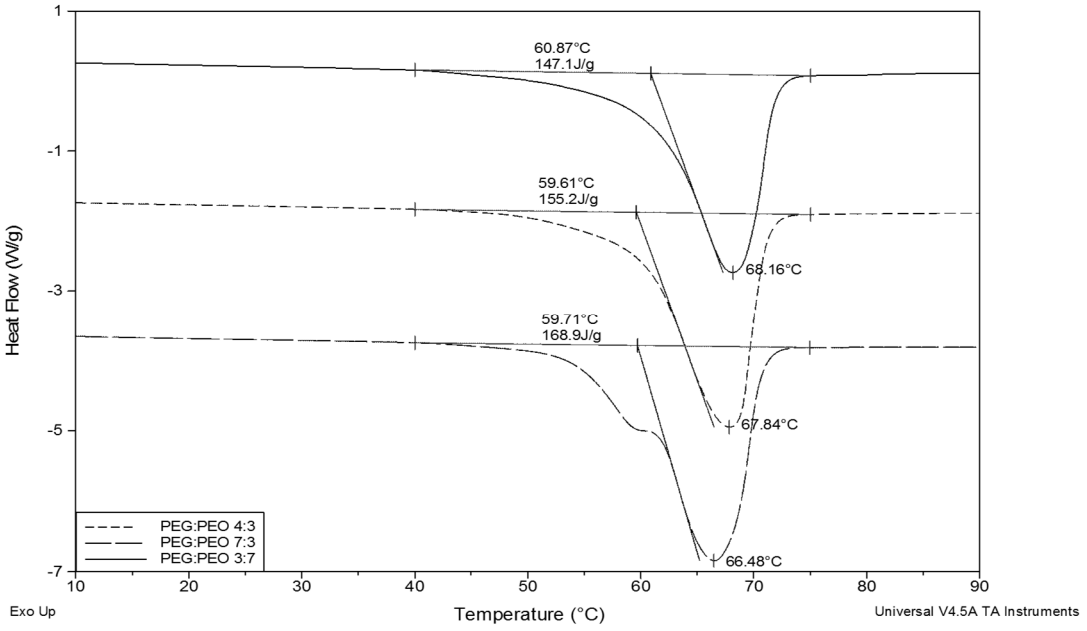

Figure 3.28: Standard DSC thermogram showing melting peaks of PEG 4000 and PEO WSR 1105 extrudates using 10˚C / min heating ramp (n=3)

The mixture of PEG/PEO K900 in a proportion of 4:3 was selected as the suitable blend that gives a maximum reduction in polymer crystallinity (maximum amorphous fraction available for drug solubilisation) and expected to provide balancing effect of poorly water soluble drug solubilisation and mucoadhesion by the two polymers.

Figures 3.29a and b show the MTDSC thermograms of adding Tween 80 to the polymer blend as a physical mixture and HME extrudates respectively. As it is evident from the data, the transitions of the three excipients are present before processing. However, the miscibility between the ingredients is significantly improved after HME processing as indicated by the presence of single melting peak for PEG/PEO K900 blend the reduced melting peak of Tween 80. The presence of Tween 80 melting peak reflects the partial miscibility between this surfactant and the polymers. In addition, the presence of endothermic shoulder before the melting of PEG/PEO K900 blend (**Figure 3.29b**) may be due to the formation of folded form of PEG/PEO K900 polymers representing their metastable polymorphic forms (328, 330).

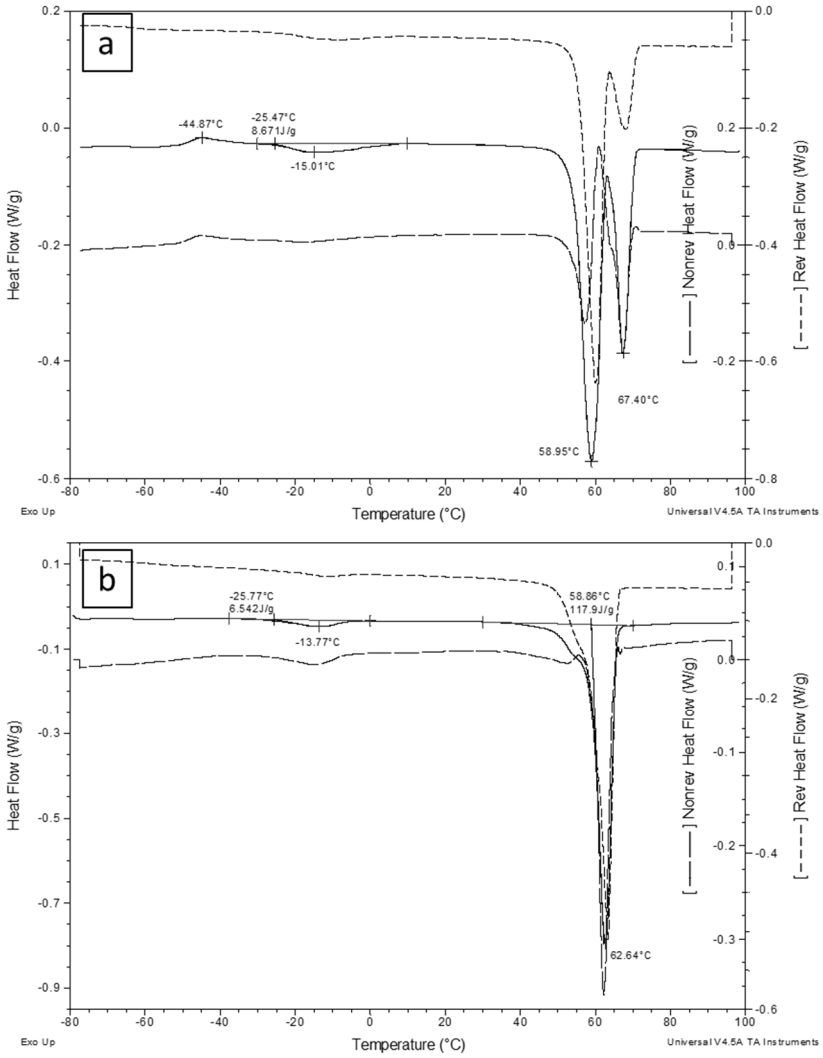

Figure 3.29: MTDSC thermogram showing transitions of PEG 4000- PEO K900-Tween 80 (4:3:3) physical mixture (a) and extrudate (b) using 2˚C / min, 0.318 amplitude and 60 sec.s period (n=3)

The addition of TPGS to the polymeric blend as a physical mixture or extrudates is shown in **Figures 3.30a and b**. The results indicate that processing also improves the miscibility of PEG/PEO K900 blend as revealed by the appearance of single melting peak of the two polymers. However, the observation of TPGS melting peak in the physical mixture and the extrudate of this blend indicates its partial miscibility with the polymeric blend.

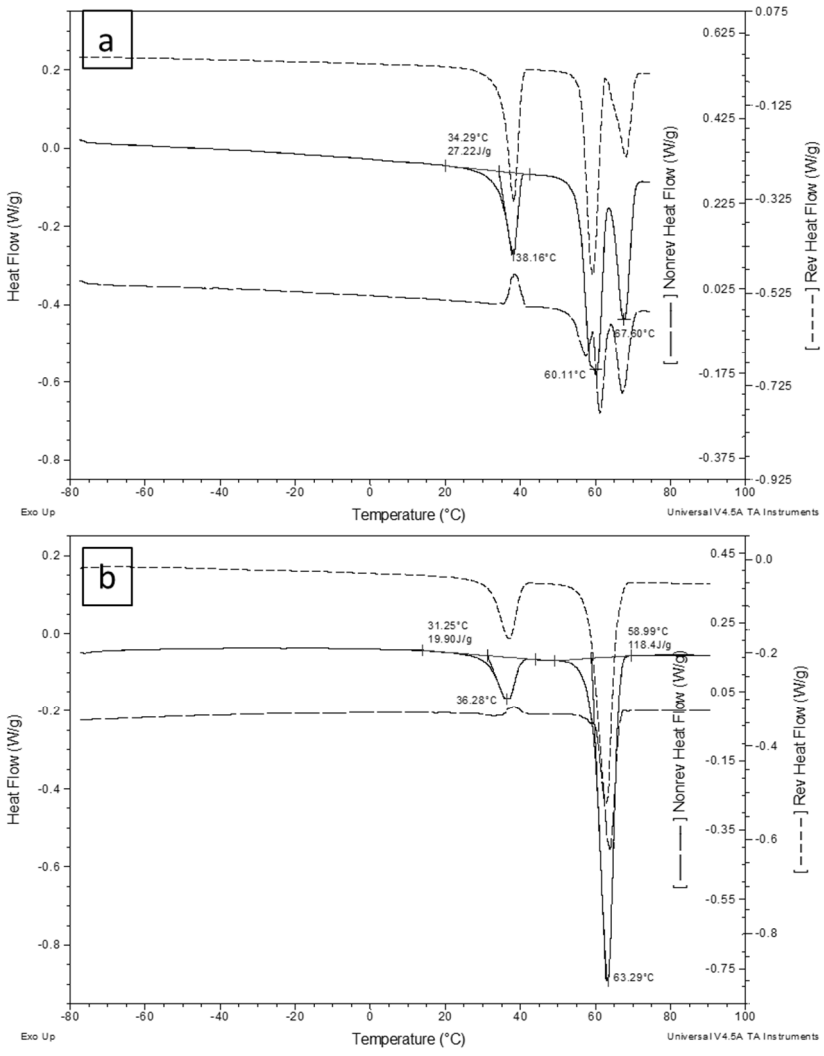

Figure 3.30: MTDSC thermogram showing transitions of PEG 4000- PEO K900-TPGS (4:3:3) physical mixture (a) and extrudate (b) using 2˚C / min, 0.318 amplitude and 60 sec.s period (n=3)

3.3.4 Estimation of the miscibility of felodipine and excipients used in HME-IM formulations

Standard DSC was used to investigate the miscibility of felodipine with the different excipients used in the fabrication of felodipine solid dispersions using HME-IM. The depression in the melting onset of felodipine was used as indicators for the miscibility of the drug in the excipients (**Figure 3.31**) (57, 87, 416, 460). The results indicate that greater depression was in the onset of melting in the mixture with PEG compared to other excipients using 0.6-0.8 w/w felodipine fractions. The depression of felodipine melting was the lowest for the mixtures containing PEO K900 in all proportions. Also, TPGS causes greater depression in the onset of felodipine melting compared to Tween 80 using felodipine fractions higher than 0.7. It should be mentioned that the experimentally measured solubility of felodipine in Tween 80 using UV-VIS spectrophotometry was 100.24 ± 0.001 mg/mL at room temperature.

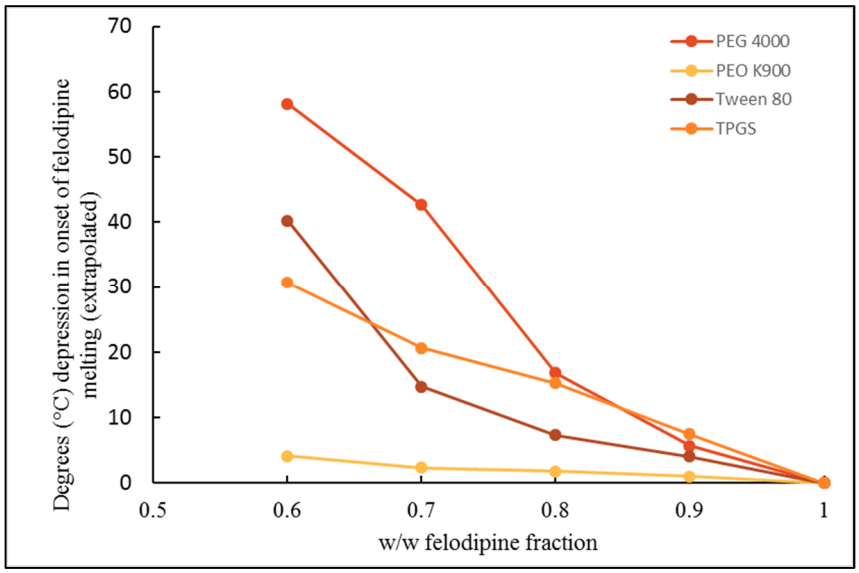

Figure 3.31: Depression in the extrapolated onset of melting of felodipine in different excipients as a function of felodipine weight fraction (n=3)

3.4 Discussion

This chapter aimed to investigate the thermal and spectroscopic properties of the raw materials used in this study as a preformulation step in order to facilitate formulations development. TGA results showed that all excipients utilised in the different formulations were more thermally stable

compared to felodipine which is more susceptible to thermal degradation at approximately 166℃. This may suggest a maximum processing temperature of 150℃ for safe processing of this model drug using HME-IM and FDM 3D printing. Processing PEG 4000 with PEO K900 using HME at 65℃ for 5 minutes using different proportions shows mixing improvement of the two polymers compared to physical mixtures. The two polymers with 4:3 and 7:3 blends of PEG 4000 and PEO K900 respectively show single melting peaks indicating the formation of single semicrystalline structure. In order to provide good solubilisation and mucoadhesion properties for the intended felodipine buccal patches formulations, PEG 4000-PEO K900 4:3 blend was selected as it shows good mixing properties between the two polymers.

Tween 80 and TPGS are non-ionic surfactants with semicrystalline properties. Due to the partial miscibility between these two surfactants with PEG-PEO K900 polymer blend, the phase separated surfactant domains will be used as a solubilisation compartments to solubilise and stabilise felodipine as an embedded molecular dispersion within the matrix. According to solubility parameter predictions and the depression of onset of melting, TPGS has higher solubilisation capacity for felodipine compared to Tween 80. This is expected to play a significant role in the solubilisation and stabilisation of felodipine in the formulations. In addition, TPGS has higher temperatures of melting, crystallisation and T_g compared to Tween 80. Due to its melting at approximately 37℃, TPGS is not expected to be 100% available for felodipine solubilisation as Tween 80 (liquid at room temperature) assuming no depression in its melting occurs when mixed with the drug. This may affect the extent of felodipine solubilisation by TPGS. On the other hand, the semisolid nature of TPGS may act as stabilisation parameter that restrict the diffusion of molecularly dispersed felodipine to form aggregates leading to phase separation.

DSC results indicate that the melting temperature and crystallinity of polyethylene oxide polymer grades are affected by thermal treatment. The reduction in the melting points and crystallinity indicates the conversion of part of the polymer to the less stable and more folded forms. Changes in crystallinity of the polymers can be considered as an important parameter that may affect the solubilisation capacity of the carrier mixture. Reduction in crystallinity (increasing amorphous fraction) of the carrier polymers is expected to increase the solubilisation capacity for the drug. On the other hand, the stability of the amorphous and crystalline domains of the carrier mixtures can play a critical role in the stability of the prepared solid dispersions. Instability of the amorphous domains and the tendency of the polymer to increase its crystallinity may act as a contributing factor for drug phase separation. Therefore, monitoring the physical stability of semicrystalline excipients used for preparing solid dispersions is necessary.

As mentioned in Chapter 1, FDM 3D printing technology is recently introduced to the pharmaceutical field as a promising technique to provide patients individualised medicine (224-226). Due to the limited number of pharmaceutically approved excipients are only available to use for fabricating formulations using this method, the use of excipient blends is suggested as an approach to improve the printability of excipients and provide different functionalities for formulations using this technique. Soluplus and eudragit E PO are widely used polymers for preparing solid dispersions of poorly soluble drugs using HME due to their good thermoplastic and solubilisation properties (73, 87, 149, 461). Blending these two polymers with polymers like PEG, PEO K100 and/or Tween 80 is expected to form miscible mixtures based on solubility parameter calculations. As mentioned in Chapter 2, PEG, PEO K100 and Tween 80 possess good plasticising and drug solubilisation properties that can help to reduce the processing temperature of FDM 3D printing and solubilise the incorporated drug.

3.5 Conclusion

Preformulation studies conducted in this chapter aimed to provide an insight into the fundamental physicochemical properties of the raw materials (model drug and excipients) and their mixing behaviour prior to their incorporation in the formulation using HME-IM and FDM 3D printing. Thermal, spectroscopic and imaging characterisation techniques were used to achieve this purpose. Prediction studies using group contribution and the depression in the melting onset were used to provide an estimation about the miscibility of the excipients with felodipine. Theoretical calculations revealed that felodipine is expected to have good miscibility with all excipients except with PVA. The various excipients have a solubility parameter differences (from lower to higher) relative to felodipine with an order of magnitude ranked as TPGS > soluplus > (PEG 4000, PEO K900, PEO K100) > Tween 80 > eudragit E PO > PVA. The addition of Tween 80 and TPGS surfactants as plasticisers to PEG/PEO K900 polymeric blend leads to the formation of surfactant phase in addition to the two phases of the semicrystalline polymeric blend. The surfactant phase separate domains can provide a solubilisation compartments for the poorly water soluble model drug used in this study. This will be used as a formulation strategy as illustrated in Chapter 4. Finally, polymer blends are suggested as an approach to improve the printability of pharmaceutical excipients to produce personalised medicines using FDM 3D printing technology.

Chapter 4. Design, characterisation and evaluation of felodipine loaded HME-IM mucoadhesive buccal patches

4.1 Introduction

Poor aqueous solubility and/or dissolution of many active pharmaceutical ingredients (APIs) including BCS class II drugs like felodipine is a challenging problem that affects their systemic absorption due to slower dissolution compared to permeation leading to inter- and intra-patient pharmacokinetics and absorption variations (1, 2, 462). Felodipine is widely used calcium channel antagonist as a potent antihypertensive and for prevention of angina pectoris. However, this drug is extensively metabolised in the liver (84%) into inactive metabolites which further reduce its systemic bioavailability (310, 462).

As discussed earlier in Chapter 1, solid dispersion technology is considered as an effective formulation-based method used to overcome the poor dissolution problem with high flexibility in processing techniques and excipients' choices (25, 31, 177). Fabricating transmucosal solid dispersions to be delivered via the buccal route processed by HME-IM offers a number of potential advantages including avoiding hepatic first pass effect and improving the dissolution profile of this poorly water soluble drug which was suggested as an approach to improve its systemic bioavailability (372, 463-466). HME-IM is a single step, environmentally friendly and cost-effective processing technique capable of producing final dosage forms with uniform content and thickness and much defined shape and geometry compared to the conventional solvent casting and direct compression methods normally used to prepare buccal formulations (208, 372, 467).

In order to prepare solid dispersions to be used as buccal patches for delivering felodipine, two matrices composed of PEG 4000 and PEO K900 polymeric blend with either liquid (Tween 80) or waxy solid (vitamin E TPGS) non-ionic surfactants were used as carrier mixtures (abbreviated as CM1 for Tween 80 and CM2 for TPGS containing formulations) in this study. The excipients used in the fabrication of felodipine buccal patches were selected to provide solubilisation, stabilisation, plasticisation and promote mucoadhesive functionality to the formulations with easy peel-off from the IM mould (62, 151, 326, 327, 355, 360, 361, 373, 468). The theoretical and experimental approaches to assess the miscibility between the different constituents of the formulations were discussed in details in Chapter 3. Based on the miscibility predictions, the hypothesis of the phase behaviour of the formulation can be generated. The hypothesis behind the solubilisation and stabilisation of the carrier matrices is based on creating surfactant-rich solubilisation compartments via phase separation between the components of the carrier mixtures. Within this chapter, the effects of the type of surfactants used in the dispersion patches on the

physicochemical properties and *in vitro* performance of the patches were compared and discussed in order to gain insights into how to choose the suitable surfactants for such formulations.

Research Objectives:

1. To design and manufacture felodipine mucoadhesive buccal patches containing surfactant-rich solubilisation compartments that function to solubilise and stabilise felodipine using HME-IM as a single step processing at low temperature (65℃).
2. To investigate the phase separation behaviour and microstructure of the designed buccal patches using a range of thermal, microscopic and spectroscopic characterisation techniques including DSC, MTDSC, SEM, EDS, ATR-FTIR, PXRD and IR imaging.
3. To evaluate the enhancement in the *in vitro* release profiles compared to crystalline felodipine and investigate the mucoadhesion properties of the fabricated patches.

4.2 Materials and Methods

4.2.1 Materials

The selected API for this project, felodipine (batch no. FP140602), was purchased from Afine Chemicals Ltd (Hangzhou, China). Polysorbate (Tween® 80) MWT is 1310 g/mole was ordered from Sigma-Aldrich (Dorset, UK). Polyethylene glycol (PEG) 4000 average MWT is 4060 g/mole was supplied from Sigma-Aldrich (Poole, UK). Polyethylene Oxide (PEO) WSR 1105 (average MWT= 900,000 g/mole) was kindly donated by Colorcon Ltd (Dartford, UK). Vitamin E TPGS MWT is 1513 g/mole was kindly donated by BASF (Ludwigshafen, Germany).

4.2.2 Felodipine loaded buccal patches prepared by HME-IM

Felodipine loaded in **CM1** (**Tween 80** containing carrier mixture) and **CM2** (**TPGS** containing carrier mixture) buccal patches were prepared using HME-IM with mixing proportions as shown in **Table 4.1**.

Table 4.1: Composition of felodipine loaded CM1 and CM2 buccal patches produced by HME-IM technique

Formulation	Felodipine (w/w)	PEG 4000 (w/w)	PEO K900 (w/w)	Tween 80 (w/w)	TPGS (w/w)
Placebo CM1	-----	40%	30%	30%	-----
10% w/w CM1	10%	36%	27%	27%	-----
20% w/w CM1	20%	32%	24%	24%	-----
30% w/w CM1	30%	28%	21%	21%	-----
Placebo CM2	-----	40%	30%	-----	30%
10% w/w CM2	10%	36%	27%	-----	27%
20% w/w CM2	20%	32%	24%	-----	24%
30% w/w CM2	30%	28%	21%	-----	21%

The buccal patches were prepared using a co-rotating twin screw mini-extruder (HAAKE™ MiniLab II Micro Compounder, Thermo Electron, Karlsruhe, Germany) connected to injection moulding apparatus (HAAKE™ MiniJet System, Thermo Electron Corporation, Karlsruhe, Germany). Felodipine and Tween 80 or TPGS (melted at 65℃) were pre-mixed before being blended with PEG and PEO using mortar and pestle for approximately 2 minutes. The physical mixtures were fed into the extruder and extruded at 65˚C with a screw speed of 100 rpm and 5 minutes of residence time. The reason for selecting 65˚C for HME-IM in this study was to minimise any possible thermally induced degradation (oxidation) of PEG and PEO K900 and still provide complete melting and sufficient mixing of the excipients. After HME, the extruded materials were directly flushed into the reservoir of the IM machine for producing the final buccal patches. The reservoir and mould temperatures were set at 65˚C for the IM process with 300 bars of moulding pressure for 20 seconds. After the injection process, the mould with an inner film-shaped cavity dimension of 25 mm × 25 mm × 0.5 mm, was removed from the apparatus and allowed to cool at room temperature for 1 hour followed by the disassembly of the mould and the collection of the final HME-IM patches. The relative w/w ratios of the components of the carrier mixtures remain constant for all formulations with different drug loading. Images for the prepared patches were presented in **Figure 4.1**.

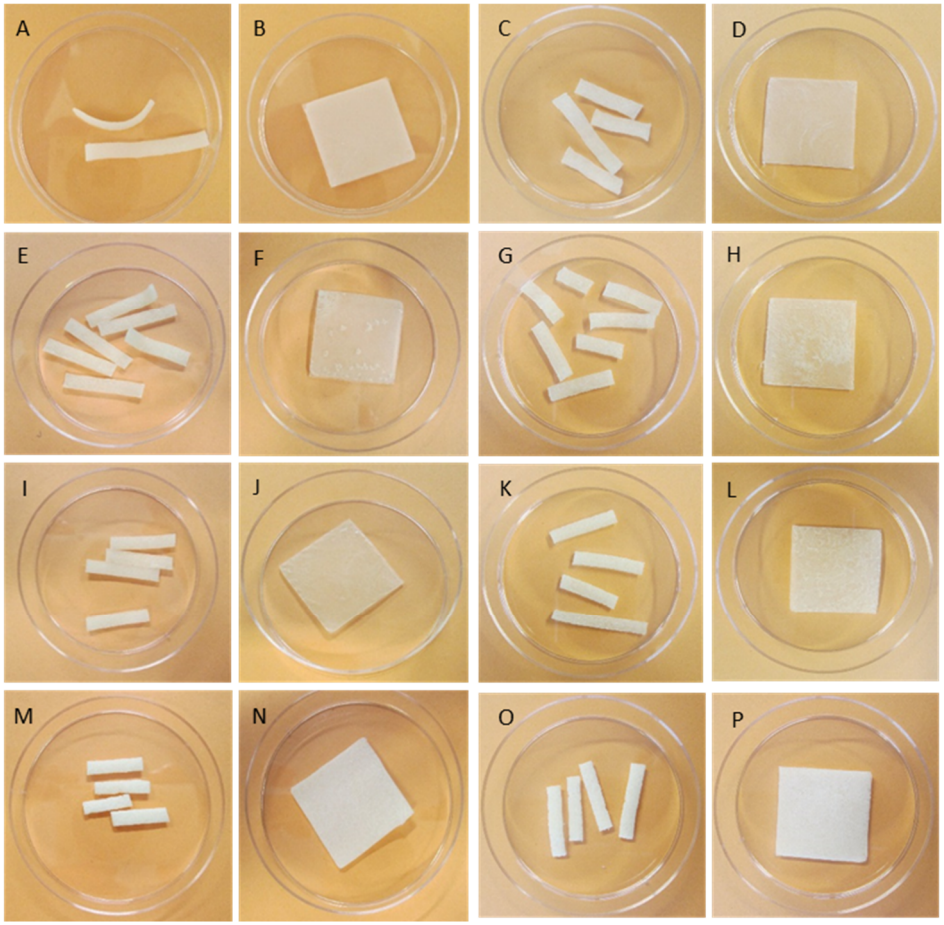

Figure 4.1: Images of the felodipine loaded HME-IM extrudates and buccal patches: A and C are placebo CM1 and CM2 extrudates respectively, B and D are placebo CM1 and CM2 buccal patches respectively, E and G are 10% w/w felodipine CM1 and CM2 extrudates respectively, F and H are 10% felodipine CM1 and CM2 buccal patches respectively, I and K are 20% w/w felodipine CM1 and CM2 extrudates respectively, J and L are 20% felodipine CM1 and CM2 buccal patches respectively, M and O are 30% w/w felodipine CM1 and CM2 extrudates respectively and N and P are 30% felodipine CM1 and CM2 buccal patches respectively

4.2.3 Physicochemical characterisation and evaluation of CM1 and CM2 formulations

4.2.3.1 Differential scanning calorimetry (DSC) and modulated temperature DSC (MTDSC)

All samples investigated in this study using standard DSC and MTDSC were analysed using the same parameters as described in Chapter 3, section 3.2.2.2.2.

4.2.3.2 Scanning electron microscopy (SEM) and energy dispersive spectroscopy (EDS)

A JSM 5900LV Field Emission Scanning Electron Microscope (Jeol Ltd, Japan) equipped with a tungsten hairpin electron gun was used to visualise the surfaces and the cross-sections of placebo and felodipine loaded buccal patches. For the surface investigation, samples were used directly with care to avoid damaging their surfaces, while for cross-section examinations the samples were cut immediately after dipping the samples into liquid nitrogen. The samples were attached to SEM specimen stubs by double-side tape and coated with gold using Polaron SC7640 sputter gold coater (Quorum Technologies, Laughton, UK) before imaging. Elemental analysis imaging using EDS was performed to understand the uniformity of drug distribution on the flat surface of the patches by tracking the chlorine (Cl) atoms present in the structure of felodipine. EDS (INCA Energy manufactured by Oxford Instruments, Abingdon, UK) connected to the SEM was used to map the distribution of drug clusters using Cl in felodipine as the marker. Samples were tested using mapping mode.

4.2.3.3 Powder X-ray diffraction (PXRD)

PXRD parameters as mentioned in Chapter 3, section 3.2.2.2.6 were utilised to analyse all samples investigated in this study using this characterisation technique.

4.2.3.4 Attenuated total reflectance-Fourier transform infrared spectroscopy (ATR-FTIR)

ATR-FTIR scanning for all samples was carried out using the same experimental parameters as mentioned in Chapter 3, section 3.2.2.2.4.

4.2.3.5 Fourier transform infrared microscopy imaging

The heterogeneity of the surface composition was assayed with a Nicolet iN10MX infrared microscope. (Thermo Fisher Scientific, Madison, WI, USA) with 25 μm spatial resolution in reflection mode, using an aluminium mirror as a reference. Fast maps were acquired with 1 scan at 16 cm^{-1} resolution per pixel, and detailed maps with 64 scans at 4 cm^{-1} resolution. Principal component analysis (PCA) of the spectra data in the 1800-900 cm^{-1} region was used to deconvolute the spectra in order to map the distribution of the individual components.

4.2.3.6 *In vitro* mucoadhesion study

The *in vitro* mucoadhesive measurements were carried out on felodipine buccal patches using a TA-XT2 Texture Analyser (Stable Micro Systems, Surrey, UK) fitted with a 5 kg load cell in tension mode (442, 469, 470). Felodipine loaded buccal patches (n=5) having an area of 1.56 cm^2 were attached to the cylindrical perspex probe (1.2 cm diameter and 4.5 cm length) using double-sided adhesive tapes. Aqueous gelatin solution in a concentration of 6.67% w/v was allowed to set as solid gel in a petri-dish (diameter 88 mm), which was used to simulate the adhesion of buccal mucosa. Before each measurement, the gelatinous substrates were equilibrated with 1 mL of 2% w/v porcine mucin solution (pH of 6.8) and fixed on the platform of the texture analyser. For all tests, the probe moved at a pre-test speed of 0.5 mm/s, a test speed of 0.5 mm/s and a post-test speed of 1 mm/s, with an applied force of 0.5 Kg and a return distance of 10 mm and a contact time of 60 s. During the post-test period, the probe was lifted automatically with 0.05 Kg force.

4.2.3.7 *In vitro* drug release studies

The *in vitro* drug release profiles were measured in dissolution testing apparatus (Caleva 8ST, Germany) using paddle over disc method (similar to USP apparatus 5) in which a unidirectional release is achieved to simulate the situation inside the buccal cavity. A paddle rotation speed of

100 rpm and 900 mL of phosphate buffer saline pH 6.8 (simulated salivary fluid) at 37 ± 0.5 ˚C was used for all measurements. Patches containing 10 mg of the drug were fixed to glass disks (5 cm in diameter) using double adhesive tape to allow complete immersion of these patches into the dissolution media. For sink condition dissolution tests, 0.5% (v/v) Tween 80 was added to the dissolution media. For the non-sink condition dissolution tests, no additional surfactant was added into the dissolution media. 5mL of the dissolution samples were withdrawn at pre-determined time intervals. The samples were directly filtered through a membrane filter with 0.45 µm pore size (Minisart NML single use syringe, Sartorius, UK). For the non-sink condition tests, the filtered sample solutions were diluted with equal volume of ethanol. 5 mL of fresh pre-warmed (37 ± 0.5 ˚C) dissolution media was added to the dissolution vessel after each sampling. The samples were measured using a UV–VIS spectrophotometer (Perkin-Elmer Lambda 35, USA) at 363 nm. The measured absorbance values for the dissolution samples at different time intervals were converted to concentration values using the calibration curves described in Appendix 1. All drug release studies were conducted in triplicates.

4.3 Results

4.3.1 Physicochemical characterisation of placebo and felodipine loaded HME-IM buccal patches

4.3.1.1 Thermal characterisation of CM1 and CM2

In this Chapter, DSC and MTDSC were used to investigate the solubilisation limits of CM1 and CM2 matrices for felodipine different loadings, felodipine physical state in the different formulations and the impacts of felodipine loading on the behaviour of CM1 and CM2 phases before and after HME-IM processing. Preformulation studies indicated that CM1 and CM2 are partially miscible with detectable Tween 80 and TPGS surfactant phases even after processing using HME. As PEG and PEO K900 are semi-crystalline polymers, in literature APIs have been claimed to be solubilised in the amorphous regions of these two polymers for the drugs having favourable interactions with them (471-474). Therefore, this study takes the assumption that the formation of amorphous molecular dispersion with felodipine largely occurs in the amorphous regions of CM1 and CM2 blends as suggested in the literature (471-474).

CM1 patches

For CM1 system, as mentioned in Chapter 2, felodipine has an experimentally measured solubility of 100.24 ± 0.001 mg/mL in Tween 80 at room temperature. Based on the prediction of the drug containing binary systems, Tween 80 has more solubilisation capacity for felodipine, followed by PEG and PEO K900 due to the low proportion of amorphous content in these polymers. Therefore, one could predict that an under-saturated drug dispersion containing all these materials should contain three types of domains of Tween 80-felodipine, amorphous PEG-PEO -felodipine and crystalline PEG-PEO K900, with Tween 80-felodipine domains having the higher drug content than PEG-PEO-felodipine domains. However, this prediction is based on the assumption of minimal interaction between Tween 80 and PEG-PEO K900 phases. Within the thermodynamic solubility between all ingredients, domains with complex compositions containing more than two ingredients may also present. Altering the concentration of any one of the ingredients in the quaternary system could lead to dynamic changes in the phase separation behaviour of the system. **Figure 4.2** shows there is no melting of crystalline felodipine was detected in the physical mixtures and HME-IM CM1 patches loaded with 10-30% felodipine. The disappearance of drug melting peak in all loaded formulations is due to thermal dissolution of crystalline felodipine fraction in samples loaded with 20-30% drug loading during DSC ramps in the lower melting excipients forming CM1 blend as confirmed by other characterisation techniques like SEM, EDS, ATR-FTIR and PXRD shown later in this chapter.

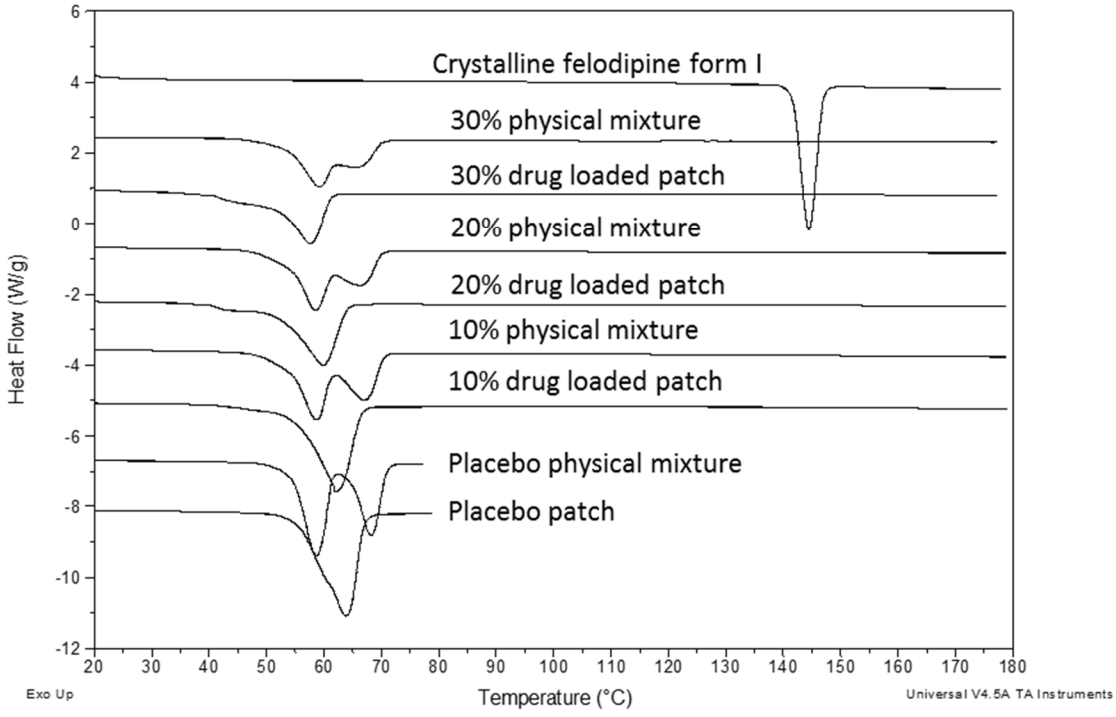

Figure 4.2: Standard DSC (10ºC/min scanning rate) thermograms of CM1 physical mixtures and drug loaded patches with 10-30% loading (n=3)

It is also noted that the onset and peak temperatures of the melting transitions PEG-PEO K900 of all felodipine loaded CM1 matrices are lower than the ones of the placebo patches **(Figure 4.2** and **Table 4.2**). It can be seen that with increasing the drug load from placebo to 20%, the melting peak temperatures depressed by approximately 3.6 ˚C. The depression in the melting of crystalline PEG-PEO K900 is likely to be associated with the dissolution of felodipine in the amorphous fractions of the mixture, which leads to reduced degree of order and possibly smaller size of crystalline regions of the polymers (475). Increasing the loading percentage to 30% causes less depression in melting temperatures compared to lower loading percentages. This may be attributed to the saturation of felodipine in the PEG-PEO K900 phase (as evidenced by the presence of the crystalline drug in these patches). Thus no additional drug is dissolved in PEG-PEO K900 phase to cause further melting depression. The melting enthalpy values can be used as a measure of the crystallinity level of the polymers. There is no significant reduction in the crystallinity of the polymers are observed after drug incorporation up to 20% loading considering the proportion of the two polymers in the different mixtures. However, samples loaded with 30% felodipine show 8.2% reduction in crystallinity compared to placebo sample. The decrease in crystallinity of 30% loaded samples may be attributed to the presence of the crystalline fraction

of felodipine leading to defective crystallisation of PEG-PEO K900 blend reflected as a reduction in crystallinity.

Table 4.2: Melting Temperature (T_m) depression of PEG-PEO K900 and surfactant phases caused by drug loading in different CM1 HME-IM patches using DSC at 10°C/ min (n=3; average ± SD)

Formulation	PEG-PEO K900 T_m Peak (˚C)	PEG-PEO K900 ΔH_f (J/g)	Tween 80 T_m Peak (˚C)	Tween 80 ΔH_f (J/g)
Placebo CM1	63.6 ± 0.3	125.3 ± 0.4	-10.3 ± 0.2	6.2 ± 0.1
10% CM1	61.8 ± 0.1	112.0 ± 3.9	---	---
20% CM1	60.0 ± 0.1	98.9 ± 1.8	---	---
30% CM1	59.7 ± 0.1	80.5 ± 0.9	---	---

Compared to placebo CM1 patch, the melting of Tween 80 almost disappeared in the non-reversing signals of all felodipine-loaded CM1 patches as seen in **Figure 4.3**. The fact that during the pre-mixing and HME-IM process, crystalline felodipine was pre-dispersed and some proportion was dissolved in the Tween 80 is possibly responsible for the absence of the melting of Tween 80 in these systems. The dissolved felodipine in the Tween 80 could significantly disrupt and even prevent the crystallisation of Tween 80. In addition, the incorporation of the hydrophobic drug in the mixture could improve the miscibility of Tween 80 and PEG-PEO K900, as the drug could better mix with the hydrophobic tail group of Tween 80 and allow better interaction of the hydrophilic head group of Tween 80 with PEG-PEO K900. This again can prevent the crystallisation of Tween 80; thus no melting of Tween 80 was observed. This may suggest the creation of single Tween 80- rich amorphous phase which can act as a solubilisation domains for felodipine.

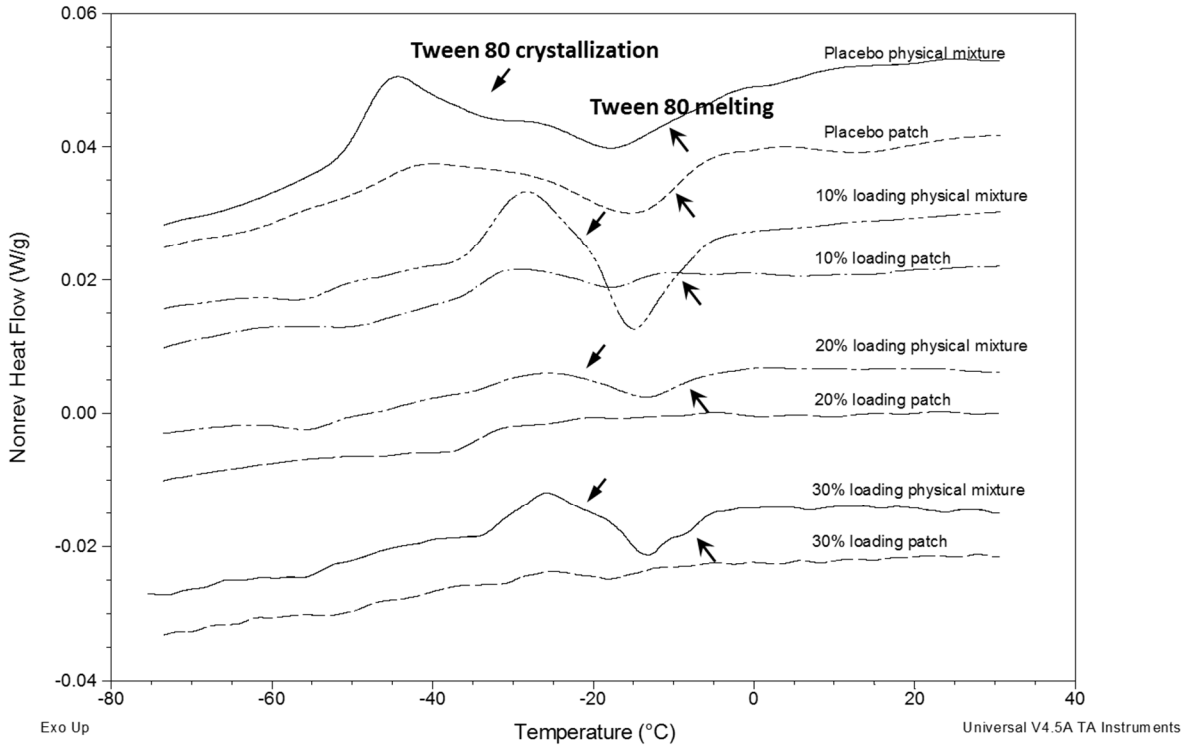

Figure 4.3: Non-reversing heat flow signal of the MTDSC results of CM1 physical mixes and buccal patches of placebo and patches loaded with 10% - 30% w/w felodipine (n=3)

The T_g values of PEO K900, Tween 80 and TPGS were measured as -53.9 ± 1.9, -64.2 ± 0.6 and -20.0 ± 0.9 ºC, respectively. The T_g values for PEG was reported in the literature as -61 (449, 453). Drug incorporation also led to the changes in the T_g of CM1 patches. As seen in **Figure 4.4** and **Table 4.3**, although PEG and PEO K900 are semi-crystalline polymers, a single T_g of the amorphous portions of their mixture with Tween 80 can be clearly detected indicating single amorphous phase for three compounds within the detection limits of the DSC. For CM1 patches with 10 and 20% drug loading, the amorphous content of the matrices increased by approximately 20% and 52% (w/w), respectively compared to physical mixtures using the ΔC_p values as shown in **Table 4.3**. This may indicate the increase in miscibility between the PEG-PEO K900 and Tween 80 caused by drug solubilisation in the amorphous fraction. There is no significant increase in amorphous fraction after HME-IM in the patches with 30% felodipine loading compared to the physical mixture.

By comparing the ΔC_p values of the physical mixtures (without pre-heating) at the glass transition, it is noted that adding a crystalline drug to the physical mixture of PEG-PEO-Tween 80 leads to

increase in ΔC_p values. This increase in ΔC_p could be explained by the dissolution of felodipine in PEG-PEO-Tween 80 amorphous phase during mixing.

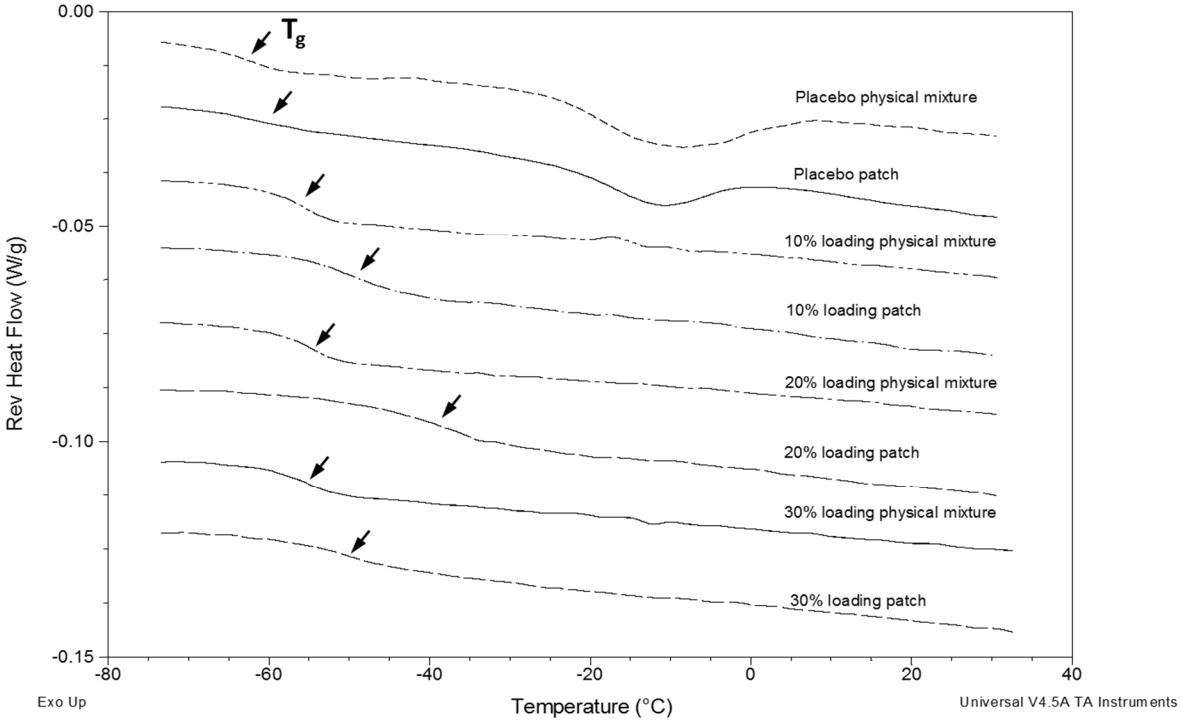

Figure 4.4: MTDSC Reversing heat flow signals of CM1 physical mixes and buccal patches of placebo and patches loaded with 10% - 30% w/w felodipine (n=3)

It should be borne in mind that the formation of molecular dispersions of felodipine in the matrix should shift the T_g to a higher temperature, as the T_g of amorphous felodipine is 46.5 ± 0.2 ºC (measured by MTDSC as shown in Chapter 3). The increases in the T_g temperatures (by up to approximately 6.7 ± 0.3 ºC) of the physical mixtures with felodipine in comparison to the placebo physical mixture further confirm the hypothesis of felodipine being dissolved into the Tween 80 rich phase. Further increases of T_g values are clearly observed for all CM1 HME-IM drug-loaded patches indicating higher level of molecular mixing of felodipine into the Tween 80-PEG-PEO K900 amorphous phase. However, with 30% drug loading the T_g of the patches shifted to similar temperature as 10% loaded systems, indicating similar amount drug to the 10% systems was molecularly dispersed in the matrices. This effect of drug loading on the ternary blend of Tween 80-PEG-PEO K 900 can be clearly seen in **Table 4.3** and **Figure 4.5** in the changes in both the T_g temperature and ΔC_p values at T_g with drug loading. **Table 4.3** shows the detailed measurements of the values of ΔC_p and T_g of the glass transition regions of all physical mixtures and patches. It can be clearly seen that placebo mixtures and patches have the lowest T_g and the incorporation of

felodipine increases the T_g of the mixtures and patches. With increasing the drug loading from 0-20%, the T_g and ΔC_P values increase indicating the increased amount of amorphous material in CM1 patches. However, further increasing the drug loading to 30% led to the presence of the crystalline drug in the formulation and this is also reflected by the reduced T_g and ΔC_P values in comparison to the values of the samples with 20% drug loading. These results indicate that 20% drug loaded patches are likely to be supersaturated with dissolved drug.

Table 4.3: T_g and ΔC_p values of placebo and felodipine loaded CM1 physical mixtures and HME-IM patches (10% - 30% w/w) measured using MTDSC (n=3; average ± SD)

Drug loading	T_g (˚C) mid-point	ΔC_P (J/g.°C)
Placebo CM1 PM	-62.1 ± 0.5	0.18 ± 0.03
Placebo CM1 patch	-60.8 ± 0.6	0.13 ± 0.01
10% CM1 PM	-56.4 ± 0.1	0.25 ± 0.03
10% CM1 patch	-51.0 ± 0.2	0.30 ± 0.02
20% CM1 PM	-55.4 ± 0.3	0.23 ± 0.01
20% CM1 patch	-38.7 ± 0.2	0.35 ± 0.03
30% CM1 PM	-55.9 ± 0.0	0.25 ± 0.00
30% CM1 patch	-51.3 ± 0.5	0.24 ± 0.02

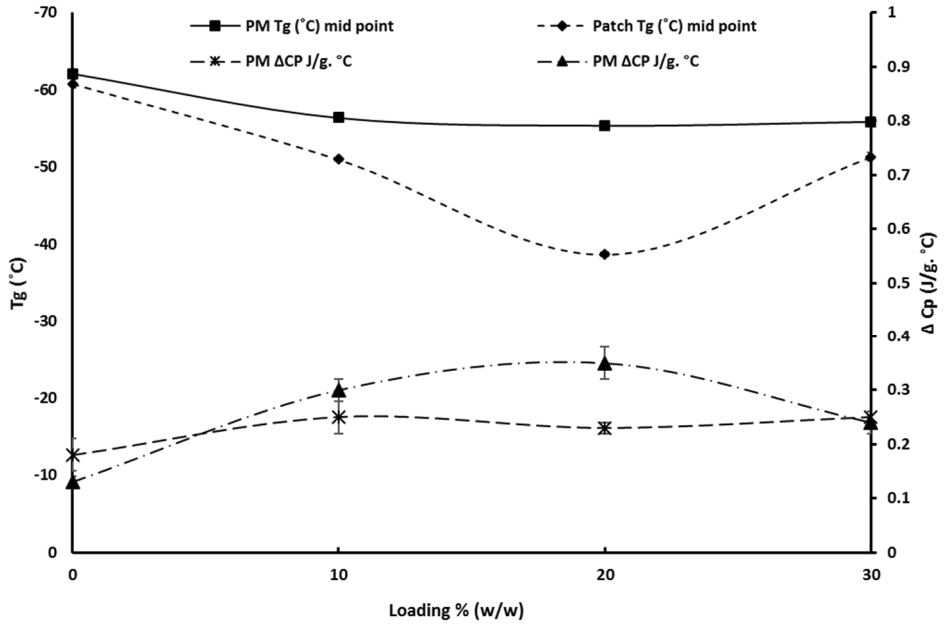

Figure 4.5: T_g and ΔC_p values of the CM1 samples plotted against felodipine loading percentage (10% - 30% w/w) using MTDSC (n=3; average ± SD)

CM2 patches

The predicted miscibility of felodipine with different excipients used in CM2 revealed that TPGS has better solubilisation properties for felodipine compared PEG-PEO K900 polymeric blend. In addition, the miscibility of felodipine in TPGS is also predicted to be higher than that of Tween 80. On the other hand, TPGS has shown to have lower miscibility with PEG and PEO K900. All these preformulation predictions may provide an indication that the phase behaviour of CM2 will be different compared to CM1 formulations. After felodipine had been incorporated in the CM2 patches, no crystalline felodipine melting was detected by DSC in any patches as seen in **Figure 4.6**. As earlier, the ATR-FTIR and PXRD results indicated that crystalline felodipine was present in at least in the 30% drug loaded patches, this result suggests that thermal dissolution of crystalline felodipine in the molten excipients occurred during DSC runs. These results are also confirmed by the absence of felodipine melting peak in felodipine 10-30% w/w loaded CM2 physical mixtures.

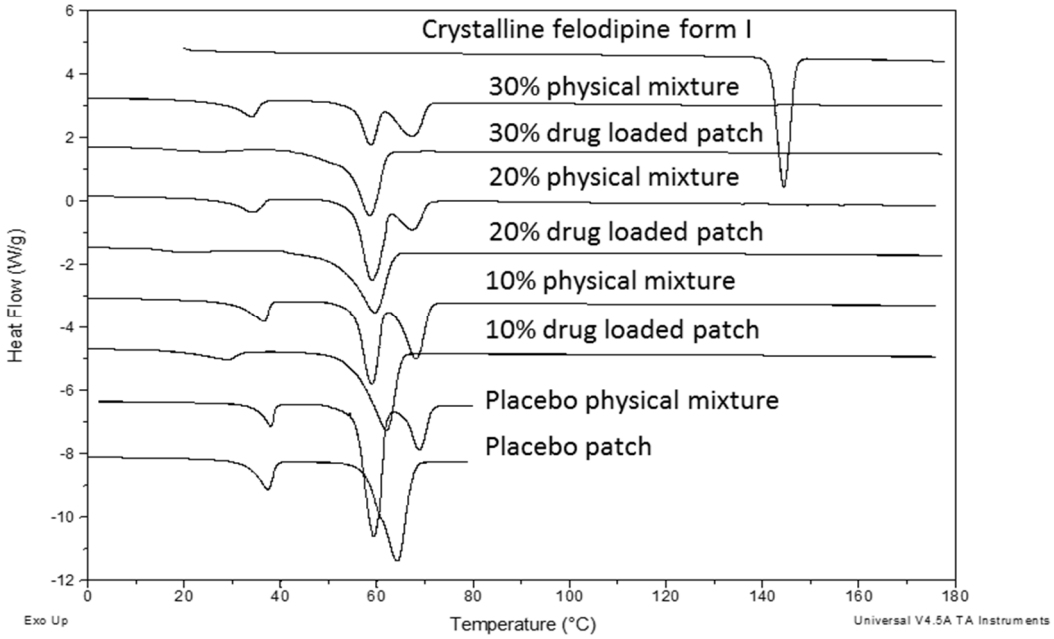

Figure 4.6: Standard DSC (10ºC/min scanning rate) thermogram of CM2 physical mixtures and drug loaded patches with 10-30% loading (n=3)

For CM2 felodipine loaded HME-IM samples, **Figure 4.6** and **Table 4.4** indicate that the TPGS crystalline phase is detectable in all samples with different drug loadings. The melting transitions of TPGS and PEG-PEO K900 in the drug loaded patches shifted to lower temperatures than those observed for the placebo CM2 patches. These melting point depressions of the excipients are likely caused by the dissolved felodipine in the TPGS and PEG-PEO K900 phases during the HME-IM process which may lead to higher level of crystal defects compared to the placebo CM2 formulation (476). In addition, no significant reduction in the crystallinity of the PEG-PEO K900 polymers is observed after drug incorporation up to 20% loading. However, samples loaded with 30% felodipine show 4.5% reduction in crystallinity compared to placebo CM2 sample. This slight reduction in crystallinity may be attributed to the presence of the crystalline fraction of felodipine leading to defective crystallisation of PEG-PEO K900 blend. The melting transition temperatures show drug-loading dependence, as seen in **Figure 4.6** and **Table 4.4**. It was noted that the lowest melting points of TPGS and PEG-PEO K900 were obtained in the patches with 20% drug loading. This may indicate that the 20% patches contain most solubilised drug in the matrices which approaches the saturation or even potentially supersaturation of the drug in the polymer matrices. Further increasing the drug loading to 30% leads to the presence of undissolved/recrystallised crystalline drug accompanied by a shift in the melting peaks of TPGS to higher temperatures than were observed in the 10 and 20% loaded patches. However, the

melting temperatures of TPGS are still lower than those of the placebo suggesting the presence of solubilised drug in the matrices.

Table 4.4: Melting temperature (T_m) depression of PEG-PEO K900 and surfactant phases caused by drug loading in different CM2 HME-IM patches DSC 10°C/ min (n=3, average ± SD)

Formulation	PEG-PEO K900 T_m Peak (˚C)	PEG-PEO K900 ΔH_f (J/g)	TPGS T_m Peak (˚C)	TPGS ΔH_f (J/g)
Placebo CM2	64.1 ± 0.3	124.7 ± 2.1	37.5 ± 0.1	22.2 ± 1.0
10% CM2	62.1 ± 0.3	105.5 ± 5.6	28.9 ± 0.3	15.2 ± 0.9
20% CM2	59.6 ± 0.1	96.8 ± 3.0	20.4 ± 0.4	6.2 ± 0.4
30% CM2	58.4 ± 0.3	83.9 ± 0.3	24.9 ± 1.5	5.6 ± 1.0

For CM2 formulations, due to the high semi-crystalline nature of PEG, PEO K900 and TPGS, no T_g was detected for the placebo samples using standard and MTDSC modes of the DSC for both the physical mixture and the HME-IM samples. In addition, no T_g also was detected for the physical mixtures of all felodipine loaded mixtures as seen in **Figure 4.7** indicating limited miscibility between TPGS and PEG-PEO K900 phases and limited miscibility of felodipine in the phase separated domains. However, loading felodipine in the HME-IM CM2 matrices causes the appearance of T_g events close to the detected T_g of TPGS at -20.0 ± 0.9 ºC. As seen in **Figure 4.7**, the T_g for the 10, 20 and 30% w/w were detected at -23.7 ± 0.4, -22.2 ± 0.4 and -21.4 ± 0.8 ºC respectively. The detection of the T_g values close to that of pure TPGS together with depression in the melting of this surfactant strongly suggests felodipine solubilisation in TPGS phase. Slight shifting the T_g values to higher temperature reveals the antiplasticising effect of the drug. The measured ΔC_p values for the 10,20 and 30% w/w were 0.24 ± 0.04, 0.33 ± 0.02 and 0.29 ± 0.02 J/ g.°C respectively indicating more amorphous fraction present following this order: 20% > 30% > 10% drug loading. The increase in the felodipine -TPGS amorphous fraction is attributed to the reduction in the crystallinity of TPGS and the solubilisation of felodipine in the created solubilisation amorphous compartment of TPGS.

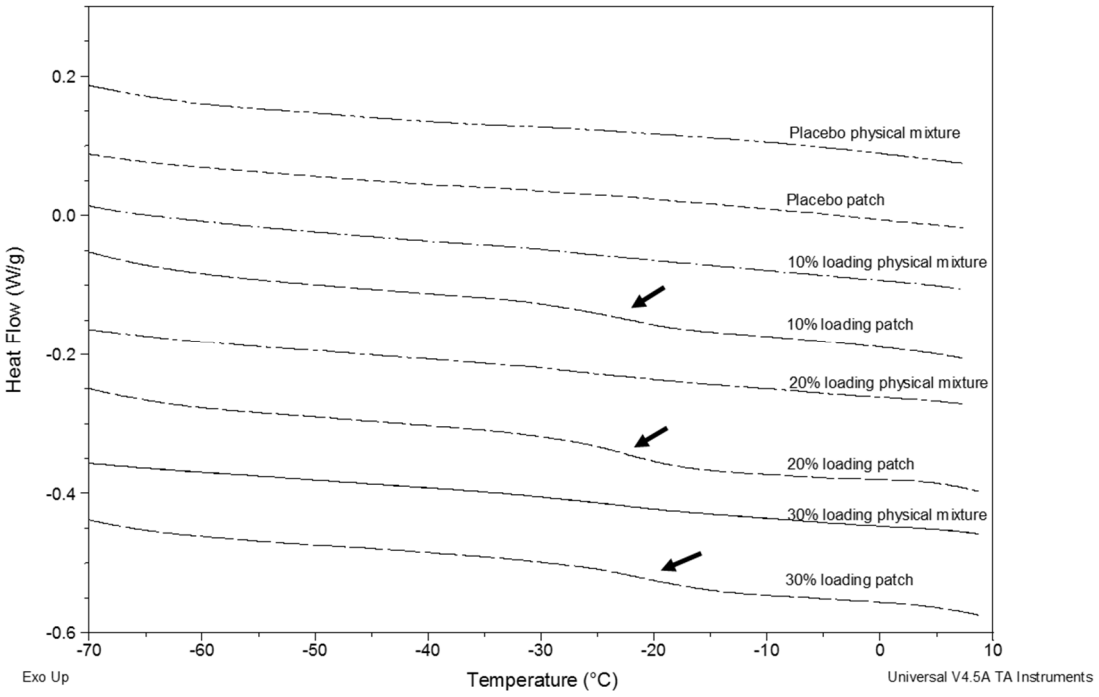

Figure 4.7: Standard DSC results of CM2 physical mixes and buccal patches of placebo and patches loaded with 10% - 30% w/w felodipine (n=3)

A brief comparison between CM1 and CM2 mixtures can be concluded based on the observed thermal events of the two series of mixtures. Felodipine was solubilised in the PEG-PEO K900-Tween 80 amorphous phase of CM1 HME-IM patches while in case of CM2 formulations, the drug was mostly dispersed in the TPGS phase. The melting peak of TPGS was detected in all placebo and felodipine loaded CM2 patches, while in CM1 formulations, the Tween 80 phase was only detected in placebo CM1 sample. This indicates that loading felodipine enhances the miscibility of Tween 80 with PEG-PEO K900 blend in CM1 loaded formulations. For CM2, drug loading did not show any observable improvement in the miscibility of CM2 carrier components. In addition, drug loading was found to antiplasticise the amorphous phase of CM1 patches to greater extent compared to the antiplasticisation effect of the drug on the TPGS phase. This is indicated by the larger increase in the T_g of the solubilising phase in CM1 compared to CM2 mixtures. It should be mentioned that the ΔH_f values of the PEG-PEO K900 in CM1 and CM2 formulations with the same loading percentages were comparable.

4.3.1.2 Comparisons of morphological properties of CM1 and CM2 patches

As seen in **Figure 4.8**, SEM images of placebo and felodipine loaded CM1 patches show similar elongated micron-pore structures at the surfaces and cross-sections with the exception of the clear presence of particles with defined edges and 10-20 µm in diameter in the patches with 30% drug loading. In addition, SEM images captured for CM2 placebo and loaded patches (**Figure 4.9**) revealed that the surfaces of the solid dispersion patches, except for those with 20% drug loading, show the presence of small cracks and air voids and increased roughness with increasing the drug loading. The cross-sectional images of the patches show increased roughness in the interior in comparison to the surfaces and a clear porous character for all samples. Large air pockets between 100-300 µm in diameter and particles (often with defined edges) with diameters of 10-20 µm, can be observed only in the patches with 30% drug loading.

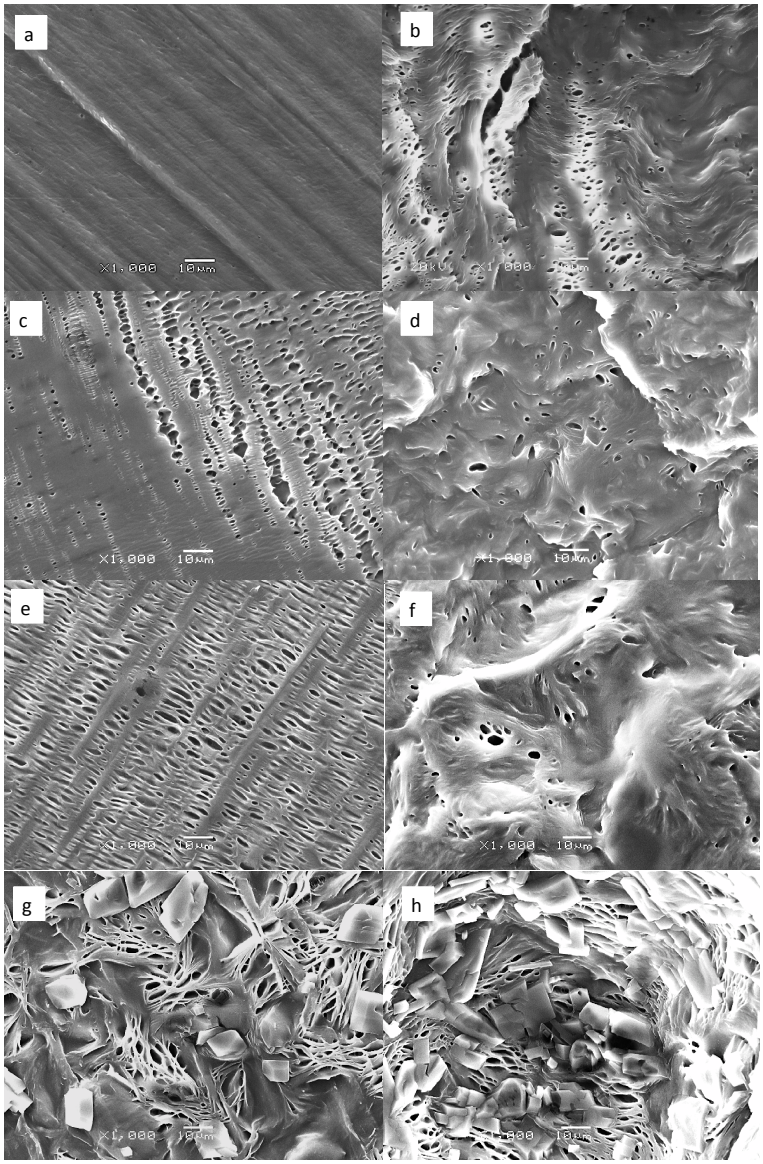

Figure 4.8: SEM images surfaces (a, c, e, g) of CM1 placebo and patches with 10%, 20% and 30% felodipine loading and their corresponding cross-sections (b, d, f, h)

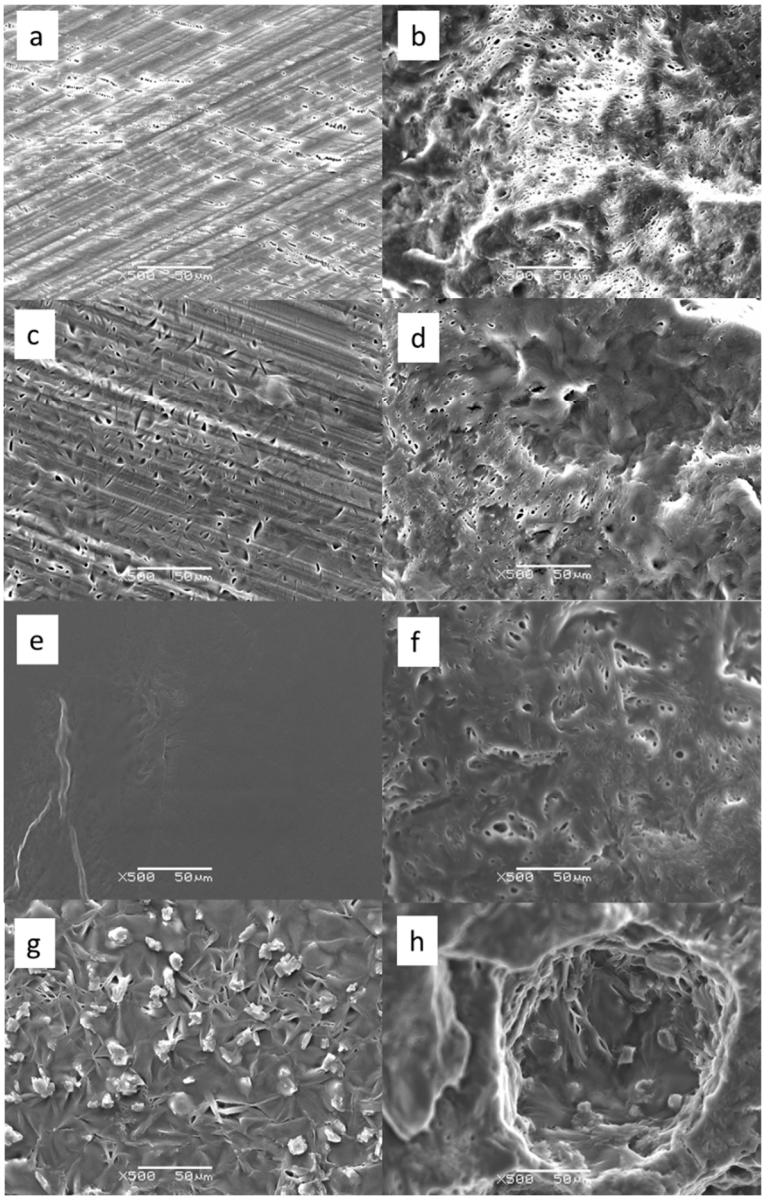

Figure 4.9: SEM images surfaces (a, c, e, g) of CM2 placebo and patches with 10%, 20% and 30% felodipine loading and their corresponding cross-sections (b, d, f, h)

Using the chlorine (Cl) in felodipine molecules as a chemical marker, the elemental analysis performed by EDS for the SEM images of both CM1 and CM2 loaded samples confirmed these particles being highly concentrated felodipine clusters (**Figure 4.10**). This leads to the conclusion that these clusters being crystal felodipine due to the absence of chlorine in the structures of the other excipients used in fabricating CM1 and CM2 HME-IM patches. This is also confirmed by the PXRD and ATR-FTIR data shown later.

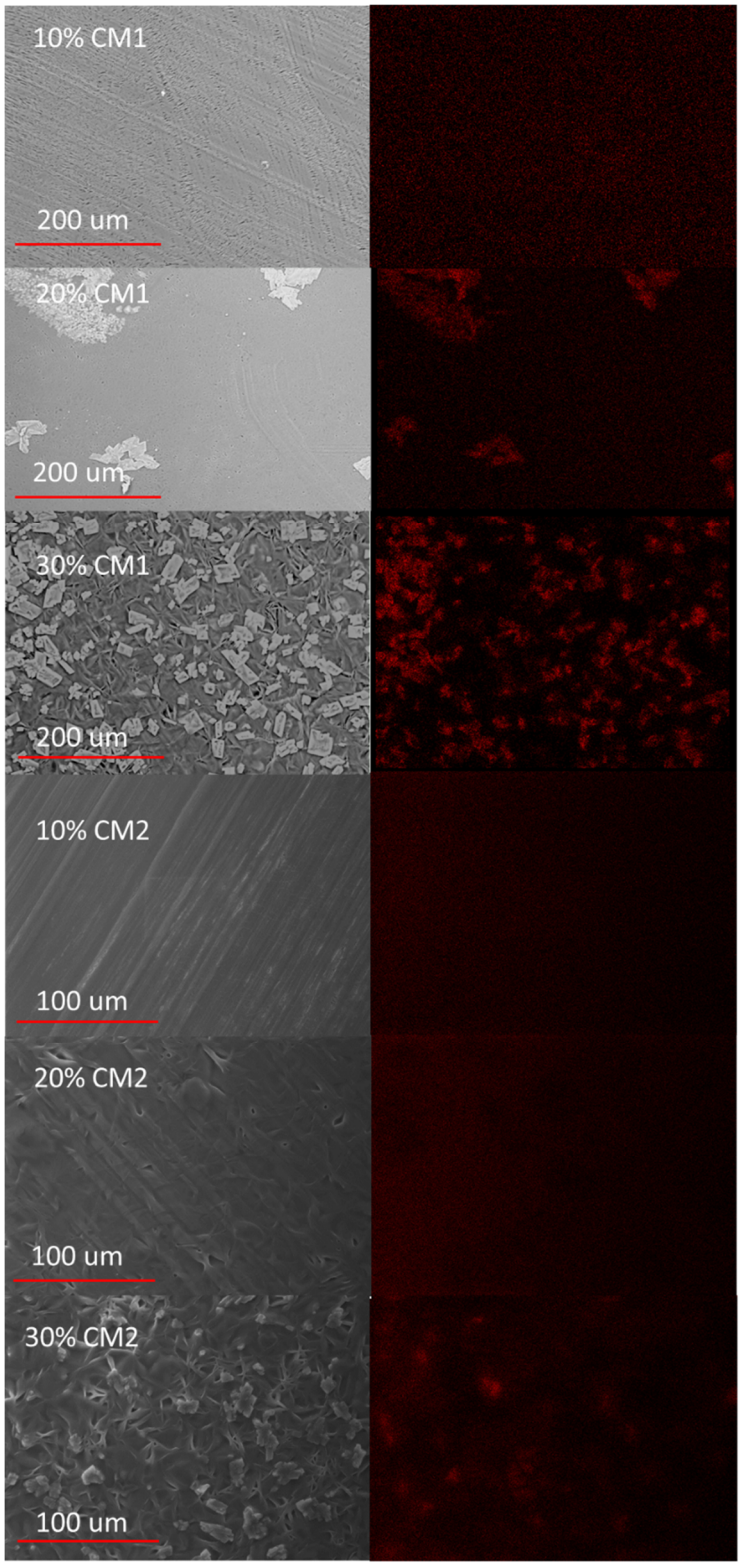

Figure 4.10: Scanning electron microscopic (left) and elemental analysis images (right) of the surfaces of CM1 and CM2 patches with different drug loadings

4.3.1.3 PXRD and IR characterisation of CM1 and CM2 patches

As seen in **Figure 4.11 A and B**, clear crystalline felodipine form I diffraction peaks at 9.3˚, 10.2˚, 16.3˚and 16.6˚ can be identified in the diffraction pattern of the patches with 30% drug loading for both formulations (312). For all drug-loaded CM1 and CM2 patches, no significant changes of matrix excipient related peaks were observed. Knowing the presence of crystalline felodipine in 30% loaded patches, the absence of crystalline felodipine melting in the DSC results shown in **Figures 4.2 and 4.6** indicates the felodipine dissolved in the molten matrices at temperatures above the polymers melting points during the DSC runs. Therefore, only the melting transitions of PEG-PEO K900 matrices were observed.

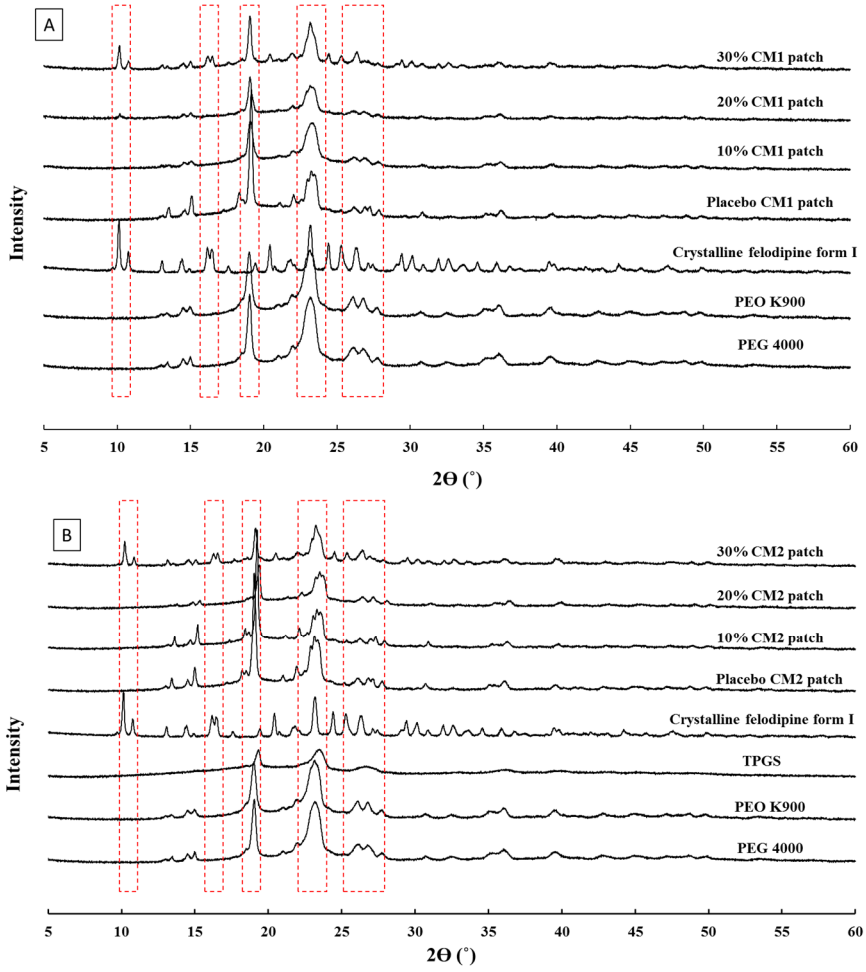

Figure 4.11: PXRD patterns of A) raw materials, CM1 placebo and 10-30% (w/w) felodipine loaded felodipine patches and B) raw materials, CM2 placebo and 10-30% (w/w) felodipine loaded felodipine patches

ATR-FTIR spectra of CM1 and CM2 HME-IM patches are shown in **Figures 4.12 a and b**. Patches with 30% drug loading revealed an NH peak at 3367 cm^{-1} which is assigned to crystalline felodipine form I. This is also confirmed by the results obtained from the PXRD. The detection of the NH stretching of felodipine in the spectrum of 30% loaded samples confirming the presence of crystalline felodipine in these patches.

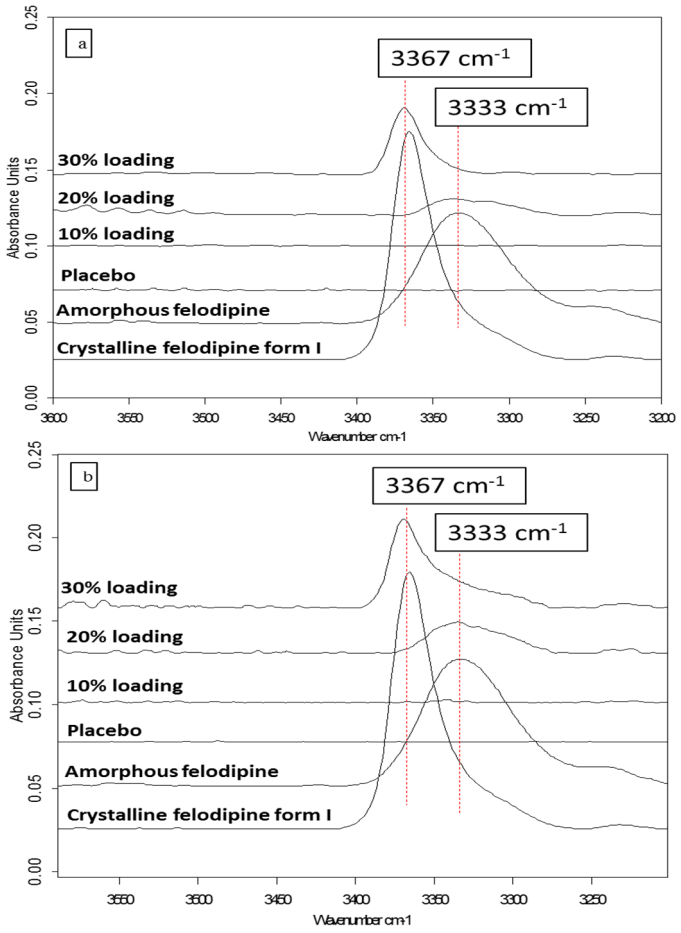

Figure 4.12: Partial ATR-FTIR spectra of felodipine NH stretching region of CM1 (a) and CM2 (b) HME-IM patches with different drug loadings in comparison to crystalline and amorphous felodipine. The dotted lines highlight the signature crystallisation and amorphous felodipine peaks (n=3)

It should also be mentioned that the shape of the NH peak of 30% loaded CM2 patches is asymmetric, with absorbance in a region corresponding to amorphous felodipine, indicating the coexistence of amorphous and crystalline materials (108, 316, 317). However, CM1 loaded with 30% w/w felodipine samples show a more symmetric NH stretching peak indicating less amorphous and more crystalline felodipine existing in the patch compared to 30% CM2

formulation. This is also confirming the higher solubilisation capacity of CM2 compared to CM1 mixtures. For the patches with 10% and 20% drug loading, no crystalline felodipine NH peak was observed (**Figure 4.12**).

The analysis of the spectra of carbonyl region of felodipine between 1800 and 1400 cm^{-1} for CM1 and CM2 patches is shown in **Figures 4.13a and b** respectively. The C=O peaks of crystalline felodipine detected at 1688 cm^{-1} (dotted line) are upshifted to 1697cm^{-1} for the patches with 10 and 20% drug loading of both CM1 and CM2 formulations. This perfectly aligns with the C=O peak of the amorphous felodipine indicating the amorphous nature of the drug in patches with 20% drug loaded patches due to the stronger amorphous felodipine-felodipine intermolecular hydrogen bonding (448). In addition, this also may indicate the formation of hydrogen bonds between the NH group of felodipine and the -C-O-C backbone of ethylene oxide moieties of the other formulation components especially for samples with a drug loading of 10% w/w (68). A shift to lower wavenumber towards the C=O of crystalline felodipine for CM1 and CM2 patches with 30% drug loading at 1693 cm^{-1} and 1695 cm^{-1} respectively may be a result of the presence of both crystalline and amorphous felodipine (108, 316, 317).

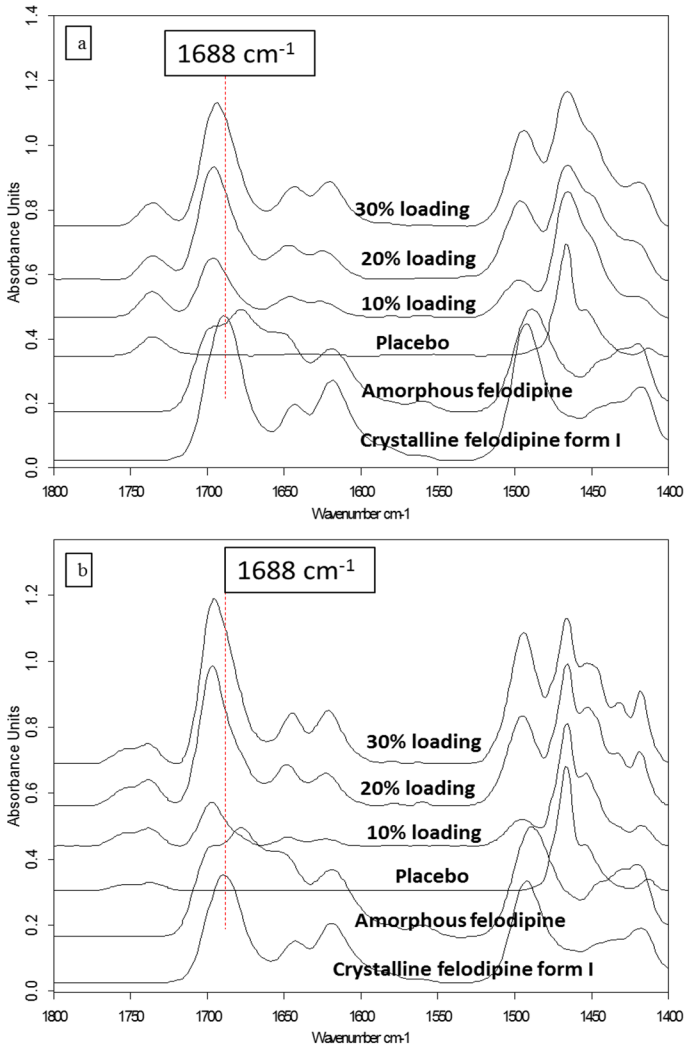

Figure 4.13: Partial ATR-FTIR spectra of felodipine C=O carbonyl region of CM1 (a) and CM2 (b) HME-IM patches with different drug loadings in comparison to crystalline and amorphous felodipine (n=3)

The interpretation of the CN region is shown in **Figures 4.14a and b** for CM1 and CM2 patches respectively. The CN peak of pure amorphous felodipine shifted to 1206 cm^{-1} (dotted line) in comparison to the 1202 cm^{-1} CN peak of crystalline felodipine indicating stronger intermolecular H-bonding in the amorphous state (448). The CN peak further shifted further to 1210 cm^{-1} for the patches with 10% and 20% drug loading of both formulations, indicating the presence of additional hydrogen bonding between the drug and the ethylene oxide chains which may contribute to the formation of a molecular dispersion of felodipine in amorphous fractions of CM1 and CM2 carriers. However, the CN peak of the CM1 and CM2 patches with 30% loading was observed at 1206 cm^{-1}. This is consistent with the presence of crystalline together with amorphous

and/or molecularly dispersed felodipine interacting with the other excipients (448). It should be mentioned that there is no change in the position of the C=O stretching groups of both Tween 80 and TPGS indicating the absence of felodipine hydrogen bonding with these groups of the surfactants.

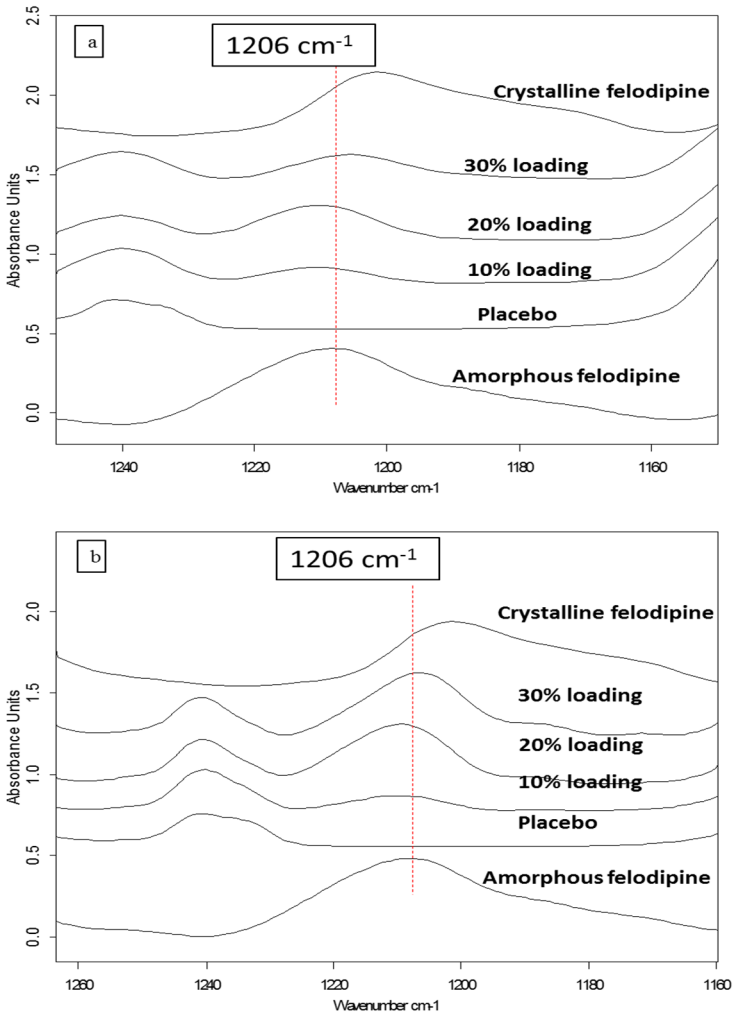

Figure 4.14: Partial ATR-FTIR spectra of felodipine CN stretching region of CM1 and CM2 HME-IM patches with different drug loadings in comparison to crystalline and amorphous felodipine (n=3)

4.3.1.4 Investigation of heterogeneity HME-IM patches using IR imaging

IR imaging was utilised in the first instance to rapidly screen compositional heterogeneity of CM1 and CM2 HME-IM patches and confirm the phase separation being drug loading dependent. Increased compositional heterogeneity was observed with increasing the drug loading. As it was preliminary fast screening, the IR imaging was constructed based on both compositional and light

reflectivity difference at the surface of the samples. The combinations of these differences were analysed using principle component analysis (PCA) to construct the IR map seen in **Figure 4.15**. It can be seen that the IR spectra of the areas with red, green and blue are distinctively different, indicating areas with different colours are also with different chemical composition (**Figure 4.15a**). The IR images of the surfaces of the placebo and 10% CM1 loaded patches are dominated by red colour with a spectrum containing a little contribution of drug spectrum loading indicating a lower level of heterogeneity (**Figure 4.15b and c**). At 10% drug loading, most of the surface was dominated by PEG-PEO K900. Increased heterogeneity of the colour differences is observed in the patches with higher drug loadings. With 20% CM1 HME-IM (**Figure 4.15d**) the surface showed a few isolated domains which appeared to be drug-rich and the rest of the surface had similar IR features as the patches with 10% loading. However, the spectra of the surfaces of the patches with 30% drug loading (**Figure 4.15e**), were interpreted as a patchwork of small PEG-PEO K900-rich and Tween 80-rich areas, the latter showing small bands which may indicate the presence of dissolved felodipine. It was noticed that the sizes of the separated domains are larger for 20% than for 30% patches. In addition, many domains with spectra in the 30% loaded patches indicating high crystalline drug loading can be seen.

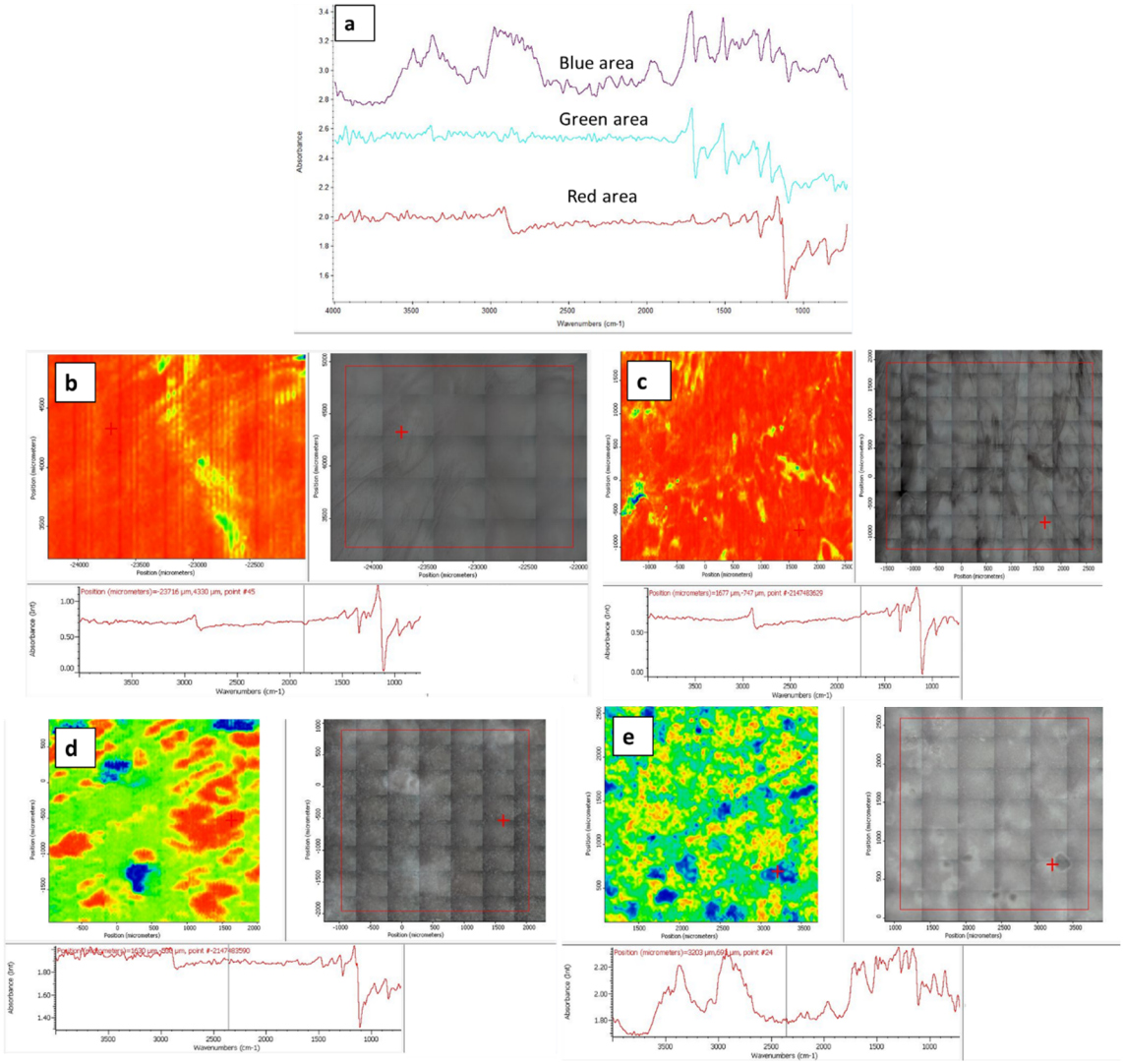

Figure 4.15: (a) IR reflectance spectra are coding for the composition of different colours in the IR images. Red spectrum indicates areas containing drug as molecularly dispersed or amorphous form; green spectrum indicating areas indicating areas rich with the drug (supersaturated matrix which may contain very tiny crystals); purple spectrum indicating areas with crystalline drug); correlation IR map (left), optical image (right) and the IR spectrum of the point of interest (bottom) of the surfaces of CM1 HME-IM patches with (b) placebo, (c) 10%, (d) 20% and (e) 30% felodipine loading

IR imaging (**Figure 4.16**) shows that CM2 patches with up to 20% w/w loadings have a very homogenous composition (no heterogeneity within the limits of the scrutiny of the instrument). For example, comparing the red with the green spots in the 10 and 20% w/w loadings shows identical spectra. Differences in correlation coefficients are probably only due to physical effects such as reflection and/or surface roughness indicating no microscale phase separation on the surface of these samples. However, the 30% loading patches show the presence of the blue spots

with different spectrum indicating the phase separation of the crystalline drug on the surface of the sample.

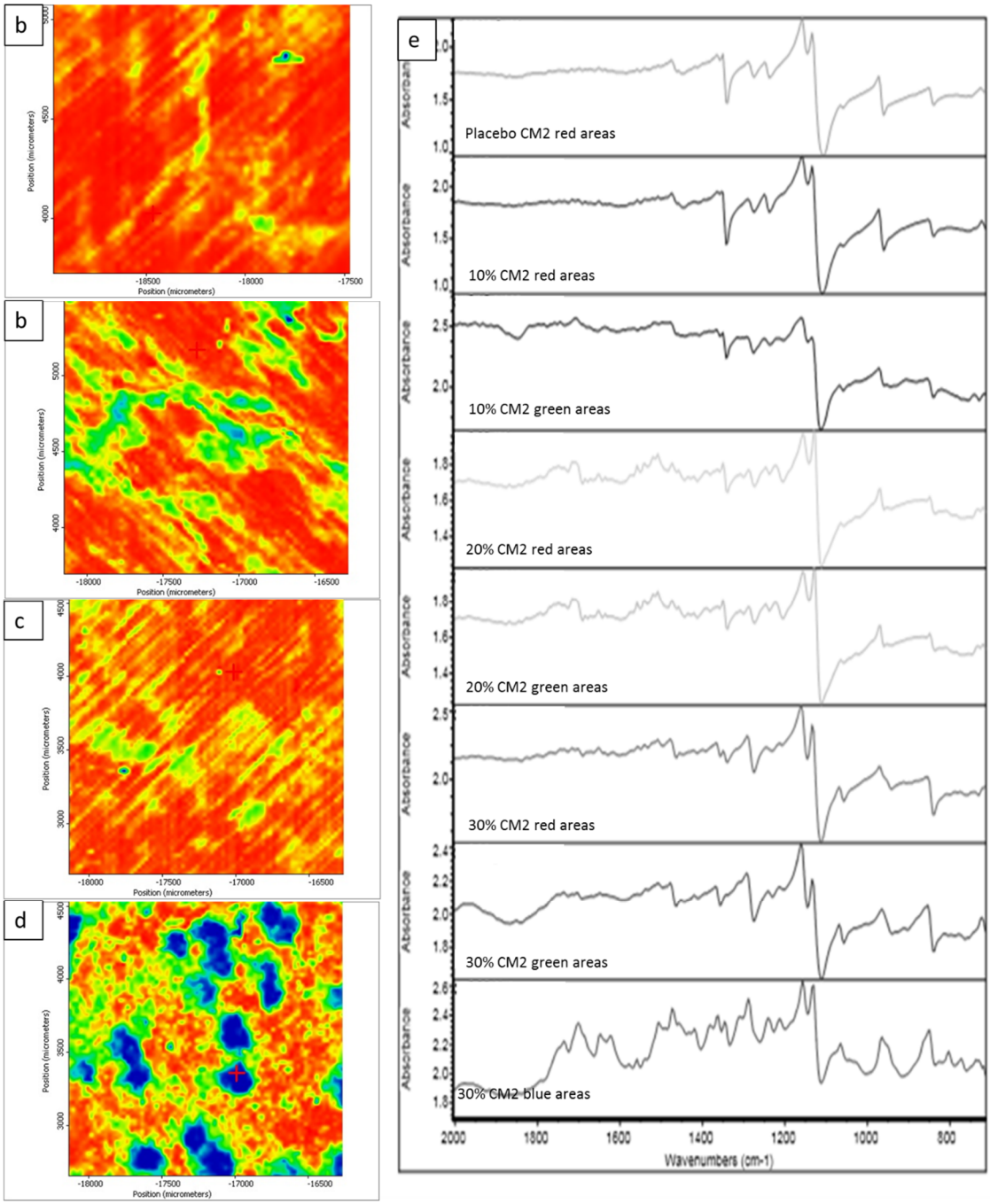

Figure 4.16: Correlation IR maps for placebo (a), 10% (b), 20% (c) and 30% (d) CM2 HME-IM patches; (e) is the IR reflectance spectra for the different areas of the maps

4.3.2 Influence of drug loading and phase separation on mucoadhesion

The mucoadhesion properties of CM1 and CM2 HME-IM patches were estimated using standard adhesion testing (477). As the focus of this study is to investigate the effect of phase separation on the *in vitro* performance of the patches, mucoadhesion results presented here are purely for comparison purpose between different formulations. **Figure 4.17** shows representative mucoadhesion analysis using TA-XT2 Texture Analyser for placebo CM1 patch. As seen in **Table 4.5**, no significant difference is seen in the mucoadhesivness of the placebo and 10% drug loaded CM1 patches. This indicates that 10% drug loading as molecular dispersion did not significantly affect the surface hydrophobicity and overall mucoadhesive properties of the patches. However, with increasing the drug loading the mucoadhesivness of the patches reduces. It should be borne in mind that the content of the main mucoadhesive material, PEO K900, reduced by 22% (w/w) from 10% loaded patches to 30% loaded patches. However, the mucoadhesion force reduced by 40% and 39% for CM1 and CM2 respectively indicating the effect is not only related to the lowered mucoadhesive material content. The increased amount of hydrophobic drug could also increase the overall hydrophobicity of the surface of the patches and reduce the wetting and mucoadhesion of the patches. The presence of phase-separated Tween 80 and PEG-PEO K900 areas may also lead to the patch surface with discontinuous adhesive areas which also contributed to the reduced adhesion of the patches.

Compared to CM1, CM2 placebo and 10% w/w loaded patches showed an insignificant reduction in their mucoadhesive properties revealing that changing surfactant type has no effect on these properties below the saturation limits of the two systems. However, the mucoadhesion of 20% w/w loaded patches were found to be significantly lower than that of the corresponding CM1 matrices. This may be due to the lower miscibility of TPGS phase compared to Tween 80 phase with the PEG-PEO K900 polymeric blend and the depressed melting of TPGS by the dissolved drug. The molten TPGS phase at room temperature on the surface of the patches may decrease the adhesion properties of the system. Additionally, phase separation of 30% w/w felodipine loaded CM2 patches together with the presence of the crystalline fraction of felodipine may be the causes for the reduction in the mucoadhesive properties of the formulation.

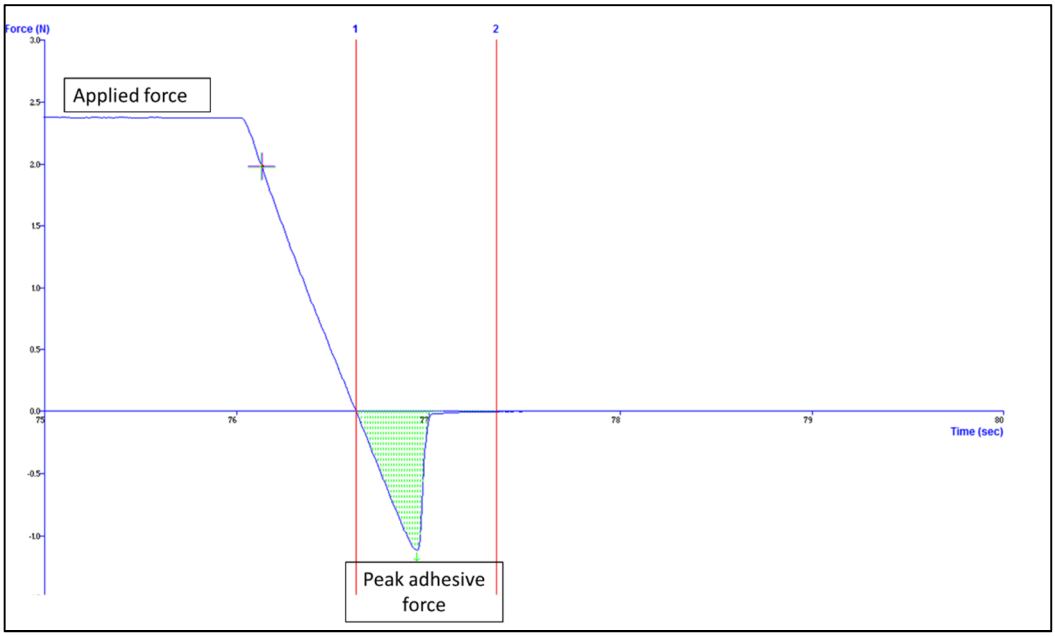

Figure 4.17: Mucoadhesion analysis for placebo CM1 sample using TA-XT2 Texture Analyser

Table 4.5: *In vitro* mucoadhesion measurements of CM1 and CM2 placebo and felodipine loaded HME-IM buccal patches (n = 5, average ± SD)

Formulation	Peak adhesive force (N)	Total work of adhesion (N.mm)
Placebo CM1	0.825 ± 0.115	0.159 ±0.030
10% w/w CM1	0.927± 0.149	0.194± 0.046
20% w/w CM1	0.775± 0.090	0.158± 0.027
30% w/w CM1	0.536± 0.040	0.100± 0.005
Placebo CM2	0.992 ± 0.340	0.211 ±0.087
10% w/w CM2	0.882 ± 0.304	0.205 ± 0.079
20% w/w CM2	0.393 ± 0.090	0.086 ± 0.016
30% w/w CM2	0.345 ± 0.171	0.076 ± 0.028

4.3.3 Influence of drug loading and phase separation on the *in vitro* felodipine release profiles from the HME-IM patches

Figure 4.18 shows the *in vitro* unidirectional drug release behaviour of CM1 and CM2 patches under sink (PBS pH = 6.8 containing 0.5% v/v Tween 80) and non-sink (PBS pH = 6.8 only) conditions. The release profile of CM1 patches under sink condition (**Figure 4.18a**), with the presence of surfactants in the dissolution media, no significant difference in the release profiles of felodipine from the HME-IM patches with different loading percentages can be identified. The release is dominated by zero-order kinetics. This indicates that the dissolution is not controlled or affected by the phase separation and presence of the crystalline drug. In this case, it is likely that the dissolution of the matrix is the rate-limiting factor of the drug release.

The *in vitro* release of CM1 under non-sink condition was conducted to eliminate the impact of the sink condition promoting surfactant on the release profile of different mucoadhesive patches. The supersaturation of felodipine in the dissolution media had a clear impact on the release profiles of the patches. As seen in **Figure 4.18b**, the patches with 30% drug loading show similar dissolution behaviour as pure crystalline felodipine, indicating the dissolution of the crystalline drug is the rate-limiting factor in this case. The patches with 10 and 20% drug loadings showed higher dissolution rates and better maintained supersaturation state of felodipine in dissolution media than the patches with 30% drug loading.

The unidirectional felodipine release profile from CM2 patches with different drug loading tested under non-sink conditions are shown in **Figure 4.18c**. For the 10% and 20% patches, 10-15 fold increases in maximum drug release were achieved within 2-2.25 hours in comparison to the crystalline drug alone. This may be attributed to the fact that the majority of the drug in these two formulations is in the molecularly dispersed and the amorphous states, which led to faster dissolution. However, with increasing the drug loading to 30%, the increase in drug release reduced to only 2-fold increase in comparison to the pure crystalline drug. The presence of phase separated crystalline drug in the patches is likely to be responsible for this result. The dissolution results indicate that the phase-separated carrier systems that contain no crystalline drug can significantly improve drug release. Even with only one side of the intact patches in contact with the dissolution media, this dissolution enhancement is comparable with other binary solid dispersion systems reported in the literature where milled extrusion powders with a much higher total surface area for dissolution were used (73).

The two mixtures show approximately similar release percentages at the corresponding loading fraction of felodipine. The only difference noticed between the two formulations is the higher ability of CM2 patches loaded with 20% felodipine to stabilise the dissolved felodipine in the dissolution media compared to CM1 constituents. These self-emulsified drug delivery systems are assumed to prevent the after dissolution crystallisation of felodipine. Knowing that the proportions and the constituents of the two mixtures at this loading percentage are the same except the type of the surfactants, this difference in felodipine stabilisation in the dissolution media is more likely due to the more stabilisation effect of TPGS compared to Tween 80. It should be mentioned that the concentrations of both surfactants in the dissolution medium after their dissolution is less than their CMC reported in the literature (363, 375).

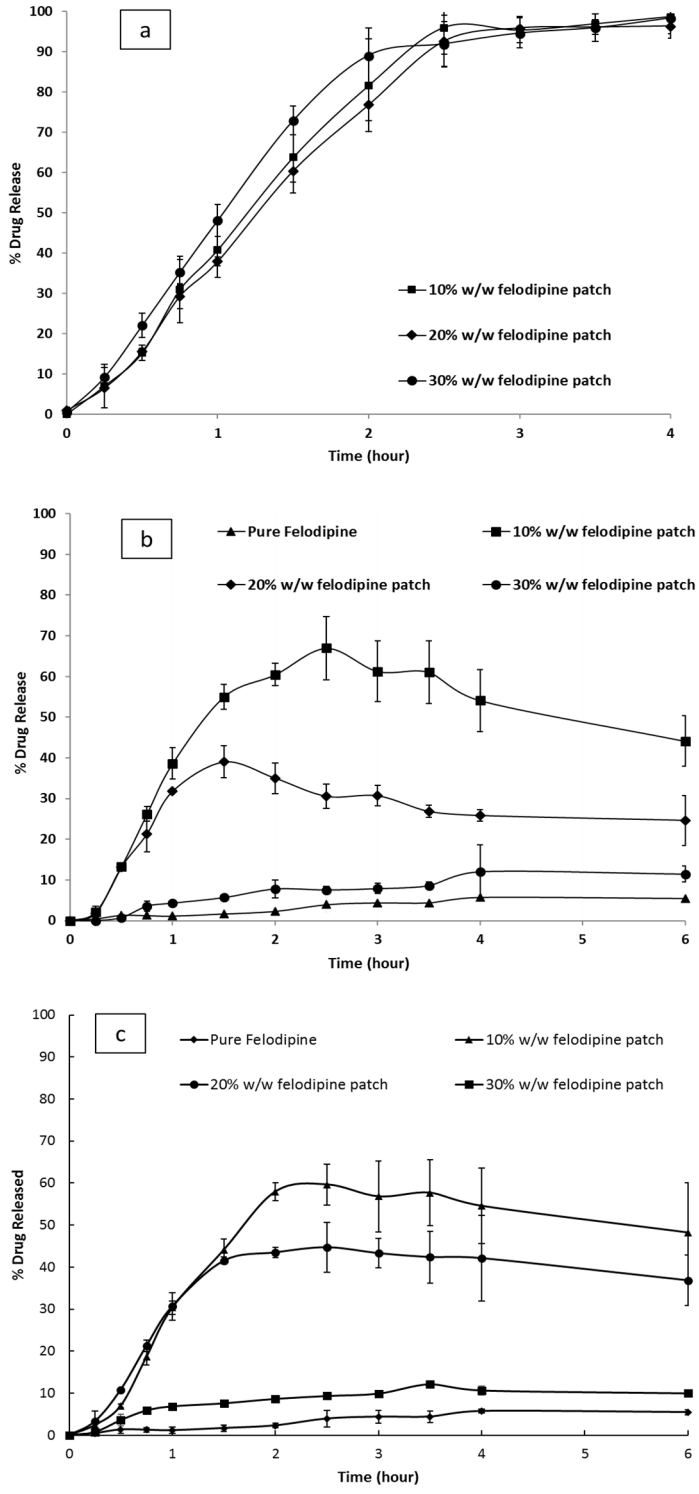

Figure 4.18: *In vitro* release profiles of felodipine from HME-IM buccal mucoadhesive patches; a) CM1 patches under sink conditions, a) CM1 patches under non-sink conditions and c) CM2 patches under non-sink conditions (n=3; average ± SD)

4.4 Discussion

Formulating solid dispersions of poorly water soluble drugs like felodipine using HME-IM as single step processing is an attractive approach for improving their dissolution properties with fast and environmentally friendly processing. However, in order to achieve the desired formulation features of the product such as systemic delivery via the buccal cavity in this study to avoid the extensive liver inactivation of 84% of the drug in addition to dissolution enhancement, it requires the inclusion of a number of excipients resulting in an increase in the complexity of the system. The primary objective of this chapter was to design and investigate the physicochemical properties of felodipine quaternary solid dispersions using carefully selected excipients to solubilise and stabilise the dispersed drug in the matrices. Liquid (Tween 80) and waxy solid (vitamin E TPGS) surfactants were used as intentionally created solubilisation compartments. In addition, the excipients also chosen to permit processing at low temperature (65 ºC) with easy to peel off from the mould after cooling which cannot be achieved for the vast majority of excipients used in HME due to the requirement of high processing temperature and stickiness to the mould after moulding which interferes with the purpose of using this processing technique.

The binary miscibility between excipients was first estimated in order to establish the preliminary understanding of the complex phase separation of the quaternary dispersions. Crystalline felodipine showed good solubility in Tween 80 and TPGS surfactants. The partial miscibility of Tween 80 and TPGS with PEG-PEO K900 was indicated by the thermal method leads to the formation of phase-separated systems. Felodipine was predicted be to miscible with PEG-PEO K900 by solubility parameter method but was experimentally proven to be very low due to the low amorphous content of PEG-PEO K900 at the stated processing parameters. The ability of semi-crystalline PEG-PEO K900 mixture to solubilise poorly water-soluble drugs is generally governed by the kinetics of crystallisation of the drug and the presence of favourable interactions between the drug and the polymers below their saturation capacity. Dissolved drugs are normally occupying the amorphous fraction of the polymeric blend. Drugs with weak interactions with these polymers or strong devitrification tendencies are most likely translocate to the interfibrillar or interspherulitic regions. The magnitude of drug solubilisation has significant impact on the size of the amorphous fraction and consequently their overall crystallinity (88).

Thermal and spectroscopic characterisation techniques like DSC, MTDSC, SEM, EDS, ATR-FTIR and PXRD were used to characterise the prepared HME-IM matrices. SEM, EDS and

PXRD revealed that dispersions with up to 10% CM1 and 20% CM2 are free of crystalline fraction of felodipine. Samples with 20% CM1 and 30% CM2 loading clearly showed the presence of crystalline felodipine form I as indicated by the identified felodipine crystals on the surface and interface of the samples using SEM and EDS and the appearance of the characteristics diffraction peaks of form I using PXRD. Using ATR-FTIR, the physical state of the drug in the different dispersions was revealed. Broadening of the NH stretching peak of felodipine in the 10% loading most likely indicating that the drug is molecularly dispersed in the phase separated. The appearance of felodipine NH stretching in 3333 cm^{-1} suggesting the presence of the drug as amorphous domains in the matrix. The asymmetric NH stretching peak detected at 3367 cm^{-1} in the spectrum of the 30% loading indicate that felodipine exists as crystalline and amorphous fractions in the mixture. These results also supported by changes in the CN stretching of the drug. IR imaging revealed the same conclusion obtained from the other techniques indicating microscale heterogeneity of 30% loaded patches.

DSC analysis provided more information about the miscibility of the PEG-PEO K900 and Tween 80 or TPGS phases and the impact of drug loading on the phase separation in the different HME-IM buccal patches. As revealed from melting point depression approach in Chapter 3, TPGS has higher solubilisation capacity for felodipine than PEG-PEO K900 blend and Tween 80. The phase separated Tween 80 phase detected in placebo CM1 patches is completely absent by felodipine loading revealing improved miscibility of the phases by drug solubilisation. The high semicrystalline nature of TPGS and the presence of vitamin E moiety in its structure limits its miscibility with the hydrophilic PEG-PEO K900 polymer blend. Dispersing felodipine in CM2 phase separated system is strongly depressing the melting of TPGS compared to PEG-PEO K 900 up to 20% loading supporting that TPGS acts as semisolid phase separated solubilisation compartments embedded in the patches. This is also clearly reflected in the T_g region analysis. Due to the high semi-crystalline character of TPGS and PEG-PEO K 900 phases and their limited miscibility, the T_g of either of them was undetectable in the placebo CM2 sample. Interestingly, as the loading percent of the drug increase, a clear T_g in a temperature very close to the T_g of TPGS was detected indicating an increase in the amorphous fraction of TPGS by felodipine solubilisation. It should be mentioned that felodipine has less antiplasticising effect on TPGS phase of CM2 formulations compared to CM1 loaded patches. In addition, the dissolved drug in TPGS seems has no effect on increasing the miscibility of the separate phases compared to CM1 formulations.

It was found that the saturation limit and the concentration of the drug affecting the mucoadhesion parameters of the fabricated HME-IM patches of CM1 and CM2 blends. Samples below the

saturation (10% loading) revealed similar mucoadhesion properties, however, increasing drug loading to 20-30% loading significantly reduced the force and work of adhesion may be due to the presence of a crystalline fraction of felodipine and/or lowering the melting of the surfactant phase. The designed felodipine loaded CM1 and CM2 mucoadhesive buccal patches also showed an enhancement in the dissolution properties of felodipine with 10% loading being the maximum with approximately 60% drug release after 2.5 hours under non-sink conditions compared to the crystalline drug. This significant enhancement in the solubility/dissolution properties of felodipine using the HME-IM fabricated patches together with using the buccal route for systemic delivery of felodipine is expected to improve the bioavailability of the drug under investigation.

4.5 Conclusion

Formation of phase separated compartments in-situ with different functionalities that can improve the bioavailability of poorly soluble drugs was the main formulation strategy presented in this chapter. The characterisation results presented in this chapter confirmed the formation of the phase-separated systems with the drug being solubilised predominately in the Tween 80 and TPGS rich phases. The results of this chapter have also demonstrated the feasibility of using HME-IM as a simple pharmaceutical process to produce patches that are suitable for the buccal route of administration which can provide the advantage of avoiding the first-pass metabolism. Using the solubility difference between the excipients and drug, Tween 80-rich or TPGS-rich compartments with the primary function of solubilising drug and PEG-PEO-rich phase with the main function of providing mucoadhesion and acting as a hydrophilic carrier for easing dissolution were successfully created in-situ. To be able to formulate such phase separated systems requires a clear understanding of the miscibility between ingredients. Successfully designed mucoadhesive patches show good mucoadhesive properties and maximum *in vitro* release profile with matrices loaded with 10% felodipine. With this information, formulations with the desired level and type of phase separation can be designed and produced by varying the composition of the different ingredients in the mixtures. However, despite the clear indications of the phase separation in the patches, it is not possible to obtain detailed information on the spatial distribution of the separate phases. This characterisation challenge is addressed in Chapter 5.

Chapter 5. Characterisation of heterogeneity and spatial distribution of phases in felodipine HME-IM patches using thermal analysis by structural characterisation and X-ray micro computed tomography

5.1 Introduction

The heterogeneity of material in a complex formulation is often a key parameter that requires monitoring during quality control of pharmaceutical products. In multi-component formulations, which is the case for most pharmaceutical products, the uniformity of the distribution of excipients and active therapeutic drugs across the dosage form is extremely important for ensuring the quality such as physical stability over shelf-life and *in vivo* performance such as drug release rate, which are critically responsible for the overall therapeutic efficiency of the product (175). However, to characterise and assess heterogeneity within a single formulation often requires the use of multiple off-line localised analytical techniques, which is time-consuming and costly process. In the case of the solid dispersion based patches produced in this project, the multi-components also phase separate in the patches. The understanding of how these separate phases distribute across the patches is important for further investigation and modification of the *in vitro* stability and drug release behaviour of the patches.

Traditionally, solid dispersions have been often loosely classified into single-phase molecular dispersions and phase separated systems with varying degrees of structural complexity (474, 478, 479). Phase separation in solid dispersions is the result of the diversity in the physicochemical properties of the drugs and excipients used in the formulations which affects their miscibility. Normally, phase separation of drug from the excipients has often been considered as an indication of instability or incompatibility between the drug and excipients and therefore been avoided in industrial formulation development (480, 481). The most commonly detected phase separation behaviour in solid dispersions is the separation of the dispersed drug from the carrier matrix (8, 24) as either amorphous or crystalline domain (129, 482, 483). However, in this project phase separation was intentionally used as a strategy to improve stability and modulate the drug release profile. As described in Chapter 4, for both CM1 and CM2, the conventional characterisation results indicated that the excipients used showed partial miscibility which led to phase separation of the excipients. Each separate excipient phase contained different amount of solubilised drug.

Although conventional characterisation techniques such as DSC, MTDSC, PXRD and spectroscopic methods including IR, Raman and terahertz spectroscopy often allow the confirmation of the presence of phase separation, understanding the phase separation behaviour in solid dispersions can still be challenging. The overlapping diffraction patterns or spectra from different phases or the thermal dissolution of one phase into another during heating in the DSC often lead to the difficulty in accurate data interpretation (385, 484, 485). Many excipients and

active ingredients are organic materials which make SEM analysis in combination with EDS powerless for identifying detailed phase separation due to the lack of elemental variability between samples. In addition, the conventional characterisation methods mentioned above have not been able to effectively provide information on two important aspects of phase separation in formulations, heterogeneity and the 3D spatial distribution of different phases. Addressing these two aspects of phase separated solid dispersions will advance our understanding of how to control the formation and kinetics of phase separation behaviour in complex solid formulations and in turn enable the rapid development of phase separated dispersions which may be used for the delivery of multiple active pharmaceutical ingredients in one formulation. It should be mentioned that micro/nano thermal analysis using a heated probe in a scanning probe microscope can provide information on sample heterogeneity using either local thermal analysis or photothermal IR spectroscopy (486-488). However, it is slow and can take over an hour for a single high spatial resolution image using TTM (489).

This chapter introduces the use of two non-conventional methods, thermal analysis by structural characterisation (TASC) and X-ray micro computed tomography (XμCT), as novel techniques for studying phase separation in complex pharmaceutical products designed by HME-IM. The potential of these techniques has been evaluated for characterising heterogeneity and spatial distribution of phases in the prepared samples. TASC uses conventional and user-friendly hot stage microscopy with a novel algorithm for quantifying changes in successive micrographs of the samples during heating or cooling. The detailed working principle of TASC has been explained previously in Chapter 2. The subtle changes in the appearance of the sample during heating or cooling detected by TASC can then be converted into thermal transition graphs. XμCT used as a non-invasive method to investigate the 3D internal microstructure of the patches and to estimate the size, shape and spatial distribution of the phases in situ. In this technique, the absorption of X-rays results in the generation of series of images in a manner similar to transmission microscopy. Different phases having different electron densities depending on the characteristics of their elements can be differentiated by XμCT and represented as 3D models. In this chapter, the same series of complex solid dispersions studied in Chapter 4 (placebo and 10-30% w/w felodipine loaded CM1 and CM2 HME-IM mucoadhesive buccal patches) were analysed using TASC and XμCT.

Research objectives

1. To use TASC as a new, fast and cheap thermal characterisation technique for detecting heterogeneity in complex solid dispersions prepared by HME-IM technique.
2. To compare the data generated by TASC with results obtained by standard DSC in order to observe the possible additional advantages of TASC analysis like detecting thermal dissolution, providing localised analysis and impacts of the rate of heating and cooling ramps during thermal analysis.
3. To investigate the ability of XμCT to detect heterogeneity and spatial distribution of phase separation in the prepared solid dispersions at micron-scale.
4. To assess the use of XμCT for providing quantitative/semi-quantitative information about the phase separation of drug above the saturation limits of the carrier mixture.

5.2 Materials and Methods

5.2.1 Materials

Same batches of the HME-IM patches studied in Chapter 4 were prepared and characterised using TASC and XμCT.

5.2.2 Methods

5.2.2.1 Thermal analysis by structural characterisation (TASC)

The TASC system was composed of a temperature controlled heating/cooling Linkam MDSG600 automated stage fixed to a Linkam imaging station that was attached to a microscope working in reflective mode (LED light source and X10 magnification lens) and was equipped with a digital camera to capture images that correspond to thermal events as a function of temperature. For cooling ramps, the temperature of the stage is controlled using a cooling unit that operates by purging liquid nitrogen into the stage.

For all samples analysed, thin slices of the prepared patches (0.6 - 1.2 mm × 0.6 mm × 0.2 mm) were cut using a sharp blade and placed in standard DSC pans (TA Instruments, Newcastle, USA). A pre-designed temperature program (10 °C/min) for heating, cooling and reheating cycles with

an isothermal period of 1 minute separating the ramps was applied to the prepared samples within the range of -10 to 150 °C. Before starting the experiments, the image-capturing mode was activated at an image acquisition rate of 1 frame/ ˚C. The captured images were then collected and analysed using the TASC software provided by Cyversa (Norwich, UK). The results obtained were statistically analysed by using one way analysis of variance (ANOVA). Statistical significance was accepted at the $p \leq 0.05$ level.

5.2.2.2 Differential scanning calorimetry (DSC) and modulated temperature DSC (MTDSC)

All samples investigated in this study using standard DSC were analysed using the same parameters as described in Chapter 3, section 3.2.2.2.2. Heating only MTDSC experiments were also performed (at 2 ºC/min scanning rate, 40 sec period and 0.212 ºC amplitude) to investigate the hidden melt-recrystallisation behaviour of the patches. All samples analysed have a weight of about 2-3 mg and standard TA crimped pans (TA Instruments, Newcastle, USA) were used. All analyses were performed in triplicates.

5.2.2.3 Variable temperature attenuated total reflectance Fourier transform infrared spectroscopy (VT-ATR-FTIR)

All experiments were conducted using an IFS 66/S FTIR spectrometer (Bruker Optics Ltd, Coventry, UK) fitted with a Golden Gate® ATR accessory with a temperature-controllable top plate (Orpington, UK) equipped with diamond internal reflection element. ATR-FTIR spectra, in absorbance mode, were obtained using a scanning resolution of 2 cm^{-1} and 32 scans for each sample. The system was connected to a high stability temperature controller (Specac, USA) and the VT-ATR-FTIR spectra were collected using heat-cool-heat program with a heating rate of 2ºC/min. All spectra were analysed using OPUS software.

5.2.2.4 X-ray micro computed tomography (XμCT)

Two XμCT types of equipment were used to investigate CM1 and CM2 buccal patches designed using HME-IM. XμCT images for the placebo and felodipine loaded CM1 patches were characterised using a Phoenix v[tome]x m system (General Electric, Wunstorf, Germany). 3D images of the formulations were reconstructed from a large series of two-dimensional

radiographic images taken around a single axis of rotation. The following settings were applied: voxel size: 4μm, number of images: 1500, Voltage 60 kV, Current 100 μA and timing 500: ms. For CM2 samples, CM2 felodipine solid dispersions with different drug loading percentages were analysed using SkyScan1172 high-resolution X-ray micro computed tomography (XμCT) scanner (Bruker-microCT, Kontich, Antwerp, Belgium). The analysed samples were imaged using an aluminium filter to cut-off high energy X-rays at an isotropic voxel resolution of 3 μm over a total of 20 min acquisition time and a subsequent image reconstruction time took approximately 20 min per sample, using the NRecon program (version 1.6.8.0, Bruker-microCT). The reconstructed images were analysed using CTan and CTvol software in which the images for a small section (designated as a region of interest ROI) for each sample are converted to binary images followed by thresholding each component according to differences in density and represented in 3D models. CM2 Powder compacts made of the physical mixtures of crystalline felodipine and the rest of the excipients with consistent compositions to those used in the HME-IM formulations were prepared for the quantitative studies. The compacts (13 mm in diameter) were prepared by compressing (500 mg) of the premixed physical blends into flat-faced disks using an IR press (Specac, Kent, UK) with 10 kN pressure held for 5 minutes.

5.3 Results

5.3.1 TASC analysis of the phase separation of the HME-IM patches

5.3.1.1 Fast detection of heterogeneity in solid dosage forms

The TASC software is designed to track changes in the sample during heating or cooling ramps and any change in the structure as seen by the microscope can be detected. Samples frequently move when heated or cooled, but TASC tracks these movements and compensates for them, so only structural changes are measured. As seen in **Figure 5.1**, the blue frame is the region of interest (ROI) while the red square defines the target area (TA) scanned by the centre of the ROI thus movement over this range is compensated for. TASC tracks these movements by fixing on an optical feature.

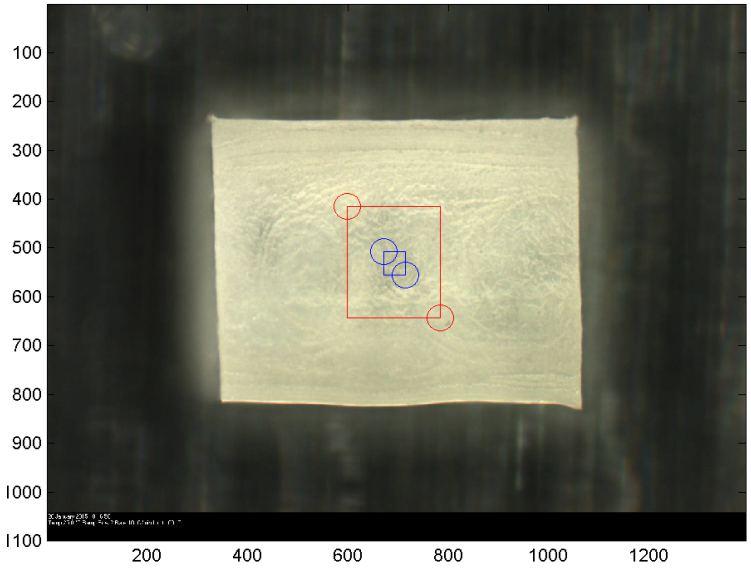

Figure 5.1: Light microscopic image of an example slice of 10% w/w CM1 felodipine mucoadhesive buccal patch analysed by TASC software

Sequences of images were collected during the heating or cooling of patches using TASC. Initially, the ROI was selected as shown in **Figure 5.1**. TASC follows the subtle changes of structure of the selected ROI and converts this information into phase transition signals plotted against temperature. The detailed algorithm of TASC is described in chapters 2. **Figure 5.2** shows an example for the thermal events detected by TASC algorithm.

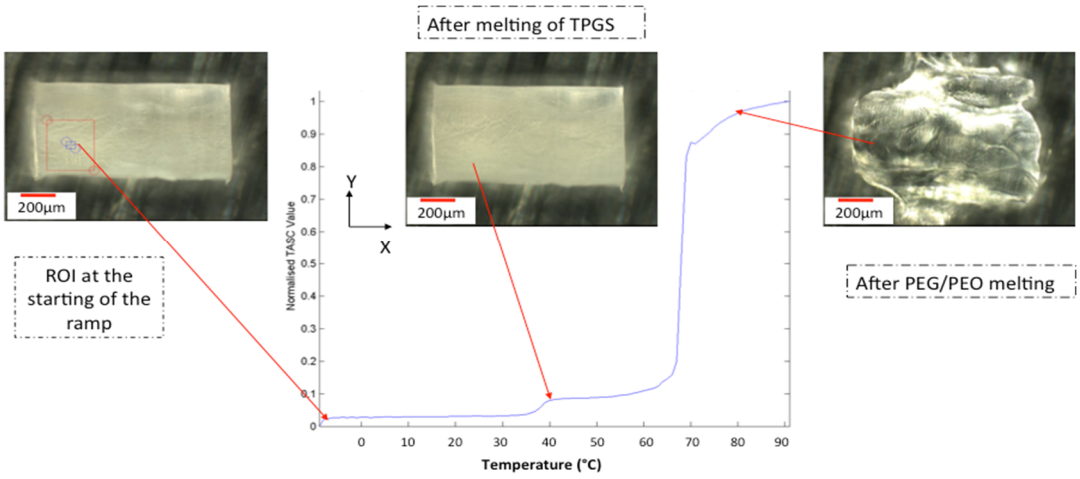

Figure 5.2: Thermal events of placebo CM2 sample detected by TASC at different points (-10°C, 40°C, and 80°C) during the heating ramp at 10 °C/ min

Compared to DSC, TASC detected the of thermal transitions of placebo CM1 and CM2 for the heating -cooling and reheating cycles in temperatures comparable to DSC as shown in **Figure 5.3**. TASC detected the offset of melting transitions of PEG-PEO K900 and TPGS at similar temperatures for all cycles. Similar results are also obtained for the onset and offset of crystallisation events during the cooling cycles. However, the detection of the onset of melting transitions is delayed in the heating cycles because the method of detection by TASC is different from that of DSC. TASC detects the change on the top surface of the sample, which means that when the lower part of the sample in contact with the pan starts to melt (onset of melting in DSC) no TASC signal can be detected until the change appears on the top surface where the algorithm is scanning for the ROI change. This is the case when the sample under investigation is opaque as the matrices used in this study due to the semicrystalline nature of some of the excipients used in this study. This leads to a temperature gradient sometimes appears as a delay in the TASC signal compared to DSC.

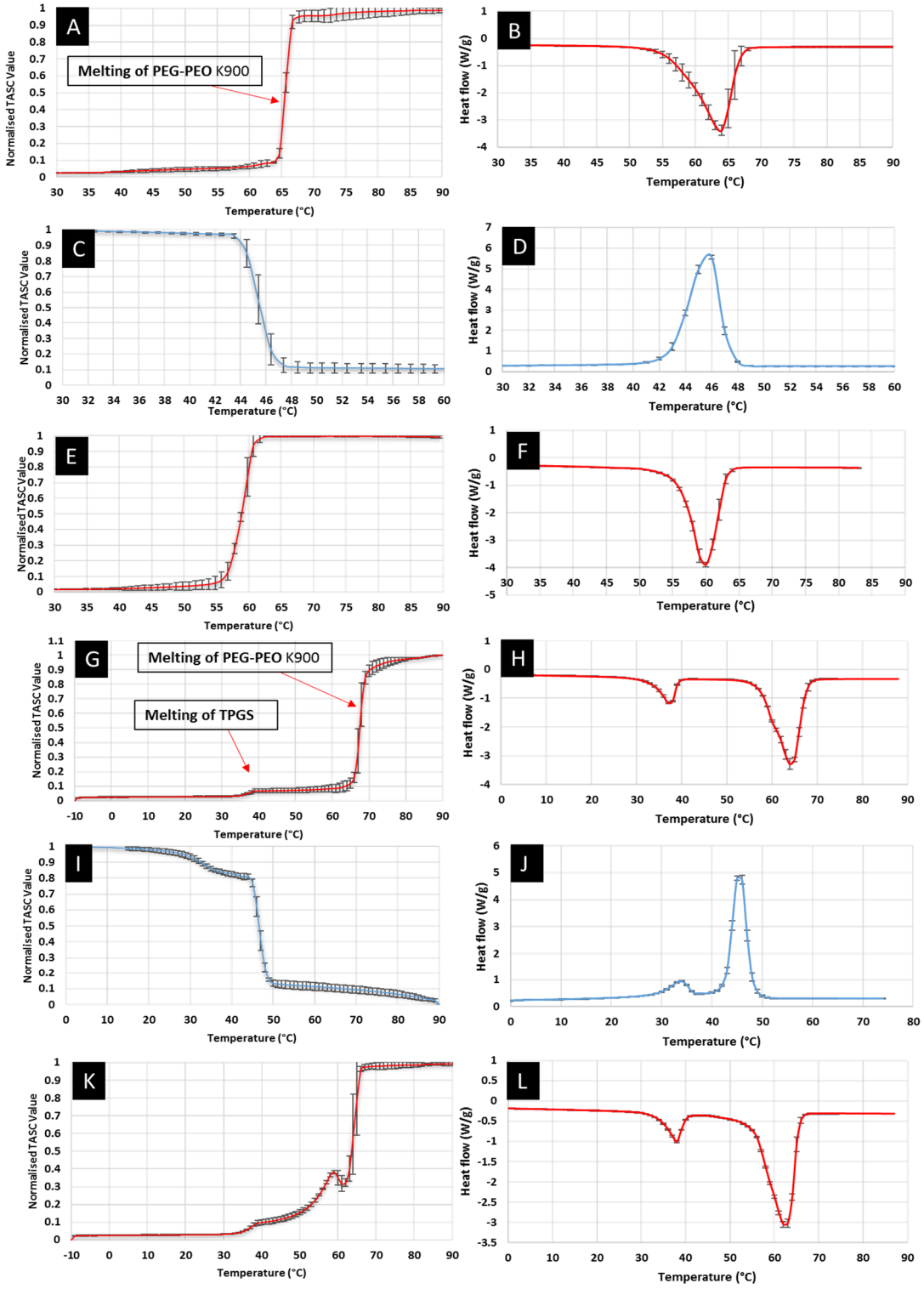

Figure 5.3: TASC compared to standard DSC averaged thermograms of placebo CM1 during the heating (A and B), cooling (C and D) and reheating (E and F) cycles and placebo CM2 during the heating (G and H), cooling (I and J) and reheating (K and L) cycles at 10 °C/ min for all cycles (n=3; average ± SD)

For CM1 and CM2 placebo and patches with up to 20% w/w drug loading, the results obtained from TASC were more reproducible (low standard deviation for 3-5 repeated tests) for the heating, cooling and reheating cycles than the data obtained from the system with 30% drug loading (**Figures 5.3-5.5**). This low inter-sample variation indicates a low level of heterogeneity, at least at this scale of scrutiny, of the formulations with drug loadings at and below 20% loading. This is confirmed by the SEM results of the internal microstructure of the patches as seen in Chapter 4. The reproducibility of the TASC results of the patches with 30% felodipine was much lower as reflected by the high variation of the TASC data for the initial heating cycle of the patches (**Figure 5.6**), note that regions of similar area were used for all of the samples. As TASC is a form of local thermal analysis, each testing area is different from another (such as containing different amount of crystalline/amorphous material or structural features). Therefore, the high inter-sample variation (with statistically significance $P < 0.5$) in the 30% patches should be an indication of high heterogeneity of the sample with average testing areas of (2500-10000 μm^2).

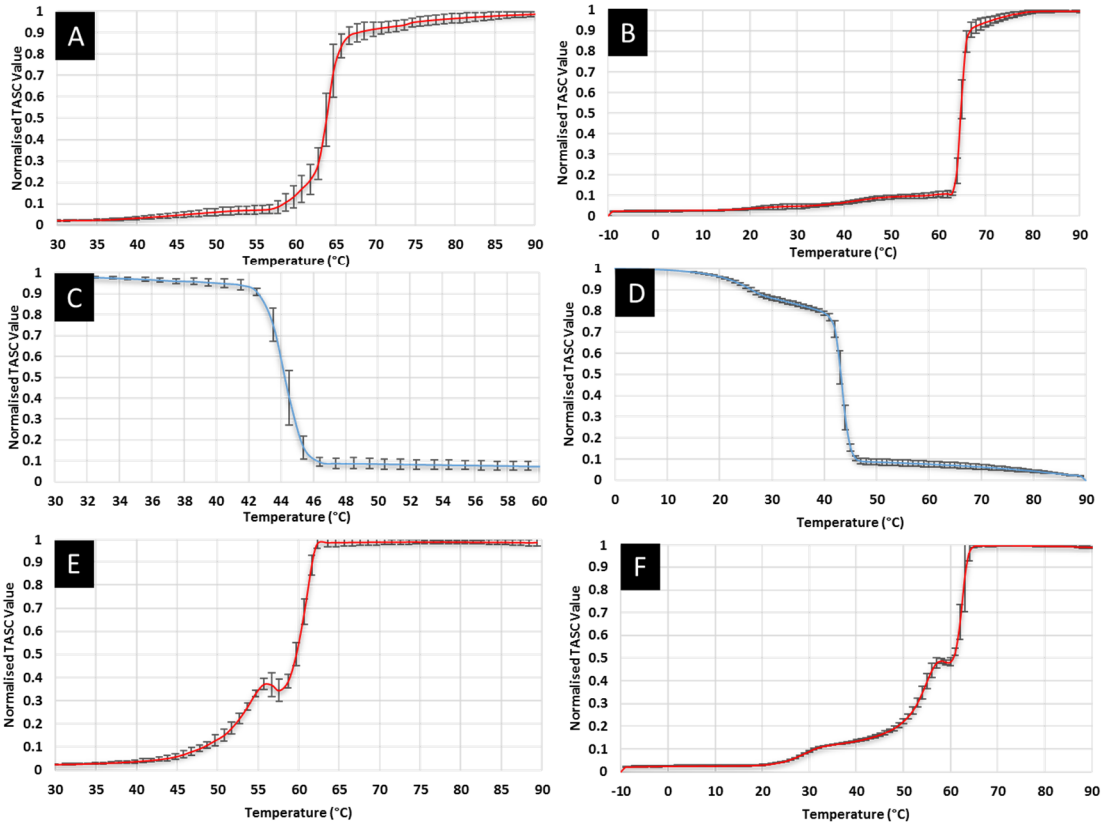

Figure 5.4: TASC thermograms of 10% felodipine in CM1 during the heating (A), cooling (C) and reheating (E) cycles; and 10% felodipine in CM2 during the heating (B), cooling (D) and reheating (F) cycles using 10 °C/ min for all cycles (n=3; average ± SD)

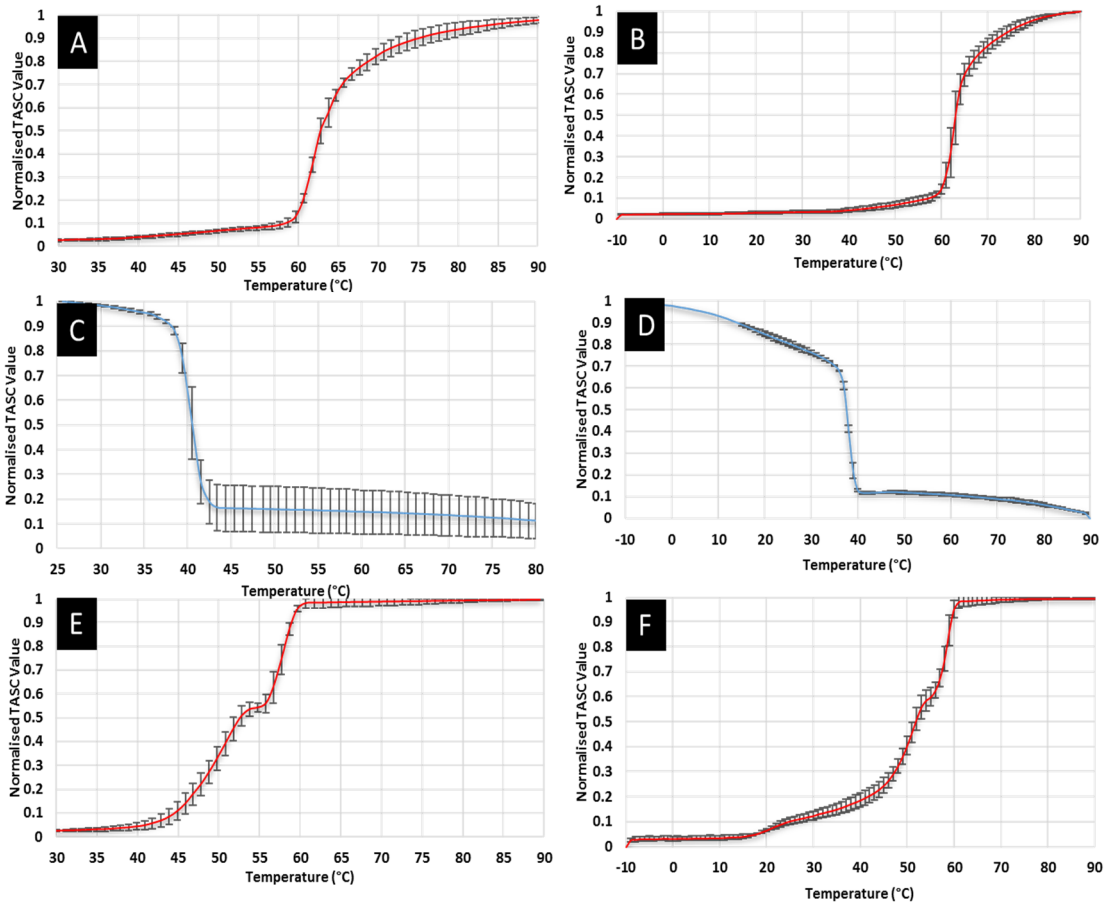

Figure 5.5: TASC thermograms of 20% felodipine in CM1 during the heating (A), cooling (C) and reheating (E) cycles; and 20% felodipine in CM2 during the heating (B), cooling (D) and reheating (F) cycles using 10 °C/ min for all cycles (n=3; average ± SD)

The TASC results of CM2 patches with 30% w/w felodipine content (**Figure 5.6B**) show a complex triple transition. The melting peak of TPGS can be clearly seen at approximately 33ºC which is in agreement with the DSC data. Two further melting transitions were detected at 60 and 76ºC followed by the absence of the plateau region seen in the placebo and 10% loaded samples. DSC data of the 30% loaded patches only show the melting of the PEG-PEO K900 phase at 60ºC (**Figure 5.7B**). However, it is known from the other characterisation methods in Chapter 4 that there were crystalline drug particles present in the 30% patches. Therefore, the 76ºC transition detected by TASC is likely to be associated with the thermal dissolution of the remaining crystalline drug into the molten matrix. The absence of a plateau region indicates the continuous changes captured by TASC were not completed at 90 ºC. The poorer reproducibility of data in the high temperature region was also noted in comparison to the results of the samples with lower drug loadings. It should be mentioned that the 30% CM2 loaded patches show better

reproducibility compared to the corresponding CM1 patches confirming the results of better solubilisation capacity of CM2 for felodipine compared to CM1.

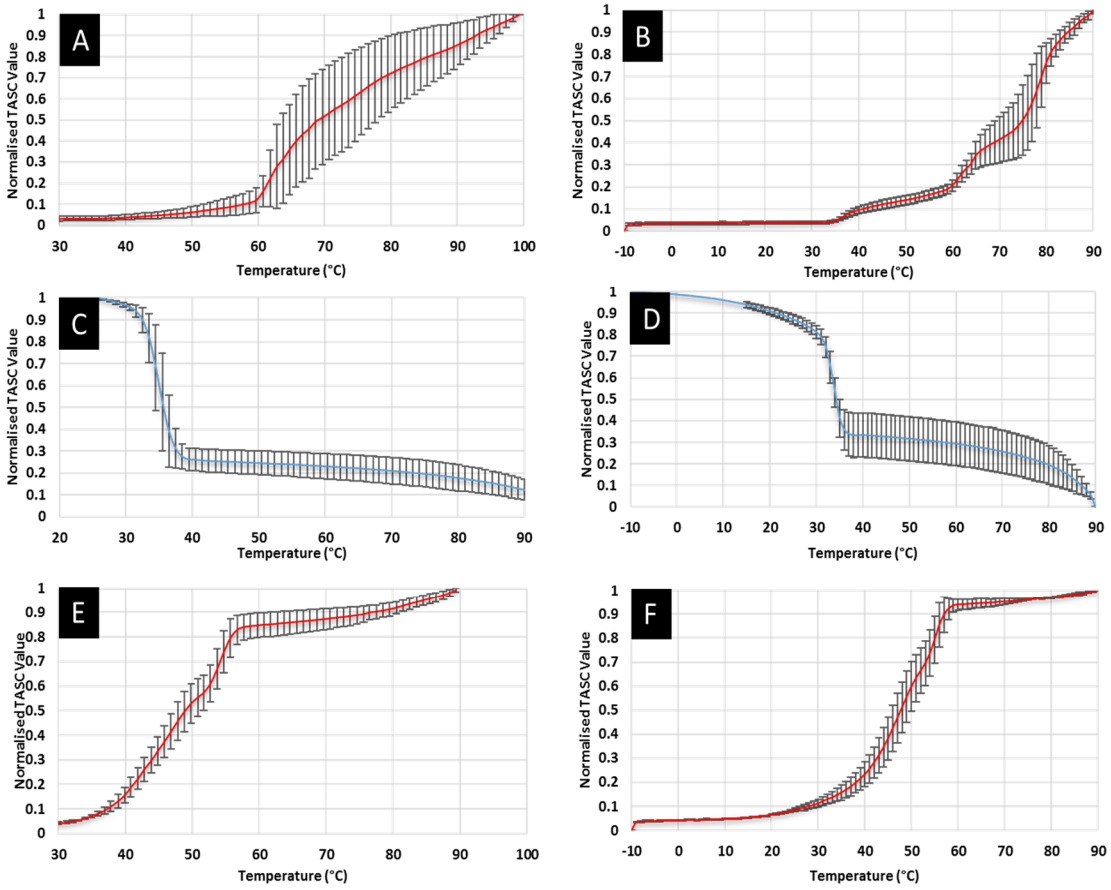

Figure 5.6: TASC thermograms of 30% felodipine in CM1 during the heating (A), cooling (C) and reheating (E) cycles; and 30% felodipine in CM2 during the heating (B), cooling (D) and reheating (F) cycles using 10 °C/ min for all cycles (n=3; average ± SD)

The high heterogeneity of the patches with 30% load is confirmed by the rich variety of interior features of the patches seen by SEM (Chapter 4; **Figures 4.4g and h** and **Figure 4.5g and h**) including the presences of air pockets and non uniform distribution of particles with 5-20μm in average diameter and defined edges which are likely to be felodipine crystals.

As seen in **Figure 5.7**, this sensitivity to the heterogeneity of the sample is absent in the DSC results which provide only global information. The significant difference in weight of sample analysed by the two methods may contribute to the difference in their detective sensitivities. The calculated weight range of the analysed areas by TASC (the area framed by the blue square indicated in **Figure 5.2**) was estimated to be 0.6-3.7 μg in comparison to 2-3 mg sample size used

in the DSC experiments. As a consequence of this, as seen in **Figure 5.7B and D**, the 30% loaded samples analysed by DSC showed high reproducibility.

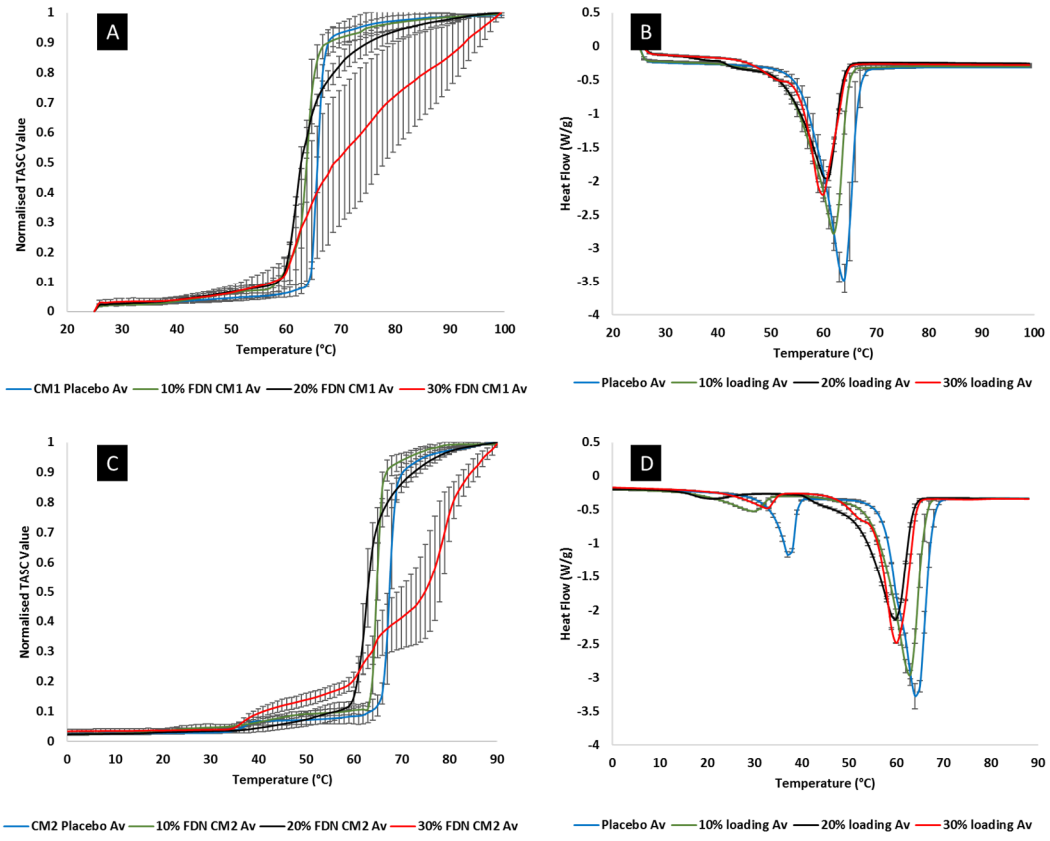

Figure 5.7: TASC and DSC results of the heating cycle of CM1 (A and B) and CM2 (C and D) placebo and felodipine loaded mucoadhesive buccal patches with 10, 20 and 30% w/w loading (n=3; average ± SD)

The low reproducibility and failure to reach a plateau with the individual replicates of the 30% w/w loaded CM1 and CM2 formulations were further investigated by altering the size of ROI and increasing the terminal temperature of the analysis to above the melting point of crystalline felodipine. As seen in **Figure 5.8**, the reproducibility of the data collected by analysing small areas (ROIs, approximately between 2.5×10^{-3} and 10×10^{-3} mm^2) is lower than that obtained from larger areas (between 40×10^{-3} and 90×10^{-3} mm^2). The results obtained using larger tested areas often overlooks the differences present locally on a micro scale (heterogeneity). This is demonstrated by the highly reproducible DSC data in which the samples were tested as a bulk material with no localised information being obtainable (**Figure 5.7B and D**). The poor reproducibility of the TASC results obtained from small ROIs indicates a high variability in the thermal transitions detected locally. The size of drug crystals detected by SEM is approximately

10-20 μm in diameter which is smaller than the smallest ROI used in this analyses. The thermal properties detected for each ROI is the average of all materials within the area which should, therefore, be a mixture of drug crystals, excipients and amorphous dispersions of drug dissolved in the excipients. The variation of the thermal properties is likely to represent differing amounts of drug crystals, excipients and amorphous drug dispersions being present in each ROI. This was not observed in placebo and samples with 10% drug loading (**Figure 5.9**). This is a clear indication of the high heterogeneity of the distribution of the separate phases in the patches with 30% drug loading at the micron scale. The attempt of validating such finding by XμCT is described later in this chapter.

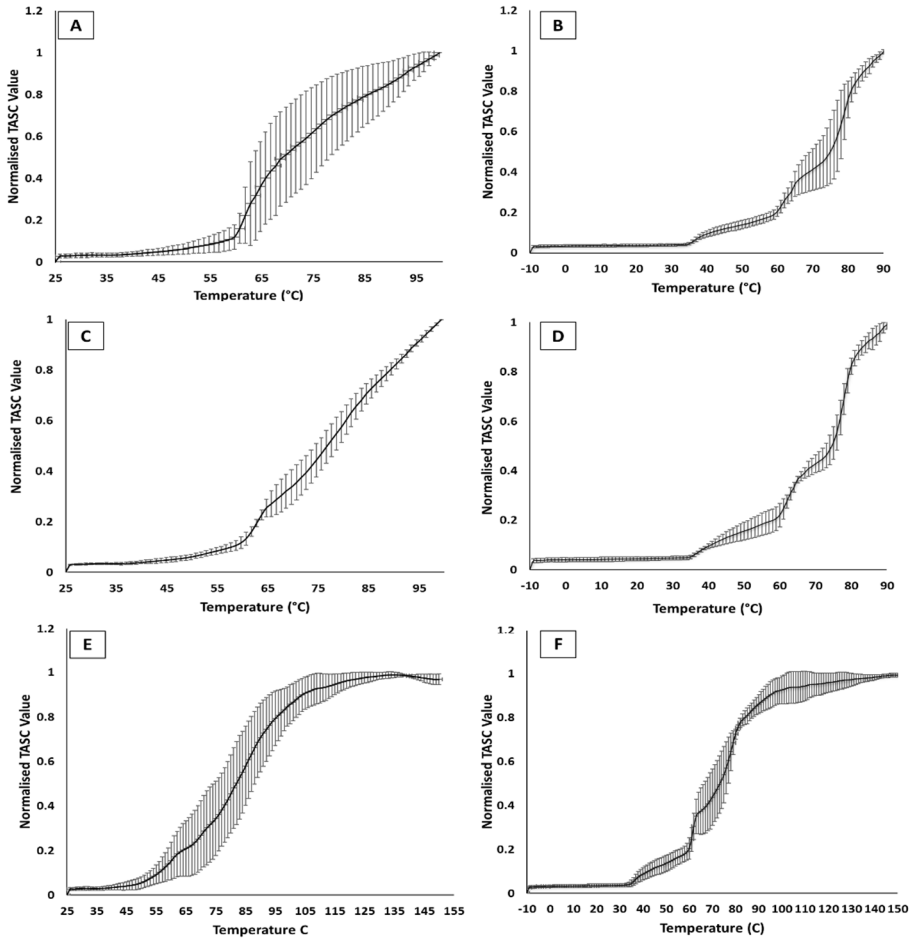

Figure 5.8: Comparison of the TASC results of the heating cycle of CM1 (left) and CM2 (right) 30% w/w felodipine patches using (A, B) small sampling spots (to provide localise thermal analysis), (C and D) larger sampling spots; (E and F) extended heating to 150ºC to demonstrate that the drug dissolution/melting occurred in the 30% drug loaded samples as the TASC signal reaches the plateau at higher temperature above 100 °C (n=3; average ± SD)

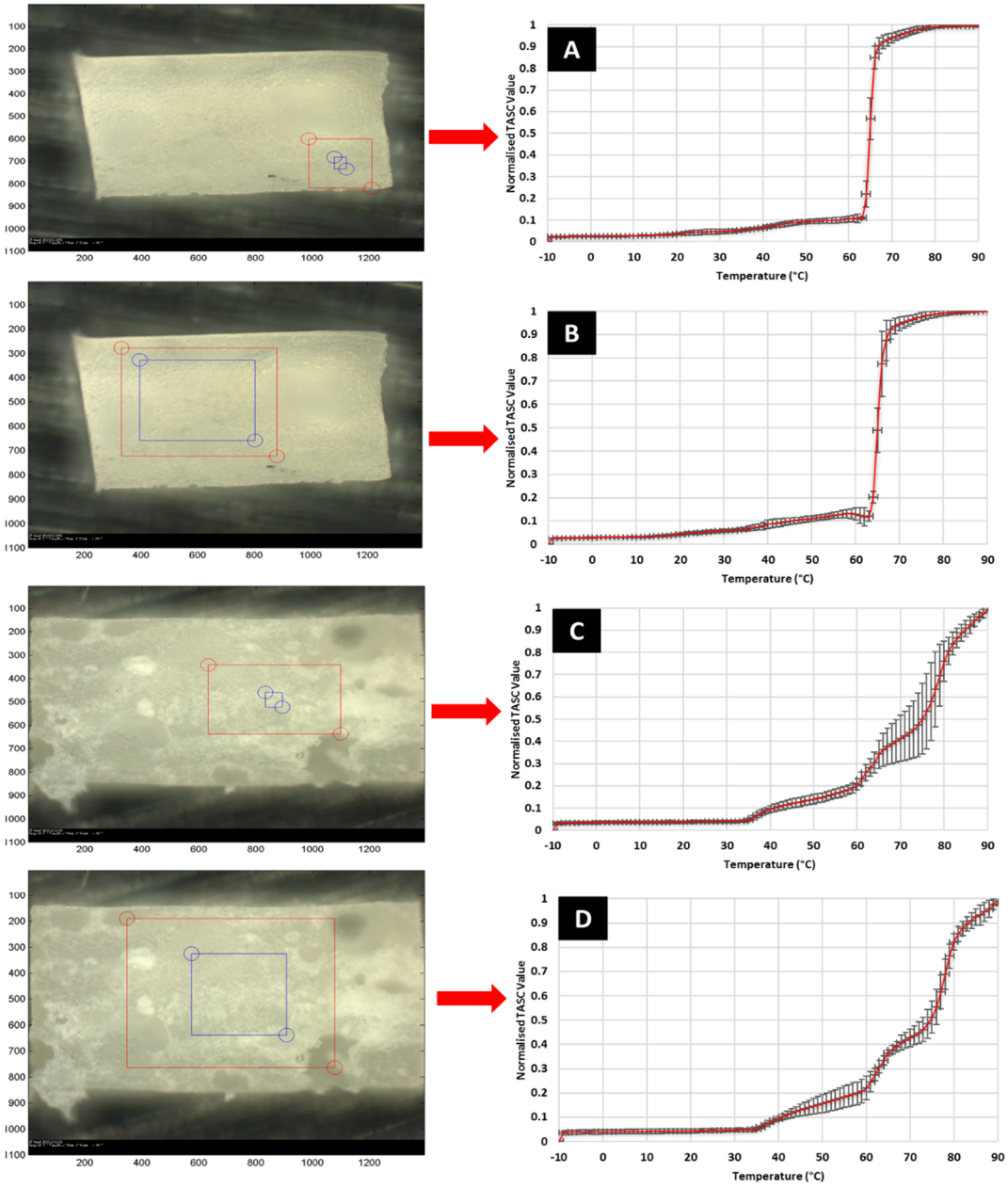

Figure 5.9: The TASC results of the heating cycle of 10% (A and B) and 30% (C and D) CM2 felodipine loaded patches using a small sampling area (A and C) and a larger sampling area (B and D). It can be seen that there is no obvious difference in the error bars of the data collected from the two areas with different sizes for 10% indicating the high homogeneity of the samples with low drug loading compared to 30% loading (n=3; average ± SD)

It was also noticed that TASC was able to detect the double crystallisation in CM2 placebo sample at a temperature comparable to that of the DSC as seen in **Figure 5.10**. There is also a reduction of the crystallisation temperatures with increasing drug loading of all CM1 and CM2 which can

be explained by the incorporation of drug in the different phases (although not necessarily in equal proportions) which disrupted the crystallisation of the excipients. However, only a single phase can be seen in the TASC and DSC results of the cooling cycles of the patches with 30% CM2 drug loaded patches. This may indicate that TPGS did not crystallise due to the presence of the dissolved drug in these patches.

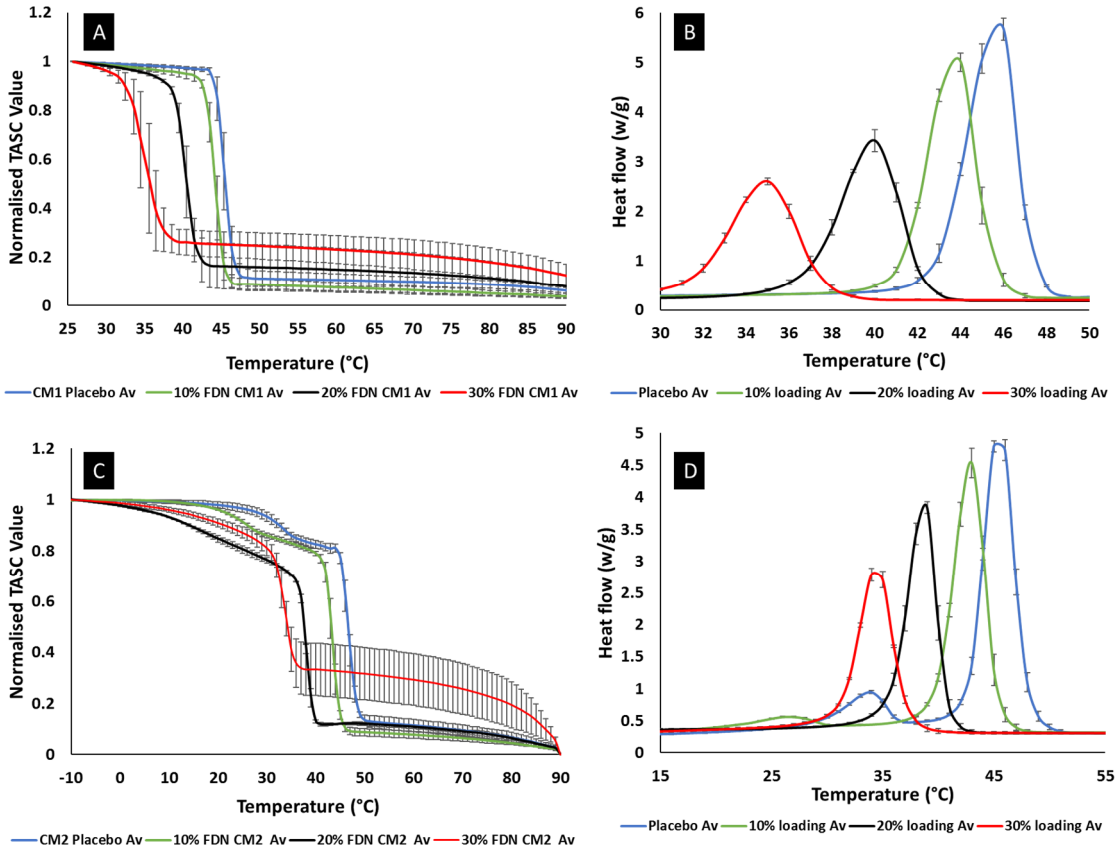

Figure 5.10: TASC and DSC results of the cooling cycle of CM1 (A and B) and CM2 (C and D) placebo and felodipine loaded mucoadhesive buccal patches with 10, 20 and 30% w/w loading (n=3; average ± SD)

5.3.1.2 Detection of thermal dissolution of crystalline drug in excipients

The presence of crystalline felodipine in the patches cannot be detected using DSC because the drug crystals are thermally dissolved in the molten carrier matrices. TASC results of the samples with 30% CM1 and CM2 drug loadings have shown clear indication of a process occurs above the melting temperatures of PEG-PEO K900 blend. As seen in **Figure 5.7A and C**, in the initial heating cycle the TASC signals reach a plateau at higher temperatures as the drug load increases.

This effect is particularly significant for the patches with 30% felodipine. As seen in **Figure 5.8E and F**, a reproducible TASC signals of the 30% patches only reaches the plateau when the temperature is close to the melting temperature of crystalline felodipine (100-140 ºC). This result suggests the dissolution process of felodipine in the molten excipients' blends can be detected by TASC.

The dissolution of the crystalline drug into the molten carrier mixture during heating was confirmed by the variable-temperature ATR-FTIR. As seen in **Figure 5.11**, the disappearance of the NH stretching peak characteristic of crystalline felodipine at 3367cm^{-1} during heating between 60-70 ºC indicating the loss of drug crystallinity and the dissolution of the drug into the molten carrier matrix.

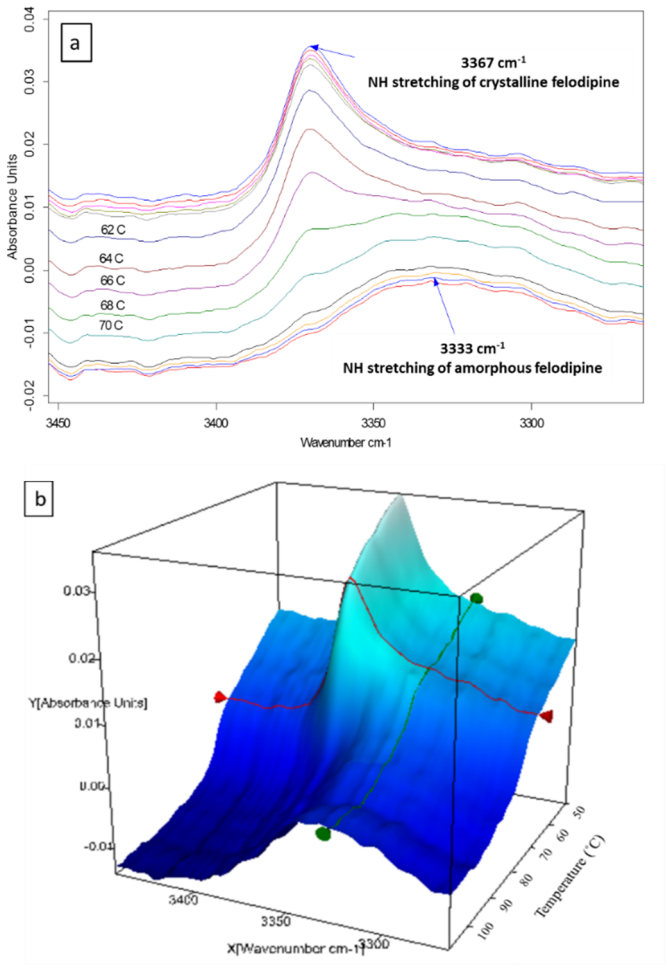

Figure 5.11: VT- ATR-FTIR (a) 2D and (b) 3D spectra of demonstrating the dissolution of the crystalline drug in CM1 matrix in the patches with 30% drug loading during heating

5.3.1.3 Sensitivity to the presence of metastable form of PEG

For all samples, the transition temperatures detected by TASC during the first heating and cooling cycles are highly comparable with the DSC data. However, double transitions are clearly detected by TASC during the reheating cycle as seen in **Figure 5.12A and C**. The detection of the double transitions seen as a shouldered peak is highly reproducible indicating the occurrence of a true thermal event. The double transitions may be associated with the melting of the folded and extended forms of the PEG 4000 as the transition temperature is just below the melting of PEG/PEO K900 (328, 330, 337). However, this bimodality is not detected by conventional DSC (as seen in **Figure 5.12B and D**) using the same scanning rate which is 10ºC/min in this case. The changes seen by TASC are subtle while simple inspection of the images does not suggest complex behaviour as illustrated in **Figure 5.13** for CM1 as representative results. In addition, these two evident thermal events tend to overlap as the percentage of drug loading increased as indicated by the reduction in the temperature range between them due to drug solubilisation inside the matrix. It should be mentioned that CM1 placebo sample does not show this shoulder which may be attributed to the low fraction of the folded form present in this sample.

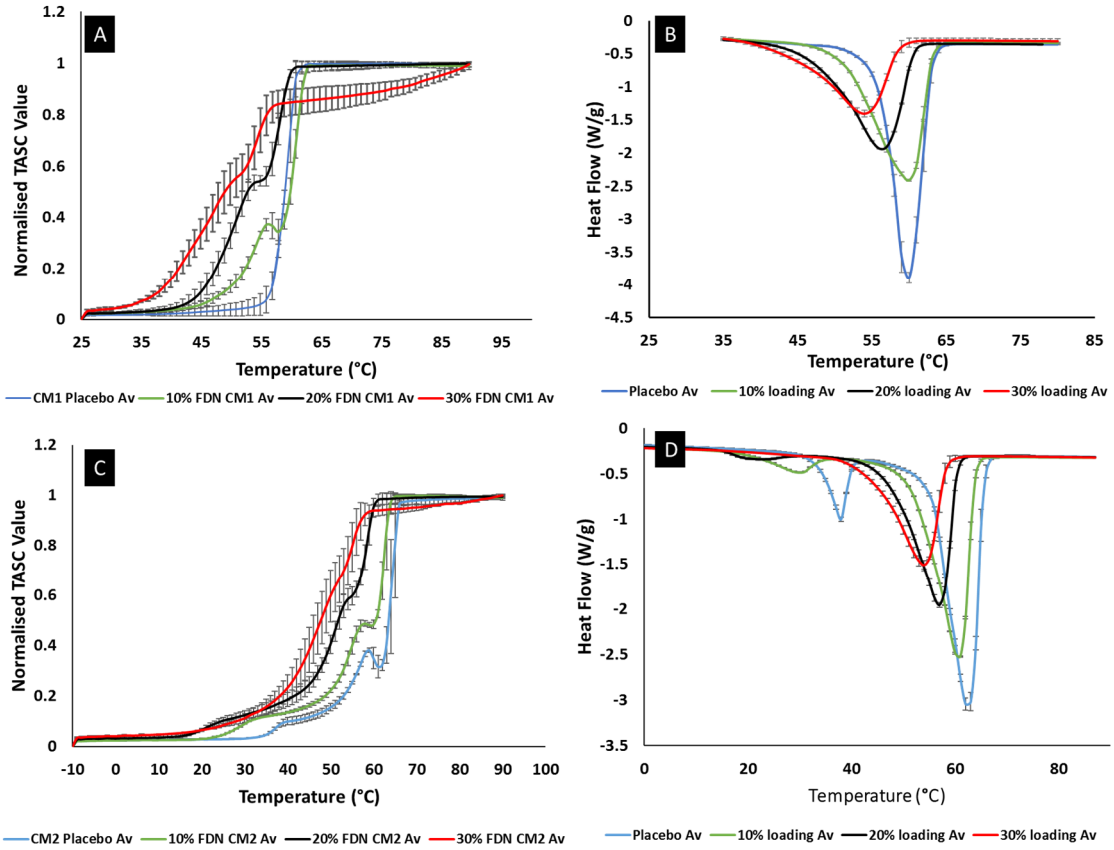

Figure 5.12: TASC and DSC results of the reheating cycle of CM1 (A and B) and CM2 (C and D) placebo and felodipine loaded mucoadhesive buccal patches with 10, 20 and 30% w/w loading showing the detection of metastable folded form of PEG by TASC (n=3; average ± SD)

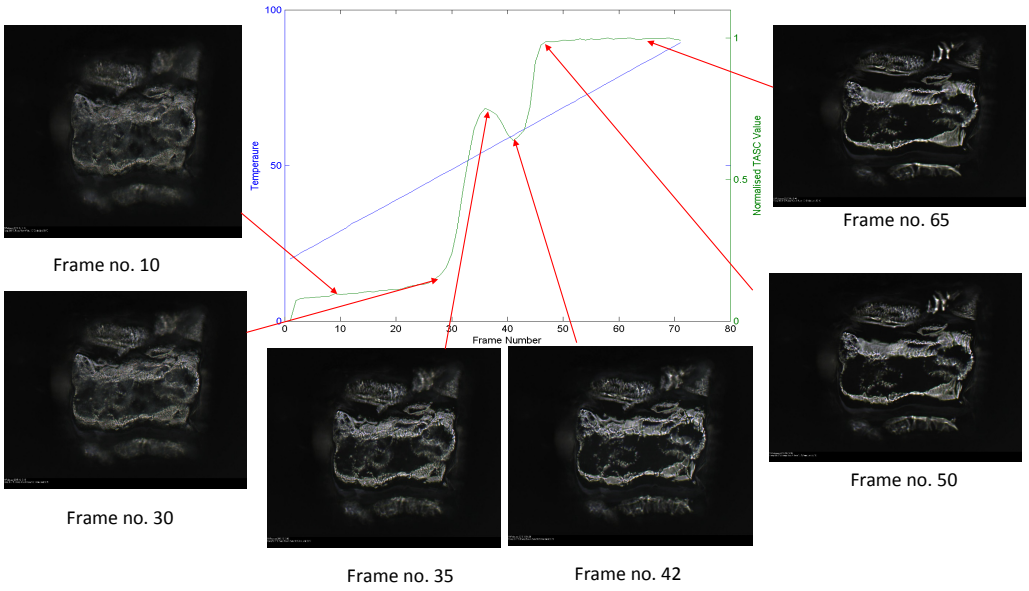

Figure 5.13: Enhanced sensitivity for the detection of hidden thermal transitions. Optical images at different temperatures of the TASC measurement during heating of the PEG/PEO K900 based CM1 patch with 10% drug loading. The areas with no specular effect were chosen for the measurements

In order to further investigate the details of the samples' structure, MTDSC and VT-ATR-FTIR were used. The MTDSC data of the reheating cycle of the patch with 10% drug loading, shown in **Figure 5.14**, unambiguously confirms bimodal behaviour in both reversing and non-reversing signals at a temperature between 45 to 58 ºC, which are below the main melting of PEG-PEO K900 (62ºC). In the non-reversing signal, an endothermic (melting) followed by an exothermic (recrystallisation) peak can be clearly seen.

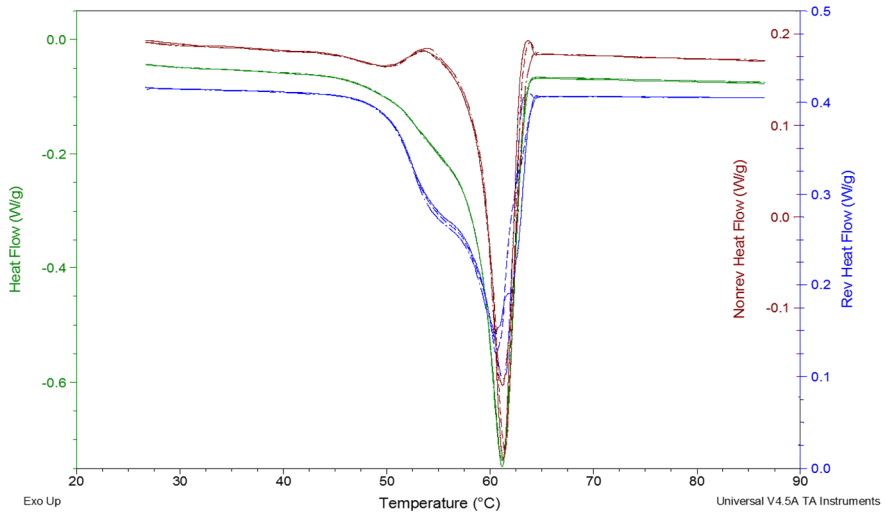

Figure 5.14: MTDSC results of the melting region of CM1 patches with 10% drug loading indicating the present of solid form transformation of PEG at the transition temperature identified by TASC during the reheating cycle (n=3)

The first heating cycle of the VT-ATR-FTIR data (**Figure 5.15a**) shows the melting of crystalline PEG-PEO K900 blend that agrees well with the spectra reported in the literature for these semi-crystalline polymers (328, 332). However, the spectra of the reheating cycle following the cooling of the first heating cycle, shown in **Figure 5.15b** (highlighted by the dash-line box and a red arrow), demonstrate the appearance of an additional peak at 1106 cm^{-1}. The intensity of this new peak decreases with increasing temperature during heating and disappears when the temperature reaches above 70°C when PEO K900 melts (**Figure 5.15c**). It suggests that the material created by the cooling cycle is different from the as-received material, something that is clearly indicated by TASC but is not immediately obvious from the DSC results. Although in literature there is no report of this particular IR band being associated with a metastable form of PEG, the thermal behaviour of the PEG detected by MTDSC matches the documented thermal events related to the metastable PEG (328, 332, 490). All these data confirm the presence of a metastable form of PEG after heating followed by immediately cooling which support the TASC data. It follows that in this case at least, TASC is sensitive to an event that conventional DSC does not clearly detect using the same heating rate at 10ºC/min. DSC shows only one process because the two melting events are broad and overlap. The reversing signal from the MTDSC experiment detected a two-stage process because it is sensitive to re-arrangement, in effect it is more directly influenced by the kinetics of the melting process than the total signal. It is reasonable to infer that these kinetics will influence the softening process; as melting starts there is an increase in fluidity but this is arrested because at least some recrystallisation occurs as the more stable form is created before it,

in turn, melts. In this way, TASC can follow the consequences of changing the structure on a length scale it cannot directly interrogate.

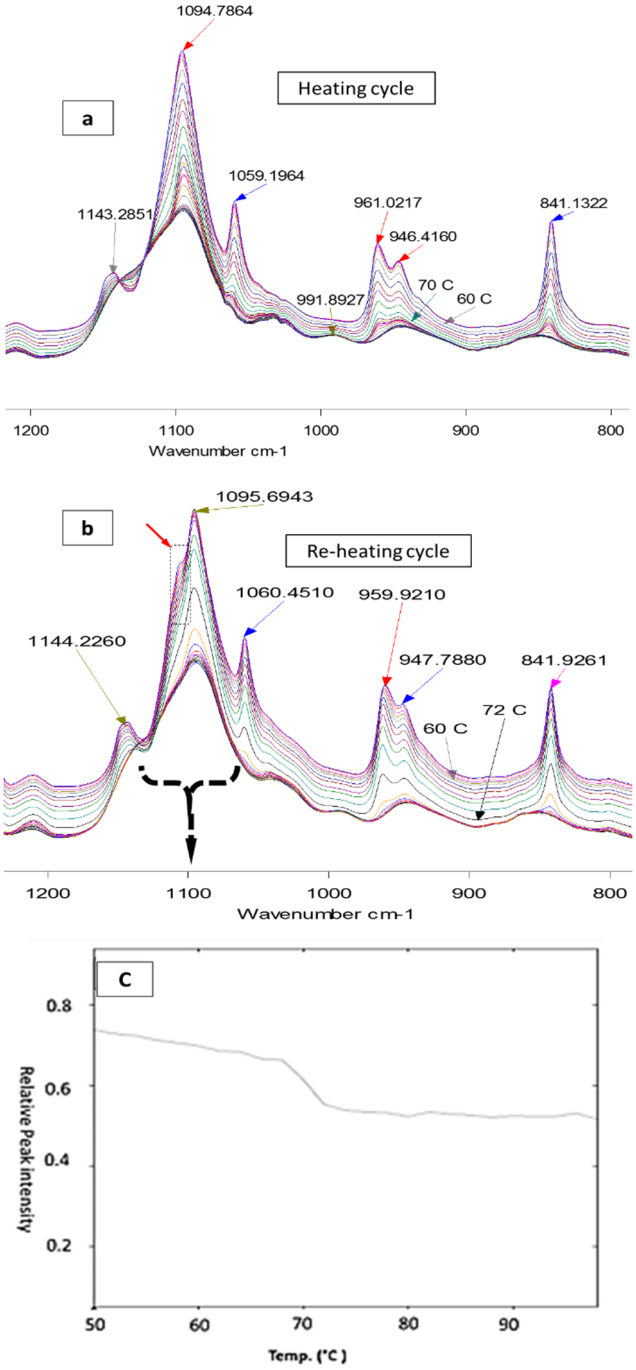

Figure 5.15: VT- ATR-FTIR spectra of the heating a and c reheating cycle of the CM1 10% loaded patches indicating the crystallisation and melting of the metastable form of PEG; and (d) the ATR-FTIR spectra intensity changes of the additional peak at 1106 cm^{-1} with temperature indicating the presence of metastable form PEG

5.3.1.4 Scanning rate effects on the detection sensitivity

Resolving events that have similar transition temperatures is typically more easily achieved at slow heating rates. This is particularly true when the events take place over a wide temperature interval and overlap. When using conventional DSC, low heating rates can improve resolution but decrease sensitivity; they also increase the time taken for the analysis. In **Figure 5.16** DSC results are shown in a variety of heating rates, they reflect the range typically used for routine DSC work, 10 to 40 ºC/min. In no case is a bimodal event detected. The TASC results detect the bimodal character of the sample's behaviour during the reheating segment even at the fastest heating rate. This suggests TASC is suitable for routine rapid analysis such as that often required for quality control without any reduction in sensitivity and resolution.

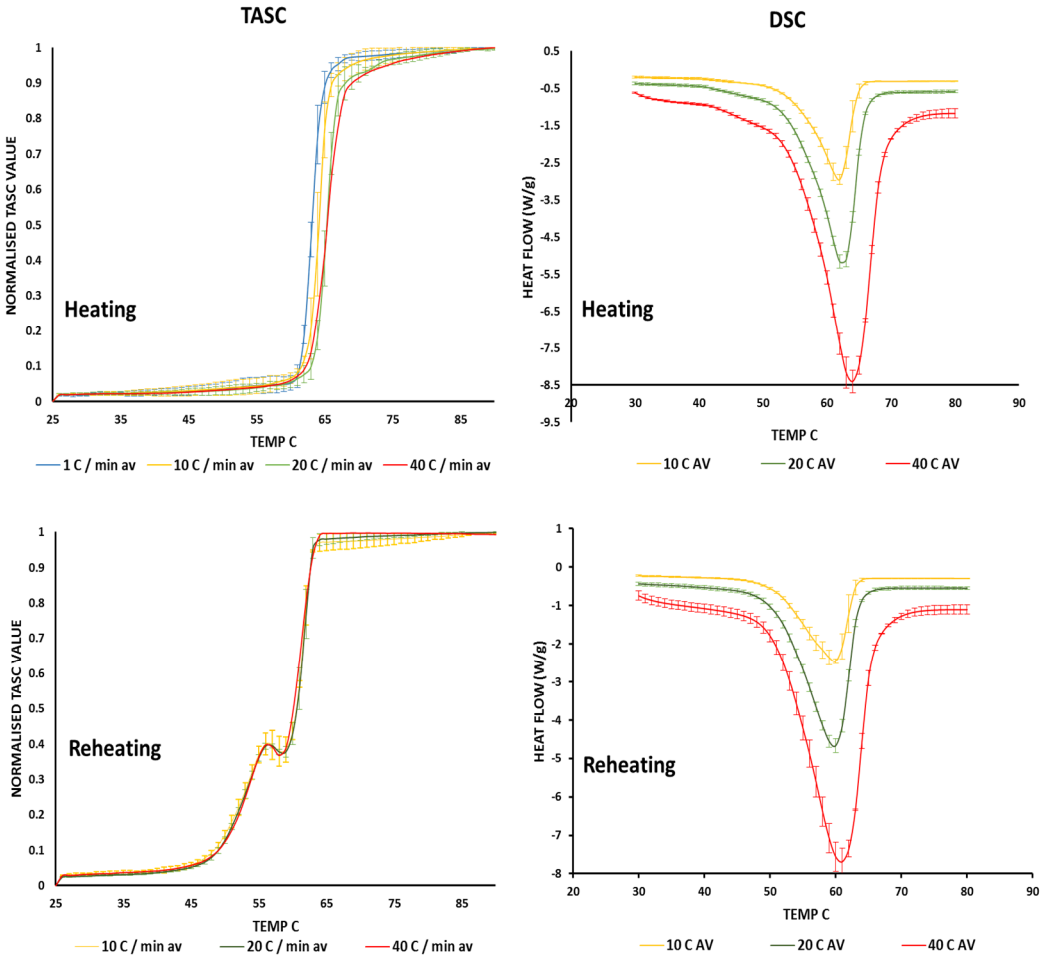

Figure 5.16: Influence of heating rate on TASC response in comparison to conventional DSC. CM1 patches loaded with 10% felodipine were tested using TASC and DSC at 10, 20 and 40ºC/min. First heating and reheating cycle were recorded and compared (n=3; average ± SD)

5.3.2 XμCT analysis of phase separations in the HME-IM patches

5.3.2.1 XμCT analysis of internal microstructure and spatial distribution of phase separations

It is well known in the literature that the surface and interior of many extruded samples exhibit significantly different features (483, 491). Therefore, XμCT was further used as a non-invasive method to study the 3D microstructure of the patches and to estimate the size, shape and spatial distribution of the phases in the prepared formulations. It is important to bear in mind that the spatial resolution of XμCT is limited to micron scale (which is 4 μm in this case). Thus nanoscale phase separation cannot be detected by this technique. Two XμCT types of equipment were used in the investigation of CM1 and CM2 formulations as mentioned in the experimental part of this chapter. The XμCT images of CM1 placebo and the patches with 10% drug loading (**Figure 5.17a-d**) revealed some dark and light blue colour distributed in the matrices of these samples. This effect is within the noise level of the measurement thus not a true feature of the samples. Therefore, no micron-scale phase separation is detected using micro-CT under the limit of detection of XμCT.

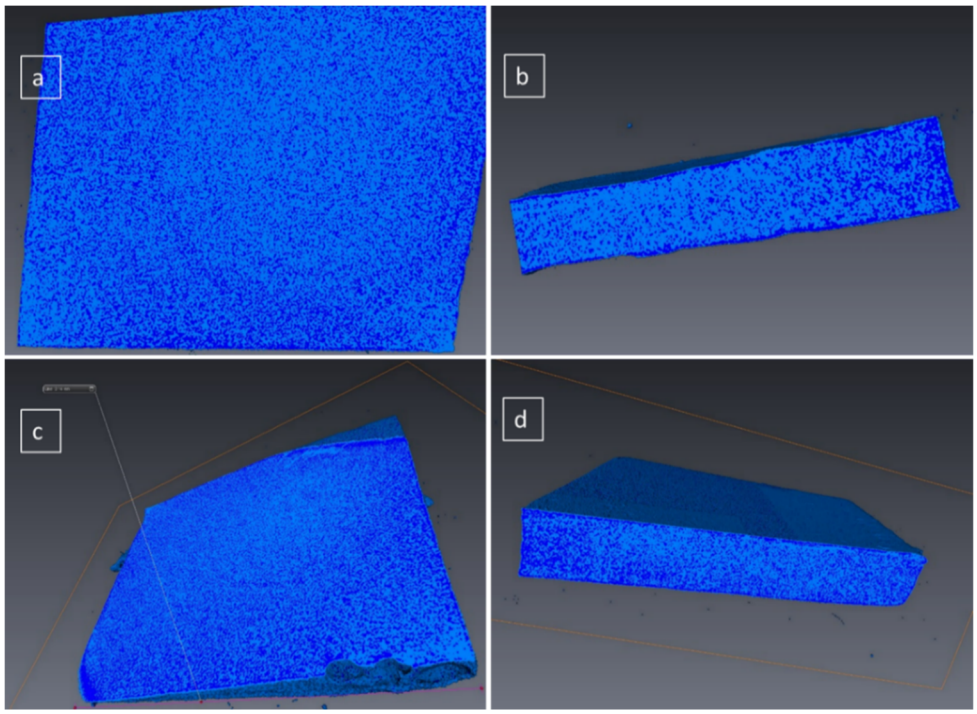

Figure 5.17: XμCT images of CM1 placebo surface and cross-section images (a, b) and CM1 10% surface and cross-section images (c, d)

With increasing the drug loading to 20% (w/w), large clusters (approximately 100 μm in diameter) and small (approximately 5-20 μm in diameter) particles with higher density (red dots and clusters) can be observed being predominately distributed at the surface and interior of the patches, respectively, as seen in **Figure 5.18**. The small particles are likely to be crystalline felodipine as crystalline material has higher density than the molecularly dispersed state and chlorine in the chemical structure of felodipine also provides improved electron density thus gives higher contrast in comparison to PEG, PEO K900 and Tween 80 (492). The presence of drug particles in the matrices agrees well with the SEM results shown in Chapter 4. The fact that significant amount of dense drug areas at the surface of the patches may be associated with the faster cooling rate at the surface after HME-IM, which promote the phase separation of drug from the matrix. This surface crystallisation phenomenon is also reported to present in other drug-polymer extrudates in the literature (483, 491). This important 3D spatial distribution of the phase separated drug particles cannot be observed using other conventional characterisation methods.

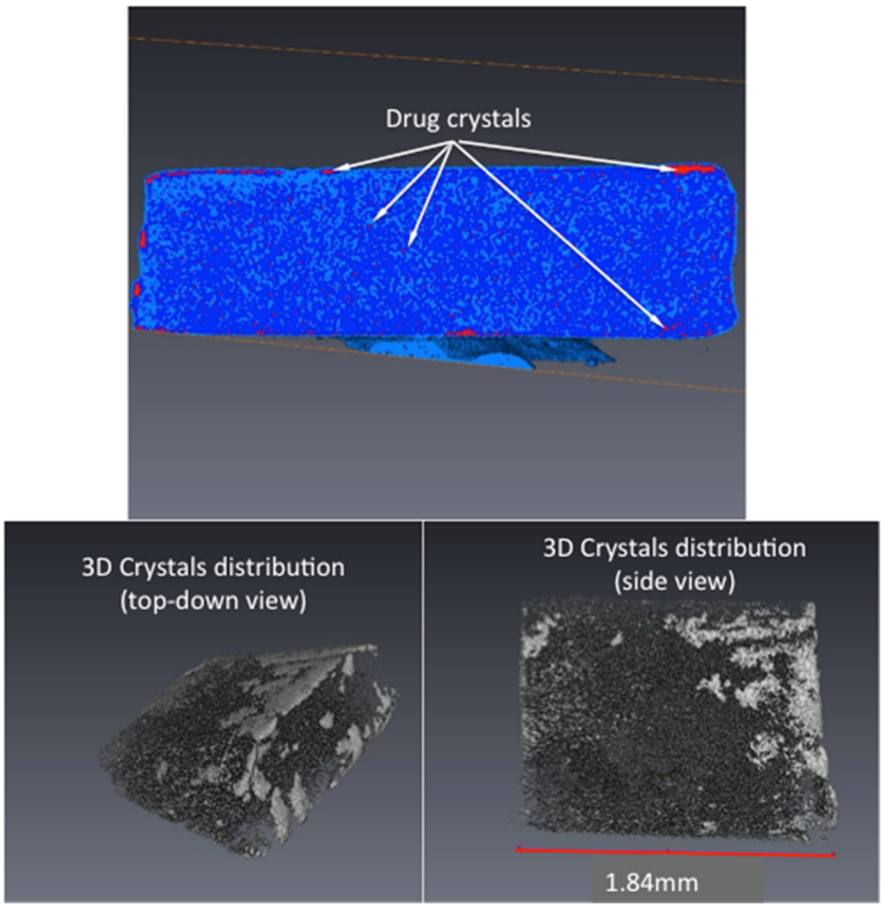

Figure 5.18: XμCT images of CM1 HME-IM patches containing 20% (w/w) felodipine

The XμCT images of the HME-IM patches with 30% drug loading (**Figure 5.19**) revealed rich interior features including evenly distributed air pockets and dense drug particles with a larger particle size (approximately at or below 150 μm) than the ones observed in the patches with 20% loading. It is also possible to distinguish phases with different densities (discontinuous light blue having a lower density and dark blue having a higher density). It is interesting to note that the dense drug particles are mostly distributed in the dark blue phases and many located at the edges of air pockets. According to literature data, the true density of PEG and PEO K900 are 1.15-1.21g/mL and 1.3g/mL at 25°C, respectively, whereas Tween 80 has a true density of 1.064g/mL (348, 493, 494). Taking into account the previous results indicating the low miscibility of Tween 80 and PEG-PEO K900, it is reasonable to argue that the light blue phases, with an average diameter of 250-750 μm are Tween 80 rich phases and the dark blue areas are PEG-PEO K900 rich phases. As the solubility of felodipine in PEG-PEO K900 is limited by the low quantity of amorphous polymer, it is possible that the drug dissolved in the PEG-PEO-rich phase during melt extrusion at an elevated temperature above the melting of PEG-PEO K900 and crystallised out when the patches cooled and equilibrated at room temperature.

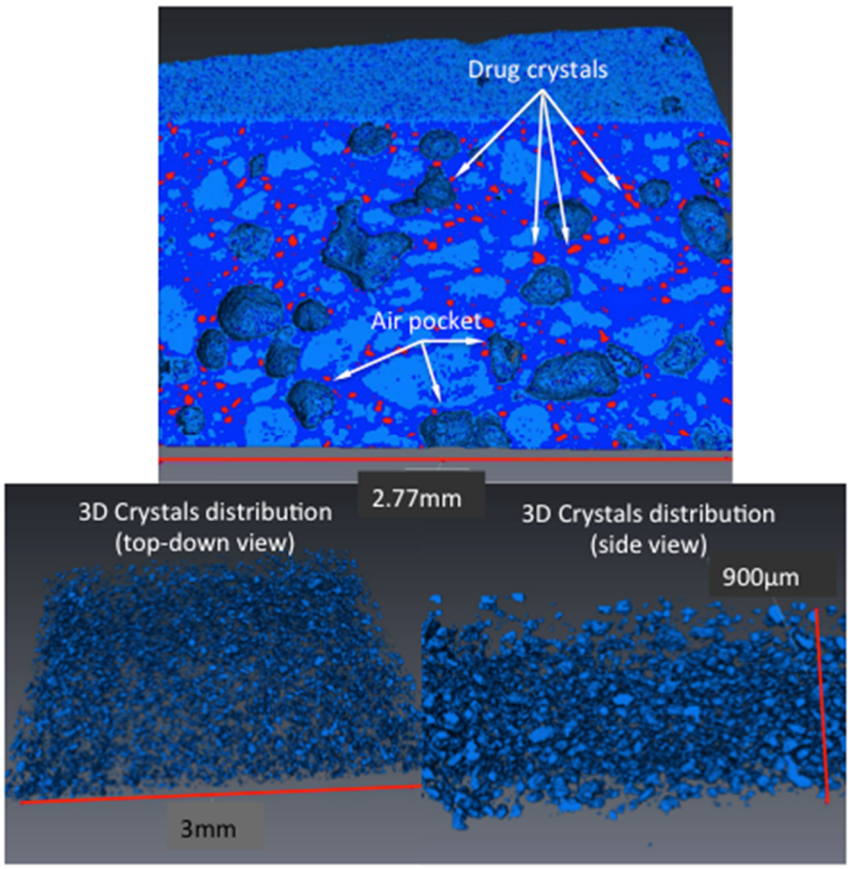

Figure 5.19: XμCT images HME-IM CM1 patches containing 30% (w/w) felodipine.

XμCT analysis of CM2 placebo patches revealed that they are pore-free with little interior microstructure at the resolution used in XμCT (**Figure 5.20**)

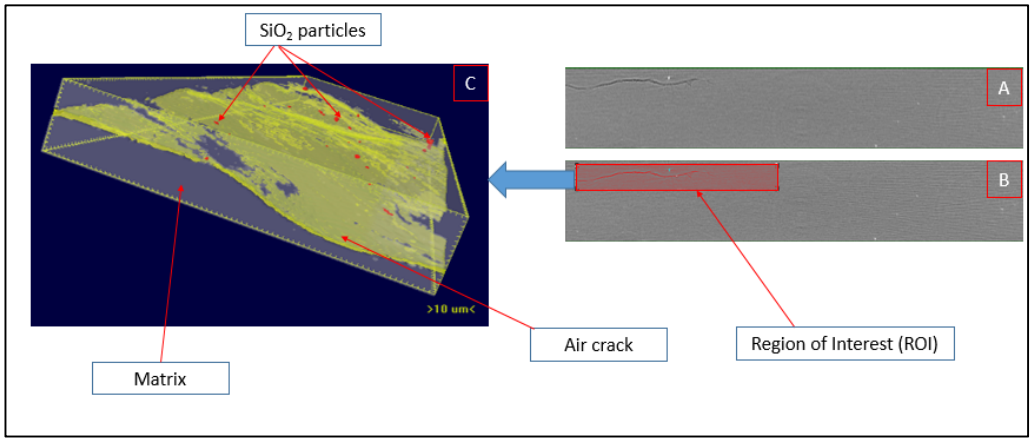

Figure 5.20: XμCT analysis of CM2 placebo sample; A) an example of a reconstructed binary image; B) selected Region of Interest (ROI) for analysis C) 3D object representing the different components according to their densities present in the selected ROI

At 10 and 20% drug loading, some internal air pockets are evident as seen in **Figure 5.21**. These occasional air pockets have no defined structure. With increasing the drug loading, the volume fraction of the patches occupied by the air voids was also increased. The few particles with high density shown as bright spots in the matrix were identified as silicone dioxide (SiO_2) (with a density of 2.65 g/mL), which is an inorganic material present in the powder of PEO K900 at a concentration of 0.8-3 % w/w as a powder flowability enhancer (495).

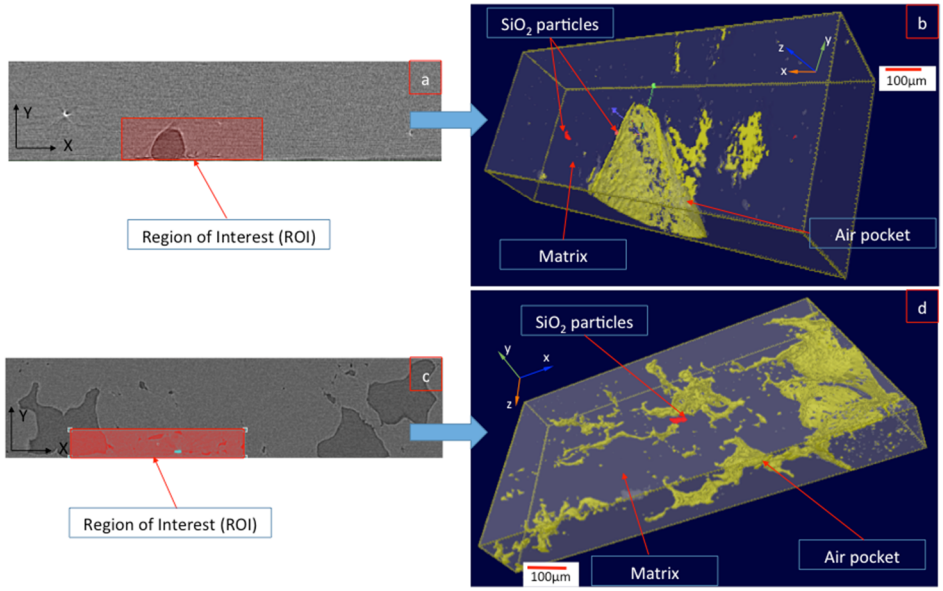

Figure 5.21: (a) XμCT reconstruction of binary image of 10% CM2 loaded sample with selected Region of Interest (ROI) for analysis; b) 3D object representing the different components according to their densities present in the selected ROI; (c) XμCT reconstruction of binary image of 20% CM2 loaded patches with selected Region of Interest (ROI) for analysis; d) 3D object representing the different components according to their densities present in the selected ROI

No other phase separation can be observed in these patches with 10 and 20% drug loading. Although DSC and TASC confirmed the presence of separate TPGS and PEG-PEO K900 phases, both are organic materials with similar elemental composition in their structure which provide no electron density contrast that can be used in XμCT to resolve the different phases. Felodipine has chlorine atoms in its structure which have higher electron density compared to the elements in the excipients. When felodipine dissolved in the excipients as a molecular dispersion, the overall electron density of the local area will be elevated by the presence of felodipine. The fact that no isolated drug clusters can be identified using XμCT for these two patches indicates that felodipine is relatively evenly distributed across the patches. It should also be mentioned that the spatial resolution of XμCT used in this study is within the micron range. Therefore, if any drug clusters occur with sizes smaller than few microns, they would not be detectable by XμCT.

As seen in **Figure 5.22**, the XμCT images of the CM2 patches with 30% drug loading show the presence of clear drug clusters and air voids with well-defined spherical shape. As PXRD and ATR-FTIR spectroscopy results (as mentioned in Chapter 4) indicated the presence of the crystalline drug, it can be stated with some confidence that these drug clusters, represent the crystalline felodipine particles and be described as crystalline drug particles in the following discussions. The crystalline drug particles are 10-20 μm in diameter, which is similar to the

crystals observed using SEM in Chapter 4.

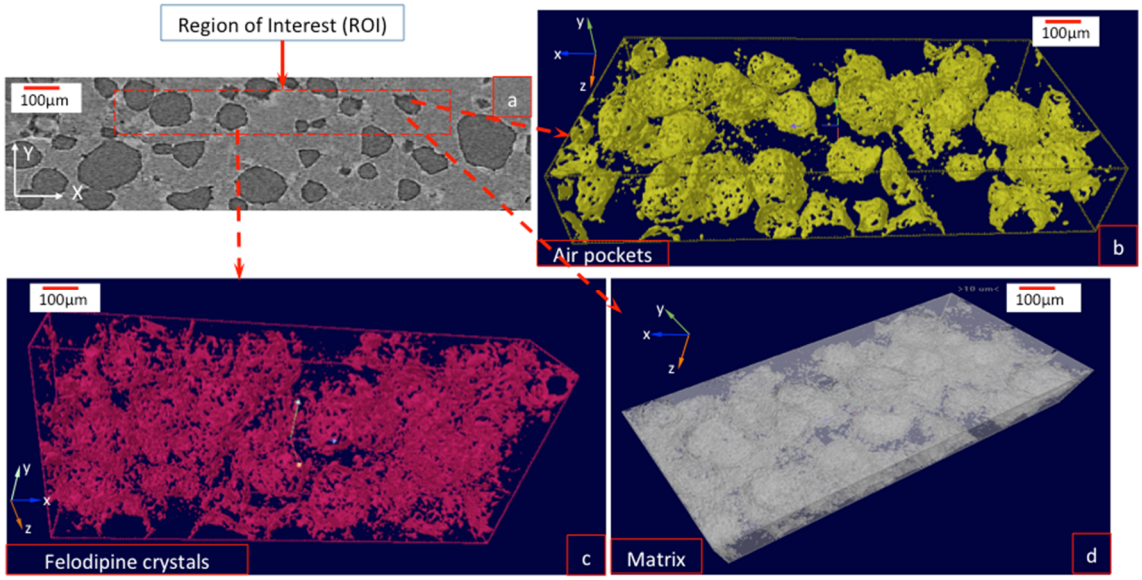

Figure 5.22: XμCT analysis of CM2 30% loaded sample; a) an example of reconstructed binary image with selected Region of Interest (ROI) for analysis b) 3D object representing the air pockets entrapped in the sample; c) 3D object representing the phase separated crystalline felodipine particles; d) 3D object representing the matrix

As seen in **Figure 5.22a**, the crystals (light spots) are more frequently distributed at the interfaces between the air voids and the matrix. This is an interesting feature which was not detected by any other characterisation method used in this study. The DSC results indicate that felodipine has a higher miscibility with TPGS than PEG-PEO K900 and hence drug crystallisation after reaching supersaturation is more likely to occur in PEG-PEO K900-rich domains than in TPGS-rich domains. Therefore, it is reasonable to speculate that these crystalline felodipine-rich areas around the air pockets are also PEG-PEO K900 rich regions.

5.3.2.2 XμCT analysis as a potential semi-quantitative method to study crystalline drug content

In order to further explore the possibility of using XμCT as a quantitative method for characterising phase separation in solid dispersions, compressed compacts of CM2 physical mixes of crystalline felodipine with known drug content (the same drug content as was used in CM2 patches) were prepared and analysed. As seen in **Figure 5.23**, crystalline felodipine particles are evenly distributed across the matrices. The volume fraction of the space occupied by the

crystalline drug particles can be measured and the values for the compacts with 10-60% crystalline drug loading were plotted against their known drug contents (**Figure 5.23d**). It was noted that the linearity of the correlation was not ideal (with a regression R^2 of 0.92). Therefore, these results should be regarded as semi-quantitative. It was noted that the compacts were much softer after compression than normal solid tablets and the surfaces of the compacts were slightly tacky. This softening indicates the lowered melting point of the mixture which could be caused by solubilisation of crystalline drug in the low melting excipients such as TPGS during the high-pressure compression process. This may explain why the 60% drug loaded physical mixture shows more deviation from the linear correlation in comparison to results obtained from the 10-40% drug loaded physical mixtures. Using systems that do not have dissolution or physical form changes of the drug during compaction with excipients may improve the accuracy and linear correlation between drug loading and XμCT measured volume. Nevertheless, the attempt of using the correlation as a calibration curve was made to estimate the amount crystalline drug in the HME-IM CM2 patches with 30% drug loading.

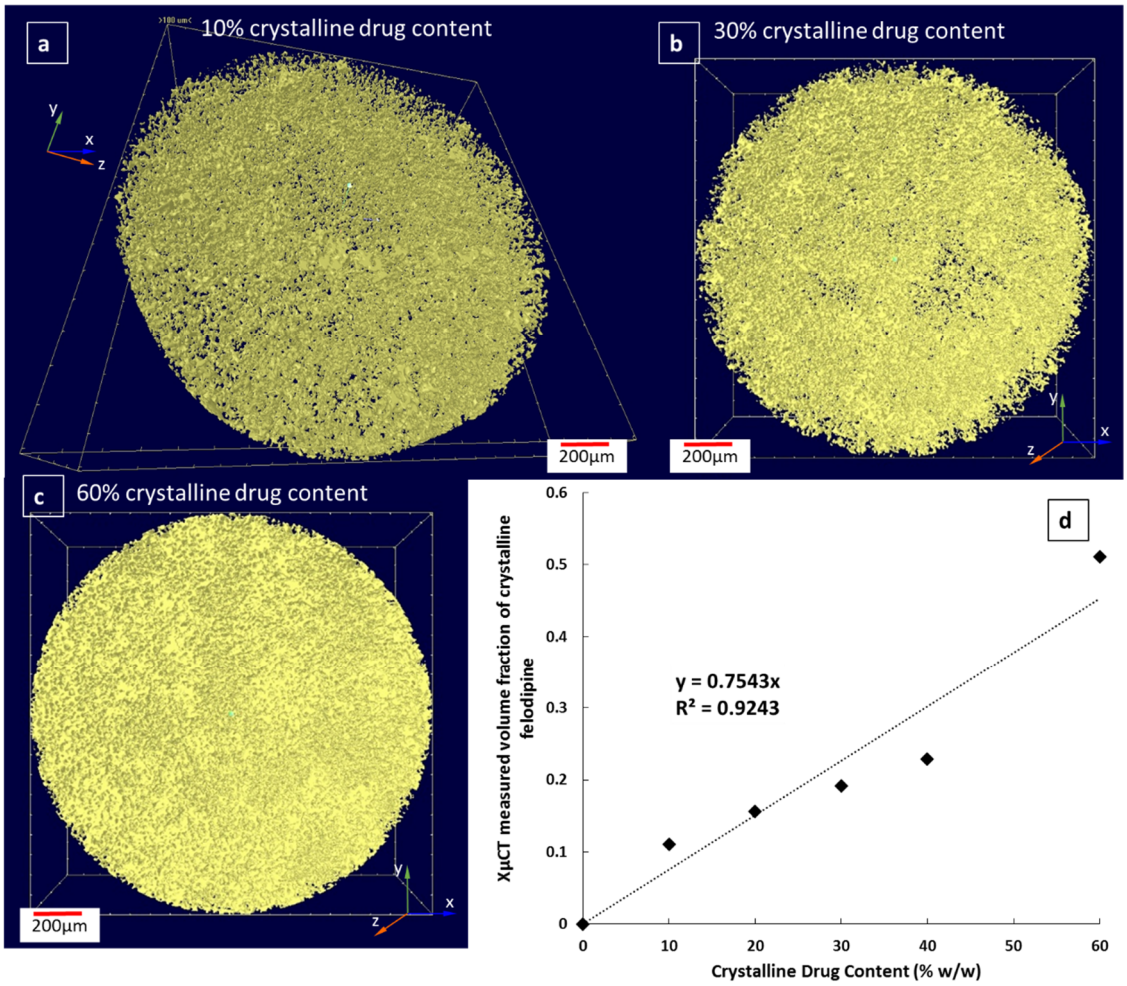

Figure 5.23: Representative 3D XμCT images of the distribution of crystalline felodipine in the compacts made of the physical mixes of crystalline felodipine-TPGS-PEG-PEO K900 with (a) 10%; (b) 30%; and (c) 60% crystalline felodipine loadings. (d) the correlation between crystalline drug content in these compacts and measured volume fraction of felodipine in their 3D XμCT images, which was used as a calibration curve for the quantitative estimation of crystalline felodipine in HME-IM patches with 30% drug loading

The volume fraction of the crystalline drug particles in the 30% CM2 patches observed in **Figure 5.22** is 0.078. Using the linear correlation shown in **Figure 5.23d** the weight fraction of the crystalline drug can be calculated as 10.3% (w/w). This indicates that 19.7% felodipine was molecularly dispersed in the matrices in the HME-IM CM2 patches with 30% drug loading. As no crystalline drug was detected in the HME-IM patches with 20% drug loading, it indicates that the 20% is close to the saturation of the solubility of felodipine in the matrices. Therefore, for the patches with 30% loading, approximately 10% w/w drug should be phase separated as a crystalline drug. The XμCT quantitative estimation agrees well with this.

5.3.3 Comparison of heterogeneity assessment by XμCT and TASC

The heterogeneity of CM2 patches with 30% drug loading was studied using XμCT in order to make a comparison with the measurements on heterogeneity performed by TASC. The same methodology used with TASC for measuring heterogeneity was adapted, and areas of interests (ROI) with various sizes were taken from 2D XμCT images. Using the quantitative calibration described above, the amount of crystalline felodipine in each ROI were calculated. As shown in **Figure 5.24a**, a single XμCT slice (grey scale image) was used and 6 small (100 × 100 μm equivalent to 10×10^{-3} mm^2) ROIs and 6 large ROIs (300 × 300 μm equivalent to 90×10^{-3} mm^2) were randomly selected and analysed. These areas are similar in size to the ones used in TASC measurements. Same thresholding procedure was adapted for the estimation of the volume fraction of phase separated crystalline felodipine in all of these ROIs. It can be seen in **Figure 5.24b** that the amounts of crystalline felodipine measured in larger ROIs have a lower standard deviation in comparison to those measured in the smaller ROIs indicating the high heterogeneity at the scale of 100 × 100 μm. These findings agree well with the results obtained by TASC and confirm that integrating large areas reduces the sensitivity to heterogeneity and explained why heterogeneity is not detected by DSC analysis.

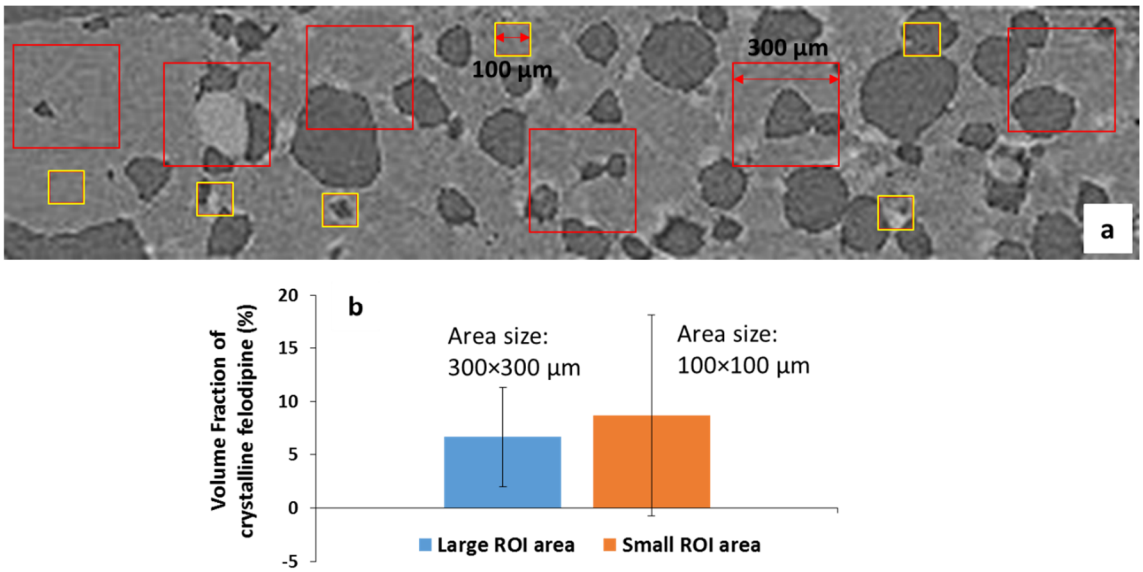

Figure 5.24: Estimation of heterogeneity by XμCT: (a) Illustration of the selection of a range of ROIs with different sizes on a representative 2D XμCT image of CM2 patches with 30% drug loading; (b) the comparison of the calculated volume fraction of crystalline felodipine in the ROIs with large (300×300 μm) and small (100×100 μm) areas

5.4 Discussion

Formulating solid dispersions of poorly water soluble drugs using HME-IM as single step processing is an attractive approach for improving their dissolution properties with fast and environmentally friendly processing. However, in order to achieve the desired formulation features of the product such as systemic delivery via the buccal cavity in this study, it requires the inclusion of a number of excipients resulting in an increase in the complexity of the system. In Chapter 4, two sets of HME-IM mucoadhesive buccal patches were designed and characterised using conventional characterisation techniques like DSC, MTDSC, ATR-FTIR, SEM, EDS, PXRD and IR imaging. Due to the nature of the fabricated systems being intentionally phase separated to provide surfactant-rich solubilisation and stabilisation domains for felodipine, it is important to further investigate the heterogeneity of the different phases and their microstructure spatial distribution. This chapter investigated the effect of drug-excipient miscibility on the heterogeneity and spatial distribution of phase separation in pharmaceutical solid dispersions at a micron-scale using two novel and complementary characterisation techniques, TASC and XμCT, to provide complimentary information in conjunction with conventional characterisation methods used in Chapter 4.

As a recently developed characterisation technique, TASC was used to assess the heterogeneity of placebo and felodipine loaded HME-IM patches. As a rapid and cheap technique, TASC revealed the melting transitions of the PEG-PEO K900 and/or TPGS separate phases in the different CM1 and CM2 formulations. CM1 samples up to 20% w/w loading have homogeneous microstructure compared to 30% w/w loading. In addition, increasing the loading percentage of the drug in CM2 blend up to 20%, the TPGS phase is reduced in intensity and shifted to lower temperature compared to the PEG-PEO K900 phase. This may indicate the solubilisation of the drug in TPGS phase is more than that in PEG-PEO K900 phase. However, increasing the loading percentage to 30% in CM2 mixture resulting in an increase in the intensity of the TPGS peak revealing the phase separation of the crystalline fraction of felodipine from this phase.

Due to the low melting transitions of the components of both CM1 and CM2 HME-IM mixtures, melting transition of the crystalline fraction cannot be detected using standard DSC experiments due to the thermal dissolution during the heating ramp. However, using TASC, it was possible to detected thermal dissolution due to the ability to detect changes before reaching equilibrium. Reaching the plateau with TASC signal indicates that the system in a state of equilibrium. Placebo and 10% loaded CM1 and CM2 samples reach the sharp plateau revealing that equilibrium was

achieved after the melting of PEG-PEO K900 polymer blend. The less sharp plateau was detected with 20% loading of both mixtures indicates the small fraction of crystalline drug present in the formulations. However, failure to achieve the equilibrium compared to lower loadings significantly indicate the presence of considerable amount of crystalline drug in the matrices of both CM1 and CM2 blends. Using this analysis, it would be possible to detect the thermal dissolution of the drug in the molten carrier and consequently assess the saturation limits of the carrier for a particular drug. This hidden thermal dissolution can be easily detected using this technique compared to DSC as the complete dissolution of felodipine is only achieved when the TASC signal reaches the plateau which is also confirmed by VT-ATR-FTIR using 30% CM1 sample. In addition, because TASC can perform microscale thermal analysis for the sample using single experiment with multiple data-based analysis which can be considered as time and cost saving approach, it could be possible to detect microscale heterogeneity of the samples. Reproducibility of TASC signal indicates microscale homogeneity as seen in the case of placebo and loaded patches up to 20% loading. However, the signals of the 30% loading were irreproducible resulting in large error bars representing intra- and inter- sample variations. The heterogeneous distribution of crystalline fraction is more likely the cause of the lack of reproducibility of the samples. The detected heterogeneity of 30% CM1 patches was higher compared to CM2 reflected by the lower reproducibility of former than the later indicating more drug phase separation and lower solubilisation capacity in CM1 compared to CM2 blend. Furthermore, the reheating cycles of TASC analysis were sensitive for the detection of metastable folded forms of PEG 4000 which is not observable using DSC using the same heating rate. It should be mentioned that the results collected by TASC analysis are not affected by the heating rate indicating the potential of this thermal analysis technique for achieving the same results as DSC at shorter time without a decrease in the sensitivity.

Using previous characterisation techniques revealed valuable information about the microstructure of the samples. However, the spatial distribution of phases cannot be revealed by any of the aforementioned techniques. XμCT was used as a novel technique to detect and simulate the distribution of phase separate solid dispersions using the difference in their electron densities. The distribution of crystalline felodipine predominately in the PEG-PEO K900-rich phase is not detected by any other characterisation methods but XμCT. This observation can be explained by the difference in the solubility values of felodipine in Tween 80 and semi-crystalline PEG-PEO K900. XμCT results not only confirmed the findings from the thermal and spectroscopic methods but also allowed the estimations of the size, shape and spatial distribution of different phases and revealed the distinct interior microstructure difference between dispersions with different drug

loadings. Due to the similarity in density between the PEG-PEO K900 and TPGS phases and the possible nanoscale phase separation, XμCT was unable to detect the phase separation of the different phases of the carrier. However, the high electron density of felodipine compared to the other components of the carrier mixture, crystalline drug fraction in 30% loaded samples can be thresholded and represented in 3D views together with some processing malfunctions such as the presence of air voids and heavy metal impurities. In addition, this study also explored the use of felodipine physical mixtures compacted discs loaded with 0-60% w/w that can be used as a calibration curve of the crystalline fraction of felodipine. Using this method, the fraction of crystalline felodipine in 30% loaded patches was estimated semiquantitatively and found to be 10.3% w/w.

5.5 Conclusion

This chapter introduces the use of two novel characterisation methods for studying phase separation behaviour in pharmaceutical solid dispersions, TASC and XμCT. The characterisation techniques were challenged by the set of complex multi-component solid dispersions studied in Chapter 4. The results confirmed that both techniques not only could provide complementary information to conventional characterisation tools, including DSC, MTDSC, PXRD, ATR-FTIR, SEM and EDS to reveal the correlation between drug-excipient miscibility and phase separation but also are able to provide a new and important understanding of the heterogeneity and distribution of separate phases in the systems. TASC allowed rapid identification of heterogeneity in the dispersions containing phase separation but does not have the capability of analysing the spatial distribution of the phases. As a non-destructive technique, XμCT analysis provided the 3D microstructure of the interior of the patches and the spatial distribution of the separated phases. This detailed understanding of the dispersions will provide confidence in product quality of dispersions formulations. However, it should be highlighted that XμCT cannot be used as identification method on its own for distinguishing crystalline and amorphous drug domains. The first attempt of using XμCT as a quantitative method to estimate phase separated drug clusters (identified as crystalline drug with confirmation by PXRD and ATR-FTIR) in processed formulations indicated its potential application for such purposes. However, the results reported here can only be regarded as semi-quantitative. Further studies are needed to validate XμCT as a quantitative method.

Chapter 6. Effect of surfactants on the physical stability of solid dispersions and felodipine crystallisation

6.1 Introduction

Surfactants, such as Tween 80 and TPGS, have been suggested in the literature for use as plasticisers for HME based solid dispersions (200, 329, 361, 496, 497). In Chapter 4, the addition of a significant amount of surfactant was adapted as a strategy aiming to improve the solubility of the poorly soluble drugs in the matrix via creating phase separated surfactant concentrated drug solubilisation compartments (498, 499). However, it was reported that surfactants can destabilise the drug and cause crystallisation of drug from the dispersions during storage (93, 201, 385, 500). The mechanism of this destabilising effect has been mainly attributed to the low T_g of such materials. It should be mentioned that the benefit of facilitating processing was described as often outweighing the minimal amount of destabilisation, thus the addition of surfactants is often recommended (201, 385, 501). However, there is no fully developed guidance for surfactant selection and how to minimise their destabilising effects in the literature.

This chapter aimed to contribute to a fuller understanding of the destabilisation effect of the use of surfactants in hot melt extruded formulations by investigating the stability of two types surfactant-containing hot melt injection moulded patches. CM1 and CM2 placebo and 10-30% w/w felodipine loaded HME-IM patches were used as surfactant containing solid dispersions in this chapter. Due to their complex phase behaviour resulting from the differences in the miscibilities between the individual constituents, their stabilities can be affected by storage temperature and relative humidity. Both of these storing conditions can affect molecular mobility in the formulations (97, 100). For the well-studied molecular dispersions of a binary polymer-drug system, a single global mobility is generally reflected by a single T_g. Water has a strong plasticising activity and moisture uptake from humid environment during storage is known to increase the global mobility of the system enhancing phase separation of the drug from its dispersion (106-110). In terms of storage temperature, as a general rule amorphous dispersions are stored at temperatures 50℃ below their T_g to minimise the crystallisation tendency of the drug (24). However, the effects of storage temperature are often more complex. For example, storing amorphous polymeric based solid dispersions at low temperatures can decrease the recrystallisation rate of the molecularly dispersed drug because of reduced molecular mobility. However, at lower temperatures, the miscibility of the polymer and drug is usually decreased leading to increased risks of increasing the degree of saturation of the drug in the dispersions (24, 105). When the supersaturation is reached, if the molecular mobility allows, the drug could still crystallise even at low temperatures. Therefore, the storage temperature may have a positive or

negative impact on the physical stability of the system under investigation depending on the balance between the speed of diffusion of the drug molecules and the thermodynamics of the mixing between the drug and the polymers.

In this study, the effects of humidity and/or temperature on the individual phases and overall stability of placebo and felodipine loaded CM1 and CM2 HME-IM patches was examined in order to provide an insight into the how the complex interplay of the effect of surfactants, the stability of the semi-crystalline carrier material and the degree of drug saturation in the formulation can impact on the stability of the entire dispersions.

Research objectives

1. To investigate the impacts of storing temperature and relative humidity on the stability of CM1 and CM2 placebo and 10-30% w/w felodipine patches.
2. To understand the effect of surfactants on the stability of different formulations.
3. To compare the two formulations to provide good understanding of the selection criteria that governs the suitability of surfactants for solid dispersions prepared by HME-IM technique.
4. To assess the crystallisation tendency of felodipine from formulations at different conditions and evaluating the most important parameters that control the crystallisation process.

6.2 Materials and Methods

6.2.1 Materials

The raw materials used for the fabrication of placebo and felodipine loaded CM1 and CM2 HME-IM buccal patches were the same as those mentioned in Chapter 4, section 4.2.1 except for using different batch no. of felodipine (20100601) from the same supplier. Phosphorus pentoxide (P_2O_5) 99.0 % was ordered from Sigma-Aldrich (Dorset, UK) and NaCl extra pure (≥ 99.0 %) was purchased from Thermo Fisher Scientific (Geel, Belgium).

6.2.2 Methods

6.2.2.1 Storage conditions for HME-IM patches and amorphous felodipine

After the preparation of the placebo and drug loaded HME-IM patches (as described in Chapter 4, section 4.2.2), they were immediately stored at four different conditions of temperature and relative humidity (%RH): room temperature and 0% RH (condition A), room temperature and 75 % RH (condition B), 40℃ and 0% RH (condition C) and 40℃ and 75% RH (condition D). The conditions selected are the most likely used conditions for investigating the stability of pharmaceutical products. Storing jars containing phosphorus pentoxide (P_2O_5) were used to represent the 0% RH while supersaturated NaCl solution was used to provide the 75% RH. In order to investigate the dual effect of relative humidity and the temperature, two sets of the humidity conditioned jars (0 and 75%) were stored either at room temperature or incubated in an incubator (Genlab incubator, Genlab Ltd, Cheshire, UK) operating at 40℃. The stored samples were characterised to investigate the stability of the system especially the crystallisation tendency of felodipine. After incubation for 3 months, the samples were analysed to monitor the changes in each sample resulting from aging at each storing condition. Amorphous felodipine samples were immediately stored at 40℃ and 75% RH for 7 days after preparation (as described in Chapter 3, section 3.2.2.1) before characterisation using different techniques.

6.2.3 Characterisation of HME-IM aged solid dispersions

The HME-IM patches and amorphous felodipine were characterised using the SEM, DSC, ATR-FTIR, PXRD and TGA using the same methods previously described in Chapters' sections 3.2 and 4.2. EDS characterisation was performed using the same method described in Chapter 4.2 except for using single point X-ray acquisition mode (at least 3 points were analysed for each morphological feature such as crystals, matrix surface, matrix cross-section) instead of the mapping mode. The results obtained using DSC were statistically analysed using (ANOVA). Differences of $p < 0.05$ were considered to be significant.

6.3 Results

6.3.1 Effect of surfactant on the stability of semi-crystalline carrier in placebo patches

The addition of surfactant to a semicrystalline mixture of PEG and PEO K900 contains two phases: an amorphous phase and a crystalline phase may result in the formation of an extra phase(s) depending on the physical state of the surfactant and its miscibility in the amorphous fraction of the blend. As seen in **Figure 6.1 and 6.2**, in the fresh placebos both Tween and TPGS were phase separated as indicated by their detectable melting endothermic peaks at -10.3 ± 0.2 and 37.5 ± 0.1 °C, respectively. This implies that CM1 contains a liquid Tween surfactant phase at ambient temperature whereas CM2 contains a solid TPGS phase. The melting enthalpy values of pure Tween 80 and TPGS are known to be 45.53 ± 0.59 and 100.01 ± 1.09 J/g, respectively, it is possible to estimate the degree of crystallinity of the two surfactants in the freshly prepared placebo patches. These are for Tween in CM1 45.5% which is significantly less than the one of TPGS in CM2 (74.1%) with considering the fraction of each surfactant incorporated in the formulations. This result indicates that higher weight percentage of Tween is mixed with PEG-PEO K900 in the CM1 than TPGS in CM2. This difference in the physical state of the phase separated surfactant domains may affect the stability as the diffusion rate of drug molecules in the liquid state in general is faster than in solid and semi-solid environments which may promote faster nucleation and crystallisation of drug. The melting peaks of raw PEG and PEO K900 are 59.3 ± 0.3 and 70.2 ± 0.3 while their crystallinity are 87.6% and 84.1% calculated by dividing the melting enthalpy of studied samples by the melting enthalpy of fully crystalline polymers values obtained from the literature (449, 455, 456), which are 214.6 J/g and 205 J/g respectively. The PEG-PEO K900 melting points of the fresh placebo CM1 and CM2 samples are 63.6 ± 0.2 and 64.1 ± 0.3 respectively. The proportion of PEG to PEO K900 in both mixtures is 4:3 which means that the theoretical % of crystallinity is 86.1% assuming no interaction between the two polymers. The calculated % of crystallinity based on experimental results of PEG-PEO K900 polymers in placebo CM1 and CM2 were found to be 59.5% and 59.2% indicate a significant reduction in their crystallinity.

The DSC results of placebo CM1 samples are shown in **Figure 6.1**. It was noticed that all aged samples maintain their solid structures except the patches stored at 40°C/75%RH. Placebo CM1 patches stored at 40°C/75%RH lost their solid structure 'liquefied' after storage at condition D.

The liquefied samples show complex behaviour: a recrystallisation peak at about the crystallisation temperature of Tween 80. However, the enthalpy of the peak is 39.3 J/g which is much higher than 7.9 J/g the expected crystallisation enthalpy for Tween 80. A single endothermic phase transition at 33.5°C is also observed. There are no melting peaks of Tween and PEG-PEO K900. This indicates the presence of low molecular weight degradation products of PEG-PEO K900 which crystallise and form complexes with Tween at a lower temperature and subsequently melt at 33.5°C (144, 145, 502-505).

DSC investigation indicates that good physical stability of CM2 placebo under conditions A, B and C, but some changes after 3-month ageing under 40°C/75%RH (**Figure 6.2**). There are no significant changes in the TPGS phase. Two additional shoulder peaks at 55 and 59.5 °C are observed at the melting of PEG-PEO K900 phase which may be attributed to a small extent of degradation of PEG-PEO K900. The significantly less degradation of CM2 is highly likely to be associated with antioxidant nature of TPGS which protected PEG-PEO K900 from extensive oxidation (144, 207, 386, 387).

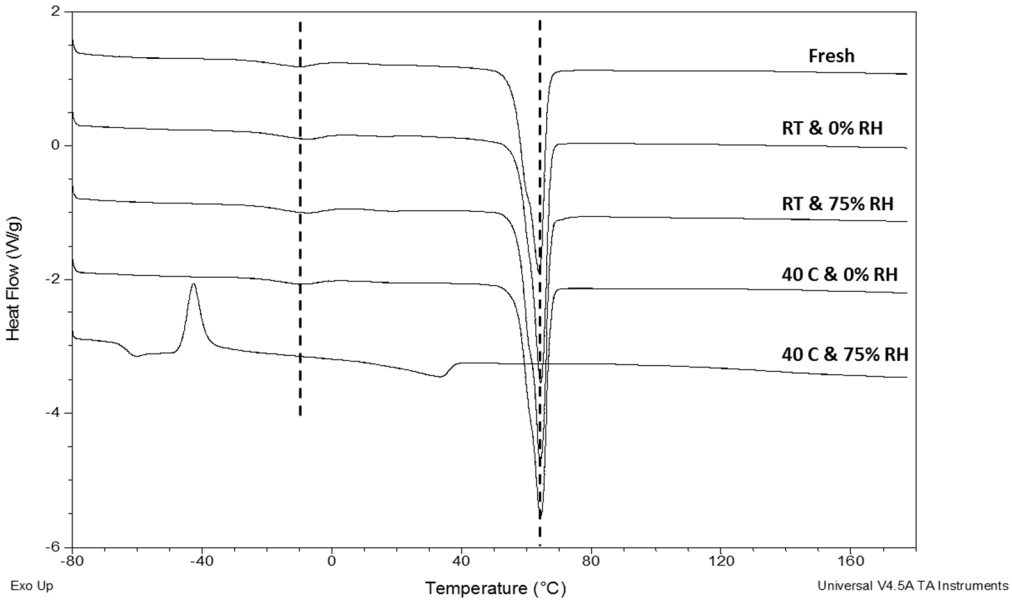

Figure 6.1: DSC thermograms of placebo CM1 fresh and aged samples using 10℃/ min (n=3)

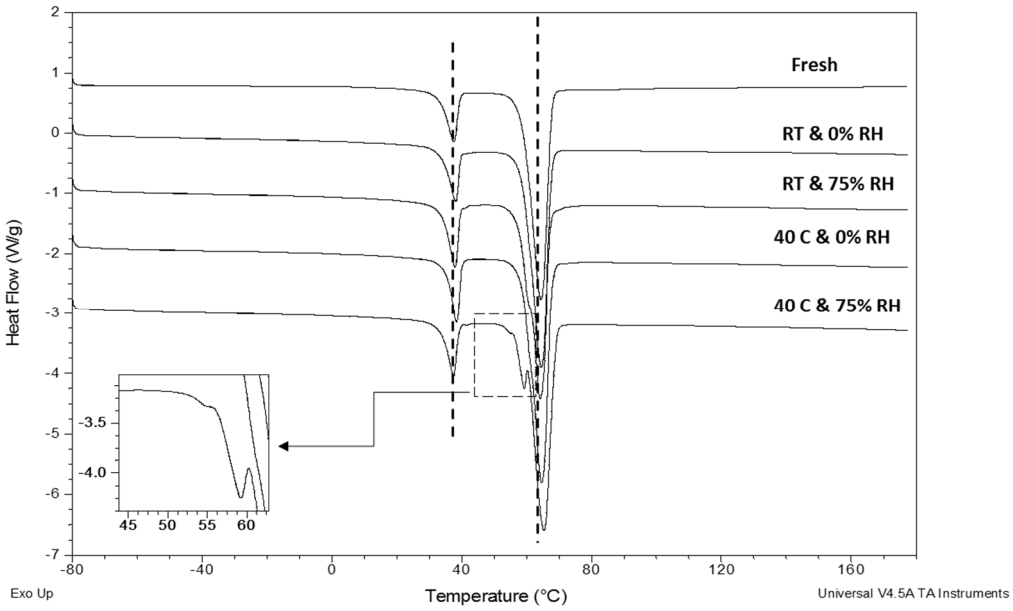

Figure 6.2: DSC thermograms of placebo CM2 fresh and aged samples using 10℃/ min (n=3)

After ageing, SEM images revealed no significant morphological changes for both placebo CM1 and CM2 at different ageing conditions (**Figures 6.3-4**) except for CM1 patches which lost their original shape and liquefied under 40ºC/75% RH (condition D).

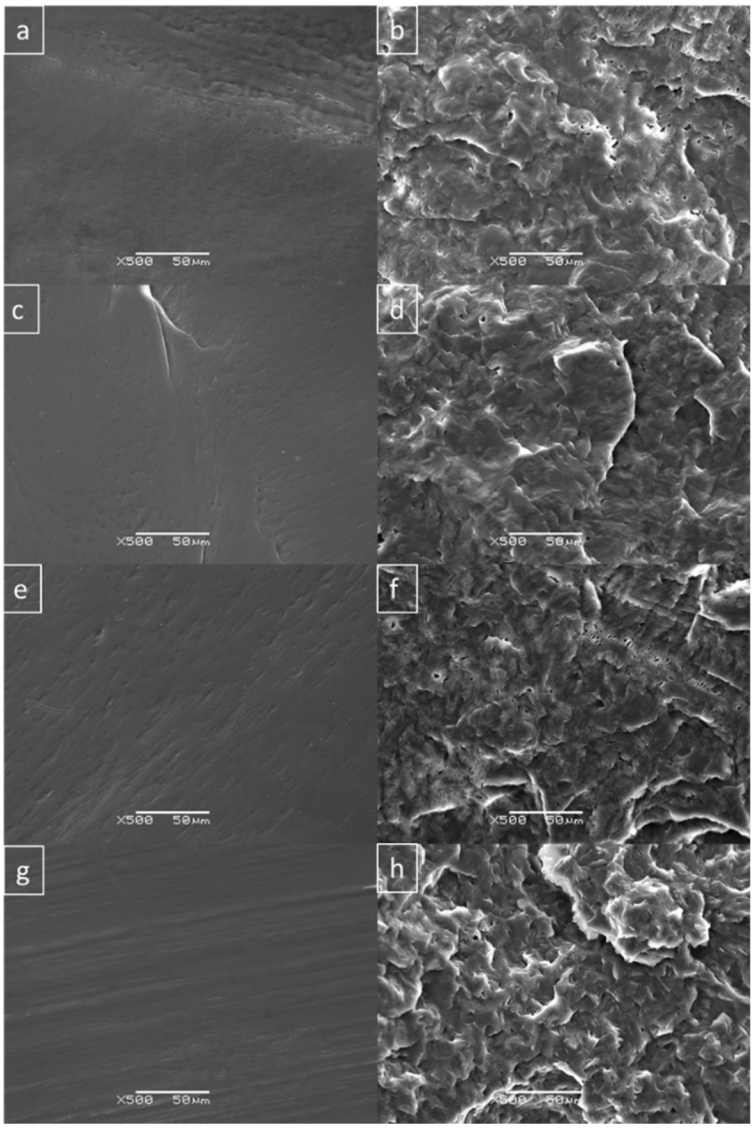

Figure 6.3: SEM images for CM1 placebo fresh and 3 months aged samples; (a and b) are surface and cross-section of fresh sample, (c and d) are surface and cross-section of sample stored at condition A, (e and f) are surface and cross-section of sample stored at condition B and (g and h) are surface and cross-section of sample stored at condition C

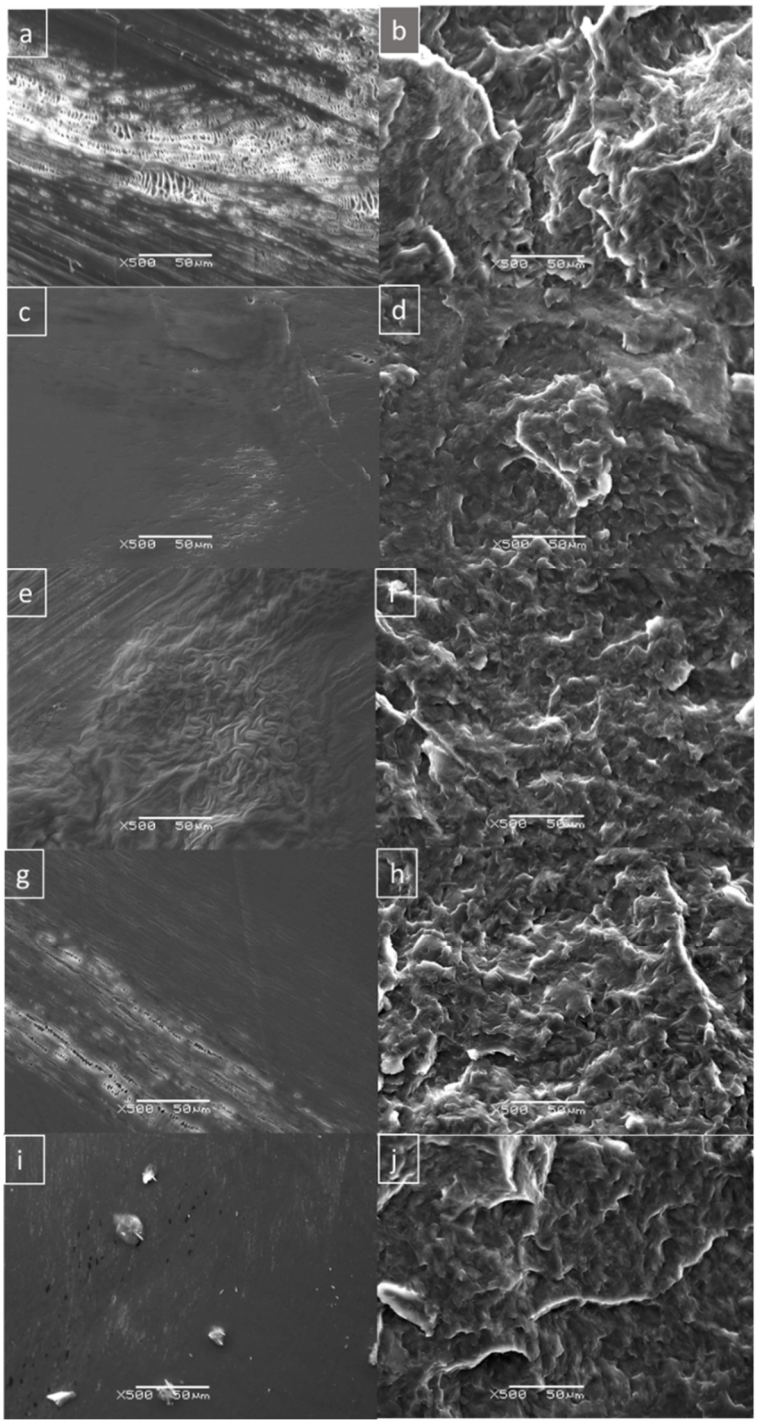

Figure 6.4: SEM images for CM2 placebo fresh and 3 months aged samples; (a and b) are surface and cross-section of fresh sample, (c and d) are surface and cross-section of sample stored at condition A, (e and f) are surface and cross-section of sample stored at condition B, (g and h) are surface and cross-section of sample stored at condition C, and (i and j) are surface and cross-section of sample stored at condition D

As mentined in Chapter 3, isohume (at 75%RH) DVS studies of Tween 80 and TPGS revealed that they could take up to 14.44 ± 0.89 % and 12.80 ± 0.72% w/w moistures, respectively, whereas PEG and PEO K900 only could take up less than 2% w/w moisture when reached equilibrium. Using these data, it is possible to estimate the theoretical moisture uptake of the two placebos (assuming of the ingredients have complete phase separation) being 5.35 ± 0.28 and 4.85 ± 0.23 % (w/w) for CM1 and CM2, respectively. As seen in **Figure 6.5** and **Table 6.1**, a significant amount of weight loss up to 100 °C (14.48 ± 1.28 % w/w) during TGA measurement was observed in the liquefied CM1 placebo after 3-month storage under 40ºC/75%RH. This is more than the theoretical amount of moisture uptake capacity estimated using the individual ingredient data. It is also noted that the weight loss of the 40ºC/75%RH aged CM1 placebo sharply increased by 5.44 % up to 150 °C. It is well-known in literature that Tween and PEG-PEO K900 exhibits thermally initiated autoxidation (143, 145, 206, 506, 507). Thus, this continued weight loss at temperature below the thermal decomposition temperatures of the constituents of the mixture (which are 376.3 ± 5.0, 369.3 ± 0.3 and 372.4 ± 0.8 °C for PEG, PEO and Tween 80, respectively) is likely to be attributed to the loss of low molecular weight degradation products during heating. It should be mentioned that the apparent weight gain at 0% RH samples is more likely due to moisture uptake in handling after removal of from the storage. The moisture uptake of CM2 placebo after 3-month at 40ºC/75%RH shows close to the theoretical estimation indicates TPGS exhibited its full capacity.

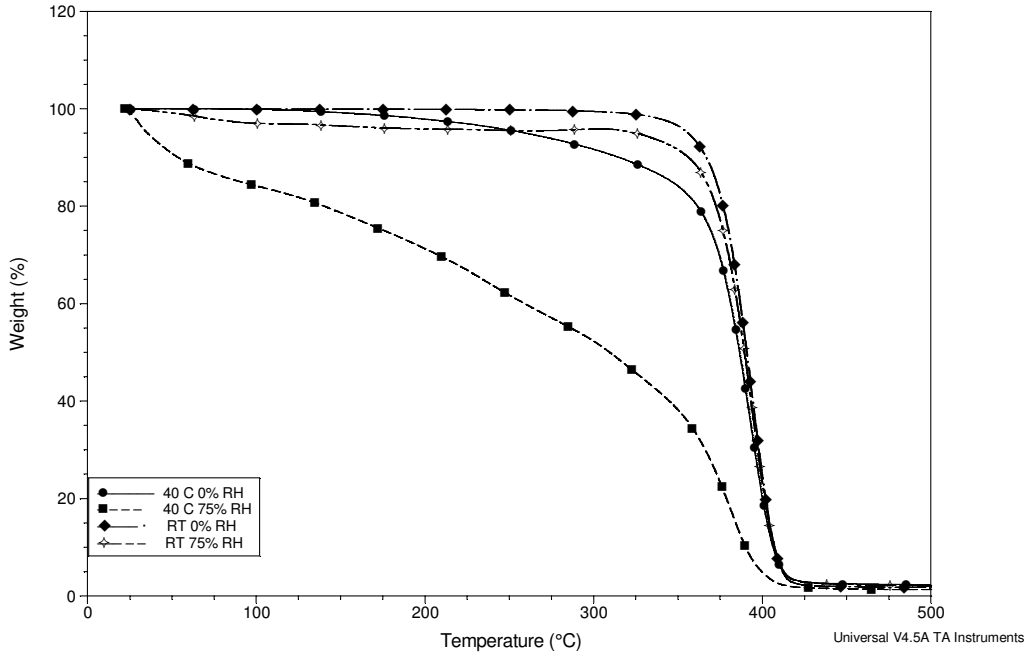

Figure 6.5: TGA results of 3-month aged CM1 placebo patches (n=3)

Table 6.1: Percentage of weight loss of the formulations measured by TGA after three months ageing (n=3, average ± SD)

Formulation	Condition A	Condition B	Condition C	Condition D
Placebo CM1	0.12 ± 0.00	2.6 ± 0.52	0.18 ± 0.10	14.48 ± 1.28
10% CM1	0.08 ± 0.04	5.00 ± 0.33	0.10 ± 0.05	3.40 ± 0.12
20% CM1	0.10 ± 0.01	2.99 ± 0.38	0.05 ± 0.03	3.32 ± 0.22
30% CM1	0.04 ± 0.00	2.48 ± 0.11	0.03 ± 0.00	2.43 ± 0.07
Placebo CM2	0.11 ± 0.03	3.02 ± 0.00	0.12 ± 0.03	3.40 ± 0.12
10% CM2	0.05 ± 0.01	2.67 ± 0.08	0.15 ± 0.06	3.37 ± 0.13
20% CM2	0.04 ± 0.01	2.14 ± 0.05	0.05 ± 0.01	2.73 ± 0.17
30% CM2	0.02 ± 0.02	1.74 ± 0.04	0.03 ± 0.00	1.90 ± 0.07

This is also supported by the ATR-FTIR spectrum of the sample seen in **Figure 6.6a and b**. The placebo CM1 sample after three months shows a broad band centred around 3409 cm^{-1} and new peaks at 1645 and 1750 cm^{-1}. The peaks at 1750 and 1645 cm^{-1} were assigned to water and carbonyl respectively. The broad peak is from water and hydroxyl groups. There is also a loss of resolution across the whole spectrum consistent with degradation and loss of crystallinity (145, 506).

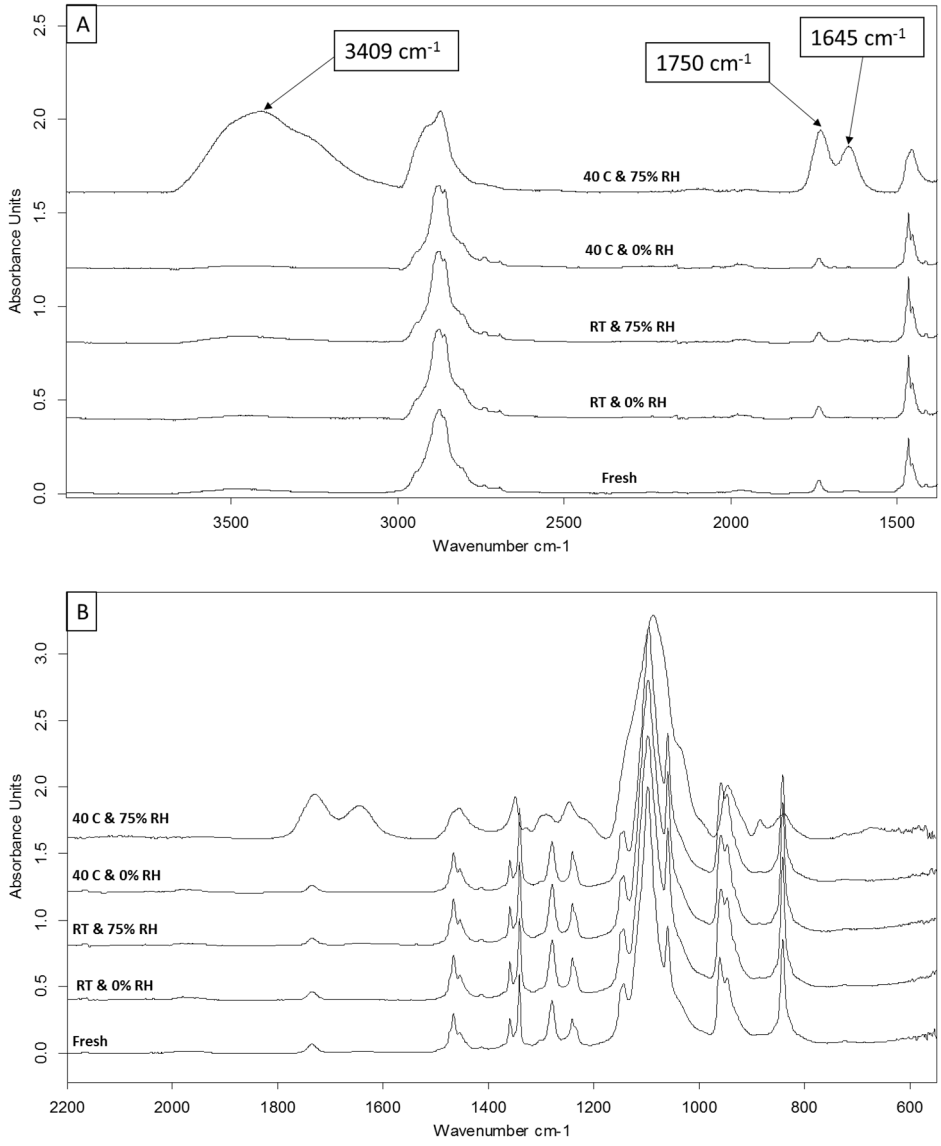

Figure 6.6: A) The high wavenumber and B) is the low wavenumber ATR-FTIR spectra of placebo CM1 fresh and aged samples (n=3)

6.3.2 Effect of drug loading on semi-crystalline carrier

The morphologies of the surfaces and cross-sections of the patches after drug incorporation (10-30% w/w) in both CM1 and CM2 blends can be seen in **Figure 6.7-12**. With increasing the drug loading for both formulations, the roughness of the samples increased. These figures will be used explain the crystallisation tendency of felodipine from aged samples later in this chapter.

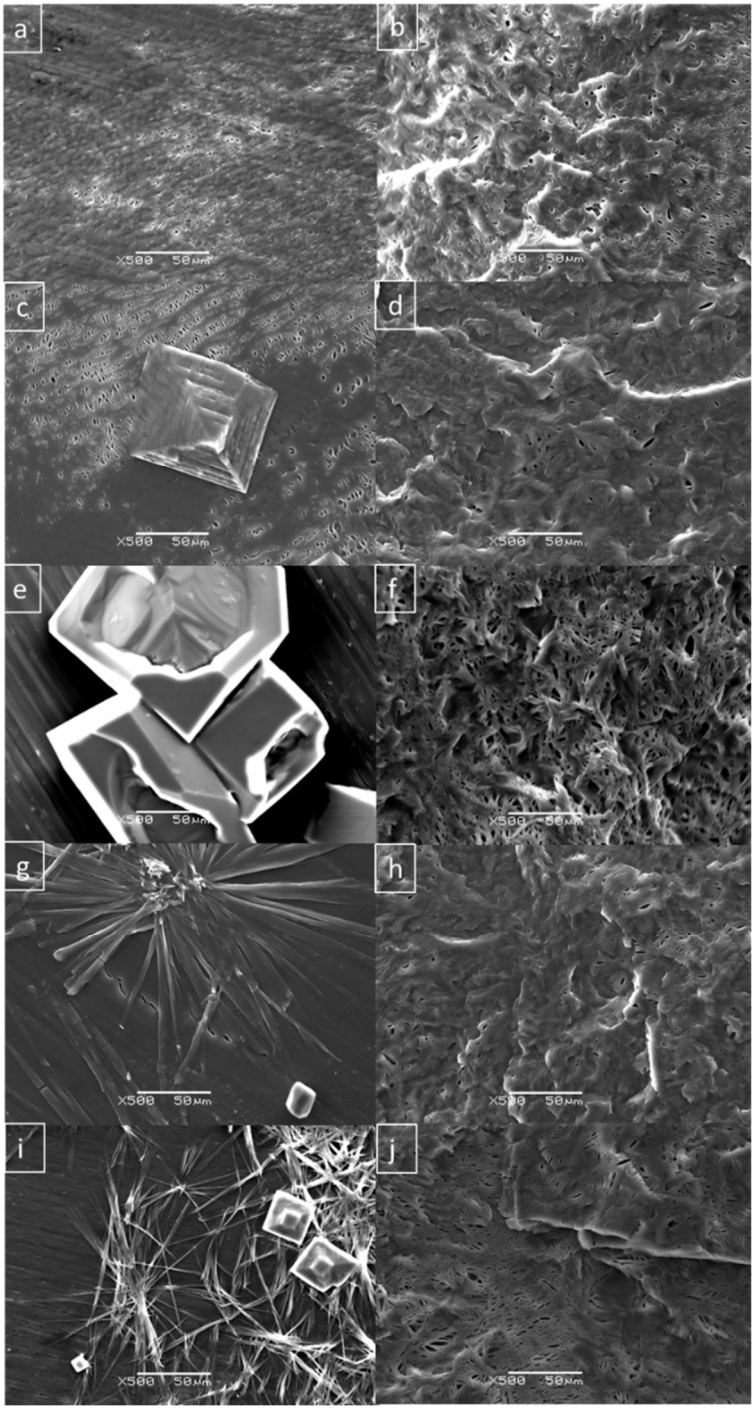

Figure 6.7: SEM images for 10% CM1 fresh and 3 months aged samples; (a and b) are surface and cross-section of fresh sample, (c and d) are surface and cross-section of sample stored at condition A, (e and f) are surface and cross-section of sample stored at condition B, (g and h) are surface and cross-section of sample stored at condition C, and (i and j) are surface and cross-section of sample stored at condition D

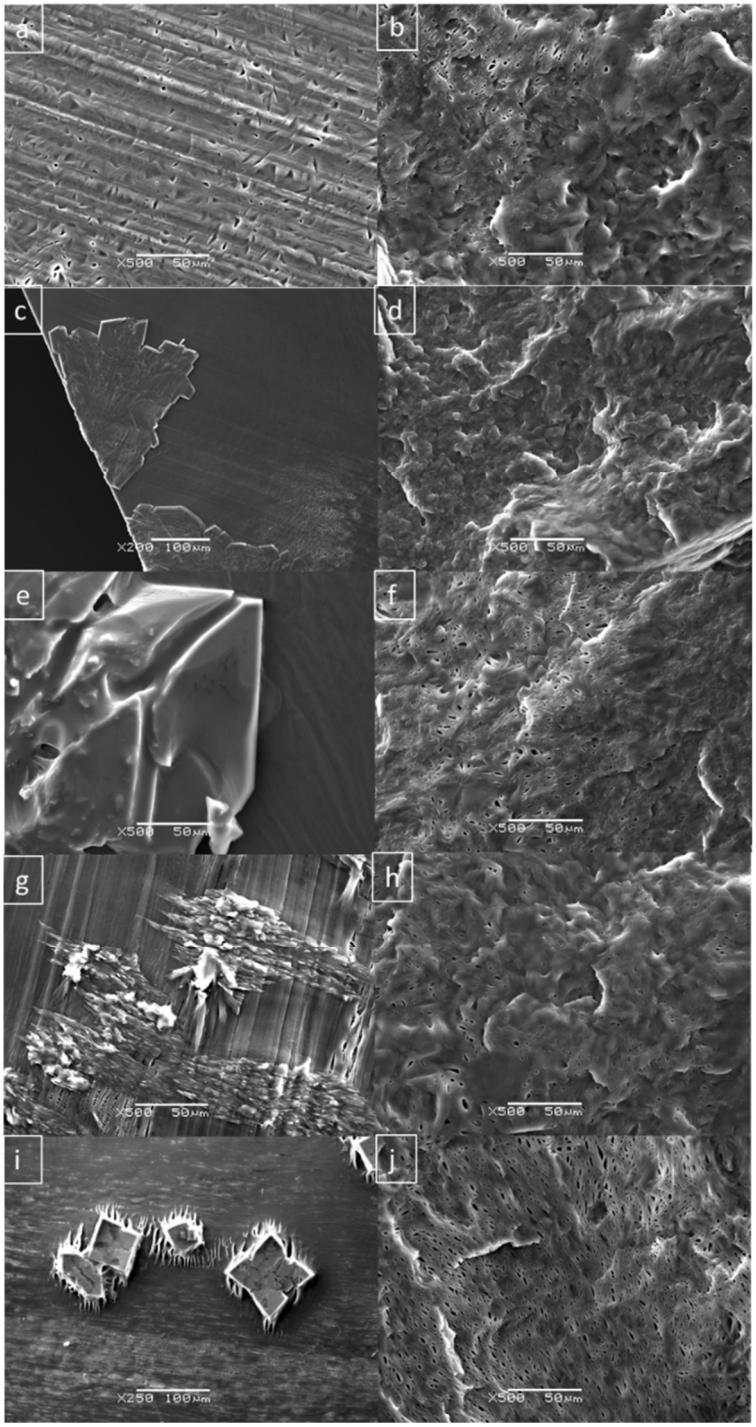

Figure 6.8: SEM images for 10% CM2 fresh and 3 months aged samples; (a and b) are surface and cross-section of fresh sample, (c and d) are surface and cross-section of sample stored at condition A, (e and f) are surface and cross-section of sample stored at condition B, (g and h) are surface and cross-section of sample stored at condition C, and (i and j) are surface and cross-section of sample stored at condition D

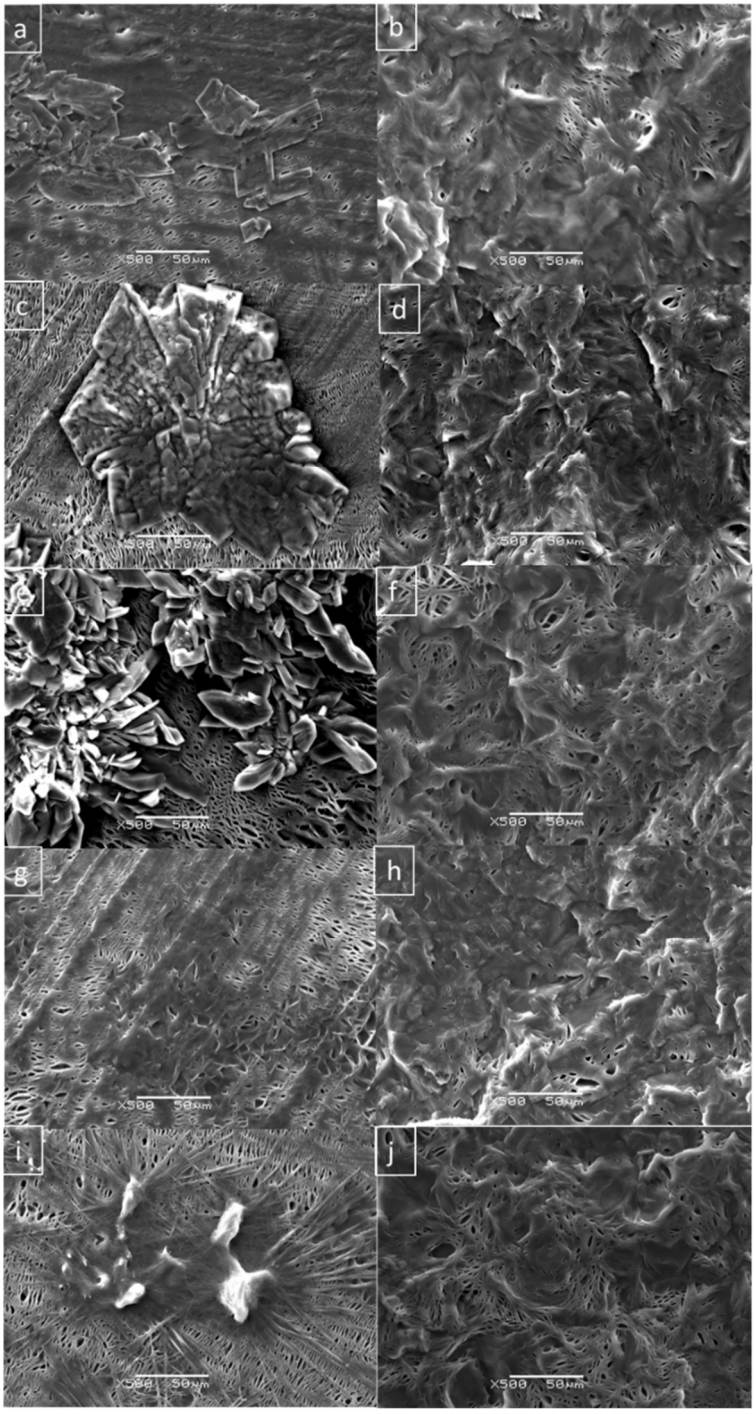

Figure 6.9: SEM images for 20% CM1 fresh and 3 months aged samples; (a and b) are surface and cross-section of fresh sample, (c and d) are surface and cross-section of sample stored at condition A, (e and f) are surface and cross-section of sample stored at condition B, (g and h) are surface and cross-section of sample stored at condition C, and (i and j) are surface and cross-section of sample stored at condition D

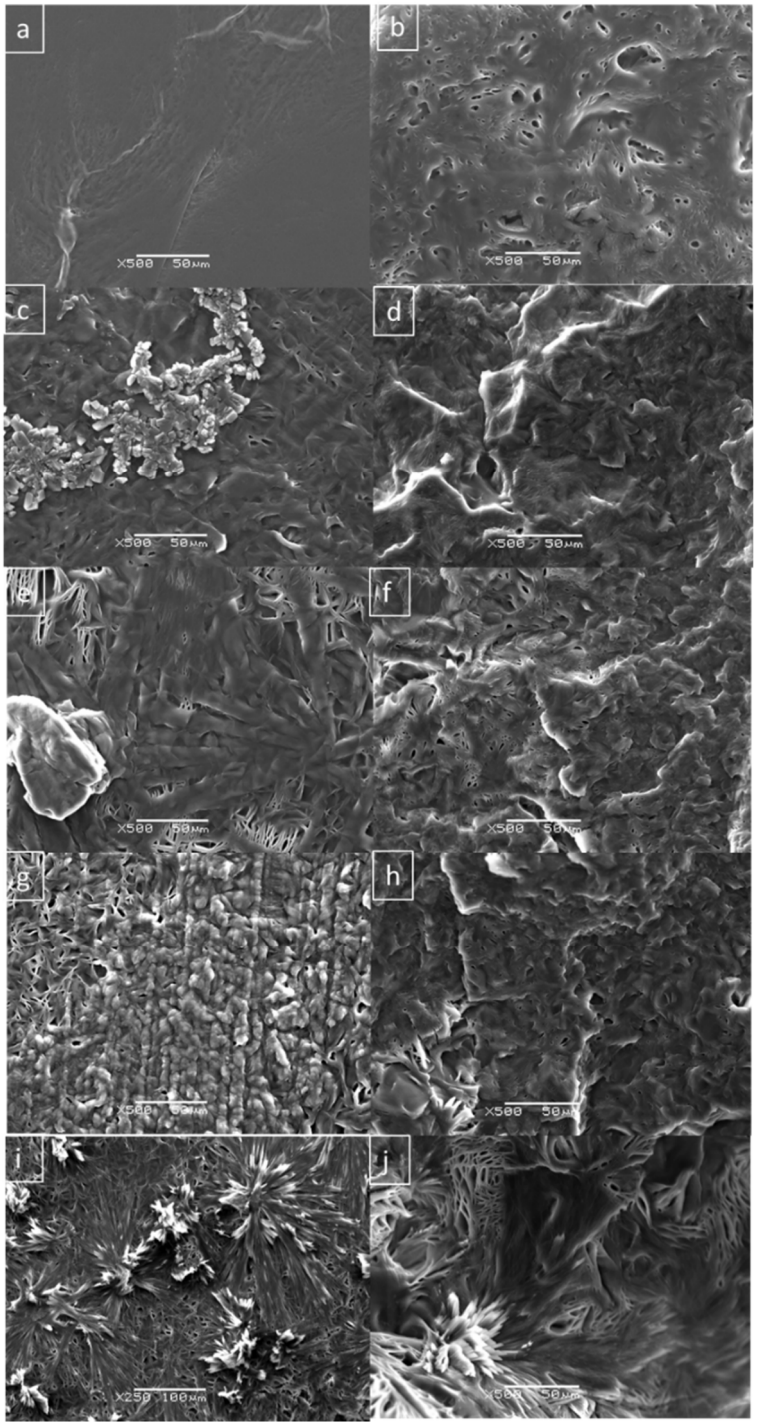

Figure 6.10: SEM images for 20% CM2 fresh and 3 months aged samples; (a and b) are surface and cross-section of fresh sample, (c and d) are surface and cross-section of sample stored at condition A, (e and f) are surface and cross-section of sample stored at condition B, (g and h) are surface and cross-section of sample stored at condition C, and (i and j) are surface and cross-section of sample stored at condition D

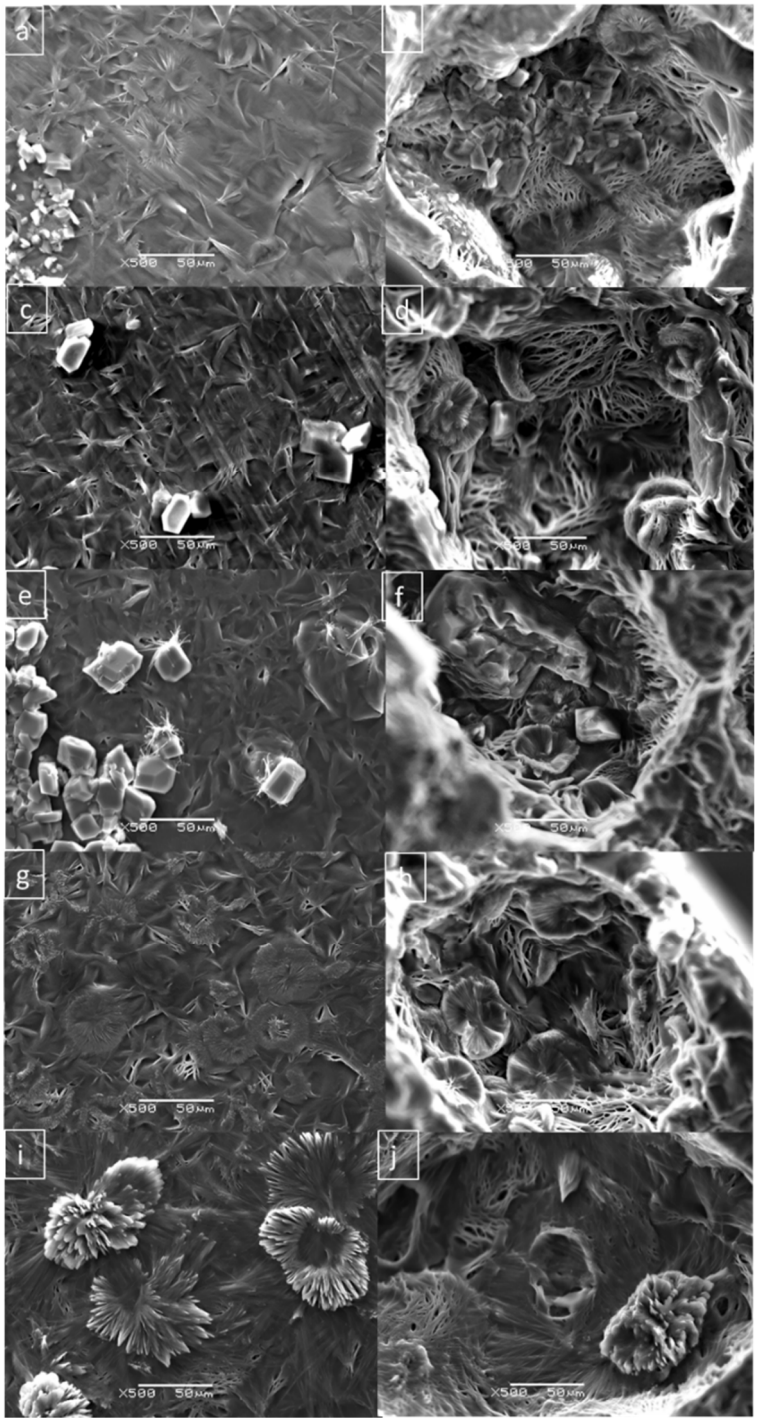

Figure 6.11: SEM images for 30% CM1 fresh and 3 months aged samples; (a and b) are surface and cross-section of fresh sample, (c and d) are surface and cross-section of sample stored at condition A, (e and f) are surface and cross-section of sample stored at condition B, (g and h) are surface and cross-section of sample stored at condition C, and (i and j) are surface and cross-section of sample stored at condition D

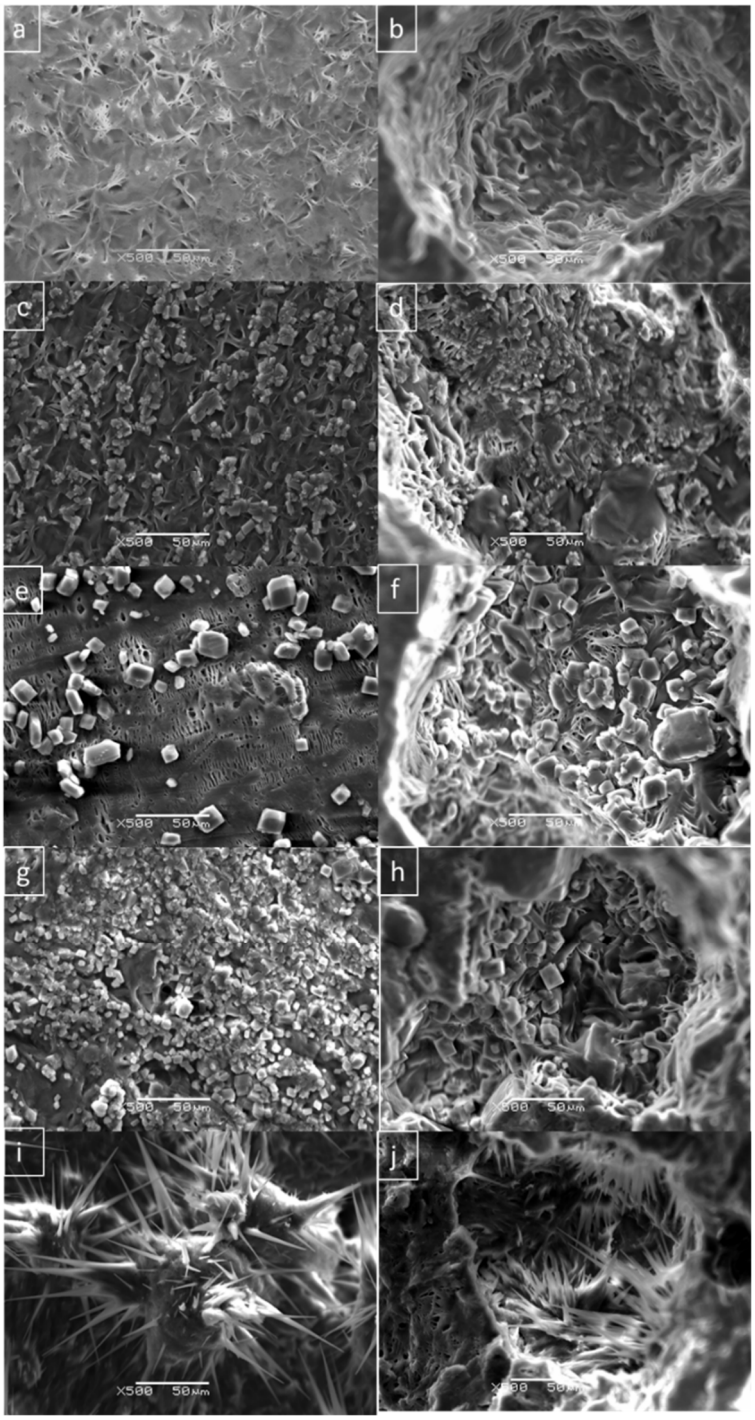

Figure 6.12: SEM images for 30% CM2 fresh and 3 months aged samples; (a and b) are surface and cross-section of fresh sample, (c and d) are surface and cross-section of sample stored at condition A, (e and f) are surface and cross-section of sample stored at condition B, (g and h) are surface and cross-section of sample stored at condition C, and (i and j) are surface and cross-section of sample stored at condition D

The phase behaviour of the patches can be analysed using the DSC. For CM1 loaded samples (**Figures 6.13-15**), in contrast to the placebo samples, no melting of Tween was observed. A shoulder at the onset of the melting of PEG-PEO K900 is developed with increasing the drug load above 10%. At 30% drug loading, a separate melting at 87 °C can be seen. This is assigned to the depressed melting of crystalline felodipine, indicating the presence of significant amount of crystalline felodipine in CM1 patches with 30% drug loading. The detection of felodipine melting peak in the 30% CM1 loading fresh sample (**Figure 6.15**) was attributed to the difference in particle size between the two batches of pure felodipine used in this study. The characterisation of the two batches of the pure drug is shown in Appendix 3.

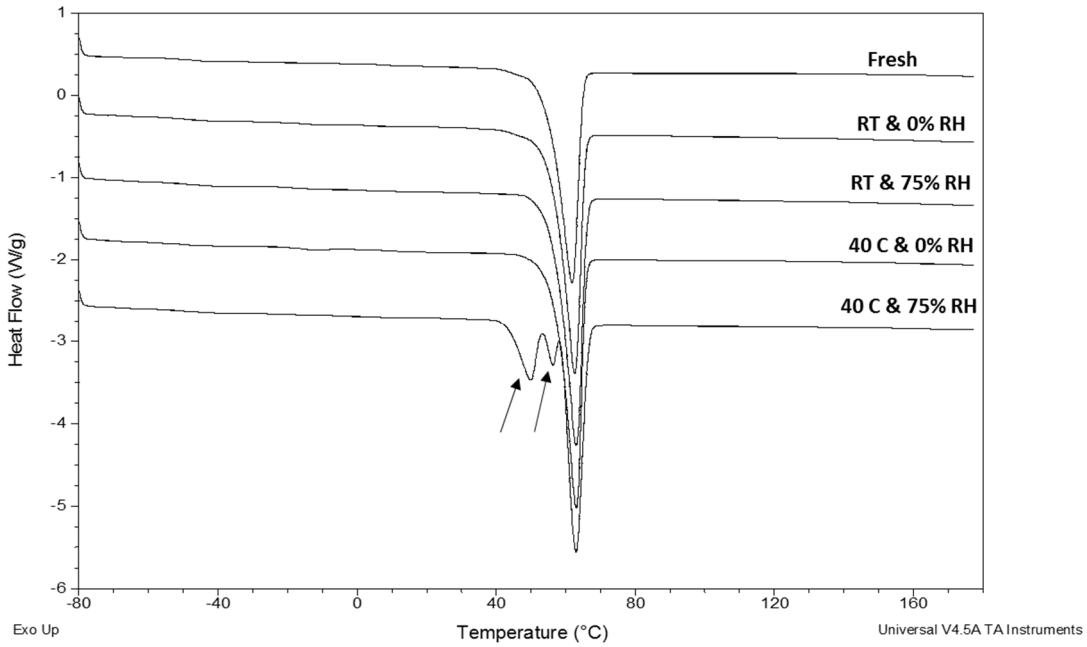

Figure 6.13: DSC thermograms of 10% CM1 fresh and three months aged samples using 10℃/ min heating ramp (n=3)

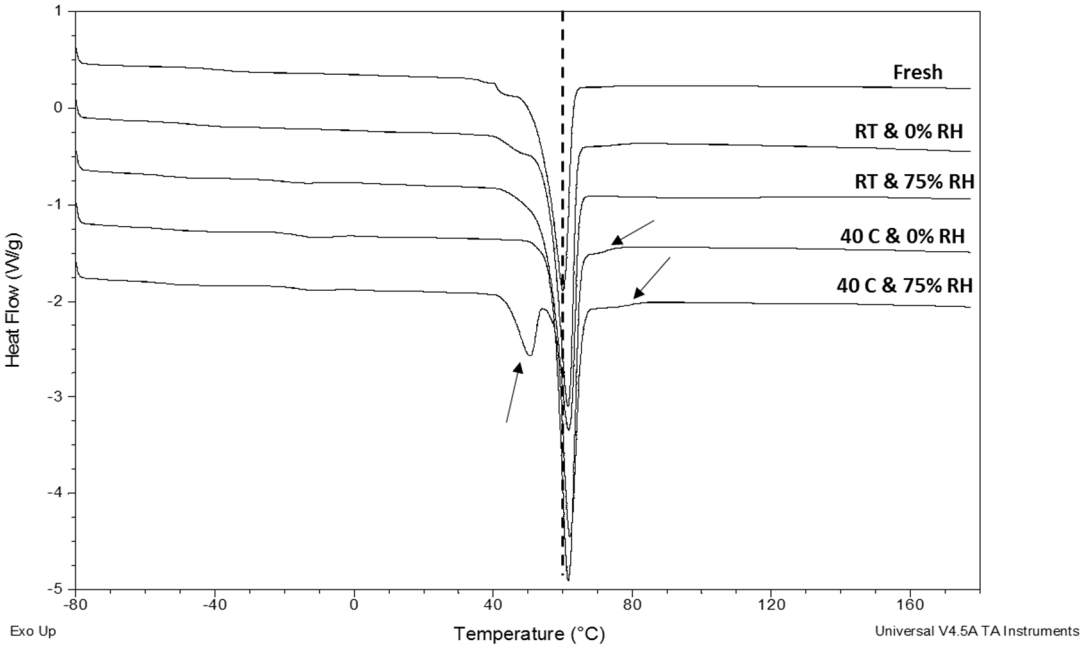

Figure 6.14: DSC thermograms of 20% CM1 fresh and three months aged samples using 10℃/ min heating ramp (n=3)

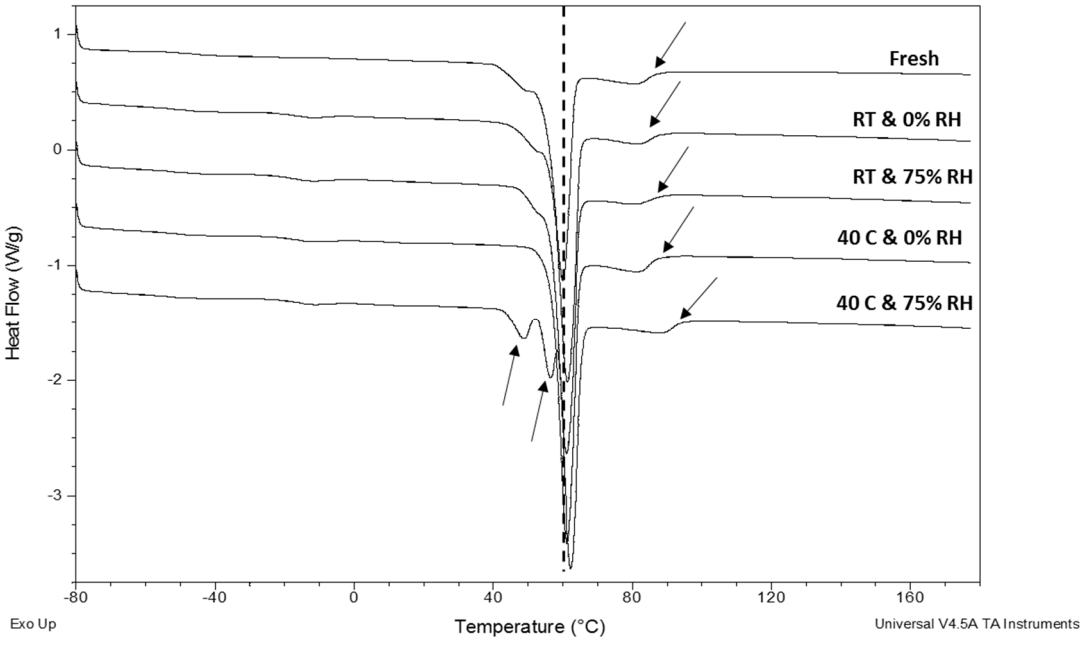

Figure 6.15: DSC thermograms of 30% CM1 fresh and three months aged samples using 10℃/ min heating ramp (n=3)

Investigating the T_g regions (**Figures 6.16-18**) revealing the detection of single T_g temperatures for all drug loaded fresh CM1 patches at -49.0 ± 0.6, -38.0 ± 0.3 and -46.6 ± 0.5 °C for 10, 20 and 30% w/w drug loadings, respectively. As shown in Chapter 4, the presence of felodipine in the Tween 80/PEG/PEO K900 system results in a single amorphous phase consisting of four components. The increase of T_g for 20% CM1 patches indicates the increased amount of molecularly dispersed drug in the Tween rich phase. The decrease of T_g of 30% CM1 is consistent with the increased amount of crystalline drug in the samples indicating drug phase separation.

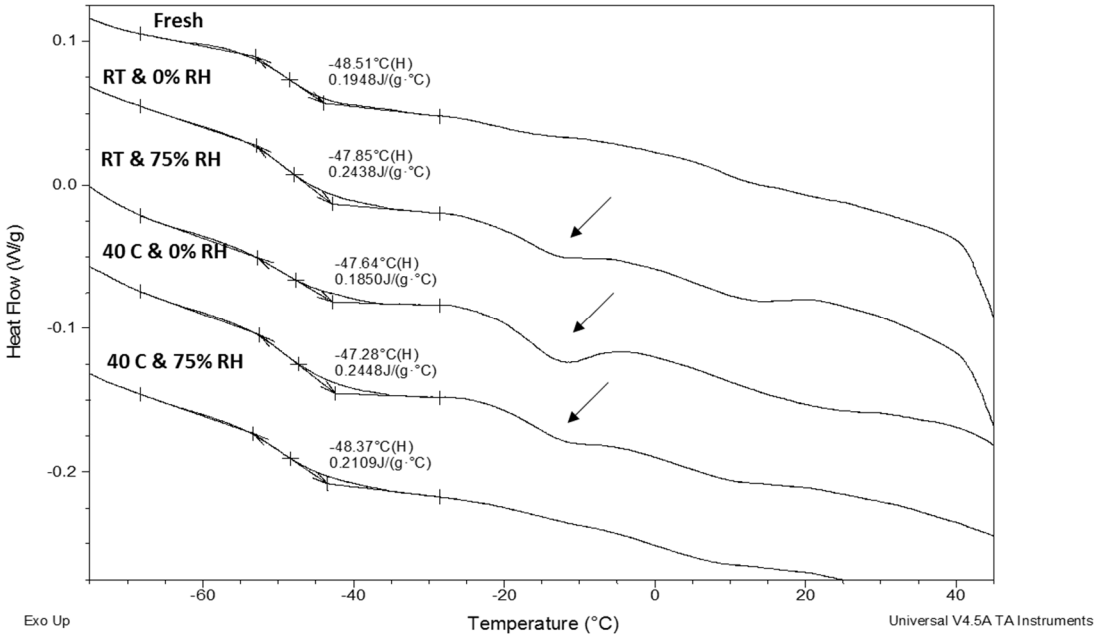

Figure 6.16: Part of DSC thermograms samples showing the T_g regions of 10% CM1 fresh and three months aged samples using 10℃/ min heating rate (n=3)

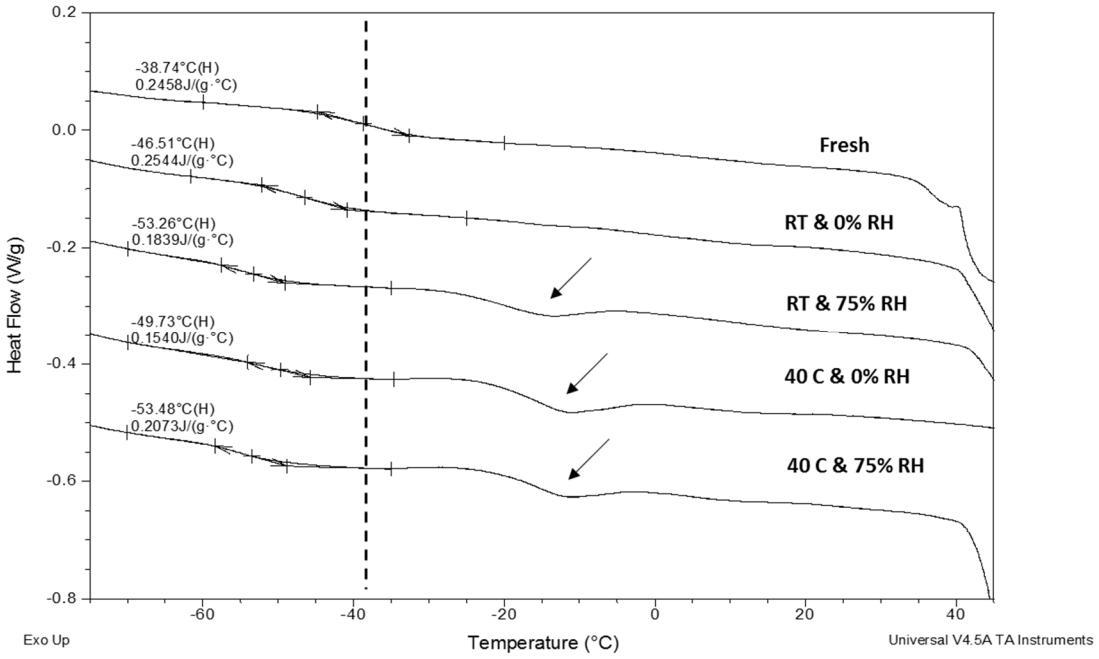

Figure 6.17: Part of DSC thermograms samples showing the T_g regions of 20% CM1 fresh and three months aged samples using 10℃/ min heating rate (n=3)

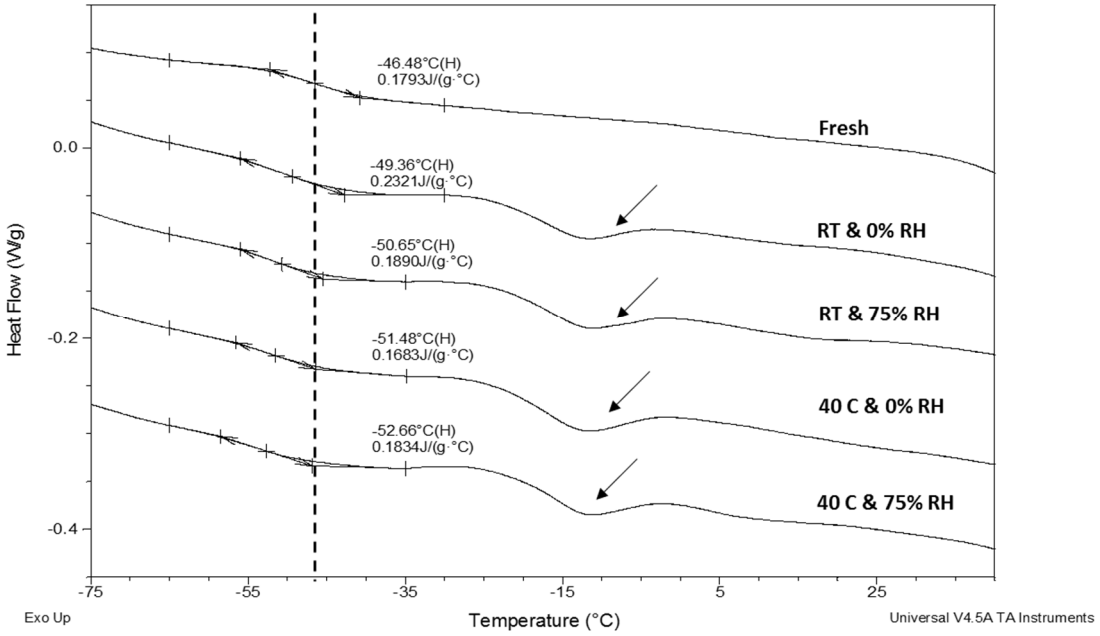

Figure 6.18: Part of DSC thermograms samples showing the T_g regions of 30% CM1 fresh and three months aged samples using 10℃/ min heating rate (n=3)

As seen in **Figures 6.19-21**, drug loaded fresh CM2 patches show the separate melting peaks of the TPGS phase at 28.9 ± 0.3, 20.4 ± 0.4 and 24.9 ± 1.5 °C for 10, 20, and 30% w/w drug loaded systems, respectively. The drug solubilised in TPGS phase would cause the significant depression of the TPGS melting compared to the pure TPGS. Assuming the lowering of melting point is an indicator of drug solubility it is clear that 20% drug loaded systems had more drug dissolved in the TPGS than 10 and 30% loaded systems. For the 30% drug loaded system, in comparison CM1, no depressed drug melting is detected indicating the higher drug solubilisation capacity of the CM2 carrier than CM1. In contrast to CM1, no melting of felodipine is seen in the 30% loaded sample of CM2 although there is evidence from FTIR and PXRD that crystals exist. It was assumed therefore that on heating crystalline felodipine dissolves in the molten TPGS phase.

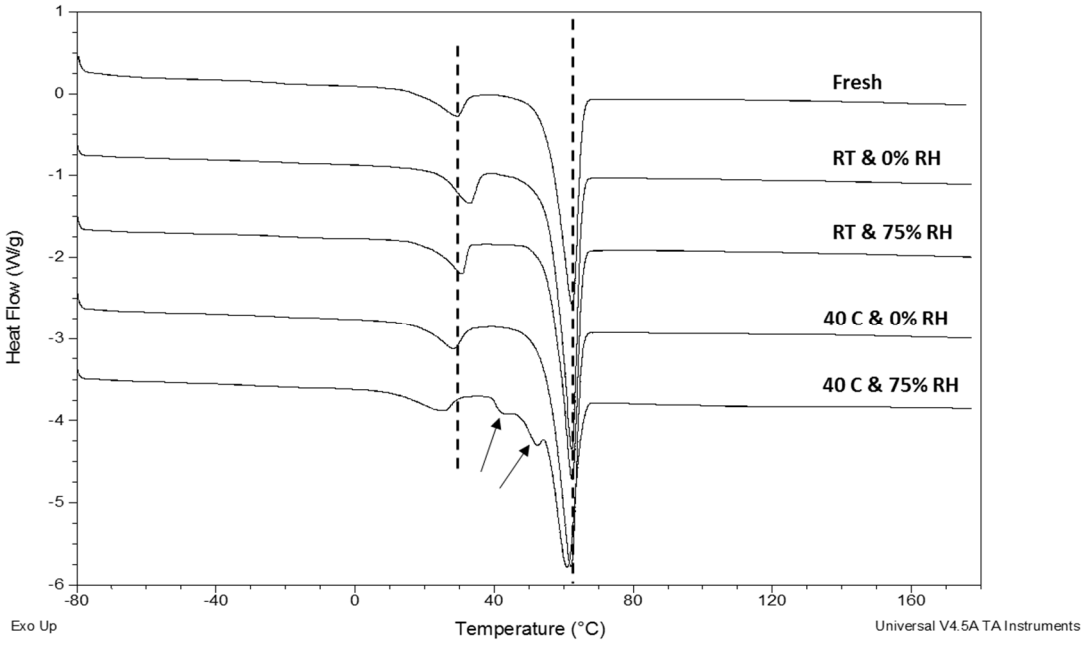

Figure 6.19: DSC thermograms of 10% CM2 fresh and three months aged samples using 10℃/ min heating ramp (n=3)

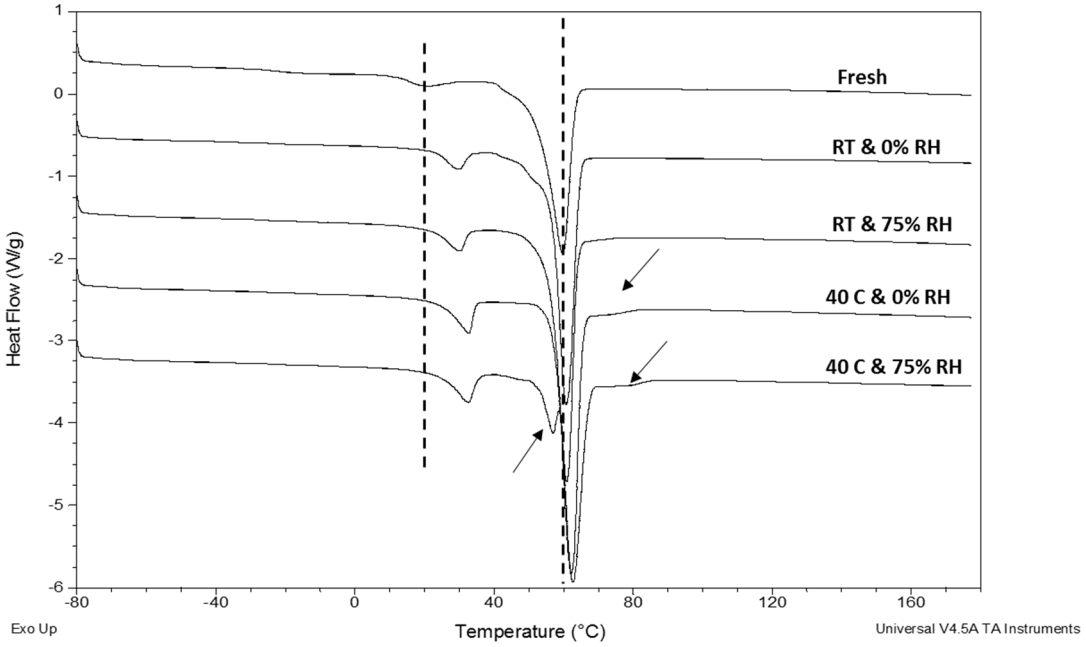

Figure 6.20: DSC thermograms of 20% CM2 fresh and three months aged samples using 10℃/ min heating ramp (n=3)

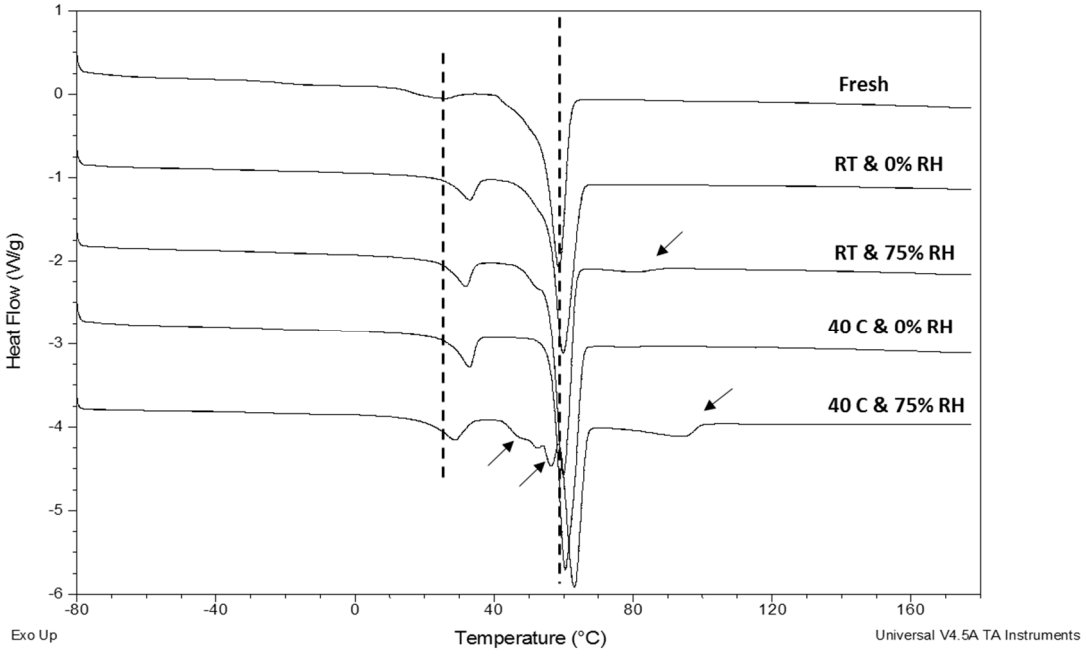

Figure 6.21: DSC thermograms of 30% CM2 fresh and three months aged samples using 10℃/ min heating ramp (n=3)

As mentioned in Chapter 4, DSC analysis of T_g regions of fresh1 0, 20 and 30% drug loaded CM2 formulations indicated the detection of single T_g at -23.7 ± 0.4, -22.2 ± 0.4 and -21.4 ± 0.8 ºC respectively. The impacts of different storing conditions on CM2 formulations are shown in **Figures 6.22-24** and will be discussed in the next sections.

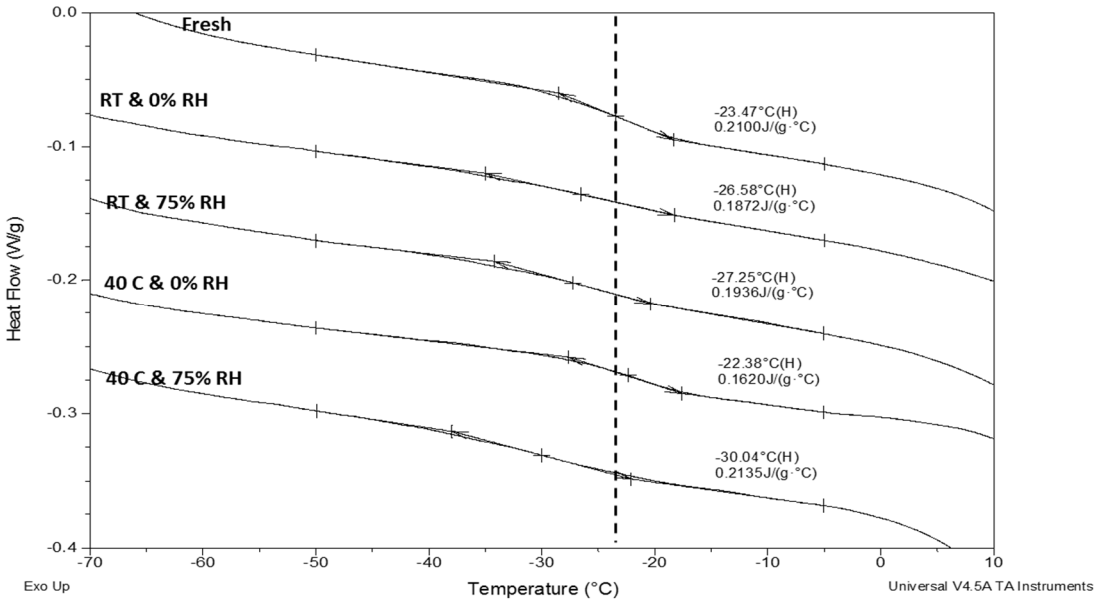

Figure 6.22: Part of DSC thermograms samples showing the T_g regions of 10% CM2 fresh and three months aged samples using 10℃/ min heating rate (n=3)

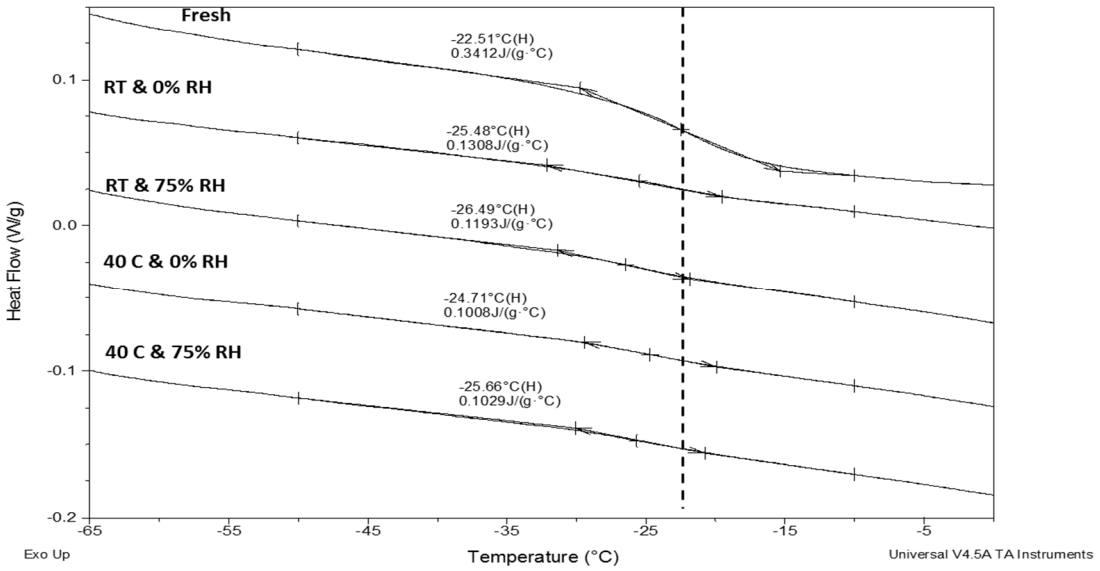

Figure 6.23: Part of DSC thermograms samples showing the T_g regions of 20% CM2 fresh and three months aged samples using 10℃/ min heating rate (n=3)

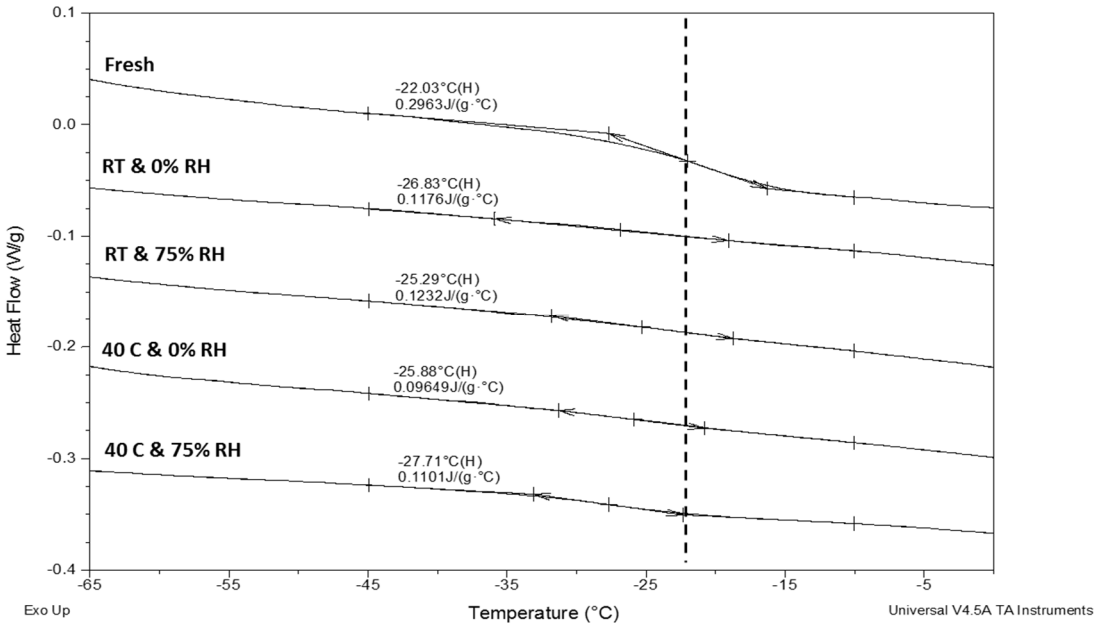

Figure 6.24: Part of DSC thermograms samples showing the T_g regions of 30% CM2 fresh and three months aged samples using 10℃/ min heating rate (n=3)

6.3.3 Carrier stability of drug loaded patches aged under 0%RH

The changes of the drug loaded patches on ageing were monitored by examination of four transition regions in the DSC experiments: the T_g region and the melting regions associated with Tween, TPGS and PEG-PEO K900. Results are summarised in **Table 6.2**.

Table 6.2: Summary of the changes of thermal properties of the aged patches in comparison to the properties of the fresh patches

Thermal Transition	Storing condition	Formulations							
		CM1(Tween 80)				CM2 (TPGS)			
		0%	10%	20%	30%	0%	10%	20%	30%
T_g	A	↔	↔	↓	↓	↔	↓	↓	↓
	B	↔	↔	↓	↓	↔	↓	↓	↓
	C	↔	↔	↓	↓	↔	↔	↓	↓
	D	↔	↔	↓	↓	↔	↓	↓	↓
ΔC_p	A	↔	↔	↔	↔	↔	↓	↓	↓
	B	↔	↔	↓	↔	↔	↔	↓	↓
	C	↔	↔	↓	↑	↔	↔	↓	↓
	D	↔	↔	↓	↔	↔	↔	↓	↓
PEG/PEO T_m	A	↑	↑	↑	↑	↔	↔	↑	↑
	B	↑	↑	↑	↑	↔	↔	↑	↑
	C	↑	↑	↑	↑	↑	↔	↑	↑
	D	*	↔	↑	↑	↑	↔	↑	↑
PEG/PEO ΔH_f	A	↑	↔	↔	↑	↑	↑	↔	↑
	B	↑	↔	↔	↑	↑	↔	↔	↔
	C	↑	↑	↑	↑	↑	↔	↑	↑
	D	*	↔	↑	↔	↑	↔	↔	↔
Surfactant T_m	A	↑	**X**	↔	**X**	↑	↑	↑	↑
	B	↑	**X**	**X**	**X**	↔	↓	↑	↑
	C	↑	**X**	**X**	**X**	↑	↑	↑	↑
	D	*	↔	**X**	**X**	↔	↓	↑	↑
Surfactant ΔH_f	A	↑	↑	↔	↑	↔	↔	↑	↑
	B	↓	↑	↑	↑	↑	↔	↑	↑
	C	↑	↑	↑	↑	↑	↔	↑	↑
	D	*	↔	↑	↑	↔	↔	↑	↑

(*) Stands for the sample liquefied after three months storage and not testable
(↑) Value increased in comparison to fresh samples
(↓) Value decreased in comparison to fresh samples

(↔) Value showed no significant change in comparison to fresh samples
(X) Detection of Tween 80 melting peak

For placebo CM1 and CM2 samples, no changes in the T_g regions were observed, and there was a significant increase in the melting temperature and corresponding heat of fusion of PEG-PEO K900. This is attributed to the removal of moisture from the patches leading the formation of more crystals. For 10% drug loaded, CM1 samples stored at both room temperature and 40 °C ageing resulted in the appearance of Tween melting transitions in these samples. There was also increase in the crystallinity of the PEG-PEO K900 reflected by the increase in the melting point and/or ΔH_f. On the other hand, only 10% CM2 samples stored at room temperature showed a decrease in T_g and ΔC_p with an increase in PEG-PEO K900 crystallinity. However, both samples stored at room temperature and 40 °C revealed a significant increase in TPGS melting with no change in ΔH_f as illustrated in **Table 6.2**.

For the aged CM1 and CM2 patches with 20 and 30% drug loadings, both T_g and associated ΔC_p tended to be reduced. As discussed above, the observation of a single T_g in the system implies that the glassy material is a mixture of the surfactant and the amorphous PEG/PEO K900 with drug dissolved in it. As the drug behaves as an antiplasticiser, the decreases in T_g values after ageing are an indication of a reduction in the amount of drug in the surfactant-rich phases. For both CM1 and CM2, the changes much more greater for patches with 20% drug loading than the 30% samples. This may be attributed to the supersaturation of 20% loaded samples and the lower content of solubilised felodipine in 30% compared to 20% patches.

In the PEG-PEO K900 melting region, peak shape changes are observed. As seen in **Figures 6.14, 6.15, 6.20 and 6.21** the shoulder before the onset of PEG-PEO K900 melting for 20 and 30% CM1 and CM2 samples stored at 0% RH and 40 °C is absent indicating unfolding of the folded form of PEG-PEO K900 polymers. For 30% drug loaded CM1 samples, stored at room temperature and 40 °C, clearly partially separated depressed melting of crystalline felodipine with melting peak ranging at temperatures 81-89 °C can be identified suggesting a significant amount of crystalline felodipine present.

For the 20 and 30% CM1 samples, the melting of Tween is detectable for all aged samples except the 20% aged at room temperature and 0%RH. There was a slight difference in Tween melting peak temperatures and heat of fusion between the aged samples. In CM2 patches, the melting peak of TPGS moved to a higher temperature closer to the melting point of pure TPGS with increased melting enthalpy values. This indicates drug phase separation and increased the degree of crystallinity of TPGS after ageing. The enthalpy of melting of the TPGS in the 30% sample is

greater than that of the 20% sample. This implies more drug dissolved in the TPGS in the 20% sample than the 30% sample. It should be mentioned that storing 20 and 30% CM2 patches at 40 °C leads to greater increases in the melting enthalpy values of the surfactant than room temperature. In addition, this melting enthalpy increases of the surfactant phases are more profound for CM2 compared to CM1. Once the surfactants are phase separated in their crystalline form, it is likely that drug is no longer solubilised in the surfactant phases. This suggests that more crystalline drug is likely to be present in 30% drug loaded samples under 40 °C and 0% RH.

6.3.4 Carrier stability of drug loaded patches under 75%RH

Under 40 °C/75%RH, the development of multiple peaks on the shoulder of the peak of the melting of PEG-PEO K900 were observed in all samples. These peaks were assigned to the melting of degradation products of PEG-PEO K900 due to the random chain scission of the two polymers caused by oxidative thermal degradation (144, 145, 502-505). Except this feature, little significant changes as indicated in **Table 6.2** were seen for 10% loaded CM1 and CM2. The depression of T_g of the surfactant phase is greater for 20 and 30% drug loaded samples compared to 10% loading. However, there is a significantly higher degree of T_g shift for 20-30% samples stored at 75% RH in comparison to the samples aged under 0% RH. The increases in the melting peak points of PEG-PEO K900 (compared to fresh samples) showed no significant difference to the aged samples under 0%RH. For 30% drug loaded CM2 samples, depressed melting of felodipine can be detected under both room temperature and 40 °C which were absent in the samples aged under 0%RH. This indicates that high humidity led to more drug crystallisation in TPGS containing samples.

6.3.5 Effect of surfactant on crystallisation tendency and crystal growth of felodipine on ageing

As mentioned in Chapters 2 and 3, the flexibility of felodipine molecular structure is responsible about the appearance of its polymorphic forms (312, 508). Four polymorphic forms (I-IV) were obtained by precipitation from various solvents (312-315, 318, 319). This part of the study focuses on the felodipine crystallisation within the aged samples and the identification of the polymorphs formed. SEM was used to study the crystal growth of felodipine in the patches. Using chlorine as a marker for felodipine, it is possible to identify the grown crystals in the formulations using EDS.

Table 6.3 summarises the drug crystallisation tendency and crystal habits after three months ageing under the four different conditions. The SEM data of the fresh samples indicates that CM2 is better at solubilising felodipine than CM1 as no drug crystals were observed in any patches with 10-30% loading. This highlights the better drug solubilisation capacity of TPGS than Tween as discussed earlier. As seen in **Figures 6.7-12**, drug recrystallisation at the surfaces during ageing occurred to all formulations, except 20% CM1 under condition C (40˚C and 0% RH) and 10% CM2 under condition D (40˚C and 75 % RH). Generally, more drug crystallisation was observed on the surface of the patches and the interior of the air pockets than the bulk matrix of the samples. This is likely to be due to the surface being the hydrophobic (air exposed) interface experiencing highest temperature and humidity at least at the initial few hours of the ageing process. These results are consistent with data reported in literature revealing faster surface to bulk drug crystallisation (509, 510). There are three main types of felodipine crystal habits observed, blocks, plate and needles arranged in spherulitic pattern as illustrated in **Figures 6.7-12**. In the literature the crystal habits of the polymorphs were reported to be blocks shaped for polymorphs I and II and plate-like crystals for form III, but no available information about the crystal habit of polymorph IV of felodipine is available (319). In this study the spherulitic crystals only tend to growth either in the interior or after ageing under 40 °C. The blocks and plate crystals are more common than the needle crystals and their growths are promoted by ageing on the surfaces and interior of most formulations as summerised in **Table 6.3**.

Table 6.3: Summary of surface morphology and crystal growth of the 3-month aged HME-IM patches

Drug loading	Formulation	CM1 (with Tween 80)								CM2 (with TPGS)							
	Location	Surface				Cross-section				Surface				Cross-section			
	Ageing condition	A	B	C	D	A	B	C	D	A	B	C	D	A	B	C	D
10% w/w	Fresh	-				-				-				-			
	Aged	B	B	B+S	S	-	-	-	-	P	B	P	-	-	-	-	-
20% w/w	Fresh	P				-				-				-			
	Aged	P	P	-	S	-	-	-	-	B	B	P	S	-	-	-	S
30% w/w	Fresh	B				P+S				-				-			
	Aged	B	B	S	S	S	B+S	S	S	B	B	B	S	B	B	B	S

(S) Spherulitic crystals; (B) Blocky crystals; (P) Plate crystals and (-) No crystals were detected

In order to further identify the polymorphic form of the recrystallised felodipine, PXRD and ATR-FTIR were used to characterise the aged samples. No clear drug PXRD crystallisation peaks were observed in any of CM1 and CM2 10% drug loaded patches (**Figures 6.25-26**).

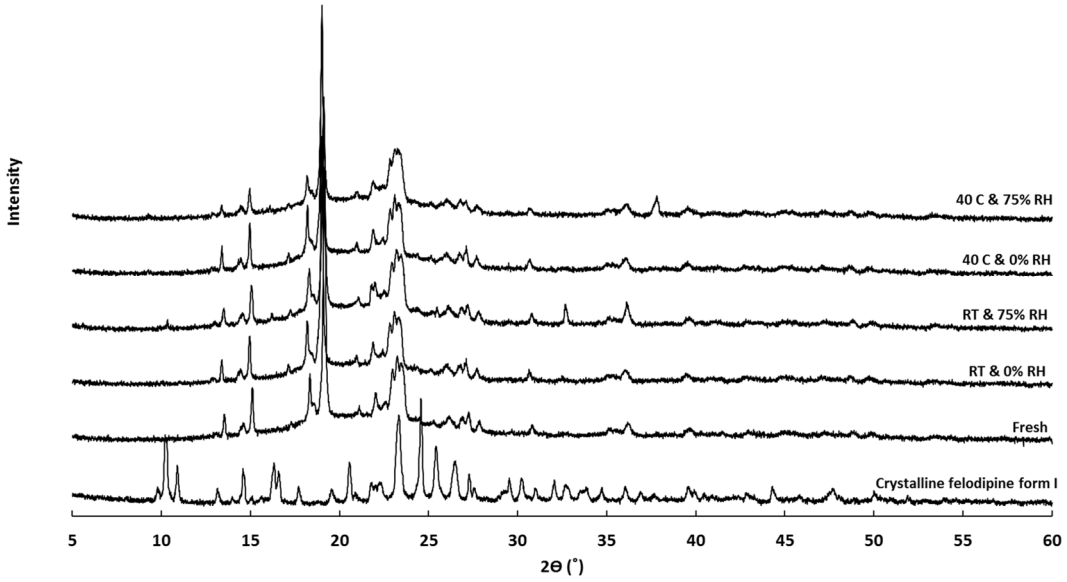

Figure 6.25: PXRD patterns of 10% w/w fresh and three months aged CM1 drug loaded patches

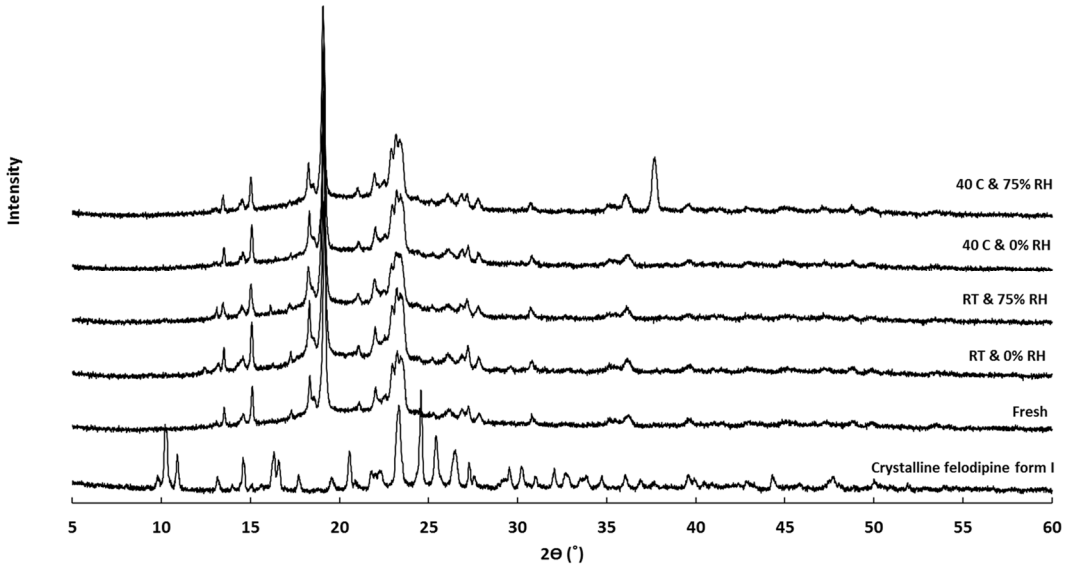

Figure 6.26: PXRD patterns of 10% w/w fresh and three months aged CM2 drug loaded patches

As seen in **Figure 6.27** for 20% w/w CM1 patch, the appearance of diffraction peaks in the pattern of the aged sample stored in condition A indicates the presence of form I which are consistent with those of raw felodipine pattern and with the reported data in the literature (312). This is consistent with the SEM results as form I is the usually present in the block-shaped habit (319). The PXRD results of the CM1 sample stored in condition B indicate the presence of a mixture of form I and II. New peaks at 9.3˚and 12.4˚are observed in the diffraction patterns of the sample stored in condition C and D. These diffraction peaks do not match with any known polymorphs of felodipine in the literature, suggesting the presence of unknown new polymorph growth.

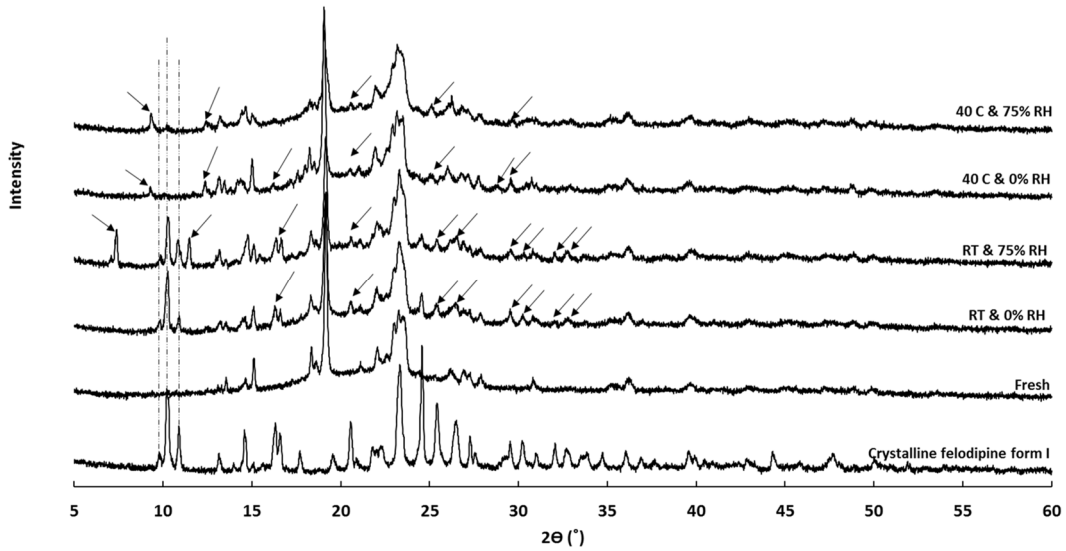

Figure 6.27: PXRD patterns of 20% w/w fresh and three months aged CM1 drug loaded patches

For 20% w/w CM2 samples (**Figure 6.28**), fewer recrystallisation diffraction peaks were identified compared to the corresponding CM1 loaded samples owing to the higher solubilisation capacity and stabilisation ability of TPGS containing matrix compared to Tween 80. The diffraction peaks at 9.3˚, 10.2˚(form I) and 12.4˚are all visible in all CM2 samples stored at all conditions indicating the mixture of form I and the new form and the crystallisation of the new polymorph favoring the TPGS containing matrices.

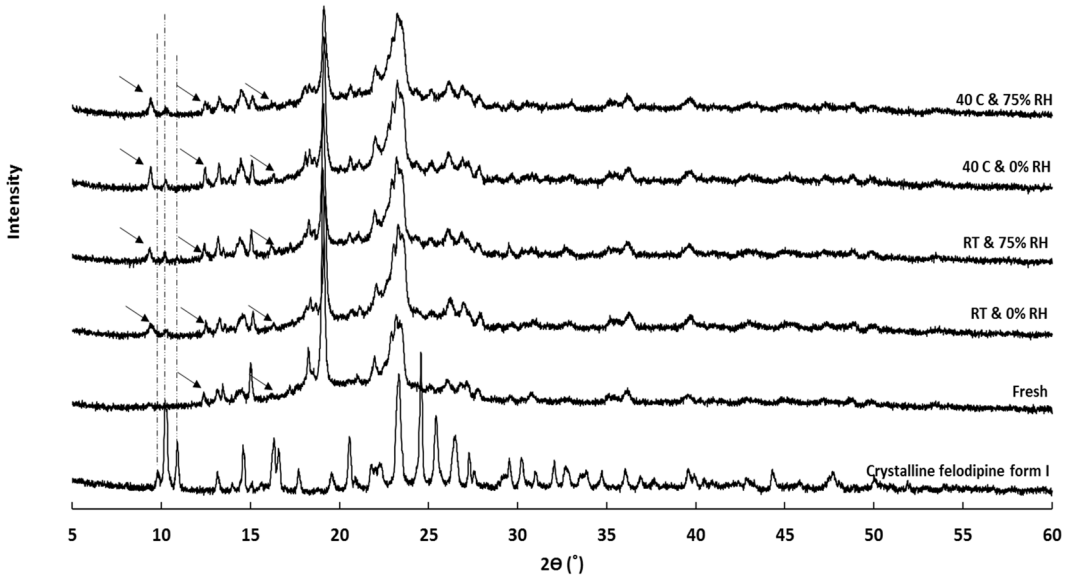

Figure 6.28: PXRD patterns of 20% w/w fresh and three months aged CM2 drug loaded patches

For the 30% w/w drug loaded samples (**Figure 6.29-30**), it is noted that there are form I drug crystals present in both the fresh CM1 and CM2 samples. The diffraction patterns of the 30% w/w CM1 samples indicate the coexistence of the new form and form I. However, it is noted that regardless of the humidity, room temperature storage resulted in the formation of more form I than the new form. However, at 40 °C more of new form than form I was formed. For 30% w/w CM2 formulations stored in the conditions A, B, C, diffraction patterns of the crystallised drug indicated the presence of form I; whereas the sample stored in condition D (40°C 75% RH) formed needle felodipine crystals showing diffraction peaks of both form I and the new form. The 30% loaded samples contain crystallised drug immediately after extrusion. The presence of these crystals favour the formation of form I. However high temperature and humidity can initiate the formation of the new form. It should be mentioned that felodipine undergoes form I to metastable form II polymorphic transformation in the presence or absence of polymeric additives at different temperatures (511, 512).

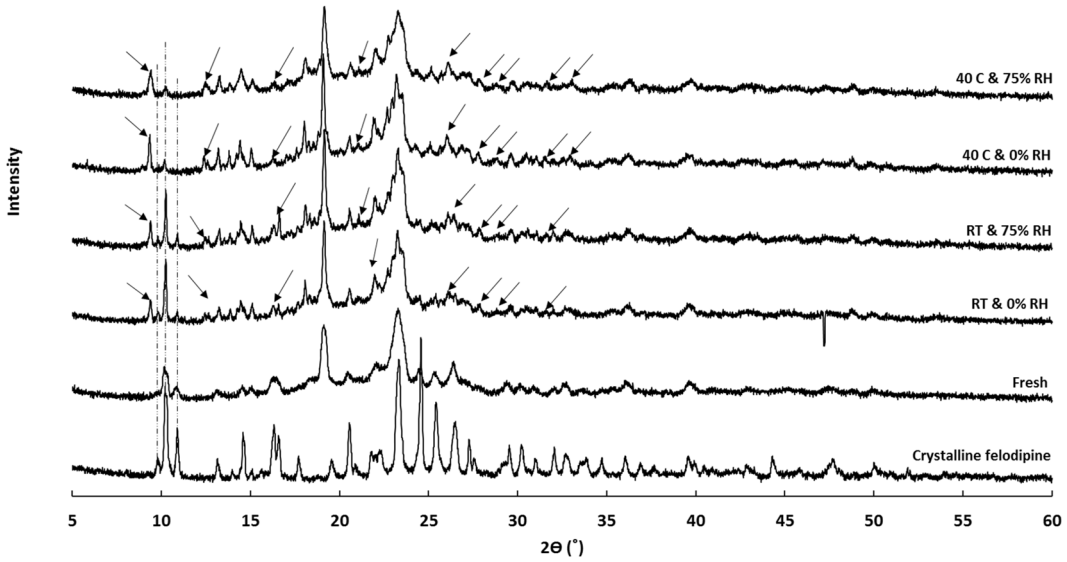

Figure 6.29: PXRD patterns of 30% w/w fresh and three months aged CM1 drug loaded patches

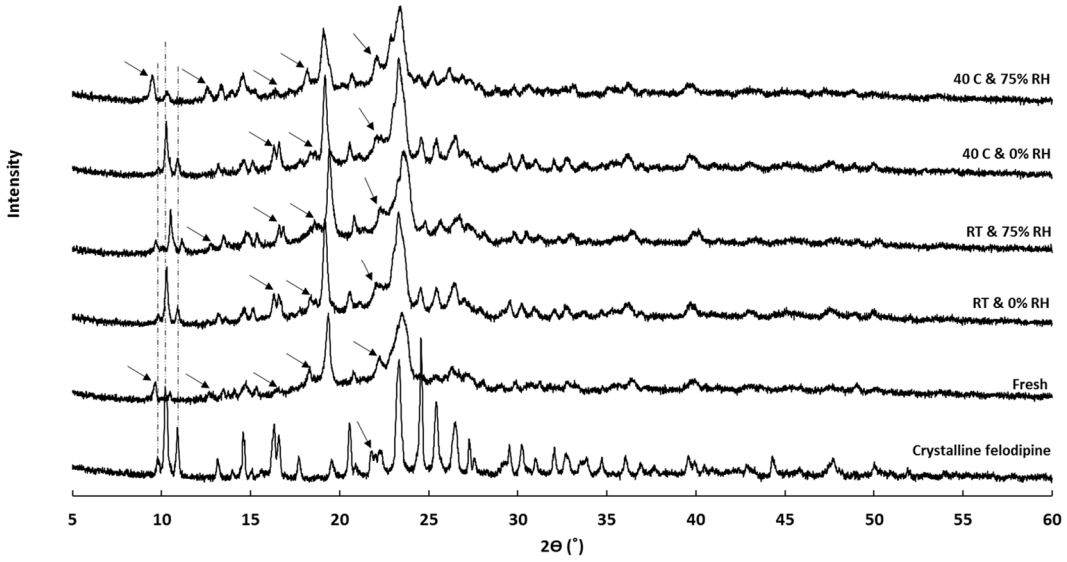

Figure 6.30: PXRD patterns of 30% w/w fresh and three months aged CM2 drug loaded patches

As mentioned in Chapter 3, the NH stretching vibration in the infrared has been reported at 3372, 3334, 3370, 3329 cm^{-1} for the four crystalline polymorphic forms I-IV, respectively (313-315, 318). Furthermore, the amorphous form showed an NH stretching peak at ~ 3339 cm^{-1} and peaks at 1701 and 1682 cm^{-1} corresponding to the non-hydrogen bonded C=O group and the hydrogen-bonded C=O group respectively (316, 317). Using these signature peaks, it is possible to facilitate

the identification of the polymorphic forms detected by PXRD. **Figures 6.31-34** illustrate the ATR-FTIR spectra for CM1 and CM2 10% loaded samples before and after ageing at different conditions.

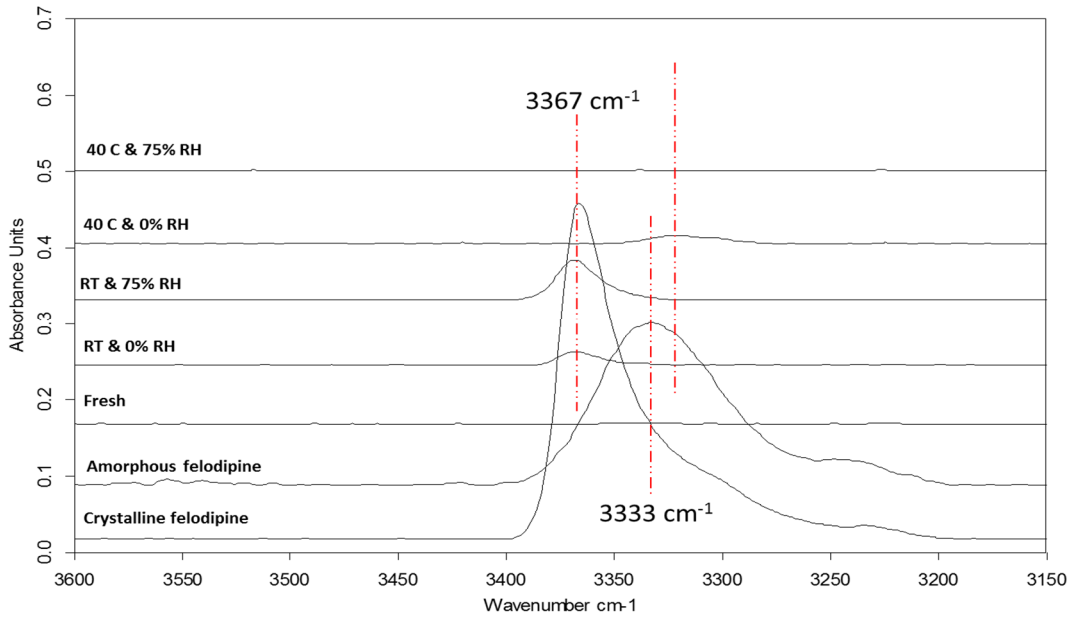

Figure 6.31: The NH stretching region of the ATR-FTIR spectra of CM1 10% fresh and aged samples (n=3)

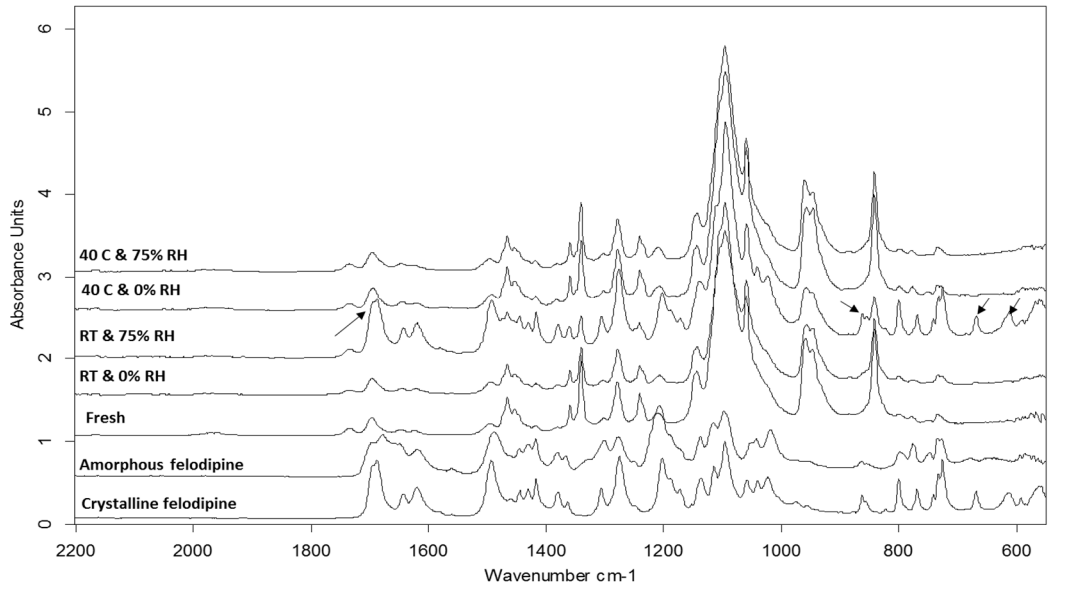

Figure 6.32: Partial ATR-FTIR spectra of CM1 10% fresh and aged samples for the low wavenumber range (n=3)

As seen in **Figure 6.31-32**, only sample stored at room temperature and 75% RH clearly shows the characteristic NH stretching at 3367 cm^{-1}, the C=O stretching is more similar to that of the raw crystalline felodipine (form I), the appearance of other peaks at 865 and 725 cm^{-1} indicating recrystallisation of felodipine into form I. For 10% CM2 samples (**Figures 6.33-34**), no significant changes in the spectra of the aged samples compared to freshly prepared samples.

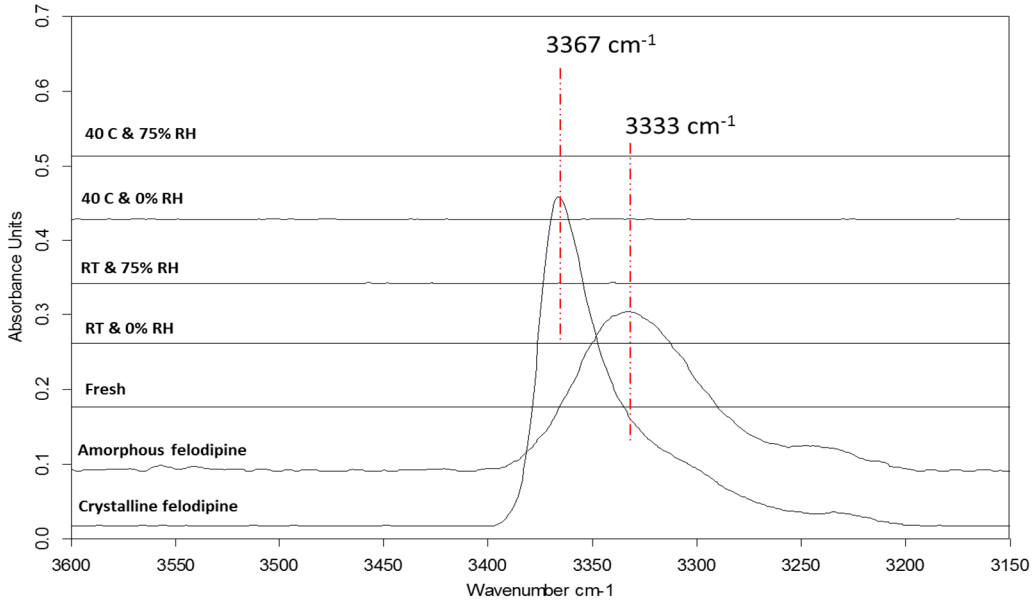

Figure 6.33: The NH stretching region of the ATR-FTIR spectra of CM2 10% fresh and aged samples (n=3)

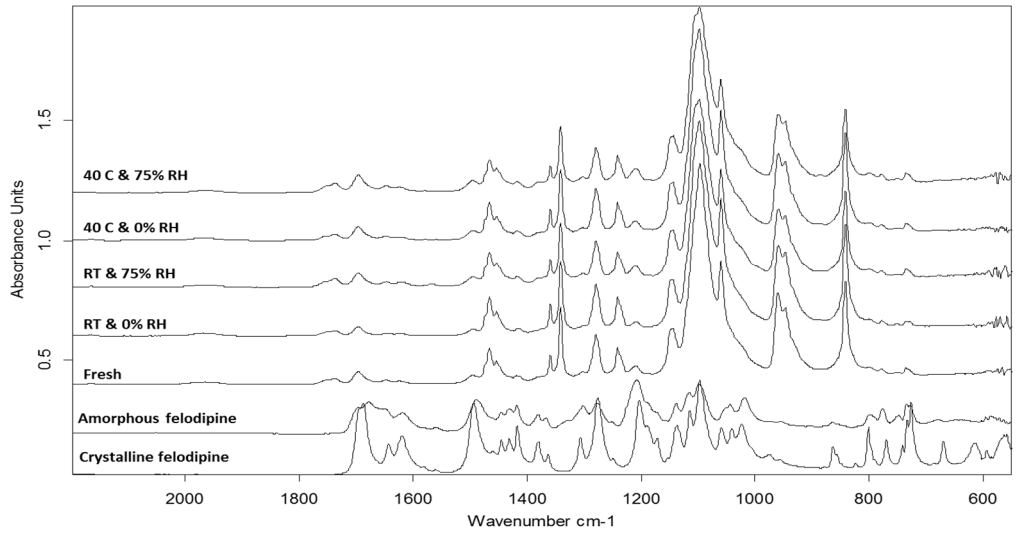

Figure 6.34: Partial ATR-FTIR spectra of CM2 10% fresh and aged samples for the low wavenumber range (n=3)

20 and 30% w/w CM1 samples stored at 40℃ and CM2 samples stored at all conditions revealed the NH stretching at 3321 cm^{-1} which is not related any known polymorphs or the amorphous form (**Figures 6.35-42**).

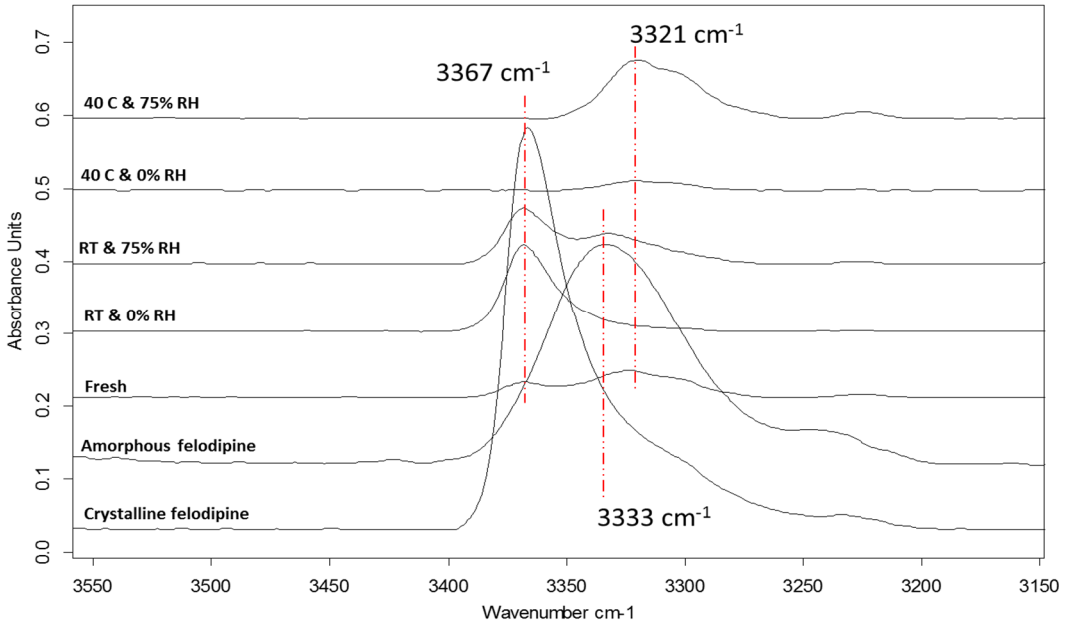

Figure 6.35: The NH stretching region of the ATR-FTIR spectra of CM1 20% fresh and aged samples (n=3)

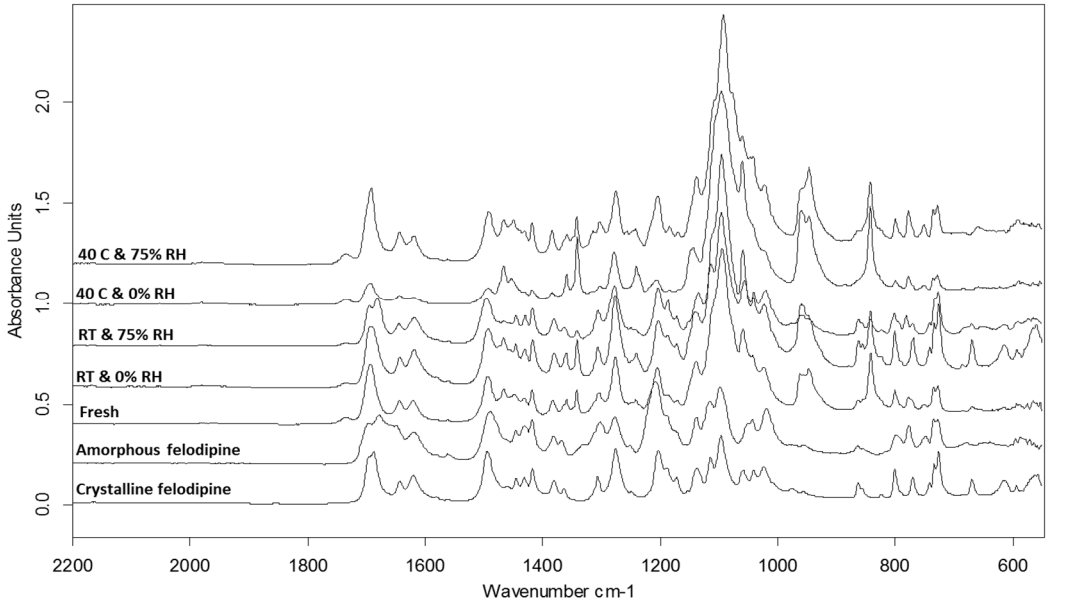

Figure 6.36: Partial ATR-FTIR spectra of CM1 20% fresh and aged samples for the low wavenumber range (n=3)

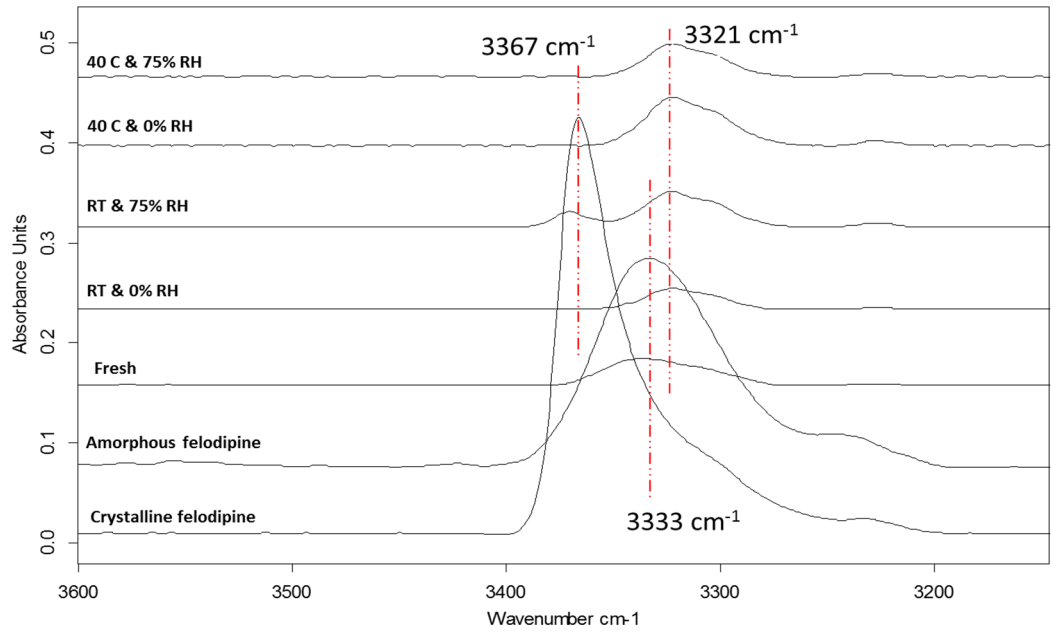

Figure 6.37: The NH stretching region of the ATR-FTIR spectra of CM2 20% fresh and aged samples (n=3)

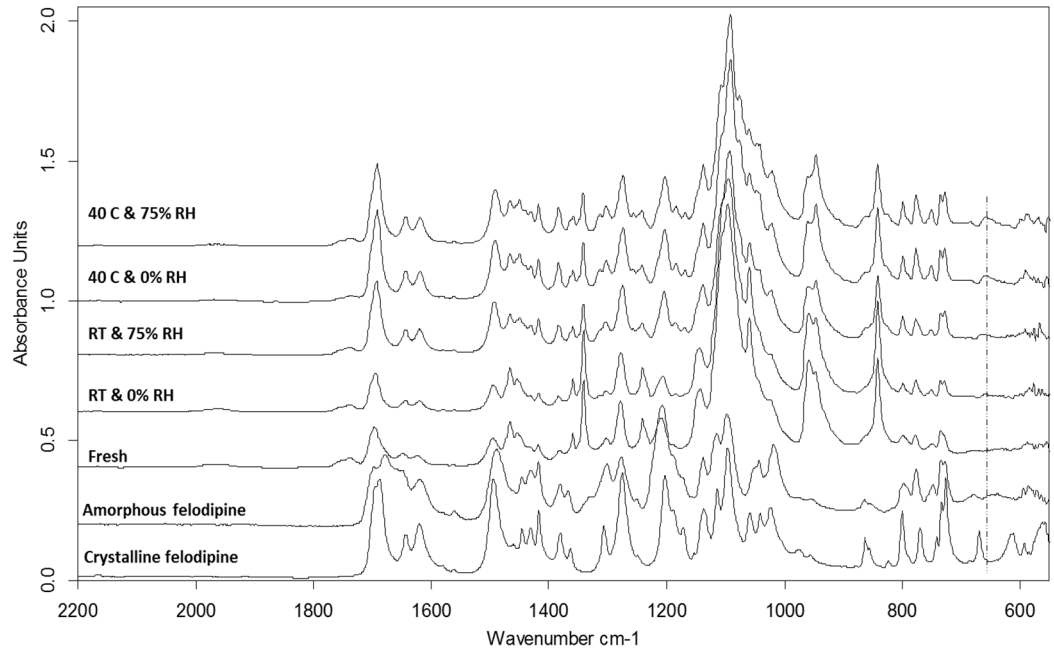

Figure 6.38: Partial ATR-FTIR spectra of CM2 20% fresh and aged samples for the low wavenumber range (n=3)

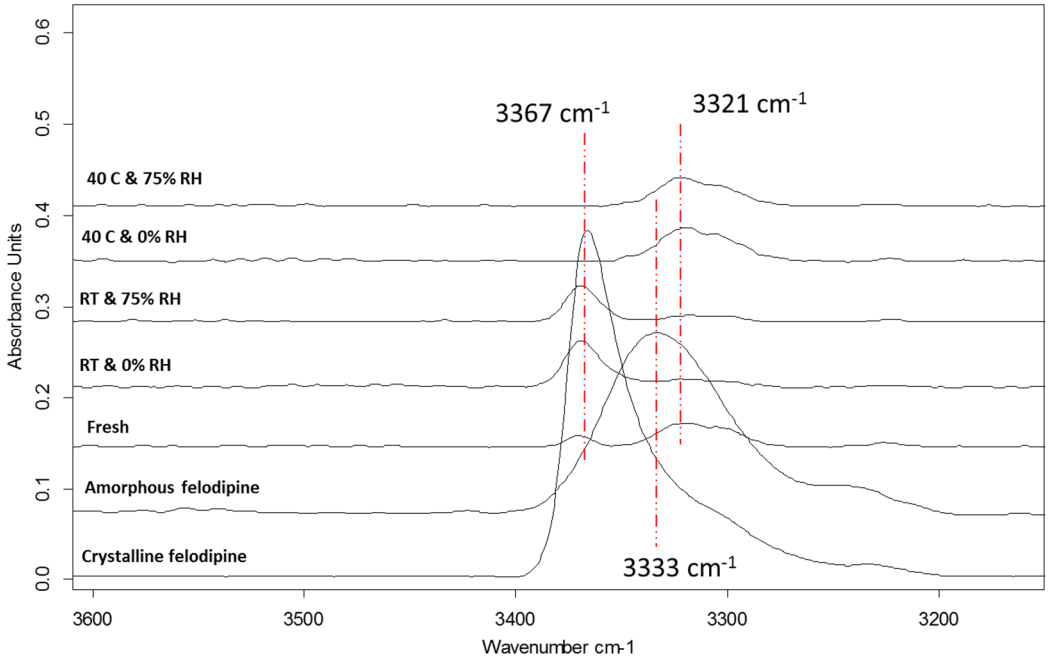

Figure 6.39: The NH stretching region of the ATR-FTIR spectra of CM1 30% fresh and aged samples (n=3)

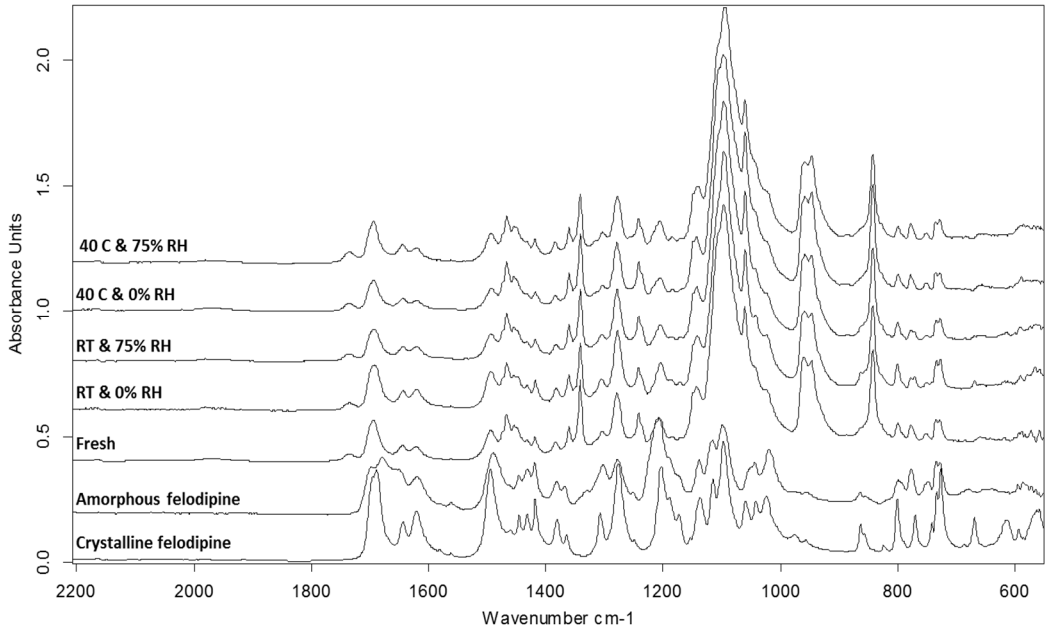

Figure 6.40: Partial ATR-FTIR spectra of CM1 30% fresh and aged samples for the low wavenumber range (n=3)

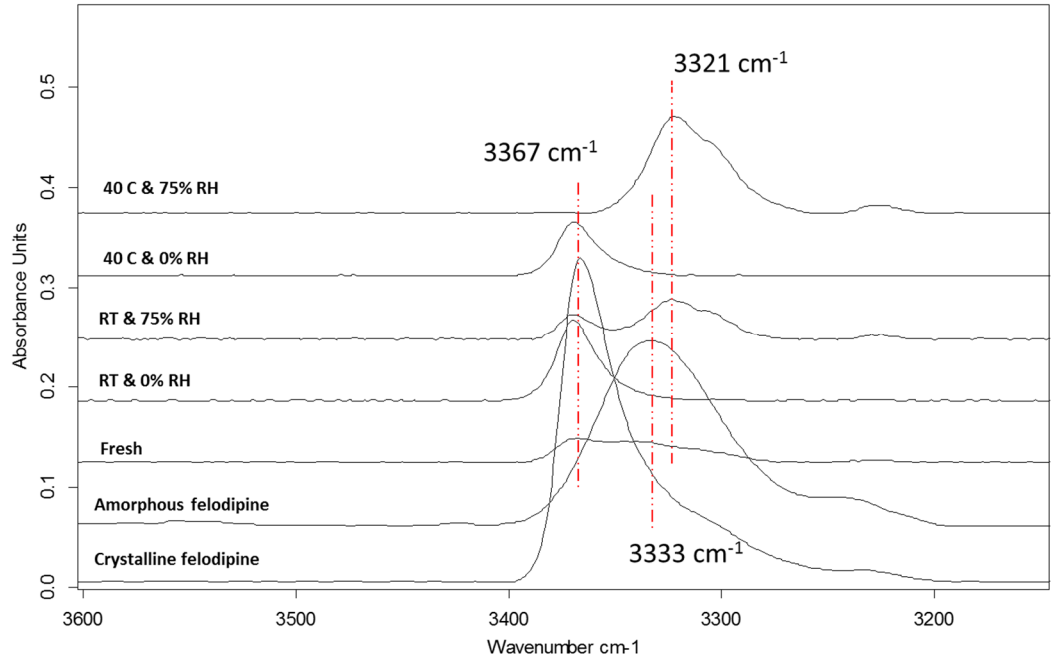

Figure 6.41: The NH stretching region of the ATR-FTIR spectra of CM2 30% fresh and aged samples (n=3)

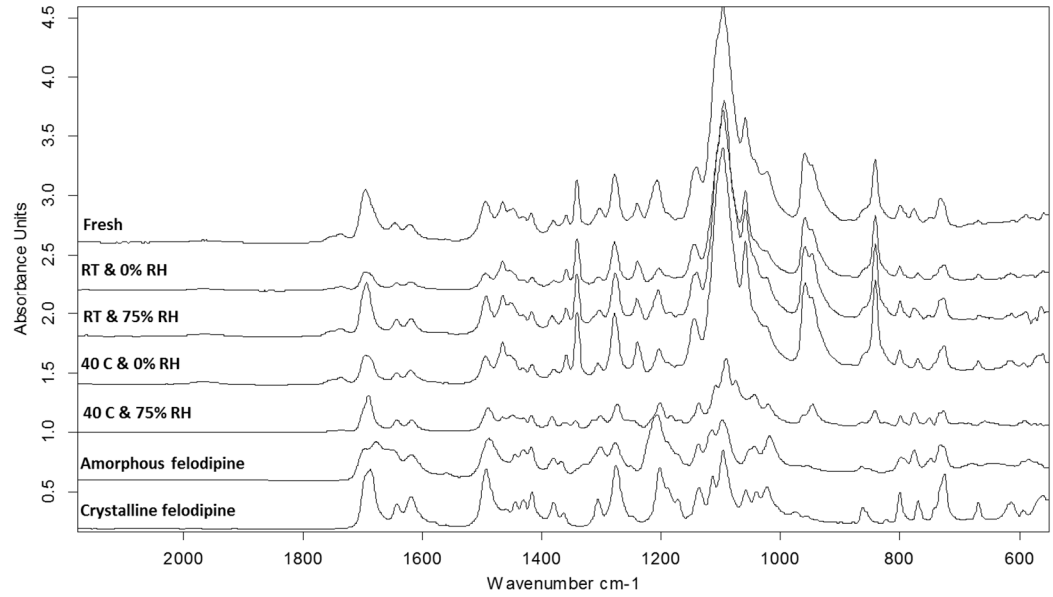

Figure 6.42: Partial ATR-FTIR spectra of CM2 30% fresh and aged samples for the low wavenumber range (n=3)

As the PXRD results indicated that the growth of the new form is favoured at 40℃, it is reasonable to suggest that the NH stretching peak at 3321 cm^{-1} is a possible signature peak for a new

polymorphic crystal form of felodipine. The ATR-FTIR results show good agreement with PXRD data.

In summary, it is clear that the growth of the new polymorphic form favours TPGS containing dispersions when the drug loading at the border of being saturated. When form I already present in the fresh samples, the growth of the new form is more in favoured by higher storage temperature but not sensitive to humidity.

6.3.6 Characterisation of felodipine recrystallised from its glassy state under stressful conditions of temperature and humidity

In order to provide better understanding of the crystallisation of felodipine from its solid dispersion matrices especially those with the higher loading percentage and investigate the impact of other excipients on the process, amorphous felodipine was prepared from crystalline felodipine form I melt by quench cooling and subsequent storage at 40℃ and 75% RH as this condition is the most likely driving the drug in its formulation to recrytallise in its spherulitic (needle) pattern having different characterisation properties as seen above. Images of the prepared glassy felodipine samples before (A) and after recrystallisation at 40℃ and 75% RH (B) are shown in **Figure 6.43**.

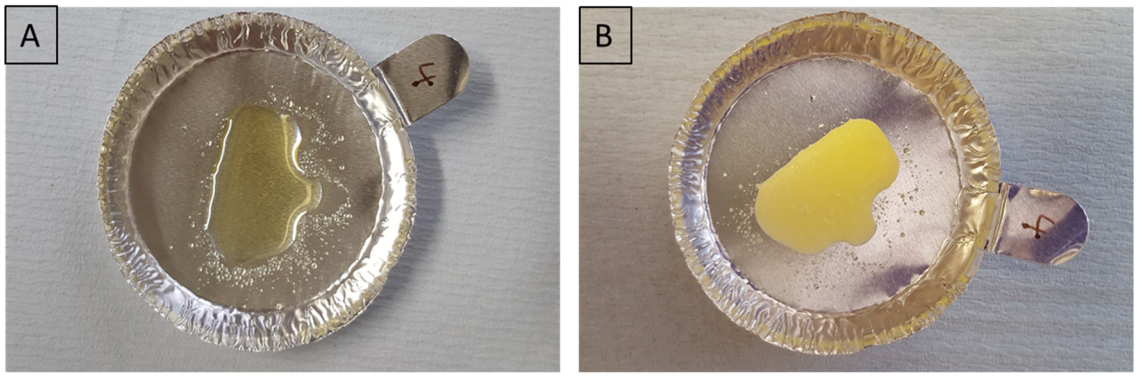

Figure 6.43: Images of felodipine in its glassy state (A) and after recrystallisation at 40℃ and 75% RH (B)

SEM images (**Figure 6.44**) illustrated that the upper surface of the recrystallised drug shows a spherulitic pattern while this pattern is absent in the lower surface (in contact with the Aluminium dish). This indicates that the spherulitic growth is more likely to occur in free surfaces exposed to high humidity air at a temperature close to the T_g of felodipine.

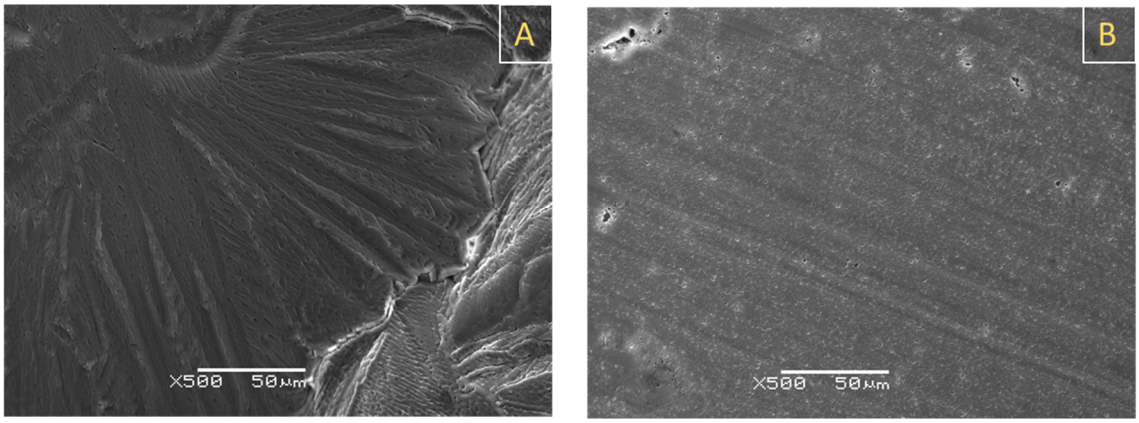

Figure 6.44: SEM images of felodipine after recrystallisation at 40℃ and 75% RH; A is the upper surface and (B) is the lower surface of the sample

In addition, DSC analysis (**Figure 6.45**) shows an interesting finding related to the melting of felodipine compared to the formulations where its melting is absent due to thermal dissolution in the molten excipients during the DSC heating ramp. The melting peak onset of raw pure crystalline felodipine form I used in this study is 140.9 ± 0.1℃. However, pieces of the recrystallised drug without milling shows the appearance of two partially separated melting peaks having onsets at 118.3 ± 0.1℃ for the smaller peak and 136.0 ± 0.9℃ for the larger peak. These results clearly indicate that at least the lower melting peak is belonging to a new polymorphic crystal growth of felodipine. Milling the recrystallised sample using mortar and pestle shows significant reduction in the intensity of the lower melting peak indicating polymorphic transformation into the more stable form aided by milling and/or exposure to air. It should be mentioned that the melting onset of the higher melting peak of the milled recrystallised sample is 139.5 ± 0.1℃ which may suggest the melting point depression of this peak by the lower melting fraction of felodipine.

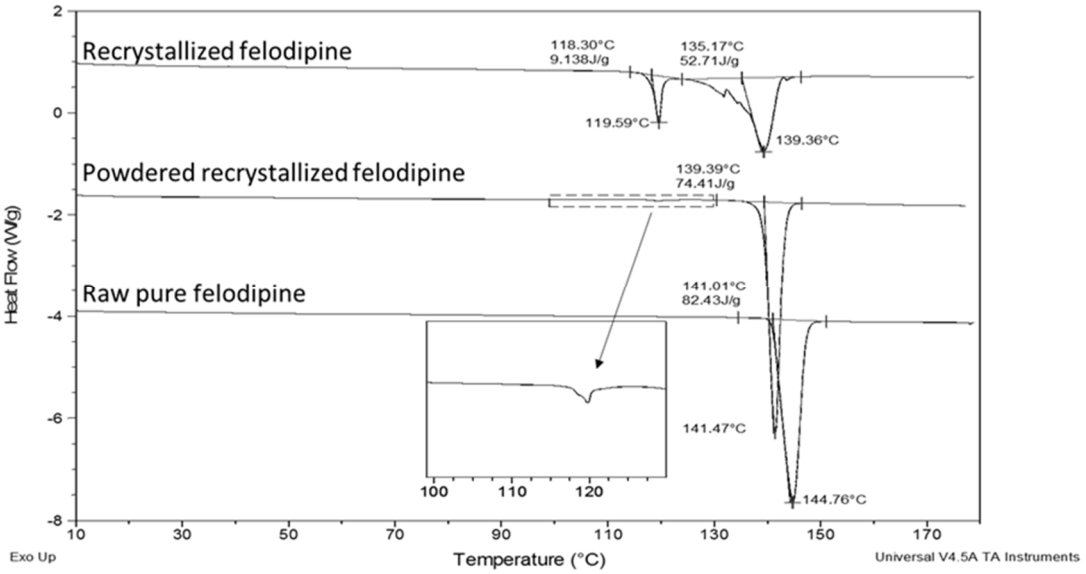

Figure 6.45: DSC thermograms illustrating melting transition of pure felodipine form I and recrystallised felodipine at 40℃ and 75% RH before and after milling (n=3)

In addition, PXRD results (**Figure 6.46**) show changes in the patterns of the recrystallised sample at 40℃ and 75% RH as small peaks at 9.3° and 12.6° as peaks of low intensity may be due to the small fraction of the new polymorphic growth.

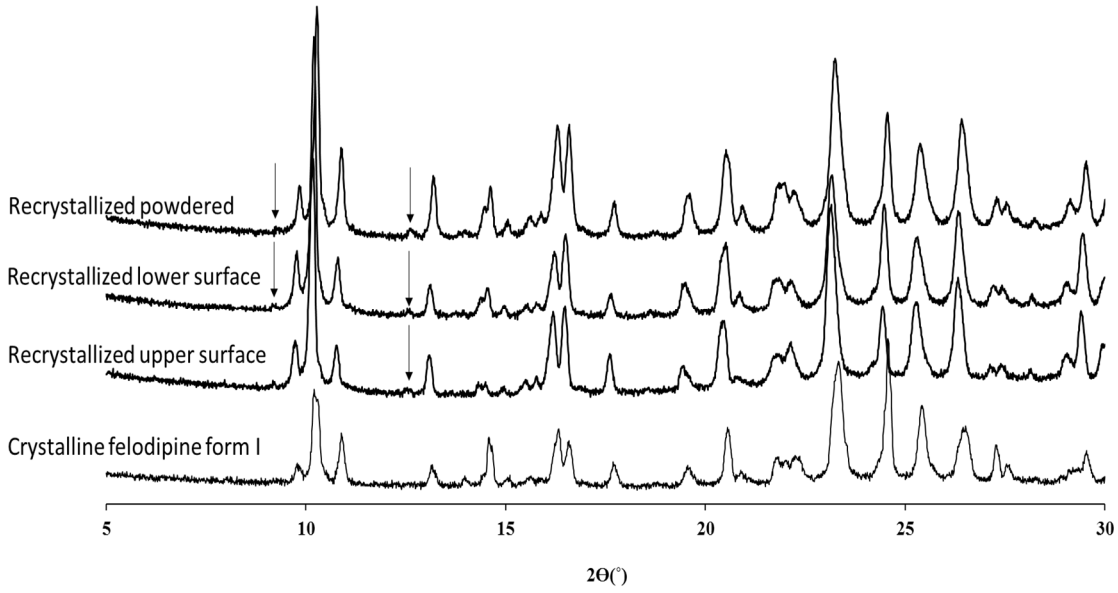

Figure 6.46: PXRD patterns of pure felodipine form I and recrystallised felodipine at 40℃ and 75% RH before and after milling

The ATR-FTIR data shown in **Figure 6.47** do not reveal any differences in the spectra for the lower surface, upper surface and the milled recrystallised sample compared to the raw pure crystalline felodipine form I. These results may suggest that the new growth is more likely in the bulk of the sample and the detection is out of the penetration depth limits of the instrument used in the analysis.

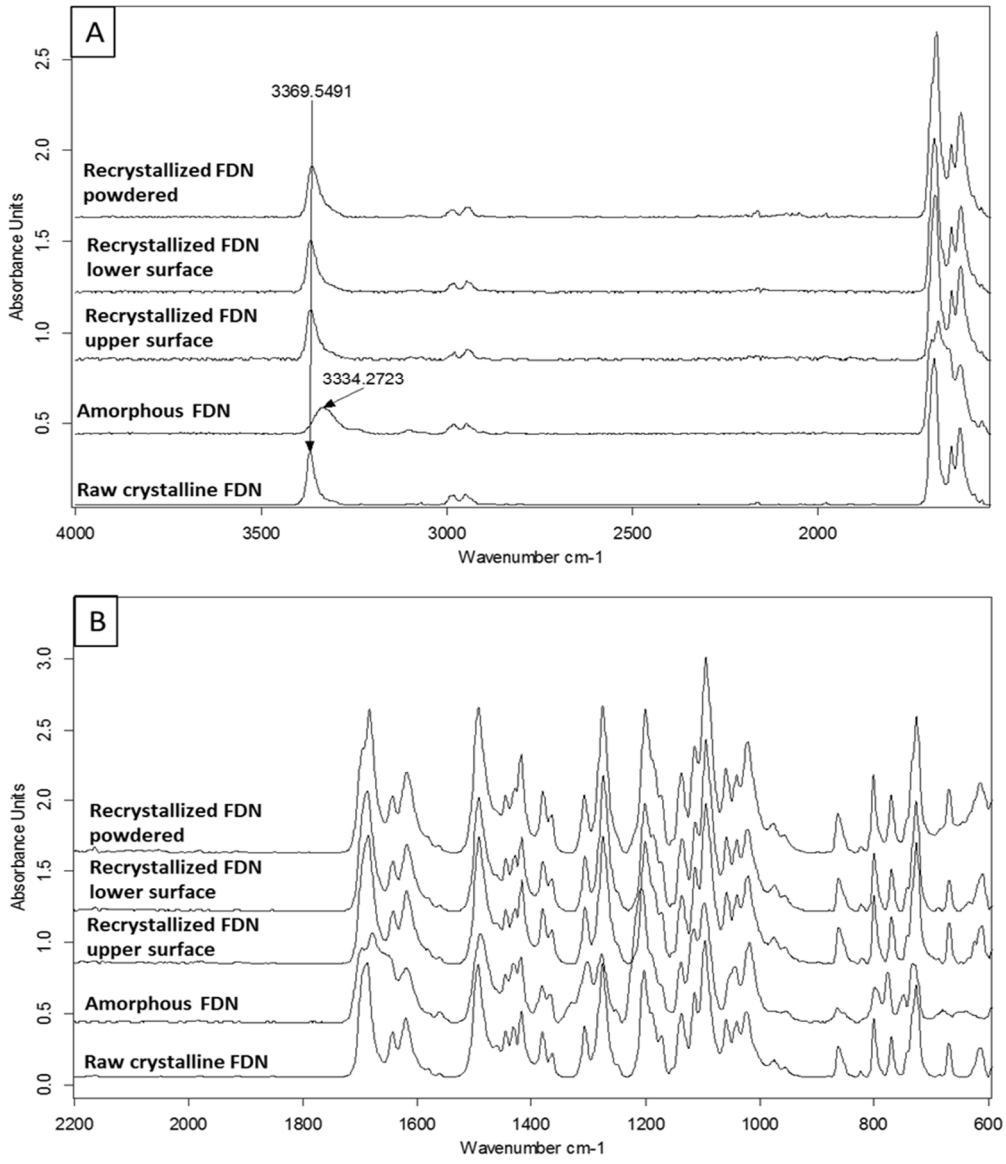

Figure 6.47: Partial ATR-FTIR spectra of pure felodipine form I and recrystallised felodipine at 40℃ and 75% RH before and after powdering; A and B are high and low wavenumber ranges respectively (n=3)

6.4 Discussion

From the data three general observations can be summarised:

1) For both 0% and 75% RH, it is clear that 40 °C led to a higher degree of phase changes than room temperature.

2) For both CM1 and CM2, drug loading has a significant impact on the ageing behaviour of the carrier materials. The CM1 and CM2 patches with 20% drug loading, which is at the boundary of reaching saturation of drug in the carrier materials, showed the highest drug phase separation activity and microstructural changes of the patches. The patches with drug loadings below and above the saturation showed less phase separation activities highlighting the important relationship between the degree of saturation and stability.

3) TPGS demonstrates better formulation and drug stabilising effects on ageing than Tween 80.

The more significant effect of temperature on the physical stability than humidity can possibly be explained by molecular mobility. Although in the fresh drug loaded samples the drug was solubilised in the surfactant-rich phases, the T_g values of the drug containing phases are ranging from -49.0 ± 0.6 °C (10% CM1) to -24.9 ± 1.5 °C (30% CM2) for CM1 and CM2 patches. The difference between these T_g values and the storing temperatures for each formulation is higher for samples stored at 40 °C compared to room temperature. The bigger the temperature gap between the storing condition temperature and the T_g of the system is expected to exhibit lower drug physical stability for systems having T_g values lower than the storing temperatures. Thus, samples stored at 40 °C is expected to have higher degree of felodipine crystallisation (lower physical stability) compared to samples aged at room temperature. It should be mentioned that the viscosity of the solubilising phase is also expected to play a role in felodipine crystallisation process. Storing the samples at 40 °C also may result in a decrease in the viscosity of the dispersing phase leading to higher rate of drug diffusion and more crystallisation compared to room temperature (24, 105). In addition, the difference between T_g of the formulations and the stability testing temperatures (either at room temperature or 40 °C) is greater for CM1 than CM2. Therefore, the mobility of drug in the Tween phase is higher than the ones in the TPGS phase. The higher molecular mobility of the drug led to higher amount of drug recrystallised in CM1 patches than CM2 patches within the same time scale of ageing. The presence of the depressed melting of the crystalline drug between 80-90 °C seen in all 30% aged CM1 patches confirms this; whereas only the CM2 with 30% aged under 75%RH show this peak. This is also evidenced by the depression

of the T_g of the surfactant phase and the PXRD results. Using the diffraction peaks within the 9-13° as the markers, it can be seen that less intensities of these peaks for aged CM2 than CM1 samples with 20 % drug loading. Therefore, during formulation development of solid dispersions containing surfactants, the thermal properties of the surfactants should be carefully considered.

The more profound changes of the 20% loaded samples on ageing demonstrated the importance of the relationship between drug-carrier solubility and stability. Boundary solubility should be avoided to minimise the instability associated with drug recrystallisation. The higher solubility of the drug in TPGS led to better drug stabilisation capacity of TPGS than Tween again indicates that impact of surfactant selection on the formulation stability.

In addition, the chemical stability of the PEG/PEO based carrier material should also be carefully considered during formulation. In comparison to Tween containing CM1 samples, TPGS containing CM2 samples is much less vulnerable to degradation owing to the antioxidant activity of TPGS (144, 207, 386, 387). For drug loaded CM1 patches, fewer signs of degradation of PEG-PEO K900 were observed under high temperature and high humidity environments in comparison to placebos suggesting the drug incorporation also had a protective effect on the carrier material from degradation, most likely to be antioxidation (513).

6.5 Conclusions

This chapter has investigated the effect of surfactants on the stability of multi-component dispersions which were intentionally formulated being phase separate. Semi-solid surfactant TPGS showed better stabilising effect on the drug than the liquid surfactant Tween 80. The higher T_g and semi-solid nature of TPGS which provides higher viscosity in the dispersion are believed to contribute to its higher stabilising effect of the model drug. However, such stabilising effect is only valid for the systems with drug loading below the saturation of drug in the carrier. With drug loading at the border and above the saturation, the stabilisation advantage is significantly reduced. In addition, a new polymorphic form of felodipine was observed in the aged samples. The crystallisation of the new form is more sensitive to temperature than humidity.

Chapter 7. Design, characterisation and evaluation of FDM 3D printed felodipine solid dispersions

7.1 Introduction

3D printing as a recently emerging technology in the pharmaceutical field has been identified as holding future promise for developing individualised medicines which in turn are expected to improve the efficacy of treatment and patients' compliance (224-226, 514, 515). FDM 3D printing can play an important role in reducing the complexity of drug regimens through the incorporation of multiple drugs into a 'polypill' type of formulations. It can also be used to achieve the required drug release profile by changing the geometry and the structure of the dosage form or through using various carriers having different release characteristics (224, 514). Although industrial scale 3D printing is used in other sectors, until now its applications in pharmaceutical research have been limited to the laboratory scale. One of the significant constraints for the development of pharmaceutical 3D printing is the extremely limited number of FDM printable materials currently available. In most reported cases, the printing of proposed solid dosage forms was performed using mostly PVA, PLA and PCL (224, 514, 516, 517). This chapter presents an approach of using polymer blends to overcome this problem and open the possibility of using pharmaceutically approved polymers in FDM printing of oral solid dosage forms. In addition, this study also demonstrates that the blends can be used to control the disintegration and drug release of the FDM printed solid dispersions.

The nature of the current state-of-art FDM printing technique leads to three significant barriers to exploiting its application in pharmaceutical solids production: (1) pre-made filaments are required as an additional process step and currently available filament extruders are largely single screw extruders which may not be able to provide sufficient compounding and mixing between the active ingredients and the excipients. Therefore, some researchers have used either a commercially available single screw filament maker or twin screw hot melt extrusion to produce the filaments for printing (224, 514, 516-519). (2) Currently, there is no effective extrusion element in commercially available FDM 3D printers instead they rely on rollers at the top of the printer to push the molten materials to the printer nozzle. Rheologically this requires the material used to have a low melt viscosity at the printing temperature. (3) The molten materials need to solidify rapidly to allow the rapid deposition and accurate buildup of the 3D object according to the pre-set digital design (229). This requires the printing materials to be highly thermoplastic whereas most pharmaceutical grade polymers are not thermoplastic.

The last two limitations of the technology can be overcome by selecting appropriate polymers. Polymers such as PVA, PLA and PCL have sufficient thermoplasticity to make them suitable for

FDM 3D printing. However, many printable grades of these polymers are not pharmaceutical grade excipients. In addition, use of these few polymers often provides little flexibility in tailoring the drug release profiles and limits the application of any delivery system produced from them. Recently the addition of plasticisers to improve the processability of controlled release polymers such as HPC and eudragit RL and RS during FDM printing has been reported (517, 518). However, to the best of our knowledge so far there is no report on the use of polymer blends to FDM print solid dispersions for the dissolution enhancement for poorly soluble drugs.

Formulations fabricated using FDM 3D printing are mostly solid dispersion based formulations (224, 514, 516, 519). This explores the feasibility of using FDM 3D orienting to produce felodipine solid dispersions. PVA was used as the benchmark polymer in this study because of its excellent thermoplasticity and FDM printability (224, 226). Eudragit E PO and soluplus both have been widely used in pharmaceutical HME indicating their good thermostability and extrudability. However, they are not FDM printable on their own. They were selected as the two model polymers which were compounded with an adjustable mixture of PEG-PEO K100 and/or Tween 80. PEG has low melt viscosity and was used to adjust the printability of the blends. As a result of its high molecular weight, PEO K100 provides mechanical flexibility to the filaments to allow easy feeding into the FDM printer. Tween 80 was used primarily as a plasticiser in order to lower the processing temperature to safe temperatures and to overcome degradation issues for the drug under investigation. The secondary functions of PEG, PEO K100 and Tween 80 are associated with their good solubilising properties for poorly water soluble drugs and plasticising characteristics for solid dispersion mixtures (361, 498, 520).

Research objectives

1. To design felodipine solid dispersions using FDM 3D printing.
2. To characterise the FDM 3D printed discs.
3. To evaluate the *in vitro* release profiles of the FDM 3D printed discs.

7.2 Materials and Methods

7.2.1 Materials

Felodipine, the model drug was purchased from Afine Chemicals Ltd (Hangzhou, China) (batch no. 20100601). Polyethylene glycol (PEG) (average MWT = 4000) was purchased from Sigma-

Aldrich (Poole, UK). Polysorbate (Tween® 80) was purchased from Acros Organics (Geel, Belgium), Polyethylene oxide (POLYOX WSR N10 LEO) MWT= 100,000, soluplus, eudragit® E PO and 33-38% partially hydrolysed polyvinyl alcohol (PVA) MWT= 18,000-25,000 were kindly donated by Colorcon Ltd. (Dartford, UK), BASF (Ludwigshafen, Germany), Evonik Industries (Darmstadt, Germany) and Kuraray Co., Ltd. (Tokyo, Japan), respectively. The chemical structures of the materials are illustrated in Chapter 2.

7.2.2 Preparation of placebo and felodipine loaded FDM filaments using HME

Placebo and 10% w/w felodipine FDM filaments consisting of three sets of excipient mixtures (compositions are shown in **Table 7.1**) were prepared using a co-rotating twin-screw extruder (Haake MiniLab II Micro Compounder, Thermo Electron, Karlsruhe, Germany). The formulations containing eudragit E PO, soluplus and PVA as the main matrix materials are labelled with the abbreviations of CME, CMS and CMV, respectively. All ingredients were accurately weighed and premixed using a mortar and pestle for 2 minutes. For each extrusion experiment, 7 g of the pre-mixed blend was fed into the extruder and 3 g was kept for the characterisation of the physical mixtures.

Table 7.1: Composition of placebo and 10% w/w felodipine loaded FDM dispersions. Proportions are expressed as % w/w

Mixture	Felodipine	Eudragit	Soluplus	PVA	Tween 80	PEG	PEO K100
Placebo CME	-----	55.56	-----	-----	11.10	16.67	16.67
10% w/w CME	10	50	-----	-----	10	15	15
Placebo CMS	-----	-----	55.56	-----	16.67	11.10	16.67
10% w/w CMS	10	-----	50	-----	15	10	15
Placebo CMV	-----	-----	-----	75	25	-----	-----
10% w/w CMV	10	-----	-----	67.5	22.5	-----	-----

The extrusion was performed at the specified extrusion temperature (**Table7.2**) with 5 minutes retention time and 100 rpm screw speed. After decreasing the rotation speed of the screws to 25 rpm, the extruded soft mass of the blends was flushed directly through a metal attachment with a

circular die of a diameter 1.75 mm onto a conveyor belt to produce placebo and 10% w/w felodipine loaded filaments.

Table 7.2: HME-3D printing processing parameters of placebo and 10% w/w loaded felodipine filaments and 3D printed discs

Mixture Code	HME temp. (˚C)	FDM printing temp. (˚C)	Extrusion torque (N.cm)
Placebo CME	100	150	24
10% w/w CME	100	150	18
Placebo CMS	120	150	7
10% w/w CMS	120	150	8
Placebo CMV	130	150	1
10% w/w CMV	130	150	1

7.2.3 Using FDM 3D printing to fabricate solid dispersions

A MakerBot Replicator II desktop 3D printer (New York, USA) equipped with two thermal extruding nozzles (diameter 400 µm) was used for printing the prepared placebo and medicated filaments. The digital file for the selected 3D shape in STL (stereolithography) format was designed using Blender software (521) and printed using MakerBot MakerWare™. In this study, a model disc shape with dimensions of 12 mm diameter and 0.6 mm thickness and was used as a standard shape to compare the characteristics of different mixtures. Printing was performed using an extrusion temperature of 150 ˚C without heating the platform. The 3D object was printed using standard mode with 0.2 mm layer thickness and 100% infill. The time required to complete printing each disc was 24.7 ± 0.1 seconds. The images of the produced 3D printed discs with their corresponding filaments are shown in **Figure 7.1**.

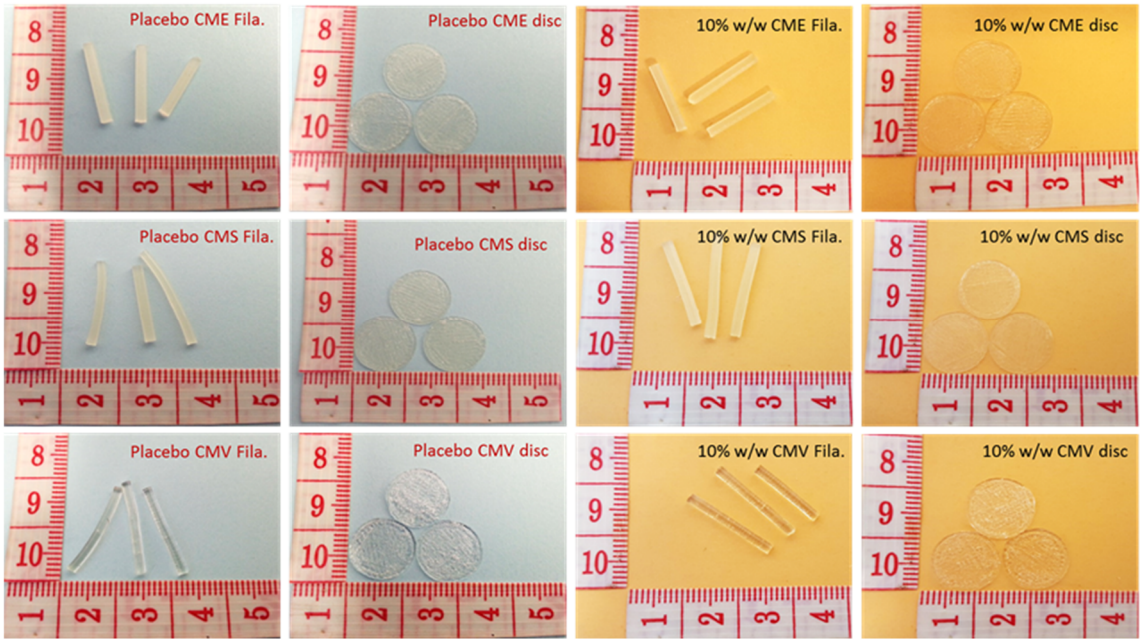

Figure 7.1: Images of the prepared HME filaments and FDM 3D printed discs

7.2.4 Characterisation and evaluation of FDM 3D printed solid dispersions

7.2.4.1 Thermal gravimetric analysis (TGA)

The same experimental setting parameters of TGA as mentioned in Chapter 3, section 3.2.2.2.1 were used to scan the samples in this study.

7.2.4.2 Differential scanning calorimetry (DSC) and temperature modulated DSC (MTDSC)

All samples investigated in this study using standard DSC were analysed using the same parameters as described in Chapter 3, section 3.2.2.2.2. MTDSC experiments were also performed using a 2 ºC/min heating rate, 60 sec period and 1 ºC or 0.318 ºC amplitude (depending on the samples) with proper MTDSC calibration to detect the T_g temperatures of the different formulations. Sample weights were 2-3 mg contained in an aluminium standard TA crimped pans and lids (TA Instruments, Newcastle, USA). Universal Analysis software was used to analyse the obtained results. All analyses were performed with 2-3 replicates for each sample.

7.2.4.3 Attenuated total reflectance Fourier transform infrared spectroscopy (ATR-FTIR)

ATR-FTIR scanning for all samples was carried out using the same experimental parameters as mentioned in Chapter 3, section 3.2.2.2.4.

7.2.4.4 Scanning electron microscopy (SEM)

The same experimental parameters of SEM as mentioned in Chapter 4, section 4.2.3.2 were used to scan the samples used in this study.

7.2.4.5 Powder X-ray diffraction (PXRD)

PXRD parameters as mentioned in Chapter 3, section 3.2.2.2.6 were utilised to analyse all samples investigated in this study using this characterisation technique.

7.2.4.6 X-ray micro-computed tomography (XµCT)

A SkyScan1172 high-resolution X-ray micro computed tomography (XµCT) scanner (Bruker-microCT, Kontich, Antwerp, Belgium) was used to 3D visualise the microstructure of the most promising blend (eudragit E PO based filaments and FDM 3D printed discs). Placebo and 10% w/w loaded samples were scanned using an aluminium filter to cut-off high energy X-rays at an isotropic voxel resolution of 3 µm over a total of 20 min acquisition time and a subsequent image reconstruction time of approximately 20 min per sample, using the NRecon program (version 1.6.8.0, Bruker-microCT). The collected data were then analysed using CTan and CTvol software in which the images for a small section (designated as a region of interest ROI) of each sample are converted to binary images followed by thresholding areas of different electron densities and represented in 3D models (499).

7.2.4.7 Determination of drug loading efficiency

Accurately weighed drug loaded FDM printed discs of different formulations were dissolved in a beaker containing 200 mL of 50:50 simulated gastric fluid pH 1.2 and absolute ethanol. The

beaker was covered with a parafilm tape to minimise solvent evaporation during dissolution. The medium was stirred using magnetic stirrer at room temperature. After complete dissolution, 5 mL samples were withdrawn and filtered using 0.45 µm pore size (Minisart NML single use syringe, Sartorius, UK). The filtered samples then scanned for their content of felodipine using a UV–VIS spectrophotometer (Perkin-Elmer Lambda 35, USA) at 363 nm. The loading efficiency measurements for the loaded discs were carried out in triplicate.

7.2.4.8 *In vitro* drug release studies

The *in vitro* drug release profiles were measured in dissolution testing apparatus (Caleva 8ST, Germany) using the paddle method (USP apparatus 1). A paddle rotation speed of 100 rpm and 900 mL of pH 1.2 HCl (simulated gastric fluid without enzymes) or phosphate buffer pH 6.8 (simulated intestinal fluid without enzymes) at 37 ± 0.5 ˚C were used for all measurements. The pure crystalline drug and disc-shaped dispersions containing the equivalent of the daily dose (5 mg) of the drug were used in this study. Under non-sink conditions, 5 mL dissolution samples were withdrawn at pre-determined time intervals. The samples were directly filtered through a membrane filter with 0.45 µm pore size (Minisart NML single use syringe, Sartorius, UK). The filtered sample solutions were diluted with equal volume of ethanol. 5 mL of fresh pre-warmed (37 ± 0.5 ˚C) dissolution media was added to the dissolution vessel after each sampling. The samples were analysed using a UV–VIS spectrophotometer (Perkin-Elmer Lambda 35, USA) at 363 nm. All drug release studies were conducted in triplicate.

7.3 Results

7.3.1 FDM 3D printing processability of placebo and drug loaded solid dispersions

The calculations of solubility parameters using group contribution methods for the individual compounds used in this chapter and their differences relative to that of felodipine were presented in Chapter 3 and Appendix 1. The solubility parameters for soluplus and the processing aid materials, PEG, PEO K100 and Tween 80, are nearly identical, indicating excellent miscibility of all excipients in CMS placebo. The $\Delta\delta$ value is less than 4 for eudragit E PO with PEO K100, PEG and Tween 80 which also indicates good miscibility between excipients used in CME

dispersions. However, the Δδ value of PVA with Tween 80 is greater than 7 suggesting partial miscibility of these two excipients for CMV formulations. Based on the ranking of the Δδ values, the highest miscibility of felodipine with the individual excipients is expected to be in the order of soluplus > PEG 4000 = PEO K100 > Tween 80> eudragit E PO > PVA. This leads to the predicted the rank of the miscibility of felodipine in FDM printed formulations being CMS > CME > CMV.

Eudragit E PO and soluplus have been widely reported for the preparation of HME solid dispersions for enhancing the dissolution of poorly soluble drugs (83, 119, 139, 522). Although both polymers on their own are HME extrudable, neither of them were FDM printable even with the addition of drug. After blending with PEG, PEO K100 and Tween 80, both polymers were FDM printable. However, due to the higher melting viscosity and lower T_g of eudragit E PO than soluplus, a greater quantity of PEG and reduced amount of Tween 80 were added to the CME blends in comparison to CMS blends (**Table 7.1**). The PVA used in this study was 33-38% hydrolysed, and the HME filament was brittle and not suitable for FDM printing. Therefore, Tween 80 was added to plasticise this material and improve the flexibility of the filaments which made feeding of the FDM printer easier.

The PVA-based filaments are highly thermoplastic. As seen in **Table 7.2**, the low extrusion torques during HME indicating low melt viscosity of the materials, but readily formed the required shape upon cooling (**Figure 7.1**). For eudragit E PO based blends, the addition of felodipine plasticised the mixtures and reduced the extrusion torque during HME which allowed FDM printing. For soluplus based blends, the plasticisation effect of the drug is not significant and may be masked by the higher Tween 80 content in these blends in comparison to eudragit E PO based blends. Although both eudragit E PO and soluplus based blends gave higher extrusion torque during HME, the mixtures were FDM printable. Moreover, no clear deformation of the shape at a micron scale can be observed using SEM (**Figure 7.2**).

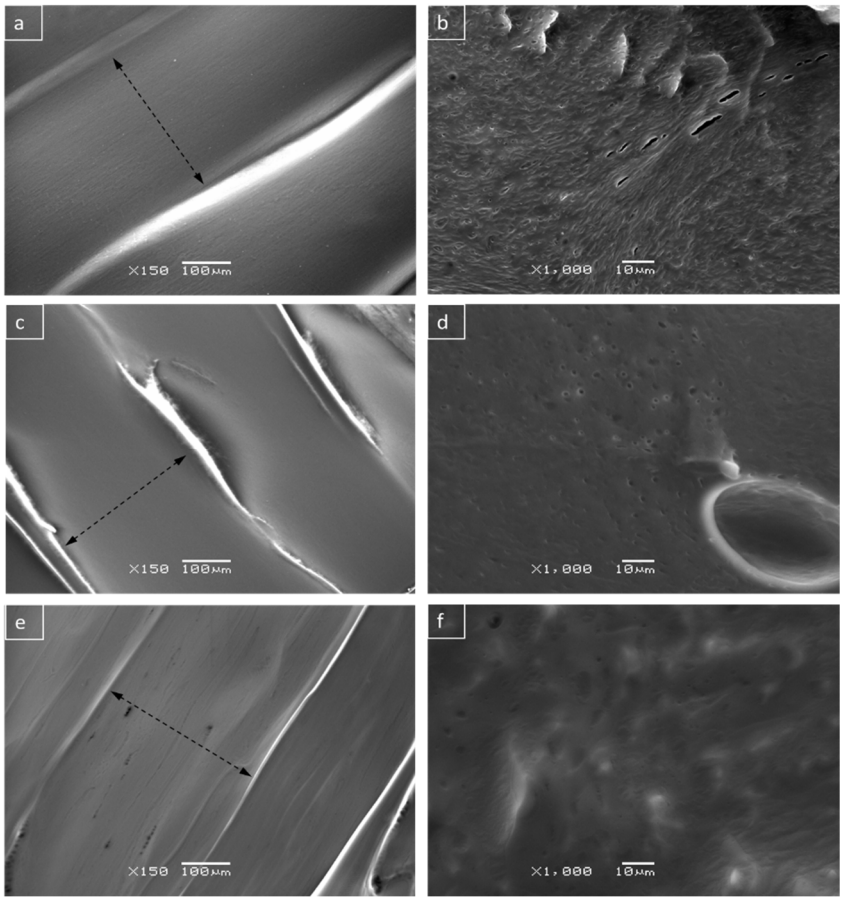

Figure 7.2: SEM images for 10% w/w felodipine loaded FDM 3D printed discs. CME (a) surface and (b) cross-section; CMS (c) surface and (d) cross-section; CMV (e) surface and (f) cross-section. The dotted lines indicate the widths of filaments strips after FDM printing

The surface roughness at the edges of each deposited strips of CMS is slightly higher than CME and CMV. This may be attributed to the combination of suitable viscosity for FDM deposition but poor thermoplasticity. The edge of each printed strip of the materials can be easily identified. It is noted that for all three formulations the road width of each strip is approximately 370 ± 10 µm instead of 400 µm which is the diameter of the printing nozzle. The uniformity of the small shrinkage of the road width of the printed materials indicates the similar thermal flow behaviour of the three blends.

XµCT was used to study the morphology and internal microstructure of the FDM samples at the hundreds of microns to the mm scale. Representative XµCT results for the placebo and 10% loaded filaments and FDM printed discs of CME blend show some level of micron scale surfaces roughness, which matches the SEM observations (**Figure 7.3**).

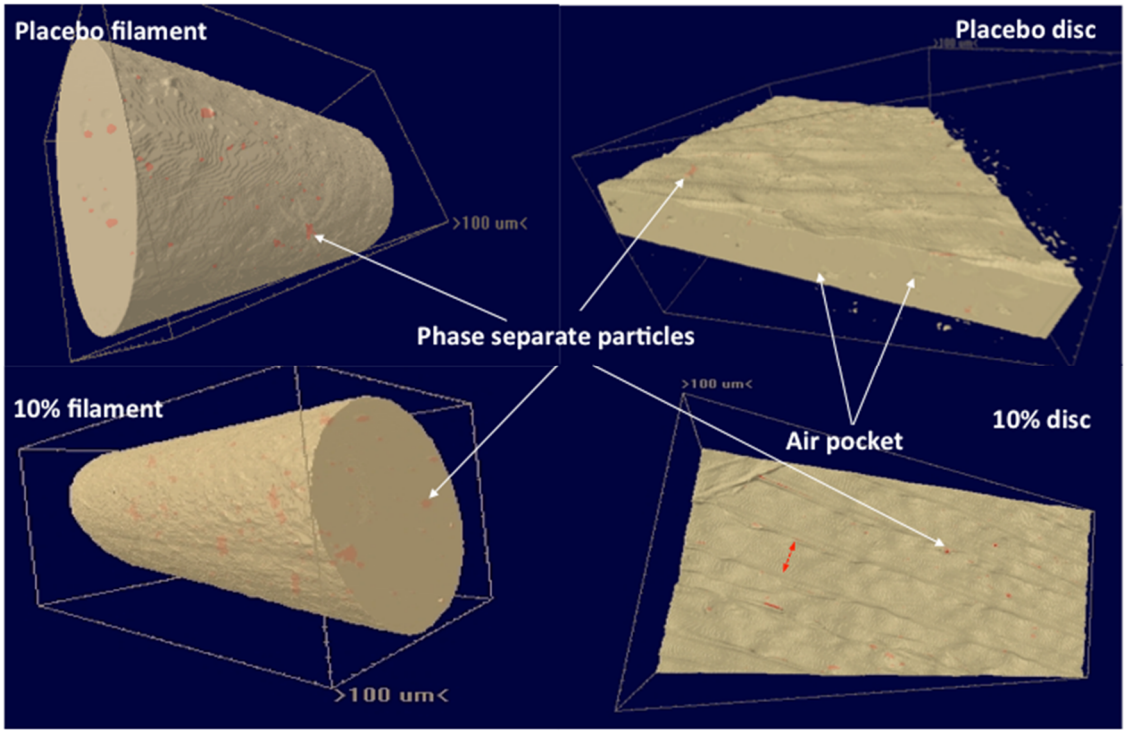

Figure 7.3: Representative XµCT reconstructed 3D images of CME placebo and 10% w/w felodipine loaded CME discs. HME filaments (left) and FDM 3D printed discs (right). The phase separate particles are likely to be metal contaminations introduced during HME and FDM printing and/or some inorganic additives included in the raw polymers (499)

The road width of the individual FDM strip also matches those observed in the SEM images. Small air pockets distributed inside the FDM printed discs can be seen which is absent in the HME filaments. The small air pockets are likely to be introduced during the deposition of each layer of strips. It was noted that for both HME filaments and FDM printed discs; some phase separated particles with high electron density are observed. It can be confirmed that they are not drug particles as they are also present in the placebo filaments and discs. They may be metal contamination introduced during the extrusion/3D printing processes and/or some inorganic additives included in the raw polymers (499).

7.3.2 Loading efficiency of FDM 3D printed felodipine solid dispersions

The weights of the designed placebo and felodipine 10% w/w loaded discs are summarised in **Table 7.3**.

Table 7.3: Weights of placebo and 10% w/w felodipine loaded FDM printed discs (n=3; average ± SD)

Mixture Code	Weights of 3D printed discs (mg)
Placebo CME	61.48 ± 8.16
10% W/W CME	61.33 ± 3.88
Placebo CMS	64.82 ± 1.46
10% W/W CMS	60.34 ± 3.27
Placebo CMV	56.93 ± 7.41
10% W/W CMV	55.34 ± 4.00

It was reported in the literature that the drug loading efficiency of the FDM 3D printed samples prepared by passive diffusion of the drug from its organic solution into the ready-made placebo PVA filaments was often lower than the theoretical value by more than 15% (224, 417, 523). Using a high printing temperature also can lead to unsatisfactory loading efficiency due to the thermal degradation of the drug (224, 417, 523). A temperature of 150 ˚C was used in this study during the FDM printing. The loading efficiencies of felodipine in the 3D printed CMS, CME and CMV discs were 95.75± 0.66%, 94.62 ± 0.56% and 86.23 ± 0.83%, respectively. This suggests that processing the mixtures using HME with subsequent FDM 3D printing at a suitable temperature can produce solid dispersions with high loading efficiency (175). In addition, this result also indicates that the 3D printing process at 150 ˚C led to no thermal degradation of the active drug which was confirmed by the results obtained by TGA (**Figures 7.4**). The lower loading efficiency for 10% CMV than CME and CMS may be attributed to the large particle size of PVA granules used during preparation which led to poor mixing with the Tween 80 and the drug.

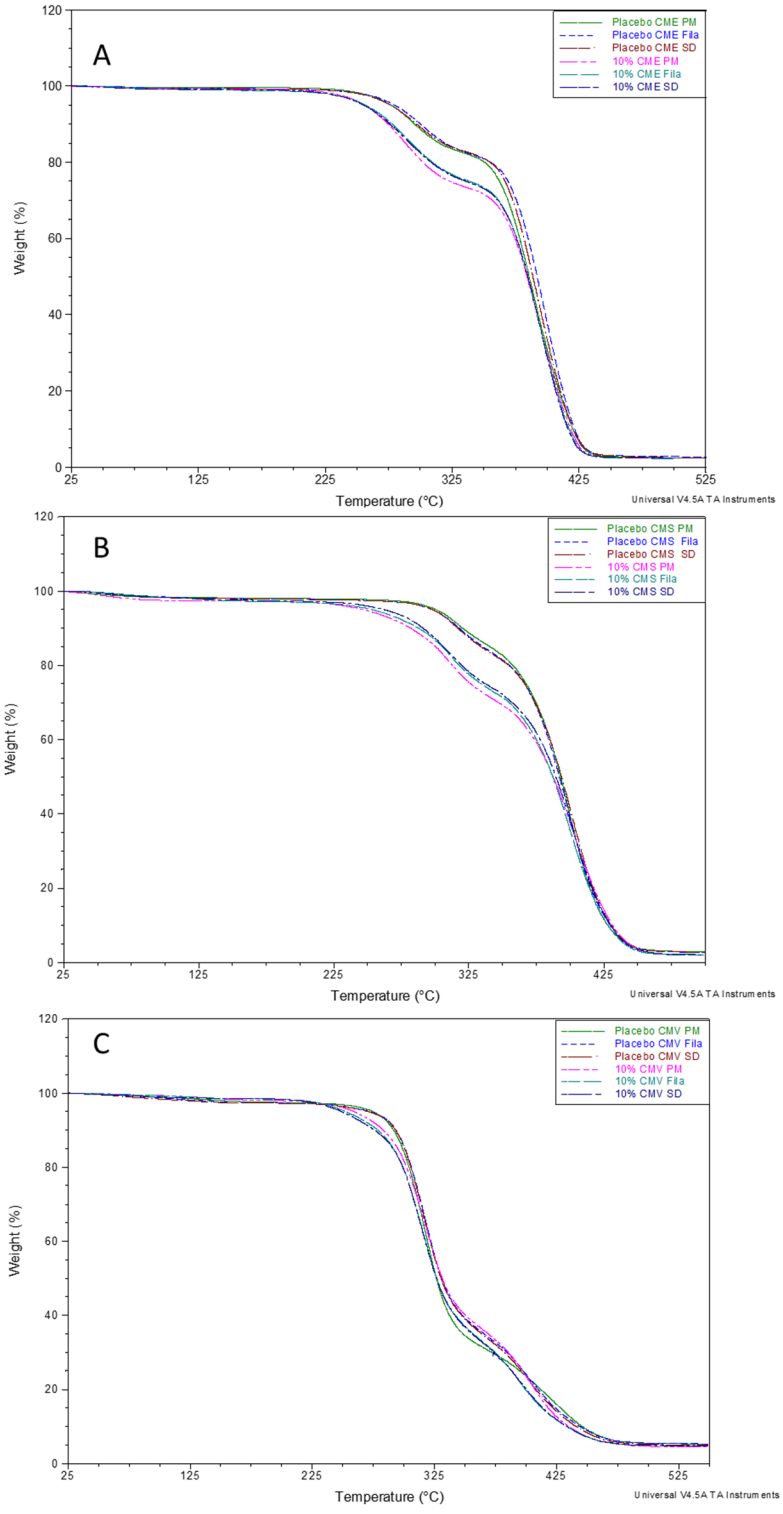

Figure 7.4: Thermal degradation of placebo and 10% w/w felodipine loaded physical mixture, filament and 3D printed discs. A) CME, B) CMS and C) CMV mixtures (n=3)

7.3.3 Physical characterisation of the FDM 3D printed solid dispersions

Thermal transitions for the raw materials used in the various formulations were measured using DSC and are illustrated in Chapter 3. The T_g of eudragit E PO, soluplus, PVA, and Tween 80 were identified at 46.7 ± 1.0, 74.1 ± 0.3, 46.1 ± 1.7, and -64.2 ± 0.6, respectively. The melting peaks of other blend excipients including Tween 80 (after crystallisation at -44.6 ± 1.2 ˚C), PEG and PEO K100 and the model drug can also be identified at -10.2 ± 2.3, 59.3 ± 0.3, 65.6 ± 0.1 and 144.6 ± 0.1 ˚C, respectively. The physical mixtures of the CME and CMS show melting of PEG and PEO K100, but no melting of the model drug (**Figure 7.5**). This is likely to be due to the thermal dissolution effect of the crystalline drug in the polymer mixtures (498). The melting of felodipine is evident in the DSC results of the physical mixtures of CMV. This confirms the partial miscibility between felodipine and PVA predicted previously.

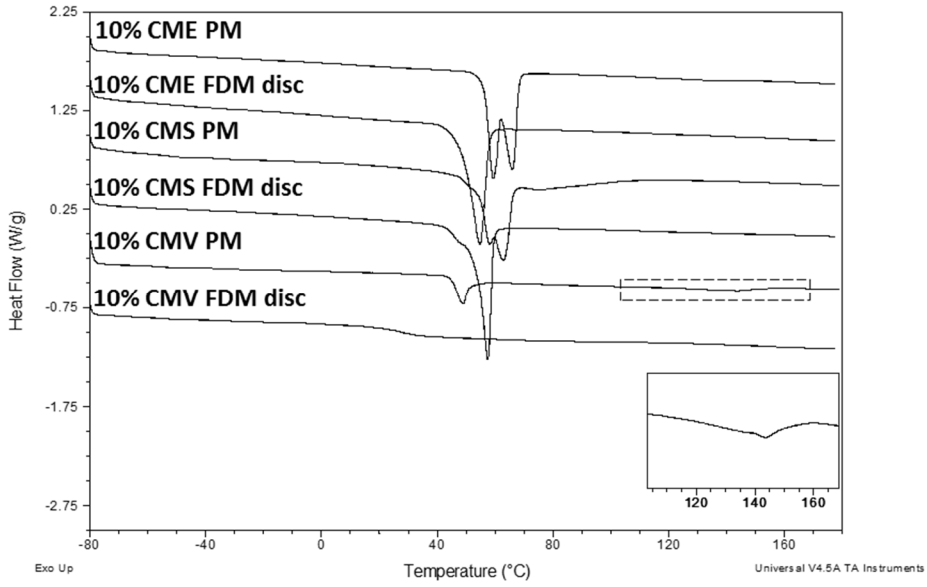

Figure 7.5: DSC thermograms illustrating different thermal events for physical mixtures and FDM 3D printed discs of placebo and 10% w/w felodipine loaded CME, CMS and CMV (n=3)

MTDSC was used to further investigate the T_g region of the samples. As seen in **Figure 7.6a**, the MTDSC results of the physical mixtures of CME show no detectable T_g. A T_g at approximately -55 ˚C can be detected for the physical mixtures of CMS which probably arises from the mixture of PEG/PEO K100/Tween 80 (**Figure 7.6b**). Two T_g temperatures can be clearly seen at -55.4 ± 0.2 and 39.4 ± 4.3 ˚C in the MTDSC results of the physical mixtures of CMV blends (**Figure 7.7**). As the first T_g is higher than the T_g of pure Tween and the second is lower than the T_g of pure PVA, they are likely to be the T_g events of Tween-drug and PVA-moisture phases, respectively.

These T_g events are shifted to higher temperatures (-51.8 ± 0.3 ˚C and 42.9 ± 4.4.5 ˚C) in the reheating cycle which may be caused by the further mixing of Tween 80 and PVA and moisture loss of the main PVA phase, respectively (**Figure 7.7**).

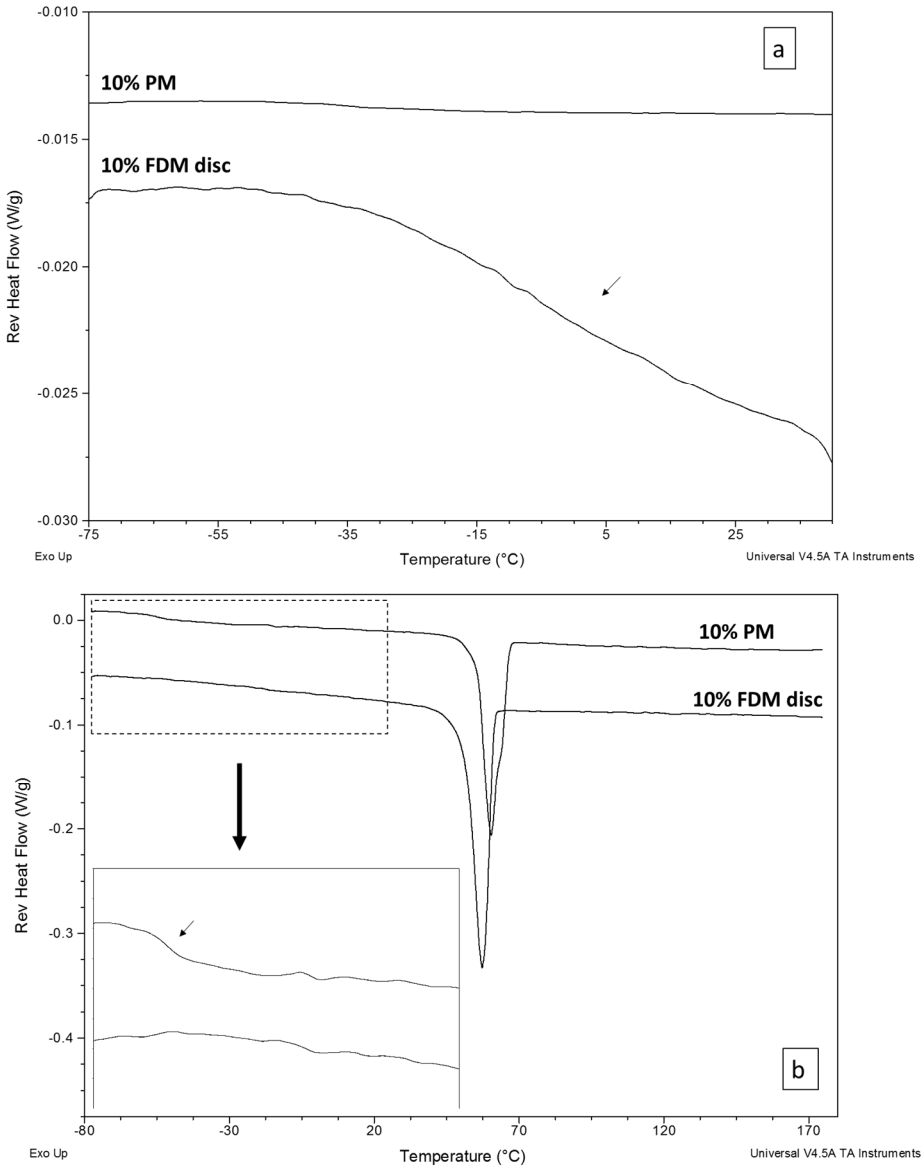

Figure 7.6: MTDSC thermograms showing the T_g events of (a) CME formulations using temperature program of 1.0 ˚C amplitude, 60 sec period and 2 ˚C/ min heating rate and (b) CMS mixtures using a heat only temperature program of 0.318 ˚C amplitude, 60 sec period and 2 ˚C/ min heating rate (n=3)

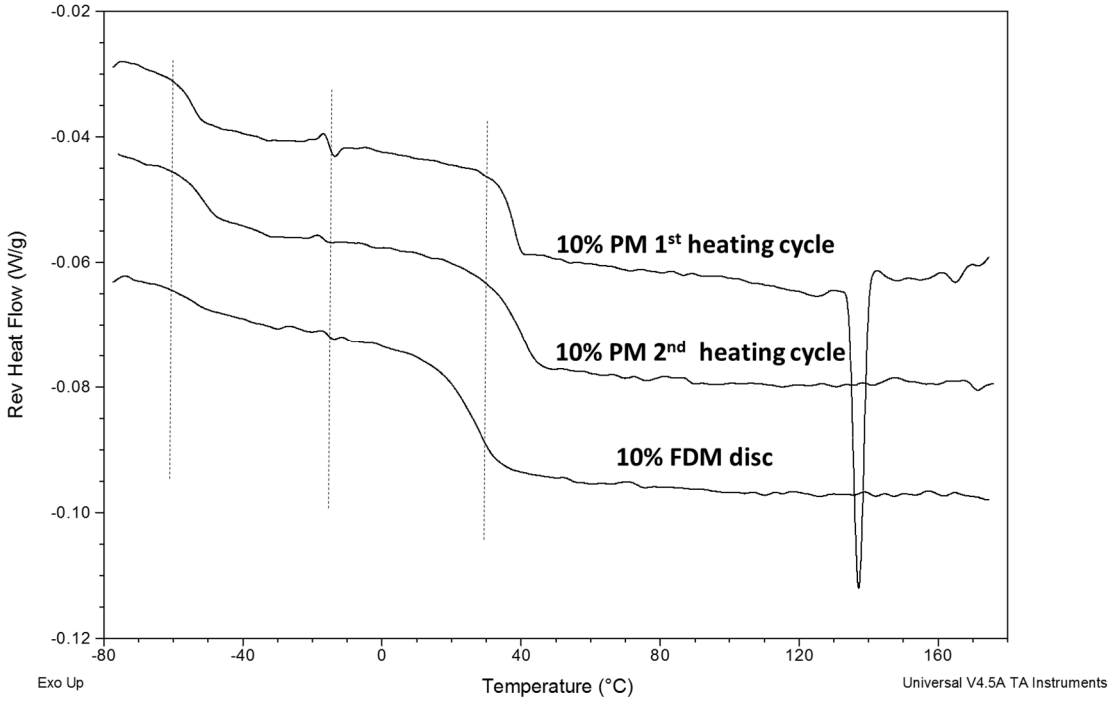

Figure 7.7: MTDSC thermograms showing the T_g events of CMV mixtures using a heat only temperature program of 0.318 ˚C amplitude, 60 sec period and 2 ˚C/ min heating rate (n=3)

In FDM printed CME and CMS discs containing 10% felodipine, DSC shows the joint melting of crystalline PEG and PEO K100. The melting enthalpy values of the crystalline PEG-PEO K100 were similar in CME and CMS. However, it should be mentioned that there was 30% w/w PEG-PEO K100 in CME and 25% in CMS. This indicates that a greater amount of the crystalline PEG-PEO K100 phase was present in CMS in comparison to CME (**Table 7.4**).

It was also noted that the melting point of the PEG-PEO K100 shifted to lower temperatures in comparison to those observed in the results of their physical mixtures. The solubilisation of other excipients and felodipine may be responsible for this melting depression of the crystalline PEG-PEO K100 phase in the printed dispersions.

Table 7.4: Experimental % crystallinity of PEG-PEO polymers in CME and CMS blends compared to the 100% theoretical values (n=3; average ± SD)

Material	1st Melting (˚C)	2nd Melting (˚C)	ΔH_f (J/(g) total	Experimental % crystallinity
Placebo CME PM	58.45± 0.15	65.41± 0.33	53.48± 5.70	87.14± 9.29
Placebo CME filament	59.56± 0.50		49.56± 0.44	80.75± 0.72
Placebo CME 3D disc	57.50± 0.66		49.56± 2.55	80.75± 4.15
10% CME PM	59.90± 1.03	66.18± 0.61	50.38± 6.26	91.23± 11.34
10% CME filament	58.15± 0.09		45.53± 1.90	82.44± 3.44
10% CME 3D disc	54.61± 0.14		46.57± 0.49	84.33± 0.89
Placebo CMS PM	56.99 ±0.65	62.75 ±0.83	55.32 ±18.49	108.67± 36.32
Placebo CMS filament	56.76 ±0.56		44.94 ±1.25	88.28± 2.46
Placebo CMS 3D disc	56.37 ±0.14		45.08 ±1.39	88.55± 2.73
10% CMS PM	58.25 ±0.25	63.43 ±0.29	43.04 ±2.00	93.91± 13.66
10% CMS filament	56.23 ±0.23		41.09 ±3.03	89.66± 6.61
10% CMS 3D disc	57.62 ±0.19		43.18 ±1.16	94.22± 2.53

For the drug loaded CME, the theoretical T_g of the blend calculated using Fox equation as described in Chapter 1, **Table 7.5** and Appendix 4 is 18.9 ˚C. This is higher than the T_g of the FDM printed CME discs measured by MTDSC which is a broad transition at approximately -6 ˚C (**Figure 7.6a**). This negative deviation from the predicted T_g value reflects non-ideality of mixing which may result from the reduced crystallinity of the semicrystalline polymers by processing, increase in the free volume caused by the diffusion of the drug inside the polymer and/or the weaker drug-polymer interactions compared to the original drug-drug interactions (24, 99). The detection of a single T_g is a good indicator of the formation of a molecular dispersion of the drug and the excipients in CME. For drug loaded CMS samples, the T_g of Tween 80 disappeared and no clear joint T_g can be detected by MTDSC (**Figure 7.6b**). No drug melting was detected in the DSC and MTDSC results of CMV processed dispersions. Two T_g events are present in the MTDSC results of the CMV dispersions (**Figure 7**) indicating the phase separation

in printed CMV dispersions. The T_g of the PVA phase shifts to a lower temperature (25.7 ± 1.3 ˚C) in the FDM printed dispersions in comparison to the physical mixture. As the T_g of PVA is lower than amorphous felodipine and higher than Tween 80, this may indicate enhanced mixing of Tween with PVA after processing. The separate T_g at -51.6 ± 2.7 ˚C can be assigned to the Tween rich phase. It is likely that felodipine is molecularly dispersed in both PVA-rich and Tween 80-rich phases.

Table 7.5: Fox equation predicted T_g temperatures for different formulations

Sample	Fox equation T_g (˚C)
Placebo CME	14.87
10% w/w CME	18.91
Placebo CMS	23.20
10% w/w CMS	25.99
Placebo CMV	3.83
10% w/w CMV	7.57

ATR-FTIR and PXRD were used to further confirm the physical states of felodipine in the solid dispersions. As seen in **Figure 7.8** the NH stretching peak of crystalline felodipine form I at 3367 cm^{-1} is visible in the physical mixtures. This peak transforms into a broad peak with low intensity in the spectra of the FDM printed CME, CMS and CMV discs. This broadening may be caused by a combination of the formulation of molecular dispersion of felodipine and the small quantity (less than 3% w/w) of moisture present in the printed discs as shown in the TGA results (**Figure 7.9**).

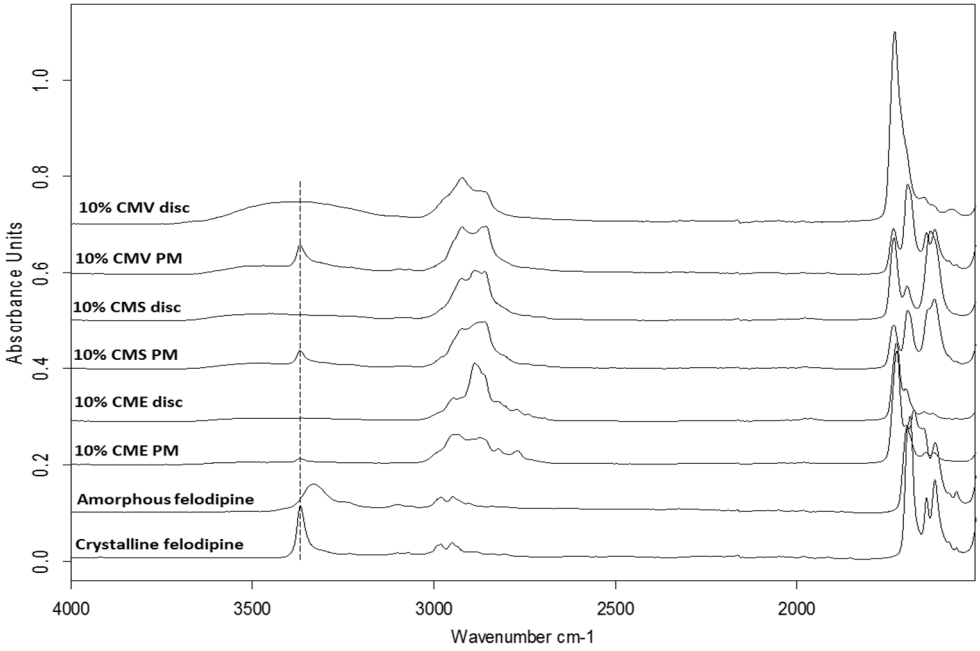

Figure 7.8: Partial ATR-FTIR spectra of the physical mixtures (PM) and felodipine loaded FDM printed discs. The NH stretching peak of crystalline felodipine is highlighted with the dashed line (n=3)

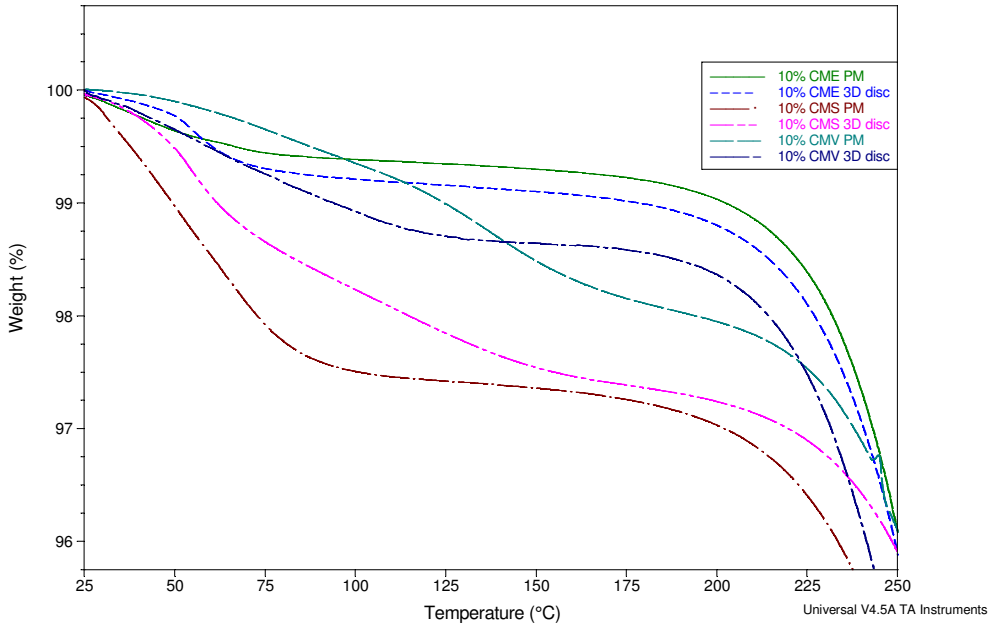

Figure 7.9: Moisture content of different FDM 3D printed discs using TGA at 10 ºC/min (n=3)

A few signature diffraction peaks of the crystalline felodipine are present in the PXRD diffraction patterns of the physical mixes for the three blends (**Figure 7.10**). Because both CME and CMS contain semi-crystalline PEG and PEO K100, the main diffraction peaks of these two polymers can be seen in the PXRD patterns of the FDM printed discs. The crystalline drug related peaks completely disappear in all patterns of the 10% w/w loaded printed discs. Taking into account of the miscibility prediction of felodipine and the excipients, the phase separation of amorphous felodipine is unlikely and the results indicate the formation of felodipine molecular dispersions at the detection limit of PXRD. These results agree well with the DSC results and confirm felodipine was molecularly dispersed in all three matrices.

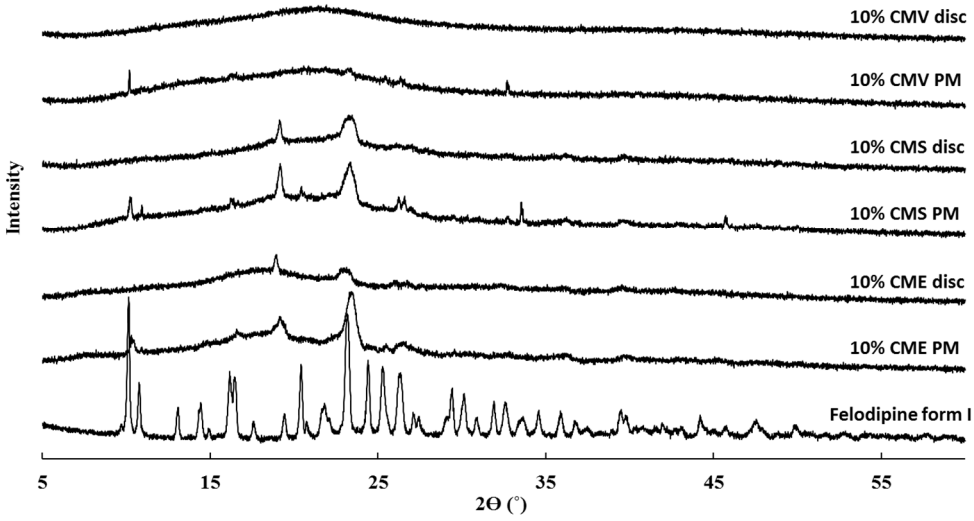

Figure 7.10: PXRD Diffraction patterns of physical mixtures and 10% w/w felodipine loaded FDM printed CME, CMS and CMV discs

7.3.4 *In vitro* disintegration and drug release study of FDM printed felodipine dispersions

A significant enhancement of the dissolution profile of felodipine from CME discs in comparison to crystalline model drug alone was obtained when pH 1.2 HCl was used as the dissolution media (**Figure 7.11a**). The rapid release of approximately 84.3% of the drug load was achieved within 30 minutes. This dissolution improvement may be attributed to the formation of the molecular drug dispersion and the high solubility of eudragit E PO in pH 1.2 HCl. The rapid disintegration

of the CME discs can be observed within the first 5 minutes of the dissolution experiments (**Figure 7.12)**.

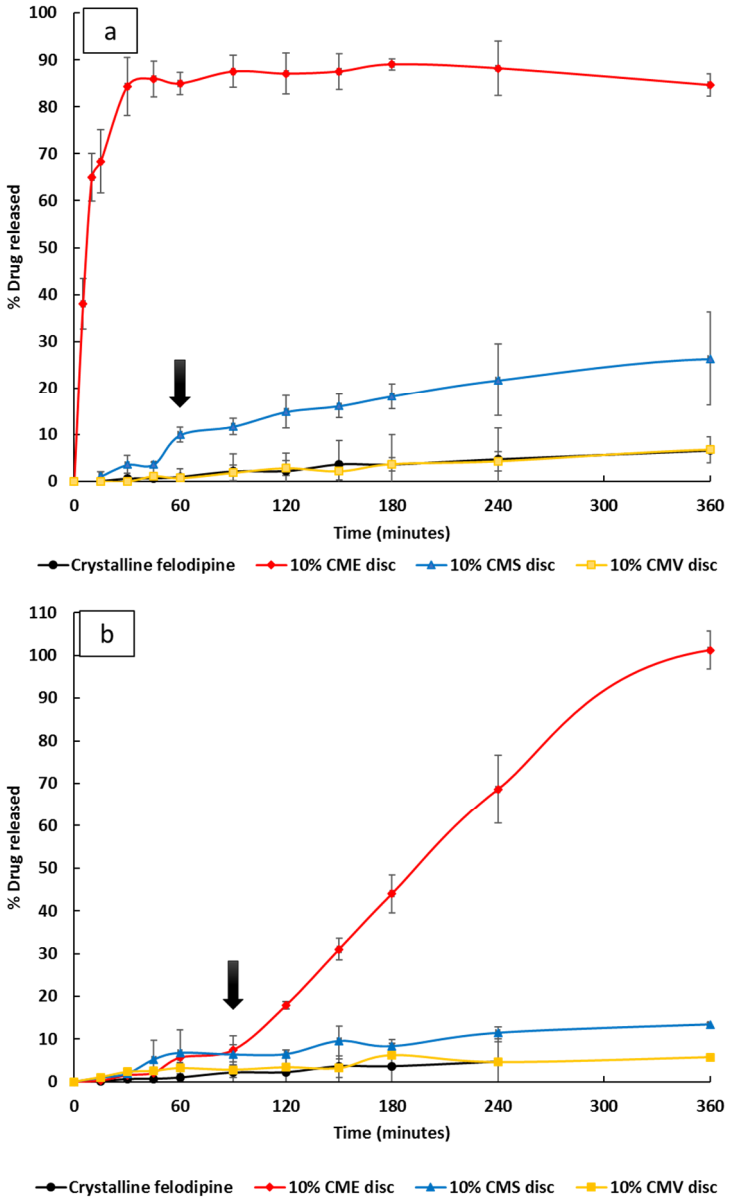

Figure 7.11: Felodipine release profile of FDM 3D printed discs using a) pH 1.2 HCl (simulated gastric fluid without enzyme) and b) pH 6.8 phosphate buffer saline (PBS) (n=3; average ± SD)

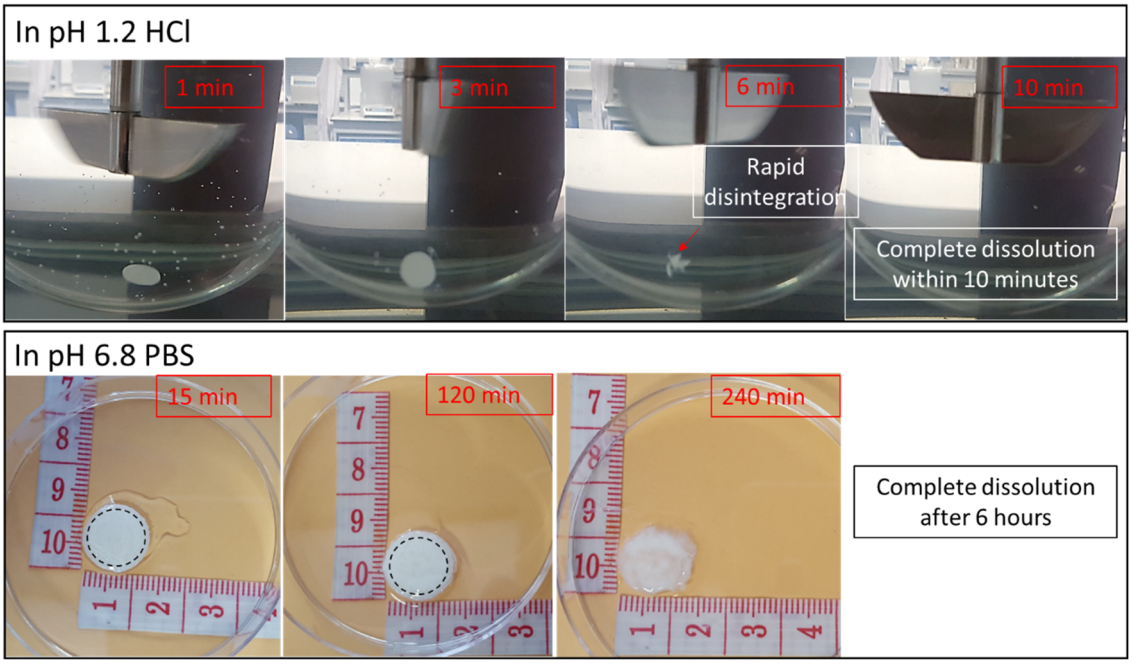

Figure 7.12: Visual appearances of felodipine loaded FDM printed CME discs during dissolution in pH 1.2 HCl and pH 6.8 PBS. The dash circles represent the diameters of freshly prepared dry CME discs

Eudragit E PO is insoluble at pH 6.8, thus little drug release from the CME was expected. However, a delayed but 100% drug release of felodipine from the CME discs in pH 6.8 PBS was obtained (**Figure 7.11b**). Less than 8% drug release occurred in the first 90 minutes. However, from 90 minutes onwards, a linear zero-order release profile with 100% drug release by 6 hours was observed. The images of the discs during the dissolution in pH 6.8 PBS show the slow bulk erosion and disintegration of the discs which was completed by 6 hours (**Figure 7.12**). A minor level of swelling of the discs prior to the complete disintegration and dissolution was observed.

CMS discs showed significantly slower drug release profile in pH 1.2 HCl than CME discs (**Figure 7.11a**). However, it is interesting to note that some improvement in drug dissolution in comparison to the crystalline drug alone was still observed from 1 hour onwards and the release follows a linear release pattern. The maximum release of 28% was achieved after 6 hours *in vitro* dissolution. Although soluplus has been reported to be a water-soluble polymer, the addition of the inorganic salts in the dissolution medium can depress the cloud point of the polymer and reduce the solubility of the polymer in the media (149). **Figure 7.13** captures the start of the disintegration process of CMS discs between 60 to 90 minutes into the dissolution test. A closer examination of the images reveals the sequence of the disintegration of CMS discs into segments of printed strips which is significantly different from the disintegration of CME in pH 6.8 PBS.

Between 60-90 minutes, the individual printed polymer strips at the outer edge of the FDM discs started to unravel into single long strands. There were three printed layers stacked together to form the discs; the outer printed layer unravelled first to reveal the middle layers. This was followed by a further breakdown of the longer polymer strips into smaller segments. This unique disintegration process contributed to the increased release of drug and led to the observed increase in the amount of drug released from 1 hour onwards (**Figure 7.11a**).

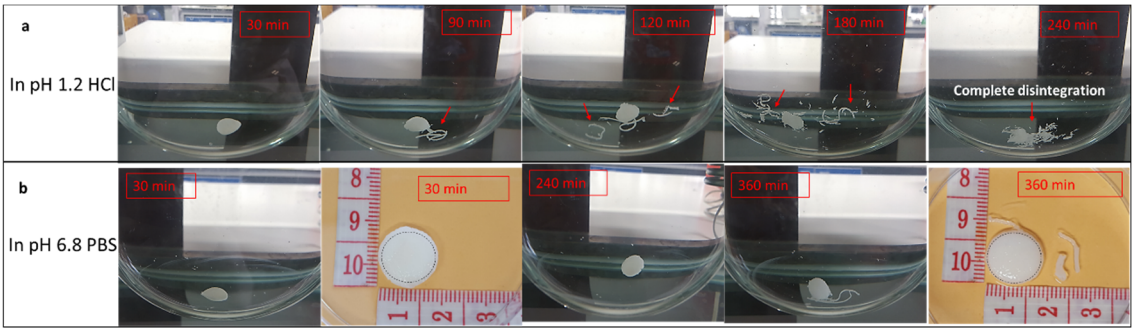

Figure 7.13: Visual appearances of the felodipine loaded FDM printed CMS discs during the dissolution tests in (a) pH 1.2 HCl and (b) pH 6.8 PBS. The dash circles in (a) and (b) represent the diameters of the dry and freshly prepared CMS discs

This indicates that the disintegration process may be the limiting step for initiating the drug release from CMS in HCl. The linear release profile also suggests that the release kinetics of felodipine from disintegrated CMS strips is close to zero-order. In pH 6.8 PBS, CMS discs show no dissolution enhancement of felodipine despite the formation of the molecular dispersions of the drug by HME and FDM 3D printing (**Figure 7.11b**). It was noted that no disintegration occurred in any FDM printed discs during the period of the dissolution tests in pH 6.8 PBS. The increased amount of inorganic salt in the PBS may contribute to further limit the solubility of soluplus in the media. No significant swelling was observed through the 6 hours of dissolution and a minimal disintegration started by 6 hours (**Figure 7.13b**).

In order to further understand the release behaviour, segments of the CMS samples after 6 hours dissolution were studied using ATR-FTIR and DSC. The ATR-FTIR results (**Figure 7.14**) show no changes of the drug and excipient peaks in comparison to the dry freshly prepared discs after 6 hours dissolution in both media.

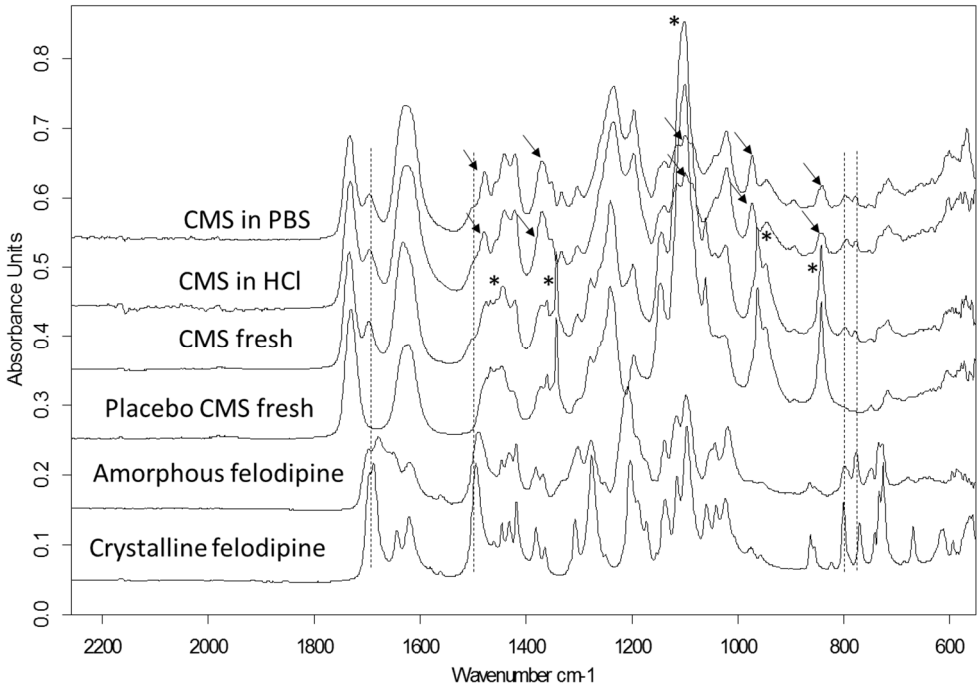

Figure 7.14: Partial ATR-FTIR spectra of CMS discs taken out of the media and dried after 6 hours dissolution. The dash lines in (c) highlight the felodipine related IR peaks and arrows highlight the changes of PEG/PEO K100 related peaks labelled with * before dissolution (n=3)

This confirms that the drug was still in amorphous dispersion with the polymer matrix. These results are consistent with the transparency of the dried matrices and the absence of drug crystals in the SEM data of these samples (**Figure 7.15**). However, the peaks associated with PEG, PEO K100 and Tween 80, such as the peaks between 1500 - 850 cm^{-1}, have shown significant changes in peak intensity and shape as observed in **Figure 7.14** indicating dissolution of these excipients during the dissolution experiments.

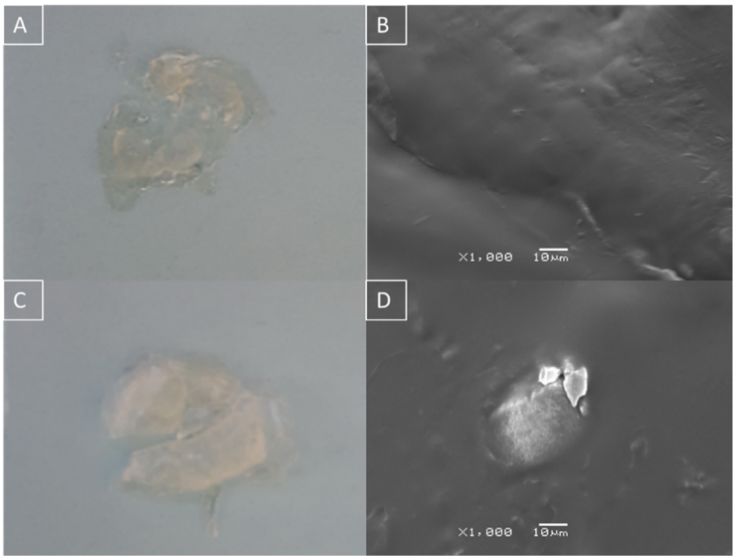

Figure 7.15: Images (A and C) and SEM images (B and D) of 10% CMS samples after dissolution for 6 hours and drying. A and B in SGF pH 1.2, while C and D in PBS pH 6.8

DSC detected much smaller PEG-PEO K100 melting peaks in the post-dissolution discs in comparison to the fresh dry sample (**Figure 7.16**), indicating the leaching of PEG-PEO K100 during dissolution. The first heating cycle showed an overlapped peak of the T_g of soluplus and dehydration of the matrix. However, the second heating cycle revealed the T_g of soluplus. These results imply that the remaining segments after dissolution are largely soluplus which retains the unreleased drug.

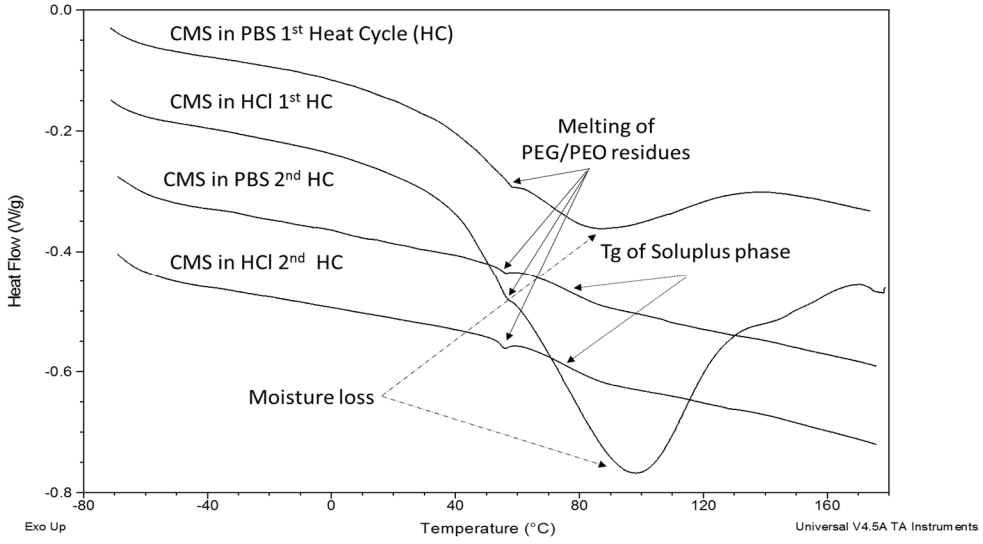

Figure 7.16: DSC thermographs of CMS discs taken out of the media and dried after 6 hours dissolution (n=3)

No significant release improvement of felodipine from CMV discs was observed in either pH 1.2 HCl or pH 6.8 PBS in comparison to the crystalline drug (**Figures 7.11a and b**). The PVA used in this study was a low hydrolysis grade which led to the poor aqueous solubility of the polymer. In addition, the effect of ionic strength of the dissolution medium may also play a role in this case, reducing the dissolution of PVA in the media (410). For both cases, a degree of gelling of the discs during dissolution can be seen in **Figures 7.17a and b**. The gelation of CMV discs can be attributed to the hydrogel formation ability of PVA reported in the literature (524, 525). The discs in pH 1.2 HCl show significant softening that led to the folding of the wetted discs (which appears as a reduction in size), whereas there was no change in the size of the discs tested in pH 6.8 PBS.

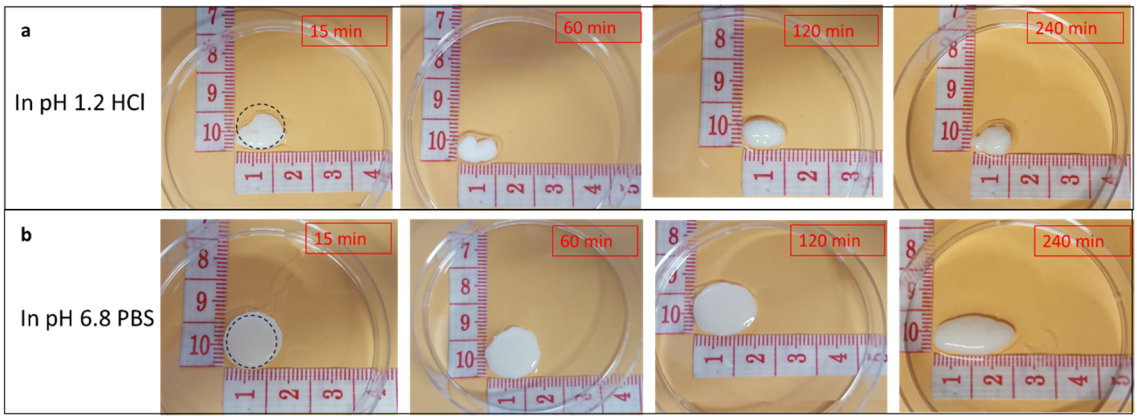

Figure 7.17: Visual appearances of the felodipine loaded FDM printed CMV discs during the dissolution tests in (a) pH 1.2 HCl and (b) pH 6.8 PBS

The ATR-FTIR results of the dried CMV samples are shown in **Figure 7.18**. No changes can be observed in comparison to the dry freshly prepared discs indicating that there was no change in the state of the drug in the CMV solid dispersions after 6 hours exposure in both media. The DSC results of the dried discs after 6 hours dissolution reveal the absence of a T_g of Tween 80 which was present in the freshly prepared discs (**Figure 7.19**). This indicates the leaching of Tween 80 during dissolution.

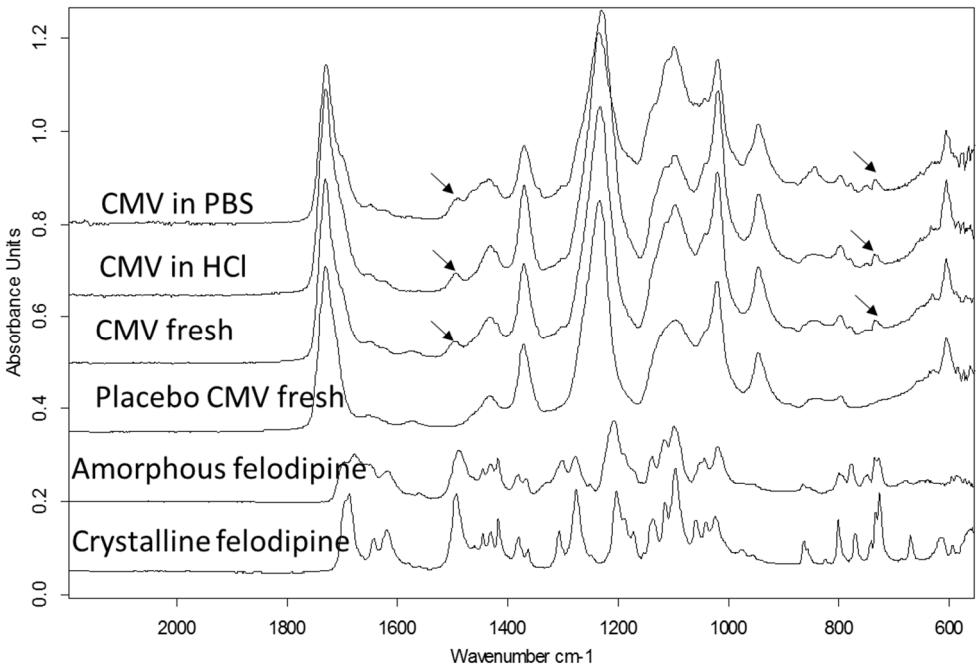

Figure 7.18: Partial ATR-FTIR spectra of CMV discs taken out of the media and dried after 6 hours dissolution. The arrows highlight felodipine related IR peaks (n=3)

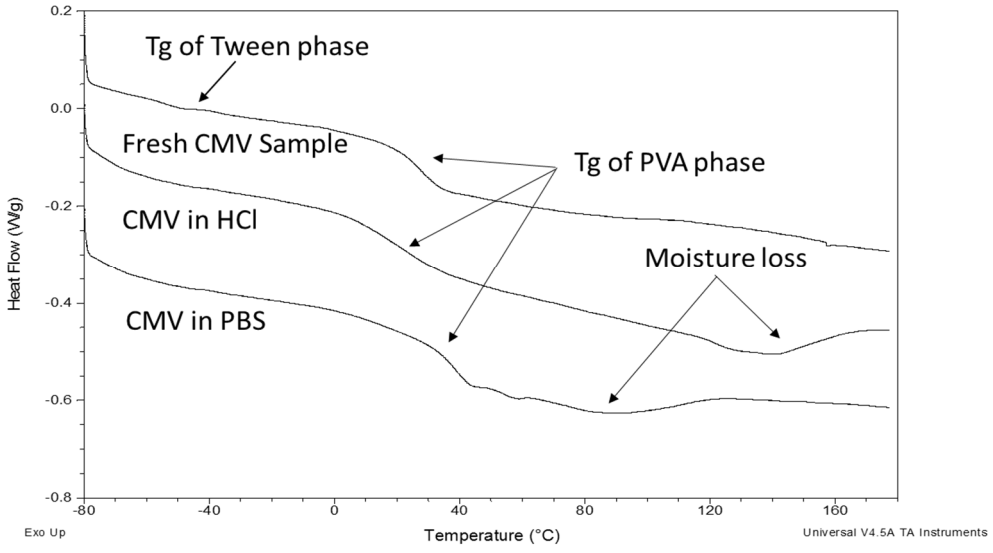

Figure 7.19: DSC thermographs of CMV discs taken out of the media and dried after 6 hours dissolution (n=3)

7.4 Discussion

7.4.1 Linking phase behaviour with FDM printability of the dispersions

Polymer blending is a widely used formulation strategy in the polymer and plastic industries to improve the processability of materials. This study tackled the FDM printability issues of two FDA approved and widely used pharmaceutical polymers, soluplus and eudragit E PO, by blending the polymers with a mixture of PEG, PEO K100 and Tween 80. Although both polymers have wide applications in preparation of pharmaceutical HME dispersions, they are not printable by conventional FDM 3D printers due to their high melt viscosity and poor fluidity. The addition of the mixture of PEG, PEO K100, Tween 80 as well as the model drug significantly improved the viscosity of the polymers during printing. As a result, these mixtures matched the printing performance of the PVA-based system that is one of the main matrix materials used currently in FDM 3D printing. This improved the thermal and mechanical properties allowing the felodipine-loaded dispersions to be printed into disc shaped, triple layered matrices. A clear understanding of the phase behaviour of the printed system is crucial for further interpretation of the mechanism of formulation stabilisation and drug release. As a result of the large number of ingredients used in the printed discs, characterisation of the phase behaviour of the systems is complex. This study took the simplified approach of ranking the miscibilities between excipients in order to gain some insight into the phase behaviour of the blend matrices and the miscibility of felodipine with different polymer blends to allow the prediction of the likelihood of the formation of molecular dispersions of the drug with polymers. The prediction revealed soluplus and eudragit E PO were miscible with PEG-PEO K100 and Tween 80; whereas PVA is only partially miscible with Tween 80. Therefore, the mechanism by which the printability of soluplus and eudragit E PO is improved by the addition of these excipients is probably the combination of improved melt viscosity and plasticisation of the polymers. Results indicated the formation of a molecular dispersion of felodipine at 10% loading in FDM printed CME and CMS dispersions. Therefore, drug incorporation further contributed to the plasticisation of the polymer matrices. The addition of Tween 80 reduced the stiffness of the PVA filaments and eased the printing process. The weakening of the stiffness may be attributed to the formation of discontinuous Tween 80 phases in PVA dispersions, as the two are partially miscible. The addition of felodipine further plasticised the polymer.

7.4.2 Linking phase behaviour with *in vitro* disintegration and dissolution performance

The phase behaviour of the printed discs is important for understanding the differences in the drug release rates of the formulations. The slower drug release from the CMS system compared to CME blend is a result of the combination of lower solubility of soluplus than eudragit E PO in the media and the physical state of the excipients in the dispersions. Although both formulations were confirmed to be molecular dispersions of felodipine, their crystalline PEG-PEO K100 contents are different. The higher crystalline PEG-PEO K100 content in the CMS compared to CME may contribute to the slower drug release from CMS discs. This is because that the crystalline PEG-PEO K100 required a wetting and hydration prior to dissolution; whereas these may not occur for the molecularly mixed PEG-PEO K100 in the polymer matrices. The reason for the higher crystalline content may be associated with the higher melt viscosity of eudragit E PO than soluplus as suggested by the HME processing torque values. As HME and FDM printing both were performed at temperatures above the melting point of the crystalline PEO K100 and PEG, higher melt viscosity of the matrix polymer would be more effective in limiting the diffusion of PEG and PEO K100 molecules to form large crystalline domains during recrystallisation on cooling (post-FDM printing). However, despite the fact that PEO K100 is a well-known controlled release matrix excipient which hydrates and swells once it is in contact with aqueous media (526-529), the limited amount of swelling observed in CME and CMS discs during dissolution, indicated that the dissolution of PEG-PEO K100 in the dispersions is the more dominant process in these blends. The intimate mixing between PEG-PEO K100 and soluplus and eudragit E PO may contribute to this observed behaviour.

Another interesting feature of the dissolution behaviour of these FDM 3D printed discs is the difference in their disintegration behaviour, which in the case of CMS in pH 1.2 HCl and CME in pH 6.8 PBS led to the 'switching on' effect of the drug release (**Figure 7.11**). It indicates that the disassembly of the bulky 3D object that was fabricated by micron-size polymeric strips may be used as a novel mechanism of the drug release performance. Therefore, a clear understanding of the disintegration behaviour of the formulation is of vital importance. In the literature, the disintegration process of FDM printed 3D matrices is still poorly understood. The results of this study revealed the unravelling of the printed strips of CMS formulation and bulk erosion behaviour of CME discs. The exact mechanism for this difference is not clear, but (1) the degree of fusion between the printed strips and layers and (2) the speed of dissolution of the matrix polymer may be relevant. As seen in **Figure 7.2**, the edges of the printed strips of CMS are much

rougher than CME discs. This may be an indication of the low melt viscosity of the materials and rapid solidification of the materials after deposition. This should lead to the better-defined interfaces between strips and layers which may contribute to the observed 'peeling' effect of strip by strip during the disintegration of CMS. The higher solubility of eudragit E PO at pH 1.2 than soluplus is believed to responsible for the rapid disintegration and dissolution of CME in pH 1.2. For CMS, the drug release results strongly indicated that disintegration is the limiting step for drug release. Following disintegration, controlled release of drug following zero-order kinetics was observed. The zero-order release of CMS in pH 1.2 media may be explained by the small diameter of each strip segment, which contributes to the short diffusion path length of the drug molecules. This short path length led to the negligible effect of changes in diffusion length during dissolution. In addition, the continuous slow breakdown into shorter segments can provide a constantly increasing release surface for the drug molecules and led to the observed zero-order like release profile. This brings insight into the potential of controlling the drug release rate via manipulation of the disintegration behaviour of the bulky solid formulation. This study has demonstrated that this is achievable using FDM printing technology, with careful selection of excipients.

Finally, the phase behaviour can also be used to explain why the prevention of drug recrystallisation in the formulations that have no drug dissolution enhancement (CMS and CMV). For CMV, as the solubility study suggested the separation of a Tween 80 rich phase and a PVA rich phase, one may expect the leaching of Tween during dissolution, which would liberate some drug. However, as extremely limited drug release was observed, it indicates that although the leaching of Tween may lead to some drug release, the majority of the drug is still held as a molecular dispersion in PVA matrices. This was confirmed by the DSC and ATR-FTIR results of the post-dissolution dried samples. The fact that no significant drug crystallisation occurred during the period of dissolution indicates that the polymer to drug ratio is efficient in stabilising and preventing crystallisation of the remaining drug in the matrices. This also applies to the CMS systems in which no drug recrystallisation was observed during 6 hours of dissolution.

7.5 Conclusion

This chapter demonstrated the use of polymer blends to overcome the poor printability of pharmaceutical polymers during FDM 3D printing. The solid dispersions of felodipine with eudragit E PO and soluplus were successfully prepared using FDM printing after blending with the process and drug release aids, PEG, PEO K100 and Tween 80. Distinctively different

disintegration behaviour of the 3D discs with different polymer blends allowed the manipulation of the rate of drug release. The results demonstrated the effect of the complex interplay between the miscibility of the excipients in the blends, the solubility of the polymer in the media and the formation of interfaces between printed strips during the FDM printing on drug release behaviour of the dispersions. This brings new insights into the design principles for controlled release formulations manufactured using FDM 3D printing by using different geometries and internal structures during the formulation development process.

Chapter 8. Concluding remarks and future work

8.1 Conclusions

8.1.1 Preformulation studies

This study introduced the use of HME-IM as a single step, solvent-free processing technique for designing mucoadhesive buccal patches for systemic delivery of felodipine with defined shape and geometry. In addition, part of the study focused on the use of FDM 3D printing for fabricating felodipine oral solid dispersions using polymeric blends as a strategy for improving the printability of pharmaceutical excipients. As a preformulation step, Chapter 3 investigated the physicochemical properties of the raw materials (felodipine and all other excipients) used throughout the different stages of the study before starting formulation development stage. This also involved the careful selection of the suitable excipients used for fabricating the formulations using these two methods. In addition, the chapter provided some theoretical and experimental predictions for the miscibility between the different excipients and the drug under investigation. Several characterisation techniques used to investigate the properties of the raw materials including DSC, MTDSC, TGA, DVS, ATR-FTIR, PXRD, SEM and EDS.

8.1.2 Formulation development strategies of felodipine HME-IM buccal patches

Several key formulation strategies were adapted to ensure the success of the formulation process using HME-IM. As the precision of product geometry is one of the major advantages of HME-IM over other methods like solvent casting for fabricating buccal and transdermal patches, the prepared patches should be easily removed from the mould after melt injection to ensure the integrity of the designed delivery systems. In order to achieve this, the excipients were selected for preparing felodipine dispersions in this study were non-sticky to the metal mould of the IM machine which facilitated the easy removal of the prepared patches after moulding. This function was provided by including PEG 4000 and PEO K900 polymeric blend as the main component of the patches. This polymeric blend provided easy peel off patches after cooling down the mould after HME-IM. Therefore, excipients should be selected carefully as sticky materials to IM moulds may be not suitable for preparing dosage forms using HME-IM.

Thermal degradation is the primary drawback for solid dispersions preparation by fusion methods in general including HME-IM. The formulation strategy to avoid thermal decomposition of formulative ingredients was through the selection of a range of excipients having low melting points which permitted processing at low and safe processing temperature (65 °C). The excipients used in the HME-IM study have melting temperatures ranging from -65 to 70°C. Thus, thermal degradation can be avoided by selecting carrier(s) having low melting points/T_g values to enable processing at safe temperatures.

The main purpose of the study using HME-IM was to design formulations (solid dispersions) for delivering felodipine to the systemic circulation via the buccal route to improve its bioavailability by solubility/dissolution enhancement and avoiding extensive liver metabolism (84%). In order to fulfil all these formulation objectives, tertiary carrier mixtures composed of PEG/ PEO K900 and either Tween 80 or TPGS blends were used as multi-functionality mixtures to provide drug solubilisation, mucoadhesion, stabilisation and absorption enhancing properties. The resultants mixtures were complex systems and they reflected the actual state of final pharmaceutical products which is rarely investigated as a strategy for preparing solid dispersion dosage forms using HME-IM.

Physical stability of molecularly solubilised drugs in solid dispersions is one of the most challenging problems in the development of successful formulations. This study adapted a strategy of creating surfactant-rich drug solubilisation and stabilisation compartments for felodipine. The created solubilisation domains were formed due to the different miscibilities of components of the CM1 and CM2 mixtures as represented in **Figure 8.1**.

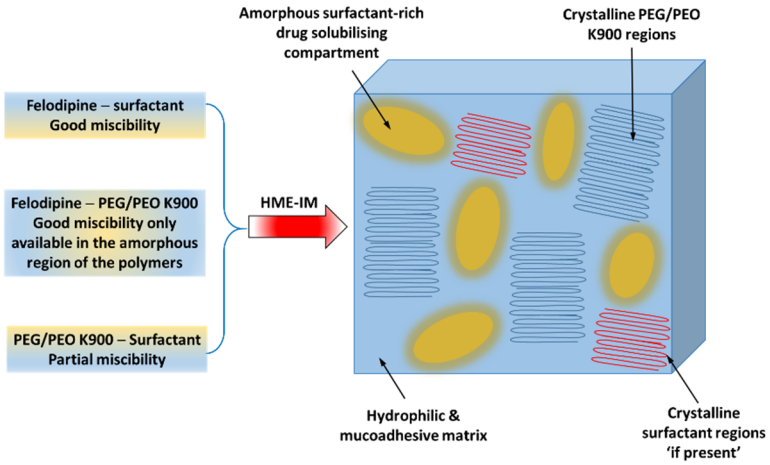

Figure 8.1: Proposed schematic illustration of felodipine loaded phase separated solubilisation compartments created by HME-IM

The investigations for the HME-IM patches presented in Chapter 4 proved that felodipine solubilisation improved the miscibility between PEG/PEO K900 polymer blend and Tween 80 as indicated by the disappearance of Tween 80 melting peak. This led to the formation of PEG-PEO K900-Tween 80 solubilisation phase for felodipine. However, for CM2 matrices, felodipine loading did not seem to improve the miscibility between TPGS and PEG-PEO K900 blend and the drug was most likely solubilised in the TPGS phase. In addition, felodipine was completely solubilised in both CM1 and CM2 at 10% w/w loading as molecularly dispersed form. The drug was dispersed in PEG-PEO K900- Tween 80 amorphous fraction for CM1 and most likely distributed in TPGS phase for CM2. The absence of felodipine crystals in the surfaces and cross-sections of the patches, broadening of felodipine NH stretching and absence of felodipine PXRD characteristic peaks indicated this. It was also found that increasing the loading percentage to 20% w/w led to more drug solubilisation in the surfactant-rich domains as revealed by the increase in the T_g of the mixtures and the ΔC_p values. Further increase in felodipine concentration to 30% w/w resulted in the detection of felodipine crystalline fraction by ATR-FTIR, SEM, EDS, PXRD, but not revealed by DSC and MTDSC due to the thermal dissolution of the crystalline drug in the molten carrier during the DSC runs. The 10% w/w loaded HME-IM patches revealed the maximum improvement in the dissolution profile of felodipine with approximately 10-12 times increase in the *in vitro* release after 2.5 hours compared to crystalline felodipine form I powder. It should be mentioned that loading felodipine at 10% w/w did not significantly affect the *in vitro* mucoadhesion properties of the HME-IM patches compared to placebo for both CM1 and CM2 mixtures. However, increasing the loading to 20-30% w/w drug loading reduced the mucoadhesion force not only because of the reduced proportion of PEO K900 but also due to saturation of the mixtures with felodipine and impacts of crystalline drug fraction in the formulations.

8.1.3 Characterisation challenges for investigating the microstructures of HME-IM patches

Conventional characterisation techniques such as DSC, MTDSC, SEM, EDS, ATR-FTIR and PXRD provided qualitative and quantitative information about the microstructure of the prepared HME-IM patches as shown in Chapter 4. However, due to the complexity of these systems and the presence of phase separation domains, it was important to understand the degree of heterogeneity in the different formulations and the impacts of drug loading on the spatial

distribution of phases. Therefore, TASC and XμCT were used to achieve this target as explained in Chapter 5.

TASC detected TPGS and PEG-PEO K900 for both CM1 and CM2 samples in comparable temperatures to standard DSC with slight variations related to the principle of detection of both techniques. DSC measures the heat flow accompanying thermal events while TASC detects changes in the appearance of the top surface of the sample under investigation. For CM1 and CM2 placebo HME-IM patches, TASC revealed that the different phases in the placebo and 10-20% w/w loaded samples were uniformly distributed within the microscale detection limits of the technique using the localised thermal analysis function for TASC. However, the 30% w/w loadings were heterogeneous reflecting microscale heterogeneity of the samples. The heterogeneity represented by the different in composition of the analysed areas using TASC algorithm. It was also found that analysing large areas of 30% w/w loaded patches reduced the heterogeneous character of these samples due to the averaging effect which in turn explained the high reproducibility of the DSC results. Unlike DSC, TASC was able to detect the thermal dissolution of the crystalline fraction of felodipine in the 30% w/w loaded samples. Placebo and 10% w/w loaded samples readily reached the plateau after the melting of PEG-PEO K900 blend. 20% w/w loaded HME-IM reached the plateau in a less sharp way compared to lower loadings. However, 30% w/w drug loading failed to reach the plateau indicating the presence of real thermal event 'thermal dissolution of crystalline felodipine' occurred after the melting of PEG-PEO K900 blend. These results complement the findings obtained by VT-ATR-FTIR. TASC also detected the unfolding of the folded form of PEG 4000 in the reheating cycle of the TASC experiments. This hidden event was unobservable using standard DSC at the same heating rate. The transformation of the folded to the more stable extended form is detected using MTDSC and VT-ATR-FTIR. In addition to be fast and cheap thermal analysis technique, TASC proved that its sensitivity is not affecting by changing the rate of heating and cooling ramps which was considered as an advantage for TASC over DSC. Thus, increasing the heating rate does not seem to reduce the resolution of analysis using TASC compared to DSC.

Since XμCT has a micron scale, phase separations between the components of CM1 and CM2 in the placebo and 10% w/w felodipine loaded samples were undetectable. The presence of a crystalline fraction of felodipine in the 20-30% w/w loadings and because the drug has higher electron density compared to other formulation ingredients, the ability of XμCT to detect and threshold crystalline felodipine clusters permitted the simulation of the spatial distribution of this phase in the higher loaded formulations. In addition, XμCT was used to provide semi-quantitative data about the concentration of felodipine in the 30% w/w felodipine loaded CM2 HME-IM

patches using a series of CM2 physical mixture discs loaded with 0-60% w/w felodipine. The results revealed the presence of 10.3% w/w crystalline felodipine in the 30% w/w CM2 patches. It was also found that thresholding small areas in the CM2 sample loaded with 30% w/w loading revealed a high degree of heterogeneity for crystalline felodipine compared to thresholding large areas. These results confirmed the localised analysis performed using TASC. XμCT was also found to be unique not only to simulate the distribution of crystalline drug fraction if it has enough electron density to perform thresholding but also to detect processing defects like the presence of air pockets and heavy metal additives because these two have very high contrast difference to be thresholded and simulated as 3D models.

8.1.4 Evaluations of physical stabilities of the HME-IM patches and their implications in formulation optimisation

After completing the formulation stage of felodipine HME-IM buccal patches using different mixtures and drug loadings, the stability of the designed preparations was investigated under four different storing conditions with respect to temperature and relative humidity for 3 months. The stability follow-up for placebo and felodipine loaded CM1 and CM2 patches was explained in details in Chapter 6. The studies conducted indicated no significant changes in the morphology and the microstructure of CM1 and CM2 placebo patches stored under all conditions except placebo CM1 sample stored at condition D (40°C and 75%RH) which lost its solid structure 'liquefied' during ageing. Using different characterisation techniques such as TGA and ATR-FTIR, this loss of solid structure was attributed to random scission oxidative degradation of PEG-PEO K900 blend and Tween 80. However, placebo CM2 samples were more resistant to oxidative degradation due to the antioxidant properties of TPGS which provided partial protection against the random polyethylene oxide chain degradation. Therefore, the prepared drug delivery system should be protected against high temperature and relative humidity conditions.

Felodipine crystallisation was detected in all loaded formulations, however, the extent of crystallisation was found to be drug concentration dependent. 10% w/w CM2 loaded HME-IM stored at condition C (40 °C and 0% RH) and condition A (room temperature and 0% RH) revealed the lowest extent of felodipine recrystallisation with only few surface crystals detected on the surface with very slight changes in the different phase separated domains. Stability investigations for 10% w/w CM1patches also showed good felodipine stabilising properties, however, they were less stable compared to corresponding CM2 formulations. These results indicated that 10% w/w

CM2 HME-IM patches are the most likely suitable formulation for the next stage of product development. Interestingly, it was found that felodipine recrystallised from formulations as a plate, block or spherulitic needle habits as observed under SEM. This phenomenon was more prominent in the higher loading formulations (20-30% w/w loadings) compared to 10% w/w loading. All habits were identified as felodipine crystals using EDS. The spherulitic needle-shaped crystals were grown on the surfaces (including the interior air pockets' surfaces) of the patches of all loaded samples stored at condition D (40°C and 75% RH) except 10% w/w CM2 patch and also seen in some of the patches aged under condition C (40°C and 0%RH). Characterisation of formulations contained the spherulitic crystals using ATR-FTIR and PXRD revealed different signatures compared to the already four identified polymorphic forms of felodipine. Most importantly, the detection of felodipine NH stretching peak at 3321 cm^{-1} in formulation loaded with 20-30% w/w loading is not related any known polymorphs or the amorphous form of the drug. In addition, the results of PXRD indicated new diffraction peaks at 9.3˚ and 12.4˚ do not match with any known polymorphs of felodipine. These observations suggested that felodipine recrystallised as spherulitic needle shaped crystals from formulations stored at 40°C with or without 75% RH is more likely new form of felodipine. The general illustration for the stability study of the HME-IM patches is shown in **Figure 8.2.**

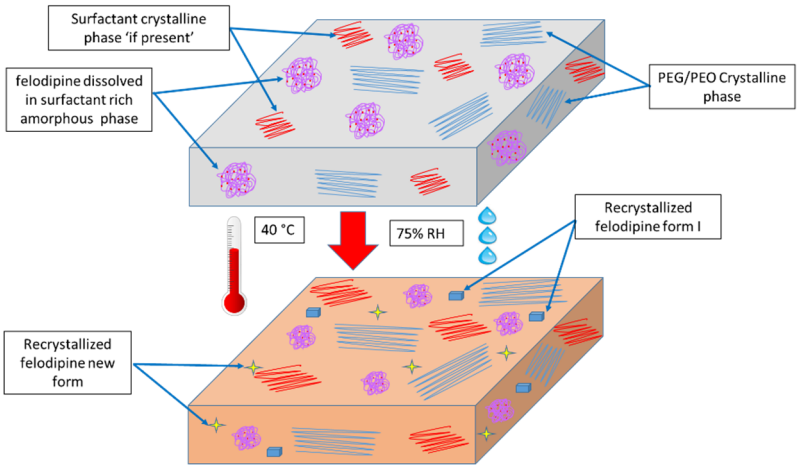

Figure 8.2: An illustration showing the impacts of storing temperature and relative humidity on the stability of felodipine loaded HME-IM patches

Crystallisation of felodipine from the glassy state under 40°C and 75% RH was also investigated and the results indicated the presence of new melting peak having an onset at 118.3 ± 0.1℃ in

addition to the main peak with onset detected at 136.0 ± 0.9℃. In addition, PXRD of the recrystallised drug revealed peaks with low intensity at 9.3° and 12.6° as peaks may be due to the small fraction of the new polymorphic growth. However, the ATR-FTIR did not show any change in the spectra of different regions of the crystallised drug compared to the raw pure crystalline felodipine form I which may be due to presence of the small fraction in the bulk of the sample which is out of the detection limits of the instrument.

8.1.5 Using polymer blends as a strategy to improve FDM 3D printability of pharmaceutical solid dosage forms

FDM 3D printing has recently attracted the attention of researchers working in pharmaceutical formulation field as a potential method for providing more personalised medicines, drug combination dosage forms and flexibility to design products with different structures, shapes and geometries. All these advantages are expected to improve patients' adherence to medications which in turn lead to better therapeutic outcomes. However, the major challenge currently is the poor printability of the vast majority of pharmaceutically approved excipients. Chapter 7 explored the possibility of using of polymer blends as a formulation strategy to overcome this limitation. Felodipine as a model drug with a range of excipients normally processed by HME (eudragit E PO, soluplus, PVA, PEG 4000, PEO K100 and Tween 80) were used to develop felodipine 10% w/w FDM 3D printed oral discs.

HME filaments and 3D printed formulation were successfully prepared using CME, CMS and CMV blends using acceptable HME and FDM 3D printing temperatures without affecting the chemical stability of all formulation ingredients. The physicochemical characterisation studies revealed that felodipine was solubilised in the three mixtures as no drug crystals were detected using SEM, the characteristics PXRD peaks were absent, and the NH stretching was very broadened using ATR-FTIR revealing molecularly dispersed drug in the systems. Felodipine was more likely dissolved in CME (eudragit E PO- PEG-PEO K100 -Tween 80) and CMS (soluplus-PEG-PEO K100 -Tween 80) amorphous phases. However, due to phase separation between PVA and Tween 80, the drug was molecularly dispersed in both PVA-rich and Tween 80-rich phases. The loading efficiency of felodipine in the different systems were 95.75 ± 0.66%, 94.62 ± 0.56% and 86.23 ± 0.83% for CME, CMS and CMV 10% w/w loaded discs, respectively. These results revealed good mixing achieved during HME processing for CME and CMS formulations, however, the large granules of PVA resulted in poor mixing with felodipine and Tween 80 and

reduced the loading efficiency of this mixture. The *in vitro* dissolution studies of felodipine showed significant enhancement in the solubility/dissolution properties of the drug from CME using 1.2 HCl as the dissolution medium. A maximum release of approximately 84.3% of loaded felodipine was achieved within the first 30 minutes which was attributed to the formation of the molecular drug dispersion and the high solubility of eudragit E PO in pH 1.2 HCl medium. In addition, the same formulation slowly but completely released in pH 6.8 PBS medium. The release of felodipine from CMS in pH 1.2 HCl medium was slightly improved and revealed an interesting fragmentation of the 3D object into the individual printing strips. However, no enhancement in the dissolution profile of felodipine was observed from CMS in pH 6.8 PBS and CMV in both media due to the entrapment of felodipine in the main insoluble polymers.

8.2 Future outlook

The conducted studies presented in this project provided information about the design, characterisation and *in vitro* evaluation of different formulations using HME-IM and FDM 3D printing. However, the most promising preparations need more investigation to ensure their suitability as candidates which may be developed to pharmaceutical products. One of most important areas to that require further investigation is the diffusion of felodipine from the most promising HME-IM buccal patches (10% w/w felodipine in CM1 and CM2 patches) through buccal mucosa from animal models or cultured buccal mucosa such as EpiOral™. These studies will provide critical information about the permeation of the drug through biological membranes to ensure the systemic delivery of felodipine. In addition, conducting an *in vivo* mucoadhesion study of the most successful formulation using buccal mucosa from animal models is also important to correlate the *in vitro* with the *in vivo* results.

According to the results obtained using different characterisation techniques, 10% w/w loaded CM1 and CM2 formulations were well below the saturation limits of the carriers. However, the stability studies revealed the presence of very few crystals on the surfaces of the patches. Thus, it is important to investigate the causes behind felodipine crystallisation in these patches and the impacts of the slight drug phase separation on its release profiles. It is also important to consider formulating felodipine at lower loading percentage such as 5% w/w to avoid crystallisation problem if this loading can provide the therapeutic dosage. Also, conducting long-term stability monitoring (9-12 months) for the most successful formulations to make sure that their physicochemical properties and structures are comparable to fresh samples. Furthermore, deep investigation is required for identifying the new polymorphic form of felodipine recrystallised

from formulations stored at 40 ℃ and 75% RH and understanding its properties using different characterisation techniques especially single crystal XRD.

In this project, the main concern behind the FDM 3D printing studies was to use excipients mixtures to enhance processing using this technique. This area needs to be expanded more to provide standard rules for selecting the suitable excipients candidates for FDM 3D printing. In addition, the prepared formulations using this technique also need to be studied further by using more sophisticated geometries, incorporating drug combinations and most importantly providing a clear vision about the future use of 3D printed medications as personalised products for patients at the care unit.

Because TASC is a very flexible and recently developed characterisation technique with many interesting applications, developing more applications for this tool in the pharmaceutical field is very crucial and provide useful information in different areas such as drug-polymer compatibility, polymorphism and thermal rheology. XμCT was found as a useful technique for understanding the spatial distribution of phases. This study provided semi-quantitative results for the crystalline fraction of felodipine as a novel method for estimating the saturation limits of the carrier. Thus, more research is required to validate the method as quantitatively used for this purpose. In addition, the spatial resolution for the experiments conducted in this project was 3-4 μm; it could be very useful if the investigation will expand to the use of higher instrument sensitivity to detect phase separation within the nanoscale.

References

References

1. Fahr A, Liu X. Drug delivery strategies for poorly water-soluble drugs. Expert Opinion on Drug Delivery. 2007;4(4):403-16.

2. Vasconcelos T, Sarmento B, Costa P. Solid dispersions as strategy to improve oral bioavailability of poor water soluble drugs. Drug Discovery Today. 2007;12(23–24):1068-75.

3. Martin AN, Sinko PJ, Singh Y. Martin's Physical Pharmacy and Pharmaceutical Sciences: Physical Chemical and Biopharmaceutical Principles in the Pharmaceutical Sciences: Lippincott Williams & Wilkins; 2011.

4. Davit BM, Kanfer I, Tsang YC, Cardot J-M. BCS Biowaivers: Similarities and Differences Among EMA, FDA, and WHO Requirements. The AAPS Journal. 2016;18(3):612-8.

5. FDA. Guidance for Industry, Waiver of in vivo bioavailability and bioequivalence studies for immediate-release solid oral dosage forms based on a biopharmaceutics classification system. 2015 17/10/2016]. Available from: http://www.fda.gov/downloads/Drugs/GuidanceComplianceRegulatoryInformation/Guidances/ucm070246.pdf

6. Bergström CAS, Andersson SBE, Fagerberg JH, Ragnarsson G, Lindahl A. Is the full potential of the biopharmaceutics classification system reached? European Journal of Pharmaceutical Sciences. 2014;57:224-31.

7. Kawabata Y, Wada K, Nakatani M, Yamada S, Onoue S. Formulation design for poorly water-soluble drugs based on biopharmaceutics classification system: Basic approaches and practical applications. International Journal of Pharmaceutics. 2011;420(1):1-10.

8. Song Y, Wang L, Yang P, Wenslow Jr RM, Tan B, Zhang H, et al. Physicochemical Characterization of Felodipine-Kollidon VA64 Amorphous Solid Dispersions Prepared by Hot-Melt Extrusion. Journal of Pharmaceutical Sciences. 2013;102(6):1915-23.

9. Aulton ME, Taylor K. Aulton's Pharmaceutics: The Design and Manufacture of Medicines. 2nd ed: Churchill Livingstone/Elsevier; 2004. 219 p.

10. Mitsuru H, Shinji N, Hisako K, Nobuyoshi K. Effect of lipid solubility on hepatic first-pass metabolism of barbiturates in rabbits. International Journal of Pharmaceutics. 1984;20(1):73-85.

11. Serajuddin ATM. Salt formation to improve drug solubility. Advanced Drug Delivery Reviews. 2007;59(7):603-16.

12. Loftsson T, Brewster ME. Pharmaceutical Applications of Cyclodextrins. 1. Drug Solubilization and Stabilization. Journal of Pharmaceutical Sciences. 1996;85(10):1017-25.

13. Blagden N, de Matas M, Gavan PT, York P. Crystal engineering of active pharmaceutical ingredients to improve solubility and dissolution rates. Advanced Drug Delivery Reviews. 2007;59(7):617-30.

14. Pawar VK, Singh Y, Meher JG, Gupta S, Chourasia MK. Engineered nanocrystal technology: In-vivo fate, targeting and applications in drug delivery. Journal of Controlled Release. 2014;183:51-66.

15. Gao L, Liu G, Ma J, Wang X, Zhou L, Li X, et al. Application of Drug Nanocrystal Technologies on Oral Drug Delivery of Poorly Soluble Drugs. Pharmaceutical Research. 2013;30(2):307-24.

16. Kapsi SG, Ayres JW. Processing factors in development of solid solution formulation of itraconazole for enhancement of drug dissolution and bioavailability. International Journal of Pharmaceutics. 2001;229(1–2):193-203.

17. Kestur US, Ivanesivic I, Alonzo DE, Taylor LS. Influence of particle size on the crystallization kinetics of amorphous felodipine powders. Powder Technology. 2013;236:197-204.

18. Serajuddin ATM. Solid dispersion of poorly water-soluble drugs: Early promises, subsequent problems, and recent breakthroughs. Journal of Pharmaceutical Sciences. 1999;88(10):1058-66.

19. Rumondor ACF, Dhareshwar SS, Kesisoglou F. Amorphous Solid Dispersions or Prodrugs: Complementary Strategies to Increase Drug Absorption. Journal of Pharmaceutical Sciences. 2016;105(9):2498-508.

20. Mu H, Holm R, Müllertz A. Lipid-based formulations for oral administration of poorly water-soluble drugs. International Journal of Pharmaceutics. 2013;453(1):215-24.

21. Jannin V, Musakhanian J, Marchaud D. Approaches for the development of solid and semi-solid lipid-based formulations. Advanced Drug Delivery Reviews. 2008;60(6):734-46.

22. Pouton CW, Porter CJH. Formulation of lipid-based delivery systems for oral administration: Materials, methods and strategies. Advanced Drug Delivery Reviews. 2008;60(6):625-37.

23. Hauss DJ. Oral lipid-based formulations. Advanced Drug Delivery Reviews. 2007;59(7):667-76.

24. Baird JA, Taylor LS. Evaluation of amorphous solid dispersion properties using thermal analysis techniques. Advanced Drug Delivery Reviews. 2012;64(5):396-421.

25. Vasconcelos T, Marques S, das Neves J, Sarmento B. Amorphous solid dispersions: Rational selection of a manufacturing process. Advanced Drug Delivery Reviews. 2016;100:85-101.

26. Faisal W, Ruane-O'Hora T, O'Driscoll CM, Griffin BT. A novel lipid-based solid dispersion for enhancing oral bioavailability of Lycopene – In vivo evaluation using a pig model. International Journal of Pharmaceutics. 2013;453(2):307-14.

27. Craig DQM. The mechanisms of drug release from solid dispersions in water-soluble polymers. International Journal of Pharmaceutics. 2002;231(2):131-44.

28. Chiou WL. Pharmaceutical Applications of Solid Dispersion Systems: X-Ray Diffraction and Aqueous Solubility Studies on Griseofulvin-Polyethylene Glycol 6000 Systems. Journal of Pharmaceutical Sciences. 1977;66(7):989-91.

29. Baghel S, Cathcart H, O'Reilly NJ. Polymeric Amorphous Solid Dispersions: A Review of Amorphization, Crystallization, Stabilization, Solid-State Characterization, and Aqueous Solubilization of Biopharmaceutical Classification System Class II Drugs. Journal of Pharmaceutical Sciences. 2016;105(9):2527-44.

30. Jani R, Patel D. Hot melt extrusion: An industrially feasible approach for casting orodispersible film. Asian Journal of Pharmaceutical Sciences. 2015;10(4):292-305.

31. Paudel A, Worku ZA, Meeus J, Guns S, Van den Mooter G. Manufacturing of solid dispersions of poorly water soluble drugs by spray drying: Formulation and process considerations. International Journal of Pharmaceutics. 2013;453(1):253-84.

32. Vo CL-N, Park C, Lee B-J. Current trends and future perspectives of solid dispersions containing poorly water-soluble drugs. European Journal of Pharmaceutics and Biopharmaceutics. 2013;85(3, Part B):799-813.

33. Abramov YA. Computational Pharmaceutical Solid State Chemistry: Wiley; 2016.

34. Rodríguez-Spong B, Acciacca A, Fleisher D, Rodríguez-Hornedo N. pH-Induced Nanosegregation of Ritonavir to Lyotropic Liquid Crystal of Higher Solubility than Crystalline Polymorphs. Molecular Pharmaceutics. 2008;5(6):956-67.

35. Lee EH. A practical guide to pharmaceutical polymorph screening & selection. Asian Journal of Pharmaceutical Sciences. 2014;9(4):163-75.

36. Chiou WL, Riegelman S. Pharmaceutical applications of solid dispersion systems. Journal of Pharmaceutical Sciences. 1971;60(9):1281-302.

37. Banker GS, Siepmann J, Rhodes C. Modern Pharmaceutics, Fourth Edition: CRC Press; 2002. 156 p.

38. Lloyd GR, Craig DQM, Smith A. An Investigation into the Melting Behavior of Binary Mixes and Solid Dispersions of Paracetamol and PEG 4000. Journal of Pharmaceutical Sciences. 1997;86(9):991-6.

39. Vippagunta SR, Wang Z, Hornung S, Krill SL. Factors Affecting the Formation of Eutectic Solid Dispersions and Their Dissolution Behavior. Journal of Pharmaceutical Sciences. 2007;96(2):294-304.

40. Gala U, Chuong MC, Varanasi R, Chauhan H. Characterization and Comparison of Lidocaine-Tetracaine and Lidocaine-Camphor Eutectic Mixtures Based on Their Crystallization and Hydrogen-Bonding Abilities. AAPS PharmSciTech. 2015;16(3):528-36.

41. Yong CS, Oh Y-K, Jung SH, Rhee J-D, Kim H-D, Kim C-K, et al. Preparation of ibuprofen-loaded liquid suppository using eutectic mixture system with menthol. European Journal of Pharmaceutical Sciences. 2004;23(4–5):347-53.

42. Aroso IM, Silva JC, Mano F, Ferreira ASD, Dionísio M, Sá-Nogueira I, et al. Dissolution enhancement of active pharmaceutical ingredients by therapeutic deep eutectic systems. European Journal of Pharmaceutics and Biopharmaceutics. 2016;98:57-66.

43. Otsuka M, Maeno Y, Fukami T, Inoue M, Tagami T, Ozeki T. Solid dispersions of efonidipine hydrochloride ethanolate with improved physicochemical and pharmacokinetic properties prepared with microwave treatment. European Journal of Pharmaceutics and Biopharmaceutics. 2016;108:25-31.

44. Chiou WL, Riegelman S. Preparation and dissolution characteristics of several fast-release solid dispersions of griseofulvin. Journal of Pharmaceutical Sciences. 1969;58(12):1505-10.

45. Goldberg AH, Gibaldi M, Kanig JL. Increasing dissolution rates and gastrointestinal absorption of drugs via solid solutions and eutectic mixtures I. Theoretical considerations and discussion of the literature. Journal of Pharmaceutical Sciences. 1965;54(8):1145-8.

46. Anguiano-Igea S, Otero-Espinar FJ, Vila-Jato JL, Blanco-Méndez J. The properties of solid dispersions of clofibrate in polyethylene glycols. Pharmaceutica Acta Helvetiae. 1995;70(1):57-66.

47. Ginés JM, Arias MJ, Moyano JR, Sánchez-Soto PJ. Thermal investigation of crystallization of polyethylene glycols in solid dispersions containing oxazepam. International Journal of Pharmaceutics. 1996;143(2):247-53.

48. Duong TV, Van Humbeeck J, Van den Mooter G. Crystallization Kinetics of Indomethacin/Polyethylene Glycol Dispersions Containing High Drug Loadings. Molecular Pharmaceutics. 2015;12(7):2493-504.

49. Schachter DM, Xiong J, Tirol GC. Solid state NMR perspective of drug–polymer solid solutions: a model system based on poly(ethylene oxide). International Journal of Pharmaceutics. 2004;281(1–2):89-101.

50. Urbanova M, Gajdosova M, Steinhart M, Vetchy D, Brus J. Molecular-Level Control of Ciclopirox Olamine Release from Poly(ethylene oxide)-Based Mucoadhesive Buccal Films: Exploration of Structure–Property Relationships with Solid-State NMR. Molecular Pharmaceutics. 2016;13(5):1551-63.

51. Van Duong T, Van den Mooter G. The role of the carrier in the formulation of pharmaceutical solid dispersions. Part I: crystalline and semi-crystalline carriers. Expert Opinion on Drug Delivery. 2016;13(11):1583-94.

52. Ford JL. The use of Thermal Analysis in the Study of Solid Dispersions. Drug Development and Industrial Pharmacy. 1987;13(9-11):1741-77.

53. Sun CC. Novel co-crystals between polyethylene glycols and 5-phenylpyrazolyl-1-benzenesulfonamides. Google Patents; 2006.

54. Yang X, Zhong Z, Huang Y. The effect of PEG molecular weights on the thermal stability and dissolution behaviors of griseofulvin-PEG crystalline inclusion complexes. International Journal of Pharmaceutics. 2016;508(1–2):51-60.

55. Zhong Z, Guo C, Chen L, Xu J, Huang Y. Co-crystal formation between poly(ethylene glycol) and a small molecular drug griseofulvin. Chemical Communications. 2014;50(48):6375-8.

56. Kolter K, Karl M, Nalawade S, Rottmann N. Hot-Melt Extrusion with BASF Pharma Polymers. Ludwigshafen, Germany: BASF, The Chemical Company; 2011.

57. Yee CS. The development of PVP-based solid dispersions using hot melt xtrusion for the preparation of immediate release formulations. School of Pharmacy: University of East Anglia; 2013.

58. Xie T, Taylor LS. Dissolution Performance of High Drug Loading Celecoxib Amorphous Solid Dispersions Formulated with Polymer Combinations. Pharmaceutical Research. 2016;33(3):739-50.

59. Jackson MJ, Kestur US, Hussain MA, Taylor LS. Dissolution of Danazol Amorphous Solid Dispersions: Supersaturation and Phase Behavior as a Function of Drug Loading and Polymer Type. Molecular Pharmaceutics. 2016;13(1):223-31.

60. Prasad D, Chauhan H, Atef E. Amorphous Stabilization and Dissolution Enhancement of Amorphous Ternary Solid Dispersions: Combination of Polymers Showing Drug–Polymer Interaction for Synergistic Effects. Journal of Pharmaceutical Sciences. 2014;103(11):3511-23.

61. Chen Z, Liu Z, Qian F. Crystallization of Bifonazole and Acetaminophen within the Matrix of Semicrystalline, PEO–PPO–PEO Triblock Copolymers. Molecular Pharmaceutics. 2015;12(2):590-9.

62. Bartsch SE, Griesser UJ. Physicochemical properties of the binary system glibenclamide and polyethylene glycol 4000. Journal of Thermal Analysis and Calorimetry. 2004;77(2):555-69.

63. Huang Y, Zu Y, Zhao X, Wu M, Feng Z, Deng Y, et al. Preparation of inclusion complex of apigenin-hydroxypropyl-β-cyclodextrin by using supercritical antisolvent process for dissolution and bioavailability enhancement. International Journal of Pharmaceutics. 2016;511(2):921-30.

64. Ouerghemmi S, Degoutin S, Tabary N, Cazaux F, Maton M, Gaucher V, et al. Triclosan loaded electrospun nanofibers based on a cyclodextrin polymer and chitosan polyelectrolyte complex. International Journal of Pharmaceutics. 2016;513(1–2):483-95.

65. Thiry J, Krier F, Ratwatte S, Thomassin J-M, Jerome C, Evrard B. Hot-melt extrusion as a continuous manufacturing process to form ternary cyclodextrin inclusion complexes. European Journal of Pharmaceutical Sciences.

66. Tran PH-L, Tran TT-D, Park JB, Lee B-J. Controlled Release Systems Containing Solid Dispersions: Strategies and Mechanisms. Pharmaceutical Research. 2011;28(10):2353-78.

67. Doherty C, York P. Mechanisms of dissolution of frusemide/PVP solid dispersions. International Journal of Pharmaceutics. 1987;34(3):197-205.

68. Karavas E, Georgarakis E, Sigalas MP, Avgoustakis K, Bikiaris D. Investigation of the release mechanism of a sparingly water-soluble drug from solid dispersions in hydrophilic carriers based on physical state of drug, particle size distribution and drug–polymer interactions. European Journal of Pharmaceutics and Biopharmaceutics. 2007;66(3):334-47.

69. Mennini N, Furlanetto S, Cirri M, Mura P. Quality by design approach for developing chitosan-Ca-alginate microspheres for colon delivery of celecoxib-hydroxypropyl-β-cyclodextrin-PVP complex. European Journal of Pharmaceutics and Biopharmaceutics. 2012;80(1):67-75.

70. Zerrouk N, Chemtob C, Arnaud P, Toscani S, Dugue J. In vitro and in vivo evaluation of carbamazepine-PEG 6000 solid dispersions. International Journal of Pharmaceutics. 2001;225(1–2):49-62.

71. Zhong Z, Guo C, Yang X, Guo B, Xu J, Huang Y. Drug Molecule Diflunisal Forms Crystalline Inclusion Complexes with Multiple Types of Linear Polymers. Crystal Growth & Design. 2016;16(3):1181-6.

72. Policianova O, Brus J, Hruby M, Urbanova M, Zhigunov A, Kredatusova J, et al. Structural Diversity of Solid Dispersions of Acetylsalicylic Acid As Seen by Solid-State NMR. Molecular Pharmaceutics. 2014;11(2):516-30.

73. Yang Z, Nollenberger K, Albers J, Craig D, Qi S. Microstructure of an Immiscible Polymer Blend and Its Stabilization Effect on Amorphous Solid Dispersions. Molecular Pharmaceutics. 2013;10(7):2767-80.

74. Cheng A, Merz KM. Prediction of Aqueous Solubility of a Diverse Set of Compounds Using Quantitative Structure−Property Relationships. Journal of Medicinal Chemistry. 2003;46(17):3572-80.

75. Gupta J, Nunes C, Vyas S, Jonnalagadda S. Prediction of Solubility Parameters and Miscibility of Pharmaceutical Compounds by Molecular Dynamics Simulations. The Journal of Physical Chemistry B. 2011;115(9):2014-23.

76. Meng F, Xu W. Drug permeability prediction using PMF method. Journal of Molecular Modeling. 2013;19(3):991-7.

77. Tian Y, Booth J, Meehan E, Jones DS, Li S, Andrews GP. Construction of Drug–Polymer Thermodynamic Phase Diagrams Using Flory–Huggins Interaction Theory: Identifying the Relevance of Temperature and Drug Weight Fraction to Phase Separation within Solid Dispersions. Molecular Pharmaceutics. 2013;10(1):236-48.

78. Tian B, Wang X, Zhang Y, Zhang K, Zhang Y, Tang X. Theoretical Prediction of a Phase Diagram for Solid Dispersions. Pharmaceutical Research. 2015;32(3):840-51.

79. Marsac PJ, Li T, Taylor LS. Estimation of Drug–Polymer Miscibility and Solubility in Amorphous Solid Dispersions Using Experimentally Determined Interaction Parameters. Pharmaceutical Research. 2008;26(1):139.

80. Greenhalgh DJ, Williams AC, Timmins P, York P. Solubility parameters as predictors of miscibility in solid dispersions. Journal of Pharmaceutical Sciences. 1999;88(11):1182-90.

81. Dahan A, Beig A, Ioffe-Dahan V, Agbaria R, Miller JM. The Twofold Advantage of the Amorphous Form as an Oral Drug Delivery Practice for Lipophilic Compounds: Increased Apparent Solubility and Drug Flux Through the Intestinal Membrane. The AAPS Journal. 2013;15(2):347-53.

82. Janssens S, Van den Mooter G. Review: physical chemistry of solid dispersions. Journal of Pharmacy and Pharmacology. 2009;61(12):1571-86.

83. Sarode AL, Sandhu H, Shah N, Malick W, Zia H. Hot melt extrusion (HME) for amorphous solid dispersions: Predictive tools for processing and impact of drug–polymer interactions on supersaturation. European Journal of Pharmaceutical Sciences. 2013;48(3):371-84.

84. Liu X, Lu M, Guo Z, Huang L, Feng X, Wu C. Improving the Chemical Stability of Amorphous Solid Dispersion with Cocrystal Technique by Hot Melt Extrusion. Pharmaceutical Research. 2012;29(3):806-17.

85. Baghel S, Cathcart H, O'Reilly NJ. Theoretical and experimental investigation of drug-polymer interaction and miscibility and its impact on drug supersaturation in aqueous medium. European Journal of Pharmaceutics and Biopharmaceutics. 2016;107:16-31.

86. Pina MF, Zhao M, Pinto JF, Sousa JJ, Craig DQM. The Influence of Drug Physical State on the Dissolution Enhancement of Solid Dispersions Prepared Via Hot-Melt Extrusion: A Case Study Using Olanzapine. Journal of Pharmaceutical Sciences. 2014;103(4):1214-23.

87. Djuris J, Nikolakakis I, Ibric S, Djuric Z, Kachrimanis K. Preparation of carbamazepine–Soluplus® solid dispersions by hot-melt extrusion, and prediction of drug–polymer miscibility by thermodynamic model fitting. European Journal of Pharmaceutics and Biopharmaceutics. 2013;84(1):228-37.

88. Marsac PJ, Shamblin SL, Taylor LS. Theoretical and Practical Approaches for Prediction of Drug–Polymer Miscibility and Solubility. Pharmaceutical Research. 2006;23(10):2417.

89. Li S, Tian Y, Jones DS, Andrews GP. Optimising Drug Solubilisation in Amorphous Polymer Dispersions: Rational Selection of Hot-melt Extrusion Processing Parameters. AAPS PharmSciTech. 2016;17(1):200-13.

90. Purohit HS, Taylor LS. Miscibility of Itraconazole–Hydroxypropyl Methylcellulose Blends: Insights with High Resolution Analytical Methodologies. Molecular Pharmaceutics. 2015;12(12):4542-53.

91. Wlodarski K, Sawicki W, Kozyra A, Tajber L. Physical stability of solid dispersions with respect to thermodynamic solubility of tadalafil in PVP-VA. European Journal of Pharmaceutics and Biopharmaceutics. 2015;96:237-46.

92. Forster A, Hempenstall J, Rades T. Characterization of glass solutions of poorly water-soluble drugs produced by melt extrusion with hydrophilic amorphous polymers. Journal of Pharmacy and Pharmacology. 2001;53(3):303-15.

93. Wang X, Michoel A, Van den Mooter G. Solid state characteristics of ternary solid dispersions composed of PVP VA64, Myrj 52 and itraconazole. International Journal of Pharmaceutics. 2005;303(1-2):54-61.

94. Craig DQM, Reading M. Thermal Analysis of Pharmaceuticals. New York: CRC Press Taylor & Francis Group; 2007.

95. Ediger MD, Angell CA, Nagel SR. Supercooled Liquids and Glasses. The Journal of Physical Chemistry. 1996;100(31):13200-12.

96. Bhattacharya S, Suryanarayanan R. Local Mobility in Amorphous Pharmaceuticals—Characterization and Implications on Stability. Journal of Pharmaceutical Sciences. 2009;98(9):2935-53.

97. Hancock BC, Zografi G. Characteristics and significance of the amorphous state in pharmaceutical systems. Journal of Pharmaceutical Sciences. 1997;86(1):1-12.

98. Barmpalexis P, Koutsidis I, Karavas E, Louka D, Papadimitriou SA, Bikiaris DN. Development of PVP/PEG mixtures as appropriate carriers for the preparation of drug solid dispersions by melt mixing technique and optimization of dissolution using artificial neural networks. European Journal of Pharmaceutics and Biopharmaceutics. 2013;85(3, Part B):1219-31.

99. Nair R, Nyamweya N, Gönen S, Martínez-Miranda LJ, Hoag SW. Influence of various drugs on the glass transition temperature of poly(vinylpyrrolidone): a thermodynamic and spectroscopic investigation. International Journal of Pharmaceutics. 2001;225(1–2):83-96.

100. Hancock BC, Shamblin SL, Zografi G. Molecular Mobility of Amorphous Pharmaceutical Solids Below Their Glass Transition Temperatures. Pharmaceutical Research. 1995;12(6):799-806.

101. Duer MJ. Solid State NMR Spectroscopy: Principles and Applications: Wiley; 2001.

102. Alie J, Menegotto J, Cardon P, Duplaa H, Caron A, Lacabanne C, et al. Dielectric study of the molecular mobility and the isothermal crystallization kinetics of an amorphous pharmaceutical drug substance. Journal of Pharmaceutical Sciences. 2004;93(1):218-33.

103. Graeser KA, Patterson JE, Zeitler JA, Gordon KC, Rades T. Correlating thermodynamic and kinetic parameters with amorphous stability. European Journal of Pharmaceutical Sciences. 2009;37(3–4):492-8.

104. Marsac PJ, Konno H, Taylor LS. A Comparison of the Physical Stability of Amorphous Felodipine and Nifedipine Systems. Pharmaceutical Research. 2006;23(10):2306-16.

105. Kestur US, Lee H, Santiago D, Rinaldi C, Won Y-Y, Taylor LS. Effects of the Molecular Weight and Concentration of Polymer Additives, and Temperature on the Melt Crystallization Kinetics of a Small Drug Molecule. Crystal Growth & Design. 2010;10(8):3585-95.

106. Johari GP, Astl G, Mayer E. Enthalpy relaxation of glassy water. The Journal of Chemical Physics. 1990;92(1):809-10.

107. Velikov V, Borick S, Angell CA. The Glass Transition of Water, Based on Hyperquenching Experiments. Science. 2001;294(5550):2335-8.

108. Konno H, Taylor LS. Ability of Different Polymers to Inhibit the Crystallization of Amorphous Felodipine in the Presence of Moisture. Pharmaceutical Research. 2008;25(4):969-78.

109. Marsac PJ, Konno H, Rumondor AC, Taylor LS. Recrystallization of nifedipine and felodipine from amorphous molecular level solid dispersions containing poly(vinylpyrrolidone) and sorbed water. Pharm Res. 2008;25(3):647-56.

110. Rumondor ACF, Stanford LA, Taylor LS. Effects of Polymer Type and Storage Relative Humidity on the Kinetics of Felodipine Crystallization from Amorphous Solid Dispersions. Pharmaceutical Research. 2009;26(12):2599-606.

111. Taylor LS, Zografi G. Spectroscopic characterization of interactions between PVP and indomethacin in amorphous molecular dispersions. Pharm Res. 1997;14(12):1691-8.

112. Thybo P, Kristensen J, Hovgaard L. Characterization and physical stability of tolfenamic acid-PVP K30 solid dispersions. Pharm Dev Technol. 2007;12(1):43-53.

113. Bley H, Fussnegger B, Bodmeier R. Characterization and stability of solid dispersions based on PEG/polymer blends. International Journal of Pharmaceutics. 2010;390(2):165-73.

114. Damian F, Blaton N, Kinget R, Van den Mooter G. Physical stability of solid dispersions of the antiviral agent UC-781 with PEG 6000, Gelucire® 44/14 and PVP K30. International Journal of Pharmaceutics. 2002;244(1–2):87-98.

115. Dordunoo SK, Ford JL, Rubinstein MH. Physical Stability of Solid Dispersions Containing Triamterene or Temazepam in Polyethylene Glycols. Journal of Pharmacy and Pharmacology. 1997;49(4):390-6.

116. Papageorgiou GZ, Bikiaris D, Karavas E, Politis S, Docoslis A, Park Y, et al. Effect of physical state and particle size distribution on dissolution enhancement of nimodipine/PEG solid dispersions prepared by melt mixing and solvent evaporation. The AAPS Journal. 2006;8(4):E623-E31.

117. Weuts I, Kempen D, Verreck G, Decorte A, Heymans K, Peeters J, et al. Study of the physicochemical properties and stability of solid dispersions of loperamide and PEG6000 prepared by spray drying. European Journal of Pharmaceutics and Biopharmaceutics. 2005;59(1):119-26.

118. Alshahrani SM, Lu W, Park J-B, Morott JT, Alsulays BB, Majumdar S, et al. Stability-enhanced Hot-melt Extruded Amorphous Solid Dispersions via Combinations of Soluplus® and HPMCAS-HF. AAPS PharmSciTech. 2015;16(4):824-34.

119. Jijun F, Lishuang X, Xiaoli W, Shu Z, Xiaoguang T, Xingna Z, et al. Nimodipine (NM) tablets with high dissolution containing NM solid dispersions prepared by hot-melt extrusion. Drug Development and Industrial Pharmacy. 2011;37(8):934-44.

120. Van den Mooter G, Wuyts M, Blaton N, Busson R, Grobet P, Augustijns P, et al. Physical stabilisation of amorphous ketoconazole in solid dispersions with polyvinylpyrrolidone K25. European Journal of Pharmaceutical Sciences. 2001;12(3):261-9.

121. Dukeck R, Sieger P, Karmwar P. Investigation and correlation of physical stability, dissolution behaviour and interaction parameter of amorphous solid dispersions of telmisartan: A drug development perspective. European Journal of Pharmaceutical Sciences. 2013;49(4):723-31.

122. Qian F, Huang J, Zhu Q, Haddadin R, Gawel J, Garmise R, et al. Is a distinctive single Tg a reliable indicator for the homogeneity of amorphous solid dispersion? International Journal of Pharmaceutics. 2010;395(1–2):232-5.

123. Mistry P, Mohapatra S, Gopinath T, Vogt FG, Suryanarayanan R. Role of the Strength of Drug–Polymer Interactions on the Molecular Mobility and Crystallization Inhibition in Ketoconazole Solid Dispersions. Molecular Pharmaceutics. 2015;12(9):3339-50.

124. Saerens L, Dierickx L, Lenain B, Vervaet C, Remon JP, Beer TD. Raman spectroscopy for the in-line polymer–drug quantification and solid state characterization during a pharmaceutical hot-melt extrusion process. European Journal of Pharmaceutics and Biopharmaceutics. 2011;77(1):158-63.

125. Weuts I, Kempen D, Decorte A, Verreck G, Peeters J, Brewster M, et al. Physical stability of the amorphous state of loperamide and two fragment molecules in solid dispersions with the polymers PVP-K30 and PVP-VA64. European Journal of Pharmaceutical Sciences. 2005;25(2–3):313-20.

126. Ahuja N, Katare OP, Singh B. Studies on dissolution enhancement and mathematical modeling of drug release of a poorly water-soluble drug using water-soluble carriers. European Journal of Pharmaceutics and Biopharmaceutics. 2007;65(1):26-38.

127. Duret C, Wauthoz N, Sebti T, Vanderbist F, Amighi K. Solid dispersions of itraconazole for inhalation with enhanced dissolution, solubility and dispersion properties. International Journal of Pharmaceutics. 2012;428(1–2):103-13.

128. Xie T, Taylor LS. Improved Release of Celecoxib from High Drug Loading Amorphous Solid Dispersions Formulated with Polyacrylic Acid and Cellulose Derivatives. Molecular Pharmaceutics. 2016;13(3):873-84.

129. Wyttenbach N, Janas C, Siam M, Lauer ME, Jacob L, Scheubel E, et al. Miniaturized screening of polymers for amorphous drug stabilization (SPADS): Rapid assessment of solid dispersion systems. European Journal of Pharmaceutics and Biopharmaceutics. 2013;84(3):583-98.

130. Raghavan SL, Trividic A, Davis AF, Hadgraft J. Crystallization of hydrocortisone acetate: influence of polymers. International Journal of Pharmaceutics. 2001;212(2):213-21.

131. Vandecruys R, Peeters J, Verreck G, Brewster ME. Use of a screening method to determine excipients which optimize the extent and stability of supersaturated drug solutions and application of this system to solid formulation design. International Journal of Pharmaceutics. 2007;342(1–2):168-75.

132. Kumar D, Thipparaboina R, Modi SR, Bansal AK, Shastri NR. Effect of HPMC concentration on crystal habit of nifedipine. CrystEngComm. 2015;17(7):1615-24.

133. Strickley RG. Solubilizing Excipients in Oral and Injectable Formulations. Pharmaceutical Research. 2004;21(2):201-30.

134. Canselier JP. The effect of surfactants and crystallization phenomena. Journal of Dispersion Science and Technology. 1993;14(6):625-44.

135. Kumar D, Thipparaboina R, Modi SR, Bansal AK, Shastri NR. Effect of surfactant concentration on nifedipine crystal habit and its related pharmaceutical properties. Journal of Crystal Growth. 2015;422:44-51.

136. Garti N, Zour H. The effect of surfactants on the crystallization and polymorphic transformation of glutamic acid. Journal of Crystal Growth. 1997;172(3):486-98.

137. Lu GW, Hawley M, Smith M, Geiger BM, Pfund W. Characterization of a novel polymorphic form of celecoxib. Journal of Pharmaceutical Sciences. 2006;95(2):305-17.

138. Iohara D, Yoshida K, Yamaguchi K, Anraku M, Motoyama K, Arima H, et al. Cyclodextrin-Induced Change in Crystal Habit of Acetylsalicylic Acid in Aqueous Solution. Crystal Growth & Design. 2012;12(4):1985-91.

139. Kalivoda A, Fischbach M, Kleinebudde P. Application of mixtures of polymeric carriers for dissolution enhancement of oxeglitazar using hot-melt extrusion. International Journal of Pharmaceutics. 2012;439(1–2):145-56.

140. Alexy P, Lacík I, Šimková B, Bakoš D, Prónayová Na, Liptaj T, et al. Effect of melt processing on thermo-mechanical degradation of poly(vinyl alcohol)s. Polymer Degradation and Stability. 2004;85(2):823-30.

141. Corrigan OI. Thermal analysis of spray dried products. Thermochimica Acta. 1995;248:245-58.

142. Kishore RSK, Kiese S, Fischer S, Pappenberger A, Grauschopf U, Mahler H-C. The Degradation of Polysorbates 20 and 80 and its Potential Impact on the Stability of Biotherapeutics. Pharmaceutical Research. 2011;28(5):1194-210.

143. Kishore RSK, Pappenberger A, Dauphin IB, Ross A, Buergi B, Staempfli A, et al. Degradation of Polysorbates 20 and 80: Studies on Thermal Autoxidation and Hydrolysis. Journal of Pharmaceutical Sciences. 2011;100(2):721-31.

144. Crowley MM, Zhang F, Koleng JJ, McGinity JW. Stability of polyethylene oxide in matrix tablets prepared by hot-melt extrusion. Biomaterials. 2002;23(21):4241-8.

145. Han S, Kim C, Kwon D. Thermal degradation of poly(ethyleneglycol). Polymer Degradation and Stability. 1995;47(2):203-8.

146. Meng J, Levina M, Rajabi-Siahboomi AR, Round AN, Reading M, Craig DQM. The Development of Thermal Nanoprobe Methods as a Means of Characterizing and Mapping Plasticizer Incorporation into Ethylcellulose Films. Pharmaceutical Research. 2012;29(8):2128-38.

147. Patel BB, Patel JK, Chakraborty S, Shukla D. Revealing facts behind spray dried solid dispersion technology used for solubility enhancement. Saudi Pharmaceutical Journal. 2015;23(4):352-65.

148. Barmpalexis P, Kachrimanis K, Georgarakis E. Solid dispersions in the development of a nimodipine floating tablet formulation and optimization by artificial neural networks and genetic programming. European Journal of Pharmaceutics and Biopharmaceutics. 2011;77(1):122-31.

149. Hughey JR, Keen JM, Miller DA, Kolter K, Langley N, McGinity JW. The use of inorganic salts to improve the dissolution characteristics of tablets containing Soluplus®-based solid dispersions. European Journal of Pharmaceutical Sciences. 2013;48(4–5):758-66.

150. Modi A, Tayade P. Enhancement of dissolution profile by solid dispersion (kneading) technique. AAPS PharmSciTech. 2006;7(3):E87.

151. Allen L. Ansel's Pharmaceutical Dosage Forms and Drug Delivery Systems: Wolters Kluwer Health; 2014. 263-98 p.

152. Rahman Z, Zidan AS, Khan MA. Risperidone solid dispersion for orally disintegrating tablet: Its formulation design and non-destructive methods of evaluation. International Journal of Pharmaceutics. 2010;400(1–2):49-58.

153. Yang Z, Nollenberger K, Albers J, Qi S. Molecular Implications of Drug–Polymer Solubility in Understanding the Destabilization of Solid Dispersions by Milling. Molecular Pharmaceutics. 2014;11(7):2453-65.

154. Ayenew Z, Paudel A, Rombaut P, Van den Mooter G. Effect of Compression on Non-isothermal Crystallization Behaviour of Amorphous Indomethacin. Pharmaceutical Research. 2012;29(9):2489-98.

155. Ayenew Z, Paudel A, Van den Mooter G. Can compression induce demixing in amorphous solid dispersions? A case study of naproxen–PVP K25. European Journal of Pharmaceutics and Biopharmaceutics. 2012;81(1):207-13.

156. Singh A, Bharati A, Frederiks P, Verkinderen O, Goderis B, Cardinaels R, et al. Effect of Compression on the Molecular Arrangement of Itraconazole–Soluplus Solid Dispersions: Induction of Liquid Crystals or Exacerbation of Phase Separation? Molecular Pharmaceutics. 2016;13(6):1879-93.

157. Löbmann K, Flouda K, Qiu D, Tsolakou T, Wang W, Rades T. The Influence of Pressure on the Intrinsic Dissolution Rate of Amorphous Indomethacin. Pharmaceutics. 2014;6(3):481.

158. Singh A, Van Humbeeck J, Van den Mooter G. A New Twist in the Old Story-can Compression Induce Mixing of Phase Separated Solid Dispersions? A Case Study of Spray-Dried Miconazole-PVP VA64 Solid Dispersions. Pharmaceutical Research. 2014;31(11):3191-200.

159. Xu W-J, Xie H-J, Cao Q-R, Shi L-L, Cao Y, Zhu X-Y, et al. Enhanced dissolution and oral bioavailability of valsartan solid dispersions prepared by a freeze-drying technique using hydrophilic polymers. Drug Delivery. 2016;23(1):41-8.

160. Bennett RC, Brough C, Miller DA, O'Donnell KP, Keen JM, Hughey JR, et al. Preparation of amorphous solid dispersions by rotary evaporation and KinetiSol Dispersing: approaches to enhance solubility of a poorly water-soluble gum extract. Drug Development and Industrial Pharmacy. 2015;41(3):382-97.

161. Wlodarski K, Tajber L, Sawicki W. Physicochemical properties of direct compression tablets with spray dried and ball milled solid dispersions of tadalafil in PVP-VA. European Journal of Pharmaceutics and Biopharmaceutics. 2016;109:14-23.

162. Tipduangta P, Belton P, Fábián L, Wang LY, Tang H, Eddleston M, et al. Electrospun Polymer Blend Nanofibers for Tunable Drug Delivery: The Role of Transformative Phase Separation on Controlling the Release Rate. Molecular Pharmaceutics. 2016;13(1):25-39.

163. Jahangiri A, Barzegar-Jalali M, Javadzadeh Y, Hamishehkar H, Adibkia K. Physicochemical characterization of atorvastatin calcium/ezetimibe amorphous nano-solid dispersions prepared by electrospraying method. Artificial Cells, Nanomedicine, and Biotechnology. 2016:1-8.

164. Potter C, Tian Y, Walker G, McCoy C, Hornsby P, Donnelly C, et al. Novel Supercritical Carbon Dioxide Impregnation Technique for the Production of Amorphous Solid Drug Dispersions: A Comparison to Hot Melt Extrusion. Molecular Pharmaceutics. 2015;12(5):1377-90.

165. Vadnere MK. Coprecipitates and melts. In: Swarbrick J, Boylan JC, editors. Encyclopedia of pharmaceutical technology. 2nd ed. New York: Marcel Dekker; 2002. p. 779.

166. Yoshihashi Y, Iijima H, Yonemochi E, Terada K. Estimationof physical stability of amorphous solid dispersion using differential scanningcalorimetry. Journal of Thermal Analysis and Calorimetry. 2006;85(3):689-92.

167. Karavas E, Georgarakis E, Bikiaris D. Application of PVP/HPMC miscible blends with enhanced mucoadhesive properties for adjusting drug release in predictable pulsatile chronotherapeutics. European Journal of Pharmaceutics and Biopharmaceutics. 2006;64(1):115-26.

168. Karavas E, Ktistis G, Xenakis A, Georgarakis E. Effect of hydrogen bonding interactions on the release mechanism of felodipine from nanodispersions with polyvinylpyrrolidone. European Journal of Pharmaceutics and Biopharmaceutics. 2006;63(2):103-14.

169. Majerik V, Charbit G, Badens E, Horváth G, Szokonya L, Bosc N, et al. Bioavailability enhancement of an active substance by supercritical antisolvent precipitation. The Journal of Supercritical Fluids. 2007;40(1):101-10.

170. Tanaka N, Imai K, Okimoto K, Ueda S, Tokunaga Y, Ohike A, et al. Development of novel sustained-release system, disintegration-controlled matrix tablet (DCMT) with solid dispersion granules of nilvadipine. Journal of Controlled Release. 2005;108(2–3):386-95.

171. Won D-H, Kim M-S, Lee S, Park J-S, Hwang S-J. Improved physicochemical characteristics of felodipine solid dispersion particles by supercritical anti-solvent precipitation process. International Journal of Pharmaceutics. 2005;301(1–2):199-208.

172. Patil H, Tiwari RV, Repka MA. Hot-Melt Extrusion: from Theory to Application in Pharmaceutical Formulation. AAPS PharmSciTech. 2016;17(1):20-42.

173. Wen H, Park K. Oral Controlled Release Formulation Design and Drug Delivery: Theory to Practice: Wiley; 2011. 266 p.

174. Narang AS, Boddu SHS. Excipient Applications in Formulation Design and Drug Delivery: Springer International Publishing; 2015. 598 p.

175. Park J-B, Kang C-Y, Kang W-S, Choi H-G, Han H-K, Lee B-J. New investigation of distribution imaging and content uniformity of very low dose drugs using hot-melt extrusion method. International Journal of Pharmaceutics. 2013;458(2):245-53.

176. Descamps M. Disordered Pharmaceutical Materials: Wiley; 2016. 477 p.

177. Démuth B, Nagy ZK, Balogh A, Vigh T, Marosi G, Verreck G, et al. Downstream processing of polymer-based amorphous solid dispersions to generate tablet formulations. International Journal of Pharmaceutics. 2015;486(1–2):268-86.

178. Ghebre-Selassie I, Martin C. Pharmaceutical Extrusion Technology: Taylor & Francis; 2003. 36-90 p.

179. Crowley MM, Zhang F, Repka MA, Thumma S, Upadhye SB, Kumar Battu S, et al. Pharmaceutical Applications of Hot-Melt Extrusion: Part I. Drug Development and Industrial Pharmacy. 2007;33(9):909-26.

180. McGinity JW, Repka MA, Zhang F, Koleng JJ. Hot-melt extrusion technology. In: Swarbrick J, Boylan JC, editors. Encyclopedia of pharmaceutical technology. 2nd ed. New York: Marcel Dekker; 2002. p. 203–66.

181. Breitenbach J. Melt extrusion: from process to drug delivery technology. European Journal of Pharmaceutics and Biopharmaceutics. 2002;54(2):107-17.

182. Chokshi RJ, Zia H. Hot-melt extrusion technique: a review. Iran J Pharm Res 2004;3:3-16.

183. Nakamichi K, Nakano T, Yasuura H, Izumi S, Kawashima Y. The role of the kneading paddle and the effects of screw revolution speed and water content on the preparation of solid dispersions using a twin-screw extruder. International Journal of Pharmaceutics. 2002;241(2):203-11.

184. Verhoeven E, De Beer TRM, Van den Mooter G, Remon JP, Vervaet C. Influence of formulation and process parameters on the release characteristics of ethylcellulose sustained-release mini-matrices produced by hot-melt extrusion. European Journal of Pharmaceutics and Biopharmaceutics. 2008;69(1):312-9.

185. Lang B, McGinity JW, Williams RO. Hot-melt extrusion – basic principles and pharmaceutical applications. Drug Development and Industrial Pharmacy. 2014;40(9):1133-55.

186. Van den Mooter G. The use of amorphous solid dispersions: A formulation strategy to overcome poor solubility and dissolution rate. Drug Discovery Today: Technologies. 2012;9(2):e79-e85.

187. LaFountaine JS, McGinity JW, Williams RO. Challenges and Strategies in Thermal Processing of Amorphous Solid Dispersions: A Review. AAPS PharmSciTech. 2016;17(1):43-55.

188. Fule R, Amin P. Development and evaluation of lafutidine solid dispersion via hot melt extrusion: Investigating drug-polymer miscibility with advanced characterisation. Asian Journal of Pharmaceutical Sciences. 2014;9(2):92-106.

189. Maniruzzaman M, Rana MM, Boateng JS, Mitchell JC, Douroumis D. Dissolution enhancement of poorly water-soluble APIs processed by hot-melt extrusion using hydrophilic polymers. Drug Development and Industrial Pharmacy. 2013;39(2):218-27.

190. Visser MR, Baert L, Klooster Gvt, Schueller L, Geldof M, Vanwelkenhuysen I, et al. Inulin solid dispersion technology to improve the absorption of the BCS Class IV drug TMC240. European Journal of Pharmaceutics and Biopharmaceutics. 2010;74(2):233-8.

191. Liu J, Zhang F, McGinity JW. Properties of lipophilic matrix tablets containing phenylpropanolamine hydrochloride prepared by hot-melt extrusion. European Journal of Pharmaceutics and Biopharmaceutics. 2001;52(2):181-90.

192. Troy DB, Remington JP, Beringer P. Remington: The Science and Practice of Pharmacy: Lippincott Williams & Wilkins; 2006. 928 p.

193. Turton R, Cheng XX. Cooling Processes and Congealing. In: Swarbrick J, Boylan JC, editors. Encyclopedia of pharmaceutical technology. 2nd ed. New York: Marcel Dekker; 2002. p. 761–74.

194. Giri TK, Kumar K, Alexander A, Ajazuddin, Badwaik H, Tripathi DK. A novel and alternative approach to controlled release drug delivery system based on solid dispersion technique. Bulletin of Faculty of Pharmacy, Cairo University. 2012;50(2):147-59.

195. Ozeki T, Yuasa H, Kanaya Y. Controlled release from solid dispersion composed of poly(ethylene oxide)–Carbopol® interpolymer complex with various cross-linking degrees of Carbopol®. Journal of Controlled Release. 2000;63(3):287-95.

196. Palem CR, Dudhipala NR, Battu SK, Repka MA, Rao Yamsani M. Development, optimization and in vivo characterization of domperidone-controlled release hot-melt-extruded films for buccal delivery. Drug Development and Industrial Pharmacy. 2016;42(3):473-84.

197. Aharoni SM. Increased glass transition temperature in motionally constrained semicrystalline polymers. Polymers for Advanced Technologies. 1998;9(3):169-201.

198. Schilling SU, McGinity JW. Novel application of hot-melt extrusion for the preparation of monolithic matrices containing enteric-coated particles. International Journal of Pharmaceutics. 2010;400(1–2):24-31.

199. Ghalanbor Z, Körber M, Bodmeier R. Protein release from poly(lactide-co-glycolide) implants prepared by hot-melt extrusion: Thioester formation as a reason for incomplete release. International Journal of Pharmaceutics. 2012;438(1–2):302-6.

200. Repka MA, McGinity JW. Influence of Vitamin E TPGS on the properties of hydrophilic films produced by hot-melt extrusion. International Journal of Pharmaceutics. 2000;202(1–2):63-70.

201. Ghebremeskel AN, Vemavarapu C, Lodaya M. Use of Surfactants as Plasticizers in Preparing Solid Dispersions of Poorly Soluble API: Stability Testing of Selected Solid Dispersions. Pharmaceutical Research. 2006;23(8):1928-36.

202. Repka MA, Shah S, Lu J, Maddineni S, Morott J, Patwardhan K, et al. Melt extrusion: process to product. Expert Opinion on Drug Delivery. 2012;9(1):105-25.

203. Maru SM, de Matas M, Kelly A, Paradkar A. Characterization of thermal and rheological properties of zidovidine, lamivudine and plasticizer blends with ethyl cellulose to assess their suitability for hot melt extrusion. European Journal of Pharmaceutical Sciences. 2011;44(4):471-8.

204. Schilling SU, Lirola HL, Shah NH, Waseem Malick A, McGinity JW. Influence of plasticizer type and level on the properties of Eudragit® S100 matrix pellets prepared by hot-melt extrusion. Journal of Microencapsulation. 2010;27(6):521-32.

205. Repka MA, Gerding TG, Repka SL, McGinity JW. Influence of Plasticizers and Drugs on the Physical-Mechanical Properties of Hydroxypropylcellulose Films Prepared by Hot Melt Extrusion. Drug Development and Industrial Pharmacy. 1999;25(5):625-33.

206. Kerwin BA. Polysorbates 20 and 80 Used in the Formulation of Protein Biotherapeutics: Structure and Degradation Pathways. Journal of Pharmaceutical Sciences. 2008;97(8):2924-35.

207. Cagno Md, Stein PC, Styskala J, Hlaváč J, Skalko-Basnet N, Bauer-Brandl A. Overcoming instability and low solubility of new cytostatic compounds: A comparison of two approaches. European Journal of Pharmaceutics and Biopharmaceutics. 2012;80(3):657-62.

208. Zema L, Loreti G, Melocchi A, Maroni A, Gazzaniga A. Injection Molding and its application to drug delivery. Journal of Controlled Release. 2012;159(3):324-31.

209. Speiser P. Injection-moulded oral medicament in solid form. Google Patents; 1969.

210. Gomes ME, Ribeiro AS, Malafaya PB, Reis RL, Cunha AM. A new approach based on injection moulding to produce biodegradable starch-based polymeric scaffolds: morphology, mechanical and degradation behaviour. Biomaterials. 2001;22(9):883-9.

211. Sammoura F, Kang J, Heo Y-M, Jung T, Lin L. Polymeric microneedle fabrication using a microinjection molding technique. Microsystem Technologies. 2007;13(5):517-22.

212. König C, Ruffieux K, Wintermantel E, Blaser J. Autosterilization of biodegradable implants by injection molding process. Journal of Biomedical Materials Research. 1997;38(2):115-9.

213. Repka MA, Majumdar S, Kumar Battu S, Srirangam R, Upadhye SB. Applications of hot-melt extrusion for drug delivery. Expert Opinion on Drug Delivery. 2008;5(12):1357-76.

214. Eith L, Stepto RFT, Tomka I, Wittwer F. The Injection-Moulded Capsule. Drug Development and Industrial Pharmacy. 1986;12(11-13):2113-26.

215. Kenyon CJ, Cole ET, Wilding IR. The effect of food on the in vivo behaviour of enteric coated starch capsules. International Journal of Pharmaceutics. 1994;112(3):207-13.

216. Eggenreich K, Windhab S, Schrank S, Treffer D, Juster H, Steinbichler G, et al. Injection molding as a one-step process for the direct production of pharmaceutical dosage forms from primary powders. International Journal of Pharmaceutics. 2016;505(1–2):341-51.

217. Quinten T, Beer T, Vervaet C, Remon J. Evaluation of injection moulding as a pharmaceutical technology to produce matrix tablets. European Journal of Pharmaceutics and Biopharmaceutics. 2009;71(1):145-54.

218. Quinten T, De Beer T, Onofre FO, Mendez-Montealvo G, Wang YJ, Remon JP, et al. Sustained-release and swelling characteristics of xanthan gum/ethylcellulose-based injection moulded matrix tablets: in vitro and in vivo evaluation. Journal of Pharmaceutical Sciences. 2011;100(7):2858-70.

219. Quinten T, Gonnissen Y, Adriaens E, Beer TD, Cnudde V, Masschaele B, et al. Development of injection moulded matrix tablets based on mixtures of ethylcellulose and low-substituted hydroxypropylcellulose. European Journal of Pharmaceutical Sciences. 2009;37(3–4):207-16.

220. Cheng L, Guo S, Wu W. Characterization and in vitro release of praziquantel from poly(ε-caprolactone) implants. International Journal of Pharmaceutics. 2009;377(1–2):112-9.

221. Rothen-Weinhold A, Besseghir K, Vuaridel E, Sublet E, Oudry N, Kubel F, et al. Injection-molding versus extrusion as manufacturing technique for the preparation of biodegradable implants. European Journal of Pharmaceutics and Biopharmaceutics. 1999;48(2):113-21.

222. Rathbone M. Development of an injection molded poly(ε-caprolactone) intravaginal insert for the delivery of progesterone to cattle. Journal of Controlled Release. 2002;85(1-3):61-71.

223. Stansbury JW, Idacavage MJ. 3D printing with polymers: Challenges among expanding options and opportunities. Dental Materials. 2016;32(1):54-64.

224. Goyanes A, Wang J, Buanz A, Martínez-Pacheco R, Telford R, Gaisford S, et al. 3D Printing of Medicines: Engineering Novel Oral Devices with Unique Design and Drug Release Characteristics. Molecular Pharmaceutics. 2015;12(11):4077-84.

225. Khaled SA, Burley JC, Alexander MR, Roberts CJ. Desktop 3D printing of controlled release pharmaceutical bilayer tablets. International Journal of Pharmaceutics. 2014;461(1–2):105-11.

226. Skowyra J, Pietrzak K, Alhnan MA. Fabrication of extended-release patient-tailored prednisolone tablets via fused deposition modelling (FDM) 3D printing. European Journal of Pharmaceutical Sciences. 2015;68:11-7.

227. Godoi FC, Prakash S, Bhandari BR. 3d printing technologies applied for food design: Status and prospects. Journal of Food Engineering. 2016;179:44-54.

228. Laura R-C, Andrew G, Callum F, Joel S, Kevin S, Jing Y. Characterisation of the surface structure of 3D printed scaffolds for cell infiltration and surgical suturing. Biofabrication. 2016;8(1):015016.

229. Chua CK, Leong KF, Lim CS. Rapid Prototyping: Principles and Applications: World Scientific; 2003. 124 p.

230. Khaled SA, Burley JC, Alexander MR, Yang J, Roberts CJ. 3D printing of five-in-one dose combination polypill with defined immediate and sustained release profiles. Journal of Controlled Release. 2015;217:308-14.

231. Ursan ID, Chiu L, Pierce A. Three-dimensional drug printing: A structured review. Journal of the American Pharmacists Association. 2013;53(2):136-44.

232. Banks J. Adding Value in Additive Manufacturing : Researchers in the United Kingdom and Europe Look to 3D Printing for Customization. IEEE Pulse. 2013;4(6):22-6.

233. Yu DG, Zhu L-M, Branford-White CJ, Yang XL. Three-Dimensional Printing in Pharmaceutics: Promises and Problems. Journal of Pharmaceutical Sciences. 2008;97(9):3666-90.

234. James CM, Carmel MH. Drug delivery: Buccal route. In: Swarbrick J, Boylan JC, editors. Encyclopedia of pharmaceutical technology. 2nd ed. New York: Marcel Dekker; 2007. p. 1071–228.

235. Shojaei AH. Buccal mucosa as a route for systemic drug delivery: a review. Journal of pharmacy & pharmaceutical sciences : a publication of the Canadian Society for Pharmaceutical Sciences, Societe canadienne des sciences pharmaceutiques. 1998;1(1):15-30.

236. Washington N, Washington C, Wilson C. Physiological Pharmaceutics: Barriers to Drug Absorption: CRC Press; 2002.

237. Montenegro-Nicolini M, Morales JO. Overview and Future Potential of Buccal Mucoadhesive Films as Drug Delivery Systems for Biologics. AAPS PharmSciTech. 2017;18(1):3-14.

238. Rathbone MJ, Hadgraft J. Absorption of drugs from the human oral cavity. International Journal of Pharmaceutics. 1991;74(1):9-24.

239. Gandhi RB, Robinson JR. Oral cavity as a site for bioadhesive drug delivery. Advanced Drug Delivery Reviews. 1994;13(1–2):43-74.

240. Harris D, Robinson JR. Drug Delivery via the Mucous Membranes of the Oral Cavity. Journal of Pharmaceutical Sciences. 1992;81(1):1-10.

241. Wertz PW, Cox PS, Squier CA, Downing DT. Lipids of epidermis and keratinized and non-keratinized oral epithelia. Comparative Biochemistry and Physiology Part B: Comparative Biochemistry. 1986;83(3):529-31.

242. Khanvilkar K. Drug transfer through mucus. Advanced Drug Delivery Reviews. 2001;48(2-3):173-93.

243. Salamatmiller N, Chittchang M, Johnston T. The use of mucoadhesive polymers in buccal drug delivery. Advanced Drug Delivery Reviews. 2005;57(11):1666-91.

244. Shi L. Mucin as biological surfactant to protect biomaterial surfaces. University of Utah: University of Utah; 1999.

245. Johnson LR. Physiology of the gastrointestinal tract: editor-in-chief, Leonard R. Johnson ; associate editors, James Christensen ... [et al.]: Raven Press; 1987.

246. Filipe MI. Mucins in the human gastrointestinal epithelium: a review. Investigative & cell pathology. 1979;2(3):195-216.

247. Roussel P, Lamblin G, Lhermitte M, Houdret N, Lafitte J-J, Perini J-M, et al. The complexity of mucins. Biochimie. 1988;70(11):1471-82.

248. Strous GJ, Dekker J. Mucin-Type Glycoproteins. Critical Reviews in Biochemistry and Molecular Biology. 1992;27(1-2):57-92.

249. Oates MDG, Rosbottom AC, Schrager J. Further investigations into the structure of human gastric mucin: The structural configuration of the oligosaccharide chains. Carbohydrate Research. 1974;34(1):115-37.

250. Carlson DM. [24] Phosphoacetylglucosamine mutase from pig submaxillary gland. Methods in Enzymology: Elsevier BV; 1966. p. 179-82.

251. Spiro RG. Glycoproteins. Annual Review of Biochemistry. 1970;39(1):599-638.

252. Gibbons RA. Polydispersity. Nature. 1963;200(4907):665-6.

253. Dekker J, Van Beurden-Lamers WMO, Oprins A, Strous GJ. Isolation and structural analysis of rat gastric mucus glycoprotein suggests a homogeneous protein backbone. Biochemical Journal. 1989;260(3):717-23.

254. Saltzman WM, Radomsky ML, Whaley KJ, Cone RA. Antibody diffusion in human cervical mucus. Biophysical Journal. 1994;66(2):508-15.

255. Niibuchi J-J, Aramaki Y, Tsuchiya S. Binding of antibiotics to rat intestinal mucin. International Journal of Pharmaceutics. 1986;30(2-3):181-7.

256. Komiya I, Park JY, Kamani A, Ho NFH, Higuchi WI. Quantitative mechanistic studies in simultaneous fluid flow and intestinal absorption using steroids as model solutes. International Journal of Pharmaceutics. 1980;4(3):249-62.

257. Franz JM, Vonderscher JP, Voges R. Contribution to the intestinal absorption of ergot peptide alkaloids. International Journal of Pharmaceutics. 1980;7(1):19-28.

258. Lindqvist L, Nord CE, Sôder PO. Origin of esterases in human whole saliva. Enzyme. 1977;22(3):166-75.

259. Rathbone MJ, Tucker IG. Mechanisms, barriers and pathways of oral mucosal drug permeation. Advanced Drug Delivery Reviews. 1993;12(1-2):41-60.

260. Sadoogh-Abasian F, Evered DF. Absorption of vitamin C from the human buccal cavity. British Journal of Nutrition. 1979;42(01):15.

261. McMullan JM, Manning AS, Evered DF. Effect of Calcium Ions on the Uptake of Sugars through the Human Buccal Mucosa. Biochemical Society Transactions. 1977;5(1):129-30.

262. Evered DF, Sadoogh-Abasian F, Patel PD. Absorption of nicotinic acid and nicotinamide across human buccal mucosa. Life Sciences. 1980;27(18):1649-51.

263. Dowly ME, Knuth KE, Robinson JR. Enzyme characterization studies on the rate-limiting barrier in rabbit buccal mucosa. International Journal of Pharmaceutics. 1992;88(1-3):293-302.

264. Squier CA, Fejerskov O, Jepsen A. The permeability of a keratinizing squamous epithelium in culture. Journal of Anatomy. 1978;126(Pt 1):103-9.

265. Squier CA, Rooney L. The permeability of keratinized and nonkeratinized oral epithelium to lanthanum in vivo. Journal of Ultrastructure Research. 1976;54(2):286-95.

266. Dowty ME, Knuth KE, Irons BK, Robinson JR. Pharmaceutical Research. 1992;09(9):1113-22.

267. Gandhi R, Robinson J. Mechanisms of penetration enhancement for transbuccal delivery of salicylic acid. International Journal of Pharmaceutics. 1992;85(1-3):129-40.

268. Lee Y, Chien YW. Oral mucosa controlled delivery of LHRH by bilayer mucoadhesive polymer systems. Journal of Controlled Release. 1995;37(3):251-61.

269. Wong C, Yuen K, Peh K. Formulation and evaluation of controlled release Eudragit buccal patches. International Journal of Pharmaceutics. 1999;178(1):11-22.

270. Hillery AM, Lloyd AW, Swarbrick J. Drug Delivery and Targeting: For Pharmacists and Pharmaceutical Scientists: Taylor & Francis; 2002. 168-89 p.

271. Smart JD. Drug delivery using buccal-adhesive systems. Advanced Drug Delivery Reviews. 1993;11(3):253-70.

272. Rossi S, Sandri G, Caramella CM. Buccal drug delivery: A challenge already won? Drug Discovery Today: Technologies. 2005;2(1):59-65.

273. Rathbone MJ, Drummond BK, Tucker IG. The oral cavity as a site for systemic drug delivery. Advanced Drug Delivery Reviews. 1994;13(1):1-22.

274. Mitra AK, Alur HH, Johnston TP. Peptides and Proteins: Buccal Absorption. In: Swarbrick J, Boylan JC, editors. Encyclopedia of pharmaceutical technology. 2nd ed. New York: Marcel Dekker; 2007. p. 2664-77.

275. Veuillez F, Kalia YN, Jacques Y, Deshusses J, Buri P. Factors and strategies for improving buccal absorption of peptides. European Journal of Pharmaceutics and Biopharmaceutics. 2001;51(2):93-109.

276. Guggi D, Kast CE, Bernkop-Schnürch A. In Vivo Evaluation of an Oral Salmon Calcitonin-Delivery System Based on a Thiolated Chitosan Carrier Matrix. Pharmaceutical Research. 2003;20(12):1989-94.

277. Alqurshi A, Kumar Z, McDonald R, Strang J, Buanz A, Ahmed S, et al. Amorphous Formulation and in Vitro Performance Testing of Instantly Disintegrating Buccal Tablets for the Emergency Delivery of Naloxone. Molecular Pharmaceutics. 2016;13(5):1688-98.

278. Lueßen HL, de Leeuw BJ, Pérard D, Lehr C-M, de Boer AG, Verhoef JC, et al. Mucoadhesive polymers in peroral peptide drug delivery. I. Influence of mucoadhesive excipients on the proteolytic activity of intestinal enzymes. European Journal of Pharmaceutical Sciences. 1996;4(2):117-28.

279. Modi P, Mihic M, Lewin A. The evolving role of oral insulin in the treatment of diabetes using a novel RapidMist? System. Diabetes/Metabolism Research and Reviews. 2002;18(S1):S38-S42.

280. Peppas NA, Buri PA. Surface, interfacial and molecular aspects of polymer bioadhesion on soft tissues. Journal of Controlled Release. 1985;2:257-75.

281. Hörstedt P, Danielsson A, Nyhlin H, Stenling R, Suhr O. Adhesion of Bacteria to the Human Small-Intestinal Mucosa. Scandinavian Journal of Gastroenterology. 1989;24(7):877-85.

282. Scrivener. D.D.S CA, Schantz CW. Penicillin: New Methods for its Use in Dentistry. The Journal of the American Dental Association. 1947;35(9):644-7.

283. Smart JD. An m vitro assessment of some mucosa-adhesive dosage forms. International Journal of Pharmaceutics. 1991;73(1):69-74.

284. Harding SE, Davis SSB, Deacon MP, Fiebrig I. Biopolymer Mucoadhesives. Biotechnology and Genetic Engineering Reviews. 1999;16(1):41-86.

285. Mathias NR, Hussain MA. Non-invasive Systemic Drug Delivery: Developability Considerations for Alternate Routes of Administration. Journal of Pharmaceutical Sciences. 2010;99(1):1-20.

286. Hornof M, Weyenberg W, Ludwig A, Bernkop-Schnürch A. Mucoadhesive ocular insert based on thiolated poly(acrylic acid): development and in vivo evaluation in humans. Journal of Controlled Release. 2003;89(3):419-28.

287. Tafaghodi M, Tabassi SAS, Jaafari M-R, Zakavi SR, Momen-nejad M. Evaluation of the clearance characteristics of various microspheres in the human nose by gamma-scintigraphy. International Journal of Pharmaceutics. 2004;280(1-2):125-35.

288. Perioli L, Ambrogi V, Pagano C, Scuota S, Rossi C. FG90 chitosan as a new polymer for metronidazole mucoadhesive tablets for vaginal administration. International Journal of Pharmaceutics. 2009;377(1-2):120-7.

289. Korbonits M, Slawik M, Cullen D, Ross RJ, Stalla G, Schneider H, et al. A Comparison of a Novel Testosterone Bioadhesive Buccal System, Striant, with a Testosterone Adhesive Patch in Hypogonadal Males. The Journal of Clinical Endocrinology & Metabolism. 2004;89(5):2039-43.

290. Bernkop-Schnurch A, Paikl C, Valenta C. Novel bioadhesive chitosan-EDTA conjugate protects leucine enkephalin from degradation by aminopeptidase N. Pharm Res. 1997;14(7):917-22.

291. Lehr CM. Bioadhesion technologies for the delivery of peptide and protein drugs to the gastrointestinal tract. Critical reviews in therapeutic drug carrier systems. 1994;11(2-3):119-60.

292. Lee JW, Park JH, Robinson JR. Bioadhesive-Based Dosage Forms: The Next Generation. Journal of Pharmaceutical Sciences. 2000;89(7):850-66.

293. Khutoryanskiy VV. Advances in Mucoadhesion and Mucoadhesive Polymers. Macromolecular Bioscience. 2011;11(6):748-64.

294. Zhang J, Bunker M, Parker A, Madden-Smith CE, Patel N, Roberts CJ. The stability of solid dispersions of felodipine in polyvinylpyrrolidone characterized by nanothermal analysis. Int J Pharm. 2011;414(1-2):210-7.

295. Ducheˇne D, Touchard F, Peppas NA. Pharmaceutical and Medical Aspects of Bioadhesive Systems for Drug Administration. Drug Development and Industrial Pharmacy. 1988;14(2-3):283-318.

296. Gu JM, Robinson JR, Leung SH. Binding of acrylic polymers to mucin/epithelial surfaces: structure-property relationships. Critical reviews in therapeutic drug carrier systems. 1988;5(1):21-67.

297. Longer MA, Robinson JR. Fundamental aspects of bioadhesion. Pharmacy International. 1986;7(5):114-7.

298. Derjaguin BV, Smilga VP. Electronic Theory of Adhesion. Journal of Applied Physics. 1967;38(12):4609-16.

299. Good RJ. Surface free energy of solids and liquids: Thermodynamics, molecular forces, and structure. Journal of Colloid and Interface Science. 1977;59(3):398-419.

300. Asane GS, Nirmal SA, Rasal KB, Naik AA, Mahadik MS, Rao YM. Polymers for Mucoadhesive Drug Delivery System: A Current Status. Drug Development and Industrial Pharmacy. 2008;34(11):1246-66.

301. Jiménez-castellanos MR, Zia H, Rhodes CT. Mucoadhesive Drug Delivery Systems. Drug Development and Industrial Pharmacy. 1993;19(1-2):143-94.

302. Baszkin A, Proust JE, Monsenego P, Boissonnade MM. Wettability of polymers by mucin aqueous solutions. Biorheology. 1990;27(3-4):503-14.

303. Mikos AG, Peppas NA. Measurement of the surface tension of mucin solutions. International Journal of Pharmaceutics. 1989;53(1):1-5.

304. Blychert E, Wingstrand K, Edgar B, Lidman K. Plasma concentration profiles and antihypertensive effect of conventional and extended-release felodipine tablets. Br J Clin Pharmacol. 1990;29(1):39-45.

305. Walton T, Symes LR. Felodipine and isradipine: new calcium-channel-blocking agents for the treatment of hypertension. Clin Pharm. 1993;12(4):261-75.

306. Pagar KP, Vavia PR. Felodipine beta-cyclodextrin complex as an active core for time delayed chronotherapeutic treatment of hypertension. Acta Pharm. 2012;62(3):395-410.

307. Patil PR, Biradar SV, Paradkar AR. Extended Release Felodipine Self-Nanoemulsifying System. AAPS PharmSciTech. 2009;10(2):515-23.

308. Committee JF. British National Formulary. 61 ed. London, UK: BMJ Group and Pharmaceutical Press; 2011. 121,30 p.

309. Edgar B, Regardh CG, Lundborg P, Romare S, Nyberg G, Ronn O. Pharmacokinetic and pharmacodynamic studies of felodipine in healthy subjects after various single, oral and intravenous doses. Biopharm Drug Dispos. 1987;8(3):235-48.

310. Edgar B, Regardh CG, Johnsson G, Johansson L, Lundborg P, Lofberg I, et al. Felodipine kinetics in healthy men. Clin Pharmacol Ther. 1985;38(2):205-11.

311. Office TS. British Pharmacopoeia. London, UK: The Stationery Office; 2016.

312. Surov AO, Solanko KA, Bond AD, Perlovich GL, Bauer-Brandl A. Crystallization and Polymorphism of Felodipine. Crystal Growth & Design. 2012;12(8):4022-30.

313. Lou B, Boström D, Velaga SP. Polymorph Control of Felodipine Form II in an Attempted Cocrystallization. Crystal Growth & Design. 2009;9(3):1254-7.

314. Wang L, Song Y, Yang P, Tan B, Zhang H, Deng Z. Preparation and thermodynamic properties of Felodipine form IV. Journal of Thermal Analysis and Calorimetry. 2015;120(1):947-51.

315. Srčič S, Kerč J, Urleb U, Zupančič I, Lahajnar G, Kofler B, et al. Investigation of felodipine polymorphism and its glassy state. International Journal of Pharmaceutics. 1992;87(1):1-10.

316. Konno H, Taylor LS. Influence of Different Polymers on the Crystallization Tendency of Molecularly Dispersed Amorphous Felodipine. Journal of Pharmaceutical Sciences. 2006;95(12):2692-705.

317. Tang XC, Pikal MJ, Taylor LS. A Spectroscopic Investigation of Hydrogen Bond Patterns in Crystalline and Amorphous Phases in Dihydropyridine Calcium Channel Blockers. Pharmaceutical Research. 2002;19(4):477-83.

318. Rollinger JM, Burger A. Polymorphism of racemic felodipine and the unusual series of solid solutions in the binary system of its enantiomers. Journal of Pharmaceutical Sciences. 2001;90(7):949-59.

319. Mishra MK, Desiraju GR, Ramamurty U, Bond AD. Studying Microstructure in Molecular Crystals With Nanoindentation: Intergrowth Polymorphism in Felodipine. Angewandte Chemie International Edition. 2014;53(48):13102-5.

320. Kestur US, Taylor LS. Evaluation of the Crystal Growth Rate of Felodipine Polymorphs in the Presence and Absence of Additives As a Function of Temperature. Crystal Growth & Design. 2013;13(10):4349-54.

321. Abrahamsson B, Johansson D, Torstensson A, Wingstrand K. Evaluation of solubilizers in the drug release testing of hydrophilic matrix extended-release tablets of felodipine. Pharm Res. 1994;11(8):1093-7.

322. Kerč J, Srčič S, Kofler B, Šmid-Korbar J. Molar solubility of felodipine in different aqueous systems. International Journal of Pharmaceutics. 1992;81(1):R1-R4.

323. Pandey MM, Jaipal A, Kumar A, Malik R, Charde SY. Determination of pKa of felodipine using UV–Visible spectroscopy. Spectrochimica Acta Part A: Molecular and Biomolecular Spectroscopy. 2013;115:887-90.

324. Landahl S, Edgar B, Gabrielsson M, Larsson M, Lernfelt B, Lundborg P, et al. Pharmacokinetics and Blood Pressure Effects of Felodipine in Elderly Hypertensive Patients. Clinical Pharmacokinetics. 1988;14(6):374-83.

325. Mohl S, Winter G. Continuous release of rh-interferon α-2a from triglyceride matrices. Journal of Controlled Release. 2004;97(1):67-78.

326. Craig DQM. Polyethyelene Glycols and Drug Release. Drug Development and Industrial Pharmacy. 1990;16(17):2501-26.

327. Smikalla MM, Urbanetz NA. The influence of povidone K17 on the storage stability of solid dispersions of nimodipine and polyethylene glycol. European Journal of Pharmaceutics and Biopharmaceutics. 2007;66(1):106-12.

328. Buckley CP, Kovacs AJ. Melting behaviour of low molecular weight poly (ethylene-oxide) fractions. Colloid and Polymer Science. 1976;254(8):695-715.

329. Morris KR, Knipp GT, Serajuddin ATM. Structural properties of polyethylene glycol—polysorbate 80 mixture, a solid dispersion vehicle. Journal of Pharmaceutical Sciences. 1992;81(12):1185-8.

330. Craig DQM. Pharmaceuticals and Thermal AnalysisA review of thermal methods used for the analysis of the crystal form, solution thermodynamics and glass transition behaviour of polyethylene glycols. Thermochimica Acta. 1995;248:189-203.

331. Yang R, Yang XR, Evans DF, Hendrickson WA, Baker J. Scanning tunneling microscopy images of poly(ethylene oxide) polymers: evidence for helical and superhelical structures. The Journal of Physical Chemistry. 1990;94(15):6123-5.

332. Buckley CP, Kovacs AJ. Melting behaviour of low molecular weight poly (ethylene-oxide) fractions. Polymere Aspekte. Darmstadt: Steinkopff; 1975. p. 44-52.

333. Bailey Jr FE, Koleske JV. Chapter 6 - PROPERTIES OF POLY(ETHYLENE OXIDE). Poly (ethylene Oxide): Academic Press; 1976. p. 105-49.

334. Kovacs AJ, Straupe C, Gonthier A. Isothermal growth, thickening, and melting of polyethylene oxide) single crystals in the bulk. II. Journal of Polymer Science: Polymer Symposia. 1977;59(1):31-54.

335. Price FP, Kilb RW. The morphology and internal structure of poly(ethylene oxide) spherulites. Journal of Polymer Science. 1962;57(165):395-403.

336. Li Y, Ma Q, Huang C, Liu G. Crystallization of Poly (ethylene glycol) in Poly (methyl methacrylate) Networks. Materials Science. 2013;19(2):147-51.

337. Koenig JL, Angood AC. Raman spectra of poly(ethylene glycols) in solution. Journal of Polymer Science Part A-2: Polymer Physics. 1970;8(10):1787-96.

338. Craig DQM, Newton JM. Characterisation of polyethylene glycols using differential scanning calorimetry. International Journal of Pharmaceutics. 1991;74(1):33-41.

339. Betageri GV, Makarla KR. Enhancement of dissolution of glyburide by solid dispersion and lyophilization techniques. International Journal of Pharmaceutics. 1995;126(1):155-60.

340. Palmieri GF, Cantalamessa F, Di Martino P, Nasuti C, Martelli S. Lonidamine Solid Dispersions: In Vitro and In Vivo Evaluation. Drug Development and Industrial Pharmacy. 2002;28(10):1241-50.

341. Pan R-N, Chen J-H, Chen RR-L. Enhancement of Dissolution and Bioavailability of Piroxicam in Solid Dispersion Systems. Drug Development and Industrial Pharmacy. 2000;26(9):989-94.

342. Perissutti B, Newton JM, Podczeck F, Rubessa F. Preparation of extruded carbamazepine and PEG 4000 as a potential rapid release dosage form. European Journal of Pharmaceutics and Biopharmaceutics. 2002;53(1):125-32.

343. Fernández M, Carmen Rodríguez I, Margarit MV, Cerezo A. Characterization of solid dispersions of piroxicam/polyethylene glycol 4000. International Journal of Pharmaceutics. 1992;84(2):197-202.

344. Kanaze FI, Kokkalou E, Niopas I, Georgarakis M, Stergiou A, Bikiaris D. Dissolution enhancement of flavonoids by solid dispersion in PVP and PEG matrixes: A comparative study. Journal of Applied Polymer Science. 2006;102(1):460-71.

345. Karavas E, Georgarakis M, Docoslis A, Bikiaris D. Combining SEM, TEM, and micro-Raman techniques to differentiate between the amorphous molecular level dispersions and nanodispersions of a poorly water-soluble drug within a polymer matrix. International Journal of Pharmaceutics. 2007;340(1–2):76-83.

346. Vélaz I, Sánchez M, Martín C, Martínez-Ohárriz MC. Effect of PEG 4000 on the dissolution rate of naproxen. European Journal of Drug Metabolism and Pharmacokinetics. 1998;23(2):103-8.

347. Crowley MM, Fredersdorf A, Schroeder B, Kucera S, Prodduturi S, Repka MA, et al. The influence of guaifenesin and ketoprofen on the properties of hot-melt extruded polyethylene oxide films. European Journal of Pharmaceutical Sciences. 2004;22(5):409-18.

348. Maximilien JS. Polyethylene Oxide. In: R. C. Rowe, P. J. Shesky, Quinn ME, editors. Handbook of Pharmaceutical Excipients. London UK and Washington USA: Pharmaceutical Press and American Pharmacists Association; 2009. p. 522-5.

349. Bailey Jr FE, Koleske JV. Chapter 1 - Introduction. Poly (ethylene Oxide): Academic Press; 1976. p. 1-4.

350. Quinten T, De Beer T, Almeida A, Vlassenbroeck J, Van Hoorebeke L, Remon JP, et al. Development and evaluation of injection-molded sustained-release tablets containing ethylcellulose and polyethylene oxide. Drug Development and Industrial Pharmacy. 2011;37(2):149-59.

351. Tajiri T, Morita S, Sakamoto R, Suzuki M, Yamanashi S, Ozaki Y, et al. Release mechanisms of acetaminophen from polyethylene oxide/polyethylene glycol matrix tablets utilizing magnetic resonance imaging. International Journal of Pharmaceutics. 2010;395(1–2):147-53.

352. Mallipeddi R, Saripella KK, Neau SH. Use of coarse ethylcellulose and PEO in beads produced by extrusion–spheronization. International Journal of Pharmaceutics. 2010;385(1–2):53-65.

353. Boateng JS, Pawar HV, Tetteh J. Polyox and carrageenan based composite film dressing containing anti-microbial and anti-inflammatory drugs for effective wound healing. International Journal of Pharmaceutics. 2013;441(1–2):181-91.

354. Kim C-J. Drug release from compressed hydrophilic POLYOX-WSR tablets. Journal of Pharmaceutical Sciences. 1995;84(3):303-6.

355. Maggi L, Segale L, Torre ML, Ochoa Machiste E, Conte U. Dissolution behaviour of hydrophilic matrix tablets containing two different polyethylene oxides (PEOs) for the controlled release of a water-soluble drug. Dimensionality study. Biomaterials. 2002;23(4):1113-9.

356. Zhang F, McGinity JW. Properties of Sustained-Release Tablets Prepared by Hot-Melt Extrusion. Pharmaceutical Development and Technology. 1999;4(2):241-50.

357. Cantin O, Siepmann F, Danede F, Willart JF, Karrout Y, Siepmann J. PEO hot melt extrudates for controlled drug delivery: Importance of the molecular weight. Journal of Drug Delivery Science and Technology. 2016;36:130-40.

358. Prodduturi S, Manek RV, Kolling WM, Stodghill SP, Repka MA. Solid-state stability and characterization of hot-melt extruded poly(ethylene oxide) films. Journal of Pharmaceutical Sciences. 2005;94(10):2232-45.

359. Thumma S, ElSohly MA, Zhang S-Q, Gul W, Repka MA. Influence of Plasticizers on the Stability and Release of a Prodrug of Δ(9)-Tetrahydrocannabinol Incorporated in Poly (Ethylene Oxide) Matrices. European journal of pharmaceutics and biopharmaceutics : official journal of Arbeitsgemeinschaft fur Pharmazeutische Verfahrenstechnik eV. 2008;70(2):605-14.

360. Zhang D. Polyoxyethylene Sorbitan Fatty Acid Esters. In: R. C. Rowe, P. J. Shesky, Quinn ME, editors. Handbook of Pharmaceutical Excipients. London UK and Washington USA: Pharmaceutical Press and American Pharmacists Association; 2009. p. 549-53.

361. Ghebremeskel AN, Vemavarapu C, Lodaya M. Use of surfactants as plasticizers in preparing solid dispersions of poorly soluble API: Selection of polymer–surfactant combinations using solubility parameters and testing the processability. International Journal of Pharmaceutics. 2007;328(2):119-29.

362. Siegel IA, Gordon HP. Surfactant-induced increases of permeability of rat oral mucosa to non-electrolytes in vivo. Arch Oral Biol. 1985;30(1):43-7.

363. Fotaki N, Brown W, Kochling J, Chokshi H, Miao H, Tang K, et al. Rationale for selection of dissolution media: Three case studies. Dissolution Technologies. 2013;20(3):6-13.

364. Varade D, Ushiyama K, Shrestha LK, Aramaki K. Wormlike micelles in Tween-80/CmEO3 mixed nonionic surfactant systems in aqueous media. Journal of Colloid and Interface Science. 2007;312(2):489-97.

365. Mura P, Faucci MT, Manderioli A, Bramanti G, Parrini P. Thermal Behavior and Dissolution Properties of Naproxen From Binary and Ternary Solid Dispersions. Drug Development and Industrial Pharmacy. 1999;25(3):257-64.

366. Mura P, Moyano JR, González-Rodríguez ML, Rabasco-Alvaréz AM, Cirri M, Maestrelli F. Characterization and Dissolution Properties of Ketoprofen in Binary and Ternary Solid Dispersions with Polyethylene Glycol and Surfactants. Drug Development and Industrial Pharmacy. 2005;31(4-5):425-34.

367. Oh DH, Park Y-J, Kang JH, Yong CS, Choi H-G. Physicochemical characterization and in vivo evaluation of flurbiprofen-loaded solid dispersion without crystalline change. Drug Delivery. 2011;18(1):46-53.

368. Wang L, Cui F-D, Sunada H. Improvement of the Dissolution Rate of Nitrendipine Using a New Pulse Combustion Drying Method. Chemical and Pharmaceutical Bulletin. 2007;55(8):1119-25.

369. Zhang H, Yao M, Morrison RA, Chong S. Commonly used surfactant, Tween 80, improves absorption of P-glycoprotein substrate, digoxin, in rats. Archives of Pharmacal Research. 2003;26(9):768-72.

370. Sarpotdar Pp, Zatz JL. Percutaneous Absorption Enhancement by Nonionic Surfactants. Drug Development and Industrial Pharmacy. 1986;12(11-13):1625-47.

371. Sarpotdar PP, Zatz JL. Evaluation of Penetration Enhancement of Lidocaine by Nonionic Surfactants Through Hairless Mouse Skin In Vitro. Journal of Pharmaceutical Sciences. 1986;75(2):176-81.

372. Sudhakar Y, Kuotsu K, Bandyopadhyay AK. Buccal bioadhesive drug delivery — A promising option for orally less efficient drugs. Journal of Controlled Release. 2006;114(1):15-40.

373. Williams AC, Barry BW. Penetration enhancers. Advanced Drug Delivery Reviews. 2004;56(5):603-18.

374. Kim J-H, Choi H-K. Effect of additives on the crystallization and the permeation of ketoprofen from adhesive matrix. International Journal of Pharmaceutics. 2002;236(1–2):81-5.

375. Guo Y, Luo J, Tan S, Otieno BO, Zhang Z. The applications of Vitamin E TPGS in drug delivery. European Journal of Pharmaceutical Sciences. 2013;49(2):175-86.

376. Shah AR, Banerjee R. Effect of d-α-tocopheryl polyethylene glycol 1000 succinate (TPGS) on surfactant monolayers. Colloids and Surfaces B: Biointerfaces. 2011;85(2):116-24.

377. Raut S, Karzuon B, Atef E. Using in situ Raman spectroscopy to study the drug precipitation inhibition and supersaturation mechanism of Vitamin E TPGS from self-emulsifying drug delivery systems (SEDDS). Journal of Pharmaceutical and Biomedical Analysis. 2015;109:121-7.

378. Varma MVS, Panchagnula R. Enhanced oral paclitaxel absorption with vitamin E-TPGS: Effect on solubility and permeability in vitro, in situ and in vivo. European Journal of Pharmaceutical Sciences. 2005;25(4–5):445-53.

379. Hong C, Dang Y, Lin G, Yao Y, Li G, Ji G, et al. Effects of stabilizing agents on the development of myricetin nanosuspension and its characterization: An in vitro and in vivo evaluation. International Journal of Pharmaceutics. 2014;477(1–2):251-60.

380. Yan A, Von Dem Bussche A, Kane AB, Hurt RH. Tocopheryl polyethylene glycol succinate as a safe, antioxidant surfactant for processing carbon nanotubes and fullerenes. Carbon. 2007;45(13):2463-70.

381. Ostacolo C, Caruso C, Tronino D, Troisi S, Laneri S, Pacente L, et al. Enhancement of corneal permeation of riboflavin-5′-phosphate through vitamin E TPGS: A promising approach in corneal trans-epithelial cross linking treatment. International Journal of Pharmaceutics. 2013;440(2):148-53.

382. Bernabeu E, Chiappetta DA. Vitamin E TPGS Used as Emulsifier in the Preparation of Nanoparticulate Systems. Journal of Biomaterials and Tissue Engineering. 2013;3(1):122-34.

383. Sokol RJ, Heubi JE, Butler-Simon N, McClung HJ, Lilly JR, Silverman A. Treatment of vitamin E deficiency during chronic childhood cholestasis with oral d-α-tocopheryl polyethylene glycol-1000 succinate. Gastroenterology. 1987;93(5):975-85.

384. Moneghini M, De Zordi N, Solinas D, Macchiavelli S, Princivalle F. Characterization of solid dispersions of itraconazole and vitamin E TPGS prepared by microwave technology. Future Med Chem. 2010;2(2):237-46.

385. Janssens S, Nagels S, Armas HNd, D'Autry W, Van Schepdael A, Van den Mooter G. Formulation and characterization of ternary solid dispersions made up of Itraconazole and two excipients, TPGS 1000 and PVPVA 64, that were selected based on a supersaturation screening study. European Journal of Pharmaceutics and Biopharmaceutics. 2008;69(1):158-66.

386. Carini R, Poli G, Dianzani MU, Maddix SP, Slater TF, Cheeseman KH. Comparative evaluation of the antioxidant activity of α-tocopherol, α-tocopherol polyethylene glycol 1000 succinate and α-tocopherol succinate in isolated hepatocytes and liver microsomal suspensions. Biochemical Pharmacology. 1990;39(10):1597-601.

387. Brouwers J, Tack J, Lammert F, Augustijns P. Intraluminal drug and formulation behavior and integration in in vitro permeability estimation: A case study with amprenavir. Journal of Pharmaceutical Sciences. 2006;95(2):372-83.

388. Chang R, Peng Y, Trivedi N, Shukla A. Polymethacrylates. In: R. C. Rowe, P. J. Shesky, Quinn ME, editors. Handbook of Pharmaceutical Excipients. London UK and Washington USA: Pharmaceutical Press and American Pharmacists Association; 2009. p. 525-33.

389. Liu H, Wang P, Zhang X, Shen F, Gogos CG. Effects of extrusion process parameters on the dissolution behavior of indomethacin in Eudragit® E PO solid dispersions. International Journal of Pharmaceutics. 2010;383(1–2):161-9.

390. Qi S, Gryczke A, Belton P, Craig DQM. Characterisation of solid dispersions of paracetamol and EUDRAGIT® E prepared by hot-melt extrusion using thermal, microthermal and spectroscopic analysis. International Journal of Pharmaceutics. 2008;354(1–2):158-67.

391. Moustafine RI, Bukhovets AV, Sitenkov AY, Kemenova VA, Rombaut P, Van den Mooter G. Eudragit E PO as a Complementary Material for Designing Oral Drug Delivery Systems with Controlled Release Properties: Comparative Evaluation of New Interpolyelectrolyte Complexes with Countercharged Eudragit L100 Copolymers. Molecular Pharmaceutics. 2013;10(7):2630-41.

392. Kojima T, Higashi K, Suzuki T, Tomono K, Moribe K, Yamamoto K. Stabilization of a Supersaturated Solution of Mefenamic Acid from a Solid Dispersion with EUDRAGIT® EPO. Pharmaceutical Research. 2012;29(10):2777-91.

393. Khan S, Kataria P, Nakhat P, Yeole P. Taste masking of ondansetron hydrochloride by polymer carrier system and formulation of rapid-disintegrating tablets. AAPS PharmSciTech. 2007;8(2):E127-E33.

394. Khachane P, Date AA, Nagarsenker MS. Eudragit EPO Nanoparticles: Application in Improving Therapeutic Efficacy and Reducing Ulcerogenicity of Meloxicam on Oral Administration. Journal of Biomedical Nanotechnology. 2011;7(4):590-7.

395. Shah N, Sandhu H, Choi DS, Chokshi H, Malick AW. Amorphous Solid Dispersions: Theory and Practice: Springer New York; 2014. 136 p.

396. Shamma RN, Basha M. Soluplus®: A novel polymeric solubilizer for optimization of Carvedilol solid dispersions: Formulation design and effect of method of preparation. Powder Technology. 2013;237:406-14.

397. Zhong Y, Jing G, Tian B, Huang H, Zhang Y, Gou J, et al. Supersaturation induced by Itraconazole/Soluplus® micelles provided high GI absorption in vivo. Asian Journal of Pharmaceutical Sciences. 2016;11(2):255-64.

398. Bahadur P, Pandya K, Almgren M, Li P, Stilbs P. Effect of inorganic salts on the micellar behaviour of ethylene oxide-propylene oxide block copolymers in aqueous solution. Colloid and Polymer Science. 1993;271(7):657-67.

399. Silva RCd, Loh W. Effect of Additives on the Cloud Points of Aqueous Solutions of Ethylene Oxide–Propylene Oxide–Ethylene Oxide Block Copolymers. Journal of Colloid and Interface Science. 1998;202(2):385-90.

400. Pygall SR, Kujawinski S, Timmins P, Melia CD. Mechanisms of drug release in citrate buffered HPMC matrices. International Journal of Pharmaceutics. 2009;370(1–2):110-20.

401. Sarkar N. Thermal gelation properties of methyl and hydroxypropyl methylcellulose. Journal of Applied Polymer Science. 1979;24(4):1073-87.

402. Li CL, Martini LG, Ford JL, Roberts M. The use of hypromellose in oral drug delivery. Journal of Pharmacy and Pharmacology. 2005;57(5):533-46.

403. Pandit NK, Wang D. Salt effects on the diffusion and release rate of propranolol from poloxamer 407 gels. International Journal of Pharmaceutics. 1998;167(1–2):183-9.

404. Nagy ZK, Balogh A, Vajna B, Farkas A, Patyi G, Kramarics Á, et al. Comparison of electrospun and extruded soluplus®-based solid dosage forms of improved dissolution. Journal of Pharmaceutical Sciences. 2012;101(1):322-32.

405. Linn M, Collnot E-M, Djuric D, Hempel K, Fabian E, Kolter K, et al. Soluplus® as an effective absorption enhancer of poorly soluble drugs in vitro and in vivo. European Journal of Pharmaceutical Sciences. 2012;45(3):336-43.

406. Ha E-S, Baek I-h, Cho W, Hwang S-J, Kim M-S. Preparation and Evaluation of Solid Dispersion of Atorvastatin Calcium with Soluplus® by Spray Drying Technique. Chemical and Pharmaceutical Bulletin. 2014;62(6):545-51.

407. Lavra ZMM, Pereira de Santana D, Ré MI. Solubility and dissolution performances of spray-dried solid dispersion of Efavirenz in Soluplus. Drug Development and Industrial Pharmacy. 2016:1-13.

408. Riekes MK, Engelen A, Appeltans B, Rombaut P, Stulzer HK, Van den Mooter G. New Perspectives for Fixed Dose Combinations of Poorly Water-Soluble Compounds: a Case Study with Ezetimibe and Lovastatin. Pharmaceutical Research. 2016;33(5):1259-75.

409. Tretinnikov ON, Zagorskaya SA. Determination of the degree of crystallinity of poly(vinyl alcohol) by FTIR spectroscopy. Journal of Applied Spectroscopy. 2012;79(4):521-6.

410. De Jaeghere W, De Beer T, Van Bocxlaer J, Remon JP, Vervaet C. Hot-melt extrusion of polyvinyl alcohol for oral immediate release applications. International Journal of Pharmaceutics. 2015;492(1–2):1-9.

411. AbuBaker O. Polyvinyl Alcohol. In: R. C. Rowe, P. J. Shesky, Quinn ME, editors. Handbook of Pharmaceutical Excipients. London UK and Washington USA: Pharmaceutical Press and American Pharmacists Association; 2009. p. 564-5.

412. Buwalda SJ, Boere KWM, Dijkstra PJ, Feijen J, Vermonden T, Hennink WE. Hydrogels in a historical perspective: From simple networks to smart materials. Journal of Controlled Release. 2014;190:254-73.

413. Singh B, Sharma V. Design of psyllium–PVA–acrylic acid based novel hydrogels for use in antibiotic drug delivery. International Journal of Pharmaceutics. 2010;389(1–2):94-106.

414. Knopp MM, Chourak N, Khan F, Wendelboe J, Langguth P, Rades T, et al. Effect of polymer type and drug dose on the in vitro and in vivo behavior of amorphous solid dispersions. European Journal of Pharmaceutics and Biopharmaceutics. 2016;105:106-14.

415. Shagholani H, Ghoreishi SM, Mousazadeh M. Improvement of interaction between PVA and chitosan via magnetite nanoparticles for drug delivery application. International Journal of Biological Macromolecules. 2015;78:130-6.

416. Forster A, Hempenstall J, Tucker I, Rades T. Selection of excipients for melt extrusion with two poorly water-soluble drugs by solubility parameter calculation and thermal analysis. International Journal of Pharmaceutics. 2001;226(1–2):147-61.

417. Goyanes A, Buanz ABM, Hatton GB, Gaisford S, Basit AW. 3D printing of modified-release aminosalicylate (4-ASA and 5-ASA) tablets. European Journal of Pharmaceutics and Biopharmaceutics. 2015;89:157-62.

418. Cyversa. Thermal analysis by structural characterisation (TASC). [online] 2016 [Available from: http://cyversa.com/tasc-explained/.

419. Reading M, Antonijevic M, Grandy D, Hourston D, Lacey A. New Methods of Thermal Analysis and Chemical Mapping on a Micro and Nano Scale by Combining Microscopy with Image Analysis. Microscopy: advances in scientific research and education. 2. Badajoz, Spain: Formatex; 2014. p. 1083-9.

420. Qi S, Belton P, McAuley W, Codoni D, Darji N. Moisture Uptake of Polyoxyethylene Glycol Glycerides Used as Matrices for Drug Delivery: Kinetic Modelling and Practical Implications. Pharmaceutical Research. 2013;30(4):1123-36.

421. Hunter NE, Frampton CS, Craig DQM, Belton PS. The use of dynamic vapour sorption methods for the characterisation of water uptake in amorphous trehalose. Carbohydrate Research. 2010;345(13):1938-44.

422. Lafontaine A, Sanselme M, Cartigny Y, Cardinael P, Coquerel G. Characterization of the transition between the monohydrate and the anhydrous citric acid. Journal of Thermal Analysis and Calorimetry. 2013;112(1):307-15.

423. Li W, Buckton G. Using DVS-NIR to assess the water sorption behaviour and stability of a griseofulvin/PVP K30 solid dispersion. International Journal of Pharmaceutics. 2015;495(2):999-1004.

424. Craig DQM, Reading M. Thermal Analysis of Pharmaceuticals: CRC Press; 2006. 1-218 p.

425. Goldstein J, Newbury DE, Echlin P, Joy DC, Romig AD, Lyman CE, et al. Scanning Electron Microscopy and X-Ray Microanalysis: A Text for Biologists, Materials Scientists, and Geologists: Springer US; 2012. 292-7 p.

426. Ngo PD. Energy Dispersive Spectroscopy. In: Wagner LC, editor. Failure Analysis of Integrated Circuits: Tools and Techniques. Boston, MA: Springer US; 1999. p. 205-15.

427. Suryanarayana C, Norton MG. X-Ray Diffraction: A Practical Approach: Springer US; 1998. 63-94 p.

428. Brittain HG. X-ray diffraction III: pharmaceutical applications. Spectroscopy. 2001;16(7):14-8.

429. Otsuka M, Ibe K, Tokudome Y, Ohshima H. Nano- and macro-geometrical structural change of caffeine and theophylline anhydrate tablets during hydration process by using X-ray computed tomography. Colloids and Surfaces B: Biointerfaces. 2009;73(2):351-9.

430. Perfetti G, Casteele EVd, Rieger B, Wildeboer WJ, Meesters GMH. X-ray micro tomography and image analysis as complementary methods for morphological characterization and coating thickness measurement of coated particles. Advanced Powder Technology. 2010;21(6):663-75.

431. Kak AC, Slaney M, Medicine IEi, Society B. Principles of Computerized Tomographic Imaging: IEEE Press; 1988.

432. Alvarez-Murga M, Bleuet P, Hodeau J-L. Diffraction/scattering computed tomography for three-dimensional characterization of multi-phase crystalline and amorphous materials. Journal of Applied Crystallography. 2012;45(6):1109-24.

433. Cloetens P, Pateyron-Salomé M, Buffiere J, Peix G, Baruchel J, Peyrin F, et al. Observation of microstructure and damage in materials by phase sensitive radiography and tomography. Journal of Applied Physics. 1997;81(9):5878-86.

434. Tokudome Y, Ohshima H, Otsuka M. Non-invasive and rapid analysis for observation of internal structure of press-coated tablet using X-ray computed tomography. Drug development and industrial pharmacy. 2009;35(6):678-82.

435. Watson DG. Pharmaceutical Analysis,A Textbook for Pharmacy Students and Pharmaceutical Chemists,3: Pharmaceutical Analysis: Elsevier Churchill Livingstone; 2012. 115-35 p.

436. Larkin P. Chapter 3 - Instrumentation and Sampling Methods. Infrared and Raman Spectroscopy. Oxford: Elsevier; 2011. p. 27-54.

437. Coutts-Lendon CA, Wright NA, Mieso EV, Koenig JL. The use of FT-IR imaging as an analytical tool for the characterization of drug delivery systems. Journal of Controlled Release. 2003;93(3):223-48.

438. Kazarian S, Kong K, Bajomo M, Van der Weerd J, Chan K. Spectroscopic imaging applied to drug release. Food and bioproducts processing. 2005;83(2):127-35.

439. Kazarian SG, Chan KLA. Applications of ATR-FTIR spectroscopic imaging to biomedical samples. Biochimica et Biophysica Acta (BBA) - Biomembranes. 2006;1758(7):858-67.

440. Shekunov BY, Chattopadhyay P, Tong HHY, Chow AHL. Particle Size Analysis in Pharmaceutics: Principles, Methods and Applications. Pharmaceutical Research. 2007;24(2):203-27.

441. Nair AB, Kumria R, Harsha S, Attimarad M, Al-Dhubiab BE, Alhaider IA. In vitro techniques to evaluate buccal films. Journal of Controlled Release. 2013;166(1):10-21.

442. Ayensu I, Mitchell JC, Boateng JS. Development and physico-mechanical characterisation of lyophilised chitosan wafers as potential protein drug delivery systems via the buccal mucosa. Colloids and Surfaces B: Biointerfaces. 2012;91:258-65.

443. Guo J-H, Cooklock KM. Bioadhesive Polymer Buccal Patches for Buprenorphine Controlled Delivery: Solubility Consideration. Drug Development and Industrial Pharmacy. 1995;21(17):2013-9.

444. Ramesha Chary RB, Vani G, Rao YM. In Vitro and In Vivo Adhesion Testing of Mucoadhesive Drug Delivery Systems. Drug Development and Industrial Pharmacy. 1999;25(5):685-90.

445. Abu-Diak OA, Jones DS, Andrews GP. An Investigation into the Dissolution Properties of Celecoxib Melt Extrudates: Understanding the Role of Polymer Type and Concentration in Stabilizing Supersaturated Drug Concentrations. Molecular Pharmaceutics. 2011;8(4):1362-71.

446. Deng W, Majumdar S, Singh A, Shah S, Mohammed NN, Jo S, et al. Stabilization of fenofibrate in low molecular weight hydroxypropylcellulose matrices produced by hot-melt extrusion. Drug Development and Industrial Pharmacy. 2013;39(2):290-8.

447. Okwuosa TC, Stefaniak D, Arafat B, Isreb A, Wan K-W, Alhnan MA. A Lower Temperature FDM 3D Printing for the Manufacture of Patient-Specific Immediate Release Tablets. Pharmaceutical Research. 2016;33(11):2704-12.

448. Suknuntha K, Jones DS, Tantishaiyakul V. Properties of felodipine-poly (vinylpyrrolidone) solid dispersion films and the impact of solvents. ScienceAsia. 2012;38:188-95.

449. Ferrarezi MMF, de Oliveira Taipina M, Escobar da Silva LC, Gonçalves MdC. Poly(Ethylene Glycol) as a Compatibilizer for Poly(Lactic Acid)/Thermoplastic Starch Blends. Journal of Polymers and the Environment. 2013;21(1):151-9.

450. Unga J, Matsson P, Mahlin D. Understanding polymer–lipid solid dispersions—The properties of incorporated lipids govern the crystallisation behaviour of PEG. International Journal of Pharmaceutics. 2010;386(1–2):61-70.

451. Ginés JM, Arias MJ, Rabasco AM, Novák C, Ruiz-Conde A, Sánchez-Soto PJ. Thermal characterization of polyethylene glycols applied in the pharmaceutical technology using differential scanning calorimetry and hot stage microscopy. Journal of thermal analysis. 1996;46(1):291-304.

452. Chatham S. Characterisation of molten filled hard gelatin capsules. London, UK: University of London 1985.

453. Bogdanov B, Vidts A, Van Den Buicke A, Verbeeck R, Schacht E. Synthesis and thermal properties of poly(ethylene glycol)-poly(ϵ-caprolactone) copolymers. Polymer. 1998;39(8):1631-6.

454. Feng L, Zhao W, Zheng J, Frisco S, Song P, Li X. The shape-stabilized phase change materials composed of polyethylene glycol and various mesoporous matrices (AC, SBA-15 and MCM-41). Solar Energy Materials and Solar Cells. 2011;95(12):3550-6.

455. Shieh Y-T, Liu G-L, Hwang KC, Chen C-C. Crystallization, melting and morphology of PEO in PEO/MWNT-g-PMMA blends. Polymer. 2005;46(24):10945-51.

456. Zhou C, Chu R, Wu R, Wu Q. Electrospun Polyethylene Oxide/Cellulose Nanocrystal Composite Nanofibrous Mats with Homogeneous and Heterogeneous Microstructures. Biomacromolecules. 2011;12(7):2617-25.

457. Otun S. Characterisation and performance assessment of semi-solid dispersions using surface active lipidic carriers Norwich, UK: University of East Anglia 2011.

458. Reintjes T. Solubility enhancement with BASF pharma polymers. Ludwigshafen, Germany: BASF, The Chemical Company; 2011.

459. Van Krevelen DW, Te Nijenhuis K. Properties of polymers. 4th ed. Oxford, UK: Elsevier Scientific Publication; 2009. 189-227 p.

460. Chadha R, Bhandari S. Drug–excipient compatibility screening—Role of thermoanalytical and spectroscopic techniques. Journal of Pharmaceutical and Biomedical Analysis. 2014;87:82-97.

461. Ng YC, Yang Z, McAuley WJ, Qi S. Stabilisation of amorphous drugs under high humidity using pharmaceutical thin films. European Journal of Pharmaceutics and Biopharmaceutics. 2013;84(3):555-65.

462. Blychert E, Edgar B, Elmfeldt D, Hedner T. A population study of the pharmacokinetics of felodipine. Br J Clin Pharmacol. 1991;31(1):15-24.

463. Gupta P, Thilagavathi R, Chakraborti AK, Bansal AK. Role of Molecular Interaction in Stability of Celecoxib−PVP Amorphous Systems. Molecular Pharmaceutics. 2005;2(5):384-91.

464. Li B, Harich K, Wegiel L, Taylor LS, Edgar KJ. Stability and solubility enhancement of ellagic acid in cellulose ester solid dispersions. Carbohydrate Polymers. 2013;92(2):1443-50.

465. Li M, Gogos CG, Ioannidis N. Improving the API dissolution rate during pharmaceutical hot-melt extrusion I: Effect of the API particle size, and the co-rotating, twin-screw extruder screw configuration on the API dissolution rate. International Journal of Pharmaceutics. 2015;478(1):103-12.

466. Lindfors L, Forssén S, Westergren J, Olsson U. Nucleation and crystal growth in supersaturated solutions of a model drug. Journal of Colloid and Interface Science. 2008;325(2):404-13.

467. Morales JO, McConville JT. Manufacture and characterization of mucoadhesive buccal films. European Journal of Pharmaceutics and Biopharmaceutics. 2011;77(2):187-99.

468. Tran PH, Tran TT, Park JB, Lee BJ. Controlled release systems containing solid dispersions: strategies and mechanisms. Pharm Res. 2011;28(10):2353-78.

469. Giovino C, Ayensu I, Tetteh J, Boateng JS. An integrated buccal delivery system combining chitosan films impregnated with peptide loaded PEG-b-PLA nanoparticles. Colloids and Surfaces B: Biointerfaces. 2013;112:9-15.

470. Ayensu I, Mitchell JC, Boateng JS. Effect of membrane dialysis on characteristics of lyophilised chitosan wafers for potential buccal delivery of proteins. International Journal of Biological Macromolecules. 2012;50(4):905-9.

471. Mahlin D, Ridell A, Frenning G, Engström S. Solid-State Characterization of PEG 4000/Monoolein Mixtures. Macromolecules. 2004;37(7):2665-7.

472. Unga J, Tajarobi F, Norder O, Frenning G, Larsson A. Relating solubility data of parabens in liquid PEG 400 to the behaviour of PEG 4000-parabens solid dispersions. European Journal of Pharmaceutics and Biopharmaceutics. 2009;73(2):260-8.

473. Zhu Q, Harris MT, Taylor LS. Time-Resolved SAXS/WAXS Study of the Phase Behavior and Microstructural Evolution of Drug/PEG Solid Dispersions. Molecular Pharmaceutics. 2011;8(3):932-9.

474. Zhu Q, Taylor LS, Harris MT. Evaluation of the Microstructure of Semicrystalline Solid Dispersions. Molecular Pharmaceutics. 2010;7(4):1291-300.

475. Flory PJ. Principles of Polymer Chemistry: Cornell University Press; 1953. 563-76 p.

476. Huang Y, Wang J, Liu X-B, Zhang H-L, Chen X-F, Zhuang W-C, et al. Crystallization, melting, and morphology of a poly(ethylene oxide) diblock copolymer containing a tablet-like block of poly{2,5-bis[(4-methoxyphenyl)oxycarbonyl]styrene}. Polymer. 2005;46(23):10148-57.

477. Grabovac V, Guggi D, Bernkop-Schnürch A. Comparison of the mucoadhesive properties of various polymers. Advanced Drug Delivery Reviews. 2005;57(11):1713-23.

478. Naima Z, Siro T, Juan-Manuel G-D, Chantal C, René C, Jerome D. Interactions between carbamazepine and polyethylene glycol (PEG) 6000: characterisations of the physical, solid dispersed and eutectic mixtures. European Journal of Pharmaceutical Sciences. 2001;12(4):395-404.

479. Sun DD, Lee PI. Probing the mechanisms of drug release from amorphous solid dispersions in medium-soluble and medium-insoluble carriers. Journal of Controlled Release. 2015;211:85-93.

480. Rumondor ACF, Taylor LS. Effect of Polymer Hygroscopicity on the Phase Behavior of Amorphous Solid Dispersions in the Presence of Moisture. Molecular Pharmaceutics. 2010;7(2):477-90.

481. Yang Z, Nollenberger K, Albers J, Moffat J, Craig D, Qi S. The effect of processing on the surface physical stability of amorphous solid dispersions. European Journal of Pharmaceutics and Biopharmaceutics. 2014;88(3):897-908.

482. Qi S, Belton P, Nollenberger K, Clayden N, Reading M, Craig DM. Characterisation and Prediction of Phase Separation in Hot-Melt Extruded Solid Dispersions: A Thermal, Microscopic and NMR Relaxometry Study. Pharmaceutical Research. 2010;27(9):1869-83.

483. Qi S, Belton P, Nollenberger K, Gryczke A, Craig DM. Compositional Analysis of Low Quantities of Phase Separation in Hot-Melt-Extruded Solid Dispersions: A Combined Atomic Force Microscopy, Photothermal Fourier-Transform Infrared Microspectroscopy, and Localised Thermal Analysis Approach. Pharmaceutical Research. 2011;28(9):2311-26.

484. Lloyd GR, Craig DQM, Smith A. An investigation into the production of paracetamol solid dispersions in PEG 4000 using hot stage differential interference contrast microscopy. International Journal of Pharmaceutics. 1997;158(1):39-46.

485. Qi S, Moffat JG, Yang Z. Early Stage Phase Separation in Pharmaceutical Solid Dispersion Thin Films under High Humidity: Improved Spatial Understanding Using Probe-Based Thermal and Spectroscopic Nanocharacterization Methods. Molecular Pharmaceutics. 2013;10(3):918-30.

486. Dai X, Moffat JG, Mayes AG, Reading M, Craig DQM, Belton PS, et al. Thermal Probe Based Analytical Microscopy: Thermal Analysis and Photothermal Fourier-Transform Infrared Microspectroscopy Together with Thermally Assisted Nanosampling Coupled with Capillary Electrophoresis. Analytical Chemistry. 2009;81(16):6612-9.

487. Harding L, Wood J, Reading M, Craig DQM. Two- and Three-Dimensional Imaging of Multicomponent Systems Using Scanning Thermal Microscopy and Localized Thermomechanical Analysis. Analytical Chemistry. 2007;79(1):129-39.

488. Moffat JG, Mayes AG, Belton PS, Craig DQM, Reading M. Compositional Analysis of Metal Chelating Materials Using Near-Field Photothermal Fourier Transform Infrared Microspectroscopy. Analytical Chemistry. 2010;82(1):91-7.

489. Dai X, Moffat JG, Wood J, Reading M. Thermal scanning probe microscopy in the development of pharmaceuticals. Advanced Drug Delivery Reviews. 2012;64(5):449-60.

490. Lisowski MS, Liu Q, Cho J, Runt J, Yeh F, Hsiao BS. Crystallization Behavior of Poly(ethylene oxide) and Its Blends Using Time-Resolved Wide- and Small-Angle X-ray Scattering. Macromolecules. 2000;33(13):4842-9.

491. Bruce CD, Fegely KA, Rajabi-Siahboomi AR, McGinity JW. The influence of heterogeneous nucleation on the surface crystallization of guaifenesin from melt extrudates containing Eudragit® L10055 or Acryl-EZE®. European Journal of Pharmaceutics and Biopharmaceutics. 2010;75(1):71-8.

492. Stock SR. MicroComputed Tomography: Methodology and Applications: CRC Press; 2008. 85-114 p.

493. Graca M, Bongaerts JHH, Stokes JR, Granick S. Friction and adsorption of aqueous polyoxyethylene (Tween) surfactants at hydrophobic surfaces. Journal of Colloid and Interface Science. 2007;315(2):662-70.

494. Wallick D. Polyoxyethylene Glycol. 2009. In: In Handbook of Pharmaceutical Excipients [Internet]. London UK: Pharmaceutical Press; [518].

495. York P. Application of powder failure testing equipment in assessing effect on glidants on flowability of cohesive pharmaceutical powders. J Pharm Sci. 1975;64(7):1216-21.

496. Goddeeris C, Willems T, Houthoofd K, Martens JA, Van den Mooter G. Dissolution enhancement of the anti-HIV drug UC 781 by formulation in a ternary solid dispersion with TPGS 1000 and Eudragit E100. European Journal of Pharmaceutics and Biopharmaceutics. 2008;70(3):861-8.

497. Repka MA, McGinity JW. Bioadhesive properties of hydroxypropylcellulose topical films produced by hot-melt extrusion. Journal of Controlled Release. 2001;70(3):341-51.

498. Alhijjaj M, Bouman J, Wellner N, Belton P, Qi S. Creating Drug Solubilization Compartments via Phase Separation in Multicomponent Buccal Patches Prepared by Direct Hot Melt Extrusion–Injection Molding. Molecular Pharmaceutics. 2015;12(12):4349-62.

499. Alhijjaj M, Yassin S, Reading M, Zeitler JA, Belton P, Qi S. Characterization of Heterogeneity and Spatial Distribution of Phases in Complex Solid Dispersions by Thermal Analysis by Structural Characterization and X-ray Micro Computed Tomography. Pharmaceutical Research. 2016:1-19.

500. Galop M. Study of Pharmaceutical Solid Dispersions by Microthermal Analysis. Pharmaceutical Research. 2005;22(2):293-302.

501. Mosquera-Giraldo LI, Trasi NS, Taylor LS. Impact of surfactants on the crystal growth of amorphous celecoxib. International Journal of Pharmaceutics. 2014;461(1–2):251-7.

502. Glastrup J. Degradation of polyethylene glycol. A study of the reaction mechanism in a model molecule: Tetraethylene glycol. Polymer Degradation and Stability. 1996;52(3):217-22.

503. Han S, Kim C, Kwon D. Thermal/oxidative degradation and stabilization of polyethylene glycol. Polymer. 1997;38(2):317-23.

504. Voorhees KJ, Baugh SF, Stevenson DN. An investigation of the thermal degradation of poly(ethylene glycol). Journal of Analytical and Applied Pyrolysis. 1994;30(1):47-57.

505. Pielichowski K, Flejtuch K. Non-oxidative thermal degradation of poly(ethylene oxide): kinetic and thermoanalytical study. Journal of Analytical and Applied Pyrolysis. 2005;73(1):131-8.

506. Lai W-C, Liau W-B. Thermo-oxidative degradation of poly(ethylene glycol)/poly(l-lactic acid) blends. Polymer. 2003;44(26):8103-9.

507. Ha E, Wang W, John Wang Y. Peroxide formation in polysorbate 80 and protein stability. Journal of Pharmaceutical Sciences. 2002;91(10):2252-64.

508. Akune Y, Gontani H, Hirosawa R, Koseki A, Matsumoto S. The effects of molecular flexibility and substituents on conformational polymorphism in a series of 2,5-diamino-3,6-dicyanopyrazine dyes with highly flexible groups. CrystEngComm. 2015;17(30):5789-800.

509. Wu T, Yu L. Surface Crystallization of Indomethacin Below T g. Pharmaceutical Research. 2006;23(10):2350-5.

510. Zhu L, Wong L, Yu L. Surface-Enhanced Crystallization of Amorphous Nifedipine. Molecular Pharmaceutics. 2008;5(6):921-6.

511. Kestur US, Taylor LS. Role of polymer chemistry in influencing crystal growth rates from amorphous felodipine. CrystEngComm. 2010;12(8):2390-7.

512. Tian Y, Jones DS, Andrews GP. An Investigation into the Role of Polymeric Carriers on Crystal Growth within Amorphous Solid Dispersion Systems. Molecular Pharmaceutics. 2015;12(4):1180-92.

513. Sugawara H, Tobise K, Kikuchi K. Antioxidant Effects of Calcium Antagonists on Rat Myocardial Membrane Lipid Peroxidation. Hypertension Research. 1996;19(4):223-8.

514. Goyanes A, Robles Martinez P, Buanz A, Basit AW, Gaisford S. Effect of geometry on drug release from 3D printed tablets. International Journal of Pharmaceutics. 2015;494(2):657-63.

515. Jonathan G, Karim A. 3D printing in pharmaceutics: A new tool for designing customized drug delivery systems. International Journal of Pharmaceutics. 2016;499(1–2):376-94.

516. Holländer J, Genina N, Jukarainen H, Khajeheian M, Rosling A, Mäkilä E, et al. Three-Dimensional Printed PCL-Based Implantable Prototypes of Medical Devices for Controlled Drug Delivery. Journal of Pharmaceutical Sciences.

517. Melocchi A, Parietti F, Loreti G, Maroni A, Gazzaniga A, Zema L. 3D printing by fused deposition modeling (FDM) of a swellable/erodible capsular device for oral pulsatile release of drugs. Journal of Drug Delivery Science and Technology. 2015;30, Part B:360-7.

518. Pietrzak K, Isreb A, Alhnan MA. A flexible-dose dispenser for immediate and extended release 3D printed tablets. European Journal of Pharmaceutics and Biopharmaceutics. 2015;96:380-7.

519. Sandler N, Salmela I, Fallarero A, Rosling A, Khajeheian M, Kolakovic R, et al. Towards fabrication of 3D printed medical devices to prevent biofilm formation. International Journal of Pharmaceutics. 2014;459(1–2):62-4.

520. Regardh CG, Edgar B, Olsson R, Kendall M, Collste P, Shansky C. Pharmacokinetics of felodipine in patients with liver disease. Eur J Clin Pharmacol. 1989;36(5):473-9.

521. Adamkiewicz M, Rubinsky B. Cryogenic 3D printing for tissue engineering. Cryobiology. 2015;71(3):518-21.

522. Liu J, Cao F, Zhang C, Ping Q. Use of polymer combinations in the preparation of solid dispersions of a thermally unstable drug by hot-melt extrusion. Acta Pharmaceutica Sinica B. 2013;3(4):263-72.

523. Goyanes A, Buanz ABM, Basit AW, Gaisford S. Fused-filament 3D printing (3DP) for fabrication of tablets. International Journal of Pharmaceutics. 2014;476(1–2):88-92.

524. Jensen BEB, Dávila I, Zelikin AN. Poly(vinyl alcohol) Physical Hydrogels: Matrix-Mediated Drug Delivery Using Spontaneously Eroding Substrate. The Journal of Physical Chemistry B. 2016;120(26):5916-26.

525. Jiang S, Liu S, Feng W. PVA hydrogel properties for biomedical application. Journal of the Mechanical Behavior of Biomedical Materials. 2011;4(7):1228-33.

526. Colombo P, Bettini R, Santi P, Peppas NA. Swellable matrices for controlled drug delivery: gel-layer behaviour, mechanisms and optimal performance. Pharmaceutical Science & Technology Today. 2000;3(6):198-204.

527. Li H, Hardy RJ, Gu X. Effect of Drug Solubility on Polymer Hydration and Drug Dissolution from Polyethylene Oxide (PEO) Matrix Tablets. AAPS PharmSciTech. 2008;9(2):437-43.

528. Ma L, Deng L, Chen J. Applications of poly(ethylene oxide) in controlled release tablet systems: a review. Drug Development and Industrial Pharmacy. 2014;40(7):845-51.

529. Maggi L, Bruni R, Conte U. High molecular weight polyethylene oxides (PEOs) as an alternative to HPMC in controlled release dosage forms. International Journal of Pharmaceutics. 2000;195(1–2):229-38.

Appendices

Appendix 1: Solubility parameter calculations using group contribution methods

The calculated solubility parameters of felodipine (chemical structure shown in Chapter 2) using Hoftyzer and Van Krevelen and Hoy methods the are presented in **Tables 1 and 2.**

Table (1): Hoftyzer and Van Krevelen group contribution calculations used for the estimation of felodipine solubility parameter

Structural Group	No. of groups	F_{di} $(MJ/m^3)^{½}$. mol^{-1}	F_{pi}^2 (MJ/m^3) . mol^{-2}	Eh_i J . mol^{-1}
CH_3	4	1680	0	0
CH_2	1	270	0	0
COO	2	780	480200	14000
tri-substituted benzene ring	1	1270	12100	0
=C<	4	280	0	0
CH	1	200	0	0
NH	1	160	44100	3100
Cl	2	900	605000	800
Ring	1	190	0	0
Σ		5730	1141400	17900

$V = 304.77\ cm^3.\ mol^{-1}$

$$\delta d = \frac{\Sigma F_{di}}{V} = 18.80\ (MJ/m^3)^{½}$$

$$\delta p = \frac{\sqrt{\Sigma F^2_{pi}}}{V} = 3.51\ (MJ/m^3)^{½}$$

$$\delta h = \sqrt{\frac{\Sigma E_{hi}}{V}} = 7.66\ (MJ/m^3)^{½}$$

$\delta = \sqrt{\delta_d^2 + \delta_p^2 + \delta_h^2} = 20.60\ (MJ/m^3)^{½}$

Table (2): Hoy group contribution calculations used for the estimation of felodipine solubility parameter

Structural Group	No. of groups	F_t $(MJ/m^3)^{½}$. mol^{-1}	V cm^3. mol^{-1}
CH3	4	1214	86.2
CH2	1	269	15.55
COO	2	1280	47.4
C ar	1	1407	51.94
CH ar	4	964	53.68
NH	1	368	11
Cl	1	660	39
6 ring	2	-48	0
Ortho	1	20.2	0
Meta	1	13.5	0
Σ		6147.7	304.77

V = 304.77 cm^3. mol^{-1}

$\delta t = \frac{(F_i + B)}{V} = 21.08\ (MJ/m^3)^{½}$

For PEG and PEO polymer grades (molecular formulas are shown in Chapter 2), the calculated solubility parameters calculated by both methods are presented in **Tables 3 and 4**.

Table (3): Hoftyzer and Van Krevelen group contribution calculations used for the estimation of PEG & PEO solubility parameters

Structural Group	No. of groups	F_{di} $(MJ/m^3)^{½}$. mol^{-1}	F_{pi}^2 (MJ/m^3) . mol^{-2}	Eh_i J . mol^{-1}
CH_2	2	540	0	0
O	1	100	160000	3000
Σ		640	160000	3000

$V = 37.55\ cm^3\ .\ mol^{-1}$.

$\delta d = \frac{\Sigma Fdi}{V} = 17.04\ (MJ/m^3)^{½}$

$\delta p = \frac{\sqrt{\Sigma F^2 pi}}{V} = 400\ (MJ/m^3)^{½}$

$\delta h = \sqrt{\frac{\Sigma Ehi}{V}} = 106.52\ (MJ/m^3)^{½}$

$\delta = \sqrt{\delta_d^2 + \delta_p^2 + \delta_h^2} = 22.00\ (MJ/m^3)^{½}$

Table (4): Hoy group contribution calculations used for the estimation of PEG and PEO solubility parameters

Structural Group	No. of groups	F_t $(MJ/m^3)^{½}$. mol^{-1}	ΔT	V cm^3. mol^{-1}
CH_2	2	538	0.02	15.55
O	1	235	0.018	6.45
Σ		773	0.058	37.55

$V = 37.55\ cm^3.\ mol^{-1}$

$n = 0.5/\Delta T = 8.62$

$\delta t = \frac{(F_i + B/n)}{V} = 21.44\ (MJ/m^3)^{½}$

For Tween 80 (chemical structure is shown in Chapter 2), the calculated solubility parameters calculated by both methods are presented in **Tables 5 and 6**.

Table (5): Hoftyzer and Van Krevelen group contribution calculations used for the estimation of Tween 80 solubility parameter

Structural Group	No. of groups	F_{di} $(MJ/m^3)^{½}$. mol^{-1}	F_{pi}^2 (MJ/m^3) . mol^{-2}	Eh_i J . mol^{-1}
CH	4	320	0	0
CH2	58	15660	0	0
O	41	4100	6560000	123000
5 Ring	1	190	0	0
OH	3	630	750000	60000
COO	1	390	240100	7000
CH3	1	420	0	0
Σ		21710	7550100	190000

$V = 1287.19\ cm^3 . mol^{-1}$

$\delta d = \frac{\Sigma F_{di}}{V} = 16.87\ (MJ/m^3)^{½}$

$\delta p = \frac{\sqrt{\Sigma F^2_{pi}}}{V} = 2.13\ (MJ/m^3)^{½}$

$\delta h = \sqrt{\frac{\Sigma E_{hi}}{V}} = 12.15\ (MJ/m^3)^{½}$

$\delta = \sqrt{\delta_d^2 + \delta_p^2 + \delta_h^2} = 20.90\ (MJ/m^3)^{½}$

Table (6): Hoy group contribution calculations used for the estimation of Tween 80 solubility parameter

Structural Group	No. of groups	F_t $(MJ/m^3)^{½}$. mol^{-1}	V cm^3. mol^{-1}
CH	4	704	38.24
CH2	58	15602	901.9
O	41	9635	264.45
5 Ring	1	43	0
OH	3	2025	37.35
COO	1	640	23.7
CH3	1	303.5	21.55
Σ		28952.5	1287.19

V = 1287.19 cm^3. mol^{-1}

$$\delta t = \frac{(F_i + B)}{V} = 22.71\ (MJ/m^3)^{½}$$

For TPGS (chemical structure is shown in Chapter 2), the calculated solubility parameters calculated by both methods are presented in **Tables 7 and 8**.

Table (7): Hoftyzer and Van Krevelen group contribution calculations used for the estimation of TPGS solubility parameter

Structural Group	No. of groups	F_{di} $(MJ/m^3)^{½}$. mol^{-1}	F_{pi}^2 (MJ/m^3) . mol^{-2}	Eh_i J . mol^{-1}
C	1	-70	0	0
CH	3	240	0	0
CH2	56	15120	0	0
O	23	2300	3680000	69000
6 Ring	1	190	0	0
OH	1	210	250000	20000
COO	2	780	480200	14000
CH3	8	3360	0	0
Σ		23400	4422300	103000

$V = 1283.64\ cm^3.\ mol^{-1}$

$\delta d = \frac{\Sigma F_{di}}{V} = 18.23\ (MJ/m^3)^{½}$

$\delta p = \frac{\sqrt{\Sigma F^2_{pi}}}{V} = 1.64\ (MJ/m^3)^{½}$

$\delta h = \sqrt{\frac{\Sigma E_{hi}}{V}} = 8.96\ (MJ/m^3)^{½}$

$\delta = \sqrt{\delta_d^2 + \delta_p^2 + \delta_h^2} = 20.38\ (MJ/m^3)^{½}$

Table (8): Hoy group contribution calculations used for the estimation of TPGS solubility parameter

Structural Group	No. of groups	F_t $(MJ/m^3)^{½}$. mol^{-1}	V cm^3. mol^{-1}
C	1	65.5	3.56
C aromatic	6	1206	44.52
CH	3	582	28.68
CH_2	56	15064	870.8
O	23	5405	148.35
6 Ring	1	-48	0
OH	1	675	12.45
COO	2	1280	47.4
CH3	8	2428	172.4
Benzene ring substitutions (ortho, meta, para)	1	231.4	0
Σ		26834.9	1280.08

V = 1280.08 cm^3. mol^{-1}

$$\delta t = \frac{(F_i + B)}{V} = 21.18\ (MJ/m^3)^{½}$$

For eudragit E PO (chemical structure is shown in Chapter 2), the calculated solubility parameters calculated by both methods are presented in **Tables 9 and 10**.

Table (9): Hoftyzer and Van Krevelen group contribution calculations used for the estimation of eudragit E PO solubility parameter.

Structural Group	No. of groups	F_{di} $(MJ/m^3)^{½}$. mol^{-1}	F_{pi}^2 (MJ/m^3) . mol^{-2}	Eh_i J . mol^{-1}
>C<	3	-210	0	0
CH2	7	1890	0	0
N	1	20	640000	5000
COO	3	1170	720300	21000
CH3	7	2940	0	0
Σ		5810	1360300	26000

V = 150.85 cm^3 . mol^{-1}.

$$\delta d = \frac{\Sigma Fdi}{V} = 16.41\ (MJ/m^3)^{½}$$

$$\delta p = \frac{\sqrt{\Sigma F^2 pi}}{V} = 3.29\ (MJ/m^3)^{½}$$

$$\delta h = \sqrt{\frac{\Sigma Ehi}{V}} = 8.57\ (MJ/m^3)^{½}$$

$$\delta = \sqrt{\delta_d^2 + \delta_p^2 + \delta_h^2} = 18.80\ (MJ/m^3)^{½}$$

Table (10): Hoy group contribution calculations used for the estimation of eudragit E PO solubility parameter

Structural Group	No. of groups	F_t $(MJ/m^3)^{½}$. mol^{-1}	ΔT	V cm^3. mol^{-1}
>C<	3	196.5	0.12	10.68
CH_2	7	1883	0.14	108.85
N	1	125	0.009	12.6
COO	3	1920	0.15	71.1
CH_3	7	2124.5	0.154	150.85
Σ		6249	0.573	354.08

V = 354.08 cm^3. mol^{-1}

n = 0.5/ΔT = 0.87

$$\delta t = \frac{(F_i + B/n)}{V} = 18.55\ (MJ/m^3)^{½}$$

For soluplus (chemical structure is shown in Chapter 2), the calculated solubility parameters calculated by both methods are presented in **Tables 11 and 12**:

Table 11: Hoftyzer and Van Krevelen group contribution calculations used for the estimation of soluplus solubility parameter

Structural Group	No. of groups	F_{di} $(MJ/m^3)^{½}$. mol^{-1}	F_{pi}^2 (MJ/m^3) . mol^{-2}	Eh_i J . mol^{-1}
CH	3	240	0	0
CH2	9	2430	0	0
O	1	100	160000	3000
N	1	20	640000	5000
7 membered ring	1	190	0	0
COO	1	390	240100	7000
CH3	2	840	0	0
CO	1	290	592900	2000
Σ		4500	1633000	17000

$V = 271.78\ cm^3\ .\ mol^{-1}$.

$$\delta d = \frac{\Sigma Fdi}{V} = 16.56\ (MJ/m^3)^{½}$$

$$\delta p = \frac{\sqrt{\Sigma F^2 pi}}{V} = 4.70\ (MJ/m^3)^{½}$$

$$\delta h = \sqrt{\frac{\Sigma Ehi}{V}} = 7.91\ (MJ/m^3)^{½}$$

$$\delta = \sqrt{\delta_d^2 + \delta_p^2 + \delta_h^2} = 18.94\ (MJ/m^3)^{½}$$

Table 8.12: Hoy group contribution calculations used for the estimation of soluplus solubility parameter

Structural Group	No. of groups	F_t $(MJ/m^3)^{½}$. mol^{-1}	ΔT	V cm^3. mol^{-1}
CH	3	528	0.039	28.68
CH2	9	2421	0.18	139.95
O	1	235	0.018	6.45
N	1	125	0.009	12.6
7 membered ring	1	92	0.007	0
COO	1	640	0.05	23.7
CO	1	538	0.04	17.3
Σ		6400	0.387	271.78

V = 271.78 cm^3. mol^{-1}

n = 0.5/ΔT = 1.29

$\delta t = \frac{(F_i + B/n)}{V}$ = 24.34 $(MJ/m^3)^{½}$

For PVA (chemical structure shown in Chapter 2), the calculated solubility parameters calculated using both methods are presented in **Tables 13 and 14**.

Table (13): Hoftyzer and Van Krevelen group contribution calculations used for the estimation of PVA solubility parameter

Structural Group	No. of groups	F_{di} $(MJ/m^3)^{½}$. mol^{-1}	F_{pi}^2 (MJ/m^3) . mol^{-2}	Eh_i J . mol^{-1}
CH2	1	270	0	0
OH	1	210	250000	20000
CH	1	80	0	0
Σ		560	250000	20000

$V = 37.56\ cm^3\ .\ mol^{-1}$

$\delta d = \frac{\Sigma\ Fdi}{V} = 14.91\ (MJ/m^3)^{½}$

$\delta p = \frac{\sqrt{\Sigma\ F^2\ pi}}{V} = 13.31\ (MJ/m^3)^{½}$

$\delta h = \sqrt{\frac{\Sigma\ Ehi}{V}} = 23.08\ (MJ/m^3)^{½}$

$\delta = \sqrt{\delta_d^2 + \delta_p^2 + \delta_h^2} = 30.53\ (MJ/m^3)^{½}$

Table (14): Hoy group contribution calculations used for the estimation of PVA solubility parameter

Structural Group	No. of groups	F_t $(MJ/m^3)^{½}$. mol^{-1}	ΔT	V cm^3. mol^{-1}
CH2	**1**	269	0.02	15.55
OH	**1**	591	0.049	12.45
CH	**1**	176	0.013	9.56
Σ		1036	0.082	37.56

$V = 37.56\ cm^3.\ mol^{-1}$

$n = 0.5/\Delta T = 6.10$

$\delta t = \frac{(F_i + B/n)}{V} = 28.79\ (MJ/m^3)^{½}$

Appendix 2: UV-Visible scans and standard calibration curves of felodipine in different dissolution media

The UV-VIS scan for felodipine in PBS pH =6.8 indicated that the drug has λ_{max} at 363 nm as shown in **Figure 1**.

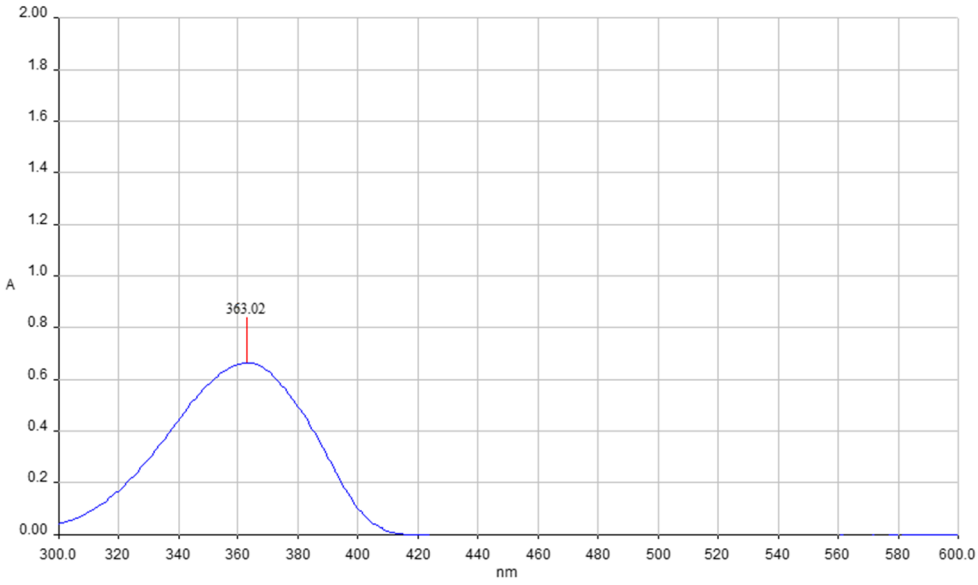

Figure (1): UV-Visible scan showing the λ_{max} of felodipine (n=3)

The calibration curves of felodipine in the different dissolution media are shown in **Figures 2-4**.

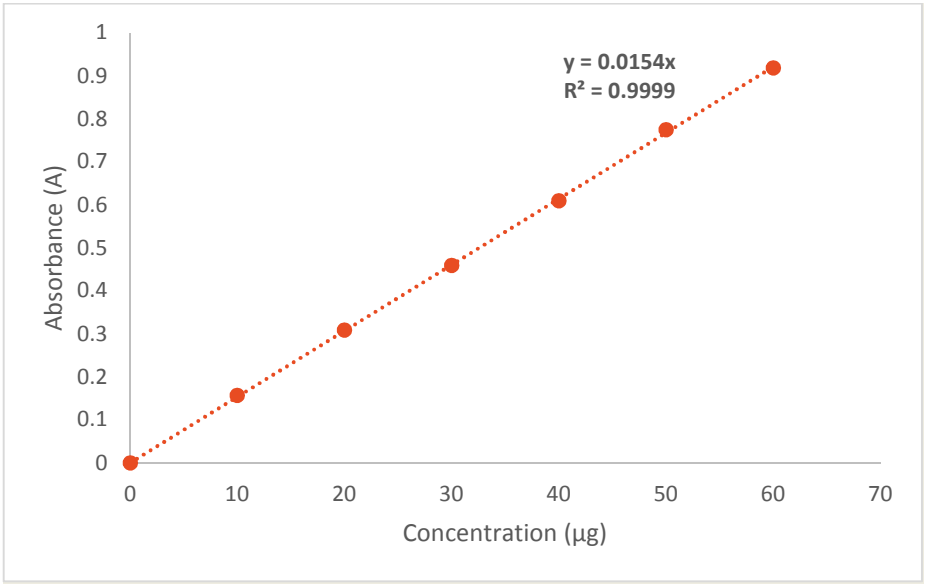

Figure (2): Calibration curve of felodipine in phosphate buffer saline (pH = 6.8) containing 0.05% (V/V) Tween 80 at 363 nm **(n=3)**

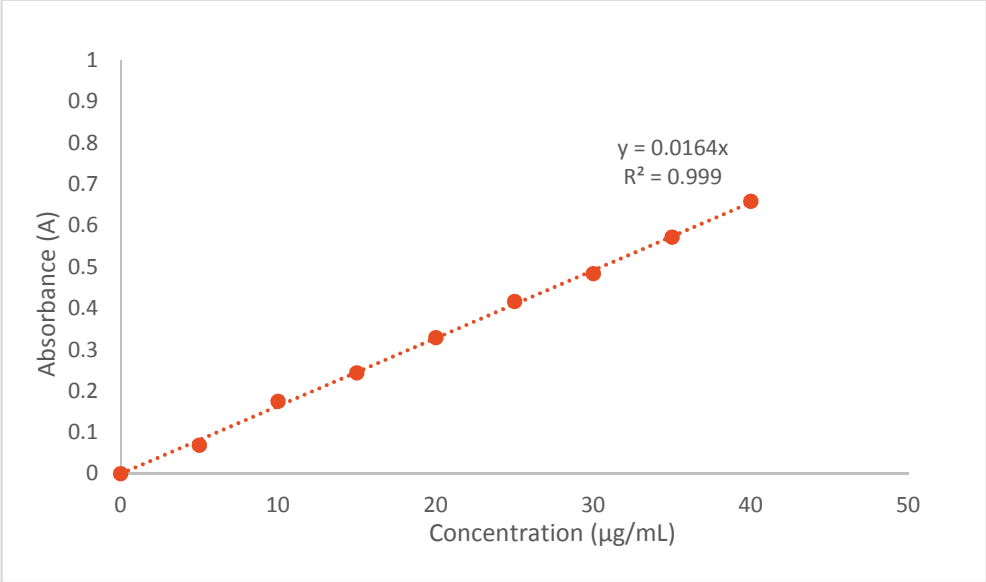

Figure (3): Calibration curve of felodipine in phosphate buffer saline (PBS) (pH = 6.8) with absolute ethanol 50:50 measured at 363 nm (n=3)

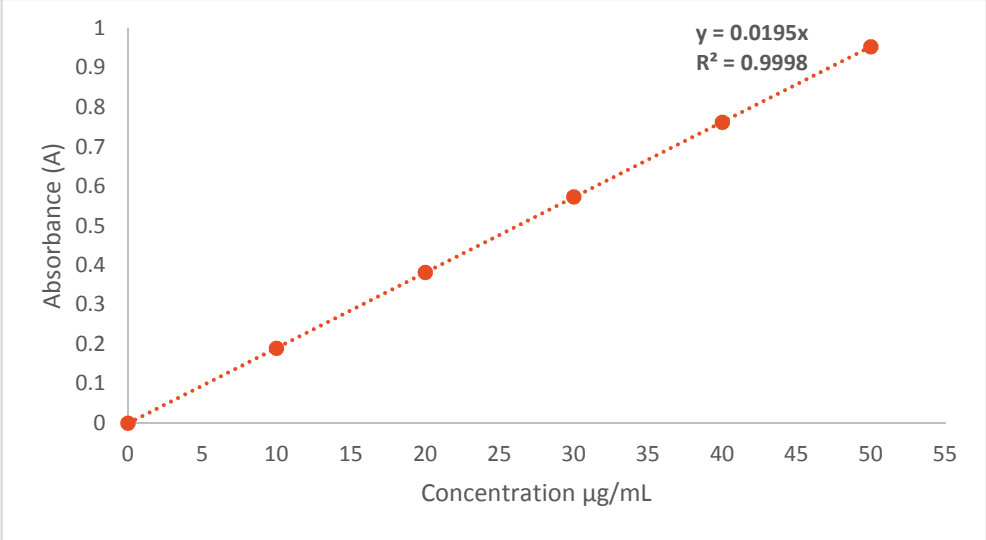

Figure (4): Calibration curve of felodipine in HCl simulated gastric fluid (SGF) without enzymes (pH = 1.2) with absolute ethanol 50:50 measured at 363 nm (n=3)

Appendix 3: Characterisation of different batches of pure felodipine samples

Two batches of felodipine were used in this study: sample 1 (batch no. FP140602) and sample 2 (batch no. 20100601). DSC, ATR-FTIR, PXRD, SEM and LD were used for characterising these samples.

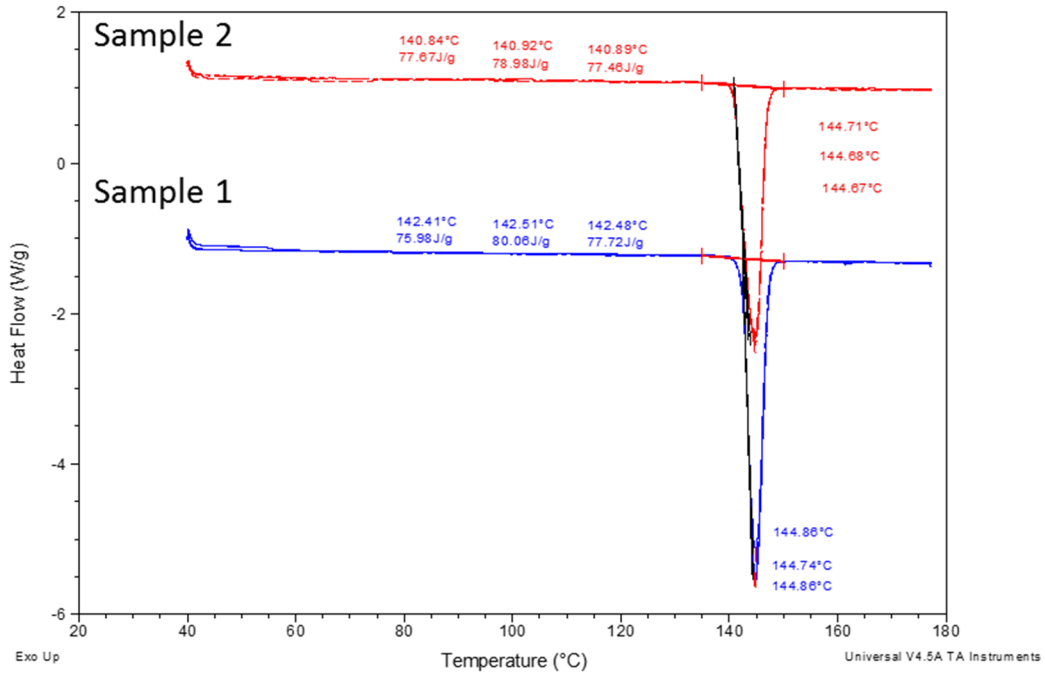

Figure (5): Standard DSC thermograms showing the melting of the two samples of felodipine using 10 °C/min heating rate (n=3)

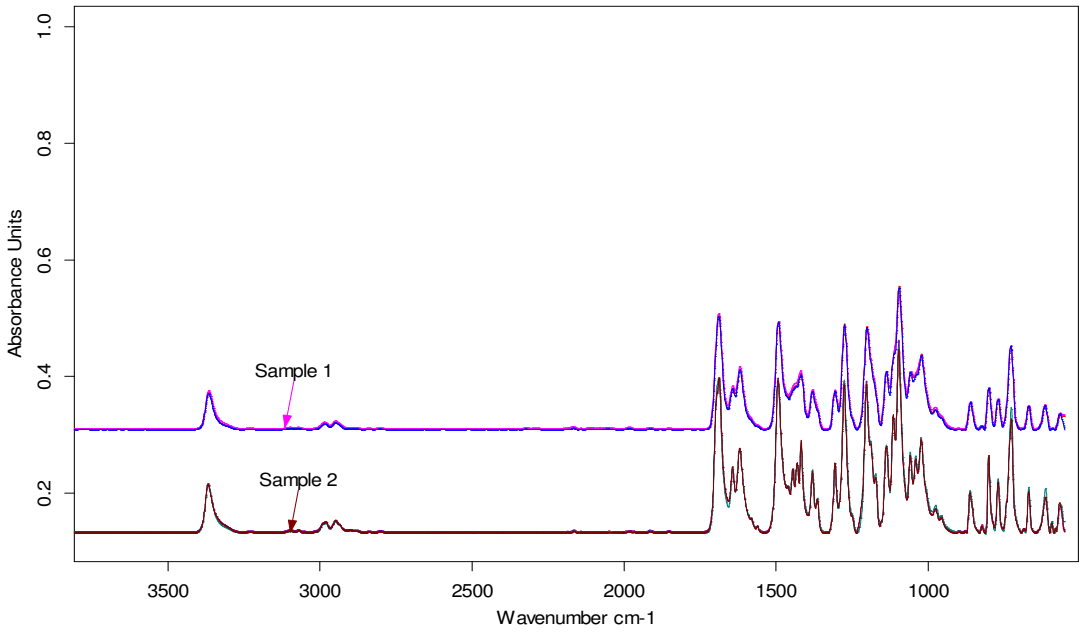

Figure (6): ATR-FTIR spectra of the two samples of felodipine scanned at 2 cm^{-1} and 32 repeated scans in absorbance mode (n=3)

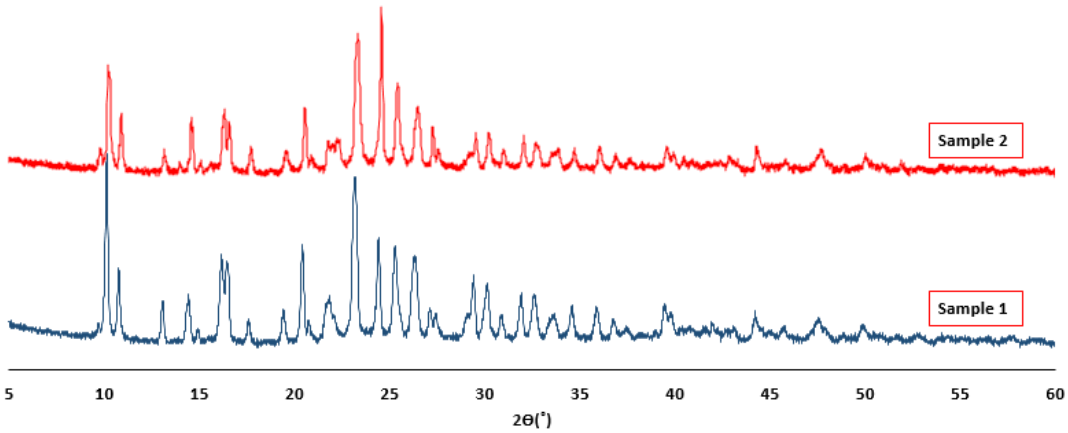

Figure (7): PXRD patterns of the two samples of felodipine scanned using the same method mentioned in Chapter 3, section 3.2.2.3.6

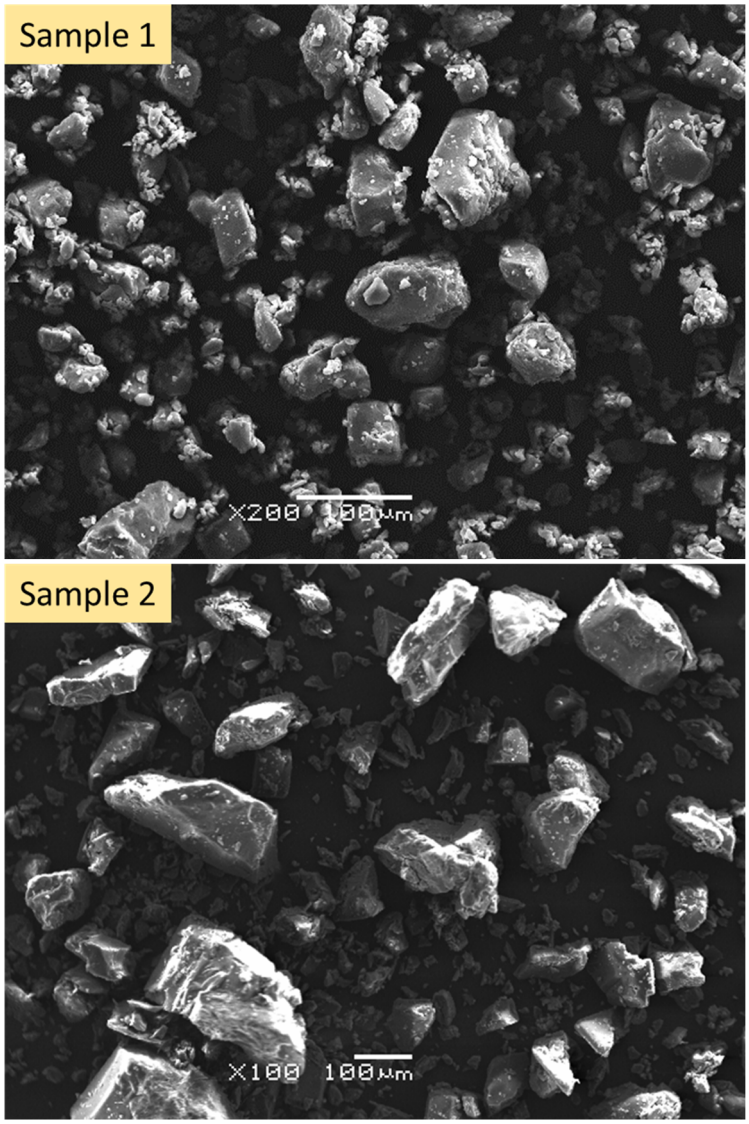

Figure (8): SEM images of the two samples of felodipine scanned using the same method mentioned in Chapter 3, section 3.2.2.3.4

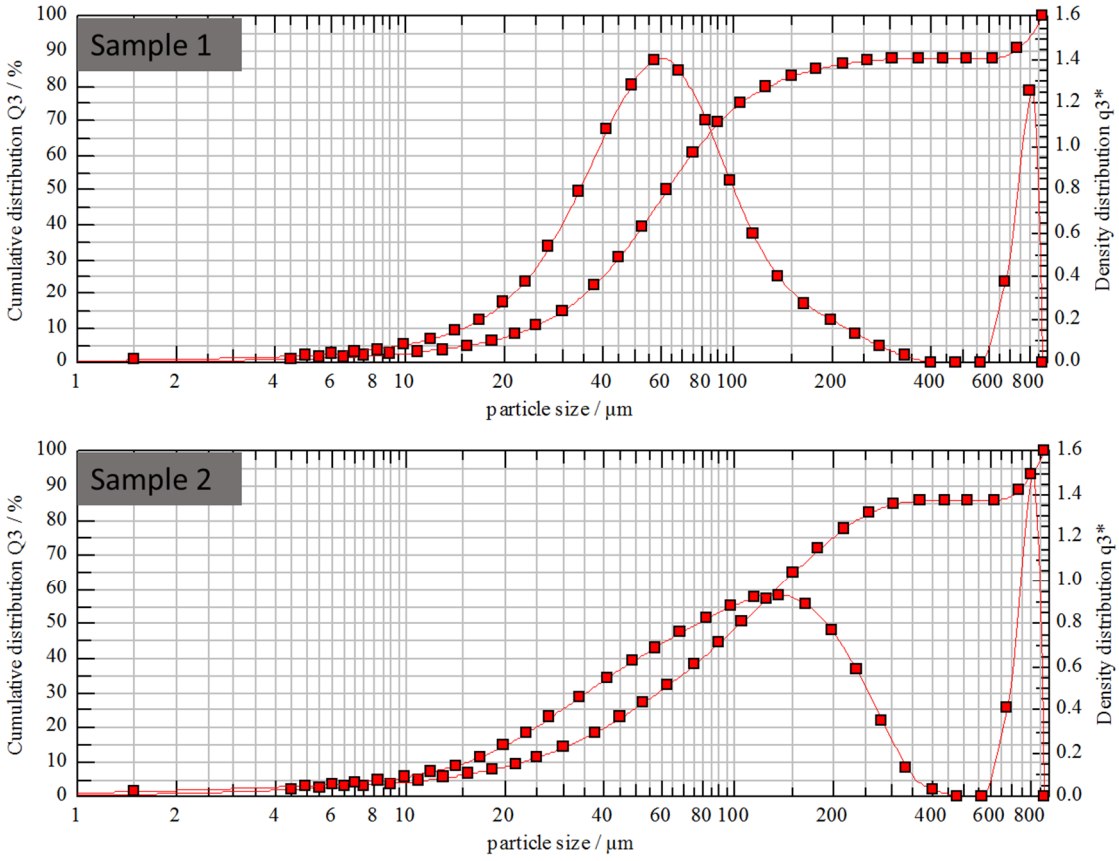

Figure (9): LD particle size analysis of the two samples of felodipine scanned using the same method mentioned in Chapter 2, section 2.3.12 (n=6)

Appendix 4: Calculation of T_g using Fox equation

Fox equation was used to calculate the T_g for the different blends utilised in the fabrication of solid dispersions by FDM 3D printing (Chapter 7). The following method was adapted in the determination of these values:

Fox equation for 10% w/w CME blend:

$$1/T_{g\ mix} = (w_{felodipine}/T_{g\ felodipine}) + (w_{PEG}/T_{g\ PEG}) + (w_{PEO}/T_{g\ PEO}) + (w_{eudragit\ E\ PO}/T_{g\ eudragit\ E\ PO}) + (w_{Tween\ 80}/T_{g\ Tween\ 80})$$

The T_g values and weight fractions of the different compounds (after normalisation based on the amorphous fraction of PEG and PEO) are:

$w_{felodipine} = 0.1358$; $T_g = 319.6$ K

$w_{PEG} = 0.0246$; $T_g = 212.2$ K

$w_{PEO} = 0.0250$; $T_g = 223.4$ K

$w_{eudragit\ E\ PO} = 0.6788$; $T_g = 319.9$ K

$w_{Tween\ 80} = 0.1358$; $T_g = 209.2$ K

$T_{g\ mix} = 292.1$ K = 18.9 °C